HEMODYNAMIC FORCES AND ENDOTHELIAL MECHANOBIOLOGY IN VASCULAR DISEASES

EDITED BY: Chih-Yu Yang, Der-Cherng Tarng, Yan-Ting Shiu and Katherine Yanhang Zhang

PUBLISHED IN: Frontiers in Bioengineering and Biotechnology

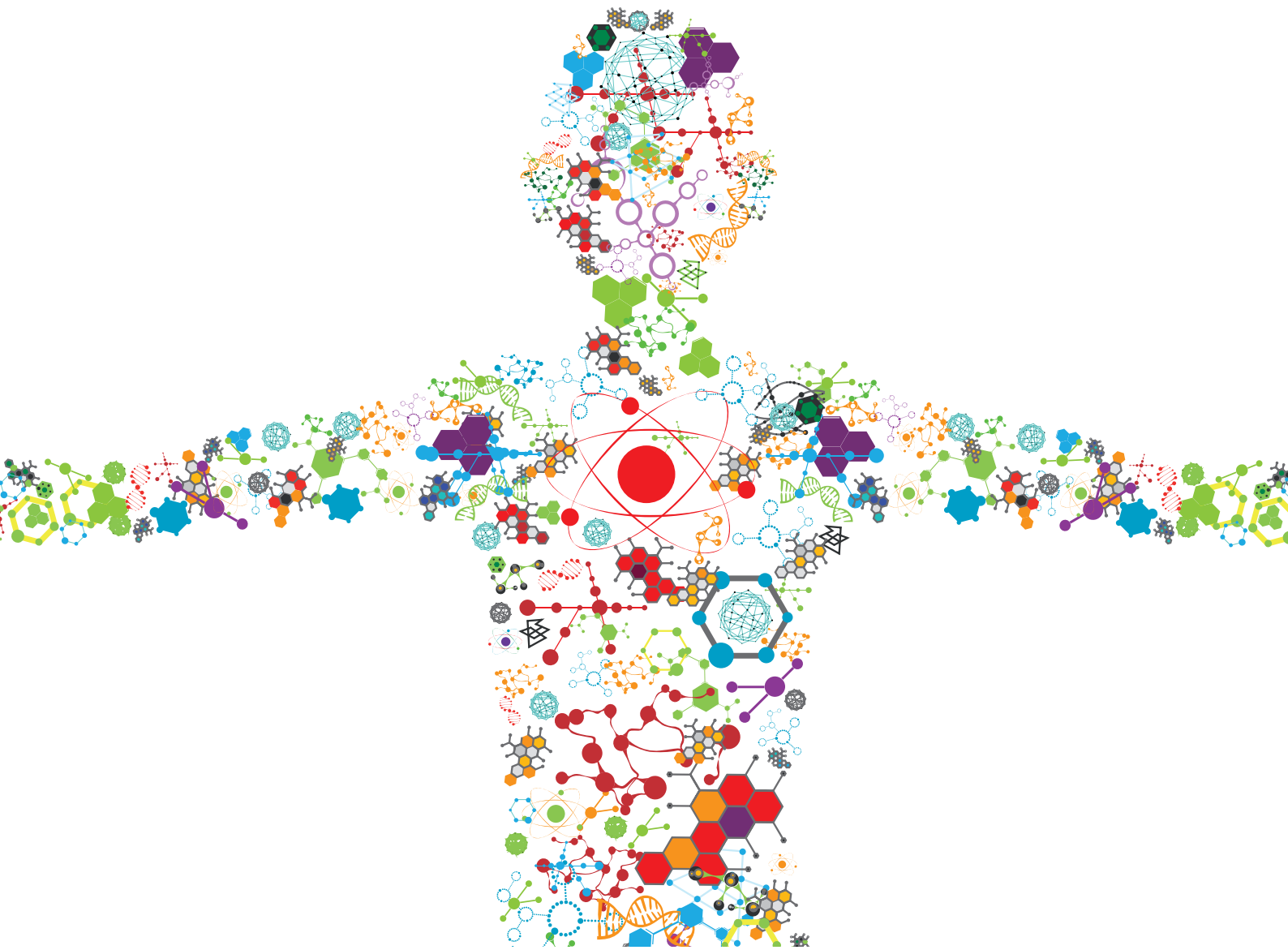

frontiers Research Topics

frontiers

ISSN 1664-8714
ISBN 978-2-88976-851-6
DOI 10.3389/978-2-88976-851-6

About Frontiers

Frontiers is more than just an open-access publisher of scholarly articles: it is a pioneering approach to the world of academia, radically improving the way scholarly research is managed. The grand vision of Frontiers is a world where all people have an equal opportunity to seek, share and generate knowledge. Frontiers provides immediate and permanent online open access to all its publications, but this alone is not enough to realize our grand goals.

Frontiers Journal Series

The Frontiers Journal Series is a multi-tier and interdisciplinary set of open-access, online journals, promising a paradigm shift from the current review, selection and dissemination processes in academic publishing. All Frontiers journals are driven by researchers for researchers; therefore, they constitute a service to the scholarly community. At the same time, the Frontiers Journal Series operates on a revolutionary invention, the tiered publishing system, initially addressing specific communities of scholars, and gradually climbing up to broader public understanding, thus serving the interests of the lay society, too.

Dedication to Quality

Each Frontiers article is a landmark of the highest quality, thanks to genuinely collaborative interactions between authors and review editors, who include some of the world's best academicians. Research must be certified by peers before entering a stream of knowledge that may eventually reach the public - and shape society; therefore, Frontiers only applies the most rigorous and unbiased reviews.
Frontiers revolutionizes research publishing by freely delivering the most outstanding research, evaluated with no bias from both the academic and social point of view. By applying the most advanced information technologies, Frontiers is catapulting scholarly publishing into a new generation.

What are Frontiers Research Topics?

Frontiers Research Topics are very popular trademarks of the Frontiers Journals Series: they are collections of at least ten articles, all centered on a particular subject. With their unique mix of varied contributions from Original Research to Review Articles, Frontiers Research Topics unify the most influential researchers, the latest key findings and historical advances in a hot research area! Find out more on how to host your own Frontiers Research Topic or contribute to one as an author by contacting the Frontiers Editorial Office: frontiersin.org/about/contact

HEMODYNAMIC FORCES AND ENDOTHELIAL MECHANOBIOLOGY IN VASCULAR DISEASES

Topic Editors:
Chih-Yu Yang, Division of Nephrology, Department of Medicine, Taipei Veterans General Hospital, Taiwan
Der-Cherng Tarng, Taipei Veterans General Hospital, Taiwan
Yan-Ting Shiu, The University of Utah Salt, United States
Katherine Yanhang Zhang, Boston University, United States

Citation: Yang, C.-Y., Tarng, D.-C., Shiu, Y.-T., Zhang, K. Y., eds. (2022). Hemodynamic Forces and Endothelial Mechanobiology in Vascular Diseases. Lausanne: Frontiers Media SA. doi: 10.3389/978-2-88976-851-6

Table of Contents

frontiers in Bioengineering and Biotechnology

ORIGINAL RESEARCH
published: 07 December 2021
doi: 10.3389/fbioe.2021.774954

In-vitro and *In-Vivo* Assessment of 4D Flow MRI Reynolds Stress Mapping for Pulsatile Blood Flow

Hojin Ha[1], Hyung Kyu Huh[2], Kyung Jin Park[3,4], Petter Dyverfeldt[5,6], Tino Ebbers[5,6], Dae-Hee Kim[7†] and Dong Hyun Yang[4†]*

[1]Department of Mechanical and Biomedical Engineering, Kangwon National University, Chuncheon, South Korea, [2]Daegu-Gyeongbuk Medical Innovation Foundation, Medical Device Development Center, Daegu, South Korea, [3]Department of Electrical and Electronic Engineering, Yonsei Univeristy, Seoul, South Korea, [4]Department of Radiology, Asan Medical Center, University of Ulsan College of Medicine, Seoul, South Korea, [5]Department of Health, Medicine and Caring Science, Linköping University, Linköping, Sweden, [6]Center for Medical Image Science and Visualization (CMIV), Linköping University, Linköping, Sweden, [7]Department of Cardiology, Asan Medical Center, University of Ulsan College of Medicine, Seoul, South Korea

OPEN ACCESS

Edited by:
Katherine Yanhang Zhang, Boston University, United States

Reviewed by:
Hui Tang, Hong Kong Polytechnic University, Hong Kong SAR, China
Harvey Ho, The University of Auckland, New Zealand

***Correspondence:**
Dong Hyun Yang
donghyun.yang@gmail.com

†These authors have contributed equally to this work and share last authorship

Specialty section:
This article was submitted to Biomechanics, a section of the journal Frontiers in Bioengineering and Biotechnology

Received: *13 September 2021*
Accepted: *16 November 2021*
Published: *07 December 2021*

Citation:
Ha H, Huh HK, Park KJ, Dyverfeldt P, Ebbers T, Kim D-H and Yang DH (2021) In-vitro *and* In-Vivo *Assessment of 4D Flow MRI Reynolds Stress Mapping for Pulsatile Blood Flow. Front. Bioeng. Biotechnol. 9:774954. doi: 10.3389/fbioe.2021.774954*

Imaging hemodynamics play an important role in the diagnosis of abnormal blood flow due to vascular and valvular diseases as well as in monitoring the recovery of normal blood flow after surgical or interventional treatment. Recently, characterization of turbulent blood flow using 4D flow magnetic resonance imaging (MRI) has been demonstrated by utilizing the changes in signal magnitude depending on intravoxel spin distribution. The imaging sequence was extended with a six-directional icosahedral (ICOSA6) flow-encoding to characterize all elements of the Reynolds stress tensor (RST) in turbulent blood flow. In the present study, we aimed to demonstrate the feasibility of full RST analysis using ICOSA6 4D flow MRI under physiological conditions. First, the turbulence analysis was performed through *in vitro* experiments with a physiological pulsatile flow condition. Second, a total of 12 normal subjects and one patient with severe aortic stenosis were analyzed using the same sequence. The *in-vitro* study showed that total turbulent kinetic energy (TKE) was less affected by the signal-to-noise ratio (SNR), however, maximum principal turbulence shear stress (MPTSS) and total turbulence production (TP) had a noise-induced bias. Smaller degree of the bias was observed for TP compared to MPTSS. *In-vivo* study showed that the subject-variability on turbulence quantification was relatively low for the consistent scan protocol. The *in vivo* demonstration of the stenosis patient showed that the turbulence analysis could clearly distinguish the difference in all turbulence parameters as they were at least an order of magnitude larger than those from the normal subjects.

Keywords: magnetic resonace imaging, turbulence measurement, turbulent kinetic energy, turbulence production, hemodynamics

INTRODUCTION

Imaging hemodynamics plays an important role in the diagnosis of abnormal blood flow due to vascular and valvular diseases and monitoring the recovery of normal blood flow after surgical or interventional treatment (Ragosta, 2017; Members et al., 2021). Non-invasive measurement of hemodynamic parameters, such as velocity, pressure loss, and perfusion, has been an important marker for the management and therapy of patients with vascular diseases (Ragosta, 2017; Members et al., 2021).

While echocardiography is still a dominant imaging tool for assessing hemodynamics in clinics, volume acquisition of phase-contrast magnetic resonance imaging, also termed 4D flow MRI, is an emerging technique to characterize multi-dimensional features of hemodynamics (Caruthers et al., 2003; Falahatpisheh et al., 2016; Donati et al., 2017). 4D flow MRI quantifies not only the velocity and flow rate, but also provides various dynamic and kinematic properties of the blood flow, such as wall shear stress (WSS) (Barker et al., 2012; Bissell et al., 2013), turbulent kinetic energy (TKE) (Dyverfeldt et al., 2008; Dyverfeldt et al., 2009a; Dyverfeldt et al., 2013), vorticity (Kim et al., 2015; von Spiczak et al., 2015), pressure gradient (Ebbers et al., 2001; Krittian et al., 2012; Donati et al., 2015), and pulse wave velocity (PWV) (Markl et al., 2010; Markl et al., 2012). In addition, numerous applications of 4D flow MRI for different cardiac and vascular diseases have been introduced, and its clinical implications beyond conventional echocardiography or other diagnostic tools have been successfully demonstrated (Stankovic et al., 2014; Ha et al., 2016d; Soulat et al., 2020; Rizk, 2021).

Characterization of turbulent blood flow in the circulation system has received attention from researchers as it provides additional insights into the extent of spatiotemporal velocity fluctuation and the corresponding stress and energy. The development of turbulent flow dissipates kinetic energy into internal energy by viscous shear stress, which elevates the energy and pressure loss accordingly (Pope, 2001). The elevated viscous shear stress due to the stochastic velocity fluctuation also increases damage to the blood components, promoting hemolysis and thrombosis (Mustard et al., 1962; Smith et al., 1972; Sallam and Hwang, 1983; Lu et al., 2001; Yen et al., 2014). As the mechanical stimuli of turbulent flow are detected and transduced into endothelial cells, the pathophysiology of turbulence on the progression of atherosclerosis and vascular remodeling has also been investigated (Davies et al., 1986; Davies, 1989; Prado et al., 2006).

Although turbulence measurement using medical instruments is still challenging, there has been continuing research on turbulence quantification for developing novel hemodynamic markers. Previously, a catheter-based hot-film anemometer was used to quantify the turbulence level in the aortic flow. The turbulent intensity, frequency, and energy density of the normal and stenotic flows were, thus, successfully analyzed (Stein and Sabbah, 1976; Yamaguchi et al., 1983; Hanai et al., 1991). Since the catheter-based method is currently limited due to its invasiveness, turbulence characterization using non-invasive 4D flow MRI has been widely carried out (Dyverfeldt et al., 2006; Dyverfeldt et al., 2008; Dyverfeldt et al., 2009a; Dyverfeldt et al., 2013).

Conventional velocity measurement from the phase image of 4D flow MRI acquisition does not include turbulent flow features. The MRI sequence fills k-space data from multiple cardiac cycles. The reconstructed velocity field inherently is an ensemble average of many repeated signal acquisitions. As the reconstruction of the MRI signal using a discrete inverse Fourier transform gives the representative value of the whole spin signals within the voxel, the voxel data are also spatially averaged (Brown et al., 2014).

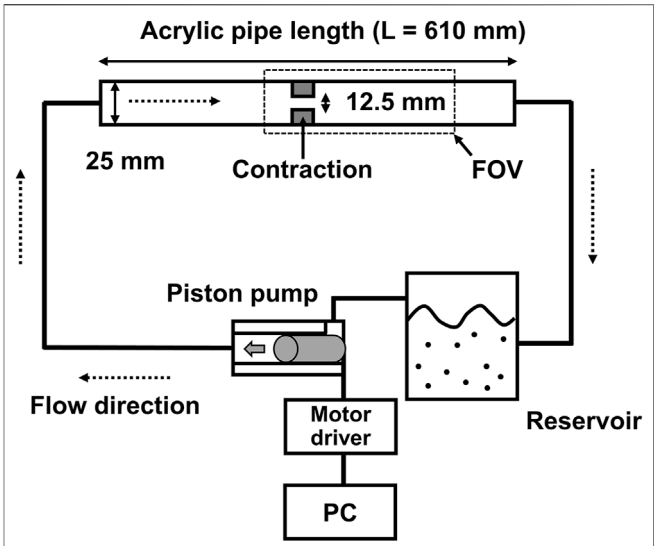

FIGURE 1 | A schematic for *in-vitro* experiments.

Recently, the application of 4D flow MRI for turbulence estimation has been widely demonstrated by utilizing the changes in MRI signal magnitude depending on intravoxel spin distribution (Dyverfeldt et al., 2006; Dyverfeldt et al., 2008; Dyverfeldt et al., 2009a; Dyverfeldt et al., 2013). Previously, TKE, which is the trace of the Reynolds stress tensor (RST), was estimated using the conventional 4D flow MRI sequence for the non-invasive measurement of turbulence in the aortic blood flow (Dyverfeldt et al., 2008). This 4D flow MRI sequence was further extended with a six-directional icosahedral (ICOSA6) flow-encoding scheme to measure all elements of RST, rather than only three diagonal elements, in turbulent flows (Ha et al., 2016e; Ha et al., 2017b; Haraldsson et al., 2018; Ha et al., 2019). Recently, it was found that multi-point flow encoding with a highly under-sampled acquisition successfully quantified the turbulence within ten minutes of scanning (Walheim et al., 2019).

Although preliminary studies on the quantification of full RST using extended 4D flow MRI have demonstrated its potential in medicine, the practical feasibility of turbulence analysis under physiological conditions has rarely been demonstrated. Most *in vitro* demonstrations have used the steady flow condition to optimize the experimental environments, such as signal-to-noise ratio (SNR) and scan time. A previous study demonstrating multi-point measurement for full RST analysis in two normal subjects and patients with valvular diseases has been the only *in vivo* study performed till date (Walheim et al., 2019). Therefore, questions still remain to be answered, for example; whether the turbulence analysis provides robust results and what happens if parameter dependency arises in cases for highly pulsatile flows, particularly for *in vivo* scan conditions.

This study aimed to investigate the performance of full RST analysis using ICOSA6 4D flow MRI under physiological conditions. First, we confirmed the feasibility of the turbulence analysis at different velocity encoding (Venc) conditions using

in vitro experiments with a pulsatile flow condition. Second, a total of 12 normal subjects and one patient with aortic stenosis were scanned with the same sequence. The extent of the turbulence parameters from *in vivo* measurements was analyzed accordingly.

MATERIALS AND METHODS

In-vitro Experimental Setup

In vitro measurements of 4D flow MRI were performed using an acrylic flow phantom and a cardiovascular-mimicking pulsatile flow pump (**Figure 1**). The stenotic phantom had a 50% reduction in length, which corresponds to a 75% reduction in area with a rectangular cross-sectional shape. The upstream and downstream diameters, without stenosis, were 25 mm. To minimize the entrance effect, 0.3 m of the straight inlet upstream of the stenosis was used to minimize the entrance effect. In addition, the same length of the outlet part was used downstream of the stenosis. The working fluids were a mixture of 60% water and 40% glycerol by mass. The density was 1,053.8 kg/m^3, which corresponded to a dynamic viscosity of 3.72×10^{-3} kg/m s. The working fluid was circulated through the flow phantom with a physiological pulsatile waveform using an in-house cardiovascular pulse duplication pump (Kim et al., 2020). The in-house pulsatile pump uses a programmable piston pump to replicate human aortic blood flow waveforms at 60 beats per minute (bpm). The corresponding Womersley number $\alpha = D/2\sqrt{\rho 2\pi f/\mu}$ in the pulsatile flow was 16.7, where D is the diameter, ρ is the density, μ is the dynamic viscosity, and f is the frequency. The mean and maximum flow rates of the pulsatile flow were 3.95 L/min and 13.1 L/min, respectively. The corresponding peak Reynolds number, $\mathrm{Re} = \rho uD/\mu = \rho QD/\mu A$, at the inlet and stenosis regions were 2,735 and 5,471, respectively, where Q is the flow rate and A is the area (**Supplementary Figure S1**). The temperature of the working fluid was maintained at 20°C during the experiment to maintain the fluid properties. A 30 ml volume of MRI contrast agent (0.5 mmol/kg, gadofosveset trisodium, VasovistVR, Bayer Schering Pharma AG, Berlin, Germany) was mixed to working fluid (40 L) for better SNR during *in-vitro* measurement.

Recruitment of Normal Subjects and Patient for In-Vivo Study

Twelve healthy volunteers and one patient with severe aortic stenosis were prospectively enrolled in this study. This study was approved by the Institutional Review Board of the Asan Medical Center (approval number: 2020-1698, Seoul, Korea). Written informed consent was obtained from all the participants. Normal subjects were confirmed to have no severe cardiovascular disease from the cardiology department before they were scanned using 4D flow MRI. One patient with severe aortic stenosis was registered for comparison with normal subjects. Echocardiography showed that the patient had a peak velocity of 4.7 m/s, which corresponds to the mean and peak pressure gradients of 53 and 89 mmHg, respectively. A demographic summary of the *in vivo* subjects is summarized in **Table 1**.

4D Flow MRI Measurement

The 4D flow MRI measurements for the *in vitro* experiments were as follows: A commercial 1.5T MRI scanner (1.5T Philips Achieva, Philips Medical Systems, Best, Netherlands) with a 32-channel torso coil performed the ICOSA6 sequence, which was modified to employ icosahedral flow encoding (six-directional) with a single flow-compensated reference encoding. Various velocity-encoding (Venc) parameter values (100–350 cm/s) were selected for the turbulence analysis, and 350 cm/s was used for velocity measurement. The echo time, temporal resolution, flip angle and matrix size were 2.5 ms, 3.9 ms, 10° and 128 × 128 × 25 (2.0 mm isotropic voxel), respectively. To obtain the shortest TE, a partial echo factor was set to 0.725. The total scan time for the *in vitro* study was approximately 30 min per case.

The 4D flow MRI parameters for the *in vivo* study, other than those described below, were the same as those for the *in vitro* experiments. A dStream Flex coil (Philips Medical Systems, Best, Netherlands) was used with various Venc parameters ranging from 80 to 100 cm/s for the normal subjects and 300 cm/s for the stenosis patient for turbulence quantification. TE and temporal resolution were slightly adjusted according to the scan condition, ranging from 1.9 to 2.7 ms and 3.8–4.4 ms, respectively. The matrix size range was 112–128 × 112–128 × 23–30 voxels (2.5–3.0 mm isotropic voxel). The scan time for the *in vivo* study was approximately 23 min.

Post-processing of 4D Flow MRI Data

Raw data were exported using Pack'n Go and reconstructed offline using ReconFrame (ReconFrame, Gyrotool LLC, Zurich, Switzerland). A custom MATLAB (The MathWorks, Inc., Natick, MA) code was used to solve the linear equations to recover the velocity vector and RST, as described in previous works (Ha et al., 2017a; Ha et al., 2019). To correct the background phase errors, a no-flow velocity field (flow off) was subtracted from the *in vitro* data (Ha et al., 2019) and weighted 2nd order fitting to static tissue was used for the *in vivo* data (Ebbers et al., 2008).

Magnitude and velocity images were imported into the ITK-SNAP software (v.3.8.0, University of Utah, Salt Lake City, UT) to segment the aortic flow region. The aorta was subdivided into the ascending aorta (AA), descending aorta (DA), and aortic arch (arch) by the brachiocephalic artery and the left subclavian artery (**Figure 2**). Aortic branches were excluded from the analysis.

4D Flow MRI Turbulence Quantification

The intravoxel velocity variance (IVVV) of the turbulent flow in I direction (σ_i^2) was calculated by dividing the velocity-encoded signal magnitude $S_i(k_v)$ from the reference signal magnitude S (0) and as **Eq. 1** (Dyverfeldt et al., 2009b):

TABLE 1 | Demographic characteristics of the *in-vivo* subjects.

	Case	Age (years)	Sex (F/M)	Height (cm)	Weight (kg)	BSA (m^2)	LV EDV (mL)	LV ESV (mL)	LVEF (%)	LA diameter (mm)	Aorta (mm)
Normal	1	51	M	169.8	60.6	1.7	76	26	66	31	39
	2	59	F	161.3	61.8	1.65	70	31	56	36	27
	3	62	F	151.7	55.7	1.51	74	25	66	31	21
	4	31	M	175.7	74.7	1.9	113	41	64	29	33
	5	52	M	175.1	70.5	1.85	169	65	62	36	31
	6	67	F	151.6	61.2	1.57	102	34	67	35	30
	7	36	F	165.8	51.4	1.56	68	22	68	28	29
	8	51	F	154.4	45.6	1.41	76	29	62	26	27
	9	72	M	170.2	67.2	1.78	106	42	60	40	33
	10	56	F	160.0	60.0	1.62	102	35	66	36	30
	11	49	M	177.1	84.2	2.02	133	48	64	39	39
	12	76	F	143.9	43.5	1.31	68	27	60	28	32
Patient	1	64	M	169.4	74.2	1.85	130	46	65	37	37

BSA, body surface area; LV, left ventricle; EDV, end-diastolic volume; ESV, end-systolic volume; LVEF, left ventricular ejection fraction; LA, left atrium.

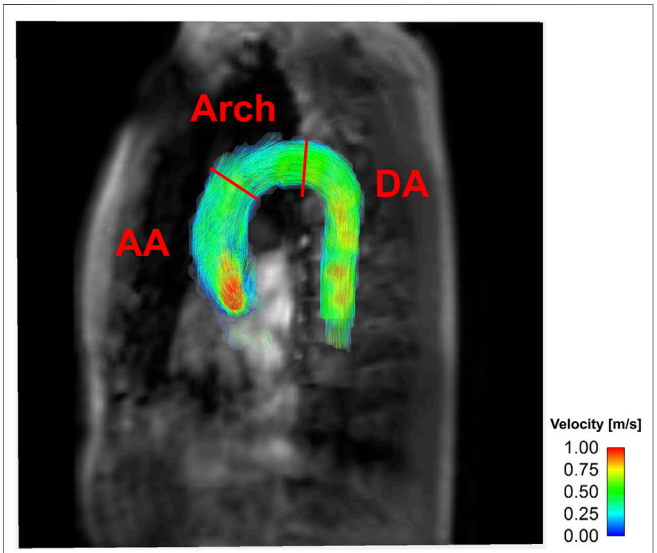

FIGURE 2 | Representative velocity mapping of ICOSA6 4D flow MRI for *in-vivo*.

$$\sigma_i^2 = \overline{u_i' u_i'} = \frac{2}{k_v^2} \ln\left(\frac{|S(0)|}{|S_i(k_v)|}\right), \left(\frac{m^2}{s_2}\right) \quad (1)$$

where u_i' denotes fluctuating velocity component and $\bar{}$ denotes an averaging operation.

Orthogonal components (velocity vectors u, v, and w) and covariance components (Reynolds stress tensor R_{ij}, a six-element symmetric tensor in **Eq. 2**) can be simultaneously calculated by solving linear equations from six non-orthogonal velocity encodings (**Figure 3**) (Haraldsson et al., 2018; Ha et al., 2019).

$$R = -\rho \begin{bmatrix} \overline{u_1' u_1'} & \overline{u_1' u_2'} & \overline{u_1' u_3'} \\ \overline{u_2' u_1'} & \overline{u_2' u_2'} & \overline{u_2' u_3'} \\ \overline{u_3' u_1'} & \overline{u_3' u_2'} & \overline{u_3' u_3'} \end{bmatrix} \quad (2)$$

The turbulent kinetic energy TKE with in the flow can be described from the IVVV of each direction as follows:

$$TKE = \frac{1}{2}\rho \sum_{i=1}^{3} \sigma_i^2 = \frac{1}{2}\rho\left(\overline{u_1' u_1'} + \overline{u_2' u_2'} + \overline{u_3' u_3'}\right), \left(\frac{J}{m^3}\right) \quad (3)$$

where ρ is the fluid density. The voxel-wise integration of TKE provides total TKE with units of J or mJ.

The maximum principal turbulent shear stress (MPTSS) was estimated using principal stress analysis. MPTSS can be calculated as follows:

$$MPTSS = \frac{1}{2}(\delta_1 - \delta_3), \text{(Pa)} \quad (4)$$

where the δ is the eigenvalues of RST $(\delta_1 > \delta_2 > \delta_3)$.

Turbulent production (TP) can directly be computed as follows (Ha et al., 2017a; Ha et al., 2019):

$$TP = R_{ij} S_{ij}, \left(\frac{W}{m^3}\right) \quad (5)$$

Here, S_{ij} denotes the strain rate tensor of the velocity field. Voxel-wise integration of TP and multiplying the density provides a total TP with a unit of W or mW.

The turbulence parameters near the luminal surface were estimated separately to estimate the impact of turbulence on the vessel wall. Near-wall TKE (nwTKE), near-wall MPTSS (nwMPTSS), and near-wall TP (nwTP) were calculated as previously described (Ziegler et al., 2017). In short, for near-wall estimation, the number of turbulence parameters near the luminal surface was obtained using a convolution kernel with a 3 × 3 mean filter.

Statistics

A Shapiro–Wilk test was performed to check the normality of the data. The parametric data were described as mean ± standard deviation, while non-parametric data were described as median (1st quartile, 3rd quartile) throughout the manuscript.

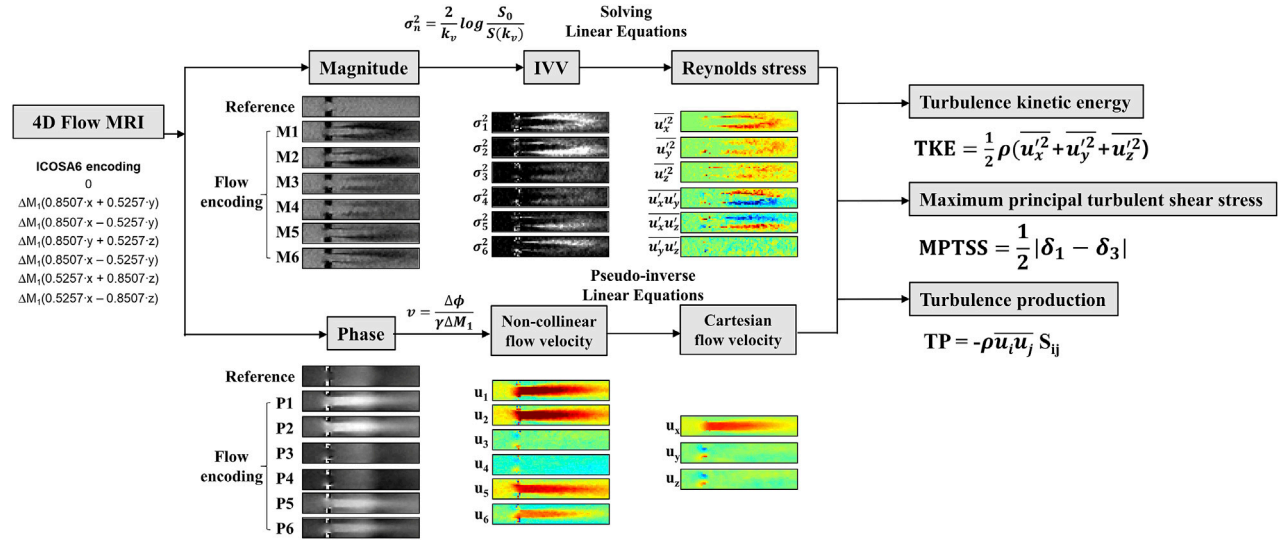

FIGURE 3 | Illustration of Reynolds stress measurement and turbulence parameter analysis.

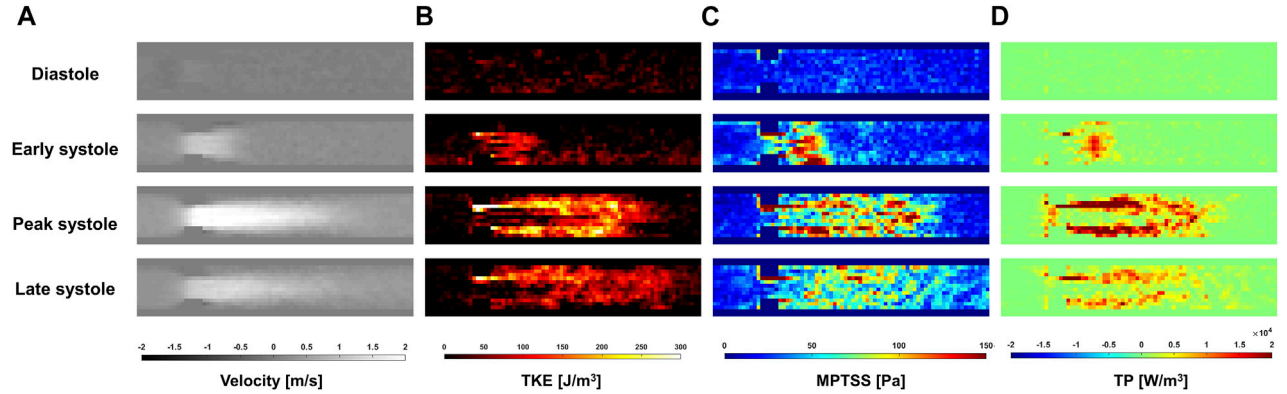

FIGURE 4 | Temporal variation of **(A)** Velocity, **(B)** turbulent kinetic energy (TKE), **(C)** maximum principal turbulent shear stress (MPTSS), **(D)** turbulence production (TP) through the stenosis at Venc of 200 cm/s.

RESULTS

In-vitro Turbulence Quantification Under Pulsatile Flow

The ICOSA6 4D Flow MRI successfully visualized the pulsatile flow waveform that generated a strong jet flow through the stenosis (**Figure 4**). These turbulence parameters exhibited the highest values around the boundary layer of the jet flow. Turbulence parameters (TKE, MPTSS, and TP) started to increase during the early systole phase and reached a maximum at the peak systole phase of the cycle (**Figures 4**, **5**). The mean and peak velocity during the pulsatile cycle were 0.83 m/s and 2.26 m/s and corresponding flow rates were 3.95 L/min and 13.1 L/min, respectively.

The quality of turbulence quantification was dependent on the Venc parameter, which determines the SNR of the measurement (**Figures 5**, **6**). The effect of the Venc-dependent SNR on turbulence quantification varied with the turbulence parameters. The measurement with a higher Venc resulted in a higher noise level in TKE (**Figures 5**, **6A**). The maximum difference due to Venc was 26.9 and 10.3% for the mean and maximum total TKE, respectively (**Table 2**). In contrast, a higher Venc resulted in a noise-induced bias in the MPTSS and TP (**Figures 6B,C**). Mean and maximum MPTSS at Venc = 350 cm/s were 5.1 and 3.0 folds larger than those at Venc = 100 cm/s. Mean and maximum total TP at Venc = 350 cm/s were 2.4 and 1.4 folds larger than those at Venc = 100 cm/s. The near-wall turbulence parameters exhibited similar behaviors (**Table 2**).

In-vivo Turbulence Analysis

Twelve normal volunteers were scanned with the ICOSA6 sequence to perform flow and turbulence quantification. The

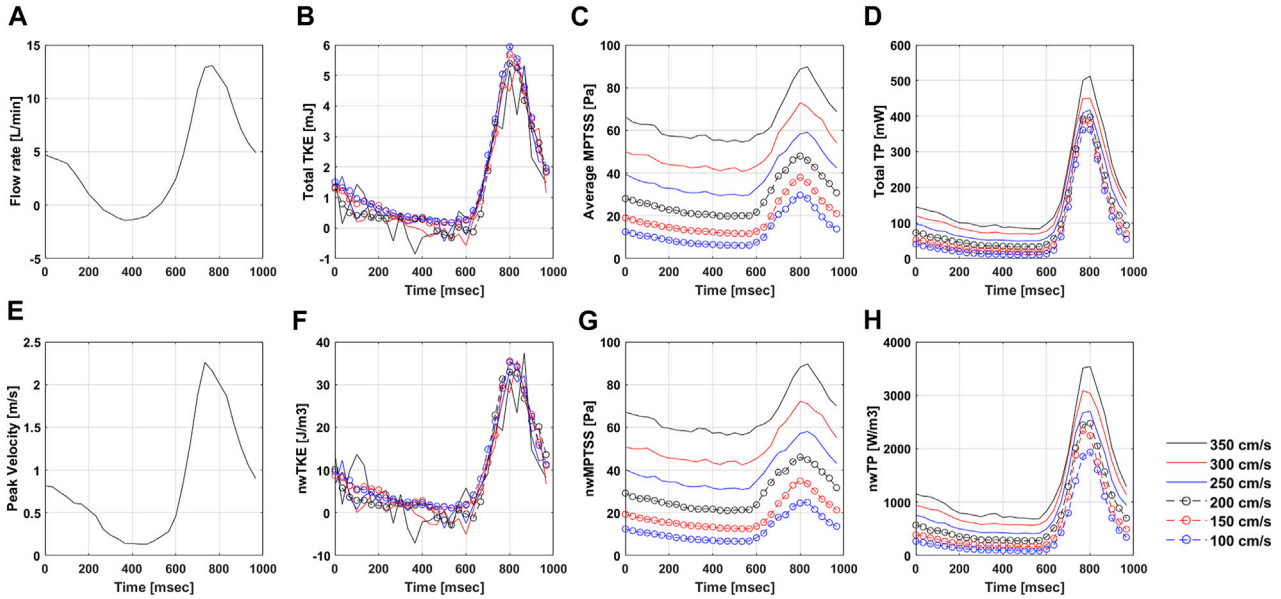

FIGURE 5 | Temporal variation of **(A)** Flow rate, **(B)** total TKE, **(C)** Average MPTSS, **(D)** total TP, **(E)** Peak velocity, **(F)** nwTKE, **(G)** nwMPTSS, and **(H)** nwTP at different Venc parameters. Note that the flow rate and peak velocity are only measured at Venc of 350 cm/s.

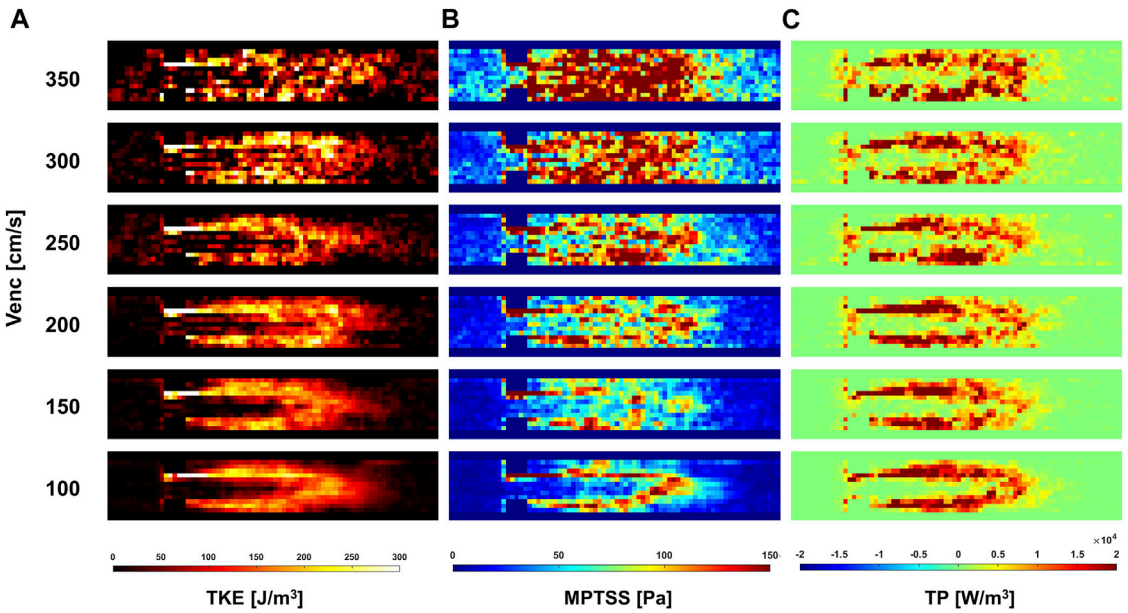

FIGURE 6 | Effect of Venc on **(A)** TKE, **(B)** MPTSS, **(C)** TP at peak systole.

blood flow through the aortic valve developed a high-velocity jet flow in the ascending aorta (**Figure 7**). TKE, MPTSS, and TP mapping at the peak systole phase clearly visualized the local development of turbulence with a reasonable SNR (**Supplementary Figures S2–S5**).

Most of the hemodynamic parameters of the normal subjects were within the confined range (**Figure 8**). The peak velocities of the normal subjects were 1.2 m/s (1.2 m/s, 1.3 m/s). Data are shown as median (1st quartile, 3rd quartile). The total TKE, MPTSS and TP of the normal subjects at the peak systole were 4.6 mJ (3.1 mJ, 5.9 mJ), 71.3 Pa (58.7 Pa, 79.8 Pa), 365.7 mW (263.8 mW, 425.0 mW), respectively. Among them, most of the turbulence was focused on the ascending aorta.

The turbulence parameters at the diastolic phase were significantly smaller than those at the peak systolic phase. Total TKE and total TP were at least an order of magnitude

TABLE 2 | Summary of turbulence parameters from the *in-vitro* experiments.

Venc (cm/s)	Total TKE (mJ)		Average MPTSS (Pa)		Total TP (mW)		nwTKE (J/m^3)		nwMPTSS (Pa)		nwTP (kW/m^3)	
	Mean	Max	Mean	Max	Mean	Max	Mean	Max	Mean	Max	Mean	Max
350	1.2	5.3	64.7	89.8	177.6	512.5	7.9	37.4	66.1	89.7	1.4	3.5
300	1.2	5.4	50.5	72.9	154.8	450.0	7.5	35.6	51.7	72.2	1.2	3.1
250	1.4	5.4	38.7	59.1	128.7	417.7	8.2	33.3	39.7	58.1	0.9	2.7
200	1.3	5.4	28.4	48.0	106.9	397.6	8.4	32.9	29.2	46.1	0.8	2.5
150	1.5	5.7	19.1	38.0	89.5	387.2	9.5	35.5	19.1	34.9	0.6	2.3
100	1.6	5.9	12.8	29.7	73.2	361.7	9.9	35.2	12.2	24.9	0.5	1.9

TKE, turbulent kinetic energy; MPTSS, maximum principal turbulence shear stress; TP, turbulence production; nw, near-wall.

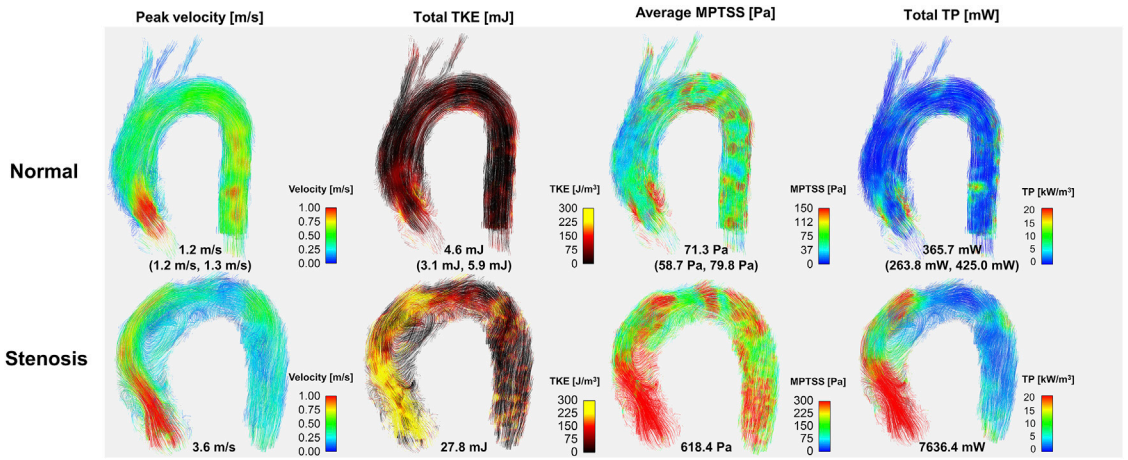

FIGURE 7 | Comparison hemodynamics in normal subjects and patient with severe aortic stenosis. Note that representative normal subject (case #1) was used for color mapping. Values for the normal subject are median (1st quartile, 3rd quartile) of the data. Velocity, TKE, MPTSS and TP for all normal subjects are also shown in the **Supplementary Figures S2–S5**.

smaller than those at the peak systolic phase. The average MPTSS was approximately one-third of that at the peak systole phase (**Figure 8** and **Table 3**). The total TKE, MPTSS and total TP of the normal subjects at the diastolic phase were −0.2 mJ (−0.3 mJ, −0.1 mJ), 19.3 Pa (16.1 Pa, 22.1 Pa), 8.6 mW (6.6 mW, 12.3 mW), respectively. While the total TKE values at the diastolic phase were almost negligible regardless of the vascular region, almost half of the MPTSS and total TP developed at the ascending aorta.

The near-wall turbulence parameters were the largest in the ascending aorta (**Table3** and **Supplementary Figure S6**). The nwTKE, nwMPTSS and nwTP of the ascending aorta at the peak systole were 69.0 J/m^3 (47.7 J/m^3, 78.2 J/m^3), 80.4 Pa (72.2 Pa, 94.4 Pa), 5,634.0 W/m^3 (4,175.9 W/m^3, 6,771.9 W/m^3), respectively, while those of the whole aorta were 44.1 J/m^3 (34.8 J/m^3, 57.4 J/m^3), 72.1 Pa (61.2 Pa, 80.9 Pa), 3,620.8 W/m^3 (3,160.1 W/m^3, 4,627.6 W/m^3), respectively. Diastolic nwTKE and nwTP were at least an order of magnitude smaller than those at the peak systolic phase. The nwMPTSS was approximately one-third of that at the peak systole phase (**Table 3**).

The *in vivo* demonstration of ICOSA6 turbulence quantification for a stenosis patient with an aortic velocity of 3.6 m/s showed that all turbulence parameters were at least an order of magnitude larger (**Figure 7**). The total TKE, MPTSS, and total TP of the patient at the peak systole were 27.8, 618.4 Pa and 7,636.4 mW, respectively.

DISCUSSION

This study focuses on demonstrating the performance of full RST analysis using ICOSA6 4D flow MRI under physiological conditions. The key results of the study are as follows:

1) Turbulence quantification from *in vitro* pulsatile flow experiments can be affected by the SNR of the measurement. The effect of the Venc-dependent SNR on turbulence quantification varied with the turbulence parameters. While total TKE was less affected, MPTSS and TP had a noise-induced bias.
2) An *in vivo* study of normal subjects showed that most of the hemodynamic parameters were within the confined range. The impact of the subject-variability on turbulence quantification was relatively low for the consistent scan protocol.

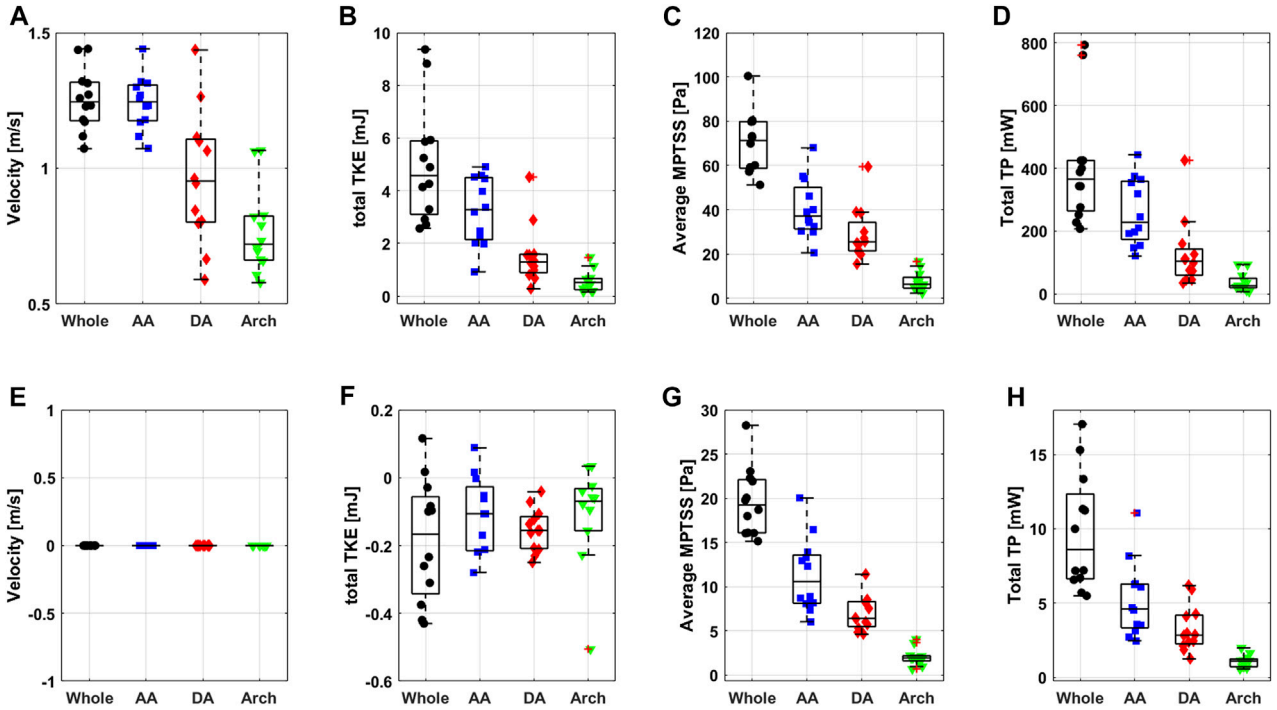

FIGURE 8 | Boxplot of peak systolic **(A)** velocity, **(B)** total TKE, **(C)** average MPTSS, **(D)** total TP and diastolic **(E)** velocity, **(F)** total TKE, **(G)** average MPTSS and **(H)** total TP.

TABLE 3 | Summary of turbulence parameters from the *in-vivo* normal subjects.

		Total TKE (mJ)		
	Whole	AA	DA	Arch
Peak Systole	4.6 (3.1, 5.9)	3.3 (2.1, 4.5)	1.3 (0.9, 1.6)	0.5 (0.2, 0.7)
Diastole	−0.2 (−0.3, −0.1)	−0.1 (−0.2, 0.0)	−0.2 (−0.2, −0.1)	−0.1 (−0.2, 0.0)
		Average MPTSS (Pa)		
	Whole	AA	DA	Arch
Peak Systole	71.3 (58.7, 79.8)	37.1 (31.3, 50.1)	25.4 (21.4, 34.2)	6.4 (4.6, 9.4)
Diastole	19.3 (16.1, 22.1)	10.6 (8.1, 13.6)	6.4 (5.5, 8.3)	1.9 (1.6, 2.2)
		total TP (mW)		
	Whole	AA	DA	Arch
Peak Systole	365.7 (263.8, 425.0)	227.6 (173.2, 358.9)	104.4 (19.7, 49.7)	25.9 (19.7, 49.7)
Diastole	8.6 (6.6, 12.3)	4.6 (3.3, 6.3)	2.8 (2.3, 4.2)	1.1 (0.7, 1.2)
		nwTKE (J/m^3)		
	Whole	AA	DA	Arch
Peak Systole	44.1 (34.8, 57.4)	69.0 (47.7, 78.2)	36.1 (28.1, 47.1)	29.2 (24.3, 40.3)
Diastole	−2.0 (−4.0, −1.4)	−2.8 (−4.7, −0.7)	−4.3 (−6.1, −2.6)	−4.9 (−13.9, −2.8)
		nwMPTSS (Pa)		
	Whole	AA	DA	Arch
Peak Systole	72.1 (61.2, 80.9)	80.4 (72.2, 94.4)	73.0 (64.8, 88.1)	51.2 (38.4, 69.2)
Diastole	19.2 (16.1, 22.0)	20.1 (18.0, 23.8)	16.4 (14.6, 18.8)	15.0 (13.7, 18.2)

(Continued on following page)

TABLE 3 | (*Continued*) Summary of turbulence parameters from the *in-vivo* normal subjects.

	Total TKE (mJ)			
	nwTP (W/m^3)			
	Whole	AA	DA	Arch
Peak Systole	3,620.8 (3,160.1, 4,627.6)	5,634.0 (4,175.9, 6,771.9)	3,173.0 (2092.3, 3,788.3)	2,024.7 (1370.2, 3,128.6)
Diastole	93.4 (80.6, 127.0)	102.9 (85.6, 138.6)	85.7 (63.8, 103.7)	76.6 (61.6, 85.1)

TKE, turbulent kinetic energy; MPTSS, maximum principal turbulence shear stress; TP, turbulence production; nw, near-wall; AA, ascending aorta; DA, descending aorta. Data are shown as median (1st quartile, 3rd quartile).

3) The *in vivo* demonstration of the stenosis patient showed that the turbulence analysis could clearly distinguish the differences of all turbulence parameters as they were at least an order of magnitude larger than those from the normal subjects. The discrepancy between the normal and patient was much larger than the effect of SNR.

Validation of novel hemodynamic parameters under various conditions is crucial for the transition of a new biomarker from research to clinical routine. Since the TKE estimation using 4D flow MRI was demonstrated at the *in vitro* stenotic flow phantom (Dyverfeldt et al., 2006), various subsequent experiments confirmed the feasibility of the method under various measurement conditions (Dyverfeldt et al., 2006; Ha et al., 2016a; Petersson et al., 2016; Ziegler et al., 2017). Based on the results of *in vitro* experiments, TKE has been widely investigated as a clinical biomarker (Dyverfeldt et al., 2013; Zajac et al., 2015; Fredriksson et al., 2018; Ha et al., 2018). In contrast to TKE, other turbulence parameters from the RST have not yet been investigated. Since full RST measurements were demonstrated (Haraldsson et al., 2018), the following studies have attempted to study the accuracy and robustness of the RST measurement under limited steady flow conditions (Ha et al., 2020; Kim et al., 2021). The present study strengthens the feasibility of full RST analysis by adding the results under physiological pulsatile flow conditions. It is noted that the sample size for the *in vivo* normal study was small. We added one patient data set to show that the degree of turbulence in the patient is at least an order of magnitude higher than in the normal subjects. Elevated turbulence level in patients with valvular and vascular disease has also been reported previously (Dyverfeldt et al., 2008; Dyverfeldt et al., 2013). Adding a few more patients would not affect the results of the present study. Successful demonstration of RST analysis for a small group of *in vivo* studies will be an important bridge for upcoming large clinical trials.

The turbulence parameters from the full RST characterize different clinical aspects of turbulent flow. TKE is the kinetic energy associated with eddies in turbulent flow. Physically, TKE is a measure of how much turbulent energy is currently developed due to vascular coactation or valvular stenosis. The MPTSS indicates the extent to which shear stress is developed due to turbulence. Elevation of turbulent shear stress on the vessel wall or blood components can describe the risk of hemolysis (Grigioni et al., 1999). TP indicates how much TKE is produced, which will eventually dissipate. This indicates how much energy is taken from the mean flow to produce turbulence, and how much energy is dissipated into internal energy such as heat (Tennekes and Lumley, 1972). The TP has been investigated to indicate the irreversible pressure loss due to turbulence (Ha et al., 2019). Although conventional 4D flow MRI can also measure TKE, MPTSS and TP, it can only be estimated with full elements of the RST. The ICOSA6 4D flow MRI used in this study provides all turbulence parameters in compensation for three additional flow encodings and corresponding scan times.

The *in vitro* demonstration shows that the effect of the SNR on the turbulence quantification differs between the turbulence parameters. The Venc-dependent SNR adds the Gaussian noise distribution on TKE unless too much turbulence causes the flow-encoded signal magnitude to be less than the noise level (Dyverfeldt et al., 2009b; Ha et al., 2016a). Therefore, the choice of Venc affects the uncertainty of the TKE, but not the accuracy. The TKE results from the present study agree with those of previous studies. Compared to the measurement at the lowest Venc, higher Venc measurements showed larger noise-induced fluctuations (**Figure 5**). In contrast to TKE, MPTSS largely varied with the SNR. MPTSS is estimated from the eigenvalues of the RST, which are the solutions of the characteristic equation (Fung, 1977). The coefficients of the characteristic equation are obtained from the summation and multiplication of the RST elements. Therefore, the Gaussian noise distribution on the elements of the RST does not produce the same noise distribution on the MPTSS. When the MPTSS is expressed with the principal stress, it includes the square root of the principal stress squared. Therefore, a higher noise level increases the MPTSS, as shown in **Figures 5**, **6**. The overestimation of MPTSS was also described in a previous study using Monte Carlo simulation (Walheim et al., 2019). While it was less obvious than MPTSS, TP also showed a Venc-dependent bias. The mean and maximum MPTSS at Venc = 350 cm/s were 5.1 and 3.0 folds larger than those at Venc = 100 cm/s, and the mean and maximum total TP were 2.4 and 1.4 folds larger at the same conditions. Considering that the clinical protocol for turbulence quantification using 4D flow MRI usually uses the same or similar parameters for all cohorts, such large discrepancies due to Venc-dependent SNR changes will only be shown in the worst-case scenario (Dyverfeldt et al., 2008; Dyverfeldt et al., 2013).

The subject-variability including subject-dependent SNR-variability played a minor role in turbulence quantification in the *in vivo* study. Hemodynamic parameters for the normal subjects were relatively similar despite a wide spectrum of age and corresponding height, weight, and cardiovascular indices (**Figure 5** and **Table 1**). This was mostly because consistent scan

parameters were used throughout the *in vivo* study. Venc between 80 cm/s to 100 cm/s and the voxel resolution between 2.5 and 3.0 mm were used for the normal subjects. Despite the *in vitro* experiments on steady flow, a previous study also showed that the turbulence quantification changes less than 11.5% for TKE and 33.9% for TP when the practical range of Venc between 100 cm/s and 200 cm/s was used (Ha et al., 2020). Walheim et al. also analyzed the effect of the SNR on the turbulence parameters (Walheim et al., 2019). Monte-Carlo simulation from the study also showed that SNR played a minor role in TKE and MPTSS compared to the effect of image resolution.

The feasibility of ICOSA6 4D flow MRI for patients with aortic stenosis showed that the turbulence analysis could clearly distinguish the differences in all turbulence parameters. TKE, MPTSS, and TP were at least an order of magnitude larger than those in the normal subjects. It is noteworthy that the optimum choice of Venc for 4D flow MRI turbulence quantification is related to the extent of turbulence in the flow. The use of a very small Venc value may result in excessive turbulence-related signal loss, which can lead to the underestimation of turbulence parameters owing to the Rician noise distribution (Dyverfeldt et al., 2009a). For this reason, usually, a larger Venc for stenotic flow than that for normal aortic flow is used (Dyverfeldt et al., 2013). Therefore, the turbulence parameters for the patient can be overestimated, particularly for the MPTSS and TP. Considering that the *in vitro* study showed that maximum MPTSS and TP at Venc = 350 cm/s were 3.0 folds and 1.4 folds larger than those at Venc = 100 cm/s, the elevation of turbulence parameters in the stenosis patient observed in this study is far beyond the effect of the Venc-dependency effect. However, care should be taken when turbulence parameters from different Venc parameters are to be compared.

It should be noted that turbulence measurement using 4D flow MRI can result in unphysical values, such as negative TKE at some voxels. This phenomenon is mostly due to background noise in the magnitude image. Since, the development of turbulence increases the signal loss in the flow-encoded image, the turbulence level is quantified by determining the signal loss in the flow-encoded image compared to the reference image (Dyverfeldt et al., 2009b). When turbulence-related signal loss is relatively small because the extent of turbulence is negligible or the first moment of bipolar gradient is too small to produce intravoxel dephasing, there are some chances for some voxels of the flow-encoded image have larger intensity than those of the reference image (Ha et al., 2016a). In contrast, the signal loss at the flow-encoded image quantifies the positive IVVV; a larger intensity in the flow-coded image is interpreted as negative IVVV. In general, this noise distribution affects the voxel-wise TKE but has less effect on the total TKE because the noise cancels out during the volumetric integration (Ha et al., 2016b). Despite volumetric integration, some extent of uncertainty may still affect the results, so that total TKE becomes negative when the turbulence is almost negligible (Ha et al., 2016b). To minimize the effect of noise on turbulence quantification, multi-Venc measurements have been used to optimize the results by finding the best possible estimates (Ha et al., 2019). A recent study filtered negative diagonal components of the RST to enforce positive IVVV (Marlevi et al., 2020). Filtering based on the physically realizable states of turbulence was also considered (Andersson et al., 2021).

The increased acquisition time of ICOSA6 4D flow MRI has been an inherent drawback for clinical use. Unlike conventional four-directional encoding, this sequence employs seven flow encodings, which increase the scan time by up to 75%. However, recent developments in various acceleration techniques, including compressed sensing and local low-rank, have been successfully applied to reduce the scan time without sacrificing the critical flow information (Zhang et al., 2015; Ma et al., 2019). In addition, Walheim et al. reported that faster turbulence quantification can be performed within ten minutes using highly under-sampled 5D flow MRI acquisition with locally low-rank image reconstruction (Walheim et al., 2019). We speculate that the scan time of turbulence quantification will become trivial as acceleration techniques are further developed.

It is noted that this study does not include the validation of MRI turbulence measurements against other engineering flow measurements. However, the feasibility and validation of MRI turbulence measurements have been previously demonstrated again laser Doppler anemometer (Dyverfeldt et al., 2006), particle image velocimetry (Knobloch et al., 2014; Ha et al., 2016c), and computational fluid dynamics (Petersson et al., 2016).

One of the limitations of the present study is that the uncertainty level of each measurement has not been presented. This would require multiple measurements of the same flow conditions, which is not feasible for *in-vivo* subjects due to the long scan time. Instead, the present study investigated the same flow conditions at different Venc and SNR. In addition, a level of uncertainty for *in-vivo* measurements has been studied by observing the range of the turbulence parameters in the normal cohort.

Another limitation of the present study is that the sample size for the *in vivo* normal study was small. The current results do not represent the true normal turbulence level. Based on the successful demonstration of turbulence analysis for a small group study, this will trigger upcoming large clinical trials. The atlas of turbulence parameters at different age, sex, and disease groups will be followed in the future.

DATA AVAILABILITY STATEMENT

The original contributions presented in the study are included in the article/**Supplementary Material**, further inquiries can be directed to the corresponding author.

ETHICS STATEMENT

The studies involving human participants were reviewed and approved by This study was approved by the Institutional Review Board of the Asan Medical Center (approval number: 2020-1698, Seoul, Korea). The patients/participants provided their written informed consent to participate in this study.

AUTHOR CONTRIBUTIONS

HH, DK, DY designed the study and discussed the results; HH and KP contributed to the MRI experiments and data analysis; PD and TE contributed to the ICOSA6 MRI sequence and discussed the results; HH drafted the manuscript; all authors reviewed the manuscript.

FUNDING

This research was supported by the Basic Science Research Program through the National Research Foundation of Korea, which is funded by the Ministry of Education (NRF-2018R1D1A1A02043249, NRF-2021R1I1A3040346, NRF-2020R1A2C200384, NRF- 2021R1C1C1003481, NRF-2020R1A4A1019475). This research was also supported by the Basic Science Research Program and Medical Cluster R and D project, through the National Research Foundation of Korea (NRF), funded by the Ministry of Science, ICT and Future Planning (NRF-2020R1A2C2003843, HI19C0760).

SUPPLEMENTARY MATERIAL

The Supplementary Material for this article can be found online at: https://www.frontiersin.org/articles/10.3389/fbioe.2021.774954/full#supplementary-material

REFERENCES

Andersson, M., Karlsson, M., and Mechanobiology, M. I. (2021). Characterization of Anisotropic Turbulence Behavior in Pulsatile Blood Flow. *Biomech. Model. Mechanobiol* 20 (2), 491–506. doi:10.1007/s10237-020-01396-3

Barker, A. J., Markl, M., Bürk, J., Lorenz, R., Bock, J., Bauer, S., et al. (2012). Bicuspid Aortic Valve Is Associated with Altered wall Shear Stress in the Ascending Aorta. *Circ. Cardiovasc. Imaging* 5 (4), 457–466. doi:10.1161/circimaging.112.973370

Bissell, M. M., Hess, A. T., Biasiolli, L., Glaze, S. J., Loudon, M., Pitcher, A., et al. (2013). Aortic Dilation in Bicuspid Aortic Valve Disease. *Circ. Cardiovasc. Imaging* 6 (4), 499–507. doi:10.1161/circimaging.113.000528

Brown, R. W., Cheng, Y.-C. N., Haacke, E. M., Thompson, M. R., and Venkatesan, R. (2014). *Magnetic Resonance Imaging: Physical Principles and Sequence Design*. Hoboken, New Jersey: John Wiley & Sons.

Caruthers, S. D., Lin, S. J., Brown, P., Watkins, M. P., Williams, T. A., Lehr, K. A., et al. (2003). Practical Value of Cardiac Magnetic Resonance Imaging for Clinical Quantification of Aortic Valve Stenosis. *Circulation* 108 (18), 2236–2243. doi:10.1161/01.cir.0000095268.47282.a1

Davies, P. F., Remuzzi, A., Gordon, E. J., Dewey, C. F., and Gimbrone, M. A. (1986). Turbulent Fluid Shear Stress Induces Vascular Endothelial Cell Turnover *In Vitro*. *Proc. Natl. Acad. Sci.* 83 (7), 2114–2117. doi:10.1073/pnas.83.7.2114

Davies, P. (1989). How Do Vascular Endothelial Cells Respond to Flow? *Physiology* 4 (1), 22–25. doi:10.1152/physiologyonline.1989.4.1.22

Donati, F., Myerson, S., Bissell, M. M., Smith, N. P., Neubauer, S., Monaghan, M. J., et al. (2017). Beyond Bernoulli: Improving the Accuracy and Precision of Noninvasive Estimation of Peak Pressure Drops. *Circ. Cardiovasc. Imaging* 10 (1), e005207. doi:10.1161/CIRCIMAGING.116.005207

Donati, F., Figueroa, C. A., Smith, N. P., Lamata, P., and Nordsletten, D. A. (2015). Non-invasive Pressure Difference Estimation from PC-MRI Using the Work-Energy Equation. *Med. Image Anal.* 26 (1), 159–172. doi:10.1016/j.media.2015.08.012

Dyverfeldt, P., Gårdhagen, R., Sigfridsson, A., Karlsson, M., and Ebbers, T. (2009a). On MRI Turbulence Quantification. *Magn. Reson. Imaging* 27 (7), 913–922. doi:10.1016/j.mri.2009.05.004

Dyverfeldt, P., Gårdhagen, R., Sigfridsson, A., Karlsson, M., and Ebbers, T. (2009b). On MRI Turbulence Quantification. *Magn. Reson. Imaging* 27 (7), 913–922. doi:10.1016/j.mri.2009.05.004

Dyverfeldt, P., Hope, M. D., Tseng, E. E., and Saloner, D. (2013). Magnetic Resonance Measurement of Turbulent Kinetic Energy for the Estimation of Irreversible Pressure Loss in Aortic Stenosis. *JACC: Cardiovasc. Imaging* 6 (1), 64–71. doi:10.1016/j.jcmg.2012.07.017

Dyverfeldt, P., Kvitting, J.-P. E., Sigfridsson, A., Engvall, J., Bolger, A. F., and Ebbers, T. (2008). Assessment of Fluctuating Velocities in Disturbed Cardiovascular Blood Flow: *In Vivo* Feasibility of Generalized Phase-Contrast MRI. *J. Magn. Reson. Imaging* 28 (3), 655–663. doi:10.1002/jmri.21475

Dyverfeldt, P., Sigfridsson, A., Kvitting, J.-P. E., and Ebbers, T. (2006). Quantification of Intravoxel Velocity Standard Deviation and Turbulence Intensity by Generalizing Phase-Contrast MRI. *Magn. Reson. Med.* 56 (4), 850–858. doi:10.1002/mrm.21022

Ebbers, T., Haraldsson, H., Dyverfeldt, P., Sigfridsson, A., Warntjes, M. J. B., and Wigström, L. (2008). "Higher Order Weighted Least-Squares Phase Offset Correction for Improved Accuracy in Phase-Contrast MRI," in Proceedings of the International Society for Magnetic Resonance in Medicine. 16, Toronto, Ontario, May 2008.

Ebbers, T., Wigström, L., Bolger, A. F., Engvall, J., and Karlsson, M. (2001). Estimation of Relative Cardiovascular Pressures Using Time-Resolved Three-Dimensional Phase Contrast MRI. *Magn. Reson. Med.* 45 (5), 872–879. doi:10.1002/mrm.1116

Falahatpisheh, A., Rickers, C., Gabbert, D., Heng, E. L., Stalder, A., Kramer, H.-H., et al. (2016). Simplified Bernoulli's Method Significantly Underestimates Pulmonary Transvalvular Pressure Drop. *J. Magn. Reson. Imaging* 43 (6), 1313–1319. doi:10.1002/jmri.25097

Fredriksson, A., Trzebiatowska-Krzynska, A., Dyverfeldt, P., Engvall, J., Ebbers, T., and Carlhäll, C. J. (2018). Turbulent Kinetic Energy in the Right Ventricle: Potential MR Marker for Risk Stratification of Adults with Repaired Tetralogy of Fallot. *J. Magn. Reson. Imaging* 47 (4), 1043–1053. doi:10.1002/jmri.25830

Fung, Y.-c. (1977). *A First Course in Continuum Mechanics*. Englewood Cliffs: Cambridge University Press.

Grigioni, M., Daniele, C., D'avenio, G., and Barbaro, V. (1999). A Discussion on the Threshold Limit for Hemolysis Related to Reynolds Shear Stress. *J. Biomech.* 32 (10), 1107–1112. doi:10.1016/s0021-9290(99)00063-9

Ha, H., Lantz, J., Haraldsson, H., Casas, B., Ziegler, M., Karlsson, M., et al. (2016e). Assessment of Turbulent Viscous Stress Using ICOSA 4D Flow MRI for Prediction of Hemodynamic Blood Damage. *Sci. Rep.* 6 (1), 39773–39814. doi:10.1038/srep39773

Ha, H., Lantz, J., Ziegler, M., Casas, B., Karlsson, M., Dyverfeldt, P., et al. (2017a). Estimating the Irreversible Pressure Drop across a Stenosis by Quantifying Turbulence Production Using 4D Flow MRI. *Sci. Rep.* 7 (1), 46618–46714. doi:10.1038/srep46618

Ha, H., Hwang, D., Kim, G. B., Kweon, J., Lee, S. J., Baek, J., et al. (2016a). Estimation of Turbulent Kinetic Energy Using 4D Phase-Contrast MRI: Effect of Scan Parameters and Target Vessel Size. *Magn. Reson. Imaging* 34 (6), 715–723. doi:10.1016/j.mri.2016.03.008

Ha, H., Hwang, D., Kim, G. B., Kweon, J., Lee, S. J., Baek, J., et al. (2016b). Reply to Letter by Dyverfeldt and Ebbers Regarding the Article "Estimation of Turbulent Kinetic Energy Using 4D Phase-Contrast MRI: Effect of Scan Parameters and Target Vessel Size". *Magn. Reson. Imaging* 34 (9), 1338–1340. doi:10.1016/j.mri.2016.07.014

Ha, H., Kim, G. B., Kweon, J., Huh, H. K., Lee, S. J., Koo, H. J., et al. (2016c). Turbulent Kinetic Energy Measurement Using Phase Contrast MRI for Estimating the post-stenotic Pressure Drop: *In Vitro* Validation and Clinical Application. *PLoS ONE* 11 (3), e0151540. doi:10.1371/journal.pone.0151540

Ha, H., Kim, G. B., Kweon, J., Lee, S. J., Kim, Y.-H., Lee, D. H., et al. (2016d). Hemodynamic Measurement Using Four-Dimensional Phase-Contrast MRI: Quantification of Hemodynamic Parameters and Clinical Applications. *Korean J. Radiol.* 17 (4), 445–462. doi:10.3348/kjr.2016.17.4.445

Ha, H., Kvitting, J., Dyverfeldt, P., and Ebbers, T. (2019). Validation of Pressure Drop Assessment Using 4D Flow MRI-based Turbulence Production in Various Shapes of Aortic Stenoses. *Magn. Reson. Med.* 81 (2), 893–906. doi:10.1002/mrm.27437

Ha, H., Lantz, J., Ziegler, M., Casas, B., Karlsson, M., Dyverfeldt, P., et al. (2017b). Estimating the Irreversible Pressure Drop across a Stenosis by Quantifying Turbulence Production Using 4D Flow MRI. *Sci. Rep.* 7, 46618. doi:10.1038/srep46618

Ha, H., Park, K. J., Dyverfeldt, P., Ebbers, T., and Yang, D. H. (2020). *In Vitro* experiments on ICOSA6 4D Flow MRI Measurement for the Quantification of Velocity and Turbulence Parameters. *Magn. Reson. Imaging* 72, 49–60. doi:10.1016/j.mri.2020.06.020

Ha, H., Ziegler, M., Welander, M., Bjarnegård, N., Carlhäll, C.-J., Lindenberger, M., et al. (2018). Age-related Vascular Changes Affect Turbulence in Aortic Blood Flow. *Front. Physiol.* 9, 36. doi:10.3389/fphys.2018.00036

Hanai, S., Yamaguchi, T., and Kikkawa, S. (1991). Turbulence in the Canine Ascending Aorta and the Blood Pressure. *Biorheology* 28 (1-2), 107–116. doi:10.3233/bir-1991-281-211

Haraldsson, H., Kefayati, S., Ahn, S., Dyverfeldt, P., Lantz, J., Karlsson, M., et al. (2018). Assessment of Reynolds Stress Components and Turbulent Pressure Loss Using 4D Flow MRI with Extended Motion Encoding. *Magn. Reson. Med.* 79 (4), 1962–1971. doi:10.1002/mrm.26853

Kim, D., Kang, J., Adeeb, E., Lee, G.-H., Yang, D. H., and Ha, H. (2021). Comparison of Four-Dimensional Flow Magnetic Resonance Imaging and Particle Image Velocimetry to Quantify Velocity and Turbulence Parameters. *Fluids* 6 (8), 277. doi:10.3390/fluids6080277

Kim, G. B., Ha, H., Kweon, J., Lee, S. J., Kim, Y.-H., Yang, D. H., et al. (2015). Post-stenotic Plug-like Jet with a Vortex Ring Demonstrated by 4D Flow MRI. *Magn. Reson. Imaging* 34, 371–375. doi:10.1016/j.mri.2015.11.010

Kim, J., Lee, Y., Choi, S., and Ha, H. (2020). Pulsatile Flow Pump Based on an Iterative Controlled Piston Pump Actuator as an *In-Vitro* Cardiovascular Flow Model. *Med. Eng. Phys.* 77, 118–124. doi:10.1016/j.medengphy.2019.10.020

Knobloch, V., Binter, C., Gülan, U., Sigfridsson, A., Holzner, M., Lüthi, B., et al. (2014). Mapping Mean and Fluctuating Velocities by Bayesian Multipoint MR Velocity Encoding-Validation against 3D Particle Tracking Velocimetry. *Magn. Reson. Med.* 71 (4), 1405–1415. doi:10.1002/mrm.24785

Krittian, S. B. S., Lamata, P., Michler, C., Nordsletten, D. A., Bock, J., Bradley, C. P., et al. (2012). A Finite-Element Approach to the Direct Computation of Relative Cardiovascular Pressure from Time-Resolved MR Velocity Data. *Med. image Anal.* 16 (5), 1029–1037. doi:10.1016/j.media.2012.04.003

Lu, P. C., Lai, H. C., and Liu, J. S. (2001). A Reevaluation and Discussion on the Threshold Limit for Hemolysis in a Turbulent Shear Flow. *J. Biomech.* 34 (10), 1361–1364. doi:10.1016/s0021-9290(01)00084-7

Ma, L. E., Markl, M., Chow, K., Huh, H., Forman, C., Vali, A., et al. (2019). Aortic 4D Flow MRI in 2 minutes Using Compressed Sensing, Respiratory Controlled Adaptive K-Space Reordering, and Inline Reconstruction. *Magn. Reson. Med.* 81 (6), 3675–3690. doi:10.1002/mrm.27684

Markl, M., Wallis, W., Brendecke, S., Simon, J., Frydrychowicz, A., and Harloff, A. (2010). Estimation of Global Aortic Pulse Wave Velocity by Flow-Sensitive 4D MRI. *Magn. Reson. Med.* 63 (6), 1575–1582. doi:10.1002/mrm.22353

Markl, M., Wallis, W., Strecker, C., Gladstone, B. P., Vach, W., and Harloff, A. (2012). Analysis of Pulse Wave Velocity in the Thoracic Aorta by Flow-Sensitive Four-Dimensional MRI: Reproducibility and Correlation with Characteristics in Patients with Aortic Atherosclerosis. *J. Magn. Reson. Imaging* 35 (5), 1162–1168. doi:10.1002/jmri.22856

Marlevi, D., Ha, H., Dillon-Murphy, D., Fernandes, J. F., Fovargue, D., Colarieti-Tosti, M., et al. (2020). Non-invasive Estimation of Relative Pressure in Turbulent Flow Using Virtual Work-Energy. *Med. Image Anal.* 60, 101627. doi:10.1016/j.media.2019.101627

Members, W. C., Otto, C. M., Nishimura, R. A., Bonow, R. O., Carabello, B. A., Erwin, J. P., III, et al. (2021). 2020 ACC/AHA Guideline for the Management of Patients with Valvular Heart Disease: a Report of the American College of Cardiology/American Heart Association Joint Committee on Clinical Practice Guidelines. *J. J. Am. Coll. Cardiol.* 77 (4), e25–e197.

Mustard, J. F., Murphy, E. A., Rowsell, H. C., and Downie, H. G. (1962). Factors Influencing Thrombus Formation *In Vivo*. *Am. J. Med.* 33 (5), 621–647. doi:10.1016/0002-9343(62)90243-7

Petersson, S., Dyverfeldt, P., Sigfridsson, A., Lantz, J., Carlhäll, C. J., and Ebbers, T. (2016). Quantification of Turbulence and Velocity in Stenotic Flow Using Spiral Three-dimensional Phase-contrast MRI. *Magn. Reson. Med.* 75 (3), 1249–1255. doi:10.1002/mrm.25698

Pope, S. B. (2001). *Turbulent Flows*. Bristol, United Kingdom: IOP Publishing.

Prado, C. M., Ramos, S. G., Alves-Filho, J. C., Elias, J., Jr, Cunha, F. Q., and Rossi, M. A. (2006). Turbulent Flow/low wall Shear Stress and Stretch Differentially Affect Aorta Remodeling in Rats. *J. J. Hypertens.* 24 (3), 503–515. doi:10.1097/01.hjh.0000209987.51606.23

Ragosta, M. (2017). *Textbook of Clinical Hemodynamics E-Book*. Amsterdam, Netherlands: Elsevier Health Sciences.

Rizk, J. (2021). 4D Flow MRI Applications in Congenital Heart Disease. *Eur. Radiol.* 31 (2), 1160–1174. doi:10.1007/s00330-020-07210-z

Sallam, A. M., and Hwang, N. H. (1983). Human Red Blood Cell Hemolysis in a Turbulent Shear Flow: Contribution of Reynolds Shear Stresses. *Biorheology* 21 (6), 783–797. doi:10.3233/bir-1984-21605

Smith, R. L., Blick, E. F., Coalson, J., and Stein, P. D. (1972). Thrombus Production by Turbulence. *J. Appl. Physiol.* 32 (2), 261–264. doi:10.1152/jappl.1972.32.2.261

Soulat, G., McCarthy, P., and Markl, M. (2020). 4D Flow with MRI. *Annu. Rev. Biomed. Eng.* 22, 103–126. doi:10.1146/annurev-bioeng-100219-110055

Stankovic, Z., Allen, B. D., Garcia, J., Jarvis, K. B., and Markl, M. (2014). 4D Flow Imaging with MRI. *Cardiovasc. Diagn. Ther.* 4 (2), 173–192. doi:10.3978/j.issn.2223-3652.2014.01.02

Stein, P. D., and Sabbah, H. N. (1976). Turbulent Blood Flow in the Ascending Aorta of Humans with normal and Diseased Aortic Valves. *Circ. Res.* 39 (1), 58–65. doi:10.1161/01.res.39.1.58

Tennekes, H., and Lumley, J. L. (1972). *A First Course in Turbulence*. Cambridge, Massachusetts: MIT press.

von Spiczak, J., Crelier, G., Giese, D., Kozerke, S., Maintz, D., and Bunck, A. C. (2015). Quantitative Analysis of Vortical Blood Flow in the Thoracic Aorta Using 4D Phase Contrast MRI. *PloS one* 10 (9), e0139025. doi:10.1371/journal.pone.0139025

Walheim, J., Dillinger, H., Gotschy, A., and Kozerke, S. (2019). 5D Flow Tensor MRI to Efficiently Map Reynolds Stresses of Aortic Blood Flow *In-Vivo*. *Sci. Rep.* 9 (1), 18794–18812. doi:10.1038/s41598-019-55353-x

Yamaguchi, T., Kikkawa, S., Yoshikawa, T., Tanishita, K., and Sugawara, M. (1983). Measurement of Turbulence Intensity in the center of the Canine Ascending Aorta with a Hot-Film Anemometer. *J. biomechanical Eng.* 105 (2), 177–187. doi:10.1115/1.3138403

Yen, J.-H., Chen, S.-F., Chern, M.-K., and Lu, P.-C. (2014). The Effect of Turbulent Viscous Shear Stress on Red Blood Cell Hemolysis. *J. Artif. Organs* 17 (2), 178–185. doi:10.1007/s10047-014-0755-3

Zajac, J., Eriksson, J., Dyverfeldt, P., Bolger, A. F., Ebbers, T., and Carlhäll, C.-J. (2015). Turbulent Kinetic Energy in normal and Myopathic Left Ventricles. *J. Magn. Reson. Imaging* 41 (4), 1021–1029. doi:10.1002/jmri.24633

Zhang, T., Pauly, J. M., and Levesque, I. R. (2015). Accelerating Parameter Mapping with a Locally Low Rank Constraint. *Magn. Reson. Med.* 73 (2), 655–661. doi:10.1002/mrm.25161

Ziegler, M., Lantz, J., Ebbers, T., and Dyverfeldt, P. (2017). Assessment of Turbulent Flow Effects on the Vessel wall Using Four-Dimensional Flow MRI. *Magn. Reson. Med.* 77 (6), 2310–2319. doi:10.1002/mrm.26308

Conflict of Interest: The authors declare that the research was conducted in the absence of any commercial or financial relationships that could be construed as a potential conflict of interest.

Publisher's Note: All claims expressed in this article are solely those of the authors and do not necessarily represent those of their affiliated organizations or those of the publisher, the editors, and the reviewers. Any product that may be evaluated in this article, or claim that may be made by its manufacturer, is not guaranteed or endorsed by the publisher.

frontiers in Bioengineering and Biotechnology

ORIGINAL RESEARCH
published: 28 January 2022
doi: 10.3389/fbioe.2021.828577

The Correlation Between Wall Shear Stress and Plaque Composition in Advanced Human Carotid Atherosclerosis

*A. M. Moerman[1], S. Korteland[1], K. Dilba[1], K. van Gaalen[1], D. H. J. Poot[2], A. van Der Lugt[2], H. J. M. Verhagen[3], J. J. Wentzel[1], A. F. W. van Der Steen[1], F. J. H. Gijsen[1,4] and K. Van der Heiden[1]**

[1]Department of Biomedical Engineering, Thorax Center, Erasmus MC, Rotterdam, Netherlands, [2]Department of Radiology and Nuclear Medicine, Erasmus MC, Rotterdam, Netherlands, [3]Department of Vascular Surgery, Erasmus MC, Rotterdam, Netherlands, [4]Department of Biomedical Engineering, Delft University of Technology, Delft, Netherlands

OPEN ACCESS

Edited by:
Der-Cherng Tarng, Taipei Veterans General Hospital, Taiwan

Reviewed by:
Dalin Tang, Worcester Polytechnic Institute, United States
Aike Qiao, Beijing University of Technology, China

***Correspondence:**
K. Van der Heiden
K.vanderheiden@erasmusmc.nl

Specialty section:
This article was submitted to Biomechanics, a section of the journal Frontiers in Bioengineering and Biotechnology

Received: *03 December 2021*
Accepted: *29 December 2021*
Published: *28 January 2022*

Citation:
Moerman AM, Korteland S, Dilba K, van Gaalen K, Poot DHJ, van Der Lugt A, Verhagen HJ, Wentzel J, van Der Steen AFW, Gijsen FJ and Van der Heiden K (2022) The Correlation Between Wall Shear Stress and Plaque Composition in Advanced Human Carotid Atherosclerosis. Front. Bioeng. Biotechnol. 9:828577. doi: 10.3389/fbioe.2021.828577

The role of wall shear stress (WSS) in atherosclerotic plaque development is evident, but the relation between WSS and plaque composition in advanced atherosclerosis, potentially resulting in plaque destabilization, is a topic of discussion. Using our previously developed image registration pipeline, we investigated the relation between two WSS metrics, time-averaged WSS (TAWSS) and the oscillatory shear index (OSI), and the local histologically determined plaque composition in a set of advanced human carotid plaques. Our dataset of 11 carotid endarterectomy samples yielded 87 histological cross-sections, which yielded 511 radial bins for analysis. Both TAWSS and OSI values were subdivided into patient-specific low, mid, and high tertiles. This cross-sectional study shows that necrotic core (NC) size and macrophage area are significantly larger in areas exposed to high TAWSS or low OSI. Local TAWSS and OSI tertile values were generally inversely related, as described in the literature, but other combinations were also found. Investigating the relation between plaque vulnerability features and different combinations of TAWSS and OSI tertile values revealed a significantly larger cap thickness in areas exposed to both low TAWSS and low OSI. In conclusion, our study confirmed previous findings, correlating high TAWSS to larger macrophage areas and necrotic core sizes. In addition, our study demonstrated new relations, correlating low OSI to larger macrophage areas, and a combination of low TAWSS and low OSI to larger cap thickness.

Keywords: atherosclerosis, wall shear stress, oscillatory shear index, vulnerable plaque, plaque composition, MRI, image registration pipeline

INTRODUCTION

Atherosclerosis is a gradually progressing disease of the arteries characterized by vessel wall thickening due to the accumulation of lipids and inflammatory cells. This is referred to as plaque formation. Atherosclerosis is a multifactorial disease that can be aggravated not only by lifestyle factors, such as high caloric diet, physical inactivity, and smoking, but also by genetic factors. The initiation of plaque formation, however, has been strongly linked to a hemodynamic parameter: wall shear stress (WSS). WSS is the frictional force exerted by flowing blood on the vessel wall.

Atherosclerotic plaques form at predetermined locations where WSS is low and/or oscillatory, which increases endothelial cell permeability and subsequent retention of lipoproteins (Lusis, 2000) and regulates pro-inflammatory signaling pathways in the endothelium, resulting in an increased influx of inflammatory cells (Gimbrone and García-Cardeña, 2013). The causal role of WSS in plaque initiation is evident (Kwak et al., 2014; Cunningham and Gotlieb, 2005); however, the influence of WSS on plaque progression is less clear. Initial plaque growth is generally accompanied by outward remodeling and preservation of low and/or oscillatory WSS levels. With disease progression, however, plaques will start to intrude the lumen, thereby affecting local hemodynamics. Upstream and at the throat of the plaque, WSS levels are high, while low WSS is found downstream (Slager et al., 2005). Based on their composition and the resulting risk of rupture, plaques are classified as stable or vulnerable. Vulnerable plaques are characterized by a thin cap, covering a large necrotic core (NC), and often present with high inflammatory activity and decreased smooth muscle cell content (Schaar et al., 2004). Intraplaque hemorrhage (IPH) can also be present (Virmani et al., 2000). The morphology and composition of advanced plaques were shown to be inhomogenous, both in the axial and in the circumferential direction (Richardson et al., 1989; Dirksen et al., 1998; Burke et al., 1999; Wentzel et al., 2003; Cicha et al., 2011), which could indicate a relation between local hemodynamics and plaque composition. In addition, plaque rupture is most often encountered at the high WSS–exposed upstream site (de Weert et al., 2009). The interplay between WSS and plaque composition is a subject of debate: both low and high WSS have been linked to features of plaque vulnerability (Lovett and Rothwell, 2003; Cicha et al., 2011; Eshtehardi et al., 2012; Wentzel et al., 2012; Vergallo et al., 2014; Tuenter et al., 2016; Yamamoto et al., 2019). However, these studies differ in imaging modality used for assessing plaque composition, complicating one-to-one comparison of their results. In addition, studies of the carotid artery are often based on assumed WSS levels (Dirksen et al., 1998; Lovett and Rothwell, 2003; Fagerberg et al., 2010) or used animal models, which are not truly representative (Winkel et al., 2015; Daugherty et al., 2017). Since histology is the gold standard for the assessment of human plaque composition in high resolution, we previously developed a framework for accurate registration of MRI-derived WSS patterns to histological cross-sections (Moerman et al., 2019). In this study, we investigated the correlation between WSS and histologically identified components of plaque vulnerability in a dataset of advanced human carotid atherosclerotic plaques.

METHODS

MR Imaging, Tissue Collection, and Histological Processing

MR imaging, tissue collection, tissue processing, and image registration procedures have been described in detail elsewhere (Moerman et al., 2019). In short, we imaged the carotid bifurcations of 11 patients scheduled for carotid endarterectomy (CEA) surgery in a 3.0-T MRI scanner (GE Healthcare, Milwaukee, United States). The MRI protocol consisted of a 3D black-blood fast spin-echo (3D-BB-FSE) sequence with variable flip angles (TR/TE: 1000/16 ms; FOV: 15 cm; slice thickness: 0.8 mm; matrix: 160 × 160; number of excitations 1; scan time: 190 s), which was optimized for visualizing lumen and outer wall geometry. CEA specimens were collected within 30 min after surgical resection, snap-frozen in liquid nitrogen, and stored at −80°C until *ex vivo* scans and histology were performed. Upon processing, CEA specimens were thawed, fixed in 4% formaldehyde, and immersed in PBS. *Ex vivo* MRI scans (T2w fast recovery FSE (frFSE); TR/TE: 2,500/66 ms; in-plane resolution: 0.1 × 0.1 mm; slice thickness: 0.5 mm; matrix: 256 × 256; scan time: ~20 min; number of slices: 66) were performed using a 7.0-T MRI scanner (7.0T Discovery MR901, GE Healthcare, Milwaukee, United States).

CEA specimens were decalcified and cut into 1 mm thick consecutive axial cross-sections. "En face photos" were taken (IXUS 60, Canon, Tokyo, Japan) of the proximal side of each cross-section. The en face photos contained landmarks to facilitate registration of each en face photo to the photo of the adjacent cross-section, enabling reconstruction of a 3D stack of en face photos. After photographing, the 1-mm-thick axial cross-sections were embedded in paraffin. Each paraffin block was cut into consecutive 5 μm thick sections, which were processed for a series of histochemical staining procedures, that is, Miller's elastic stain, hematoxylin–eosin, Martius scarlet blue, and Picrosirius red, as well as two immunohistological staining procedures for macrophages (CD68, Abcam, United Kingdom) and endothelial cells (CD31, Abcam, United Kingdom). For each tissue section, compositional characteristics of plaque vulnerability, that is, necrotic core (NC) and the IPH-associated protein fibrin, were delineated in a segmentation image (BioPix iQ3.2). This segmentation was based on the total set of histochemical stains. Based on the immunohistological staining for CD68, we made segmentation masks of the CD68-positive pixels by applying a color deconvolution filter in Fiji (Ruifrok and Johnston, 2001; Schindelin et al., 2012). Tissue areas containing artifacts and NC led to false-positive results and were removed from CD68-positive pixel selection.

Computational Fluid Dynamics for Wall Shear Stress Calculation

Lumen contours of the stenosed bifurcations were delineated on the *in vivo* MRI scan using ITK-snap (Yushkevich et al., 2006) and exported as surface geometry VMTK (Antiga et al., 2008) was used for surface smoothing and centerline calculation. Clipping of inlet and outlets normal to the centerline was performed in ICEM (ANSYS ICEM 17.1, United States), and flow extensions were applied on the inlet and outlets using the VMTK. The length of the added flow extensions was five times the radius of the inlet or outlets. Subsequently, ICEM was used to generate a volume mesh containing on average 7 million elements. The volume mesh consisted of tetrahedral elements with five layers of prism elements at the wall. On the inlet of the common carotid artery (CCA), we applied a transient flow velocity profile using

the theory of Womersley (Xu et al., 2018). This transient profile was based on the average flow waveform over one heart cycle and the heart rate reported by Lee et al. (2008). For each patient, the transient flow waveform was scaled to obtain an average WSS in the common carotid artery of 0.9 Pa (Lee et al., 2009) (Gnasso et al., 1997). As outlet boundary condition, the relative outflow to the internal carotid artery (ICA) and external carotid artery (ECA) was defined based on the stenosis degree (Groen et al., 2010). Blood density was set to 1060 kg/m^3, and non-Newtonian fluid behavior was mimicked by the Carreau–Yasuda model using the parameters reported by Seo et al. (2005). The Navier–Stokes equations were solved numerically (ANSYS Fluent 17.1, United States) (convergence criteria: 1E-4 for continuity residual; 1E-5 for x-velocity, y-velocity, and z-velocity residuals; time step was 0.004 s) over 2 heart cycles. Time-dependent time-averaged wall shear stress (TAWSS) and oscillatory shear index (OSI) (Ku et al., 1985) were computed over the second heart cycle to account for initialization effects.

Image Registration of MRI, CFD, and Histology

Image registration was performed according to the methods we described previously (Moerman et al., 2019). In short, *via* a series of rigid and nonrigid image registrations and transformations, the *in vivo* MRI lumen and its corresponding WSS map were transformed consecutively to the *ex vivo* and the en face image domain. Histology images were axially stacked and registered to the en face domain as well, resulting in co-registration of *in vivo* MRI-derived WSS and histology.

Analysis and Exclusion Criteria

For a detailed description of data selection and analysis procedures, we refer to our previous publication (Moerman et al., 2019). In short, WSS patterns were axially averaged over −0.3 mm to +0.3 mm with respect to the axial location of the nearest histology section. Transversally, the WSS distribution over each lumen was discretized into eight radial bins (bin radius 45°). The points on the centerline of the transformed 3D WSS map were used as center points to create the radial bins. Plaque component measures were averaged in each radial bin. Per bin, we investigated the relation between local WSS and tissue composition of total intima depth. The dataset of 11 CEA samples yielded 183 axial cross-sections, of which 87 (48%) were included in the final analysis, yielding a total of 696 radial bins, of which 511 (73%) were included in the final analysis.

We excluded data, both axial cross-sections and radial bins, based on a set of criteria. Axial cross-sections were excluded if A) a part of the excised CEA lumen showed severe and nonuniform deformation with respect to the rest of the lumen, for example, large lumen collapse in the ICA compared to the CCA. The applied nonrigid lumen registration algorithms act on the global 3D geometry and are not able to correct for local severe tissue deformations; thus, accurate registration was impaired in such cross-sections. B) Lumen diameter on *in vivo* MRI was <3 pixels and/or showed a very large axial gradient. As discussed previously (Moerman et al., 2019), the applicability of our method should be carefully assessed in these cases since WSS calculations in highly stenotic areas are very sensitive to minor variations in lumen size, and a small mismatch in registration accuracy in regions with large axial gradients has a relatively large effect on the relation found between WSS and plaque composition. C) Low signal-to-noise ratio of the *in vivo* MRI images, which impaired reliable lumen segmentation. The radial bins were excluded based on the presence of 1) histological processing artifacts, 2) a mismatch in lumen registration between en face and histology images, or 3) a mismatch in lumen registration between *in vivo* MRI and en face images (Moerman et al., 2019). For the included radial bins, we quantified registration performance by calculating the average Hausdorff distance (HD) and dice similarity coefficients (DSCs) between en face and histology lumen segmentations and en face and *in vivo* MRI lumen segmentations (Moerman et al., 2019).

Statistical Analysis

The range of absolute TAWSS and OSI values varied per artery. To define low, mid, and high WSS metric regions within each artery, patient-specific TAWSS and OSI tertiles were calculated. Statistical analysis was performed using a linear mixed effects model: WSS tertiles or OSI tertiles were set as a fixed factor and patient as a random factor. In addition, we tested the combination of WSS tertiles and OSI tertiles, including their interaction term, in one model to estimate the various parameters. Bonferroni correction was applied to adjust for multiple comparisons between WSS tertiles. The estimated means and standard error are reported. P-values < 0.05 were considered statistically significant.

RESULTS

Registration Performance

The dataset of 11 CEA samples yielded 183 axial cross-sections, of which 87 (48%) were included in the final analysis. Ninety-six axial cross-sections were excluded; the majority of exclusions (59) were due to severe nonuniform deformation in the excised tissue or processing artifacts. Twenty axial cross-sections were excluded because the *in vivo* lumen was highly stenotic or had a large axial gradient, impairing accurate lumen segmentation for CFD simulations. Seventeen cross-sections were excluded because of bad signal-to-noise ratio on *in vivo* MRI. The 87 included axial cross-sections were divided into 8 radial bins, yielding a total of 696 radial bins, of which 511 (73%) were included in the final analysis. The majority of excluded radial bins (111) presented with histological artifacts. After the exclusion procedure, registration accuracy of the remaining dataset was quantified by calculating the dice similarity coefficient (DSC) and Hausdorff distance (HD) between the lumen segmentations of the en face and histology cross-sections and between the en face and the transformed *in vivo* cross-sections. For the histology-to-en face registration, we found a mean HD of 0.55 ± 0.07 (SEM) mm and a mean DSC of 0.85 ± 0.02 (SEM). The registration performance between *in vivo* MRI and en face was slightly better: the mean HD was 0.36 ± 0.06 (SEM) mm and the mean DSC was 0.91 ± 0.02 (SEM). These values were in the order of magnitude of previously reported similarity indices, describing

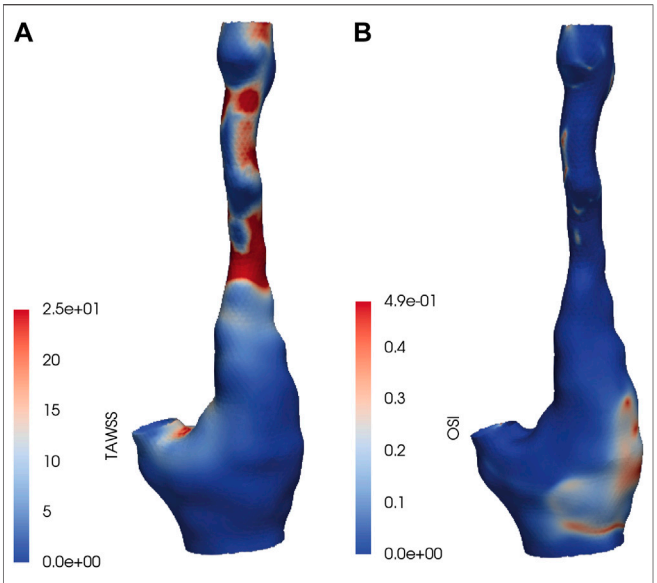

FIGURE 1 | (A) Time-averaged wall shear stress (TAWSS) and **(B)** oscillatory shear index (OSI) values on a carotid bifurcation included in the dataset.

registration of images of CEA specimens by multiple imaging modalities (Boekhoven et al., 2013).

Wall Shear Stress Patterns in Advanced Carotid Atherosclerosis

In **Figure 1** the TAWSS and OSI patterns on a carotid bifurcation are shown. In all included carotid arteries, relatively high TAWSS was mainly located at the flow divider, at the ECA inlet, and upstream to and at locations of the maximally narrowed lumen. Low TAWSS was mainly found in the proximal CCA, at the lateral side of the carotid bulb, and at sites of relative lumen dilation. High OSI was generally found at the lateral side of the carotid bulb and downstream of stenoses, while low OSI was seen in relatively straight arterial segments, such as the proximal CCA, and at sites of lumen narrowing. The range of absolute TAWSS and OSI values varied per artery. After registration of the WSS maps to histology, WSS values were axially and radially averaged. In **Table 1** the patient-specific tertile boundaries and the ranges of average TAWSS and OSI values, after registration and averaging per bin, are reported. In **Table 2**, the co-occurrences of TAWSS and OSI tertile values are reported. An inverse relation between TAWSS and OSI tertile values was most frequently encountered, but other combinations were also found.

Histologically Determined Plaque Composition in Advanced Carotid Atherosclerosis

In **Figure 2**, a selection of representative histological cross-sections is shown, along with the segmentation of lumen, fibrin, intima, NC, and macrophages. In general, histological cross-sections originating from the CCA showed a thickened intima with one or more NCs and small, elongated patches of macrophages. Both the NCs and the macrophages were generally located from the lumen up to a depth of half of the intima (**Figure 2A**). Relatively small fibrin areas could be observed as well. When moving from the proximal to distal region through the bulb, the plaque thickness varied in circumferential direction: plaque area and NC size were larger at the lateral side of the bifurcation (**Figures 2B,C**). Largest plaque area and eccentric plaque growth were observed in cross-sections harvested from the ICA (**Figures 2D,E**). Large NCs were present and showed large fibrin-positive areas. In these cross-sections, macrophages were generally distributed around the circumference of the lumen, were present in the cap, and were also seen deeper in the intima and at the edges of the NCs (**Figure 2E**). The amount of fibrous tissue was relatively low compared to proximal axial locations.

Relation Between Wall Shear Stress Metrics and Plaque Composition

For all included radial bins, we compared the average TAWSS and OSI levels, subdivided into patient-specific low, mid, and high

TABLE 1 | Patient-specific tertile boundaries and ranges of wall shear stress (WSS) metrics averaged on radial bins. TAWSS, time-averaged WSS; OSI, oscillatory shear index.

Patient	TAWSS tertile boundary low–mid [Pa]	TAWSS tertile boundary mid–high [Pa]	Range TAWSS—averaged over bins [Pa]	OSI tertile boundary low–mid [Pa]	OSI tertile boundary mid–high [Pa]	Range OSI—averaged over bins [Pa]
1	2.1	4.5	0.5–10.4	0.003	0.010	0–0.092
2	1.0	1.9	0.3–3.8	0.004	0.018	0–0.386
3	1.5	2.0	1.0–3.3	0.000	0.001	0–0.005
4	1.3	2.0	0.5–3.5	0.011	0.021	0–0.169
5	1.1	2.5	0.2–8.0	0.001	0.014	0–0.093
6	1.2	2.8	0.5–34.8	0.002	0.044	0–0.344
7	1.1	2.9	0.2–6.0	0.002	0.008	0–0.111
8	0.6	1.5	0.2–5.8	0.007	0.032	0–0.232
9	1.8	8.8	0.1–52.6	0.000	0.013	0–0.308
10	1.7	2.7	1.0–11.1	0.000	0.004	0–0.091
11	0.8	2.5	0.3–11.7	0.004	0.031	0–0.156

TABLE 2 | Co-occurrence of TAWSS and OSI tertiles.

	Low OSI	Mid OSI	High OSI
Low TAWSS	11	38	120
Mid TAWSS	42	89	35
High TAWSS	116	39	14

tertiles, to the composition of the underlying plaque (NC area, fibrin area, macrophage area, and cap thickness). In **Figure 3**, the relations between WSS metrics and plaque composition are visualized. When considering the plaque composition of the total intimal area per radial bin, we found significantly larger NC areas in plaque regions exposed to high TAWSS, compared to low TAWSS ($p = 0.000$) and mid TAWSS ($p = 0.004$). In addition, we found significantly larger NC areas in plaque regions exposed to low OSI, compared to high OSI ($p = 0.000$) and mid OSI ($p = 0.007$). Regarding macrophage area, we found significantly larger macrophage areas in regions exposed to high TAWSS than in regions exposed to low TAWSS ($p = 0.007$). In addition, we found significantly larger macrophage areas in plaque regions exposed to low OSI, compared to high OSI ($p = 0.002$) and mid OSI ($p = 0.002$). When different combinations of TAWSS and OSI tertile values were analyzed, we found a significantly larger cap thickness in plaque regions exposed to both low TAWSS and low OSI, compared to low TAWSS and high OSI ($p = 0.013$). In the regions exposed to low OSI, a trend is observed for decreasing cap thickness with increasing TAWSS (low vs. mid TAWSS $p = 0.076$ and low vs. high TAWSS $p = 0.060$). No relations were found between the WSS metrics and fibrin area.

DISCUSSION

This was the first study that was able to make a direct comparison between local WSS metrics and histologically determined compositional characteristics of plaque vulnerability in a substantial number of human carotid plaques. The applied image registration pipeline allowed for a very accurate, localized assessment of this relation. We were able to take into account not just axial but also rotational matching of WSS and histology. Our cross-sectional analysis showed a relation between NC area and macrophage area with high TAWSS, as well as low OSI in advanced carotid atherosclerosis. Of these correlations, only a relation between presumed (because of the upstream location) high TAWSS and macrophage area was previously reported (Dirksen et al., 1998; Fagerberg et al., 2010). The relations between high TAWSS and cap thickness (Wentzel et al., 2013) in human coronaries and high TAWSS and IPH (Groen et al., 2007; Tuenter et al., 2016) in human carotids (Dirksen et al., 1998; Fagerberg et al., 2010), as previously reported, were not present in this dataset. When analyzing combinations of TAWSS and OSI tertile values, we found a significantly larger cap thickness in plaque regions exposed to

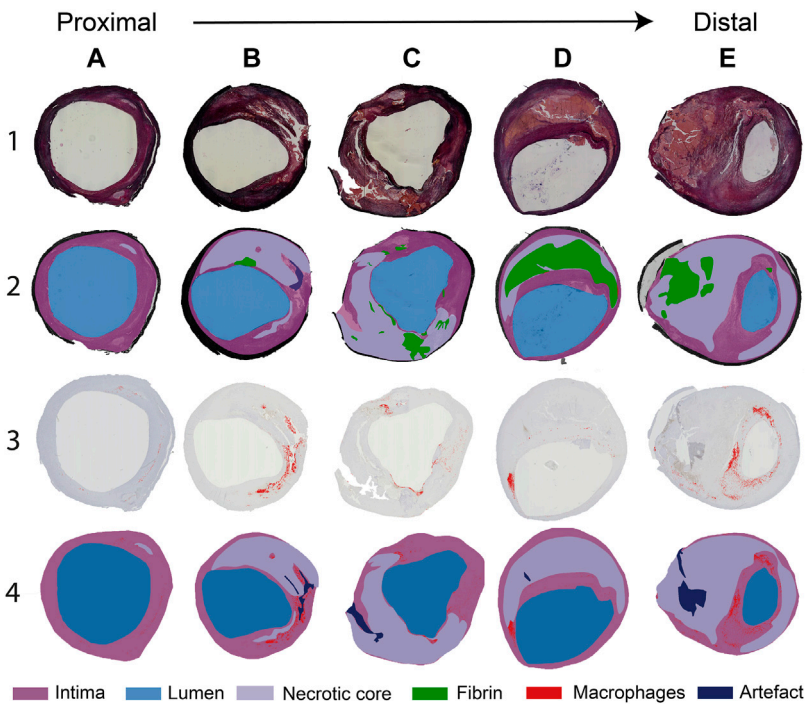

FIGURE 2 | (A–E). Selection of typical histology cross-sections of carotid plaques seen when moving from proximal to distal along the length of the carotid plaque. Cross-sections **(A–C)** are seen proximal to the flow divider and **(D,E)** distal to the flow divider. Row 1: Miller's elastic stain. Row 2: segmentation of the necrotic core (NC), fibrin, and artifact, based on the combination of histochemical staining procedures performed. Row 3: $CD68^+$ immunohistochemical stain. CD68-positive areas are marked in red. Row 4: segmentation of $CD68^+$ stained slides, showing macrophage areas, NC, and artifacts.

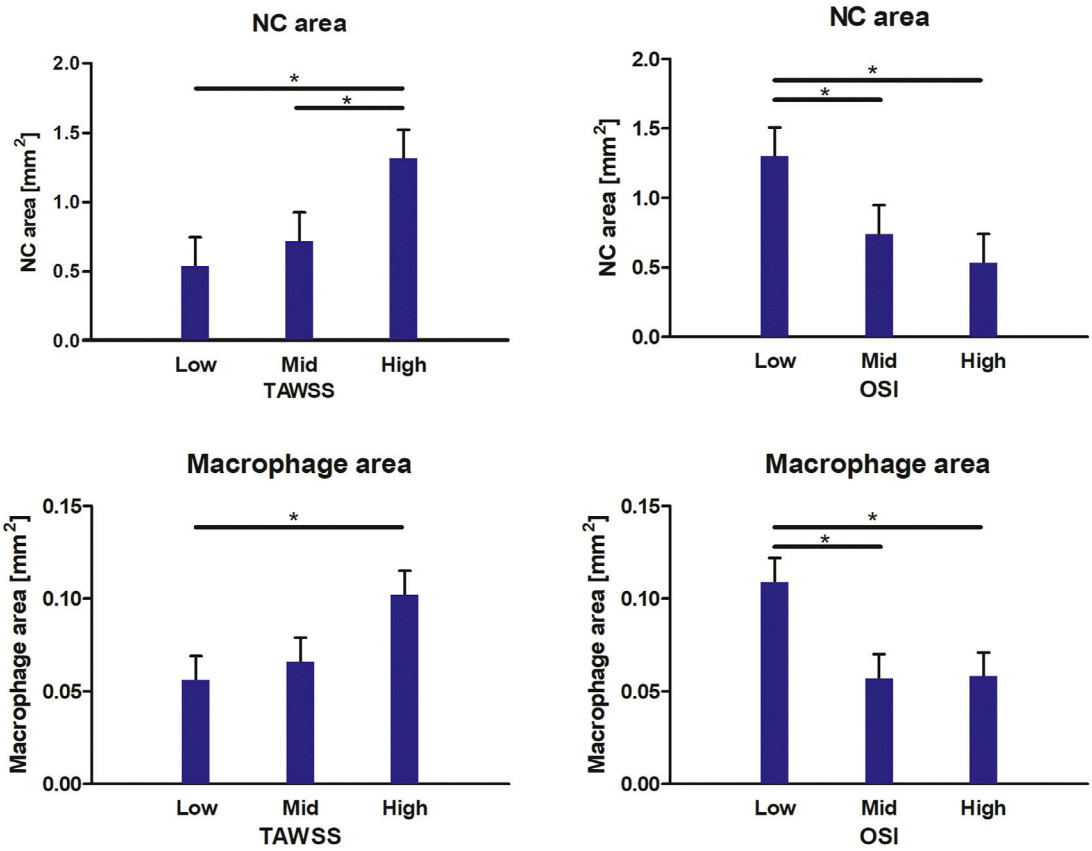

FIGURE 3 | Relations between WSS metrics and plaque compositional characteristics. In high TAWSS-exposed regions and low OSI-exposed regions, a larger NC area and macrophage area are found. At low TAWSS and low OSI, a larger cap thickness is found. Data are presented as estimated mean +standard error. *$p < 0.05$.

both low TAWSS and low OSI, compared to low TAWSS and high OSI. The observed trend for decreasing cap thickness with increasing TAWSS in regions exposed to low OSI confirmed previous findings.[12,20]

Wall Shear Stress Patterns in Advanced Carotid Atherosclerosis

The TAWSS patterns observed in this set of carotid arteries were in line with findings previously described in the literature (Ku et al., 1985; Kaazempur-Mofrad et al., 2004; Ladisa et al., 2010; Gallo et al., 2016; van Ooij et al., 2018; Vamsi Krishna et al., 2020). That is, low TAWSS was present at the CCA, at the lateral side of the carotid bulb, while high TAWSS was mainly seen at the upstream side of lumen stenoses. Generally, an inverse relation between TAWSS and OSI was found, as described before (Gallo et al., 2016). However, a subset of radial bins showed other relations between these two WSS metrics. As inflow boundary conditions, we did not use measured patient-specific flow profiles but applied estimated patient-specific flow profiles, scaled by inlet diameter, as we previously found that the absolute WSS levels in highly stenotic carotid arteries were affected mostly by the patient-specific geometry rather than the flow (Groen et al., 2010). Yet, large variations in WSS and OSI values were still encountered between patients, which stresses the large influence of geometrical factors on WSS patterns. Because of the large variation in WSS ranges between patients, it would be impossible to draw conclusions on the relation between WSS and plaque composition by using absolute WSS values. Therefore, we calculated patient-specific WSS tertiles. The use of relative instead of absolute WSS levels has the additional advantage of diminishing the sensitivity of the CFD results to the approximated boundary conditions that were applied.

Histologically Determined Plaque Composition in Advanced Carotid Atherosclerosis

The histologically determined composition seen in this set of carotid plaques reflected histology results reported in the literature (Virmani et al., 2006b). That is, the greatest plaque cross-sectional area and smallest lumens were found in the ICA

at cross-sections where the largest NCs were present, sometimes accompanied by fibrin-positivity, reflecting IPH. The majority of the excluded axial cross-sections and radial bins presented with processing artifacts, especially in the distal part of the plaque. The relatively "soft" necrotic and thrombotic tissue areas were more prone to deformation than tissue areas containing a higher amount of fibrous tissue. In addition, the tissue structure at areas that contained a high amount of calcium lost rigidity after decalcification, making these regions also susceptible to processing artifacts. The exclusion of these necrotic and calcified areas may have introduced a bias in our dataset toward moderately diseased tissue segments. The effect of this bias on the obtained results is unpredictable.

Relation Between Wall Shear Stress Metrics and Plaque Composition

Our study was designed to assess the correlations between WSS metrics and compositional features of plaque vulnerability in carotid plaques. We found relations between TAWSS and OSI with NC area, macrophage area, and cap thickness. Regarding NC area, we found that NCs were significantly larger at locations exposed to high TAWSS. Besides the existence of a direct correlation between TAWSS and NC size, this finding might be explained by the fact that progression of atherosclerosis is accompanied by plaque growth and subsequent lumen intrusion. This local lumen narrowing will affect TAWSS patterns, inducing a local high TAWSS at the upstream side and at the throat of the stenosis. In addition, plaque area has been shown to be correlated to NC size (Wentzel et al., 2013; Ahmadi et al., 2015), a finding that links the co-existence of high TAWSS and NC size. A positive correlation between TAWSS and NC has been reported before in both carotid plaques (Yang et al., 2010) and in coronary plaques (Samady et al., 2011; Eshtehardi et al., 2012; Wentzel et al., 2013; Park et al., 2016). Similarly, we also found significantly larger NCs at regions exposed to low OSI. The OSI value describes how much the WSS vector deviates from its average direction. Thus, low OSI, indicating a relative constant WSS direction, is mainly expected at regions with high flow velocity and high TAWSS. Although a large NC size has been shown to be associated with rupture (Virmani et al., 2006a; Falk et al., 2013), based on this cross-sectional study, we cannot differentiate whether we are looking at a "true" relation between WSS-induced NC growth and vulnerability or simply at the effect of stenosis-induced altered hemodynamics. In addition to a larger NC area, we found significantly larger macrophage areas in plaque regions where OSI levels were low or TAWSS was high. Our findings confirmed the previously reported relation between presumed (because of the upstream location) high TAWSS and macrophage area (Dirksen et al., 1998; Fagerberg et al., 2010). To the best of our knowledge, we are the first to report a relation between low OSI and macrophage area. We found a new relation between cap thickness and WSS metrics when analyzing combinations of TAWSS and OSI tertile values. In plaque regions exposed to both low TAWSS and low OSI, cap thickness was significantly higher than in areas exposed to low TAWSS and high OSI. In addition, we observed a trend for decreasing cap thickness with increasing TAWSS in regions exposed to low OSI, confirming previous findings.[12,20]

Implications of This Study

The relation between WSS and plaque vulnerability has been a topic of discussion for many years. Finding a direct association between WSS and risk of rupture might guide diagnostic approaches to identify the patient at risk or drive therapeutic development to stagnate disease progression. A combination of various study designs is necessary for finding evidence to reach these ultimate goals: both longitudinal studies, investigating the *in vivo* relation between WSS and plaque progression (Kumar et al., 2018; Stone et al., 2018); *in vitro* assays, investigating the pathways underlying the response of endothelial cells to WSS; and cross-sectional investigations, proving the existence and applicability of these relations.

The variability in results between previous studies and ours might be due to different reasons. First, differences in geometry, size, and/or origin of the vascular bed might influence the nature of the relation between plaque composition and a hemodynamic parameter, such as WSS. This, in combination with the generally small sample sizes in this kind of studies, increases the likelihood of varying outcomes. Second, the degree of disease progression is likely to influence findings in cross-sectional setups. As plaque histology could only be obtained from subjects who are eligible for an endarterectomy procedure, the study population involved elderly patients with advanced disease. As relations between WSS and plaque composition is dynamic and disease stage–dependent, these relations could be less obvious in our study population. Third, the study setup might be of influence. Only one previous study compared TAWSS and OSI to histologically determined vulnerability features in four CEA samples (Kaazempur-Mofrad et al., 2004) and found no correlations. In all other cross-sectional studies, plaque composition was determined by *in vivo* imaging, or relative WSS levels were assumed based on axial location instead of calculations. Finally, we studied relative differences in WSS parameters, not absolute levels, in a cross-sectional setup. With time, technological improvements regarding higher *in vivo* imaging resolutions might allow patient-specific flow data and high-resolution compositional information to be obtained. This in combination with a larger study number would be required to analyze whether WSS parameters can be used as a predictor of plaque composition and ultimately rupture risk.

In conclusion, our image registration pipeline can match histology to patient-derived WSS metrics and can be used to investigate the relation between these WSS metrics and features of plaque vulnerability. We found relations between TAWSS and NC area and between TAWSS and macrophage area, which were in agreement with the literature. To our knowledge, our study is the first to show significant relations between OSI and features of human plaque vulnerability. Unlike the general assumption, low OSI areas did not always coincide with high TAWSS. In fact, areas exposed to both low OSI and low TAWSS showed significantly thicker caps.

DATA AVAILABILITY STATEMENT

The datasets presented in this article are not readily available because the data is generated in a consortium. Approval by the consortium is needed before the data can be shared. Requests to access the datasets should be directed to k.vanderheiden@erasmusmc.nl.

ETHICS STATEMENT

The studies involving human participants were reviewed and approved by the Institutional Medical Ethical Committee. The patients/participants provided their written informed consent to participate in this study.

AUTHOR CONTRIBUTIONS

KH and FG contributed to conception and design of the study. AM, KD, DP, and KG performed the experiments and/or general analysis. SK and AM performed the computational modeling. AM, KH, FG, and AS interpreted the data. AM, KH, and JW performed the statistical analysis. KH, AL, and HV organized the human carotid plaque samples. AM and KH wrote the first draft of the manuscript. All authors contributed to manuscript revision, read, and approved the submitted version.

FUNDING

AM and KH are funded by the Netherlands Heart Foundation (NHS2014T096).

REFERENCES

Ahmadi, A., Leipsic, J., Blankstein, R., Taylor, C., Hecht, H., Stone, G. W., et al. (2015). Do Plaques Rapidly Progress Prior to Myocardial Infarction? *Circ. Res.* 117, 99–104. doi:10.1161/CIRCRESAHA.117.305637

Antiga, L., Piccinelli, M., Botti, L., Ene-Iordache, B., Remuzzi, A., and Steinman, D. A. (2008). An Image-Based Modeling Framework for Patient-specific Computational Hemodynamics. *Med. Biol. Eng. Comput.* 46, 1097–1112. doi:10.1007/s11517-008-0420-1

Boekhoven, R. W., Lopata, R. G. P., van Sambeek, M. R., van de Vosse, F. N., and Rutten, M. C. M. (2013). A Novel Experimental Approach for Three-Dimensional Geometry Assessment of Calcified Human Stenotic Arteries *In Vitro*. *Ultrasound Med. Biol.* 39, 1875–1886. doi:10.1016/j.ultrasmedbio.2013.03.019

Burke, A. P., Farb, A., Malcom, G. T., Liang, Y.-h., Smialek, J. E., and Virmani, R. (1999). Plaque Rupture and Sudden Death Related to Exertion in Men with Coronary Artery Disease. *Jama* 281, 921–926. doi:10.1001/jama.281.10.921

Cicha, I., Wörner, A., Urschel, K., Beronov, K., Goppelt-Struebe, M., Verhoeven, E., et al. (2011). Carotid Plaque Vulnerability. *Stroke* 42, 3502–3510. doi:10.1161/strokeaha.111.627265

Cunningham, K. S., and Gotlieb, A. I. (2005). The Role of Shear Stress in the Pathogenesis of Atherosclerosis. *Lab. Invest.* 85, 9–23. doi:10.1038/labinvest.3700215

Daugherty, A., Tall, A. R., Daemen, M. J. A. P., Falk, E., Fisher, E. A., García-Cardeña, G., et al. (2017). Recommendation on Design, Execution, and Reporting of Animal Atherosclerosis Studies: A Scientific Statement from the American Heart Association. *Arterioscler Thromb. Vasc. Biol.* 37, e131–e157. doi:10.1161/ATV.0000000000000062

de Weert, T. T., Cretier, S., Groen, H. C., Homburg, P., Cakir, H., Wentzel, J. J., et al. (2009). Atherosclerotic Plaque Surface Morphology in the Carotid Bifurcation Assessed with Multidetector Computed Tomography Angiography. *Stroke* 40, 1334–1340. doi:10.1161/STROKEAHA.108.538439

Dirksen, M. T., van der Wal, A. C., van den Berg, F. M., van der Loos, C. M., and Becker, A. E. (1998). Distribution of Inflammatory Cells in Atherosclerotic Plaques Relates to the Direction of Flow. *Circulation* 98, 2000–2003. doi:10.1161/01.cir.98.19.2000

Eshtehardi, P., McDaniel, M. C., Suo, J., Dhawan, S. S., Timmins, L. H., Binongo, J. N. G., et al. (2012). Association of Coronary wall Shear Stress with Atherosclerotic Plaque burden, Composition, and Distribution in Patients with Coronary Artery Disease. *Jaha. Assoc.* 1, e002543. doi:10.1161/JAHA.112.002543

Fagerberg, B., Ryndel, M., Kjelldahl, J., Akyürek, L. M., Rosengren, L., Karlström, L., et al. (2010). Differences in Lesion Severity and Cellular Composition between *In Vivo* Assessed Upstream and Downstream Sides of Human Symptomatic Carotid Atherosclerotic Plaques. *J. Vasc. Res.* 47, 221–230. doi:10.1159/000255965

Falk, E., Nakano, M., Bentzon, J. F., Finn, A. V., and Virmani, R. (2013). Update on Acute Coronary Syndromes: the Pathologists' View. *Eur. Heart J.* 34, 719–728. doi:10.1093/eurheartj/ehs411

Gallo, D., Steinman, D. A., and Morbiducci, U. (2016). Insights into the Co-localization of Magnitude-Based versus Direction-Based Indicators of Disturbed Shear at the Carotid Bifurcation. *J. Biomech.* 49, 2413–2419. doi:10.1016/j.jbiomech.2016.02.010

Gimbrone, M. A., and García-Cardeña, G. (2013). Vascular Endothelium, Hemodynamics, and the Pathobiology of Atherosclerosis. *Cardiovasc. Pathol.* 22 (1), 9–15. doi:10.1016/j.carpath.2012.06.006

Gnasso, A., Irace, C., Carallo, C., De Franceschi, M. S., Motti, C., Mattioli, P. L., et al. (1997). *In Vivo* Association between Low Wall Shear Stress and Plaque in Subjects with Asymmetrical Carotid Atherosclerosis. *Stroke* 28, 993–998. doi:10.1161/01.STR.28.5.993

Groen, H. C., Gijsen, F. J. H., van der Lugt, A., Ferguson, M. S., Hatsukami, T. S., van der Steen, A. F. W., et al. (2007). Plaque Rupture in the Carotid Artery Is Localized at the High Shear Stress Region. *Stroke* 38, 2379–2381. doi:10.1161/STROKEAHA.107.484766

Groen, H. C., Simons, L., van den Bouwhuijsen, Q. J. A., Bosboom, E. M. H., Gijsen, F. J. H., Van Der Giessen, A. G., et al. (2010). MRI-based Quantification of Outflow Boundary Conditions for Computational Fluid Dynamics of Stenosed Human Carotid Arteries. *J. Biomech.* 43, 2332–2338. doi:10.1016/j.jbiomech.2010.04.039

Kaazempur-Mofrad, M. R., Isasi, A. G., Younis, H. F., Chan, R. C., Hinton, D. P., Sukhova, G., et al. (2004). Characterization of the Atherosclerotic Carotid Bifurcation Using MRI, Finite Element Modeling, and Histology. *Ann. Biomed. Eng.* 32, 932–946. doi:10.1023/b:abme.0000032456.16097.e0

Ku, D. N., Giddens, D. P., Zarins, C. K., and Glagov, S. (1985). Pulsatile Flow and Atherosclerosis in the Human Carotid Bifurcation. Positive Correlation between Plaque Location and Low Oscillating Shear Stress. *Arteriosclerosis* 5, 293–302. doi:10.1161/01.ATV.5.3.293

Kumar, A., Thompson, E. W., Lefieux, A., Molony, D. S., Davis, E. L., Chand, N., et al. (2018). High Coronary Shear Stress in Patients with Coronary Artery Disease Predicts Myocardial Infarction. *J. Am. Coll. Cardiol.* 72, 1926–1935. doi:10.1016/j.jacc.2018.07.075

Kwak, B. R., Bäck, M., Bochaton-Piallat, M.-L., Caligiuri, G., Daemen, M. J. A. P., Davies, P. F., et al. (2014). Biomechanical Factors in Atherosclerosis: Mechanisms and Clinical Implications. *Eur. Heart J.* 35 (43), 3013–3020. doi:10.1093/eurheartj/ehu353

Ladisa, J. F., Bowers, M., Harmann, L., Prost, R., Doppalapudi, A. V., Mohyuddin, T., et al. (2010). Time-efficient Patient-specific Quantification of Regional Carotid Artery Fluid Dynamics and Spatial Correlation with Plaque burden. *Med. Phys.* 37, 784–792. doi:10.1118/1.3292631

Lee, M.-Y., Wu, C.-M., Yu, K.-H., Chu, C.-S., Lee, K.-T., Sheu, S.-H., et al. (2009). Association between Wall Shear Stress and Carotid Atherosclerosis in Patients with Never Treated Essential Hypertension. *Am. J. Hypertens.* 22, 705–710. doi:10.1038/ajh.2009.77

Lee, S.-W., Antiga, L., Spence, J. D., and Steinman, D. A. (2008). Geometry of the Carotid Bifurcation Predicts its Exposure to Disturbed Flow. *Stroke* 39, 2341–2347. doi:10.1161/STROKEAHA.107.510644

Lovett, J. K., and Rothwell, P. M. (2003). Site of Carotid Plaque Ulceration in Relation to Direction of Blood Flow: an Angiographic and Pathological Study. *Cerebrovasc. Dis.* 16, 369–375. doi:10.1159/000072559

Lusis, A. J. (2000). Atherosclerosis. *Nature* 407, 233–241. doi:10.1038/35025203

Moerman, A. M., Dilba, K., Korteland, S., Poot, D. H. J., Klein, S., van der Lugt, A., et al. (2019). An MRI-Based Method to Register Patient-specific wall Shear Stress Data to Histology. *PLoS One* 14, e0217271. doi:10.1371/journal.pone.0217271

Park, J.-B., Choi, G., Chun, E. J., Kim, H. J., Park, J., Jung, J.-H., et al. (2016). Computational Fluid Dynamic Measures of wall Shear Stress Are Related to Coronary Lesion Characteristics. *Heart* 102, 1655–1661. doi:10.1136/heartjnl-2016-309299

Richardson, P., Davies, M. J., and Born, G. V. R. (1989). Influence of Plaque Configuration and Stress Distribution on Fissuring of Coronary Atherosclerotic Plaques. *The Lancet* 334, 941–944. doi:10.1016/S0140-6736(89)90953-7

Ruifrok, A. C., and Johnston, D. A. (2001). Quantification of Histochemical Staining by Color Deconvolution. *Anal. Quant. Cytol. Histol.* 23, 291–299.

Samady, H., Eshtehardi, P., McDaniel, M. C., Suo, J., Dhawan, S. S., Maynard, C., et al. (2011). Coronary Artery wall Shear Stress Is Associated with Progression and Transformation of Atherosclerotic Plaque and Arterial Remodeling in Patients with Coronary Artery Disease. *Circulation* 124, 779–788. doi:10.1161/CIRCULATIONAHA.111.021824

Schaar, J., Muller, J. E., Falk, E., Virmani, R., Fuster, V., Serruys, P. W., et al. (2004). Terminology for High-Risk and Vulnerable Coronary Artery Plaques. *Eur. Heart J.* 25, 1077–1082. doi:10.1016/j.ehj.2004.01.002

Schindelin, J., Arganda-Carreras, I., Frise, E., Kaynig, V., Longair, M., Pietzsch, T., et al. (2012). Fiji: An Open-Source Platform for Biological-Image Analysis. *Nat. Methods* 9, 676–682. doi:10.1038/nmeth.2019

Seo, T., Schachter, L. G., and Barakat, A. I. (2005). Computational Study of Fluid Mechanical Disturbance Induced by Endovascular Stents. *Ann. Biomed. Eng.* 33, 444–456. doi:10.1007/s10439-005-2499-y

Slager, C., Wentzel, J., Gijsen, F., Thury, A., van der Wal, A., Schaar, J., et al. (2005). The Role of Shear Stress in the Destabilization of Vulnerable Plaques and Related Therapeutic Implications. *Nat. Rev. Cardiol.* 2, 456–464. doi:10.1038/ncpcardio0298

Stone, P. H., Maehara, A., Coskun, A. U., Maynard, C. C., Zaromytidou, M., Siasos, G., et al. (2018). Role of Low Endothelial Shear Stress and Plaque Characteristics in the Prediction of Nonculprit Major Adverse Cardiac Events. *JACC: Cardiovasc. Imaging* 11, 462–471. doi:10.1016/j.jcmg.2017.01.031

Tuenter, A., Selwaness, M., Arias Lorza, A., Schuurbiers, J. C. H., Speelman, L., Cibis, M., et al. (2016). High Shear Stress Relates to Intraplaque Haemorrhage in Asymptomatic Carotid Plaques. *Atherosclerosis* 251, 348–354. doi:10.1016/j.atherosclerosis.2016.05.018

Vamsi Krishna, C., Chandran Suja, V., Watton, P. N., Arakeri, J. H., and Gundiah, N. (2020). Shear Stress Rosettes Capture the Complex Flow Physics in Diseased Arteries. *J. Biomech.* 104, 109721. doi:10.1016/j.jbiomech.2020.109721

van Ooij, P., Cibis, M., Rowland, E. M., Vernooij, M. W., van der Lugt, A., Weinberg, P. D., et al. (2018). Spatial Correlations between MRI-Derived wall Shear Stress and Vessel wall Thickness in the Carotid Bifurcation. *Eur. Radiol. Exp.* 2, 27. doi:10.1186/s41747-018-0058-1

Vergallo, R., Papafaklis, M. I., Yonetsu, T., Bourantas, C. V., Andreou, I., Wang, Z., et al. (2014). Endothelial Shear Stress and Coronary Plaque Characteristics in Humans. *Circ. Cardiovasc. Imaging* 7, 905–911. doi:10.1161/circimaging.114.001932

Virmani, R., Ladich, E. R., Burke, A. P., and Kolodgie, F. D. (2006b). Histopathology of Carotid Atherosclerotic Disease. *Neurosurgery* 59, S3-219–S3-227. doi:10.1227/01.NEU.0000239895.00373.E4

Virmani, R., Burke, A. P., Farb, A., and Kolodgie, F. D. (2006a). Vulnerable Plaque Symposium, Boston, Massachusetts, USA, October 2003. *J. Am. Coll. Cardiol.* 47, C1–C103. doi:10.1016/j.jacc.2005.06.090

Virmani, R., Kolodgie, F. D., Burke, A. P., Farb, A., and Schwartz, S. M. (2000). Lessons from Sudden Coronary Death. *Atvb* 20, 1262–1275. doi:10.1161/01.atv.20.5.1262

Wentzel, J. J., Chatzizisis, Y. S., Gijsen, F. J. H., Giannoglou, G. D., Feldman, C. L., and Stone, P. H. (2012). Endothelial Shear Stress in the Evolution of Coronary Atherosclerotic Plaque and Vascular Remodelling: Current Understanding and Remaining Questions. *Cardiovasc. Res.* 96 (2), 234–243. doi:10.1093/cvr/cvs217

Wentzel, J. J., Janssen, E., Vos, J., Schuurbiers, J. C. H., Krams, R., Serruys, P. W., et al. (2003). Extension of Increased Atherosclerotic wall Thickness into High Shear Stress Regions Is Associated with Loss of Compensatory Remodeling. *Circulation* 108, 17–23. doi:10.1161/01.CIR.0000078637.21322.D3

Wentzel, J. J., Schuurbiers, J. C. H., Gonzalo Lopez, N., Gijsen, F. J. H., van der Giessen, A. G., Groen, H. C., et al. (2013). *In Vivo* assessment of the Relationship between Shear Stress and Necrotic Core in Early and Advanced Coronary Artery Disease. *EuroIntervention* 9, 989–995. doi:10.4244/EIJV9I8A165

Winkel, L. C., Hoogendoorn, A., Xing, R., Wentzel, J. J., and Van der Heiden, K. (2015). Animal Models of Surgically Manipulated Flow Velocities to Study Shear Stress-Induced Atherosclerosis. *Atherosclerosis* 241, 100–110. doi:10.1016/j.atherosclerosis.2015.04.796

Xu, P., Liu, X., Zhang, H., Ghista, D., Zhang, D., Shi, C., et al. (2018). Assessment of Boundary Conditions for CFD Simulation in Human Carotid Artery. *Biomech. Model. Mechanobiol.* 17, 1581–1597. doi:10.1007/s10237-018-1045-4

Yamamoto, E., Thondapu, V., Poon, E., Sugiyama, T., Fracassi, F., Dijkstra, J., et al. (2019). Endothelial Shear Stress and Plaque Erosion. *JACC: Cardiovasc. Imaging* 12, 374–375. doi:10.1016/j.jcmg.2018.07.024

Yang, C., Canton, G., Yuan, C., Ferguson, M., Hatsukami, T. S., and Tang, D. (2010). Advanced Human Carotid Plaque Progression Correlates Positively with Flow Shear Stress Using Follow-Up Scan Data: an *In Vivo* MRI Multi-Patient 3D FSI Study. *J. Biomech.* 43, 2530–2538. doi:10.1016/j.jbiomech.2010.05.018

Yushkevich, P. A., Piven, J., Hazlett, H. C., Gerig, G., Ho, S., Gee, J. C., et al. (2006). User-guided 3D Active Contour Segmentation of Anatomical Structures: Significantly Improved Efficiency and Reliability. *Neuroimage* 31, 1116–1128. doi:10.1016/j.neuroimage.2006.01.015

Conflict of Interest: The authors declare that the research was conducted in the absence of any commercial or financial relationships that could be construed as a potential conflict of interest.

frontiers in Bioengineering and Biotechnology

ORIGINAL RESEARCH
published: 04 March 2022
doi: 10.3389/fbioe.2022.835347

Patient-Specific Cerebral Blood Flow Simulation Based on Commonly Available Clinical Datasets

Yuanyuan Shen[1†], *Yanji Wei*[2†], *Reinoud P. H. Bokkers*[3], *Maarten Uyttenboogaart*[3,4] *and J. Marc C. Van Dijk*[1*]

[1]Department of Neurosurgery, University Medical Center Groningen, University of Groningen, Groningen, Netherlands, [2]Faculty of Science and Engineering, University of Groningen, Groningen, Netherlands, [3]Department of Radiology, Medical Imaging Center, University Medical Center Groningen, University of Groningen, Groningen, Netherlands, [4]Department of Neurology, University Medical Center Groningen, University of Groningen, Groningen, Netherlands

Cerebral hemodynamics play an important role in the development of cerebrovascular diseases. In this work, we propose a numerical framework for modeling patient-specific cerebral blood flow, using commonly available clinical datasets. Our hemodynamic model was developed using Simscape Fluids library in Simulink, based on a block diagram language. Medical imaging data obtained from computerized tomography angiography (CTA) in 59 patients with aneurysmal subarachnoid hemorrhage was used to extract arterial geometry parameters. Flow information obtained from transcranial Doppler (TCD) measurement was employed to calibrate input parameters of the hemodynamic model. The results show that the proposed numerical model can reproduce blood flow in the circle of Willis (CoW) per patient per measurement set. The resistance at the distal end of each terminal branch was the predominant parameter for the flow distribution in the CoW. The proposed model may be a promising tool for assessing cerebral hemodynamics in patients with cerebrovascular disease.

Keywords: circle of Willis, hemodynamic model, cerebral blood flow, patient-specific simulation, cerebrovascular disease

OPEN ACCESS

Edited by:
Chih-Yu Yang,
Taipei Veterans General Hospital, Taiwan

Reviewed by:
Duanduan Chen,
Beijing Institute of Technology, China
Shengzhang Wang,
Fudan University, China

****Correspondence:***
J. Marc C. Van Dijk
j.m.c.van.dijk@umcg.nl

[†]*These authors have contributed equally to this work*

Specialty section:
This article was submitted to Biomechanics, a section of the journal Frontiers in Bioengineering and Biotechnology

Received: *14 December 2021*
Accepted: *31 January 2022*
Published: *04 March 2022*

Citation:
Shen Y, Wei Y, Bokkers RPH, Uyttenboogaart M and Van Dijk JMC (2022) Patient-Specific Cerebral Blood Flow Simulation Based on Commonly Available Clinical Datasets. Front. Bioeng. Biotechnol. 10:835347. doi: 10.3389/fbioe.2022.835347

1 INTRODUCTION

Fifteen percent of the total cardiac output is distributed to the brain (Burton, 1965). The circle of Willis (CoW) is a circulatory anastomosis at the base of the brain and serves as the central hub that distributes blood flow to the brain. The morphology (Kayembe et al., 1984; Chuang et al., 2008; Krasny et al., 2014) and local hemodynamic flow patterns (Li et al., 2009; Can and Du, 2015; Tuenter et al., 2016) within the CoW are associated with cerebrovascular disease, such as carotid artery stenosis and intracranial aneurysms. Numerical modeling of the blood flow through the CoW can help understand the relationship between hemodynamics in the CoW and cerebrovascular disease. However, due to the complexity of the CoW-structure and the large anatomical variation of the CoW in the population, developing a reliable patients-specific numerical model for assessing cerebral hemodynamics is a great challenge.

Various numerical models have been proposed for investigating the hemodynamics in the CoW. The zero-dimensional (0D) model is the simplest model that can provide great insight into the compensation mechanisms of the CoW (Hillen et al., 1988). One-dimensional (1D) modeling has been widely employed for studying hemodynamic effects in the CoWdue to anatomical variations and occlusions (Alastruey et al., 2007; Huang et al., 2018). The more complex three-dimensional

(3D) model became popular in recent decades, thanks to the fast development of computational fluid dynamics (CFD) (Alnæs et al., 2007). Detailed flow patterns in the intracranial aneurysms can be obtained with CFD models, which could be used to investigate the rupture risk of IAs (Asgharzadeh et al., 2020). Although the numerical models are based on the rigorous derivation of the fundamental governing equations of fluid dynamics, it was highly sensitive to the model input, particularly the inlet/outlet conditions (Venugopal et al., 2007; Balossino et al., 2009; Boccadifuoco et al., 2018).

In a recent review by Berg et al. (2019) about the hemodynamics modeling in intracranial aneurysms, it was concluded that the accuracy of the pre-and post-processing (e.g., geometry reconstruction, boundary condition setting, flow field analysis) were crucial in numerical simulation. Although many high-end numerical models have been proposed for cerebral hemodynamic studies with prospective potential for clinical practice, to the best of our knowledge, no existing numerical models have been universally accepted by clinicians to directly serve as clinical tool, due to the great uncertainty in patient-specific simulation. For patient-specific modeling, the required input not only includes patient-specific geometry, but more importantly appropriate physiological parameters, as well as proper boundary conditions per patient.

Many attempts have been made to develop patient-specific cerebral blood flow models. Zhang et al. (2016) proposed a 0D-1D coupling model and iteratively adjusted the peripheral cerebral resistance to match the measurement. They demonstrated that combining multiple sources of measurement by individual patients within the hemodynamic model can provide more comprehensive flow information. Lal et al. (2017) presented a more advanced approach for non-invasive estimation of the blood flow in the cerebral arteries, using an ensemble Kalman filter (EnKF) as an optimization tool. They utilized a 3-point clinical measurement of the transient blood flow to tune 21 input parameters. As such, they provided a feasible approach to assess blood flow at non-accessible locations in the cerebral arterial tree. Helthuis et al. (2020) introduced a patient-specific cerebral blood flow model with a structured tree and a simple auto-regulatory model at the distal boundary conditions. They validated their model with 20 healthy subjects and achieved a good agreement. Although these models can provide valuable hemodynamic information for patients, their clinical applicability was limited. The difficulties are two-fold: 1) This interdisciplinary research needs close collaboration between clinicians, biomedical engineers and computer science engineers. The clinicians commonly lack awareness on the role of hemodynamics but prefer traditional medical indices for clinical decision making (Singh et al., 2009). 2) A patient-specific model requires input that may be difficult to be obtained in clinical practice. Thus, many assumptions have to be made, which reduces the reliability of the hemodynamic assessment.

The objective of this study is to investigate cerebral hemodynamics in patients with cerebral vasospasm following aneurysmal subarachnoid hemorrhage (aSAH). A numerical model of patient-specific cerebral flow simulation is proposed, using clinical data obtained from a previously published study that investigating cerebral vasospasm in subarachnoid hemorrhage (TACTICS) study van der Harst et al. (2019). Our hemodynamic model is based on a lumped model in block diagram, which can be intuitively and easily used by clinicians. TCD measurements and common medical records are integrated to correct the input parameters of the model with a three-steps calibration procedure. The proposed model is applied to reproduce 66 cases of patient-specific hemodynamics at the time that vasospasm usually may occur. The validity of the proposed model is demonstrated by comparing the results with and without calibration procedures. The importance of the parameter calibration for the patient-specific simulation is discussed.

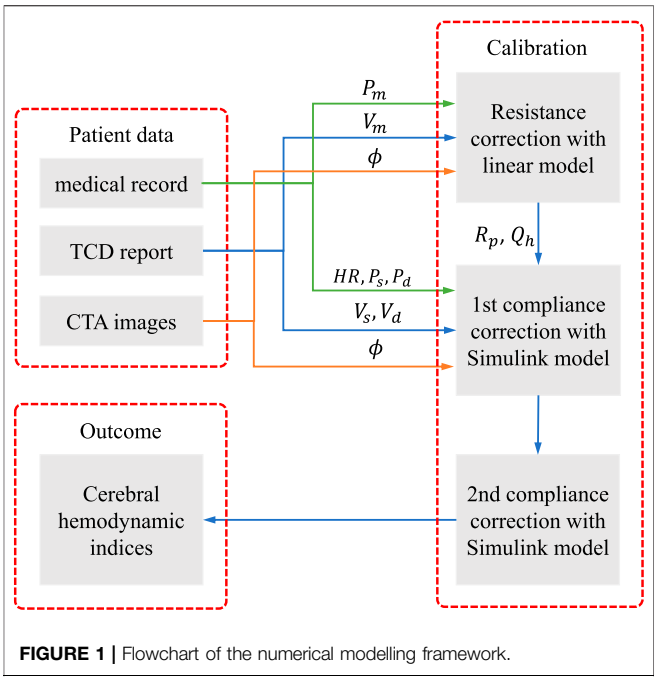

FIGURE 1 | Flowchart of the numerical modelling framework.

2 METHODOLOGY

The patients' specific data were collected from the medical record of the prospective TACTICS study, including basic medical file, CTA images and TCD reports. The CTA and TCD were performed within 24 h of each other. The brachial mean, systolic and diastolic blood pressure (P_m, P_s and P_d), and the heart rate HR were obtained from the basic medical file. The geometry of the arterial network of the CoW, e.g., the diameter of arterial segments ϕ, was extracted from CTA images. The measured mean, systolic, and diastolic blood flow velocity (V_m, V_s and V_d) at specific segments were obtained from TCD reports. **Figure 1** illustrates the steps to integrate the collected clinical data to assess patient-specific cerebral hemodynamics.

The workflow consists of three steps:

(1) determine the peripheral resistance R_p at each terminal branch and the periodical blood flow rate at the heart Q_h with a linear steady model of cerebral arterial network;

(2) correct the peripheral compliance of the body artery network and implement the tentative simulation with the Simulink model;
(3) correct the compliance of the cerebral arterial segments by adjusting the Young's modulus of the cerebral segments and implement the final simulation with the Simulink model.

The first step is to obtain the optimal blood flow distribution at the terminal branches of the cerebral arterial network, which can match the measured blood velocity by TCD. The second step provides the background pulse pressure at the entrance of the cerebral network that is in concordance with the medical record. The third step corrects the pulse waveform from the previous step to match the systolic and diastolic blood velocity by TCD measurement. The three-steps calibration procedure aims to tune the personalized model parameters to improve the fit of model predictions against measured data. The calibration is significantly important, in order to perform patient-specific simulation to reproduce the cerebral hemodynamics at the time of measurement, as will be shown in the result section.

2.1 Physiological Data

From 59 adult patients, diagnosed with aSAH within 4 days after onset, 66 sets of data were obtained. The CTA and TCD measurements have been further detailed in Shen et al. (2020).

In each CTA, the diameters of 17 cerebral segments were measured by semi-automated carotid lumen segmentation. The diameters of begin and end points of each segment were measured, while the simulation was based on an uniform diameter per segment which was calculated based on equivalent circular truncated cone volume. The thickness of arterial wall was assumed to be 25% of its radius. This was not critical, as wall thickness in conjunction with wall elasticity determine the compliance of each segment, while wall elasticity per patient per segment in the model calibration procedure will be adapted.

In each TCD, flow velocities at 11 locations on 9 cerebral segments were measured. Although patients with aSAH are prone to experience cerebral vasospasm, the measured velocity by TCD was thought to reflect the hemodynamics in the CoW at the time of CTA, since the delay between the examinations was short. Thus, patient-specific cerebral hemodynamics under vasospasm condition could be assessed by integrating the TCD and CTA measurements in the hemodynamic model.

For other required but unknown/unavailable physiological properties, such as elastic modulus of the segments, peripheral resistance, and compliance of the terminal branches, we used the same values as that in Alastruey et al. (2007), but would make corrections for each case as described in the following sections.

2.2 Simulink Model

Our hemodynamic model was developed based on Simulink, using Simscape Fluids library, which can provide an intuitive way to model the blood circulation system as a hydraulic system. The model is based on the block diagram environment that allows to easily customize the connectivity of the arterial network, as shown in **Figure 2A**.In this model, each block consists of a piece of governing equations that represents a simplified hydraulic component. The blocks are linked with connectors that form a complex hydraulic system. The system is interpreted as a set of differential or algebraic equations that are solved through symbolic formula manipulation.

In the present model, the arterial system originates from the heart (the red block) and ends at the green blocks, which depict the terminal branches. Each segment is represented with an individual blue block with the numbering and name referring to **Table 1** in Alastruey et al. (2007), while the segments in the CoW are highlighted in yellow. The polylines represents the interconnection between the segments, which passes the pressure and flow rate data in the network.

A simple heart model directly enforces a periodical inlet flow rate using the "Hydraulic Flow Rate Source" block, which describes a cardiac cycle with a half-sinusoidal flow rate wave (systole) and zero in the rest of the period (diastole) that is expressed as:

$$Q_h(t) = \begin{cases} \frac{\pi}{2\alpha_T} Q_{h,m} \sin\left(\frac{\pi t}{\alpha_T T_h}\right), & \text{if } t < t_s \\ 0, & \text{otherwise.} \end{cases} \quad (1)$$

where α_T is the ratio of systole duration over the duration of heartbeat, $\alpha_T = 0.3$ is chosen in the study; T_h is the duration of heartbeat that is obtained from the medical report; $Q_{h,m}$ is the volumetric flux of the heart, as estimated in **Section 2.3**.

The arterial segments are described with "Segmented Pipeline" block, which accounts its resistance, fluid inertia, and wall compliance, as shown in **Figure 2B**. In this block, the deformation of the segmental wall is quantified with a static pressure-diameter coefficient K_p, which establishes the relationship between pressure and internal diameter of the arterial segment at steady-state condition. K_p is determined with the common properties of each arterial segment as:

$$K_p = \frac{\phi^2}{2Eh}(1 - \sigma^2), \quad (2)$$

where ϕ is the internal diameter of the artery at the reference pressure, E is the Young's modulus of the artery, h is the thickness of the artery; σ is the Poisson's ratio, $\sigma = 0.5$. The pressure loss of the segment due to the friction is computed with the flow regime-dependable friction factor, which can take into account the possible flow separation due to the cerebral vasospasm. The friction factor in turbulent regime is determined with the Haaland approximation. In addition, the sensor blocks are used to monitor the pressure and flow rate at both ends of each segment.

A three-element Windkessel model (WK3) is embedded in the terminal branch to minimize the artificial reflection, see **Figure 2C**. A WK3 consists of two two resistances and a compliance. The "Linear Hydraulic Resistance" block is used to represent the resistance and The "Constant Volume Hydraulic Chamber" block is used to represent the peripheral compliance. Note that describing the peripheral compliance C in "Constant Volume Hydraulic Chamber" block is not straightforward, but

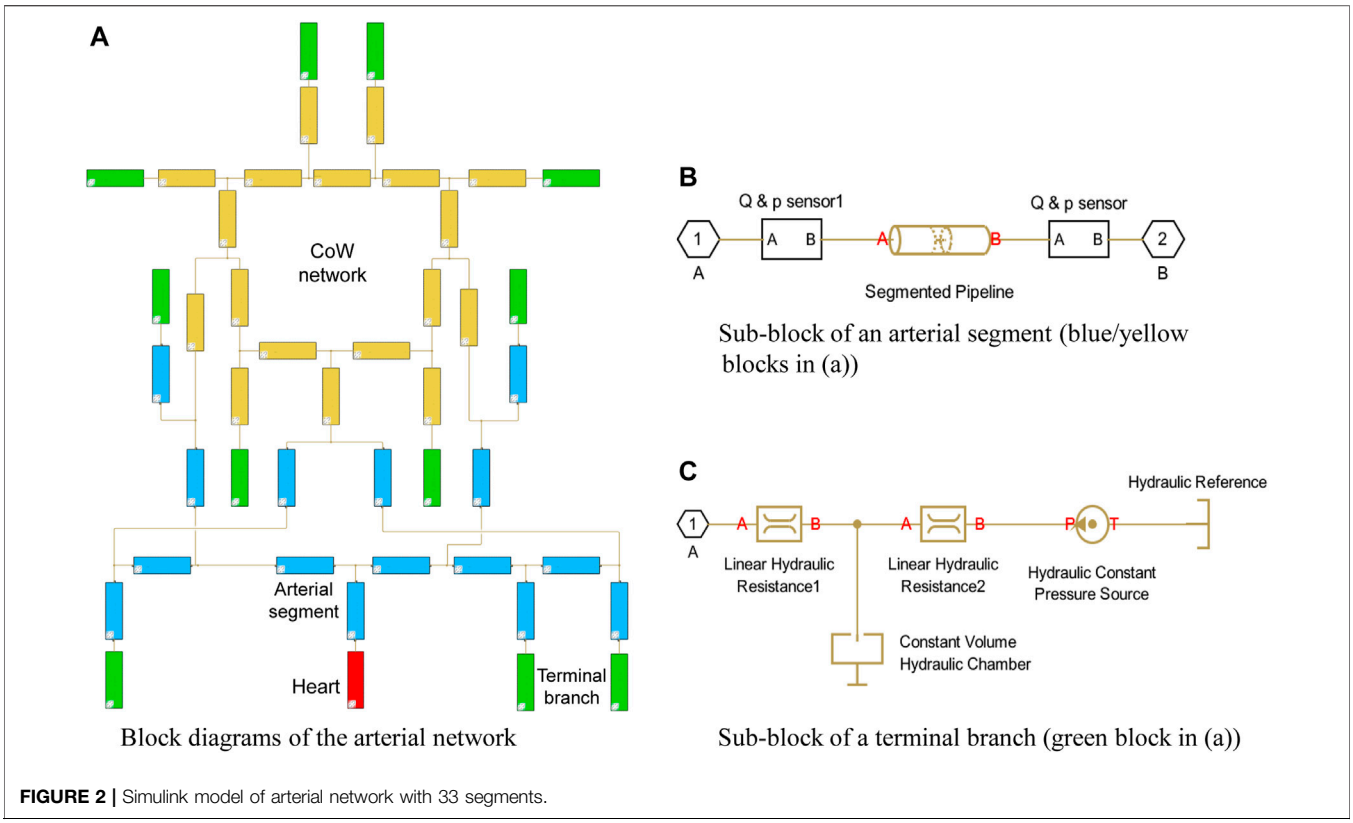

FIGURE 2 | Simulink model of arterial network with 33 segments.

TABLE 1 | ICC of various celebrate segments under various simulations.

Segment	Un-calibrated			1*st* calibrated			2*nd* calibrated		
	Q_d	Q_m	Q_s	Q_d	Q_m	Q_s	Q_d	Q_m	Q_s
ICA	0.07	0.12	0.11	0.77	0.92	0.65	0.84	0.92	0.80
MCA	0.06	0.13	0.15	0.88	0.92	0.73	0.85	0.92	0.82
ACA	0.03	0.07	0.08	0.81	0.88	0.74	0.81	0.88	0.76
PCA	0.11	0.22	0.24	0.93	0.99	0.88	0.91	0.99	0.88
BA	0.12	0.21	0.24	0.76	0.75	0.58	0.65	0.75	0.70

using an equilibrium chamber length, which is proportional to the peripheral compliance, described as:

$$l_{eq} = \frac{2C}{\pi \phi K_p}. \tag{3}$$

The peripheral compliance and two resistances in WK3 are customized per terminal branch per patient.

From the description above, we can distinguish the present model from other lumped models. The present model directly uses the hydraulic description (pipeline network) instead of the common hydraulic-electrical analogue (electrical network). It is an object-oriented model, so the interpretation of the model layout is straightforward and intuitive. We can easily build patient-specific artery network by modifying the geometrical parameters and the connectivity of the network that makes this model suitable for investigating the cerebral hemodynamics with considerable CoW variation.

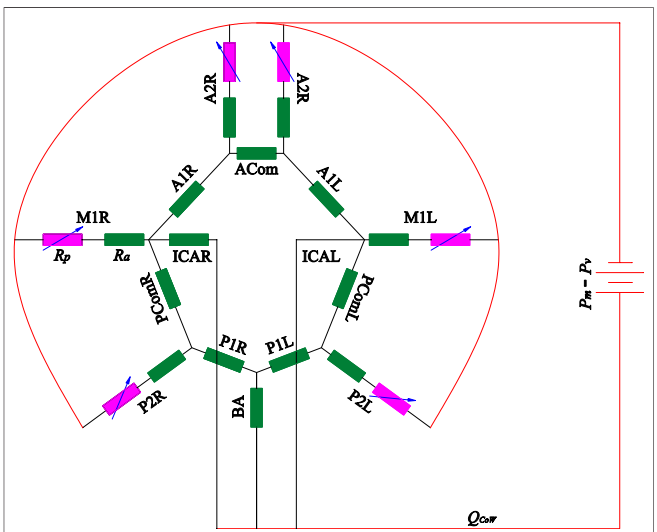

FIGURE 3 | Linear steady model of CoW arterial network.

The Simulink model uses an arterial network with 33 segments (Alastruey et al., 2007) as the basis. For each patient-specific case, the diameters of the cerebral segments are altered by the measurement from the CTA images. The resistance and the compliance in each WK3 and the wall compliance of each segment are determined by calibration procedure using TCD measurement, as described in **Section 2.3**, **2.4**.

2.3 Peripheral Resistance Correction

Analytical model by Hillen et al. (1988) has shown that the peripheral resistances dominate the flux distribution in the efferent segments and strongly influence the flux distribution in the afferent vessels. Hence, the peripheral resistance should be adapted to reflect the real flow situation at the time of the measurement for the patient-specific simulation. In the present study, a simple linear steady model was used to estimate the peripheral resistance, as shown in **Figure 3**.

The model only consisted of the CoW-segments, including three afferent arteries (left-right ICA and BA), six efferent arteries (M1L, M1R, A2L, A2R, P2L and P2R) and their interconnection. Several assumptions were made in this model: 1) The pressure drop between inlet and outlet are assumed to be equal as the difference between the mean blood pressure and the pressure at the entrance of the venous system ($\Delta P = P_m - P_v$, with $P_v = 5$ mmHg); 2) the flow is fully developed (steady and laminar), the resistance of the arterial segments R_a follows the Hagen–Poiseuille law, $R_a = 128\eta/\pi\phi^4$ with η blood viscosity; 3) the peripheral resistance R_p is considered a variable resistance, which may be adapted to alter the blood flow distribution in the CoW. Mathematically, the model is equivalent to an electric circuit with constant resistance and voltage source, which can be solved with node voltage analysis. Given specific peripheral resistance at the efferent arteries, the flow rate in each segment can be numerically obtained. TCD generally measures blood flow velocity of the target segments, while the exact location is unknown. Because the diameter varies along the vessel, the flow rate of the target segment cannot be directly determined. We measured the diameters at the start point ϕ_s and end point ϕ_e of the segment on CTA, thus the flow rate of the segment Q_m should fall within the interval $[0.25\pi\phi_e^2 V_m, 0.25\pi\phi_s^2 V_m]$, where V_m is the measured mean flow velocity. The peripheral resistance can be obtained by searching for the minimum of the norm of the relative error of the flow rates,

$$f(\boldsymbol{R}_p) = \min \sqrt{\sum_{i=1}^{N} \left(\frac{Q_n^i(\boldsymbol{R}_p) - Q_m^i}{Q_m^i} \right)^2}, \tag{4}$$

where $\boldsymbol{R}_p$ is a vector of the peripheral resistance of the six outlet arteries, $\boldsymbol{R}_p \in \mathbb{R}^6$; Q_n^i is the flow rate obtained by the linear model; N is the number of TCD measurement, $N = 9$. Due to technical limitations of TCD, e.g., inadequate acoustical temporal bone window, it is possible that there is missing data on part of the locations for some cases. In these cases, N equals to the number of locations with available data. **Eq. 4** essentially describes an optimization problem about the cerebral blood flow distribution, based on the measured velocity.

Summing up the flow rate of the three afferent arteries, we can obtain the overall blood flow rate of the CoW Q_{CoW}. Assuming 15% of the cardiac output perfuses the head (with 12% in CoW), 5% supplies each arm and 75% supplies to the rest of the body through the thoracic aorta, the mean inlet flow rate of the heart is determined as:

$$Q_{h,m} = \frac{Q_{CoW,m}}{0.12}. \tag{5}$$

Consequently, the peripheral resistance of the rest terminal branches can be determined by the ratio of the pressure drop and the flow rate. For example, the peripheral resistance of thoracic aorta is calculated by:

$$R_{body,m} = \frac{\Delta P}{0.75 Q_{h,m}}, \tag{6}$$

To minimize the reflection at the terminal branch, $R1$ in WK3 is set as the characteristic impedance of the terminal branch,

$$R1 = \frac{\rho c_0}{A_0} \tag{7}$$

with c_0 is the speed of pulse wave propagation; A_0 is the cross-section area of the segment. Then $R2$ is calculated as:

$$R2 = R_p - R1. \tag{8}$$

By using **Eq. 4**, we observed that for some cases, R_p may be smaller than $R1$, this may be caused by the uncertainty of TCD and CTA measurement, as well as the possible unexpected reflection due to the cerebral vasospasm. To avoid a negative resistance, we altered the resistance for those cases with:

$$R1 = 0.8R_p \text{ and } R2 = 0.2R_p. \tag{9}$$

With optimal peripheral resistance and proper flow rate at the heart, the obtained mean flow rate and mean blood pressure matches the measurement very well.

2.4 Compliance Correction

In a cerebral arterial network system, the mean flux distribution is mainly governed by the peripheral resistance, whereas the oscillation pattern is dominated by wall compliance and peripheral compliance. The wall compliance can be adjusted by varying Young's modulus of the segment. It is more difficult to determine the peripheral compliance because of the complex wave interaction. In the present study, the objective of the compliance correction is to match the systolic and diastolic blood pressures of the brachial artery and the systolic and diastolic cerebral blood flow velocity. Since Alastruey et al. (2007)'s model is employed as the reference model, the pressure pulse calibration can be achieved by scaling the reference model. Given a volumetric flux of the heart in the model, the amplitude of the pressure pulse is inversely proportional to the peripheral compliance. First, we computed the ratio of mean blood pressure and flow rate between patient and reference model with:

$$\alpha_1 = \frac{\Delta P Q_{ref,m}}{\Delta P_{ref} Q_{h,m}}; \tag{10}$$

where ΔP is the pressure difference between P_s and P_d, $Q_{ref,m}$ and ΔP_{ref} are the reference mean flow rate and pressure difference by the reference model, and $Q_{ref,m} = 92.6\ \mathrm{ml\,s^{-1}}$ and $\Delta P_{ref} = 55$ mmHg that is obtained from the Simulink model. The

Young's modulus and the peripheral compliance of the segments can be altered by equation:

$$E_1 = \alpha_1 E_{ref} \quad \text{and} \quad C_{p,1} = \alpha_1 C_{p,ref} \tag{11}$$

where E_{ref} and $C_{p,ref}$ represent the Young's modulus and the peripheral compliance in the reference model. With the first calibrated peripheral compliance and Young's modulus, the tentative simulation of the Simulink model is implemented. This simulation can result in a good approximation of the pulse in the aorta arteries, but may not derive a satisfactory waveform in the cerebral arteries, i.e., poor agreement with V_s and V_d in CoW, which requires a second calibration. In intra-aortic hemodynamics simulation, multiple TCD measurement can be approached by iteratively adjusting the peripheral compliance with WK3, as demonstrated by Pant et al. (2014), Bonfanti et al. (2019), while wall compliance is kept constant during the iteration. However, the intracranial arteries are stiffer than extracranial arteries, the waveform in the ICA and BA are therefor not sensitive to the peripheral compliance of the terminal branch of the CoW. Hence, the second calibration is carried out by only adjusting the Young's modulus of the cerebral arteries by an uniform factor α_2, which is estimated by:

$$\alpha_2 = \frac{\Delta Q_{ICAL,m} + \Delta Q_{ICAR,m} + \Delta Q_{BA,m}}{\Delta Q_{ICAL,n} + \Delta Q_{ICAR,n} + \Delta Q_{BA,n}}, \tag{12}$$

where ΔQ is the flow rate difference between Q_s and Q_d, with subscripts m and n refers to the measurement and numerical results respectively. The Young's modulus and the peripheral compliance of the cerebral arterial segments can be altered by equation:

$$E_2 = \alpha_2 E_1 \text{ and } C_{p,2} = \alpha_2 C_{p,1}. \tag{13}$$

Although individual calibration per arterial segment can be done with Kalman filter Pant et al. (2014), it required many iterations that made the computation inefficient. We applied an uniform factor because the flow velocity results by the tentative simulation in all cerebral segments was observed having similar trend comparing to the TCD measurement. Satisfactory results can be obtained without any complicated iteration.

2.5 Model Validation Metrics

Model validation is quantified with a number of statistical measures. The intraclass correlation coefficient (ICC) was used to assess the agreement between the results obtained by numerical simulation and the TCD measurement. Following the instruction by McGraw and Wong (1996), we selected the type of ICC(A,1) in the study, which assessed the degree of absolute agreement among simulation and measurement. The Taylor diagram (Taylor, 2001) is used to evaluate the validity of the proposed calibrations by comparing the numerical results to that by conventional boundary condition. Taylor diagram is a mathematical diagram to quantify the degree of correspondence between the modelled and observed behavior with three statistics: the Pearson correlation coefficient ρ, the centred-root-mean-square error E', and the standard deviation σ, which was intensively used in climate study (Kärnä and Baptista, 2016). Based on the definition of the three statistics, they have the following relation:

$$E'^2 = \sigma_m^2 + \sigma_n^2 - 2\sigma_m\sigma_n\rho. \tag{14}$$

where n demotes the variable by the numerical model; m demotes the measured counterpart. Making use of the law of cosines, **Eq. 14** can be interpreted as geometrical relationship of a triangle, with E', σ_m, and σ_n are the length of the sides of the triangle, and ρ is the angle between sides σ_m, and σ_n. In order to compare the data sets at multiple arterial segments in the one diagram, the normalized Taylor diagram was employed by scaling **Eq. 14** with σ_m. Thus, the measurement perfectly locates at $(R = 1, \theta = 0)$. The numerical results are displayed in polar coordinate with radial coordinate $r = \sigma_n/\sigma_m$ and angle $\theta = \arccos\rho$.

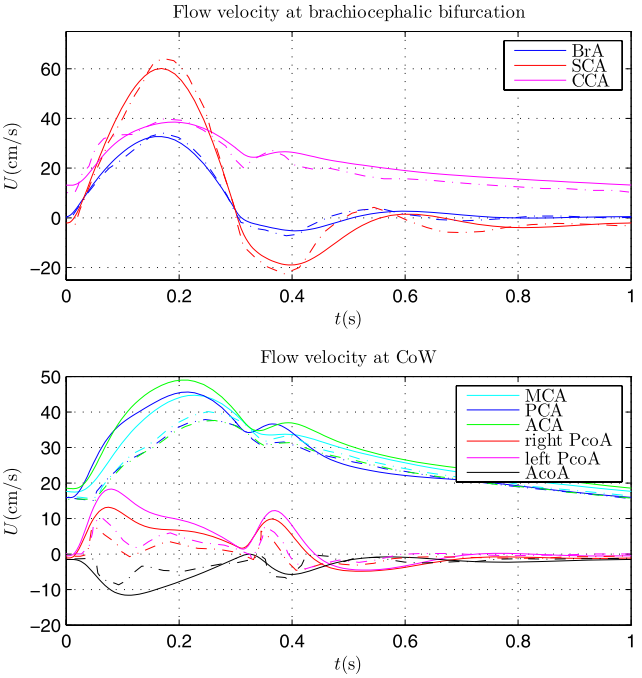

FIGURE 4 | Comparison of flow velocity at brachiocephalic bifurcation (top) and in CoW (bottom) by Simulink model (solid lines) and 1D model (dash lines).

3 RESULTS

3.1 Validation of Simulink Model

The Simulink model was firstly validated by comparing the results with that of 1D model by Alastruey et al. (2007), as presented in **Figure 4**.

The same parameters as that in Alastruey et al. (2007) were applied in the Simulink model. The flow velocity at the brachiocephalic (BrA), right subclavian (SCA) and right common carotid (CCA) showed very good agreement with that by 1D model. Some discrepancy can be found for the flow velocity in CoW. There may be two main causes: 1) wave

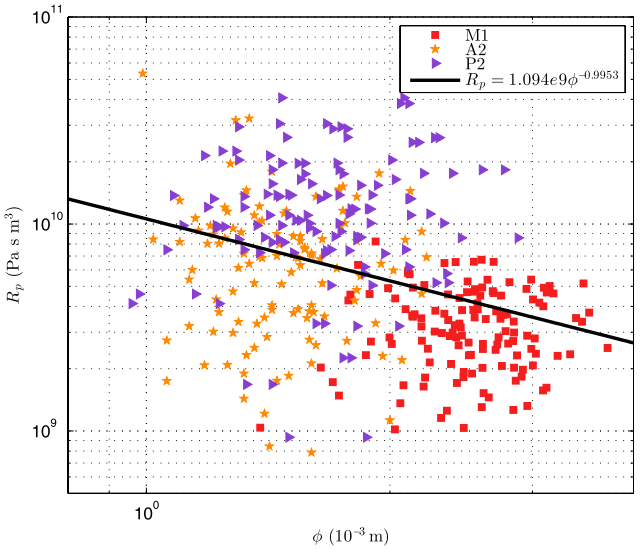

FIGURE 5 | The log-log scatter plot of the optimized peripheral resistance against the diameter of the afferent segments of CoW.

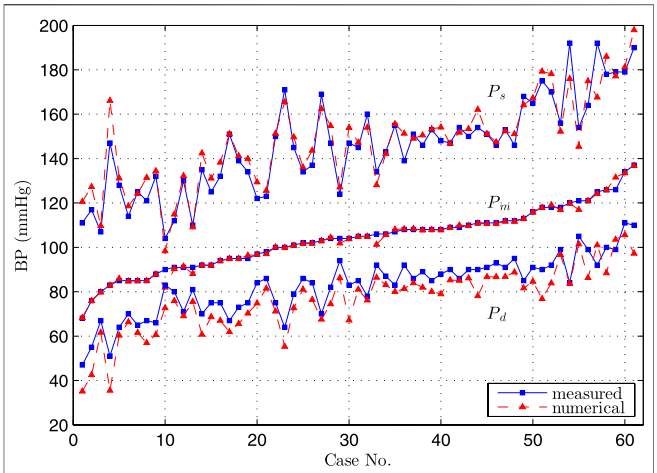

FIGURE 6 | Comparison of diastolic, systolic and mean blood pressure at brachial artery by simulation and measurement, the cases were sorted in order of low to high measured mean blood pressure.

propagation in the CoW was complex and the waveform was vulnerable to wave interference; 2) the Simulink model is a lumped model, which can be regarded as the first order discretisations of 1D systems (Milišić and Quarteroni, 2004), omitting the (nonlinear) convective acceleration term. Nevertheless, the Simulink model can capture the main waveform similar to that by 1D model, and the waveform can be further calibrated with the TCD measurement. Hence, the Simulink model can be used to investigate the patient-specific cerebral hemodynamics.

3.2 Patient-specific Simulation

In this study, 66 sets of patient-specific simulation were implemented. **Figure 5** presents the log-log scatter plot of the optimized peripheral resistance obtained by **Eq. 4** against the diameter of afferent segments of CoW, with the black line showing the log-log regression.

It can be seen that the optimized peripheral resistance showed a trench of inverse-proportional to the diameters ($R_p \propto \phi^{-0.995\ 3}$), but it was highly scattering. Alastruey et al. (2007) assumed that the peripheral resistance was inverse-proportional to the cross-sectional areas ($R_p \propto \phi^{-2}$). This suggested that this simple assumption was not valid for the patient-specific simulation as the peripheral resistance dominated the flow distribution in the CoW. In addition, the resistance of A2 segment was larger than that of P2 with similar diameter, implying that the resistance in the anterior cerebral circulation was larger than that in the posterior cerebral circulation, that was not surprise as the blood velocity in ICA was commonly larger than that in BA. **Figure 6** showed the comparison of blood pressure after the first compliance correction, i.e., **Eq. 13**.

The excellent agreement was obtained between the numerical and measured P_m, and the very good agreement was observed for P_s and P_d. Since these three parameters were commonly used to sketch the blood pressure waveform, we considered that the obtained pressure waveform by the Simulink model at the entrance of CoW represented the hemodynamic condition at the time of TCD measurement.

Figure 7 showed the comparison of flow rate in the afferent and efferent arterial segments between the measurement and the results by three simulations. The measured flow rate is indirectly obtained by solving the optimization problem of peripheral resistance, i.e., **Eq. 4**. In the "non-calibrated" simulation, we calculated the peripheral resistance and compliance in CoW of each patient based on the assumption that the blood flux of each part in the body followed a given flow distribution, and the outflow of the CoW was proportional to their initial cross-sectional areas. The agreement between the measurement and the "non-calibrated" simulation was poor, indicating that the simple assumption was not valid for the patient-specific study. The customized parameter must be applied per patient to represent the patient's hemodynamics at the time of measurement. In the "first calibrated" simulation, the calibrated peripheral resistance and compliance in the body segments was applied in the simulation. The mean flow rate in CoW by simulation agreed well with the measurement, and the results of the efferent segments outperformed that of the afferent segments. The simulation slightly underestimated the diastolic flow rate while overestimated the systolic flow rate, implying that the amplitude of the waveform was lower in simulation. In the "second calibrated" simulation, the compliance of the cerebrate segments were calibrated based on the first calibrated results. The calibration did not alter the mean flow rate in the previous simulation, while the agreement of the diastolic and systolic flow rate was improved. Since TCD-measurement has been used to calibrate the model as well as to validate the model output, it is not surprising that the flow rate by the "calibrated" simulation yields the best agreement. Based on the calibrated model, we can reproduce the cerebral hemodynamic condition for the patient at the time of

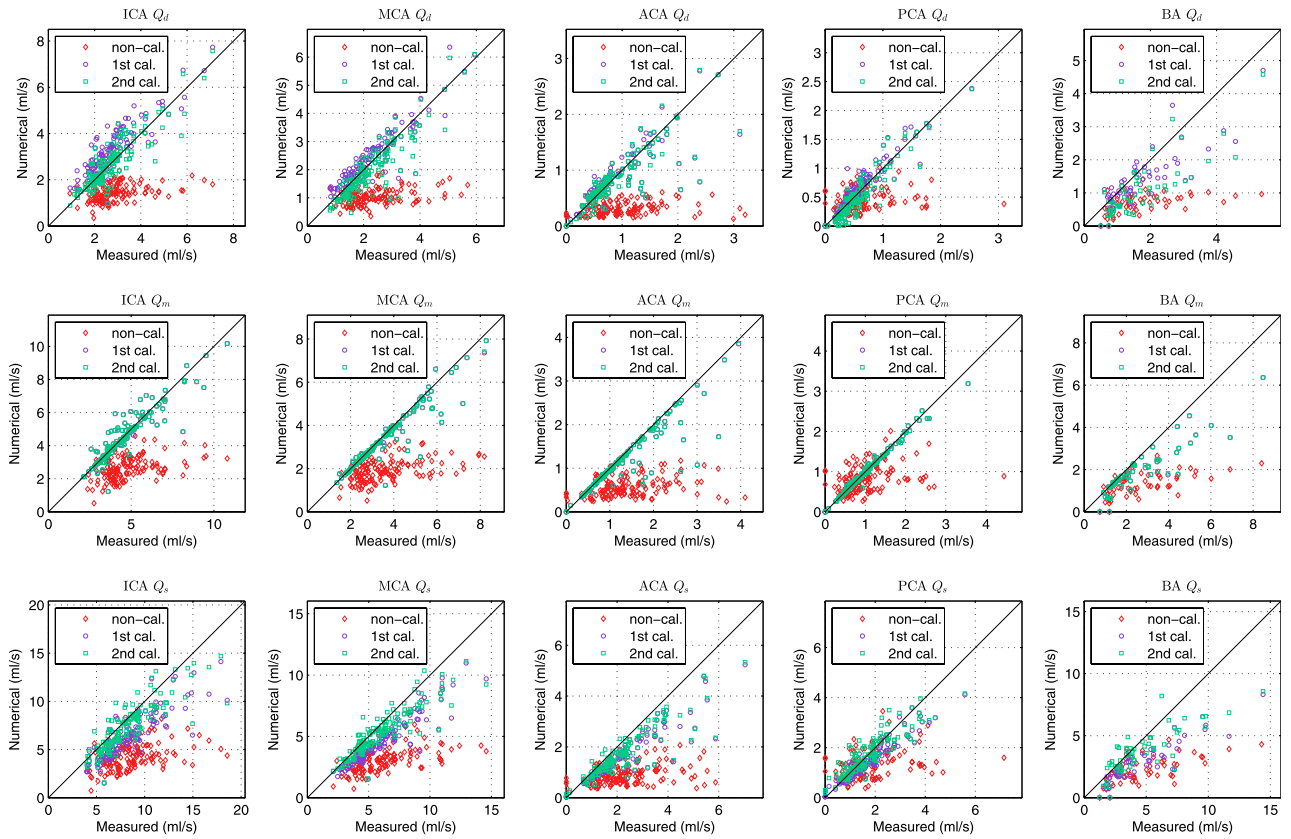

FIGURE 7 | Comparison of diastolic (1st row), mean (2nd row) and systolic (3rd row) flow rate of various cerebral segments by measurement and various simulations.

measurement and provide more comprehensive cerebral hemodynamics for the clinician.

The statistic of the results in **Figure 7** were summarized in **Table 1**. The agreement of the second calibrated results was good ($0.75 < ICC < 0.90$) to excellent ($ICC > 0.90$), except the BA. The current arterial network did not take into account the minor branches on the CoW that would introduce more error on the BA than that other segments as the BA is a relatively short segment but has the most minor branches. Q_m always presented better agreement comparing to Q_d and Q_s, this was because Q_m was strongly dominated by the peripheral resistance (the peripheral resistance was generally two order larger than the segmental resistance of the CoW). Q_d and Q_s was not only influenced by the peripheral compliance but also the compliance of the segment in CoW. Nevertheless, the agreement was satisfactory, particularly considering that only twice calibration were applied, which was significantly less iteration than using EnKF.

Figure 8 presented the normalized Taylor diagram of various segments that gave an impression of importance of the calibration procedures. The results by the three simulations were plotted in different colour, and three marker symbols were used to distinguish the results of Q_d, Q_m and Q_d. In the Taylor diagram, good results were indicated by having relatively high

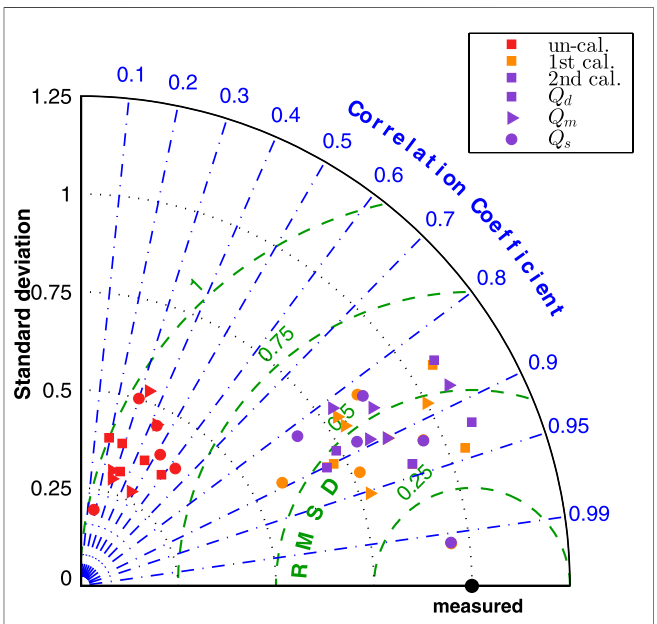

FIGURE 8 | Normalized Taylor diagram of various celebrate segments by three simulations.

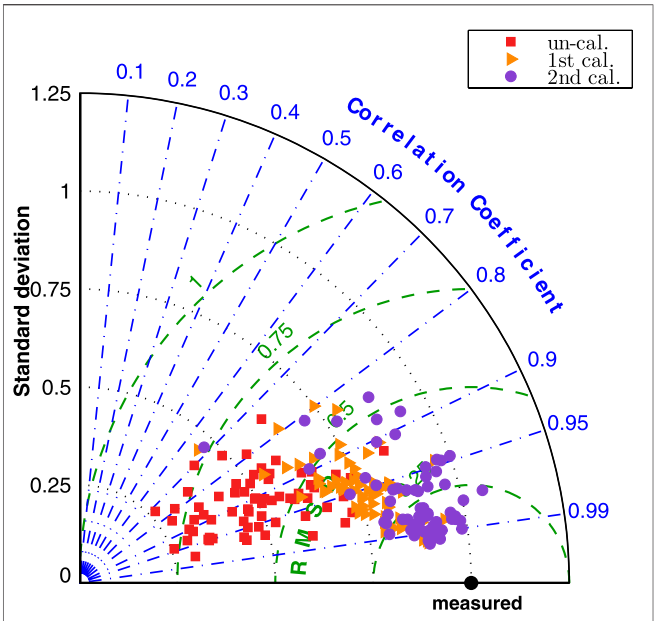

FIGURE 9 | Normalized Taylor diagram of each patient by three simulations.

correlation coefficient and low RMSE (as close to the measured point as possible). The agreement of the "un-calibrated" simulation was poor as it has very low correlation coefficient and very high RMSE, while the first and second calibrated results are much closer to the measurement.

The improvement by the calibration procedures can be seen from **Figure 9**, the normalized Taylor diagram of flow rate at 9 cerebral locations per patient. The data points cluster of the second calibrated results located at around the ~0.25 RMSE circle, while the first calibrated results shifted further from the measurement, indicating that the second calibration can describe the waveform pattern better than the first calibration.

4 DISCUSSION

When mentioning patient-specific cerebral simulation, many studies refer to the patient-specific geometry of arteries but do not take patient-specific boundary conditions into account. Our results have demonstrated the importance of boundary conditions and wall properties. Comparison by three simulations confirmed the findings of Hillen et al. (1988) that the peripheral resistance plays a predominant role in the flow distribution of the efferent arteries of the CoW. The blood flow waveform in segments in the CoW is not significantly influenced by the peripheral compliance, but would be adapted to any change of the segmental elasticity in the cerebral arterial network. To reproduce the hemodynamic environment in cerebral vasospasm, including the pulse waveform, patient-specific boundary conditions and wall properties must be corrected by integrating flow measurement. On the other hand, the model calibration relies on flow measurement on cerebral segments, which may be missing in retrospective studies, sometimes difficult to be obtained for some patients. The uncalibrated model cannot derive a reliable absolute blood flow rate, as shown in **Figure 8** that the correlation coefficient is too low. Therefore, the absolute quantitative comparison should be avoided in the statistical analysis. Alternatively, using the flow rate ratio between the segments may alleviates some of this problem and yield more meaningful results, as it can be seen from **Figure 9** that although the universal boundary condition leads to the worst results, there is not any significant difference of the correlation coefficient by three simulations. This idea is similar to the study by Lindegaard et al. (1988) that used the ratio of blood velocity in MCA and ICA by TCD to diagnose vasospasm.

The present model with personalized calibration has potential clinical applications. The model integrates the patient's morphology information and available flow measurement to provide the comprehensive cerebral hemodynamics, which may help the clinician to establish the correlations between hemodynamic indices and cerebrovascular disease. Since cerebral vasospasm due to the aSAH can result in delayed cerebral ischemia, the model can provide insight in cerebral hemodynamic development during the course of vasospasm. It may also be easily employed to predict the improvement of the blood supply after intracranial bypass operation or treatment of the carotid artery stenosis, thanks to the intuitive Simulink model. In addition, the model can also provide the boundary conditions for a patient-specific CFD model to investigate the detailed local flow in the CoW, such as the flow pattern in intracranial aneurysms. We consider the present work as the first step toward a numerical computational framework serves as a clinical decision-making tool for hemodynamic related cerebrovascular disease. The major advantage of the present model is that the model was developed with a block diagram, which is also user-friendly to the clinician. Also, the required patient's data are provided by CTA and TCD, which is commonly accessible clinical data. As such, it is easy to build up a patient-specific simulation. The calibration procedure is implemented to correct the model input with a moderate computational burden.

The present study also has limitations. The most significant limiting factor of the model is the use of indirectly obtained flow rate for calibration and validation. TCD measures flow velocity at unknown location of the target segment, the flow rate is numerically determined with a linear model of the CoW network. On one hand, the linear model obeys the law of conservation of mass and integrates the TCD velocity and dimension of segments by CTA, which estimates the flow distribution in the CoW network with minimal mass conservation error. On the other hand, the linear model uses simplified CoW network omitting the less important branch, which introduces uncertainty into the model. Finally, while we have identified the importance of the calibration procedure for patient-specific simulation, additional patient information (arterial blood pressure, TCD records) is required for calibration, which may limit its application. Nevertheless, we assume that the required data is commonly available for patients with cerebrovascular disease.

5 CONCLUSION

This paper presents a three-steps approach for implementation of a patient-specific cerebral blood flow simulation based on commonly available clinical datasets. The new approach integrates TCD and CTA data to correct the input parameters of an object-oriented hemodynamic model. Simulation with 66 sets of patient data was carried out to evaluate the validity of the model. The results demonstrated the importance of the peripheral resistance in the patient-specific cerebral blood flow simulation, and the satisfactory pulse waveforms can be reconstructed by the personalized model calibration.

The proposed method can reproduce the blood flow in the CoW where the blood flow in afferent and efferent segments was in good agreement with the TCD measurement. The model is potentially a promising tool for developing clinical understanding of cerebrovascular disease. The obtained results will be further investigated by clinical researcher to find the potential relationship between the vasospasm and the configuration of the CoW.

DATA AVAILABILITY STATEMENT

The raw data supporting the conclusion of this article will be made available by the authors, without undue reservation.

ETHICS STATEMENT

The studies involving human participants were reviewed and approved by the Institutional Ethical Review Board of the University Medical Center Groningen. Written informed consent for participation was not required for this study in accordance with the national legislation and the institutional requirements.

AUTHOR CONTRIBUTIONS

YS designed the study, collected and analyzed the data, partially drafted the manuscript. YW designed the study, developed the numerical model and performed the simulation, partially drafted the manuscript. RB assisted the data analysis, critically revised the manuscript. MU provided the patients' data, technically assisted the collection of the data, and critically revised the manuscript. JD as corresponding researcher, is responsible for the quality of the data, supervised the study, and critically revised the manuscript.

FUNDING

YS receives financial support from China Scholarship Council (CSC, File No. 201706320024).

REFERENCES

Alastruey, J., Parker, K. H., Peiró, J., Byrd, S. M., and Sherwin, S. J. (2007). Modelling the circle of willis to Assess the Effects of Anatomical Variations and Occlusions on Cerebral Flows. *J. Biomech.* 40, 1794–1805. doi:10.1016/j.jbiomech.2006.07.008

Alnæs, M. S., Isaksen, J., Mardal, K.-A., Romner, B., Morgan, M. K., and Ingebrigtsen, T. (2007). Computation of Hemodynamics in the circle of willis. *Stroke* 38, 2500–2505. doi:10.1161/STROKEAHA.107.482471

Asgharzadeh, H., Shahmohammadi, A., Varble, N., Levy, E. I., Meng, H., and Borazjani, I. (2020). A Simple Flow Classification Parameter Can Discriminate Rupture Status in Intracranial Aneurysms. *Neurosurg.* 87, E557–E564. doi:10.1093/neuros/nyaa189

Balossino, R., Pennati, G., Migliavacca, F., Formaggia, L., Veneziani, A., Tuveri, M., et al. (2009). Computational Models to Predict Stenosis Growth in Carotid Arteries: Which Is the Role of Boundary Conditions? *Comput. Methods Biomech. Biomed. Eng.* 12, 113–123. doi:10.1080/10255840802356691

Berg, P., Saalfeld, S., Voß, S., Beuing, O., and Janiga, G. (2019). A Review on the Reliability of Hemodynamic Modeling in Intracranial Aneurysms: Why Computational Fluid Dynamics Alone Cannot Solve the Equation. *Neurosurg. focus* 47, E15. doi:10.3171/2019.4.focus19181

Boccadifuoco, A., Mariotti, A., Celi, S., Martini, N., and Salvetti, M. V. (2018). Impact of Uncertainties in Outflow Boundary Conditions on the Predictions of Hemodynamic Simulations of Ascending Thoracic Aortic Aneurysms. *Comput. Fluids* 165, 96–115. doi:10.1016/j.compfluid.2018.01.012

Bonfanti, M., Franzetti, G., Maritati, G., Homer-Vanniasinkam, S., Balabani, S., and Díaz-Zuccarini, V. (2019). Patient-specific Haemodynamic Simulations of Complex Aortic Dissections Informed by Commonly Available Clinical Datasets. *Med. Eng. Phys.* 71, 45–55. doi:10.1016/j.medengphy.2019.06.012

Burton, A. C. (1965). *Physiology and Biophysics of the Circulation*. Chicago: Year Book Medical Publishers.

Can, A., and Du, R. (2015). Association of Hemodynamic Factors with Intracranial Aneurysm Formation and Rupture. *Neurosurgery* 78, 510–520. doi:10.1227/NEU.0000000000001083

Chuang, Y.-M., Liu, C.-Y., Pan, P.-J., and Lin, C.-P. (2008). Posterior Communicating Artery Hypoplasia as a Risk Factor for Acute Ischemic Stroke in the Absence of Carotid Artery Occlusion. *J. Clin. Neurosci.* 15, 1376–1381. doi:10.1016/j.jocn.2008.02.002

Helthuis, J. H. G., van Doormaal, T. P. C., Amin-Hanjani, S., Du, X., Charbel, F. T., Hillen, B., et al. (2020). A Patient-specific Cerebral Blood Flow Model. *J. Biomech.* 98, 109445. doi:10.1016/j.jbiomech.2019.109445

Hillen, B., Drinkenburg, B. A. H., Hoogstraten, H. W., and Post, L. (1988). Analysis of Flow and Vascular Resistance in a Model of the Cricle of willis. *J. Biomech.* 21, 807–814. doi:10.1016/0021-9290(88)90013-9

Huang, G. P., Yu, H., Yang, Z., Schwieterman, R., and Ludwig, B. (2018). 1d Simulation of Blood Flow Characteristics in the circle of willis Using Thinks. *Comput. Methods Biomech. Biomed. Eng.* 21, 389–397. doi:10.1080/10255842.2018.1468439

Kärnä, T., and Baptista, A. M. (2016). Evaluation of a Long-Term Hindcast Simulation for the columbia River Estuary. *Ocean Model.* 99, 1–14. doi:10.1016/j.ocemod.2015.12.007

Kayembe, K. N., Sasahara, M., and Hazama, F. (1984). Cerebral Aneurysms and Variations in the circle of willis. *Stroke* 15, 846–850. doi:10.1161/01.STR.15.5.846

Krasny, A., Nensa, F., Sandalcioglu, I. E., Göricke, S. L., Wanke, I., Gramsch, C., et al. (2014). Association of Aneurysms and Variation of the A1 Segment. *J. Neurointervent Surg.* 6, 178–183. doi:10.1136/neurintsurg-2013-010669

Lal, R., Nicoud, F., Bars, E. L., Deverdun, J., Molino, F., Costalat, V., et al. (2017). Non Invasive Blood Flow Features Estimation in Cerebral Arteries from Uncertain Medical Data. *Ann. Biomed. Eng.* 45, 2574–2591. doi:10.1007/s10439-017-1904-7

Li, Z.-Y., Taviani, V., Tang, T., Sadat, U., Young, V., Patterson, A., et al. (2009). The Mechanical Triggers of Plaque Rupture: Shear Stressvspressure Gradient. *BJR* 82, S39–S45. doi:10.1259/bjr/15036781

Lindegaard, K.-F., Nornes, H., Bakke, S. J., Sorteberg, W., and Nakstad, P. (1988). "Cerebral Vasospasm after Subarachnoid Haemorrhage Investigated by Means of Transcranial Doppler Ultrasound," in *Proceedings of the 8th European Congress of Neurosurgery Barcelona, September 6–11, 1987* (Barcelona: Springer), 81–84. doi:10.1007/978-3-7091-8975-7_16

McGraw, K. O., and Wong, S. P. (1996). Forming Inferences about Some Intraclass Correlation Coefficients. *Psychol. Methods* 1, 30–46. doi:10.1037/1082-989x.1.1.30

Milišić, V., and Quarteroni, A. (2004). Analysis of Lumped Parameter Models for Blood Flow Simulations and Their Relation with 1d Models. *ESAIM Math. Model. Numer. Anal.* 38, 613–632. doi:10.1051/m2an:2004036

Pant, S., Fabrèges, B., Gerbeau, J.-F., and Vignon-Clementel, I. E. (2014). A Methodological Paradigm for Patient-specific Multi-Scale Cfd Simulations: from Clinical Measurements to Parameter Estimates for Individual Analysis. *Int. J. Numer. Meth. Biomed. Engng.* 30, 1614–1648. doi:10.1002/cnm.2692

Shen, Y., Wei, Y., Bokkers, R. P. H., Uyttenboogaart, M., and van Dijk, J. M. C. (2020). Study Protocol of Validating a Numerical Model to Assess the Blood Flow in the circle of willis. *BMJ open* 10, e036404. doi:10.1136/bmjopen-2019-036404

Singh, P. K., Marzo, A., Coley, S. C., Berti, G., Bijlenga, P., Lawford, P. V., et al. (2009). The Role of Computational Fluid Dynamics in the Management of Unruptured Intracranial Aneurysms: a Clinicians' View. *Comput. Intell. Neurosci.* 2009, 760364. doi:10.1155/2009/760364

Taylor, K. E. (2001). Summarizing Multiple Aspects of Model Performance in a Single Diagram. *J. Geophys. Res.* 106, 7183–7192. doi:10.1029/2000JD900719

Tuenter, A., Selwaness, M., Arias Lorza, A., Schuurbiers, J. C. H., Speelman, L., Cibis, M., et al. (2016). High Shear Stress Relates to Intraplaque Haemorrhage in Asymptomatic Carotid Plaques. *Atherosclerosis* 251, 348–354. doi:10.1016/j.atherosclerosis.2016.05.018

van der Harst, J. J., Luijckx, G. R., Elting, J. W. J., Bokkers, R. P. H., van den Bergh, W. M., Eshghi, O. S., et al. (2019). Transcranial Doppler versus CT-angiography for Detection of Cerebral Vasospasm in Relation to Delayed Cerebral Ischemia after Aneurysmal Subarachnoid Hemorrhage: A Prospective Single-center Cohort Study: The Transcranial Doppler and CT-angiography for Investigating Cerebral Vasospasm in Subarachnoid Hemorrhage (TACTICS) Study. *Crit. Care Explor.* 1, e0001. doi:10.1097/CCE.0000000000000001

Venugopal, P., Valentino, D., Schmitt, H., Villablanca, J. P., Viñuela, F., and Duckwiler, G. (2007). Sensitivity of Patient-specific Numerical Simulation of Cerebal Aneurysm Hemodynamics to Inflow Boundary Conditions. *J. Neurosurg.* 106, 1051–1060. doi:10.3171/jns.2007.106.6.1051

Zhang, H., Fujiwara, N., Kobayashi, M., Yamada, S., Liang, F., Takagi, S., et al. (2016). Development of a Numerical Method for Patient-specific Cerebral Circulation Using 1D-0D Simulation of the Entire Cardiovascular System with SPECT Data. *Ann. Biomed. Eng.* 44, 2351–2363. doi:10.1007/s10439-015-1544-8

Conflict of Interest: The authors declare that the research was conducted in the absence of any commercial or financial relationships that could be construed as a potential conflict of interest.

Publisher's Note: All claims expressed in this article are solely those of the authors and do not necessarily represent those of their affiliated organizations, or those of the publisher, the editors and the reviewers. Any product that may be evaluated in this article, or claim that may be made by its manufacturer, is not guaranteed or endorsed by the publisher.

frontiers in Bioengineering and Biotechnology

REVIEW
published: 07 March 2022
doi: 10.3389/fbioe.2022.836680

Haemodynamic Wall Shear Stress, Endothelial Permeability and Atherosclerosis—A Triad of Controversy

*Peter D. Weinberg**

Department of Bioengineering, Imperial College London, London, United Kingdom

A striking feature of atherosclerosis is its patchy distribution within the vascular system; certain arteries and certain locations within each artery are preferentially affected. Identifying the local risk factors underlying this phenomenon may lead to new therapeutic strategies. The large variation in lesion prevalence in areas of curvature and branching has motivated a search for haemodynamic triggers, particular those related to wall shear stress (WSS). The fact that lesions are rich in blood-derived lipids has motivated studies of local endothelial permeability. However, the location of lesions, the underlying haemodynamic triggers, the role of permeability, the routes by which lipids cross the endothelium, and the mechanisms by which WSS affects permeability have all been areas of controversy. This review presents evidence for and against the current consensus that lesions are triggered by low and/or oscillatory WSS and that this type of shear profile leads to elevated entry of low density lipoprotein (LDL) into the wall via widened intercellular junctions; it also evaluates more recent evidence that lesion location changes with age, that multidirectional shear stress plays a key role, that LDL dominantly crosses the endothelium by transcytosis, and that the link between flow and permeability results from hitherto unrecognised shear-sensitive mediators.

Keywords: Hemodynamics, endothelial cell, OSI, transWSS, vesicles, follistatin-like 1, FSTL1, inflammation

OPEN ACCESS

Edited by:
Chih-Yu Yang,
Taipei Veterans General Hospital, Taiwan

Reviewed by:
Aike Qiao,
Beijing University of Technology, China
Bingmei M. Fu,
City College of New York (CUNY), United States
Diego Gallo,
Politecnico di Torino, Italy

***Correspondence:**
Peter D. Weinberg
p.weinberg@imperial.ac.uk

Specialty section:
This article was submitted to Biomechanics, a section of the journal Frontiers in Bioengineering and Biotechnology

Received: *15 December 2021*
Accepted: *20 January 2022*
Published: *07 March 2022*

Citation:
Weinberg PD (2022) Haemodynamic Wall Shear Stress, Endothelial Permeability and Atherosclerosis—A Triad of Controversy. Front. Bioeng. Biotechnol. 10:836680. doi: 10.3389/fbioe.2022.836680

INTRODUCTION

A striking feature of atherosclerosis is its non-uniform distribution within the arterial system. Some arteries, and some regions within individual arteries, remain free of disease even when others have developed it to a life-threatening extent (Mitchell and Schwartz, 1965). This feature implies the existence of powerful local risk factors. The identification of global risk factors such as hypertension and hyperlipidaemia has led to the development of therapies that significantly reduce the prevalence of the disease and its sequelae. The identification of local risk factors has been mired in controversy and currently no therapies are based on them.

An early hypothesis (Anitschkow, 1933) was the causal chain:

mechanical factors→enhanced uptake of circulating lipids into the wall→inflammation→disease.

A more modern addition to this insudation theory or lipid hypothesis is that the lipid needs to be modified in some way—perhaps by oxidation, aggregation or both (Quinn et al., 1987; Williams and Tabas, 1995; Javed et al., 1999; Wen and Leake, 2007; Wen et al., 2019)—before an inflammatory

response occurs. These ideas underlie the use of statins to control the development of the disease, and an extensive search for therapeutic effects of dietary antioxidants.

Despite apparent acceptance of the insudation theory, there has been debate about where lesions occur, the stresses responsible, the direction of lipid transport that is critical, the mediators linking mechanical stresses to transport, and the nature of the transport pathway. In order to derive new therapies that confer on disease-prone arteries the properties of disease-resistant ones, resolution of these controversies is required. Misidentification of, say, the mechanical triggers or the relevant transport route could lead to the design of ineffective interventions targeting inappropriate pathways. This review provides an overview of the debates and introduces recent developments in the field that suggest novel targets. It is structured and summarised as follows:

Historical Background

- Early studies showed that cholesterol-fed rabbits develop lesions downstream of aortic branch points; the pattern was explained by high haemodynamic wall shear stress (WSS) elevating endothelial permeability to circulating lipoproteins. In people, lesions were later found to occur upstream of branches; the human pattern was attributed to low and oscillatory WSS and could not be explained by elevated permeability.

Contradictions Can Be Resolved by Taking Age Into Account

- Patterns of lesions in rabbits and people switch location with age, and in the same way. The previous contradiction is attributed to immature rabbits being inappropriately compared with mature people. Age-related patterns of insudation can explain both patterns.

The Emergence of Other Disease Patterns

- Lesions occur not only upstream and downstream of branches: intermediate patterns are seen and there may be a series or continuum of changes with age.

Underlying Mechanisms

- Many other types of mechanical stresses have been implicated in atherogenesis. Is it the relation between mechanical forces and atherogenesis that changes with age, or is it the mechanical forces themselves that change? Flow-dependent NO release and its effect on permeability appear to change with age, supporting the former, but the pattern of endothelial morphology also changes, supporting the latter.

Computational Studies of Flow

- Numerical simulations have been used to further investigate if flow patterns change with age. They provide little evidence that time average or oscillatory WSS change substantially.

Potential Importance of Multidirectional Flow

- A systematic review showed that the strength of evidence for the low WSS theory is not as strong as widely supposed. The pattern of an alternative WSS metric, the transverse WSS, changes with age and correlates much better with lesion location and elevated permeability.

Further Investigation of Mechanisms Relating Flow to Permeability

- *In vivo* studies employing modern techniques suggest that "hotspots" of high endothelial permeability account for only a small fraction of uptake, at least for albumin-sized molecules, and *in silico* studies that take into account the presence of the glycocalyx suggest that concentration polarisation at the endothelial surface also has a limited effect. Recent *in vitro* studies suggest transendothelial transport of the largest macromolecules occurs by transcytosis and that it is increased by multidirectional flow.

Proposal of a Secreted Mediator

- Endothelial cells exposed to uniaxial flow *in vitro* release a soluble mediator that suppresses transcytosis of LDL. Cells exposed to multidirectional flow do not. The mediator also has anti-inflammatory effects.

The review finishes with three sections that 1) discuss limitations to the above synthesis, 2) present perspectives and suggest future work, and 3) draw conclusions.

HISTORICAL BACKGROUND

Statements about mechanical stresses and atherosclerosis appear in the 19th century (Rindfleisch, 1872) but the experimental study of localising factors began in the early 20th century with the work of Anitschkow (alt.—Anichkov, Russian—Ани́чков) and his colleagues. A retrospective review of that work (Anitschkow, 1933) remains of interest today for its scientific content, as well as for its historical significance.

The first step by the St Petersburg group was the development of the cholesterol-fed rabbit model. The Russian school at that time held that atherosclerosis was a natural consequence of aging, and also that aging was accelerated by eating meat. Rabbits fed meat did indeed develop an atherosclerosis-like disease (Steinberg, 2013). Anitschow showed, however, that it was the cholesterol in the meat that was responsible: rabbits fed diets supplemented only with cholesterol also developed lesions.

Anitschkow (1933) drew particular attention to the remarkable pattern of lipid staining seen around the ostia of side branches of the aorta. Lesions occurred in an arrowhead pattern surrounding the downstream half of the origins of the intercostal arteries (**Figure 1A**). These branch points have subsequently received much study and are the main focus of the present review. (**Supplementary Material Figure S1** shows the location of each arterial region discussed in this review; the

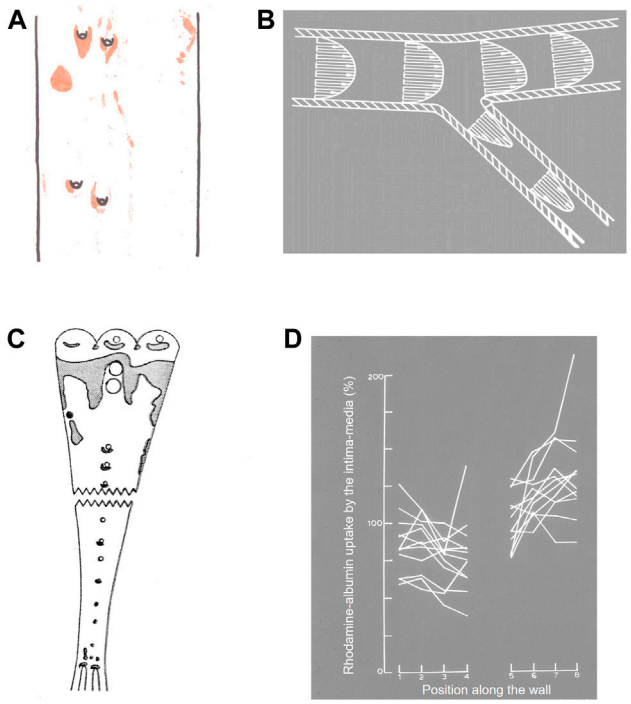

FIGURE 1 | (A) Watercolour from Anitschkow (1933) of lipid staining (red) near four intercostal branch ostia in a cholesterol-fed rabbit. The thoracic aorta is viewed *en face* and mean aortic flow is from top to bottom. **(B)** Conceptualisation of velocity vectors and velocity profiles in a 2-D model of a branching artery, after Fry (1969). **(C)** Uptake of Evans' Blue Dye (shaded areas) in the aorta of a pig (Somer and Schwartz, 1971). Note that pigs have unpaired intercostal ostia, unlike the paired ostia in human and rabbit aortas. The aorta is viewed *en face* and mean aortic flow is from top to bottom. **(D)** Uptake of rhodamine-labelled albumin into the aortic wall of rabbits up to approximately one branch diameter upstream (positions 1→4) and downstream (positions 5→8) of 12 intercostal ostia (positions 4→5), 3 h after the tracer was administered (Weinberg, 1988).

large-scale structure of the normal and diseased artery wall (Pang et al., 2021b) is shown in **Supplementary Material Figure S2**.)

It had been known since the 1850s, when microscopes were applied to pathology, that the lipid deposition in atherosclerosis occurs within the wall rather than on its surface. Anitschkow reasoned that the dietary cholesterol entered the bloodstream and that the patchy nature of the disease resulted from a patchy entry of circulating "lipoids" into the wall, as part of a process similar to the one in which lymph is formed by filtration of plasma across capillary walls. This hypothesis was supported by experiments that introduced the intravital dye Trypan Blue into the circulation of frogs. Trypan Blue, like its isomer Evans' Blue Dye (EBD), binds to circulating proteins, particularly albumin, and is carried into the wall when they enter it, leading to a blue colouration in areas where entry is particularly rapid. Petroff (1922) observed blue patches on the flow divider of branch points in large mesenteric vessels. Anitschkow (1933) suggested that mechanical forces led to this spatial variation in wall transport properties, but did not speculate further.

It was Fry (1969) who extended this view by proposing that the mechanical trigger is a pathologically elevated level of haemodynamic wall shear stress, the force per unit area acting parallel to the endothelium as a result of the flow of blood. His fluid mechanical argument is shown in **Figure 1B**. For simplicity, blood was assumed to be a continuous fluid with Newtonian rheology, flow to be steady, walls to be rigid and the geometry to be two-dimensional. Upstream of the side branch, the velocity profile is at least partially developed—that is, layers at considerable distances from the wall are slowed by viscous drag—and WSS, which is proportional to the near-wall velocity gradient, is therefore relatively low. It is the slower moving blood near the wall that enters the branch, while more rapidly moving blood, previously near the centre of the vessel, impinges on the flow divider of the branch. This fast-moving blood itself gets slowed by viscous interactions as it moves downstream but, in the region before this occurs, the velocity gradient and hence WSS are elevated. WSS would, by the same argument, be relatively high on the flow divider of a symmetrical bifurcation and lower on the outer ("lateral") walls, especially if separation were to occur.

Fry (1969) acutely exposed the luminal surface of arteries to various fluid mechanical stresses and found that WSS magnitudes above 400 dyn/cm^2 injured and, at a sufficiently high level, even removed the endothelial cells, leading to elevated influx of EBD-labelled albumin and, it was assumed, the larger lipoproteins.

Subsequent publications from Fry and colleagues recognised greater complexity: that different endothelial responses might occur over different time courses, that the structure of the underlying wall might influence the response, and that subtle features of branch geometry might have profound influences on the distribution of WSS (e.g. Fry, 1973). Nevertheless, the original hypothesis was intuitively satisfying and became the consensus view. It was supported by much subsequent data. Quantitative mapping of lesions in rabbits fed a high cholesterol diet for short periods or a lower cholesterol diet for longer periods, or in rabbits that were hypercholesterolaemic as a result of genetic mutations, all confirmed the Anitschkow pattern of lipid deposition in the aortic wall around ostia of side branches (Cornhill and Roach, 1976; Roach et al., 1978; Forster et al., 1996). Studies with intravital dyes confirmed that elevated uptake occurrs in the equivalent regions in the pig (Somer and Schwartz, 1971; **Figure 1C**). Such studies can be criticised: EBD binds to elastin (Adams, 1981) and collagen (Heinle and Lindner, 1984) once in the wall and its concentration may therefore be affected by variation in wall structure as well as in transport, whilst a fraction of the dye circulates in its free form (Lindner and Heinle, 1982) and may enter the wall by routes not available to macromolecules. However, quantitative measurements of transport using radiolabelled low-density lipoprotein (LDL) (Schwenke and Carew, 1988) or albumin covalently labelled with a fluorescent dye (Weinberg, 1988) showed that net uptake of these circulating macromolecules was likewise elevated downstream of branches in the rabbit aorta (**Figure 1D**), even though elevated EBD accumulation is hard to demonstrate in this species (Friedman and Byers, 1963).

Despite this wealth of evidence, issues arose in applying Fry's high-shear hypothesis to human disease. Mitchell and Schwartz (1965) had already noted a different distribution of lipid staining

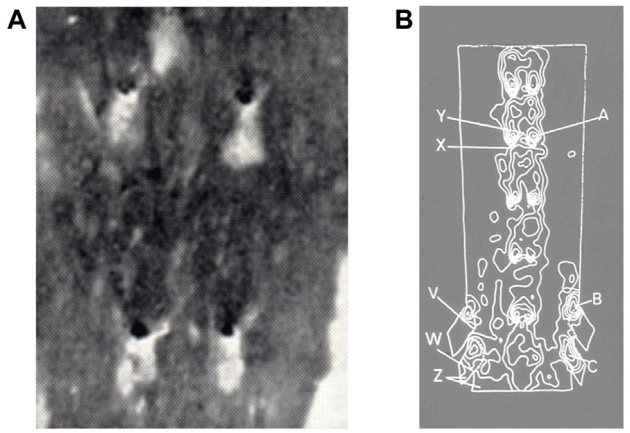

FIGURE 2 | (A) Lipid staining (black) near four intercostal branch ostia in an adult human aorta, viewed *en face* with mean aortic flow from top to bottom (Mitchell and Schwartz, 1965). **(B)** Contour map of lesion prevalence in the human aorta, opened ventrally and viewed *en face* with mean aortic flow from top to bottom. Flow dividers on the dorsal wall are indicated by bright "horseshoe" shapes. Prevalence is high at point A and low at point X (Svindland and Walløe, 1985).

in *post mortem* human specimens: Sudanophilia occurred in a dorsal streak in the descending thoracic aorta but there was striking sparing around and immediately distal to the ostia of the intercostal arteries (**Figure 2A**). Caro et al. (1971) subsequently quantified the distribution in the initial segment of the large branches of the human abdominal aorta, finding that fatty streaks were less prevalent in the quadrant containing the flow divider than in other quadrants. These distributions of human disease were confirmed and extended by Svindland and Walloe (1985; **Figure 2B**) and by Cornhill et al. (1990). Disease was again found in the inflow tract of large abdominal branches but it was also shown in the aortic wall upstream of the branches. In the thoracic segment, lipid staining was found to be maximal upstream of intercostal ostia and low distal to them.

From **Figure 1B**, it is apparent that WSS should be elevated on both the aortic and the branch side of the flow divider. Caro et al. (1971) therefore concluded from their study of lesions in the initial segment of branches that high WSS protects against the development of human disease, which instead occurs in areas of low WSS. Note that the disagreement with the high WSS hypothesis of Fry concerns the location of lesions, not the nature of local blood flow.

The low shear hypothesis of Caro et al. has been modified somewhat. Ku et al. (1985) compared the distribution of intimal thickening in the human carotid bifurcation with laser Doppler measurements of flow in anatomically realistic models of the same specimens. This work showed that intimal thickening was highest in regions where not only was time average WSS low but values of a metric called the Oscillatory Shear Index (OSI) were high. Indeed, the correlation with the OSI was stronger than with mean WSS.

Despite its name, the OSI captures any instantaneous WSS vector that is not aligned with the mean WSS vector and not just those that are at 180° degrees to it, as in oscillatory flow. As later defined by He and Ku (1996):

$$\mathbf{OSI} = \frac{1}{2}\left(1 - \frac{\left|\int_0^T \vec{\tau}_w \mathbf{d}t\right|}{\int_0^T \left|\vec{\tau}_w\right| \mathbf{d}t}\right) = \frac{1}{2}\left(1 - \frac{\left|\vec{\tau}_{mean}\right|}{\mathbf{TAWSS}}\right)$$

$$\text{where } \vec{\tau}_{mean} = \frac{1}{T}\int_0^T \vec{\tau}_w \mathbf{d}t$$

and $\vec{\tau}_w$ represents the instantaneous WSS vector, t the time and T the duration of the cardiac cycle.

The OSI tends to be high where time average WSS is low and *vice versa*. The two hypotheses have thus been conflated to some extent.

Today, the low/oscillatory WSS hypothesis is the consensus view; the paper of Caro et al. (1971), now 50 years old, is a citation classic. However, the hypothesis took many years to become widely accepted. This probably reflects the contradiction with the results of experimental studies in animals, particularly rabbits, where the location of lesions is not only different but correlates with the pattern of elevated uptake of plasma macromolecules by the wall. Caro et al. (1971) assumed that the same pattern of uptake occurred in people. To account for the discrepancy in lesion location, they had to assume different mechanisms: that plasma cholesterol concentrations were higher than wall concentrations in the rabbit, and disease therefore occurred where transport between the two compartments was fastest, whereas concentrations of cholesterol or a modified, atherogenic version of it were higher in the wall than in plasma in people, meaning that disease would occur where transport between the two compartments was slowest. This concept predicts mirror-image patterns of disease in the two species.

A corollary of the proposal, developed in a mathematical appendix to the paper, is that the level of disease in people must be independent of plasma cholesterol concentrations. Although that might have been tenable in 1971, many subsequent studies have demonstrated a link and the more recent success of cholesterol-lowering statins has made the connection practically incontrovertible. Thus there is a fundamental flaw at the centre of our understanding of atherogenesis: the accepted haemodynamic explanation for the localisation of the disease is incompatible with the most widely used therapy and the insudation theory on which it is based.

Rabbit models of atherosclerosis have been superseded to a large extent by genetically modified mouse models. Furthermore, although Anitschkow's introduction of the cholesterol-fed rabbit is eulogised by many (e.g. Steinberg, 2004), it has been anathematised by others (e.g. Stehbens, 1999). Patterns of disease and transport obtained in the rabbit are not widely discussed at present and the central inconsistency emphasised above is rarely mentioned. However, rabbits are phylogenetically the closest species to human beings outside of the primate order. Also, many haemodynamic stresses and non-dimensional groups obey allometric scaling laws and the discrepancy in their value between mice and people is therefore much greater than the

discrepancy between rabbits and people. Aortic WSS, for example, depends on body mass raised to the inverse 3/8ths power (reviewed in Weinberg and Ethier, 2007) and is thus 20-fold higher in mice than in people. Ignoring findings obtained in rabbits may be unwise.

Caro and colleagues themselves made an attempt to resolve the discrepancy. To understand their reasoning, it is first necessary to introduce some fundamentals of wall mass transport. There is a pressure gradient from the arterial lumen to the adventitia, driving a constant convective flow across the wall. Dissolved macromolecules will be advected in the same direction, but may be filtered at various interfaces though which water can move more readily than the solute. At such points, solute concentration will rise, like a filter cake, until it drives sufficient diffusion in the reverse direction to match the forward advective flux. This phenomenon is known as concentration polarisation. There have been many studies of its putative occurrence at the endothelial surface, but additional concentration polarisation may occur within the wall. For example, LDL concentrations in the arterial intima appear to be higher than those in plasma and this has been attributed to filtering by the internal elastic lamina (Smith and Staples, 1980).

Caro and Lever (1983) suggested that intimal trapping might also arise if the arterial media restricted transport of large solutes more than water. A corollary is that the degree of trapping might depend on the tone of medial smooth muscle cells, and hence could vary according to the mix of vasoactive agents present. Medial tone, by affecting porosity, would also influence the space available for solutes and hence the amount of solute present in each volume of wall tissue. Thus it is conceivable that the intimal concentration of an atherogenic macromolecule could be high in areas where the level averaged over the thickness of the wall is low; both could be caused by low medial porosity.

A phenomenon of this type might explain an apparent inverse relation between local wall uptake of plasma macromolecules and the predilection for lesions, avoiding the need to invoke transport from the wall into the lumen, with its attendant problems. However, it cannot be a complete solution to the incompatibilities noted above. First, the binding of EBD to elastin means that it should be an excellent indicator of the rate of entry of proteins into the wall, and that it should be little affected by the space available for macromolecules in the media. Second, the different sites of lesions in rabbit and human arteries remain unexplained. Like the first mechanism of Caro et al. (1971), this second attempt has not entered the mainstream. We are thus left with a paradigm in which low shear stress leads to dysfunctional, leaky endothelium and hence to disease, even though the predicted patterns of shear stress and measured patterns of permeability in the rabbit contradict it.

CONTRADICTIONS CAN BE RESOLVED BY TAKING AGE INTO ACCOUNT

A potential resolution of the apparent contradictions described above arises from the observation that anatomical patterns of transport and disease change with age. The fundamental suggestion is that immature rabbits have been inappropriately compared with mature people. Rabbits tend to be used when young because it is costly to house them for long periods. *Post mortem* human arteries generally derive from older, or at least mature, populations. When age is taken into account, there is a strong spatial correlation between sites of rabbit permeability, rabbit lesions and human lesions.

The first study (Sebkhi and Weinberg, 1994a) in the development of this concept, conducted nearly 30 years ago, showed that net uptake of circulating albumin by the aortic wall was greater downstream than upstream of intercostal branch ostia in immature rabbits, but greater upstream than downstream in mature rabbits. The transition occurred at around 6 months of age (**Figure 3A**). Mean uptake did not change, so uptake must have been decreasing downstream and increasing upstream with age. (There was a sharp drop in mean uptake shortly after weaning.)

This study assessed uptake 3 h after tracer administration. At this time, levels of labelled albumin in the wall are approaching a steady state, where they should resemble those of the native protein. Steady-state levels of an inert particle reflect three properties: the ease of entry into the wall (here termed permeability, regardless of the mechanism of entry), the ease of egress from the wall, and the space available for the particle within the wall.

A subsequent study (Sebkhi and Weinberg, 1996) examined uptake 10 min after tracer administration. After such a short period, concentrations of tracer in the space available to it are much lower than concentrations in plasma, and will be dominantly determined by ease of entry. The same age-related patterns were found, supporting the view that permeability is the limiting factor. Murphy and Lever (2002) similarly found that short-term uptake of labelled albumin was greater downstream than upstream of the renal artery in immature rabbits and showed the reverse pattern in mature ones. (However, they were unable to demonstrate a parallel pattern of quasi-steady uptake in mature animals.)

Spontaneous lipid deposition in rabbit arteries is rare, but it can be detected in weanling and old animals. A study (Barnes and Weinberg, 1998) mapping lipid deposition in rabbits of these ages found an arrowhead distribution downstream of intercostal branch ostia in the weanlings and sparing of this area in old animals, where lipid staining instead occurred further downstream and at the sides of the branch (**Figure 3B**). A trend from a downstream arrowhead to a pattern with more lateral and upstream lipid deposition was also seen at the origin of the coeliac artery. (The fact that disease developed at all in the mature animals is a challenge to the insudation theory because their average plasma cholesterol concentration was only 18 mg/dl).

The patterns in cholesterol-fed rabbits proved harder to elucidate. A small study (Sebkhi and Weinberg, 1994b) of quasi-steady albumin uptake showed that feeding mature rabbits 0.2% cholesterol for 1 week reversed the usual pattern of transport, so that uptake became greater downstream than upstream of intercostal branch ostia, as in immature animals. However, after a further week of feeding, the pattern reverted to

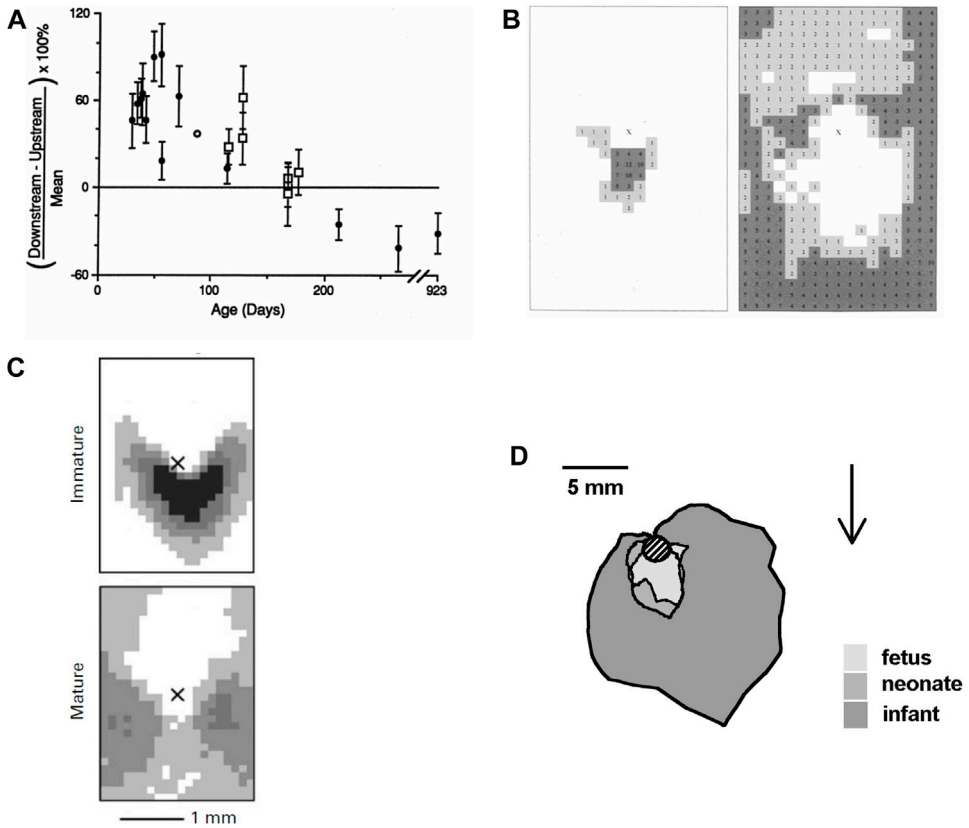

FIGURE 3 | (A) Difference between uptake of albumin downstream and upstream of intercostal branch ostia, expressed as a percentage of the mean uptake in both regions. Uptake is greater downstream in young rabbits and greater upstream in older rabbits (Sebkhi and Weinberg, 1994a). **(B)** Maps showing the prevalence of spontaneous lipid deposition around intercostal branch ostia in weanling (left) and aged (right) rabbits fed a normal diet. The centre of the ostium is marked with an "X," mean aortic flow is from top to bottom and increased lesion prevalence is indicated by numbers (% of branches affected at each site) and by darker shading (Barnes and Weinberg, 1998). **(C)** Similar maps of lesion prevalence in immature and mature rabbits fed a cholesterol-enhanced diet (Cremers et al., 2011). **(D)** Average extent of lesions from the lip of intercostal ostia (shaded circle) in human fetuses, neonates and infants up to the age of 1 year. Arrow shows mean flow direction (after Sinzinger et al., 1980).

normal. This made it uncertain whether to expect the downstream pattern of lesions if mature rabbits were fed cholesterol, or one where the area downstream of branches was spared.

In fact, both patterns—and intermediates between them—were observed. In a first trial (Barnes and Weinberg, 1999), lesions occurred in the classical Anitschkow arrowhead around the downstream margin of intercostal branch ostia in the aortas of both immature and mature animals. In a second trial (Barnes and Weinberg, 1999), mature animals had lesions lateral to the branch ostia with areas upstream and downstream of the branch being spared. The discrepancy was attributed to differences in the diet, especially since adding vitamin E to the diet in the second trial, with the aim of preserving the nitric oxide pathway, increased disease upstream of the branch.

This idea was explored in a third trial (Barnes and Weinberg, 2001) by additionally giving the cholesterol-fed rabbits either vitamin E, or L-arginine or L-N^G-nitro-arginine methyl ester (L-NAME) which are, respectively, the precursor and an inhibitor of NO production. All the diets gave a pattern that was intermediate between the two previously observed: lesions occurred downstream of the branch except along a line extending axially from the branch centreline, as if the downstream arrowhead were splitting into two lobes. A fourth trial (Barnes and Weinberg, 2001) examined the dietary fundamentals by using either of the two base diets and either of the two cholesterol regimens (0.2% for 15 weeks or 1% for 8 weeks) previously employed. Both the downstream and the lateral pattern were observed, but neither base diet and neither cholesterol regimen consistently gave one or the other.

The fourth trial was the first in which lesion patterns differed substantially between and within groups and was also the first in which it had not been possible to obtain all the rabbits from a single supplier. This motivated a retrospective analysis (Barnes and Weinberg, 2001) of mature animals from all four trials; it showed that the discrepancies could be explained completely by which strain of rabbit had been used. Although all rabbits were New Zealand Whites and >11 months old, one strain consistently showed the downstream triangle, a second consistently showed the lateral pattern, and two gave the intermediate pattern. A subsequent trial (Cremers et al., 2011) in which immature and mature rabbits of the second strain were given the same diet for

the same length of time unequivocally gave the arrowhead pattern at intercostal branch ostia of the immature animals and a more lateral pattern in the mature ones (**Figure 3C**).

To confirm that this unexpected effect of strain applies to the pattern of transport as well as lesions, short-term uptake of albumin was examined in two strains of rabbit (Staughton and Weinberg, 2004a). Both showed a gradual change with age from uptake being greater downstream of the branch to it being greater upstream of the branch, as before. However, the age at which the pattern switched—i.e. at which uptake was equal in both regions—was approximately 650 days in one strain and 1,300 days in the second. These values were significantly different, and both were markedly different to the approximately 180 days observed in the initial studies described above, which used a third strain of rabbit. Hence the switch does not necessarily occur at the age of sexual maturation, as originally supposed.

An interesting additional finding of this study was the existence of a circadian effect: the pattern of uptake was consistently biased towards the upstream pattern in the morning, compared to the afternoon. This suggests that the pattern depends in part on a physiological property that can vary over a matter of hours, in addition to any influences of more time-invariant properties such as arterial geometry.

Do parallel age-related changes occur in people? There is one quantitative study mapping the distribution of lipid deposits in *post mortem* aortas of human fetuses, neonates, and infants below the age of 1 year (Sinzinger et al., 1980). Sudanophilia was found exclusively around the downstream margins of branch ostia in the youngest aortas, and all around the branches but with highest prevalence downstream, in the older ones (**Figure 3D**). Although the authors explicitly noted that this pattern is at variance with the one obtained in adult vessels and is similar to data for the cholesterol-fed rabbit, the work has received only 5% of the citations of the paper of Caro et al. (1971), presumably because it does not fit the current consensus.

The important result of Sinzinger et al. is consistent with qualitative data from much earlier studies. Zinserling (1925) noted the presence of small, distinct spots of lipid staining, one below each intercostal ostium, and lesions in the form of a Y-shaped fork, with two stripes that join under the ostium, in children. Thus there appears to be a switch with age in the distribution of lipid deposits in the human aorta that parallels the one observed in the rabbit. It is interesting to speculate that, as with rabbits, different populations may undergo the swich at different ages.

Conclusion

The data described in this section eliminate the need to regard the cholesterol-fed rabbit model as aberrant in some way. On the contrary, both spontaneous and diet-induced lesions in the rabbit seem to replicate closely an age-related switch, largely ignored, that occurs in human vessels. Furthermore, the rabbit provides a mechanism: wall uptake of circulating macromolecules shows the same age-related switch. The permeability of the wall appears to be the critical property.

There is no need to postulate that transport out of the wall is critical, with the attendant problem in accounting for the dependence of disease on plasma cholesterol concentrations: regions downstream of branches can be diseased or spared in animals consuming diets supplemented with the same high level of cholesterol for the same duration (Cremers et al., 2011). Equally, there is no need to postulate that disease is triggered by variation in intimal macromolecule accumulation that has an undetected anatomical distribution opposite to that seen in the wall as a whole. Indeed, when uptake of albumin measured over the entire intima-media is higher downstream of branches than upstream, then the same is true for uptake in the innermost layers of the wall; there is no indication of a reversed pattern in the innermost layers that could account for an upstream distribution of lesions (Sebkhi and Weinberg, 1996).

Provided that age is taken into account, the simple insudation theory can account for the pattern of human lesions, as well as rabbit lesions. Indeed, the fact that patterns of transport and lesions remain correlated despite both changing with age greatly strengthens the insudation theory; there are many properties that vary around arterial branches, but presumably far fewer that show the necessary switch with age. The changes with age add complexity but, paradoxically, make it easier to identify localising factors.

THE EMERGENCE OF OTHER DISEASE PATTERNS

In the preceding sections, lesion prevalence and permeability have been discussed largely in a binary fashion: are they greater upstream or downstream of branch ostia? However, the patterns are more complex and more numerous than this, which has implications for the mechanisms involved.

Sloop et al. (1998) demonstrated the existence of two patterns of fatty streaks in adult human aortas. In one pattern, lesions occurred lateral to intercostal branch ostia, and in longitudinal streaks joining those areas. In a second pattern, lesions extended proximally from the inflow tract of intercostal ostia. Occasionally, both patterns were seen in a single aorta (**Figure 4A**). The average age of subjects with the first pattern was significantly lower than those with the second pattern, although the difference was remarkably small (20.5 ± 3.5 vs 25.8 ± 1.3 years, $p = 0.004$). Subjects with equal prevalence of both patterns had an intermediate age (23.5 ± 2 years). The only other variable associated with the switch was the serum isothiocyanate level, indicative of smoking.

Mitchell and Schwartz (1965) found that raised lesions in human aortas completely surround branch ostia, giving the appearance of a volcano (**Figure 4B**). The discrepancy with the pattern of lipid deposition was used to argue that fatty streaks are not precursors of raised lesions. Sloop et al. (2002) have made the same argument based on the development of raised fibroproliferative lesions in synthetic dialysis access grafts, without prior fatty streaking. This view has not been widely reported or accepted.

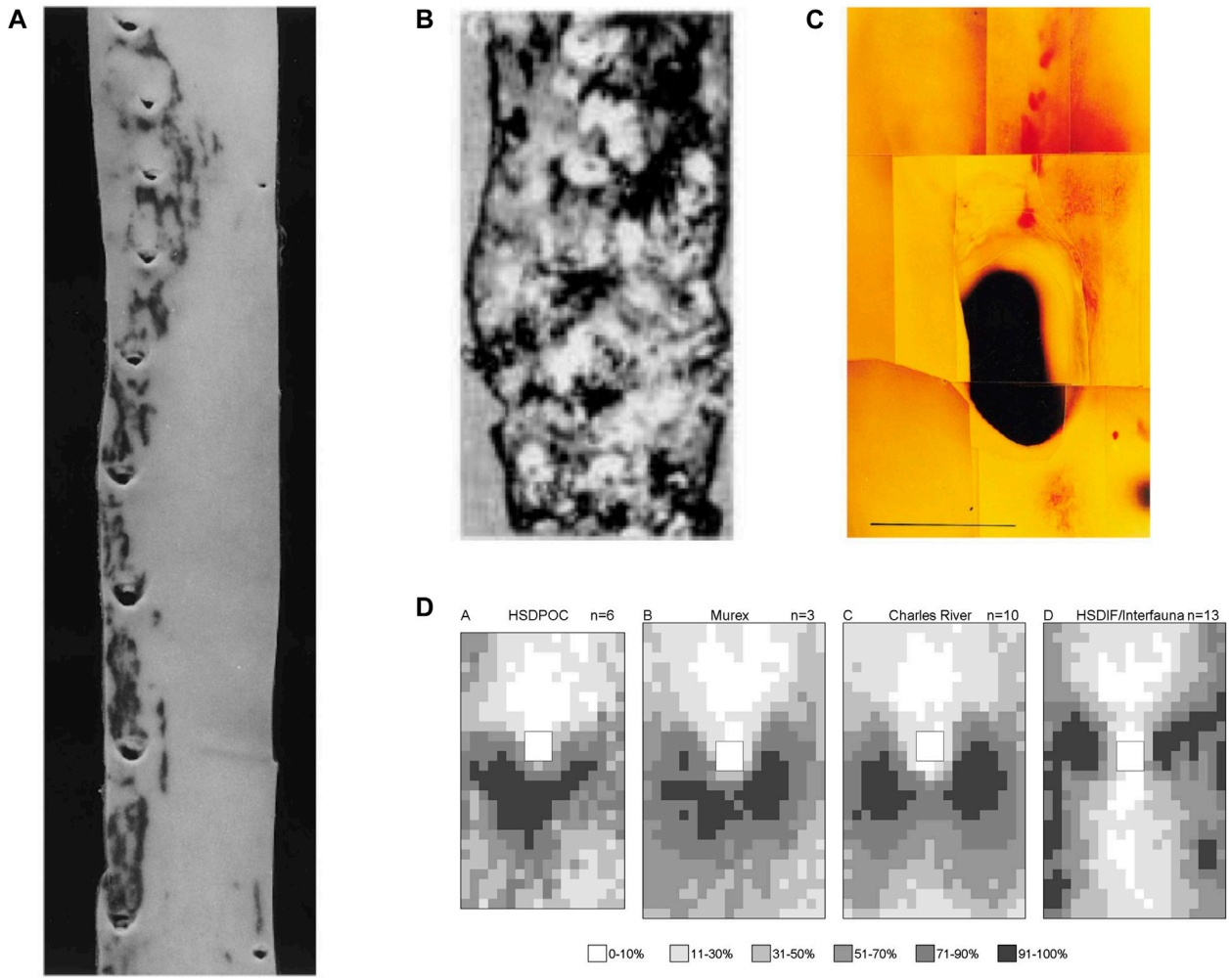

FIGURE 4 | (A) Human thoracic aorta, viewed as in **Figure 2A**, showing two patterns of lipid staining at intercostal branch ostia (Sloop et al., 1998). **(B)** Lesions in an aged human aorta, viewed as in **Figure 2A**. Fibrous caps of raised lesions appear white and can be seen completely surrounding the dark holes of branch ostia (Mitchell and Schwartz, 1965). **(C)** Spontaneous lipid deposition (red) extending upstream of the coeliac branch ostium in the abdominal aorta of an aged rabbit fed a normal diet (Barnes and Weinberg, 1998). **(D)** Maps of lesion prevalence, displayed as in **Figure 3C**, in mature rabbits of four different strains. The maps are arranged in an order that gives the impression of a trend from the downstream arrowhead to the lateral pattern of disease (Barnes and Weinberg, 2001).

Thus in people, there are downstream, lateral, and upstream fatty streaks, and raised lesions that surround ostia. There appears to be a progression in that order with increasing age. The first two have been demonstrated unequivocally in immature and mature rabbits, while the third may occur spontaneously at the coeliac branch ostium in aged animals (**Figure 4C**). The fourth has not been quantified in rabbits but example images of raised lesions in hares fed cholesterol-supplemented and normal diets, alternating every week for up to 18 months (Imai and Lee, 1983), do appear to show disease at several points around aortic branches.

Is there a continuous change in lesion pattern or a series of discrete switches from one to another? Although upstream streaks are visible at distal branches of the human aorta shown in **Figure 4A**, and lateral streaks at the proximal branches, branches at the centre of the image appear to show transitional forms. Similarly, the patterns of lesions observed in mature, cholesterol-fed rabbits of different strains, described above, can be arranged in a sequence (**Figure 4D**) that—although not corresponding to chronological age—supports the view that there is a smooth transition from the downstream to the lateral pattern rather than an abrupt switch.

Extending the argument made above, the multiplicity of lesion patterns should make the identity of a mechanism, if there is a single one, even more secure. Can permeability of the arterial wall account for all the patterns? In the studies discussed above, uptake of fluorescently-labelled albumin by the wall upstream and downstream of branches was measured in histological sections cut along the aortic axis, through the centreline of the branch. Such measurements cannot rigorously be compared to the various patterns of lesions. Indeed, the centreline through the branch defines a plane of symmetry that may behave quite

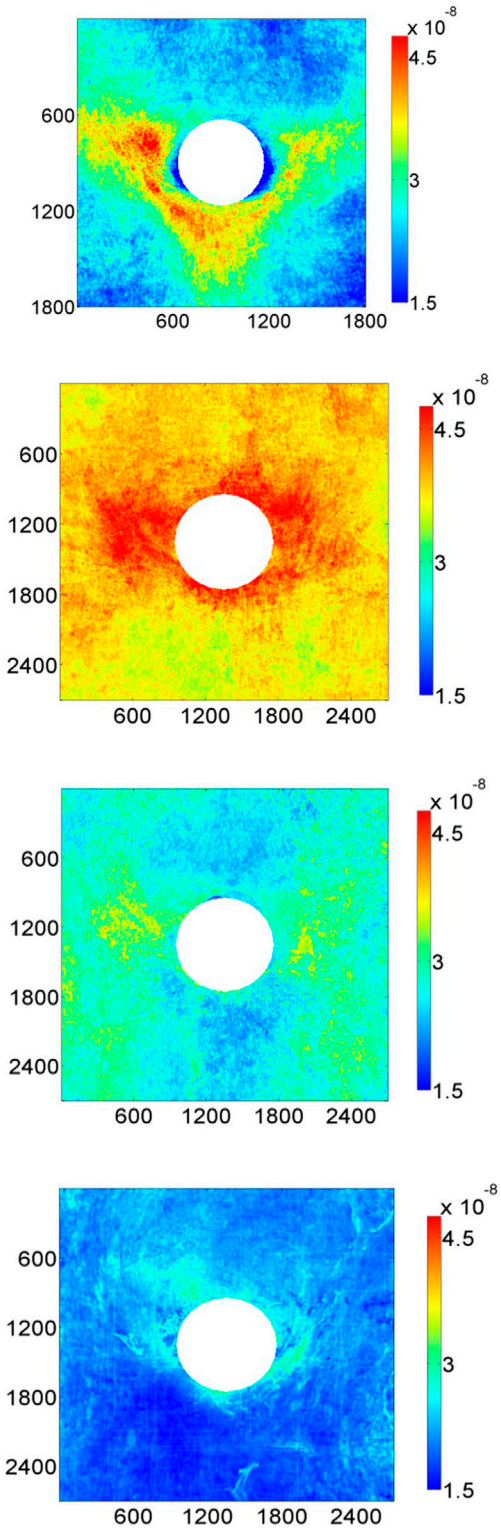

FIGURE 5 | Maps of 10-minute albumin uptake by the aortic wall of rabbits around intercostal branch ostia. The four panels represent, from top to bottom, rabbits aged 9 weeks, 6 months, 16–22 months and >5 years (Bailey et al., 2015). Uptake is expressed as mass transfer coefficients (cm/s), mean aortic flow is from top to bottom and dimensions are in μm.

differently from planes displaced even a short distance to either side.

A study (Ewins et al., 2002) that laboriously cut serial longitudinal sections across the width of the branch ostium indicated that the "downstream greater than upstream" pattern of permeability in immature rabbits was in fact a downstream arrowhead, whereas the "upstream greater than downstream" pattern in mature rabbits actually had highest uptake at the lateral margins of the branch and in streaks extending upstream and downstream from this location.

The subsequent development of rapid detection techniques based on confocal microscopy (Clarke et al., 2012) allowed 3-dimensional mapping of tracer uptake around the branch at a range of ages (Bailey et al., 2015). Maps showed a transition from the downstream triangle via an intermediate form to a lateral pattern, and then to an upstream pattern in animals >5 years old (**Figure 5**). (A reduced analysis of these four patterns showed a continuous increase in the ratio of transport directly upstream of the branch to that directly downstream.) The agreement with the distribution of fatty streaks in rabbits and people seems excellent. The mechanism underlying the development of raised lesions requires further investigation; note that such disease may affect its own progression by disturbing blood flow. An interesting feature of the data is that branches on the left and right side of the aorta showed slightly different patterns of uptake, consistent with the patterns being determined not just by the branch itself but also by larger-scale flow features.

UNDERLYING MECHANISMS

Anitschkow (1933) attributed the non-uniform pattern of transport and lesions to variation in mechanical forces. Three putative triggers have already been mentioned. They all concern WSS, although they differ as to whether it is high (Fry, 1969), low (Caro et al., 1971) or oscillatory shear (Ku et al., 1985) that is critical. Other putative triggers involving flow include turbulence (Wesolowski et al., 1965), fluctuating WSS (Fry, 1973), pulse WSS (Friedman et al., 1981), temporal WSS gradient (Bao et al., 1999), WSS harmonic content (Himburg and Friedman, 2006), spatial WSS gradient (Lei et al., 1995), WSS angle gradient (Kleinstreuer et al., 2001), the WSS angle deviation (Hyun et al., 2000), multidirectional WSS at stagnation points (McMillan, 1985a; McMillan, 1985b), multidirectional WSS generally (Peiffer et al., 2013a; Mohamied et al., 2015), particle residence time (Moore Jr et al., 1992) and relative residence time (Himburg et al., 2004). The plethora of hypotheses may explain why vascular biologist frequently use the vague and hence undesirable term "disturbed flow" to indicate atherogenic stresses.

Spatial variation in pressure, the stress normal to the wall surface, has been invoked less often. Texon (1957) suggested that the presence of lesions on the lateral walls of bifurcations could be explained by Bernoulli-type reductions in pressure. Such hypotheses have not gained acceptance, perhaps because the maximum dynamic pressure associated with the flow of blood is only around 10 mmHg (Caro et al., 1971) and hence point-to-point variation in pressure, scaled by the average value, will be much smaller than variation in WSS, similarly scaled.

Changes in blood pressure occur during each cardiac cycle and, because arteries are elastic, lead to cyclical changes in the dimensions of the wall. This strain my vary from site to site as a result of variation in wall stiffness or as a result of expansion being prevented by structures outside the wall. There is a segmental distribution of disease in the vertebral arteries, lesions occurring where the artery is free to expand, but not where it passes through the bone canal (Moossy, 1966; Solberg and Eggen, 1971). The internal carotid artery is protected from disease where it passes through the canal at the base of the skull (Glagov et al., 1988) and lesions are absent where coronary arteries pass under constraining "myocardial bridges" (Nakaura et al., 2014). Thubrikar et al. (1988) showed that lesion formation downstream of the renal artery ostium in cholesterol-fed rabbits can be prevented by restricting aortic expansion with an external cuff.

A fundamental problem with the evidence implicating arterial strain is that preventing a vessel from expanding will change not only strain but WSS as well—the time-average diameter will be smaller and hence WSS will be higher. The pattern of WSS may also be altered, if the geometry is complex. The same issue applies to *in vitro* studies examining effects of cyclic strain on cultured endothelium: when cells are stretched on a deformable membrane and there is static fluid above them, the stretch creates a relative motion with the fluid and thus generates fluid shear stresses. New techniques (e.g. Rowland et al., 2021) are required to look at more subtle, natural variations in strain, with the aim of determining whether it or WSS best explains the pattern of disease.

This summary understates the number and complexity of putative mechanical triggers. For example, there are hypotheses that depend on the temporal relation between WSS and strain (Dancu and Tarbell, 2007). What needs to be addressed is their relation to the change with age that occurs in the pattern of permeability and lesions. Broadly speaking there are two possibilities: 1) the distribution of mechanical stress is constant with age and it is the relation between mechanical stress and atherosclerosis that changes, or 2) the distribution of mechanical stress changes with age and the relation between mechanical stress and atherosclerosis remains constant.

(i) The relation between mechanical stress and atherosclerosis changes with age

A hypothetical example if this kind of mechanism would be that lesions develop at sites of high shear in immature aortas but at sites of low shear in mature aortas. That would require a change in the pathways between WSS and disease, such as in the relation between shear and permeability.

In the first study of age-related pathways (Forster and Weinberg, 1997), nitric oxide (NO) was chosen for examination because it can modify transport properties of blood vessel walls (Kubes and Granger, 1992; Yuan et al., 1992) and is influenced by age (Liu et al., 1992; Aliev et al., 1995), blood flow (Holtz et al., 1984; Rubanyi et al., 1986) and hyperlipidemia (Minor et al., 1990; Cooke et al., 1991). It was investigated in rabbit thoracic aortas; they were perfused with physiological buffer *in situ* to avoid indirect effects caused by the influence of NO on blood pressure, aortic flow, or interactions of blood cells with the vessel wall. Flow was steady. In this preparation, short-term uptake of albumin was greater downstream of branch points in immature aortas and upstream in mature aortas, as *in vivo*. That is itself interesting; it suggests that neither pattern is determined by unsteady components of luminal pressure or flow, interactions of blood cells with the vessel wall, or components of plasma, or that they are determined by these things via effects lasting longer than the 1.5 h that it took to conduct the surgery.

When NO production was inhibited with L-N^G-monomethyl arginine (L-NMMA), starting 15–25 min before the administration of tracer, the mean of uptake upstream and downstream of intercostal branches in immature aortas increased by a factor of three but the pattern was unaffected. In mature aortas, mean uptake was unaffected but the pattern was reversed—uptake became greater downstream than upstream of branches and the difference was as large as that seen in the youngest immature rabbits (**Figure 6A**). This suggests a change in endogenous NO production (e.g. from basal production to flow-dependent production) and/or a change in the effects of NO on permeability with age.

Parenthetically, it is noted that EBD inhibits acetylcholine-stimulated relaxation of preconstricted aortic rings (Forster and Weinberg, 1997), the paradigmatic property associated with the NO pathway, and studies in which this intravital dye circulates for prolonged periods may therefore give results that do not truly reflect transport of native macromolecules *in vivo*.

A follow-up study examined the effects of L-NMMA on transport and cholesterol-induced lesions in rabbits *in vivo* (Staughton and Weinberg, 2004b). Only mature animals were used. The upstream pattern of short-term albumin uptake was seen in control animals, as expected. This pattern was abolished in the rabbits administered L-NMMA. The change was statistically significant, but uptake after L-NMMA was only slightly greater downstream of the branch than upstream and the difference between regions did not reach significance (**Figure 6B**). This is markedly different from the large effect seen in perfused vessels.

Lesions in the control cholesterol-fed group clustered around the lateral margins of the branch, and in areas extending upstream and downstream from these locations, as expected. The pattern was broadly similar in animals administered L-NMMA chronically during the trial, and pilot studies with a wide range of alternative NO inhibitors also failed to give the downstream pattern of lesions in mature animals.

The discrepancy between the *in vivo* and the *in situ*-perfused transport data could reflect the influence of NO on pressure, flow and blood cell-wall interactions, which are only present in the former. Alternatively, the discrepancy could represent a difference in transport mechanisms. Albumin has a size that gives approximately equal transport via "small pores" and "large pores" in capillary endothelium *in vivo* (Levick, 1991). These pores may represent intercellular junctions and vesicular routes, respectively (see below). Permeability to albumin was elevated up to five-fold in the perfused vessels compared to *in vivo*, most likely due to an increase in transport through intercellular

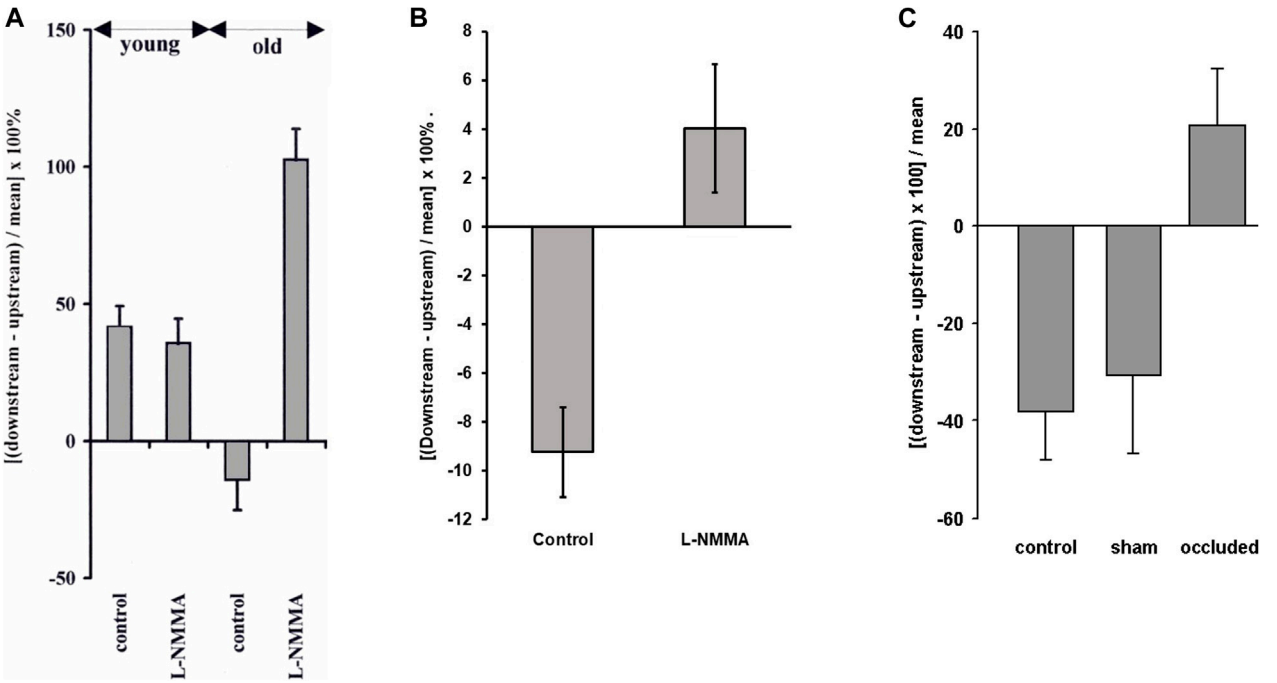

FIGURE 6 | (A) The effect of the NO inhibitor L-NMMA on the pattern of albumin uptake upstream and downstream of intercostal branch ostia in the *in situ*-perfused rabbit aorta. Positive values indicate greater uptake downstream and negative values indicate greater uptake upstream, as in **Figure 3A**. L-NMMA reversed the normal mature pattern of uptake but had no effect on the pattern in immature rabbits (Forster and Weinberg, 1997). **(B)** A similar but smaller effect was seen in mature rabbits *in vivo* (Staughton and Weinberg, 2004b). **(C)** The same trend was seen in mature rabbits when the intercostal arteries were occluded in anaesthetised mature rabbits, whereas sham operation had no effect (Staughton et al., 2001).

junctions. The junctions may be more susceptible than vesicles to the influence of NO. On the other hand, the similarity of patterns of permeability *in vivo* and in perfused vessels argues that their determinants should be broadly similar. A simpler possibility is that the discrepancy may reflect an unknown technical issue; for example, NO synthesis could be harder to inhibit *in vivo*.

Further studies (Staughton et al., 2001) investigated whether there is a change with age in the sensitivity of the transport patterns to flow. This was achieved by tying off some intercostal arteries but not others in anaesthetised rabbits; fluorescently-labelled albumin was administered 20 min after the occlusion, and was allowed to circulate for 15 min before the aorta was fixed, sectioned and imaged. Uptake was greater upstream than downstream of control branches in mature animals, as *in vivo*, but the reverse pattern was seen at occluded branches, uptake being greater downstream, while mean uptake was unchanged (**Figure 6C**).

This is the same switch that was seen when NO was inhibited in perfused vessels (Forster and Weinberg, 1997), when hypercholesterolaemia (a known inhibitor of the NO pathway) was induced for 1 week (Sebkhi and Weinberg, 1994b), and when fixation was inadvertently delayed after death in *in vivo* experiments, which left vessels exposed to tracer in the absence of pressure and flow (Sebkhi and Weinberg, 1996). A partial effect in the same direction was seen when an NO synthase inhibitor was administered *in vivo* (Staughton and Weinberg, 2004b). All these data are consistent with an underlying downstream pattern being changed to an upstream pattern in mature animals when flow-dependent synthesis of NO occurs. Since mean uptake was not altered in these experiments, shear-dependent NO production—if it is responsible—increases transport upstream of the branch and decreases it downstream. The effect is rapidly reversible. (The latter point suggests that the presence of the normal mature pattern in vessels perfused with a steady flow of physiological buffier is *not* a lingering effect of the pulsatile flow of blood 1.5 h earlier.)

An unexpected result in the branch occlusion experiments (Staughton et al., 2001) was the absence of the downstream pattern in immature animals: uptake was equal in upstream and downstream regions. Furthermore, the pattern was unaffected by occluding the branches. An additional aberration was that mean uptake at branch points was three-fold higher in the immature animals than in the mature ones, contrary to the finding in perfused vessels and in conscious animals. These results may be indicative of some important mechanism underlying the immature pattern (for example, that the pattern is dependent on strain and therefore abolished by the hypotension arising from anaesthesia) or they may reflect some trivial experimental variable; the explanation is currently unclear.

A similar experiment that examined uptake of EBD over 20–30 min at the aorto-renal branch in a small sample of anaesthetised immature animals (Murphy, 1998) did find the normal pattern—greater uptake downstream of the branch than

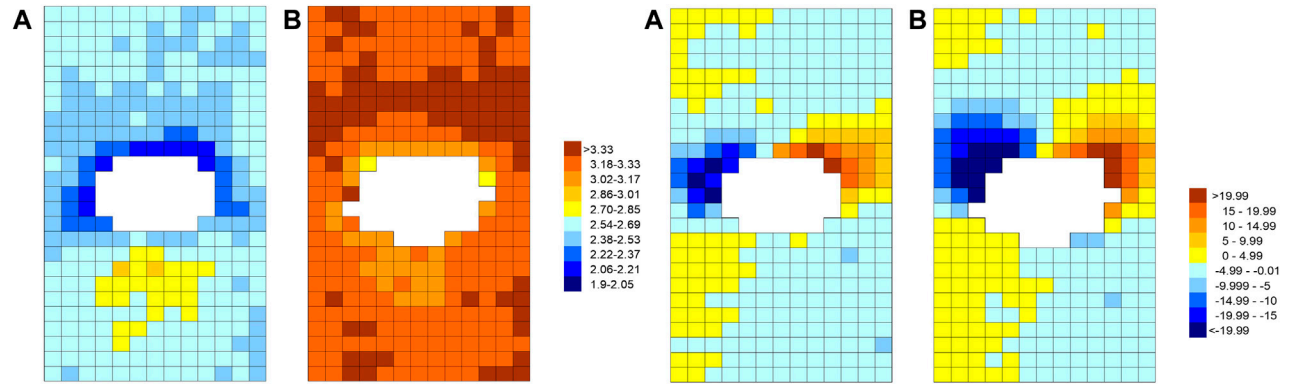

FIGURE 7 | The pattern of endothelial nuclear elongation (left pair of maps) and alignment (right pair) around intercostal branch ostia (white) for immature (A) and mature (B) rabbits. Colour coding represents length-to-width ratios (left) or angles between the nuclear long axis and the aortic axis (right, with negative angles indicating the proximal end of the nucleus is displaced to the anatomical right). Maps show an *en face* view with mean flow from top to bottom (Bond et al., 2011).

upstream—at control branches and showed that it was unaffected by partial ligation of the branch for 1.5 h. This suggests that the immature pattern does not depend on flow. Thus, different mechanisms appear to determine the uptake of albumin at immature branch points: not only is the pattern unaffected by inhibiting NO production but it also appears not to depend on flow, at least in the short term.

(ii) The distribution of mechanical stress changes with age

The data presented above strongly suggest that there is a change with age in the mechanism linking flow with patterns of transport near branches. There is no need to propose that the flow itself also changes with age. The first study (Al-Musawi et al., 2004) to test whether the pattern of flow is indeed constant exploited the relation between endothelial morphology and applied flow. Endothelial cell elongation and orientation, nuclear elongation and orientation, and the distribution of cytoskeletal F-actin all change when the direction and magnitude of the flow are modified *in vivo* (Levesque et al., 1986; Walpola et al., 1993) or *in vitro* (Dewey Jr et al., 1981; Levesque and Nerem, 1985); they have been widely used to assess WSS.

The study of Al-Musawi et al. found that endothelial cell nuclei were more elongated downstream than upstream of intercostal branch points in the aortas of immature rabbits. Lateral regions had intermediate elongations. In mature rabbits, by contrast, nuclear elongation was higher upstream than downstream; elongation in lateral regions was unchanged. This suggests that the distribution of WSS does reverse with age. The orientation of nuclei, putatively indicating the direction of near-wall flow, did not change.

This finding motivated a second study (Bond et al., 2011) in which elongation and orientation of endothelial nuclei were measured using automated methods. This permitted many more branches to be examined, and hence allowed the nuclear properties to be determined in smaller areas of the endothelium without incurring excessive variation. The resulting maps could be compared directly with maps of lesion prevalence. The study confirmed that the pattern of nuclear elongation, measured in rabbits aged 6–7 weeks and 11–22 months, reversed with age and that the pattern of nuclear orientation did not (**Figure 7**). The maps of elongation were remarkably similar to the maps of spontaneous disease in rabbits aged 4 weeks and 25–77 months (**Figure 3B**). Importantly, if cells and their nuclei elongate with increasing WSS, as commonly assumed, then this positive correlation suggests that both patterns of spontaneous rabbit lesions—and, by implication, the similar patterns of human disease—occur in regions of high rather than low WSS.

Additional findings of note, observed in the descending thoracic aorta as a whole, were: 1) a broad streak of high elongation along the dorsal surface, 2) many minor streaks of high elongation, also in the axial direction, bearing a strong resemblance to fatty streaks (which derive their name from this linear appearance), and 3) nuclear orientations that suggest counter-rotating, Dean-type vortices.

Thus, in addition to the evidence for a change in response to flow, described in the preceding section, these two studies suggest that the pattern of flow around branch points also changes with age. Only one of these mechanisms is required to account for the changing pattern of lesions. Biological systems are not selected by Occam's razor, but the finding is unexpected—nothing about the flow profiles in **Figure 1B** suggests that it should occur—and it is therefore useful to examine assumptions underlying the nuclear elongation method.

First, most studies showing that elongation depends on WSS have examined cellular rather than nuclear morphology. Nevertheless, the study of Bond et al. (2011), just described, did include validation against a smaller series of measurements concerning elongation of the whole cell; a good correlation was obtained with nuclear elongation regardless of whether the cell outline was analysed manually or by using an automated technique based on machine learning (Iftikhar et al., 2011).

Second, there are other influences on cell elongation. For example, it is affected by flow pulsatility and reversal (Helmlinger et al., 1991) and by strain (Zhao et al., 1995).

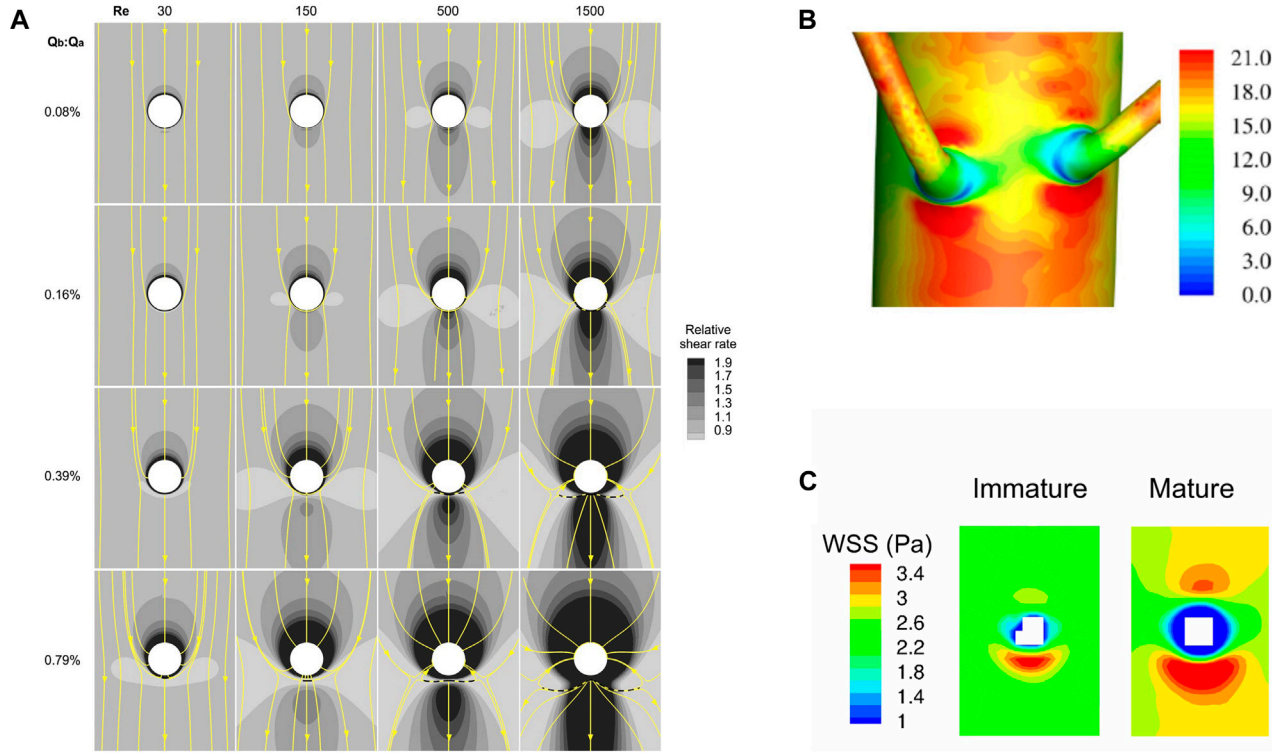

FIGURE 8 | (A) Maps of the effect of Reynolds number and the ratio of branch to aortic flow rate on computed WSS around the ostium (white) of an idealised branch emerging from a flat plate, viewed *en face* with mean flow from top to bottom (Kazakidi et al., 2009). Surface streamlines are also shown. **(B)** Patterns of WSS (Pa) around a pair of aorto-intercostal junctions, computed for steady flow in a realistic representation of the rabbit anatomy and viewed from outside the vessel, with mean flow from top to bottom (Vincent et al., 2011). **(C)** Maps of WSS around intercostal ostia (white) computed for steady flow in realistic representations of an immature and a mature rabbit anatomy, viewed *en face* with mean flow from top to bottom (Peiffer et al., 2012).

There also seems to be compensation for the increased WSS associated with smaller body size; endothelial cells know in some way the size of the body they are in (Weinberg and Ethier, 2007) and adjust their elongation accordingly. However, the effect of stretch is smaller than the effect of shear when both are applied at physiological levels (Zhao et al., 1995), the adjustment for body size should not influence local differences around branch ostia, and the influence of pulsatility and reversal do not contradict the view that the pattern of flow changes with age, only how it changes.

Third, the elongation of endothelial cells and their nuclei is a *response* to WSS. Evidence has been presented above that responses to shear can change with age. Hence it is feasible that endothelial elongation represents different flow features at different ages. The possibility that patterns of elongation reverse with age despite an unchanging flow pattern seems unlikely but cannot be ruled out *a priori*.

COMPUTATIONAL STUDIES OF FLOW

In the 1960s and early 1970s, when Fry and Caro et al. proposed their high- and low-shear hypotheses, the distribution of WSS had to be obtained by applying fundamental principles of fluid mechanics to simplified geometries or by using physical models. Over the years, models and associated measurement techniques became more advanced (e.g. Ku et al., 1985) and methods for characterising flow *in vivo* have also progressed (e.g. Riemer et al., 2021). However, current experimental methods still cannot reliably assess WSS around branch ostia.

The application of computational fluid dynamics (CFD), which occurred almost 40 years ago (Friedman and Ehrlich, 1984), was a big advance not only because it allows such assessment but also because it permits "experimental" manipulation of boundary conditions to determine their effect on the distribution of WSS; this is particularly valuable when attempting to understand effects of age.

An initial study with this aim (Kazakidi et al., 2009) determined influences of Reynolds number and side branch flow on the distribution of WSS around an ostium. The geometry was simplified by representing the branch as a cylindrical tube emerging perpendicularly from a flat surface. This assumption is justified where the parent vessel is much larger than the branch, as at an aorto-intercostal junction. The use of steady flow was justified by the desire to obtain time-average WSS and an assumption of quasi-steady flow. To examine effects of the branch alone, no attempt was made to incorporate the geometry of the aortic arch or its branches.

The objective was to confirm that WSS is high downstream and low upstream of the branch, and to examine whether this pattern can be modified. The numerical simulations showed, however, that shear is highest upstream of the branch (**Figure 8A**). This arises because it is easiest for slow-moving fluid near the wall to change direction; contrary to the impression given by 2-D representations (**Figure 1B**), flow therefore enters the branch not only from near-wall regions that lie directly upstream of the ostium but also from other near-wall regions, spread over a wider region, and less from regions further away from the wall, even if they do lie directly upstream of the branch. The near-wall streamlines converging on the branch mouth indicate accelerating fluid and the higher velocity leads to higher WSS. This effect gets stronger as Reynolds number is raised, since the increased inertia makes it even harder for fluid away from the wall to enter the branch. It also gets stronger when side branch flow rate is increased, since more fluid needs to enter the branch. A patch of high shear stress upstream of the branch is visible in the physical models of Caro et al. (1971), although not discussed by them.

WSS was low lateral to the branch (Kazakidi et al., 2009) (**Figure 8A**). In this region, some flow turned to enter the branch while neighbouring elements continued down the parent vessel, leading to diverging surface streamlines. This effect increased with Reynolds number and side branch flow rate, as above. WSS was generally elevated downstream of the branch, presumably because the development of a new boundary layer overcame the effect of the diverging streamlines in this region, but at sufficiently high branch flow rates and low Reynolds numbers shear was actually lowest downstream.

This model therefore contradicts the assumptions on which both the high- and low-WSS hypotheses were predicated. Furthermore, no low- or high-shear region had a shape that particularly resembled any of the patterns of lesions described above. The closest resemblance was between the lateral pattern of lesions and the distribution of low shear at physiological Reynolds numbers (500 for the rabbit, 1,500 for people) and side-branch flow rates (0.16% or 0.39% of the aortic flow for each intercostal) (**Figure 8A**), but even it is not striking. Resemblances were not markedly improved by modelling branches in pairs or by using more realistic geometries for the inflow tract and flow divider.

A follow-on study (Kazakidi et al., 2011) introduced unsteady flow. Adding pulsatile but non-reversing side-branch flow whilst maintaining steady flow in the aorta produced only minor changes. However, if the side-branch flow reversed direction during part of the cycle, as may occur *in vivo*, WSS patterns were substantially disrupted: in the period of reverse flow, shear was reduced rather than elevated in a small region upstream of the branch. During the subsequent switch to forward side-branch flow, shear was reduced in substantial areas both upstream and downstream of the branch, and was high at the lateral margins, a pattern that was almost the reverse of the steady-flow case. A similar pattern could be induced during certain parts of the cycle in a case with reversing aortic flow and pulsatile but non-reversing side-branch flow, as could other patterns at other times. Despite this wide variety of instantaneous WSS patterns, once again none of them resembled lesion patterns particularly closely, and neither did the patterns of time average WSS or OSI.

Vincent et al. (2011) then examined WSS patterns at aorto-intercostal junctions in a realistic rabbit aortic geometry, obtained by micro-computed tomography of a cast that was created by infusing resin into the vessel *in situ* and at pressure, allowing it to set, and then dissolving away the tissue. This method gives spatial resolution on the order of 10 μm; disturbances in WSS caused by the ductus scar, for example, were easily visible. Viewing the branch mouth *en face*, high WSS was again apparent upstream and downstream of the ostium, with low WSS laterally. Values were generally higher downstream than upstream and the shapes of these patches were stretched circumferentially, or compressed axially, compared to the simpler models. When the simulations were viewed from outside the vessel (**Figure 8B**), a fine ring of much lower shear was observed around most of the circumference of the first part of the side branch. There was still no downstream triangle or upstream streak of low shear. The anatomy of the arch produced longitudinal streaks of low and high shear in the descending segment at Reynolds numbers relevant to the rabbit and human aorta, which may reflect Dean vortices formed in the arch. When these streaks intercepted a branch, their effects on WSS were additive with the patterns produced locally by the ostium.

In the final study focusing on high and low WSS, Peiffer et al. (2012) simulated steady flow in geometries derived from corrosion casts of young and mature rabbit aortas. The anatomy changed with age: aortic curvature and torsion did not differ significantly between the groups but there was more taper between the root and first intercostal artery in mature than immature rabbits. Increased taper led to greater persistence of arch-generated Dean vortices down the descending thoracic aorta, and this in turn led to higher WSS on the dorsal wall of the mature rabbits. Despite this, the pattern around intercostal branches remained constant with age—high WSS upstream and, even more so, downstream of the branch, and low WSS laterally—therefore disagreeing with the age-related pattern of endothelial nuclear elongation (**Figure 8C**). (The results were broadly similar to an earlier study by Buchanan et al. (1999) that mapped WSS at the rabbit aorta-coeliac junction.) In a subsequent statistical comparison (Peiffer et al., 2013b) of the WSS distributions with lesion patterns obtained in cholesterol-fed rabbits (Cremers et al., 2011), the correlation was of borderline significance for immature animals and not significant for mature ones. Even where borderline significance was obtained, the relation was positive; that is, high lesion frequencies were associated with high WSS.

POTENTIAL IMPORTANCE OF MULTIDIRECTIONAL FLOW

The lack of resemblance between WSS and lesion patterns in these four CFD studies motivated a re-examination of the low WSS hypothesis. With the aim of assessing the strength of the spatial correlation in previous studies, a systematic review (Peiffer et al., 2013c) examined all papers identified with the search terms

atherosclerosis, shear and computational fluid dynamics, or synonyms of them. Twenty-seven papers remained of the original 406 after applying various pre-defined inclusion and exclusion criteria (e.g. the geometry had to be anatomically realistic, but not include severe disease that would itself have affected flow). Of these studies, 22 stated that their results agreed with the low WSS theory and only 5 (<20%), all examining thickening of human arteries, did not. That appeared to be strong evidence for the low WSS hypothesis.

However, a different picture emerged when the studies were subdivided according to the degree of data reduction and level of quantification they had employed to compare the patterns of WSS and disease. Studies that used descriptive analysis, visual comparison, simple thresholding or preselected areas unanimously supported the hypothesis. Studies that were quantitative but used substantial data reduction (circumferential or axial averaging) were evenly divided for and against the hypothesis. And all studies that conducted a quantitative, point-by-point comparison rejected the hypothesis. The fact that the most rigorous studies were the ones that rejected the hypothesis is even more striking when it is recognised that standard statistical techniques tend to over-estimate significance, due to problems with autocorrelation (Peiffer et al., 2013b; Rowland et al., 2015).

Although discussion about mechanical factors in atherogenesis has been dominated by consideration of high, low and oscillatory WSS, many other triggers have been proposed (see above). Some are physically unrealistic and no longer under active investigation, but others are based on comparison between lesion patterns and maps derived from numerical simulations of flow. Multidirectional WSS, occurring where near-wall flow changes direction over the cardiac cycle, has been the subject of several recent studies, and is discussed further here.

One metric defining multidirectional shear is the transverse WSS (transWSS) (Peiffer et al., 2013a):

$$\mathbf{transWSS} = \frac{1}{T}\int_0^T \left| \vec{\tau}_\omega \cdot \left(\vec{n} \times \frac{\int_0^T \vec{\tau}_\omega dt}{\left| \int_0^T \vec{\tau}_\omega dt \right|} \right) \right| dt$$

$$\mathbf{transWSS} = \frac{1}{T}\int_0^T \left| \vec{\tau}_\omega \cdot \left(\vec{n} \times \frac{\vec{\tau}_{mean}}{\left| \vec{\tau}_{mean} \right|} \right) \right| dt$$

where $\vec{n}$ represents the normal to the arterial surface.

It averages over the cardiac cycle those components of the instantaneous WSS vectors that are perpendicular to the mean WSS vector.

Subsequent, related metrics include the ratio of the magnitude of circumferential and axial WSS projections (Morbiducci et al., 2015) or the tangent and binormal directions (Arzani and Shadden, 2016), and the anisotropy ratio (Vamsi Krishna et al., 2020). There is also some relation to the earlier Directional Oscillatory Shear Index (DOSI) (Chakraborty et al., 2012), which captures the relative oscillatory character of flow along orthogonal axes, and the aneurysm formation indicator (AFI) (Mantha et al., 2006), which is the cosine of the angle between the instantaneous and mean WSS vectors and hence does not consider WSS magnitude; it gives more weight to reverse flow than to flow perpendicular to the mean vector.

The Cross Flow Index (CFI) (Mohamied et al., 2017) is defined in a similar way to the transWSS but, like the AFI, does not take into account the magnitude of the instantaneous vectors. The minimised transverse WSS (transWSSmin) (Ghim et al., 2017) is also defined in a similar way to the transWSS but uses as the reference not the mean WSS vector but the orientation that minimises the calculated transWSS. It is not clear that *in vivo* experiments will ever be able to discriminate between effects of these different metrics. The focus here is on transWSS and transWSSmin because they are defined with regard to endothelial biology: they describe the WSS occurring across the long axis of endothelial cells that are aligned with the mean WSS vector or that align so as to minimise such transverse WSS, respectively.

A metric characterising transverse flow is required because the OSI is increased by instantaneous WSS vectors that are aligned with the axis of the mean WSS vector but point in the opposite direction, as well as by vectors that have components at right angles to the mean vector. Hence the same value of OSI can be obtained for flows that are entirely different in character (**Figure 9A**). Uniaxial but reversing flow must occur in many straight segments of conduit arteries and should probably not be regarded as atherogenic. True multidirectionality, on the other hand, would be expected at bends and branches. It is not restricted to stagnation points, contrary to the hypothesis of McMillan (1985a,b).

The fundamental pattern of transWSS produced by a branch was investigated using the highly idealised model of a cylindrical tube emerging from a flat surface, described above (Peiffer et al., 2013a). Under pulsatile non-reversing or reversing side-branch flow, or with pulsatile aortic and branch flow, transWSS was always elevated in a four-lobed "butterfly" pattern, with high values at the proximal left, proximal right, distal left, and distal right regions around the ostium. The pattern was strikingly different from those for time average WSS, the OSI or the relative residence time.

Long, axial streaks of high transWSS were seen in anatomically realistic models of the rabbit aorta, derived from corrosion casts (Peiffer et al., 2013a). They occurred at different anatomical locations from streaks of low WSS, high OSI and high residence time, all of which coincided with one another. The streaks of high transWSS lay closer to the ostia of the intercostal branches. (There was a strong resemblance to the streaks of disease observed in mature rabbits by Cremers et al. (2011)). Of critical importance, the interaction of these streaks with the branch-dependent patterns of transWSS was not simply additive, contrary to the behaviour of WSS discussed above: the pattern around branches was changed. In cases where the ostium lay within a streak, a downstream arrowhead of high transWSS was seen, whereas when the ostium lay at the edge of a streak, high transWSS was seen at the lateral margins of the ostium, and in regions extending upstream and downstream from these locations. The patterns bore a striking resemblance to the

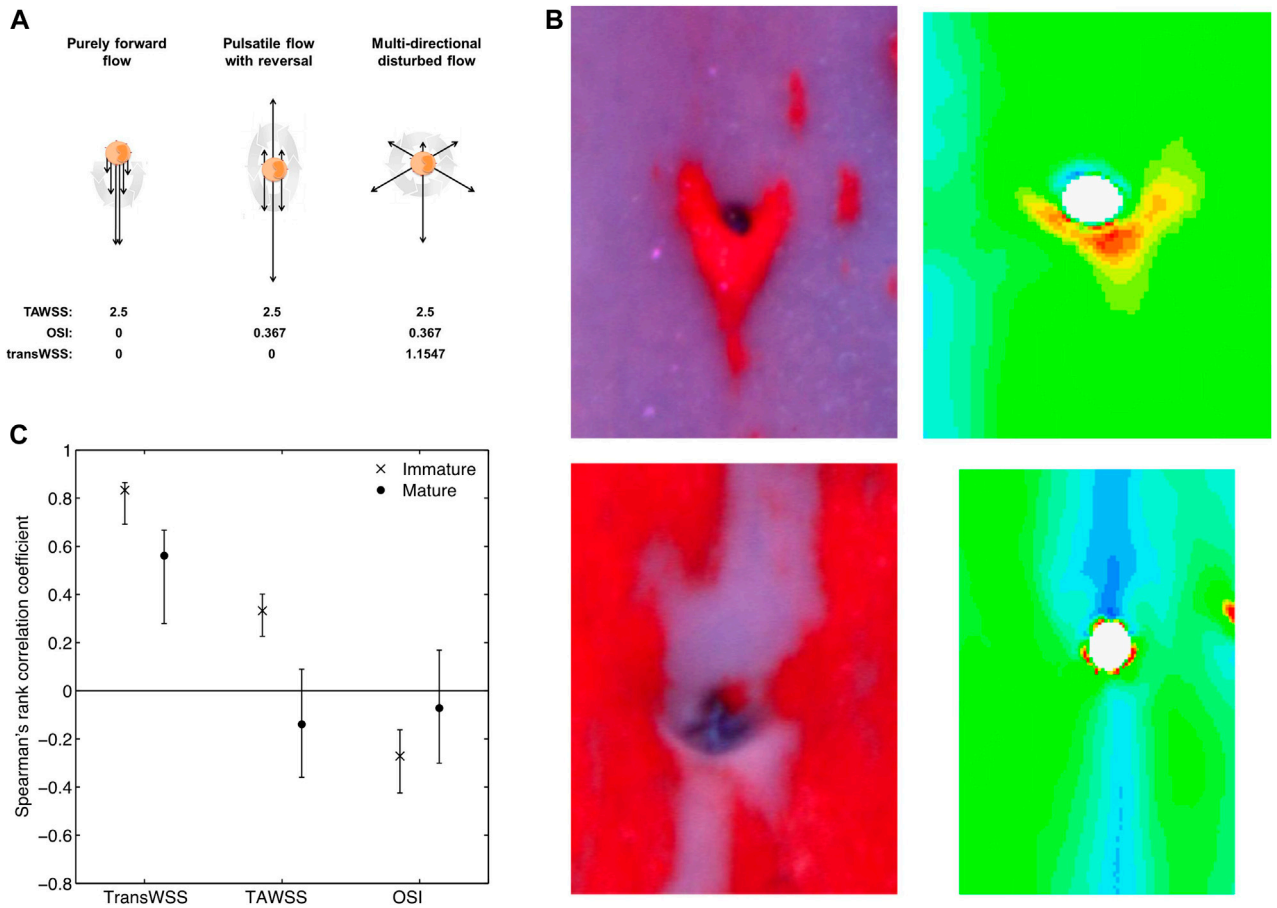

FIGURE 9 | (A) Sketch showing that the same time average WSS (TAWSS) and OSI can occur for markedly different types of flow, therefore justifying the need for the transWSS metric capturing the directionality of flow. Dark arrows represent instantaneous flow vectors and the large grey arrow represents time throughout one cycle (Peiffer et al., 2013a; Mohamied et al., 2015). **(B)** Examples of diet-induced lesions (left) and computed transWSS (right) around intercostal branch ostia in the aortas of immature (top) and mature (bottom) rabbits, viewed *en face* with mean flow from top to bottom. (Peiffer et al., 2013a). **(C)** Coefficients (mean and confidence interval) for the correlation between patterns of lesions and patterns of each of the three WSS metrics, in immature and mature rabbits. Correlations are significant if the confidence interval does not include zero (Mohamied et al., 2015).

age-related patterns of lesions seen in cholesterol-fed rabbits (**Figure 9B**).

The pattern of transWSS around branches could change with age if the streaks of high transWSS move relative to the branches, perhaps as a result of changes in aortic geometry. Patterns of transWSS were therefore computed for geometries derived from the corrosion casts of young and mature rabbit aortas (Mohamied et al., 2015), even though time average WSS itself was already known not to change. The results for transWSS, as well as for time average WSS and OSI, were compared with the earlier study of lesion patterns in cholesterol-fed rabbits (Cremers et al., 2011) using more powerful, "bootstrapping" statistical methods.

TransWSS correlated significantly with lesion prevalence in mature animals, but time average WSS and the OSI did not (Mohamied et al., 2015). TransWSS also correlated significantly with lesion prevalence in immature animals and, although the other two metrics also did so (positively for time average WSS and negatively for the OSI), the correlation with transWSS was significantly stronger. Indeed, the correlation coefficients for transWSS were approximately three times those observed for the other metrics at both ages, exceeding 0.8 for immature rabbits. No significant correlations supported the low, oscillatory WSS theory. Thus the data are consistent with lesions being triggered by high transWSS in both immature and mature aortas, and with the pattern of this metric changing with age (**Figure 9C**).

Large-scale features of the pattern of transWSS in the thoracic aorta appear to be generated during the acceleration, peak systolic and deceleration phases of the cardiac cycle; the reverse flow and subsequent diastolic phases are short or characterised by WSS magnitudes that are close to zero, respectively, and hence do not make a significant contribution (Mohamied et al., 2017). The features are insensitive to the inflow waveform but sensitive to geometry. The curvature of the arch and descending aorta produce vortical structures that are responsible for the streaks of high transWSS; streaks in the descending segment can be decoupled from those in the arch and thus appear to depend at least in part on local curvature. Non-planarity is responsible for asymmetries in the streaks and taper determines their persistence

down the aorta, as with time average WSS (Mohamied et al., 2017).

The mechanisms by which the pattern of transWSS around branches is generated, and by which it changes with age, remain under investigation but, as already noted, changes in the location of the large-scale streaks may be responsible and these could in turn be determined by alterations of geometry. Changes with age in the taper of the rabbit aorta have been discussed above. Human aortas are known to "unfold" with age—the arch gets longer and its radius of curvature increases (Redheuil et al., 2011; Rylski et al., 2014)—whilst the angle of kyphosis, indicating curvature of the upper back, increases (Fon et al., 1980). Note that the parallel change with age in rabbit and human lesion patterns does not require that geometric changes are the same, only that vortices are shifted in the same way. Note also that the sensitivity of branch patterns to geometric features means that the results of CFD simulations could depend on subtleties such as the posture of the rabbit during the aortic casting process (see below); this may explain why changes with age in the average transWSS patterns are not as dramatic as changes with age in lesion patterns (Mohamied et al., 2015), or as the examples shown in **Figure 9B**.

Interactions between branch and large-scale patterns of transWSS may help answer another long-standing issue concerning the distribution of disease, which is that the influence of branches on lipid deposition appears to propagate further from the ostium than any conceivable influence branches have on flow (Weinberg, 2002). Previously, this anomaly has been attributed to the migration of activated endothelial cells towards the heart (Weinberg, 2002) but it may more plausibly be explained by the merging of branch-dependent and vortex-dependent regions of high transWSS.

Conclusion

CFD simulations were run with the aim of resolving whether the pattern of WSS around intercostal branch ostia changes with age in a way that can explain the age-related pattern of lesions, as suggested by patterns of nuclear elongation, or whether the pattern of WSS is static and therefore a change in the response to WSS is a more likely explanation, as suggested by experiments that altered NO synthesis and flow. The simulations showed that patterns of WSS did not change markedly between immature and mature rabbits. However, they did not support the idea that a change in response was responsible either, because the patterns were not those expected from early theoretical or physical models and did not strongly resemble the pattern of lesions at any age. The CFD simulations introduced a third possibility: they showed that the pattern of a new metric—the transWSS, capturing multidirectional WSS—changed with age and showed a much stronger resemblance to the pattern of lesions at both ages.

The discrepancy between the pattern of endothelial nuclear elongation and the pattern of WSS derived from CFD was striking. Not only did the former change with age whilst the latter did not, but the pattern of elongation did not strongly resemble computations of the pattern of WSS on which it is supposed to depend. Assumptions and simplifications are always involved when computing flow but the parametric studies suggest that only a fundamental error in specifying the side-branch flow waveform would have a large enough influence to annul the discrepancy. Doppler ultrasound data of Sloop et al. (1998) are consistent with an age-related change in waveform, reverse flow disappearing in people between the ages of 30 and 40 years. However, children were not examined. Further investigation is required.

The two data sets could be resolved if endothelial cells elongated in response to high transWSS rather than to high WSS. However, several studies which applied multidirectional flow to endothelial cells *in vitro* have shown the contrary (Dardik et al., 2005; Chakraborty et al., 2012). This topic also requires further investigation. For example, the same elevated value of transWSS can be produced by high WSS with small changes in flow direction, or by low WSS with large changes in direction. It is conceivable that different combinations occur *in vivo* and *in vitro* and have different effects on elongation.

The emergence of a possible role for transWSS introduces yet another factor into the interpretation of the experimental studies that appeared to show a change with age in the response to flow. Inhibiting NO synthesis had a dramatic effect on the mature but not the immature pattern of transport, but the data were obtained in aortas perfused *in situ* with a steady flow of buffer (Forster and Weinberg, 1997). There is zero transWSS everywhere when flow does not vary cyclically. Under such conditions, other fluid mechanical stresses may assume an importance in controlling transport into the wall that they do not have when significant transWSS is present. The fact that transport was measured only in regions directly upstream and downstream of branches could have hidden changes in pattern produced by such a shift.

Limitations imposed by measuring only directly upstream and downstream may also be relevant to the studies where NO was inhibited by giving L-NMMA to mature rabbits *in vivo* (Staughton and Weinberg, 2004b); the normal pattern of uptake—transport greater upstream than downstream—was abolished, but it was not dramatically reversed, as it was in the perfused vessels. This issue was reinvestigated in the studies (Bailey et al., 2015) where transport around branches was mapped *en face* by confocal microscopy. Some rabbits were administered high dose heparin for 1 h, which is known to inhibit the synthesis of NO (VanTeeffelen et al., 2007). Only very subtle changes were seen in the map of albumin uptake for 16–22-month-old animals but, although they were visually hard to discern, they were sufficient to change the pattern directly upstream and downstream of the branch from being ≈8% greater upstream to ≈3% greater downstream; these numbers are identical to the earlier study and, as before, the change was significant. The implication is that measurements restricted to the branch centreline may give an unrepresentative view and that inhibiting NO may do very little in conditions where transWSS is present. The same argument could also apply to the effect of side-branch ligation in mature animals, which appeared to reverse the normal pattern of transport (Staughton et al., 2001): the size of the effect may similarly have been incorrectly estimated.

A final point arising from the CFD studies is that the putative effects of aortic curvature on the large-scale distribution of

transWSS, and hence on its pattern around branches, mean that the posture of the animal (or human subject) may be of importance. The *in situ* perfusion experiments, the side-branch ligation experiments and the casting of the aorta were done with the rabbits supine, whereas rabbits were upright during tracer administration in the *in vivo* experiments, including when NO was inhibited. Long-term responses, such as those responsible for endothelial nuclear elongation or lesion development, involve integration over different postures.

FURTHER INVESTIGATION OF MECHANISMS RELATING FLOW TO PERMEABILITY

In the following, it is assumed that the pattern of flow changes with age. That would be consistent with an age-*independent* set of mechanisms linking flow, via transport, to disease. Such mechanisms have been sought *in vivo*, *in silico* and—for more molecular mechanisms—*in vitro*.

(i) *In vivo*

The two-pore theory of transendothelial transport was discussed above. The normal intercellular junction cannot be the large pore because it is too narrow to allow passage of particles such as LDL (diameter 23 nm). However, the cell turnover leaky junction hypothesis of Weinbaum et al. (1985) proposes that the width of intercellular junctions temporarily increases when endothelial cells divide or die, and that large particles might then cross by this route. Consistent with this hypothesis, "hotspots" of high permeability have been observed for a range of macromolecular tracers (reviewed by Chooi et al., 2016). They are associated with enhanced entry of LDL and often, although not exclusively, with mitosis or apoptosis (Stemerman et al., 1986; Lin et al., 1988; Lin et al., 1989; Lin et al., 1990; Truskey et al., 1992; Malinauskas et al., 1995); in rabbits weighing <3 kg, they occur at high frequency downstream of aortic side branches (Barakat et al., 1992; Herrmann et al., 1994). Mitosis and apoptosis are both thought to depend on blood flow.

One study (Chooi et al., 2016) has investigated whether the pattern of hotspots and mitosis changes with age around rabbit intercostal branch ostia. EBD pre-mixed with albumin was used as the tracer; it was allowed to circulate for only 10 min in order to limit any inhibition of the NO pathway. Hotspots of high uptake, as well as normal uptake, were quantified by *en face* confocal microscopy of tracer fluorescence, and mitosis occurring over several days was mapped by adding bromodeoxyuridine to drinking water and then staining it in endothelium with a fluorescent antibody. These methods should give better quantification and higher sensitivity than was possible in some earlier studies.

The main finding was that the pattern of hotspots switched with age. Hotspots were more frequent and more leaky downstream of branches in immature animals, and in longitudinal streaks at the sides of branches in mature animals. The patterns resemble those seen for disease and for uptake of other tracers except that areas immediately lateral to the branches had few hotspots. This may have resulted from a relative paucity of elastin and collagen in such regions, since EBD binds to these proteins on entering the wall.

Despite the detection of two patterns of hotspots, closer examination of the data did not provide much support for the cell turnover leaky junction hypothesis. First, there was no discernible pattern of mitosis and no spatial correlation between the number of mitosing cells and any hotspot metric. Second, hotspots accounted for only 5% of total uptake. Third, the non-hotspot uptake showed exactly the same patterns, and so did uptake through only the largest hotspots. These observations suggest that there is a continuum of local permeability values, and that the majority of uptake does not reflect the occurrence of an aberrant event. (Hotspots may have been caused by apoptosis, which was not assayed, and hotspots might have played a more significant role if a larger tracer had been used.) The relation between mitosis or apoptosis and shear stress is also not straightforward. The paper most often cited to show that DNA synthesis depends on flow—Davies et al. (1986)—showed an effect of turbulence, but there was actually no difference between static, low shear and high shear conditions. Furthermore, shear decreases rather than increases apoptosis (Dimmeler et al., 1996).

(ii) *In silico*

Concentration polarisation at the luminal surface of the arterial wall has been investigated by both computational and experimental methods. However, the experimental studies have been conducted under conditions where concentration polarisation is expected to have been unphysiologically high (reviewed in Vincent and Weinberg, 2014), so the focus here is on *in silico* work.

Concentration polarisation is expected because the arterial wall is two orders of magnitude more permeable to water than to large particles such as LDL. It will occur at the luminal surface if the endothelium provides the major barrier to LDL entry. A number of processes would act to reduce such LDL accumulation. First, LDL does cross the endothelium into the wall at a measurable rate; this process will accelerate as the concentration of LDL increases, unless it occurs by a saturable mechanism. Second, LDL can diffuse away from the endothelium, back into the bulk of the plasma; this is the classical effect that limits polarisation. Third, the flow of blood within the lumen could advect the LDL away from the wall. Because it would influence the near-wall concentration of LDL, and hence the transport of LDL into the wall, this mechanism provides a potential link between near-wall blood flow and uptake by the wall of large molecules (Colton et al., 1972; Keller, 1974).

Considering the case of flow down an infinitely long, straight artery in which concentration polarisation has already occurred, luminal flow would have no influence on the concentration of LDL at the wall sufficiently far from the entrance. The fluid would be shifted axially at each location, by an amount that depended on the distance from the wall and on the global flow rate, but that would not affect the concentration profile within the boundary

layer, which varies only in the radial direction. An effect of blood flow rate and wall shear stress on surface LDL concentration was seen in a straight artery in the computations of Wada and Karino (1999) because the LDL concentration was assumed to be uniform across the diameter at the entrance of the artery, and the segment was only 20 diameters long; hence, the concentration profile in the boundary layer was not the same at all lengthwise locations.

A second study by the same authors (Wada and Karino, 2002) examined flow in a geometry with a double bend, where flow recirculation occurred. In this case, the presence of blood flow with radial components would be expected to modify the concentration boundary layer even in the absence of entrance effects. Local variation in the surface concentration of LDL was seen in the simulation, although the proportion due to entrance effects was not established.

It is interesting to speculate that a branch could also modify near-wall concentrations, if it were located sufficiently far from the inlet that momentum and concentration boundary layers had developed. Considering, as a simplified example, the 2-D model described in **Figure 1B**, in which the near-wall blood upstream of the branch leaves the aorta, and the wall downstream of the branch is exposed to blood that had been closer to the aortic centreline, a lower near-wall LDL concentration would be expected downstream than upstream of the branch.

How big might such effects be? Wada and Karino (2002) obtained surface LDL concentrations 35% above the bulk concentration in their model of a double bend, albeit at Reynolds numbers below those appropriate for the human or even rabbit aorta. The model assumed that the wall is uniformly permeable to water, and that there is a sharp boundary between the blood and the wall. Neither assumption is correct. Fluid flow across the endothelium occurs principally through intercellular junctions, which occupy ~0.1% of the surface area. Fluid fluxes need to be confined to these areas in computational models, and to be increased by three orders of magnitude to maintain the same global hydraulic conductance. The luminal surface of the endothelium is covered with a coat of glycoproteins, proteoglycans and adsorbed plasma macromolecules; the thickness of this glycocalyx layer is debated, but current estimates are in the micron range (van den Berg et al., 2003). The layer has a higher resistance to diffusion than blood and shields the wall from convection in the blood phase. The first effect increases concentration polarisation and shear dependence, but only by small amounts at physiological parameter values (Vincent et al., 2009). The second effect amplifies the influence of the first on concentration polarisation because of the decrease in LDL diffusion (Vincent et al., 2010). On the other hand, it reduces the influence of luminal blood flow (Vincent et al., 2010). Overall, the predicted entry of LDL into the wall is essentially independent of the applied shear.

(iii) *In vitro*

Molecular mechanisms linking flow and endothelial permeability have been extensively investigated *in vitro*. However, there are four common issues with such studies.

The first is that they usually investigate responses to acute changes in flow—most often, a step change from zero flow to some steady level. This is convenient experimentally; many methods for applying shear stress to endothelial cells do not permit long-term culture. But the responses may be different—in fact, opposite—to those caused by chronic exposure to flow, and the mechanisms also differ. In a study by Warboys et al. (2010), exposure of endothelium to shear for 1 h increased permeability to albumin whereas exposure for 1 week decreased it, compared to static culture. The effect of chronic but not acute shear was reversed by inhibiting phosphatidylinositol-3-OH kinase, NO synthesis or soluble guanylyl cyclase.

Chronic *in vitro* effects are likely to prove more relevant than acute ones to endothelial behaviour *in vivo*. It could be argued that the transient effects are relevant to the inability of endothelial cells ever to adjust to constantly changing "disturbed flow," but a control involving chronic shear would still be required in order to determine effects of such flow.

If only studies of chronic shear are admissible, then the field is a small one. To make matters worse, a second issue is that most investigations have focused on unidirectional flow or, at best, flow that is oscillatory or pulsatile along one axis. If transWSS elevates permeability, then studies of uniaxial flow are insufficient. Unfortunately, it is difficult to apply multidirectional flows *in vitro*. The standard parallel-plate flow chamber has been adapted for this purpose. Kataoka et al. (1998) added inlet and outlet ports on the sides of the chamber, allowing flow to be switched between conventional and orthogonal directions, whilst Wang et al. (2012) grew endothelial cells on a glass slide within the chamber that could be manually rotated by any angle. The flow is predictable and controllable with both methods but throughput is low, chronic exposure is challenging and the frequency of directional change is many orders of magnitude lower than *in vivo*.

An alternative is the orbital shaker or swirling well method, in which endothelial cells are grown in conventional dishes or multi-well plates placed on a horizontal platform that translates in a circular orbit in the plane of the platform. The translation induces a wave that swirls around the well, producing multidirectional flow in the centre and uniaxial flow at the edge. The method (reviewed by Warboys et al., 2019) is low cost, high throughput, and permits chronic application of multidirectional flow at an appropriate frequency. The flow can be altered by changing the orbital radius and velocity, the dish radius and the depth of medium, but it is difficult to separate the effects of different shear metrics, several of which change with increasing radial distance from the centre. Furthermore, although different flow regimes have been identified and approximate analytical methods devised (Alpresa et al., 2018a; 2018b), accurate description of the shear acting on the base of the well requires CFD models that include the orbital forcing, the free surface of the gravitational wave (Berson et al., 2008) and, in some cases, the surface tension (Arshad et al., 2022).

Over twenty studies have used the method to determine effects of shear on endothelial cells; they demonstrated more homeostatic behaviour in endothelial cells located near the edge (uniaxial flow) and more pathogenic behaviour towards

the centre (multidirectional flow) (Warboys et al., 2019). An interesting recent observation (Arshad et al., 2021) is that endothelial cells can align so as to minimise the transWSS they experience; an observation of this type could not have been made with conventional devices producing unidirectional or uniaxial flows. It suggests that the effects of transverse flow on endothelial cells are sufficiently harmful that the cells have evolved mechanisms for minimising it. The adverse effect may be as simple as the higher shear stresses, or shear stress gradients, experienced by regions of the cell membrane that cover the nucleus and protrude into the lumen (Barbee et al., 1995; Hazel and Pedley, 2000; Yamaguchi et al., 2000), or they may involve more complex events (Wang et al., 2013). In either case, the behaviour justifies using the transWSSmin metric, described above.

A third issue is that endothelial permeability to albumin is two orders of magnitude higher in culture than *in vivo* (Albelda et al., 1988). A parallel phenomenon is seen in organs or vessels that are perfused with buffer rather than blood. Many groups have searched for ways to reduce this hyperpermeability; recent studies have identified the lack of sphingosine-1-phosphate (S1P) as a key issue. In blood, S1P is chiefly carried by erythrocytes and platelets; adding it to cell culture and to perfused organs or vessels dramatically reduces paracellular permeability (Schaphorst et al., 2003; Curry et al., 2012; Warboys et al., 2012; Zhang et al., 2016). In its absence, factors controlling permeability may be misidentified.

The fourth issue is that studies of mechanisms linking flow and transport need to examine the relevant transport pathway. If, for example, it is LDL transport that is of interest, then examining effects of flow on normal intercellular junctions may have little value. Unfortunately, routes are difficult to determine because transit times are short, and because tracers that cross the endothelium via junctions can move laterally to appear under the cell body and those that cross via vesicles can similarly appear under junctions. For LDL transport, the consensus view has swung back and forth between junctions and vesicles.

A significant breakthrough was the development by Dubrovskyi et al. (2013) of a method in which endothelial cells are grown on biotinylated gelatin and a tracer comprising avidin (approx. 66–69 kDa, similar to albumin) labelled with fluorescein isothiocyanate (FITC) is added to the medium above the cells. When this tracer crosses the endothelium, it immediately binds to the substrate. Its distribution, imaged by fluorescence microscopy, can be compared with overlying structures to identify the transport route. FITC-avidin was unequivocally found under intercellular junctions.

Ghim et al. (2017) extended this concept. Using other fluorophores can give larger tracers whilst retaining the essential biotin-binding property. Labelling avidin with a phycobiliprotein gives a tracer around the size of high density lipoprotein (HDL) whilst labelling it with a quantum dot (Qdot800) gives a tracer the size of LDL. Three pathways were observed. The albumin-sized tracer crossed the endothelium via junctions between two or more cells. (The fraction crossing where two rather than three or more cells meet depends slightly on experimental conditions; human endothelial cells cultured in appropriate medium form a tighter barrier than porcine aortic endothelial cells cultured in DMEM, and less FITC-avidin is then transported through bicellular junctions (Ghim et al., 2021a).) The HDL-sized tracer crossed *only* where three or more cells came together. And, despite the elevated paracellular transport expected *in vitro*, the LDL-sized tracer crossed only through the cells (**Figure 10A**).

Accumulation of the LDL-sized tracer under the cells was reduced in the nuclear region and was not enhanced near cell junctions even after prolonged incubation (Ghim et al., 2017). Furthermore, Ghim et al. (2021b) subsequently showed that the subendothelial accumulation of the tracer, but not of FITC-avidin, was reduced by Dynasore, which is an inhibitor of the fission of clathrin-coated vesicles from the plasma membrane (Macia et al., 2006) and also of fluid-phase endocytosis and micropinocytosis (Park et al., 2013). These observations are consistent with transport by a vesicular pathway of some type. The three pathways identified by Ghim et al. (2017) are different from the three—normal junctions, transiently widened junctions and vesicles—deduced by Cancel et al. (2007); for LDL transport under convective conditions, they determined that leaky junctions were the dominant route.

Strong evidence for vesicular transport of LDL has also arisen from studies identifying receptors—scavenger receptor class B type 1 (SR-B1) (Armstrong et al., 2015; Ghaffari et al., 2018; Huang et al., 2019) and activin receptor-like kinase 1 (ALK1) (Kraehling et al., 2016)—that mediate its passage in coronary artery and aortic endothelia, and from studies showing reduced LDL transport in caveolin 1 deficient mice (Ramírez et al., 2019). (Receptor mediated transcytosis of albumin has also been proposed (Schnitzer, 1992)). The influence of receptors may have been over-estimated in some of these investigations. For example, the concentration of labelled LDL was often far below physiological levels, which would have favoured high-affinity routes. It is unlikely that a receptor exists for quantum dots, so fluid phase transcytosis seems the most plausible mechanism at least for this tracer, and perhaps also for LDL itself (Vasile et al., 1983).

The swirling well method was used to investigate effects of different types of flow on transendothelial transport of the three avidin-based tracers. The choice of culture plate, medium depth and orbital parameters gave a large difference in the directionality of WSS from the centre to the edge of the well, but a negligible change in time average WSS, according to numerical simulations that incorporated surface tension (Arshad et al., 2022). Transport of the small and medium-sized macromolecular tracers through intercellular junctions was increased in the centre of the well (multidirectional flow) and decreased at its edge (uniaxial flow) compared to static controls (Ghim et al., 2017). However, transcellular transport of the LDL-sized particle was uniformly lowered across the well.

PROPOSAL OF A SECRETED MEDIATOR

Why there should be a uniform change in LDL transport despite spatial variation in the type of flow? One possibility is that a

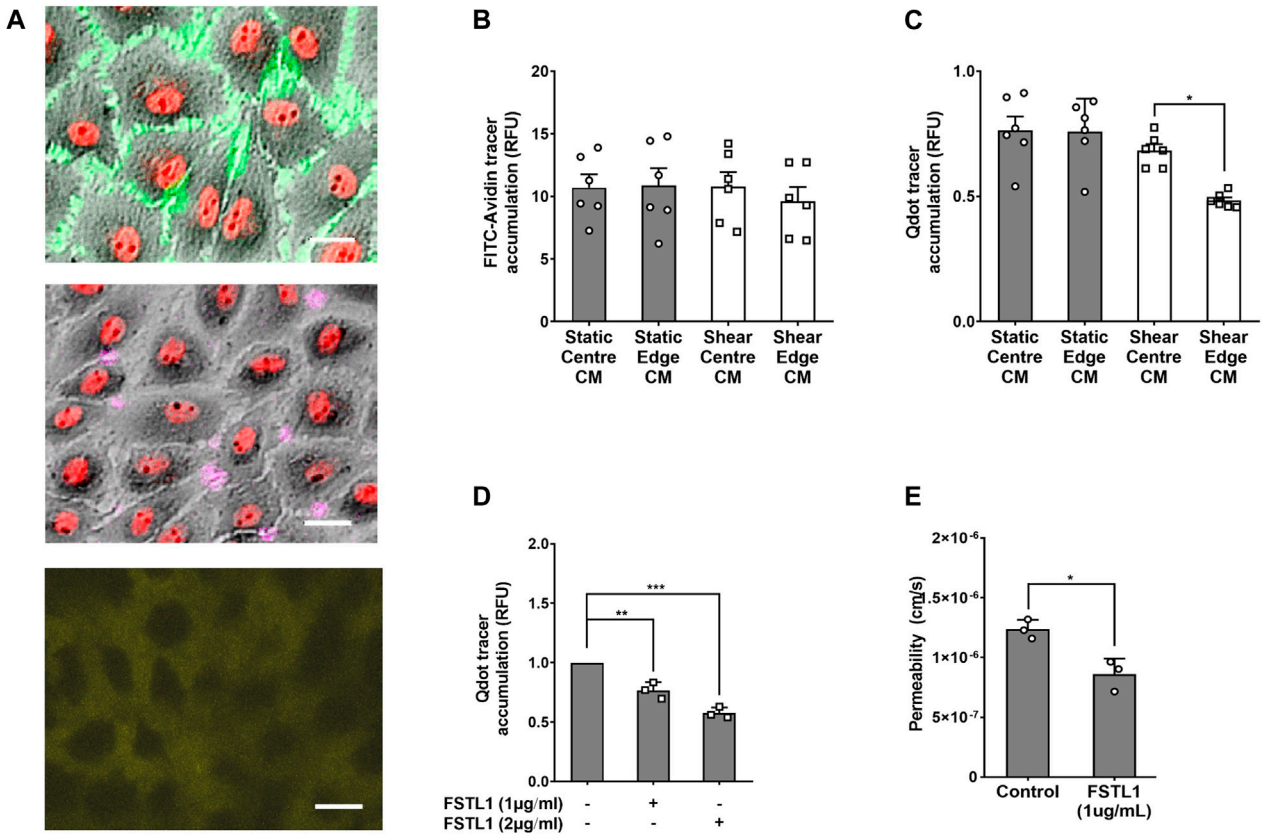

FIGURE 10 | (A) *En face* view of the uptake of avidin based tracers that have crossed cultured endothelium and then immediately bound to the biotin-labelled substrate. From top to bottom: albumin-, HDL- and LDL-sized tracers comprising avidin labelled with FITC (green), phycobiliprotein (purple) and quantum dots (yellow), respectively. Endothelial cells are visible in phase contrast and their nuclei are stained red (DRAQ-5) in the top two images. Bar = 10 µm (top and middle) or 20 µm (bottom) (Ghim et al., 2017). **(B,C)** Conditioned medium (CM) from cells at the centre or edge of swirled or static wells had no effect on the permeability of target cultured endothelium to FITC-avidin, but CM from cells swirled at the edge reduced permeability to quantum dot-labelled avidin. RFU = relative fluorescence units (Ghim et al., 2021b) **(D,E)** Exogenous recombinant FSTL1 reduced permeability of cultured endothelium to quantum dot-labelled avidin and to LDL (Ghim et al., 2021b).

soluble mediator was being secreted by cells in one region, exposed to one type of flow, and that it became well-mixed in the medium, thus affecting all regions equally, overcoming any effects of local flow on LDL permeability (Ghim et al., 2017). If correct, this would mean that the directionality of flow affects transport of both small and large macromolecules, but through different mechanisms; that might explain why transport patterns for albumin (Weinberg, 1988) and LDL (Schwenke and Carew, 1988) are similar *in vivo* even though transport might be occurring through different pathways.

To test the concept that secreted mediators could obscure the true relation between flow and endothelial phenotype, methods were developed to passivate parts of the base of the swirling well so that cells would grow only at the edge or only at the centre, even in chronic experiments (Ghim et al., 2018; Pang et al., 2021a; Ghim et al., 2021b). When the whole well was seeded with cells and swirled, there was no difference in tumor necrosis factor α (TNF-α)-induced intercellular adhesion molecule 1 (ICAM-1) or vascular cell adhesion protein 1 (VCAM-1) expression between the centre and the edge (Ghim et al., 2018). When only the centre or only the edge was seeded, expression was unchanged at the edge but elevated in the centre (Ghim et al., 2018). This demonstrates that an anti-inflammatory mediator is released from cells at the edge (uniaxial flow). When the whole well is seeded or when only the edge is seeded, the mediator limits adhesion molecule expression by all the cells. When cells are not present at the edge, there is increased expression by cells in the centre.

The method can be extended by collecting medium from fully seeded wells, or from wells where cells grow only at the centre or edge, and then applying the conditioned medium to target cells. This technique was used to unmask the true relation between flow and LDL transport across cultured endothelium (Ghim et al., 2021b). Medium conditioned by cells sheared at the edge of the well (uniaxial flow) reduced transcellular transport of the LDL-sized tracer in target cells but did not affect transport of the smaller, FITC-avidin tracer (**Figures 10B,C**). Medium conditioned by cells sheared at the centre of the well (multidirectional flow) or by static cells had no effect.

Effects of heat treatment and size filtration, an unbiased proteomic analysis and ELISA of the medium identified follistatin-like 1 protein (FSTL1) as a likely mediator (Ghim

et al., 2021b). Addition of recombinant FSTL1 reduced transport of quantum dot-labelled avidin across target endothelium in a concentration dependent manner (**Figure 10C**). It also reduced transendothelial transport of LDL itself (**Figure 10D**). (The fact that LDL and the quantum dot tracer were affected in same way is additional evidence that LDL is transported by receptor-independent, fluid-phase transcytosis.) It had no effect on transport of the smaller FITC-avidin tracer. FSTL1 and medium conditioned by cells swirled at the edge of the well also had anti-inflammatory effects, probably accounting for the results of the study of Ghim et al. (2018).

A preliminary investigation of signalling events downstream of FSTL1 (Ghim et al., 2021b) focused on the role of Bone Morphogenetic Protein 4 (BMP4) because this molecule is known to be expressed more highly in atheroprone than protected regions of the arterial tree, to be expressed more highly in the centre than the edge of swirling wells, and to be inhibited by FSTL1 (Sorescu et al., 2003; Geng et al., 2011; Souilhol et al., 2020). Exogenous recombinant human BMP4 increased transcytosis (Ghim et al., 2021b). FSTL1 blocked this barrier-disrupting effect, as did the BMP4 inhibitor noggin. However, FSTL1 was more effective: it reduced transport of the LDL-sized tracer below baseline levels, whereas noggin did not. Thus there appears to be at least one other pathway, in addition to blocking effects of BMP4, by which FSTL1 reduces permeability.

Conclusion

The swirling well method in combination with substrate-binding tracers of different size and segmentation of cell growth has demonstrated that transWSS increases both paracellular and vesicular transport across endothelium, but by different mechanisms. The effect on LDL-sized particles may be caused by a lowered secretion of FSTL1 from the endothelium, which in turn causes a disinhibition of transcytosis.

LIMITATIONS

The data and arguments presented in this review suffer from a number of limitations:

(i) There are no relevant transport data in people

It is difficult to measure transport of circulating macromolecules into the human arterial wall. Even when it has been accomplished (Tanimura et al., 1980), the fact that lesions are inevitably present makes the data of doubtful value: any spatial variation could be a result rather than a cause of disease, contrary to the situation in rabbits, where spontaneous disease is uncommon and vanishingly rare at the ages of greatest interest.

(ii) The non-human *in vivo* data derive from one site in one experimental model

The non-human *in vivo* data discussed above were obtained at side branches of the aorta in rabbits. White Carneau pigeons, which were once a popular model of atherosclerosis, and genetically modified mice, which are currently the most widely used, do not show the same age-related changes in lesion pattern at these anatomical locations (Richards and Weinberg, 2000; McGillicuddy et al., 2001).

Most conduit artery branches are bifurcations, where the parent vessel splits into two approximately equal daughter vessels, rather than T-branches like those seen in the aorta. TransWSS has been computed at the human carotid bifurcation (Gallo et al., 2016). There was no explicit comparison with disease, but high transWSS was seen on the flow divider and low transWSS was seen in the carotid sinus of many subjects, whereas disease prevalence shows broadly the opposite pattern (Grøttum et al., 1983). A formal evaluation of the spatial correlation is required.

Flow and LDL transport have been measured at the aorto-iliac bifurcation of mature rabbits by Berceli et al. (1990). LDL uptake was elevated in the lateral walls of the proximal segment of the daughter branches; high values of the OSI occurred in these segments when the vessels were perfused *in vitro*. McMillan (1985a,b) has speculated that highly multidirectional flow occurs at such locations, but the study of Berceli et al. assessed flow by Doppler techniques that could only measure velocity along the beam axis.

The relation of transWSS and disease has been assessed in coronary arteries, although not at branch points. A prospective study of human coronary arteries by Kok et al. (2019) found that transWSS was not significantly correlated with change in total plaque, fibrous tissue or fatty-fibrous tissue over time. TransWSS was significantly correlated with the increase in necrotic cores and dense calcification, but autocorrelation was not taken into account in the statistical analysis and significance will therefore have been overestimated. In a prospective study of porcine coronary arteries by Hoogendoorn et al. (2020), it is again clear that there was no relation between transverse WSS and disease progression (their Figure 1D). The association of lesion growth with other metrics such as the OSI and relative residence time may therefore reflect the fact that these metrics capture simple reversing flow as well as multidirectional flow. Neither study included cyclical motion of the coronary arteries when computing flow, and this may have introduced significant errors.

The pattern of albumin uptake around the left coronary bifurcation in rabbits showed significant changes with age but not the major reversal seen at aortic side branches (Staughton et al., 2007).

(iii) There is evidence for more than one mechanism and the evidence is self-contradictory

This limitation has been discussed at various points throughout the review. Briefly, some evidence suggests that there is a change with age in the mechanisms linking flow to transport, whilst other evidence suggests that the flow patterns themselves change with age. The former studies have largely supported the view that there is a change in the role of flow and nitric oxide, but there are inconsistencies; in particular, the effect of inhibiting NO production was unexpectedly small in mature

rabbits *in vivo* (Staughton and Weinberg, 2004b), and the disappearance of the downstream pattern of transport in one study of anaesthetised rabbits (Staughton et al., 2001) is unexplained.

One set of studies suggesting a change with age in the pattern of flow is based on measuring nuclear elongation (Al-Musawi et al., 2004; Bond et al., 2011) while another is based on computational simulations of transWSS, a metric of multidirectionality (Peiffer et al., 2013a; Mohamied et al., 2015). However, elongation is not thought to depend on transWSS. The putative role of transWSS is questioned by the finding of apparently normal patterns of permeability in aortas perfused with a steady flow of buffer (Forster and Weinberg, 1997), where transWSS will everywhere be zero.

The discrepancies may be explained by technicalities: the restriction of early studies to measuring transport in a thin axial slice along the branch centreline; the use of tracers based on albumin, which likely enters the wall by both paracellular and transcellular routes but in different proportions in different preparations; and the incomplete understanding of the cause of endothelial nuclear shape.

(iv) Proteins other than FSTL1 may mediate effects of transWSS on transcytosis of LDL

An internal inconsistency in the *in vitro* study (Ghim et al., 2021b) identifying mediators is that although exogenous recombinant FSTL1 and medium conditioned by cells at the edge of the well both reduced transport of the LDL-sized tracer, much higher concentrations of exogenous FSTL1 were required than could be detected in the conditioned medium. This may reflect aberrant folding of the recombinant FSTL1 or differences in the experimental protocol (for example, cells were exposed to conditioned medium for longer than they were exposed to exogenous FSTL1), but another possibility is that additional mediator(s) were missed in the proteomic analysis. The cells used to condition medium were isolated from porcine aortas and the porcine proteome is less well annotated than the human one.

PERSPECTIVES AND FUTURE WORK

1 TransWSS is the mechanical factor that currently best explains the age-related patterns of permeability and lesion prevalence around side-branch ostia in the aorta. Further work is required in the following areas:
   i) to understand whether the same is true in other vessels. In particular, numerical simulations of coronary arteries that take into account cyclic variation in geometry may give different results from published studies that used static geometries, given the likely relation between radius of curvature, vortical structures and flow direction.
   ii) to refine the age-related maps of transWSS. Boundary conditions used in current studies may be insufficiently precise, given the probable dependence of transWSS patterns on posture and age-related changes in geometry.
   iii) to ascertain whether other shear metrics might show comparable age-related patterns. A key question is whether altering the extent of reverse flow in the side branch might give patterns of time average WSS similar to those already obtained for transWSS.
2 The age-related patterns of aortic permeability and lesion prevalence also strongly resemble patterns of endothelial nuclear elongation around branch ostia. That is currently unexplained, since high transWSS is not expected *a priori* to cause endothelial elongation. Important points are:
   i) are these expectations correct? the influence of transWSS on endothelial morphology needs systematic investigation.
   ii) does the apparent relation with nuclear elongation but not with time average WSS suggest that the pattern of time average WSS (commonly thought to determine elongation) has been mischaracterised in the simulations? This is related to point (1.iii), above.
3 TransWSS appears to suppress the endothelial secretion of atheroprotective mediators. A candidate mediator—FSTL1—has anti-inflammatory effects and reduces transcytosis, including fluid-phase transcytosis; it reduces permeability to LDL but not to albumin-sized tracers. This raises a number of issues:
   i) why does the pattern of disease correlate *in vivo* with the pattern of albumin transport, if albumin and LDL are transported by different routes, altered by different mediators? One solution to this, again requiring investigation, is that transWSS increases permeability to both types of macromolecule but through different pathways. Based on *in vivo* studies, transWSS might be affecting transport of albumin through an NO-dependent mechanism.
   ii) through which signalling pathways and by what effects on vesicle movement does FSTL1 alter LDL transport? A role for BMP4 has been demonstrated but there is also evidence that other pathways are involved. Studies of vesicular mechanics may require the development of new methods of dynamic, super-resolution microscopy.
   iii) are mediators other than FSTL1 involved? At present, it is known that any such mediators are likely to be proteins and to have sizes between 3 and 100 kDa. Use of human rather than porcine endothelial cells would permit more detailed proteomic studies to resolve this point.

CONCLUSION

The relation between mechanical forces, transport properties of the arterial wall, and the localised occurrence of arterial disease has been investigated for over 100 years, and there has been intensive investigation of the role of WSS for over 50 years. The studies summarised above are consistent with 1) excessive net uptake of circulating macromolecules leading to a high prevalence of lesions, 2) excessive net uptake resulting from an excessive rate of influx into the wall, and 3) the pattern of influx and disease changing with age, explaining apparent discrepancies between human disease, animal disease and permeability. The

data do not appear to support the simple low WSS hypothesis. However, the WSS characteristic that is responsible and the mechanisms linking WSS to transport have not been fully resolved. The problem is not that we do not have an explanation but that we have too many.

There may not be a single trigger. It is conceivable that endothelial cells have a "comfort zone" for a number of WSS metrics (and perhaps for other mechanical stresses as well), with disease developing when one or more metrics falls outside this range—for example, if WSS is too high or too oscillatory. That would complicate the establishment of causes, although at some point the pathways should converge on a single or small number of key properties, such as the transcytosis of LDL across endothelial cells.

An alternative to the comfort zone hypothesis is that the important WSS metric may be a complex or unexpected one, not revealed by early studies. Evidence has been presented that at least for aortic side branches, highly multidirectional near-wall flow is a trigger. Preliminary studies have identified a mediator—there may be others—linking this mechanical property to transcytosis of LDL. An interesting feature of this mediator is that it appears able to influence inflammatory pathways as well as permeability.

The view that atherogenesis is triggered by excessive entry of lipoproteins into the wall has been labelled the "response to influx" hypothesis (Weinberg, 2004). There is evidence that atherosclerosis develops as a "response to retention" of lipoproteins in the wall (Williams and Tabas, 1995), but the lipoproteins first have to get into the wall. The spatial correlations presented above suggest that it is the entry of the lipoproteins that is the rate-limiting step, and that any retention is simply proportional to it.

Statins have been successful at limiting the development of arterial disease. They work chiefly by lowering plasma cholesterol concentrations and, therefore, the entry of cholesterol into the wall. The same effect could be achieved by reducing permeability. An encouraging phenomenon is that the downstream lesions present in children regress with increasing age; the response to influx hypothesis attributes this to a decrease in permeability at that location, in the absence of marked changes in plasma cholesterol levels through the transitional years. A corollary is that reducing permeability could on its own be able to reduce adult disease. The two approaches—reducing plasma cholesterol concentrations and reducing arterial wall permeability—should have a multiplicative effect. A particular advantage of identifying a pathway that mediates between atherogenic flow and elevated permeability, rather than one which affects permeability globally, is that it could be used to reduce transport only where it is inappropriately elevated, and not to alter it in regions where permeability is instead matched to physiological need and sufficiently low that lesions do not develop.

AUTHOR CONTRIBUTIONS

The author confirms being the sole contributor of this work and has approved it for publication.

FUNDING

British Heart Foundation project Grant PG/15/102/31890 Imperial College London suppports the APCs. The work was supported principally by the British Heart Foundation, directly (e.g. Grants RG/11/5/28743 and PG/15/102/31890) and through the Centres of Excellence that it has funded at Imperial College London.

ACKNOWLEDGMENTS

The author gratefully acknowledges the experimental and intellectual contributions of members of his research group and other co-authors, particularly long-term collaborator Professor SJ Sherwin.

SUPPLEMENTARY MATERIAL

The Supplementary Material for this article can be found online at: https://www.frontiersin.org/articles/10.3389/fbioe.2022.836680/full#supplementary-material

REFERENCES

Adams, C. W. M. (1981). Permeability in Atherosclerosis. *Atherosclerosis* 39 (1), 131–132. doi:10.1016/0021-9150(81)90095-2

Al-Musawi, S. L., Bishton, J., Dean, J., Williams, S., Cremers, S. G., and Weinberg, P. D. (2004). Evidence for a Reversal with Age in the Pattern of Near-Wall Blood Flow Around Aortic Branches. *Atherosclerosis* 172 (1), 79–84. doi:10.1016/j.atherosclerosis.2003.09.028

Albelda, S. M., Sampson, P. M., Haselton, F. R., McNiff, J. M., Mueller, S. N., Williams, S. K., et al. (1988). Permeability Characteristics of Cultured Endothelial Cell Monolayers. *J. Appl. Physiol.* 64 (1), 308–322. doi:10.1152/jappl.1988.64.1.308

Aliev, G., Miah, S., Turmaine, M., and Burnstock, G. (1995). An Ultrastructural and Immunocytochemical Study of Thoracic Aortic Endothelium in Aged Sprague-Dawley Rats. *J. Submicrosc Cytol. Pathol.* 27 (4), 477–490.

Alpresa, P., Sherwin, S., Weinberg, P., and van Reeuwijk, M. (2018a). Orbitally Shaken Shallow Fluid Layers. I. Regime Classification. *Phys. Fluids* 30, 032107. doi:10.1063/1.4996916

Alpresa, P., Sherwin, S., Weinberg, P., and van Reeuwijk, M. (2018b). Orbitally Shaken Shallow Fluid Layers. II. An Improved wall Shear Stress Model. *Phys. Fluids* 30, 032108. doi:10.1063/1.5016343

Anitschkow, N. (1933). "Experimental Atherosclerosis in Animals," in *Arteriosclerosis*. Editor EV Cowdry (New York: Macmillan), 271–322.

Arzani, A., and Shadden, S. C. (2016). Characterizations and Correlations of Wall Shear Stress in Aneurysmal Flow. *J. Biomech. Eng.* 138 (1), 0145031–01450310.

Armstrong, S. M., Sugiyama, M. G., Fung, K. Y. Y., Gao, Y., Wang, C., Levy, A. S., et al. (2015). A Novel Assay Uncovers an Unexpected Role for SR-BI in LDL Transcytosis. *Cardiovasc. Res.* 108 (2), 268–277. doi:10.1093/cvr/cvv218

Arshad, M., Ghim, M., Mohamied, Y., Sherwin, S. J., and Weinberg, P. D. (2021). Endothelial Cells Do Not Align with the Mean wall Shear Stress Vector. *J. Roy. Soc. Interface* 18 (174), 20200772. doi:10.1098/rsif.2020.0772

Arshad, M., Rowland, E. M., Riemer, K., Sherwin, S. J., and Weinberg, P. D. (2022). Improvement and Validation of a Computational Model of Flow in the Swirling Well Cell Culture Model. *Biotechnol. Bioeng.* 119 (1), 72–88. doi:10.1002/bit.27951

Bailey, E. L., Bazigou, E., Sowinski, P. S. J., and Weinberg, P. D. (2015). Mass Transport Properties of the Rabbit Aortic Wall. *PLoS One* 10 (3), e0120363. doi:10.1371/journal.pone.0120363

Bao, X., Lu, C., and Frangos, J. A. (1999). Temporal Gradient in Shear but Not Steady Shear Stress Induces PDGF-A and MCP-1 Expression in Endothelial Cells: Role of NO, NF Kappa B, and Egr-1. *Arterioscler. Thromb. Vasc. Biol.* 19 (4), 996–1003. doi:10.1161/01.atv.19.4.996

Barakat, A. I., Uhthoff, P. A. F., and Colton, C. K. (1992). Topographical Mapping of Sites of Enhanced HRP Permeability in the normal Rabbit Aorta. *J. Biomech. Eng.* 114 (3), 283–292. doi:10.1115/1.2891385

Barbee, K. A., Mundel, T., Lal, R., and Davies, P. F. (1995). Subcellular Distribution of Shear Stress at the Surface of Flow-Aligned and Nonaligned Endothelial Monolayers. *Am. J. Physiol.* 268 (4 Pt 2), H1765–H1772. doi:10.1152/ajpheart.1995.268.4.H1765

Barnes, S. E., and Weinberg, P. D. (1998). Contrasting Patterns of Spontaneous Aortic Disease in Young and Old Rabbits. *Arterioscler. Thromb. Vasc. Biol.* 18 (2), 300–308. doi:10.1161/01.atv.18.2.300

Barnes, S. E., and Weinberg, P. D. (2001). Strain-Dependent Differences in the Pattern of Aortic Lipid Deposition in Cholesterol-Fed Rabbits. *Exp. Mol. Pathol.* 71 (2), 161–170. doi:10.1006/exmp.2001.2395

Barnes, S. E., and Weinberg, P. D. (1999). Two Patterns of Lipid Deposition in the Cholesterol-Fed Rabbit. *Arterioscler. Thromb. Vasc. Biol.* 19 (10), 2376–2386. doi:10.1161/01.atv.19.10.2376

Berceli, S. A., Warty, V. S., Sheppeck, R. A., Mandarino, W. A., Tanksale, S. K., and Borovetz, H. S. (1990). Hemodynamics and Low Density Lipoprotein Metabolism. Rates of Low Density Lipoprotein Incorporation and Degradation along Medial and Lateral walls of the Rabbit Aorto-Iliac Bifurcation. *Arteriosclerosis* 10 (5), 686–694. doi:10.1161/01.atv.10.5.686

Berson, R. E., Purcell, M. R., and Sharp, M. K. (2008). Computationally Determined Shear on Cells Grown in Orbiting Culture Dishes. *Adv. Exp. Med. Biol.* 614, 189–198. doi:10.1007/978-0-387-74911-2_22

Bond, A. R., Iftikhar, S., Bharath, A. A., and Weinberg, P. D. (2011). Morphological Evidence for a Change in the Pattern of Aortic wall Shear Stress with Age. *Arterioscler. Thromb. Vasc. Biol.* 31 (3), 543–550. doi:10.1161/atvbaha.110.219683

Buchanan, J. R., Jr, Kleinstreuer, C., Truskey, G. A., and Lei, M. (1999). Relation between Non-Uniform Hemodynamics and Sites of Altered Permeability and Lesion Growth at the Rabbit Aorto-Celiac Junction. *Atherosclerosis* 143 (1), 27–40. doi:10.1016/s0021-9150(98)00264-0

Cancel, L. M., Fitting, A., and Tarbell, J. M. (2007). *In Vitro* study of LDL Transport under Pressurized (Convective) Conditions. *Am. J. Physiol Heart Circ. Physiol.* 293 (1), H126–H132. doi:10.1152/ajpheart.01188.2006

Caro, C. G., Fitz-Gerald, J. M., and Schroter, R. C. (1971). Atheroma and Arterial wall Shear. Observation, Correlation and Proposal of a Shear Dependent Mass Transfer Mechanism for Atherogenesis. *Proc. R. Soc. Lond. B Biol. Sci.* 177 (1046), 109–159. doi:10.1098/rspb.1971.0019

Caro, C. G., and Lever, M. J. (1983). The Mass Transport of the Arterial Wall: Effect of Mechanical Stresses and Vasoactive Agents, Including Nitrates. *Z. Kardiol* 72 (Suppl. 3), 178–181.

Chakraborty, A., Chakraborty, S., Jala, V. R., Haribabu, B., Sharp, M. K., and Berson, R. E. (2012). Effects of Biaxial Oscillatory Shear Stress on Endothelial Cell Proliferation and Morphology. *Biotechnol. Bioeng.* 109, 695–707. doi:10.1002/bit.24352

Chooi, K. Y., Comerford, A., Cremers, S. J., and Weinberg, P. D. (2016). Role of Endothelial Permeability Hotspots and Endothelial Mitosis in Determining Age-Related Patterns of Macromolecule Uptake by the Rabbit Aortic Wall near Branch Points. *Atherosclerosis* 250, 77–83.

Clarke, L. A., Mohri, Z., and Weinberg, P. D. (2012). High Throughput en Face Mapping of Arterial Permeability using Tile Scanning Confocal Microscopy. *Atherosclerosis* 224 (2), 417–425. doi:10.1016/j.atherosclerosis.2012.08.001

Colton, C. K., Friedman, S., Wilson, D. E., and Lees, R. S. (1972). Ultrafiltration of Lipoproteins through a Synthetic Membrane. Implications for the Filtration Theory of Atherogenesis. *J. Clin. Invest.* 51, 2472–2481. doi:10.1172/JCI107061

Cooke, J. P., Andon, N. A., Girerd, X. J., Hirsch, A. T., and Creager, M. A. (1991). Arginine Restores Cholinergic Relaxation of Hypercholesterolemic Rabbit Thoracic Aorta. *Circulation* 83 (3), 1057–1062. doi:10.1161/01.cir.83.3.1057

Cornhill, J. F., Herderick, E. E., and Stary, H. C. (1990). Topography of Human Aortic Sudanophilic Lesions. *Monogr. Atheroscler.* 15, 13–19.

Cremers, S. G., Wolffram, S. J., and Weinberg, P. D. (2011). Atheroprotective Effects of Dietary L-Arginine Increase with Age in Cholesterol-Fed Rabbits. *Br. J. Nutr.* 105 (10), 1439–1447. doi:10.1017/s0007114510005234

Curry, F. E., Clark, J. F., and Adamson, R. H. (2012). Erythrocyte-Derived Sphingosine-1-Phosphate Stabilizes Basal Hydraulic Conductivity and Solute Permeability in Rat Microvessels. *Am. J. Physiol Heart Circ. Physiol.* 303 (7), H825–H834. doi:10.1152/ajpheart.00181.2012

Dancu, M. B., and Tarbell, J. M. (2007). Coronary Endothelium Expresses a Pathologic Gene Pattern Compared to Aortic Endothelium: Correlation of Asynchronous Hemodynamics and Pathology *In Vivo*. *Atherosclerosis* 192 (1), 9–14. doi:10.1016/j.atherosclerosis.2006.05.042

Dardik, A., Chen, L., Frattini, J., Asada, H., Aziz, F., Kudo, F. A., et al. (2005). Differential Effects of Orbital and Laminar Shear Stress on Endothelial Cells. *J. Vasc. Surg.* 41 (5), 869–880. doi:10.1016/j.jvs.2005.01.020

Davies, P. F., Remuzzi, A., Gordon, E. J., Dewey, C. F., Jr, and Gimbrone, M. A., Jr (1986). Turbulent Fluid Shear Stress Induces Vascular Endothelial Cell Turnover *In Vitro*. *Proc. Natl. Acad. Sci.* 83 (7), 2114–2117. doi:10.1073/pnas.83.7.2114

Dewey, C. F., Jr, Bussolari, S. R., Gimbrone, M. A., Jr, and Davies, P. F. (1981). The Dynamic Response of Vascular Endothelial Cells to Fluid Shear Stress. *J. Biomech. Eng.* 103 (3), 177–185. doi:10.1115/1.3138276

Dimmeler, S., Haendeler, J., Rippmann, V., Nehls, M., and Zeiher, A. M. (1996). Shear Stress Inhibits Apoptosis of Human Endothelial Cells. *FEBS Lett.* 399 (1-2), 71–74. doi:10.1016/s0014-5793(96)01289-6

Dubrovskyi, O., Birukova, A. A., and Birukov, K. G. (2013). Measurement of Local Permeability at Subcellular Level in Cell Models of Agonist- and Ventilator-Induced Lung Injury. *Lab. Invest.* 93 (2), 254–263. doi:10.1038/labinvest.2012.159

Ewins, B. A., Majewicz, J., Staughton, T. J., and Weinberg, P. D. (2002). Two-Dimensional Maps of Short-Term Albumin Uptake by the Immature and Mature Rabbit Aortic Wall Around Branch Points. *J. Biomech. Eng.* 124 (6), 684–690. doi:10.1115/1.1517063

Fon, G., Pitt, M., and Thies, A., Jr (1980). Thoracic Kyphosis: Range in Normal Subjects. *Am. J. Roentgenology* 134 (5), 979–983. doi:10.2214/ajr.134.5.979

Forster, B. A., Javed, Q., Leake, D. S., and Weinberg, P. D. (1996). High-Resolution Mapping of the Frequency of Lipid Deposits in Thoracic Aortae from Cholesterol-Fed and Heritable Hyperlipidaemic Rabbits. *Atherosclerosis* 120 (1-2), 249–253. doi:10.1016/0021-9150(95)05718-8

Forster, B. A., and Weinberg, P. D. (1997). Evans' Blue Dye Abolishes Endothelium-Dependent Relaxation of Rabbit Aortic Rings. *Atherosclerosis* 129 (1), 129–131. doi:10.1016/s0021-9150(96)06020-0

Fredrick Cornhill, J., and Roach, M. R. (1976). A Quantitative Study of the Localization of Atherosclerotic Lesions in the Rabbit Aorta. *Atherosclerosis* 23 (3), 489–501. doi:10.1016/0021-9150(76)90009-5

Friedman, M., and Byers, S. O. (1963). Endothelial Permeability in Atherosclerosis. *Arch. Pathol.* 76, 99–105.

Friedman, M. H., and Ehrlich, L. W. (1984). Numerical Simulation of Aortic Bifurcation Flows: The Effect of Flow Divider Curvature. *J. Biomech. Eng.* 17 (12), 881–888. doi:10.1016/0021-9290(84)90001-0

Friedman, M. H., Hutchins, G. M., Bargeron, C. B., Deters, O. J., and Mark, F. F. (1981). Correlation of Human Arterial Morphology with Hemodynamic Measurements in Arterial Casts. *J. Biomechan. Eng.* 103 (3), 204–207. doi:10.1115/1.3138279

Fry, D. L. (1969). Certain Chemorheologic Considerations Regarding the Blood Vascular Wall Interface with Particular Reference to Coronary Artery Disease. *Circulation* 40 (Suppl. IV), 38–59. doi:10.1161/01.cir.40.5s4.iv-38

Fry, D. L. (1973). "Responses of the Arterial Wall to Certain Physical Factors," in *Ciba Foundation Symposium 12 - Atherogenesis: Initiating Factors*. Editors R. Porter and J. Knight. Chichester: John Wiley & Sons, Ltd, 93-125.

Gallo, D., Steinman, D. A., and Morbiducci, U. (2016). Insights into the Co-Localization of Magnitude-Based Versus Direction-Based Indicators of

Disturbed Shear at the Carotid Bifurcation. *J. Biomech.* 49 (12), 2413–2419. doi:10.1016/j.jbiomech.2016.02.010

Geng, Y., Dong, Y., Yu, M., Zhang, L., Yan, X., Sun, J., et al. (2011). Follistatin-Like 1 (Fstl1) Is a Bone Morphogenetic Protein (BMP) 4 Signaling Antagonist in Controlling Mouse Lung Development. *Proc. Natl. Acad. Sci.* 108 (17), 7058–7063. doi:10.1073/pnas.1007293108

Ghaffari, S., Naderi Nabi, F., Sugiyama, M. G., and Lee, W. L. (2018). Estrogen Inhibits LDL (Low-Density Lipoprotein) Transcytosis by Human Coronary Artery Endothelial Cells via GPER (G-Protein-Coupled Estrogen Receptor) and SR-BI (Scavenger Receptor Class B Type 1). *Arterioscler Thromb. Vasc. Biol.* 38 (10), 2283–2294. doi:10.1161/atvbaha.118.310792

Ghim, M., Alpresa, P., Yang, S.-W., Braakman, S. T., Gray, S. G., Sherwin, S. J., et al. (2017). Visualization of Three Pathways for Macromolecule Transport across Cultured Endothelium and Their Modification by Flow. *Am. J. Physiol Heart Circ. Physiol.* 313 (5), H959–H973. doi:10.1152/ajpheart.00218.2017

Ghim, M., Mohamied, Y., and Weinberg, P. D. (2021a). The Role of Tricellular Junctions in the Transport of Macromolecules across Endothelium. *Cardiovasc. Eng. Tech.* 12 (1), 101–113. doi:10.1007/s13239-020-00483-x

Ghim, M., Pang, K. T., Arshad, M., Wang, X., and Weinberg, P. D. (2018). A Novel Method for Segmenting Growth of Cells in Sheared Endothelial Culture Reveals the Secretion of an Anti-Inflammatory Mediator. *J. Biol. Eng.* 12, 15. doi:10.1186/s13036-018-0107-6

Ghim, M., Pang, K. T., Burnap, S. A., Baig, F., Yin, X., Arshad, M., et al. (2021b). Endothelial Cells Exposed to Atheroprotective Flow Secrete Follistatin-Like 1 Protein Which Reduces Transcytosis and Inflammation. *Atherosclerosis* 333, 56–66. doi:10.1016/j.atherosclerosis.2021.08.025

Glagov, S., Zarins, C., Giddens, D. P., and Ku, D. N. (1988). Hemodynamics and Atherosclerosis. Insights and Perspectives Gained from Studies of Human Arteries. *Arch. Pathol. Lab. Med.* 112 (10), 1018–1031.

Grøttum, P., Svindland, A., and Walløe, L. (1983). Localization of Early Atherosclerotic Lesions in the Right Carotid Bifurcation in Humans. *Acta Pathologica, Microbiologica, Immunologica Scand. Section A, Pathol.* 91 (1), 65–70.

Hazel, A. L., and Pedley, T. J. (2000). Vascular Endothelial Cells Minimize the Total Force on Their Nuclei. *Biophysical J.* 78 (1), 47–54. doi:10.1016/s0006-3495(00)76571-4

He, X., and Ku, D. N. (1996). Pulsatile Flow in the Human Left Coronary Artery Bifurcation: Average Conditions. *J. Biomech. Eng.* 118 (1), 74–82. doi:10.1115/1.2795948

Heinle, H., and Lindner, V. (1984). The Binding of Evans Blue to Collagen and Elastin in Elastic Tissue. *Arch. Internationales de Physiologie de Biochimie* 92 (1), 13–17. doi:10.3109/13813458409073408

Helmlinger, G., Geiger, R. V., Schreck, S., and Nerem, R. M. (1991). Effects of Pulsatile Flow on Cultured Vascular Endothelial Cell Morphology. *J. Biomech. Eng.* 113 (2), 123–131. doi:10.1115/1.2891226

Herrmann, R. A., Malinauskas, R. A., and Truskey, G. A. (1994). Characterization of Sites with Elevated LDL Permeability at Intercostal, Celiac, and Iliac Branches of the normal Rabbit Aorta. *Arterioscler Thromb.* 14 (2), 313–323. doi:10.1161/01.atv.14.2.313

Himburg, H. A., and Friedman, M. H. (2006). Correspondence of Low Mean Shear and High Harmonic Content in the Porcine Iliac Arteries. *J. Biomech. Eng.* 128 (6), 852–856. doi:10.1115/1.2354211

Himburg, H. A., Grzybowski, D. M., Hazel, A. L., LaMack, J. A., Li, X.-M., and Friedman, M. H. (2004). Spatial Comparison between wall Shear Stress Measures and Porcine Arterial Endothelial Permeability. *Am. J. Physiology-Heart Circulatory Physiol.* 286 (5), H1916–H1922. doi:10.1152/ajpheart.00897.2003

Holtz, J., Förstermann, U., Pohl, U., Giesler, M., and Bassenge, E. (1984). Flow-Dependent, Endothelium-Mediated Dilation of Epicardial Coronary Arteries in Conscious Dogs: Effects of Cyclooxygenase Inhibition. *J. Cardiovasc. Pharmacol.* 6 (6), 1161–1169. doi:10.1097/00005344-198406060-00025

Hoogendoorn, A., Kok, A. M., Hartman, E. M. J., de Nisco, G., Casadonte, L., Chiastra, C., et al. (2020). Multidirectional Wall Shear Stress Promotes Advanced Coronary Plaque Development: Comparing Five Shear Stress Metrics. *Cardiovasc. Res.* 116 (6), 1136–1146. doi:10.1093/cvr/cvz212

Huang, L., Chambliss, K. L., Gao, X., Yuhanna, I. S., Behling-Kelly, E., Bergaya, S., et al. (2019). SR-B1 Drives Endothelial Cell LDL Transcytosis via DOCK4 to Promote Atherosclerosis. *Nature* 569 (7757), 565–569. doi:10.1038/s41586-019-1140-4

Hyun, S., Kleinstreuer, C., and Archie, J. P., Jr (2000). Hemodynamics Analyses of Arterial Expansions with Implications to Thrombosis and Restenosis. *Med. Eng. Phys.* 22 (1), 13–27. doi:10.1016/s1350-4533(00)00006-0

Iftikhar, S., Bond, A. R., Wagan, A. I., Weinberg, P. D., and Bharath, A. A. (2011). Segmentation of Endothelial Cell Boundaries of Rabbit Aortic Images Using a Machine Learning Approach. *Int. J. Biomed. Imaging* 2011, 270247. doi:10.1155/2011/270247

Imai, H., and Lee, K. T. (1983). Mosaicism in Female Hybrid Hares Heterozygous for Glucose-6-Phosphate Dehydrogenase. IV. Aortic Atherosclerosis in Hybrid Hares Fed Alternating Cholesterol-Supplemented and Nonsupplemented Diets. *Exp. Mol. Pathol.* 39 (1), 11–23. doi:10.1016/0014-4800(83)90037-0

Jave, Q., Leake, D. S., and Weinberg, P. D. (1999). Quantitative Immunohistochemical Detection of Oxidized Low Density Lipoprotein in the Rabbit Arterial wall. *Exp. Mol. Pathol.* 65 (3), 121–140. doi:10.1016/s0014-4800(99)80002-1

Kataoka, N., Ujita, S., and Sato, M. (1998). Effect of Flow Direction on the Morphological Responses of Cultured Bovine Aortic Endothelial Cells. *Med. Biol. Eng. Comput.* 36 (1), 122–128. doi:10.1007/bf02522869

Kazakidi, A., Plata, A. M., Sherwin, S. J., and Weinberg, P. D. (2011). Effect of Reverse Flow on the Pattern of Wall Shear Stress Near Arterial Branches. *J. Roy. Soc. Interface* 8 (64), 1594–1603. doi:10.1098/rsif.2011.0108

Kazakidi, A., Sherwin, S. J., and Weinberg, P. D. (2009). Effect of Reynolds Number and Flow Division on Patterns of Haemodynamic Wall Shear Stress Near Branch Points in the Descending Thoracic Aorta. *J. Roy. Soc. Interface* 6 (35), 539–548. doi:10.1098/rsif.2008.0323

Keller, K. H. (1974). "The Influence of Shear Dependent Diffusion in Blood on Atherogenesis and Thrombogenesis," in *Fluid Dynamics Aspects of Arterial Disease*. Editor R. M Nerem (Columbus, Ohio: Ohio State University), 43–45.

Kleinstreuer, C., Hyun, S., Buchanan, J. R., Jr, Longest, P. W., Archie, J. P., Jr, and Truskey, G. A. (2001). Hemodynamic Parameters and Early Intimal Thickening in Branching Blood Vessels. *Crit. Rev. Biomed. Eng.* 29 (1), 1–64. doi:10.1615/critrevbiomedeng.v29.i1.10

Kok, A. M., Molony, D. S., Timmins, L. H., Ko, Y.-A., Boersma, E., Eshtehardi, P., et al. (2019). The Influence of Multidirectional Shear Stress on Plaque Progression and Composition Changes in Human Coronary Arteries. *EuroIntervention* 15 (8), 692–699. doi:10.4244/eij-d-18-00529

Kraehling, J. R., Chidlow, J. H., Rajagopal, C., Sugiyama, M. G., Fowler, J. W., Lee, M. Y., et al. (2016). Genome-Wide RNAi Screen Reveals ALK1 Mediates LDL Uptake and Transcytosis in Endothelial Cells. *Nat. Commun.* 7, 13516. doi:10.1038/ncomms13516

Ku, D. N., Giddens, D. P., Zarins, C. K., and Glagov, S. (1985). Pulsatile Flow and Atherosclerosis in the Human Carotid Bifurcation. Positive Correlation between Plaque Location and Low Oscillating Shear Stress. *Arteriosclerosis* 5 (3), 293–302. doi:10.1161/01.atv.5.3.293

Kubes, P., and Granger, D. N. (1992). Nitric Oxide Modulates Microvascular Permeability. *Am. J. Physiol.* 262 (2 Pt 2), H611–H615. doi:10.1152/ajpheart.1992.262.2.H611

Lei, M., Kleinstreuer, C., and Truskey, G. A. (1995). Numerical Investigation and Prediction of Atherogenic Sites in Branching Arteries. *J. Biomech. Eng.* 117 (3), 350–357. doi:10.1115/1.2794191

Levesque, M. J., Liepsch, D., Moravec, S., and Nerem, R. M. (1986). Correlation of Endothelial Cell Shape and Wall Shear Stress in a Stenosed Dog Aorta. *Arteriosclerosis* 6 (2), 220–229. doi:10.1161/01.atv.6.2.220

Levesque, M. J., and Nerem, R. M. (1985). The Elongation and Orientation of Cultured Endothelial Cells in Response to Shear Stress. *J. Biomech. Eng.* 107 (4), 341–347. doi:10.1115/1.3138567

Levick, J. R. (1991). *An Introduction to Cardiovascular Physiology*. London: Butterworths.

Lin, S. J., Jan, K. M., Schuessler, G., Weinbaum, S., and Chien, S. (1988). Enhanced Macromolecular Permeability of Aortic Endothelial Cells in Association with Mitosis. *Atherosclerosis* 73 (2-3), 223–232. doi:10.1016/0021-9150(88)90045-7

Lin, S. J., Jan, K. M., and Chien, S. (1990). Role of Dying Endothelial Cells in Transendothelial Macromolecular Transport. *Arteriosclerosis* 10 (5), 703–709. doi:10.1161/01.atv.10.5.703

Lin, S. J., Jan, K. M., Weinbaum, S., and Chien, S. (1989). Transendothelial Transport of Low Density Lipoprotein in Association with Cell Mitosis in Rat Aorta. *Arteriosclerosis* 9 (2), 230–236. doi:10.1161/01.atv.9.2.230

Lindner, V., and Heinle, H. (1982). Binding Properties of Circulating Evans Blue in Rabbits as Determined by Disc Electrophoresis. *Atherosclerosis* 43 (2-3), 417–422. doi:10.1016/0021-9150(82)90040-5

Liu, S. F., Hislop, A. A., Haworth, S. G., and Barnes, P. J. (1992). Developmental Changes in Endothelium-Dependent Pulmonary Vasodilatation in Pigs. *Br. J. Pharmacol.* 106 (2), 324–330. doi:10.1111/j.1476-5381.1992.tb14335.x

Macia, E., Ehrlich, M., Massol, R., Boucrot, E., Brunner, C., and Kirchhausen, T. (2006). Dynasore, a Cell-Permeable Inhibitor of Dynamin. *Dev. Cell* 10 (6), 839–850. doi:10.1016/j.devcel.2006.04.002

Malinauskas, R. A., Herrmann, R. A., and Truskey, G. A. (1995). The Distribution of Intimal white Blood Cells in the Normal Rabbit Aorta. *Atherosclerosis* 115 (2), 147–163. doi:10.1016/0021-9150(94)05497-7

Mantha, A., Karmonik, C., Benndorf, G., Strother, C., and Metcalfe, R. (2006). Hemodynamics in a Cerebral Artery before and after the Formation of an Aneurysm. *AJNR Am. J. Neuroradiol* 27, 1113–1118.

McGillicuddy, C. J., Carrier, M. J., and Weinberg, P. D. (2001). Distribution of Lipid Deposits Around Aortic Branches of Mice Lacking LDL Receptors and Apolipoprotein E. *Arterioscler. Thromb. Vasc. Biol.* 21 (7), 1220–1225. doi:10.1161/hq0701.091996

McMillan, D. E. (1985a). Hemorheologic Changes in Diabetes and Their Role in Increased Atherogenesis. *Horm. Metab. Res. Suppl.* 15, 73–79.

McMillan, D. E. (1985b). Blood Flow and the Localization of Atherosclerotic Plaques. *Stroke* 16 (4), 582–587. doi:10.1161/01.str.16.4.582

Minor, R. L., Jr, Myers, P. R., Guerra, R., Jr, Bates, J. N., and Harrison, D. G. (1990). Diet-induced Atherosclerosis Increases the Release of Nitrogen Oxides from Rabbit Aorta. *J. Clin. Invest.* 86 (6), 2109–2116. doi:10.1172/jci114949

Mitchell, J. R. A., and Schwartz, C. J. (1965). *Arterial Disease*. Oxford: Blackwell Scientific.

Mohamied, Y., Rowland, E. M., Bailey, E. L., Sherwin, S. J., Schwartz, M. A., and Weinberg, P. D. (2015). Change of Direction in the Biomechanics of Atherosclerosis. *Ann. Biomed. Eng.* 43 (1), 16–25. doi:10.1007/s10439-014-1095-4

Mohamied, Y., Sherwin, S. J., and Weinberg, P. D. (2017). Understanding the Fluid Mechanics Behind Transverse wall Shear Stress. *J. Biomech.* 50, 102–109. doi:10.1016/j.jbiomech.2016.11.035

Moore, J. E., Jr, Ku, D. N., Zarins, C. K., and Glagov, S. (1992). Pulsatile Flow Visualization in the Abdominal Aorta under Differing Physiologic Conditions: Implications for Increased Susceptibility to Atherosclerosis. *J. Biomech. Eng.* 114 (3), 391–397. doi:10.1115/1.2891400

Moossy, J. (1966). Morphology, Sites and Epidemiology of Cerebral Atherosclerosis. *Res. Publ. Assoc. Res. Nerv Ment. Dis.* 41, 1–22.

Morbiducci, U., Gallo, D., Cristofanelli, S., Ponzini, R., Deriu, M. A., Rizzo, G., et al. (2015). A Rational Approach to Defining Principal Axes of Multidirectional wall Shear Stress in Realistic Vascular Geometries, with Application to the Study of the Influence of Helical Flow on wall Shear Stress Directionality in Aorta. *J. Biomech.* 48 (6), 899–906. doi:10.1016/j.jbiomech.2015.02.027

Murphy, C. L. (1998). Arterial Mass Transport in Relation to Flow. PhD thesis. London, United Kingdom: University of London Imperial College.

Murphy, C. L., and Lever, M. J. (2002). Sulphorhodamine-B-Labelled Albumin Uptake Around the Ostium of the Renal Artery in Rabbits: Changes with Age. *J. Vasc. Res.* 39 (2), 104–113. doi:10.1159/000057759

Nakaura, T., Nagayoshi, Y., Awai, K., Utsunomiya, D., Kawano, H., Ogawa, H., et al. (2014). Myocardial Bridging Is Associated with Coronary Atherosclerosis in the Segment Proximal to the Site of Bridging. *J. Cardiol.* 63 (2), 134–139. doi:10.1016/j.jjcc.2013.07.005

Pang, K. T., Ghim, M., Arshad, M., Wang, X., and Weinberg, P. D. (2021a). Segmenting Growth of Endothelial Cells in 6-Well Plates on an Orbital Shaker for Mechanobiological Studies. *JoVE* 172, 61817. doi:10.3791/61817

Pang, K. T., Ghim, M., Liu, C., Tay, H. M., Fhu, C. W., Chia, R. N., et al. (2021b). Leucine-Rich α-2-Glycoprotein 1 Suppresses Endothelial Cell Activation through ADAM10-Mediated Shedding of TNF-α Receptor. *Front. Cell Dev. Biol.* 9, 706143. doi:10.3389/fcell.2021.706143

Park, R. J., Shen, H., Liu, L., Liu, X., Ferguson, S. M., and De Camilli, P. (2013). Dynamin Triple Knockout Cells Reveal off Target Effects of Commonly Used Dynamin Inhibitors. *J. Cell Sci.* 126 (Pt 22), 5305–5312. doi:10.1242/jcs.138578

Peiffer, V., Rowland, E. M., Cremers, S. G., Weinberg, P. D., and Sherwin, S. J. (2012). Effect of Aortic Taper on Patterns of Blood Flow and Wall Shear Stress in Rabbits: Association with Age. *Atherosclerosis* 223 (1), 114–121. doi:10.1016/j.atherosclerosis.2012.04.020

Peiffer, V., Sherwin, S. J., and Weinberg, P. D. (2013a). Computation in the Rabbit Aorta of a New Metric - The Transverse Wall Shear Stress - to Quantify the Multidirectional Character of Disturbed Blood Flow. *J. Biomech.* 46 (15), 2651–2658. doi:10.1016/j.jbiomech.2013.08.003

Peiffer, V., Bharath, A. A., Sherwin, S. J., and Weinberg, P. D. (2013b). A Novel Method for Quantifying Spatial Correlations between Patterns of Atherosclerosis and Hemodynamic Factors. *J. Biomech. Eng.* 135 (2), 021023. doi:10.1115/1.4023381

Peiffer, V., Sherwin, S. J., and Weinberg, P. D. (2013c). Does Low and Oscillatory Wall Shear Stress Correlate Spatially with Early Atherosclerosis? A Systematic Review. *Cardiovasc. Res.* 99 (2), 242–250. doi:10.1093/cvr/cvt044

Petroff, J. R. (1922). Über die vitalfärbung der Gefässwand. *Beitr Z Pathol. Anat. U Z Allg Path* 71, 115–131.

Quinn, M. T., Parthasarathy, S., Fong, L. G., and Steinberg, D. (1987). Oxidatively Modified Low Density Lipoproteins: A Potential Role in Recruitment and Retention of Monocyte/macrophages during Atherogenesis. *Proc. Natl. Acad. Sci.* 84 (9), 2995–2998. doi:10.1073/pnas.84.9.2995

Ramírez, C. M., Zhang, X., Bandyopadhyay, C., Rotllan, N., Sugiyama, M. G., Aryal, B., et al. (1992). gp60 Is an Albumin-Binding Glycoprotein Expressed by Continuous Endothelium Involved in Albumin Transcytosis. *Am. J. Physiol.* 262 (1 Pt 2), H246–H254. doi:10.1152/ajpheart.1992.262.1.H246

Redheuil, A., Yu, W.-C., Mousseaux, E., Harouni, A. A., Kachenoura, N., Wu, C. O., et al. (2011). Age-Related Changes in Aortic Arch Geometry: Relationship with Proximal Aortic Function and Left Ventricular Mass and Remodeling. *J. Am. Coll. Cardiol.* 58 (12), 1262–1270. doi:10.1016/j.jacc.2011.06.012

Richards, J. P., and Weinberg, P. D. (2000). Distribution of Disease Around the Aortocoeliac branch of white Carneau Pigeons at Different Ages. *Exp. Mol. Pathol.* 68 (2), 95–103. doi:10.1006/exmp.1999.2293

Riemer, K., Rowland, E. M., Broughton-Venner, J., Leow, C. H., Tang, M., and Weinberg, P. D. (2021). Contrast Agent-Free Assessment of Blood Flow and Wall Shear Stress in the Rabbit Aorta Using Ultrasound Image Velocimetry. *Ultrasound Med. Biol.* S0301-5629 (21), 00450–00456. doi:10.1016/j.ultrasmedbio.2021.10.010

Rindfleisch, E. (1872). *A Manual of Pathological Histology*, 1. London: New Sydenham Society.

Roach, M. R., Cornhill, J. F., and Fletcher, J. (1978). A Quantitative Study of the Development of Sudanophilic Lesions in the Aorta of Rabbits Fed a Low-Cholesterol Diet for up to Six Months. *Atherosclerosis* 29, 259–264. doi:10.1016/0021-9150(78)90013-8

Rowland, E. M., Mohamied, Y., Yean Chooi, K., Bailey, E. L., and Weinberg, P. D. (2015). Comparison of Statistical Methods for Assessing Spatial Correlations between Maps of Different Arterial Properties. *J. Biomech. Eng.* 137 (10), 101003. doi:10.1115/1.4031119

Rowland, E. M., Bailey, E. L., and Weinberg, P. D. (2021). Estimating Arterial Cyclic Strain from the Spacing of Endothelial Nuclei. *Exp. Mech.* 61 (1), 171–190. doi:10.1007/s11340-020-00655-9

Rubanyi, G. M., Romero, J. C., and Vanhoutte, P. M. (1986). Flow-Induced Release of Endothelium-Derived Relaxing Factor. *Am. J. Physiol.* 250 (6 Pt 2), H1145–H1149. doi:10.1152/ajpheart.1986.250.6.H1145

Rylski, B., Desjardins, B., Moser, W., Bavaria, J. E., and Milewski, R. K. (2014). Gender-Related Changes in Aortic Geometry throughout Life. *Eur. J. Cardio-Thoracic Surg.* 45 (5), 805–811. doi:10.1093/ejcts/ezt597

Schaphorst, K. L., Chiang, E., Jacobs, K. N., Zaiman, A., Natarajan, V., Wigley, F., et al. (2003). Role of Sphingosine-1 Phosphate in the Enhancement of Endothelial Barrier Integrity by Platelet-Released Products. *Am. J. Physiology-Lung Cell. Mol. Physiol.* 285 (1), L258–L267. doi:10.1152/ajplung.00311.2002

Schwenke, D. C., and Carew, T. E. (1988). Quantification *In Vivo* of Increased LDL Content and Rate of LDL Degradation in normal Rabbit Aorta Occurring at Sites Susceptible to Early Atherosclerotic Lesions. *Circ. Res.* 62 (4), 699–710. doi:10.1161/01.res.62.4.699

Schnitzer, J. E. (1992). gp60 is an Albumin-Binding Glycoprotein Expressed by Continuous Endothelium Involved in Albumin Transcytosis. *Am. J. Physiol.* 262 (1 Pt 2), H246–H254.

Sebkhi, A., and Weinberg, P. D. (1994a). Age-Related Variations in Transport Properties of the Rabbit Arterial Wall Near Branches. *Atherosclerosis* 106 (1), 1–8. doi:10.1016/0021-9150(94)90077-9

Sebkhi, A., and Weinberg, P. D. (1994b). Effect of Dietary Cholesterol on the Uptake of Albumin by Rabbit Aortic Wall *In Vivo*. *J. Physiol.* 479P, 77P.

Sebkhi, A., and Weinberg, P. D. (1996). Effect of Age on the Pattern of Short-Term Albumin Uptake by the Rabbit Aortic wall Near Intercostal Branch Ostia. *Arterioscler. Thromb. Vasc. Biol.* 16 (2), 317–327. doi:10.1161/01.atv.16.2.317

Sinzinger, H., Silberbauer, K., and Auerswald, W. (1980). Quantitative Investigation of Sudanophilic Lesions Around the Aortic Ostia of Human Fetuses, Newborn and Children. *J. Vasc. Res.* 17 (1), 44–52. doi:10.1159/000158233

Sloop, G. D., Fallon, K. B., and Zieske, A. W. (2002). Atherosclerotic Plaque-Like Lesions in Synthetic Arteriovenous Grafts: Implications for Atherogenesis. *Atherosclerosis* 160 (1), 133–139. doi:10.1016/s0021-9150(01)00543-3

Sloop, G. D., Perret, R. S., Brahney, J. S., and Oalmann, M. (1998). A Description of Two Morphologic Patterns of Aortic Fatty Streaks, and a Hypothesis of Their Pathogenesis. *Atherosclerosis* 141 (1), 153–160. doi:10.1016/s0021-9150(98)00167-1

Smith, E. B., and Staples, E. M. (1980). Distribution of Plasma Proteins across the Human Aortic Wall Barrier Functions of Endothelium and Internal Elastic Lamina. *Atherosclerosis* 37 (4), 579–590. doi:10.1016/0021-9150(80)90065-9

Solberg, L. A., and Eggen, D. A. (1971). Localization and Sequence of Development of Atherosclerotic Lesions in the Carotid and Vertebral Arteries. *Circulation* 43 (5), 711–724. doi:10.1161/01.cir.43.5.711

Somer, J. B., and Schwartz, C. J. (1971). Focal 3H-Cholesterol Uptake in the Pig Aorta. *Atherosclerosis* 13 (3), 293–304. doi:10.1016/0021-9150(71)90073-6

Sorescu, G. P., Sykes, M., Weiss, D., Platt, M. O., Saha, A., Hwang, J., et al. (2003). Bone Morphogenic Protein 4 Produced in Endothelial Cells by Oscillatory Shear Stress Stimulates an Inflammatory Response. *J. Biol. Chem.* 278 (33), 31128–31135. doi:10.1074/jbc.m300703200

Souilhol, C., Gauci, I., Feng, S., Tardajos Ayllon, B., Mahmoud, M., Canham, L., et al. (2020). Homeobox B9 Integrates Bone Morphogenic Protein 4 with Inflammation at Atheroprone Sites. *Cardiovasc. Res.* 116 (7), 1300–1310. doi:10.1093/cvr/cvz235

Staughton, T. J., and Weinberg, P. D. (2004a). Effect of Time of Day and Rabbit Strain on Patterns of Aortic wall Permeability. *Exp. Physiol.* 89 (1), 109–118. doi:10.1113/expphysiol.2003.002635

Staughton, T. J., and Weinberg, P. D. (2004b). "Investigation of the Role of Endogenous Nitric Oxide Synthesis in Determining Patterns of Arterial wall Permeability and Diet-Induced Lipid Deposition in the Rabbit," in *Trends in Atherosclerosis Research*. Editor L.V. Clark (New York: Nova Biomedical Books), 143–164.

Staughton, T. J., Lever, M. J., and Weinberg, P. D. (2001). Effect of Altered Flow on the Pattern of Permeability Around Rabbit Aortic Branches. *Am. J. Physiology-Heart Circulatory Physiol.* 281 (1), H53–H59. doi:10.1152/ajpheart.2001.281.1.h53

Staughton, T. J., del Rio, J. D., and Weinberg, P. D. (2007). Arterial Wall Permeability at the Left Coronary Bifurcation. *Atherosclerosis* 195 (1), 207–209. doi:10.1016/j.atherosclerosis.2006.11.034

Stehbens, W. E. (1999). Anitschkow and the Cholesterol Over-Fed Rabbit. *Cardiovasc. Pathol.* 8 (3), 177–178. doi:10.1016/s1054-8807(99)00006-x

Steinberg, D. (2013). In Celebration of the 100th Anniversary of the Lipid Hypothesis of Atherosclerosis. *J. Lipid Res.* 54 (11), 2946–2949. doi:10.1194/jlr.r043414

Steinberg, D. (2004). Thematic Review Series: the Pathogenesis of Atherosclerosis. An Interpretive History of the Cholesterol Controversy: Part I. *J. Lipid Res.* 45 (9), 1583–1593. doi:10.1194/jlr.r400003-jlr200

Stemerman, M. B., Morrel, E. M., Burke, K. R., Colton, C. K., Smith, K. A., and Lees, R. S. (1986). Local Variation in Arterial wall Permeability to Low Density Lipoprotein in normal Rabbit Aorta. *Arteriosclerosis* 6 (1), 64–69. doi:10.1161/01.atv.6.1.64

Svindland, A., and Walløe, L. (1985). Distribution Pattern of Sudanophilic Plaques in the Descending Thoracic and Proximal Abdominal Human Aorta. *Atherosclerosis* 57 (2-3), 219–224. doi:10.1016/0021-9150(85)90035-8

Ramírez, C. M., Zhang, X., Bandyopadhyay, C., Rotllan, N., Sugiyama, M. G., and Aryal, B. (2019). Caveolin-1 Regulates Atherogenesis by Attenuating Low-Density Lipoprotein Transcytosis and Vascular Inflammation Independently of Endothelial Nitric Oxide Synthase Activation. *Circulation* 140 (3), 225–239. doi:10.1161/CIRCULATIONAHA.118.038571

Tanimura, A., Adachi, K., and Nakashima, T. (1980). Permeability into Aortic Intima and Atherosclerotic Plaque. *Angiology* 31 (8), 542–548. doi:10.1177/000331978003100806

Texon, M. (1957). A Hemodynamic Concept of Atherosclerosis, with Particular Reference to Coronary Occlusion. *Arch. Intern. Med.* 99 (3), 418–427. doi:10.1001/archinte.1957.00260030100010

Thubrikar, M. J., Baker, J. W., and Nolan, S. P. (1988). Inhibition of Atherosclerosis Associated with Reduction of Arterial Intramural Stress in Rabbits. *Arteriosclerosis* 8 (4), 410–420. doi:10.1161/01.atv.8.4.410

Truskey, G. A., Roberts, W. L., Herrmann, R. A., and Malinauskas, R. A. (1992). Measurement of Endothelial Permeability to 125I-Low Density lipoproteins in Rabbit Arteries by use of en Face Preparations. *Circ. Res.* 71 (4), 883–897. doi:10.1161/01.res.71.4.883

Vamsi Krishna, C., Chandran Suja, V., Watton, P. N., Arakeri, J. H., and Gundiah, N. (2020). Shear Stress Rosettes Capture the Complex Flow Physics in Diseased Arteries. *J. Biomech.* 104, 109721. doi:10.1016/j.jbiomech.2020.109721

van den Berg, B. M., Vink, H., and Spaan, J. A. E. (2003). The Endothelial Glycocalyx Protects against Myocardial Edema. *Circ. Res.* 92 (6), 592–594. doi:10.1161/01.res.0000065917.53950.75

VanTeeffelen, J. W. G. E., Brands, J., Jansen, C., Spaan, J. A. E., and Vink, H. (2007). Heparin Impairs Glycocalyx Barrier Properties and Attenuates Shear Dependent Vasodilation in Mice. *Hypertension* 50 (1), 261–267. doi:10.1161/hypertensionaha.107.089250

Vasile, E., Simionescu, M., and Simionescu, N. (1983). Visualization of the Binding, Endocytosis, and Transcytosis of Low-Density Lipoprotein in the Arterial Endothelium *In Situ*. *J. Cell Biol.* 96 (6), 1677–1689. doi:10.1083/jcb.96.6.1677

Vincent, P. E., Plata, A. M., Hunt, A. A. E., Weinberg, P. D., and Sherwin, S. J. (2011). Blood Flow in the Rabbit Aortic Arch and Descending Thoracic Aorta. *J. Roy. Soc. Interface* 8 (65), 1708–1719. doi:10.1098/rsif.2011.0116

Vincent, P. E., Sherwin, S. J., and Weinberg, P. D. (2009). The Effect of a Spatially Heterogeneous Transmural Water Flux on Concentration Polarization of Low Density Lipoprotein in Arteries. *Biophysical J.* 96 (8), 3102–3115. doi:10.1016/j.bpj.2009.01.022

Vincent, P. E., Sherwin, S. J., and Weinberg, P. D. (2010). The Effect of the Endothelial Glycocalyx Layer on Concentration Polarisation of Low Density Lipoprotein in Arteries. *J. Theor. Biol.* 265 (1), 1–17. doi:10.1016/j.jtbi.2010.04.015

Vincent, P. E., and Weinberg, P. D. (2014). Flow-Dependent Concentration Polarization and the Endothelial Glycocalyx Layer: Multi-Scale Aspects of Arterial Mass Transport and Their Implications for Atherosclerosis. *Biomech. Model. Mechanobiol* 13 (2), 313–326. doi:10.1007/s10237-013-0512-1

Wada, S., and Karino, T. (1999). Theoretical Study on Flow-Dependent Concentration Polarization of Low Density Lipoproteins at the Luminal Surface of a Straight Artery. *Biorheology* 36 (3), 207–223.

Wada, S., and Karino, T. (2002). Theoretical Prediction of Low-Density Lipoproteins Concentration at the Luminal Surface of an Artery with a Multiple bend. *Ann. Biomed. Eng.* 30 (6), 778–791. doi:10.1114/1.1495868

Walpola, P. L., Gotlieb, A. I., and Langille, B. L. (1993). Monocyte Adhesion and Changes in Endothelial Cell Number, Morphology, and F-Actin Distribution Elicited by Low Shear Stress *In Vivo*. *Am. J. Pathol.* 142 (5), 1392–1400.

Wang, C., Baker, B. M., Chen, C. S., and Schwartz, M. A. (2013). Endothelial Cell Sensing of Flow Direction. *Arterioscler. Thromb. Vasc. Biol.* 33 (9), 2130–2136. doi:10.1161/atvbaha.113.301826

Wang, C., Lu, H., and Schwartz, M. A. (2012). A Novel *In Vitro* Flow System for Changing Flow Direction on Endothelial Cells. *J. Biomech.* 45 (7), 1212–1218. doi:10.1016/j.jbiomech.2012.01.045

Warboys, C. M., Eric Berson, R., Mann, G. E., Pearson, J. D., and Weinberg, P. D. (2010). Acute and Chronic Exposure to Shear Stress Have Opposite Effects on Endothelial Permeability to Macromolecules. *Am. J. Physiology-Heart Circulatory Physiol.* 298 (6), H1850–H1856. doi:10.1152/ajpheart.00114.2010

Warboys, C. M., Ghim, M., and Weinberg, P. D. (2019). Understanding Mechanobiology in Cultured Endothelium: A Review of the Orbital Shaker Method. *Atherosclerosis* 285, 170–177. doi:10.1016/j.atherosclerosis.2019.04.210

Warboys, C. M., Overby, D. R., and Weinberg, P. D. (2012). Dendritic Cells Lower the Permeability of Endothelial Monolayers. *Cell. Mol. Bioeng.* 5 (2), 184–193. doi:10.1007/s12195-012-0220-4

Weinbaum, S., Tzeghai, G., Ganatos, P., Pfeffer, R., and Chien, S. (1985). Effect of Cell Turnover and Leaky Junctions on Arterial Macromolecular Transport. *Am. J. Physiol.* 248 (6 Pt 2), H945–H960. doi:10.1152/ajpheart.1985.248.6.H945

Weinberg, P. D. (1988). Application of Fluorescence Densitometry to the Study of Net Albumin Uptake by the Rabbit Aortic wall up- and Downstream of Intercostal Ostia. *Atherosclerosis* 74 (1-2), 139–148. doi:10.1016/0021-9150(88)90200-6

Weinberg, P. D. (2002). Disease Patterns at Arterial Branches and Their Relation to Flow. *Biorheology* 39 (3-4), 533–537.

Weinberg, P. D. (2004). Rate-limiting Steps in the Development of Atherosclerosis: The Response-To-Influx Theory. *J. Vasc. Res.* 41 (1), 1–17. doi:10.1159/000076124

Weinberg, P. D., and Ross Ethier, C. (2007). Twenty-Fold Difference in Hemodynamic Wall Shear Stress between Murine and Human Aortas. *J. Biomech.* 40 (7), 1594–1598. doi:10.1016/j.jbiomech.2006.07.020

Wen, Y., Ahmad, F., Mohri, Z., Weinberg, P. D., and Leake, D. S. (2019). Cysteamine Inhibits Lysosomal Oxidation of Low Density Lipoprotein in Human Macrophages and Reduces Atherosclerosis in Mice. *Atherosclerosis* 291, 9–18. doi:10.1016/j.atherosclerosis.2019.09.019

Wen, Y., and Leake, D. S. (2007). Low Density Lipoprotein Undergoes Oxidation within Lysosomes in Cells. *Circ. Res.* 100 (9), 1337–1343. doi:10.1161/circresaha.107.151704

Wesolowski, S. A., Fries, C. C., Sabini, A. M., and Sawyer, P. N. (1965). The Significance of Turbulence in Hemic Systems and in the Distribution of the Atherosclerotic Lesion. *Surgery* 57, 155–162.

Williams, K. J., and Tabas, I. (1995). The Response-To-Retention Hypothesis of Early Atherogenesis. *Arterioscler. Thromb. Vasc. Biol.* 15 (5), 551–561. doi:10.1161/01.atv.15.5.551

Yamaguchi, T., Yamamoto, Y., and Liu, H. (2000). Computational Mechanical Model Studies on the Spontaneous Emergent Morphogenesis of the Cultured Endothelial Cells. *J. Biomech.* 33 (1), 115–126. doi:10.1016/s0021-9290(99)00159-1

Yuan, Y., Granger, H. J., Zawieja, D. C., and Chilian, W. M. (1992). Flow Modulates Coronary Venular Permeability by a Nitric Oxide-Related Mechanism. *Am. J. Physiol.* 263 (2 Pt 2), H641–H646. doi:10.1152/ajpheart.1992.263.2.H641

Zhang, L., Zeng, M., Fan, J., Tarbell, J. M., Curry, F.-R. E., and Fu, B. M. (2016). Sphingosine-1-Phosphate Maintains Normal Vascular Permeability by Preserving Endothelial Surface Glycocalyx in Intact Microvessels. *Microcirculation* 23 (4), 301–310. doi:10.1111/micc.12278

Zhao, S., Suciu, A., Ziegler, T., Moore, J. E., Jr, Bürki, E., Meister, J.-J., et al. (1995). Synergistic Effects of Fluid Shear Stress and Cyclic Circumferential Stretch on Vascular Endothelial Cell Morphology and Cytoskeleton. *Arterioscler. Thromb. Vasc. Biol.* 15 (10), 1781–1786. doi:10.1161/01.atv.15.10.1781

Zinserling, W. D. (1925). Untersuchungen über Atherosklerose. 1. Über die Aortaverfettung bei Kindern. *Virchows Arch. Path Anat.* 255, 677–705. doi:10.1007/bf01891708

Conflict of Interest: The author declares that the research was conducted in the absence of any commercial or financial relationships that could be construed as a potential conflict of interest.

Publisher's Note: All claims expressed in this article are solely those of the authors and do not necessarily represent those of their affiliated organizations, or those of the publisher, the editors and the reviewers. Any product that may be evaluated in this article, or claim that may be made by its manufacturer, is not guaranteed or endorsed by the publisher.

frontiers in Bioengineering and Biotechnology

ORIGINAL RESEARCH
published: 24 March 2022
doi: 10.3389/fbioe.2022.836611

Evaluation of Computational Methodologies for Accurate Prediction of Wall Shear Stress and Turbulence Parameters in a Patient-Specific Aorta

*Emily Louise Manchester[1], Selene Pirola[1], Mohammad Yousuf Salmasi[2], Declan P. O'Regan[3], Thanos Athanasiou[2] and Xiao Yun Xu[1]**

[1]Department of Chemical Engineering, Imperial College London, London, United Kingdom, [2]Department of Surgery and Cancer, Imperial College London, St Mary's Hospital, London, United Kingdom, [3]MRC London Institute of Medical Sciences, Imperial College London, Hammersmith Hospital, London, United Kingdom

OPEN ACCESS

Edited by:
Chih-Yu Yang,
Taipei Veterans General Hospital, Taiwan

Reviewed by:
Magnus Andersson,
Linköping University, Sweden
Aike Qiao,
Beijing University of Technology, China
Natalya Kizilova,
Warsaw University of Technology, Poland

***Correspondence:**
Xiao Yun Xu
yun.xu@imperial.ac.uk

Specialty section:
This article was submitted to Biomechanics, a section of the journal Frontiers in Bioengineering and Biotechnology

Received: 15 December 2021
Accepted: 07 March 2022
Published: 24 March 2022

Citation:
Manchester EL, Pirola S, Salmasi MY, O'Regan DP, Athanasiou T and Xu XY (2022) Evaluation of Computational Methodologies for Accurate Prediction of Wall Shear Stress and Turbulence Parameters in a Patient-Specific Aorta. Front. Bioeng. Biotechnol. 10:836611. doi: 10.3389/fbioe.2022.836611

Background: Recent studies suggest that blood flow in main arteries is intrinsically disturbed, even under healthy conditions. Despite this, many computational fluid dynamics (CFD) analyses of aortic haemodynamics make the assumption of laminar flow, and best practices surrounding appropriate modelling choices are lacking. This study aims to address this gap by evaluating different modelling and post-processing approaches in simulations of a patient-specific aorta.

Methods: Magnetic resonance imaging (MRI) and 4D flow MRI from a patient with aortic valve stenosis were used to reconstruct the aortic geometry and derive patient-specific inlet and outlet boundary conditions. Three different computational approaches were considered based on assumed laminar or assumed disturbed flow states including low-resolution laminar (LR-Laminar), high-resolution laminar (HR-Laminar) and large-eddy simulation (LES). Each simulation was ran for 30 cardiac cycles and post-processing was conducted on either the final cardiac cycle, or using a phase-averaged approach which utilised all 30 simulated cycles. Model capabilities were evaluated in terms of mean and turbulence-based parameters.

Results: All simulation types, regardless of post-processing approach could correctly predict velocity values and flow patterns throughout the aorta. Lower resolution simulations could not accurately predict gradient-derived parameters including wall shear stress and viscous energy loss (largest differences up to 44.6% and 130.3%, respectively), although phase-averaging these parameters improved predictions. The HR-Laminar simulation produced more comparable results to LES with largest differences in wall shear stress and viscous energy loss parameters up to 5.1% and 11.6%, respectively. Laminar-based parameters were better estimated than turbulence-based parameters.

Conclusion: Our findings suggest that well-resolved laminar simulations can accurately predict many laminar-based parameters in disturbed flows, but there is no clear benefit to running a HR-Laminar simulation over an LES simulation based on their comparable

computational cost. Additionally, post-processing "typical" laminar simulation results with a phase-averaged approach is a simple and cost-effective way to improve accuracy of lower-resolution simulation results.

Keywords: aorta, computational fluid dynamics, magnetic resonance imaging, laminar, turbulence, large-eddy simulation, wall shear stress, viscous energy loss

1 INTRODUCTION

Patient-specific computational fluid dynamic (CFD) analysis has been widely adopted in the biomedical community. Simulation outputs can be used in several ways including evaluation and design of medical devices; informing clinical decisions; and understanding disease progressions to name only a few (Saloner et al., 2006; Ge et al., 2008; Borazjani et al., 2010). Haemodynamic parameters, such as wall shear stress (WSS), are used to investigate the mechanical shearing force exerted by blood flow on the inner arterial wall and thereby endothelial cells which are in direct contact with blood. WSS is one of the factors which determine endothelium homeostasis and WSS extremes affect endothelial cell response, promoting vascular remodelling and pathologies (Cunningham and Gotlieb, 2005; Dolan et al., 2013). More specifically, prolonged exposure to high WSS is associated with aortic growth, extracellular matrix dysregulation and elastic fibre degeneration (Guzzardi et al., 2015; Bollache et al., 2018), and a recent study into ascending aortic aneurysms concluded that high WSS is associated with wall degradation in the ascending aorta (Salmasi et al., 2021). Fluctuations in WSS which occur in disturbed flows induce endothelial dysfunction (Davies et al., 1986; Chiu and Chien, 2011). Similarly, laminar and fluctuating viscous shear stresses within a fluid can be used to evaluate energy losses and haemolysis (Yen et al., 2014). Wall and viscous shear stresses are important biomarkers and it is therefore crucial that CFD models are accurate and simulation outputs are correctly processed.

There are numerous CFD studies into aortic haemodynamics, however the majority of these studies made the assumption of laminar flow. In recent years, there have been studies of aortic flows which do not assume laminarity and have shown disturbances to be present in aortas with and without pathologic conditions (Lantz et al., 2012; Lantz et al., 2013; Miyazaki et al., 2017; Xu et al., 2018; Xu et al., 2020; Manchester et al., 2021). A recent study considered flow in the healthy aorta, deducing that physiological blood flow is non-laminar and displays blood flow disturbances (Saqr et al., 2020). Recent literature suggests that the widely accepted theory of laminar flow in large arteries by the scientific community may need to be revisited. A computational study into aorta flows compared modelling capabilities of different simulation types including laminar, large-eddy simulation (LES) and the renormalisation group (RNG) $k-\epsilon$ model, although it was uncertain which modelling approach performed the best (Miyazaki et al., 2017). Lancellotti et al. (2017) considered a patient-specific stenotic carotid artery which produced a high shear and transitional flow. LES simulations with various Sigma and Smagorinsky-type subgrid-scale (SGS) models were compared to a higher-resolution simulation without SGS modelling, akin to direct numerical simulation (DNS). The static Sigma model performed best and was more robust than dynamic and mixed Sigma models. All Smagorinsky-type models were unstable and caused simulation blow-up. Similar to Lancellotti et al. (2017), Mancini et al. (2019) compared LES simulations using static Smagorinsky, dynamic Smagorinsky and static Sigma SGS models against an under-resolved DNS simulation in a stenotic carotid artery. They found that both static Sigma and dynamic Smagorinsky models could produce reliable results under pulsatile conditions, and the static Sigma model had lower computational costs than dynamic Smagorinsky. Andersson and Karlsson (2021) evaluated model-related errors in LES simulations of an aortic coarctation model. Turbulence-related tensor characteristic sensitivities to spatiotemporal resolution and phase-averaging sample size were assessed. It was found that phase-averaging errors associated with too few cardiac cycles could outweigh spatiotemporal resolution errors. Xu et al. (2020) compared laminar and LES simulations of patient-specific aortas with dilation and different aortic valve morphologies. Large-scale flow parameters were in good agreement although larger differences occurred in disturbed flow regions. Despite progression in our understanding of blood flow states, as well as efforts towards modelling guidelines in disturbed cardiovascular flows, it is still unclear which modelling approach should be selected in aortic computational simulations. This is especially true considering the high computational costs associated with LES; which are not always practicable. Understanding the capabilities of other simulation approaches without turbulence models (e.g., laminar simulation-types) in predicting both laminar and turbulence-based parameters of interest will help inform appropriate model selection in future studies.

The objective of this research is to evaluate the performance of different computational approaches used in simulations of patient-specific aortic flow. A patient with aortic valve stenosis was selected for this study as it showed blood flow disturbances (Manchester et al., 2021) and is thus expected to provide a challenging case for the various computational approaches. Three simulations are conducted including low-resolution laminar, high-resolution laminar and large-eddy simulation, and detailed comparisons are made in terms of both laminar and turbulence parameters.

2 MATERIALS AND METHODS

2.1 Data Acquisition and Magnetic Resonance Image Processing

A patient-with aortic valve stenosis was recruited from St Bartholomew's Hospital (London, United Kingdom) and underwent cardiac magnetic resonance imaging (MRI) and 4D flow MRI at Hammersmith Hospital (London, United Kingdom). The study received ethical approval from the Health Research Authority and Regional Ethics Committee (17/NI/0160) and was sponsored by the Imperial College London Joint Research and Compliance Office, as defined under the sponsorship requirements of the Research Governance Framework (2005). MRI was used to reconstruct the aorta geometry consisting of the ascending aorta down to the descending thoracic aorta and inclusive of the three supra-aortic branches. At the inlet, 4D flow MRI was used to derive a 3D velocity profile over a cardiac cycle. At the three-branch outlets the pressure-based 3-element Windkessel model is applied, with parameters determined using flow waveforms derived from 4D flow MRI and central aortic pressure measurements acquired using a brachial cuff. At the descending thoracic aorta outlet, a mass flow waveform is prescribed based on a fixed flow-split which was estimated from 4D flow MRI. The arterial wall is assumed rigid with a no-slip boundary condition. Full details on data acquisition and image processing can be found in our previous study (Manchester et al., 2021).

2.2 Computational Approaches

Two different computational approaches were considered including laminar and large-eddy simulation (LES). For a true laminar state of flow, competently executed laminar simulations can provide accurate results which rival measurements. Laminar simulations do not explicitly include a turbulence model meaning they are computationally less demanding compared to other simulation approaches. For disturbed flows, LES is better suited owing to its capabilities in modelling laminar, transitional and turbulence features. An implicit LES utilises the computational mesh to distinguish between different length scales of the flow whereby eddies larger than the mesh are directly resolved and eddies smaller than the mesh are accounted for using a subgrid-scale model. In this study, the wall-adapting local eddy-viscosity (WALE) subgrid-scale model is used (Nicoud and Ducros, 1999), with model coefficient C_w = 0.325. The LES methodology was previously validated in both idealised and patient-specific settings, and full details on the LES implementation can be found in our previous publications (Manchester and Xu, 2020; Manchester et al., 2021).

In this study, three different simulation types were considered including low-resolution laminar (LR-Laminar), high-resolution laminar (HR-Laminar) and LES. The naming conventions (LR- and HR-Laminar) refer to both spatial discretisation and temporal discretisation resolutions; where LR-Laminar indicates a lower resolution simulation with coarser mesh and larger time-step, and HR-Laminar indicates a higher resolution simulation with finer mesh and smaller time-step. In the case of laminar-type simulations of non-laminar flows, the length and time-scales of flow which are greater than the spatial and temporal discretisation of the domain are directly resolved. This means that the HR-Laminar simulation is effectively an implicit LES simulation without a subgrid-scale model, meaning the large-scale turbulence features are directly resolved and the influence of the small-scales are not included. The HR-Laminar simulation can essentially be viewed as an unresolved or quasi-direct numerical simulation. The LR-Laminar simulation is designed to be representative of "typical" laminar aortic simulations reported in previous studies (Cheng et al., 2016; Pirola et al., 2017) and both mesh size and time-step are selected accordingly. Similarly to the HR-Laminar simulation, large-scale turbulence features are resolved and the influence of the small-scales are not included. Therefore, in a coarser mesh (LR-Laminar), fewer turbulence scales are resolved.

2.2.1 Computational Mesh and Time-Step

A structured meshing approach was used with meshes generated in ANSYS ICEM (v17.0, ANSYS Inc., Canonsburg, PA). Octagonal multi-block structures were used for greater user control and to allow proper near wall treatment, ensuring $y^+ < 1$. The LES and HR-Laminar simulations used the same mesh and time-step, and LR-Laminar used a coarser mesh and larger time-step. For all meshes, the default ICEM quality metric was above 0.35. The LES and HR-Laminar mesh has a quality metric greater than 0.7 for 97% of the fluid domain, and the LR-Laminar mesh quality metric is greater than 0.7 for 96% of the fluid domain. Full mesh and time-step details used in the different simulations included in this study are provided in **Table 1**. Mesh and time-step sensitivity tests were conducted at peak systole. The LR-Laminar mesh used in this study consists of 1.8 million cells and a mesh sensitivity test was performed by refining the mesh by a factor of 1.3 in all directions, resulting in a finer mesh of 3.9 million cells. In typical laminar simulations of aorta flows, turbulence-based parameters are not included in sensitivity tests, therefore only mean kinetic energy and mean wall shear stress were considered in the mesh sensitivity analysis. Compared to the 3.9 million cell mesh, differences between 1.2% and 3.7% were observed. For the LES and HR-Laminar mesh, mean and turbulence-based parameters were converged including mean kinetic energy, turbulence kinetic energy, mean wall shear stress and turbulent wall shear stress. Full details on the mesh sensitivity can be found in Manchester et al. (2021). Two-point correlations were also used to evaluate streamwise and radial spatial resolutions in regions of elevated turbulence. The two-point correlation estimates the number of cells which resolve the largest turbulence scales and it is recommended that 8 cells or more are sufficient for LES simulations (Davidson, 2009). The mesh used for the LES and HR-Laminar simulation used at least 20 cells to resolve the largest scales in the streamwise directions and 8 cells in the radial directions, suggesting a well resolved mesh. The complete two-point correlation results can be found in **Supplementary Material**.

TABLE 1 | Numerical, mesh and time-step details.

Simulation Type	Subgrid-scale model	Number of cells [million]	Mean cell Height [mm]	First wall-adjacent cell height [mm]	Number of cells in boundary layer	Time-step [ms]
LR-Laminar	None	1.8	1.06	0.1	10	1
HR-Laminar	None	7.4	0.53	0.01	16	0.2
LES	WALE	7.4	0.53	0.01	16	0.2

TABLE 2 | Wall shear stress parameter definitions.

Parameter	Equation
WSS	$\tau_{wall}(\boldsymbol{x},t) = \mu\frac{\partial \boldsymbol{u}(\boldsymbol{x},t)}{\partial \boldsymbol{n}(\boldsymbol{x})}$
Phase-averaged WSS	$\langle\tau_{wall}\rangle(\boldsymbol{x},t) = \frac{1}{N}\sum_{n=0}^{N-1}\tau_{wall}(\boldsymbol{x},t+nT)$
Turbulent WSS	$\langle\tau'_{wall}\rangle(\boldsymbol{x},t) = \sqrt{\frac{1}{N}\sum_{n=0}^{N-1}(\tau_{wall}(\boldsymbol{x},t+nT) - \langle\tau_{wall}\rangle(\boldsymbol{x},t))^2}$
TAWSS	$\overline{\langle\tau_{wall}\rangle}(\boldsymbol{x},t) = \frac{1}{T}\int_0^T \langle\tau_{wall}\rangle(\boldsymbol{x},t)\,dt$
Turbulent-TAWSS	$\overline{\langle\tau'_{wall}\rangle}(\boldsymbol{x},t) = \frac{1}{T}\int_0^T \langle\tau'_{wall}\rangle(\boldsymbol{x},t)\,dt$

2.2.2 Numerical Details

Simulations were performed in OpenFOAM and ran on Cirrus UK National Tier-2 HPC with 216 cores. The fluid was assumed incompressible and Newtonian, with fluid properties representative of blood ($\rho = 1060\,kg/m^3$ and $\mu = 0.0035\,Pa\,s$). Temporal discretisation was achieved using a second order implicit backwards Euler scheme. For LES and HR-Laminar simulations, spatial discretisation was achieved using a second-order central differencing scheme (Gauss) and for LR-Laminar, spatial discretisation was achieved using a bounded second-order upwind scheme. Simulations were converged to a normalised residual of 1e-5 at each time-step for velocity and pressure. Pressure and velocity coupling was achieved using the PIMPLE algorithm. 30 cardiac cycles were simulated to ensure convergence of the phase-averaged parameters, as is discussed in the following section.

2.3 Post-Processing

Both laminar and turbulence-related parameters are presented including velocity, wall shear stress, viscous dissipation, and turbulence kinetic energy. Parameters are calculated using two different methods based on the expected flow state. The first implements an approach typically used to post-process laminar simulations of periodic arterial flows, and the second corresponds to an approach used to post-process simulation results of unstable or turbulent flows. In the first approach, it is assumed that the flow is laminar and pulsating, meaning flow reaches a periodically steady state, i.e., that cycle-to-cycle variations do not occur. Once a sufficient number of cardiac cycles have been simulated to reach a periodic solution, the simulation is stopped and post-processing is conducted on results obtained in the final cycle only, using instantaneous parameters. This method of post-processing is used for laminar-based parameters of the LR-Laminar simulation only using the final cardiac cycle. All parameters post-processed using this approach are referred to as ILR-Laminar (instantaneous LR-Laminar).

The second approach assumes that flow is unstable, and cycle-to-cycle variations may occur. In this case, an instantaneous variable can be decomposed into phase-averaged and fluctuating components:

$$\phi(\boldsymbol{x},t) = \langle\phi\rangle(\boldsymbol{x},t) + \phi'(\boldsymbol{x},t) \tag{1}$$

The phase-average operator, $\langle . \rangle$ acts to average a given variable at a fixed point in time (e.g., peak systole) over all simulated cardiac cycles:

$$\langle\phi\rangle(\boldsymbol{x},t) = \frac{1}{N}\sum_{n=0}^{N-1}\phi(\boldsymbol{x},t+nT) \tag{2}$$

where N is the total number of cardiac cycles, T the period of the cardiac cycle and t is a specified time within a cycle. For disturbed pulsatile flows, the phase-average provides the correct mean representation of a variable at any given time in the cardiac cycle.

The phase-averaged fluctuating component is given by the root-mean-square (RMS) of the instantaneous and phase-average variables:

$$\langle\phi'\rangle(\boldsymbol{x},t) = \sqrt{\frac{1}{N}\sum_{n=0}^{N-1}\left(\phi(\boldsymbol{x},t+nT) - \langle\phi\rangle(\boldsymbol{x},t)\right)^2} \tag{3}$$

This method of post-processing is applied to the LR-Laminar, HR-Laminar and LES simulations. Integrating any variable over the full cardiac cycle results in a cycle-average, referred to as the time-average:

$$\bar{\phi}(\boldsymbol{x},t) = \frac{1}{T}\int_0^T \phi(\boldsymbol{x},t)\,dt \tag{4}$$

Equation 4 represents the time-average of an instantaneous variable, as used in ILR-Laminar. Replacing ϕ with $\langle\phi\rangle$ gives the

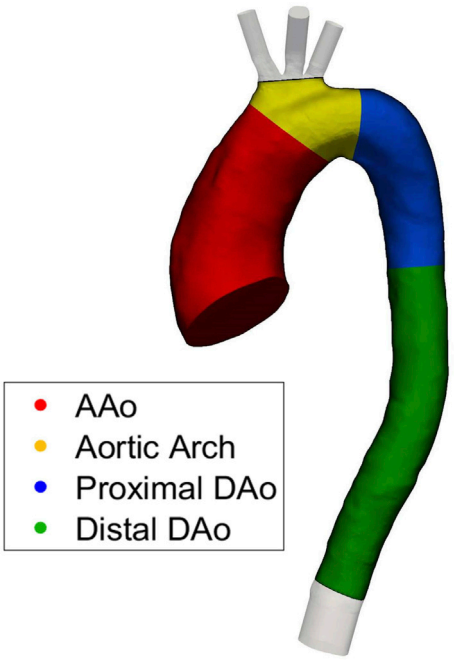

FIGURE 1 | Four regions of interest (ROIs) used for quantitative regional comparisons.

time-average of a phase-averaged mean variable, and replacing ϕ with $\langle\phi'\rangle$ gives the time-average of a phase-averaged turbulent variable. The latter substitutions are used in LR-Laminar, HR-Laminar and LES simulations. All results presented in this paper represent the phase-average, unless indicated as ILR-Laminar. Using two common methods of post-processing allows to not only assess resolution-based performance but also understand the effects of the post-processing approach.

2.3.1 Haemodynamic Parameters

Wall shear stress (WSS) is the instantaneous shearing force exerted by a fluid on the inner surface of the arterial wall. WSS can be decomposed into phase-averaged WSS, $\langle\tau_{wall}\rangle$, using **Eq. 2**, and decomposed into turbulent-WSS, $\langle\tau'_{wall}\rangle$, using **Eq. 3**. Applying **Eq. 4** to the phase-averaged WSS gives the time-averaged wall shear stress (TAWSS). Similarly, applying **Eq. 4** to the turbulent-WSS gives the turbulent time-averaged WSS (turbulent-TAWSS). All the wall shear stress-related parameters used in this study are provided in **Table 2**. Oscillatory shear index (OSI) is given by:

$$OSI = 0.5\left(1 - \frac{\left|\int_0^T \langle WSS\rangle dt\right|}{\int_0^T |\langle WSS\rangle| dt}\right) \tag{5}$$

For ILR-Laminar, $\langle WSS\rangle$ is replaced with the instantaneous WSS.

Turbulence kinetic energy (TKE) is associated with eddies in disturbed flows and can be used to quantify the level of turbulence. TKE is calculated from fluctuating velocity components:

$$TKE = \frac{\rho}{2}\sum_i u_i'^2 \qquad [Pa] \tag{6}$$

where ρ is the fluid density and i = 1, 2, 3.

Viscous dissipation is used to quantify frictional losses, which is a measure of the work done by a fluid on its adjacent layers due to shearing forces. The rate of laminar viscous energy loss can be estimated from the velocity gradient tensor by integrating the viscous dissipation function over the aortic volume:

$$\dot{EL} = \frac{\mu}{2}\int_V \sum_{i,j}\left(\frac{\partial\langle u_i\rangle}{\partial x_j} + \frac{\partial\langle u_j\rangle}{\partial x_i}\right)^2 dV \qquad [W] \tag{7}$$

Similarly, the rate of turbulent viscous energy loss is calculated using the fluctuating velocity gradient tensor:

$$\dot{EL'} = \frac{\mu}{2}\int_V \sum_{i,j}\left(\frac{\partial u_i'}{\partial x_j} + \frac{\partial u_j'}{\partial x_i}\right)^2 dV \qquad [W] \tag{8}$$

Integrating the rates of laminar and turbulent dissipation over a cardiac cycle gives the net laminar viscous energy loss and net turbulent viscous energy loss per cardiac cycle, respectively.

2.3.2 Analysis and Comparison of Results

To allow quantitative regional comparisons, the aorta was split into four regions of interest (ROIs) including the ascending aorta (AAo), aortic arch, proximal descending thoracic aorta (DAo), and distal DAo as shown in **Figure 1**. For each region, selected haemodynamic parameters are spatially integrated over each ROI, providing a spatial average.

In this study we used the LES simulation results as the baseline, meaning ILR-, LR- and HR-Laminar simulation results are compared directly to LES. Accuracy of the LES approach was previously evaluated in an idealised case (Manchester and Xu, 2020) and in the same aorta case used in this study (Manchester et al., 2021). The 4D flow MRI data acquired for this patient provides three-component velocities over the aortic volume, at 20 time points in a cardiac cycle. 4D flow MRI has limited spatiotemporal resolutions (compared to LES) which may compromise accuracy, especially for parameters derived from spatial gradients (e.g., wall shear stress) (Petersson et al., 2012). Turbulence statistics were not acquired with MRI, therefore it is only possible to make direct comparison of velocities between the computational results and 4D flow MRI measurement. All wall shear stress and turbulence-related measures are compared with those calculated from the LES results.

3 RESULTS

3.1 Simulation Comparisons

Table 3 includes details on simulation lengths and time-step convergence. The LR-Laminar simulation took ~ 1.5 days to complete 30 cardiac cycles and both the HR-Laminar and LES have comparable simulation times taking ~ 10 days for 30 cardiac cycles. On average, 32 iterations per time-step were required to achieve convergence of pressure and velocity in the LR-Laminar simulation. In the HR-Laminar and LES simulations an average of 23 and 21 iterations per

TABLE 3 | Simulation times and convergence details.

Simulation Type	Cores	Simulation time [hours]	Percentage of converged time-steps	Average iterations per converged time-step
LR-Laminar	216	37.1	100.0%	32
HR-Laminar	216	240.9	100.0%	23
LES	216	244.3	100.0%	21

TABLE 4 | Pearson correlation coefficients (R) for the three components of velocity, calculated using the entire aortic fluid domain. R is calculated using instantaneous velocities in ILR-Laminar, and phase-averaged velocities in LR-, HR-Laminar and LES.

Simulation Type	R component		
	u_x	u_y	u_z
ILR-Laminar	0.76	0.78	0.69
LR-Laminar	0.82	0.81	0.78
HR-Laminar	0.81	0.82	0.76
LES	0.84	0.83	0.80

time-step were required to achieve convergence of pressure and velocity. Convergence was achieved at all time-steps for all simulation types. Further analysis showed that HR-Laminar required more iterations throughout systolic deceleration.

3.2 Comparison with 4D Flow Magnetic Resonance Imaging

The three simulated velocity fields are quantitatively compared to 4D flow MRI using the Pearson's correlation method which gives a normalised measure of the covariance of two variables, quantifying the linearity between two data-sets Mukaka (2012). The Pearson's product-moment correlation coefficient (R) for each velocity component is calculated over the entire aortic fluid domain, providing a point-by-point comparison. CFD velocity fields are down sampled to match 4D flow MRI resolution, as recommended in Puiseux et al. (2019). Values are given in **Table 4** and correlation plots for the velocity components are provided in **Supplementary Material**. R > 0.7 indicate a high positive correlation and R > 0.5 indicate a moderate positive correlation (Mukaka, 2012). For each of the three velocity components, all simulations show a high positive correlation with 4D flow MRI velocities, except ILR-Laminar. ILR-Laminar post-processed with instantaneous velocities showed a high positive correlation in the x and y-components of velocity and a moderate positive correlation in the z-component of velocity. All simulations can accurately model velocities at peak systole–regardless of numerical or post-processing approach.

3.3 General Flow Features

Velocity magnitude streamlines at two systolic time-points are visualised in **Figure 2** for the three simulations. For LR-Laminar, both instantaneous and phase-averaged velocities are presented. For HR-Laminar and LES simulations, only phase-averaged

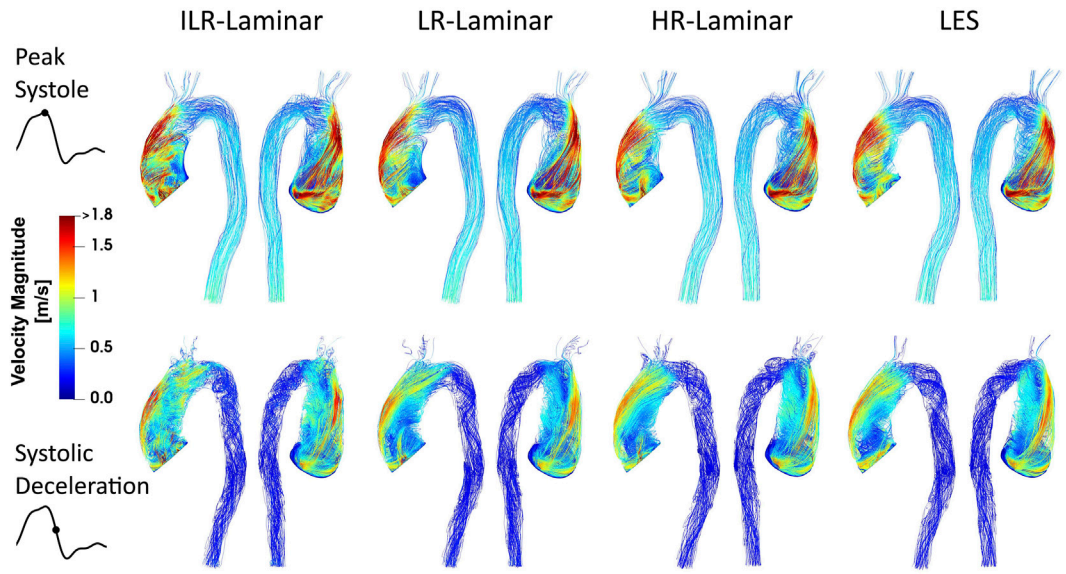

FIGURE 2 | Velocity magnitude streamlines at peak systole (top row) and systolic deceleration (bottom row) for ILR-Laminar, LR-Laminar, HR-Laminar and LES simulations.

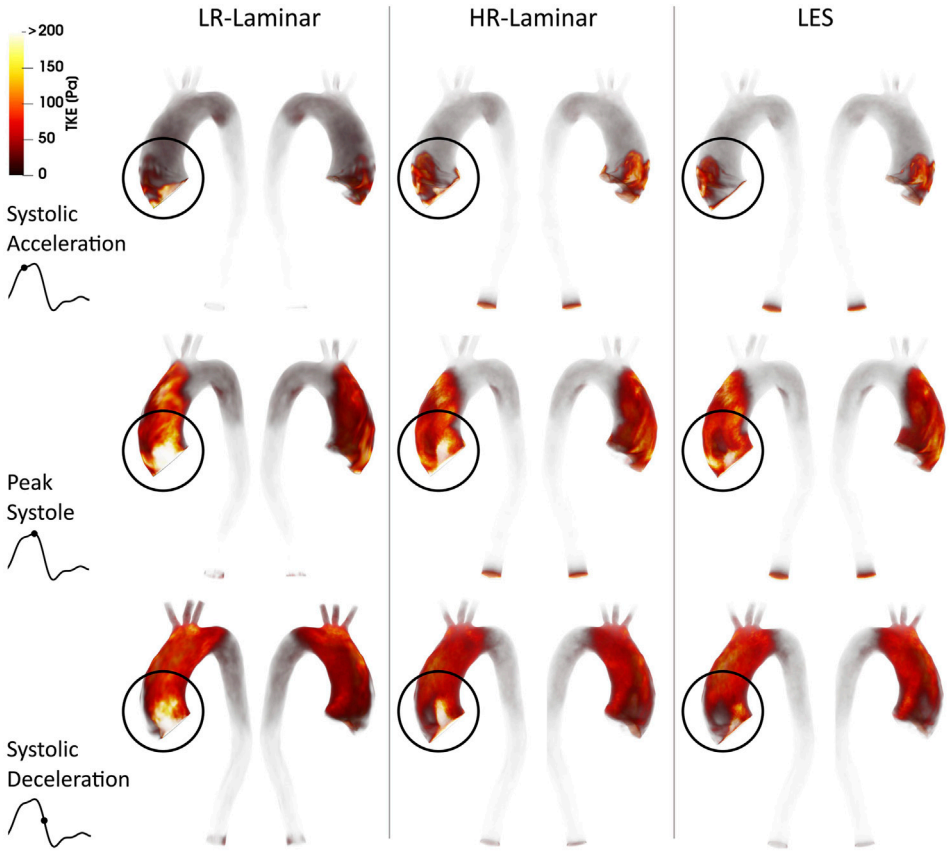

FIGURE 3 | Turbulence kinetic energy (TKE) volume renderings for LR-Laminar, HR-Laminar and LES simulations at three time-points. Top-to-bottom: systolic acceleration, peak systole and systolic deceleration. Locations of largest differences are circled.

velocities are shown. LR-Laminar and HR-Laminar velocity streamlines show good qualitative agreement with LES streamlines throughout the aorta, regardless of the post-processing approach (instantaneous or phase-average). Furthermore, there is good agreement at both peak systole and systolic deceleration. Primary flow features are well predicted, including the high velocity and skewed aortic valve flow which impinges on the anterior vessel wall. LR-Laminar instantaneous velocity streamlines (ILR-Laminar) are more chaotic, particularly in the deceleration phase.

3.4 Turbulence Kinetic Energy

Volume renderings of turbulence kinetic energy (TKE) at three time-points in the cardiac cycle are shown in **Figure 3**. Turbulence production is primarily attributed to the stenosed aortic valve which produces a high velocity and skewed jet. This jet enters the lower velocity fluid in the dilated AAo and impacts on the arterial wall, with the dilated AAo providing space for turbulence to develop. Highest TKE values are found in the AAo and aortic arch, with smaller values in the descending thoracic aorta. Visually, TKE patterns are relatively well predicted by both LR- and HR-Laminar simulations, although TKE values are notably higher near the computational model inlet. These locations of largest differences are highlighted with circles in **Figure 3**.

Figure 4 shows TKE spatially averaged over the entire aorta and each ROI, plotted over the entire cardiac cycle. Upon visual inspection all three simulations show similar trends over the cardiac cycle although values differ. Relative to LES, HR-Laminar predicts spatially averaged TKE values well, except in the AAo near peak systole and in the aortic arch during systolic deceleration. In the arch, HR-Laminar underpredicts spatially averaged TKE by up to 12.2 Pa (18.7% relative error). The LR-Laminar simulation typically overpredicts turbulence levels throughout the aorta, especially during systolic deceleration and diastole. In the AAo, spatially averaged TKE is underpredicted by 13.5 Pa (36.3% relative error) and in the arch, spatially averaged TKE is overpredicted by 17.9 Pa (38.4% relative error). Largest differences are indicated by red markers in **Figure 4**.

3.5 Wall Shear Stress

3.5.1 Laminar Wall Shear Stress

Phase-averaged WSS is averaged over the cardiac cycle to give the time-averaged wall shear stress (TAWSS) for each of the three simulations. For the LR-Laminar simulation, the TAWSS is also calculated using instantaneous wall shear stresses from the last cardiac cycle. TAWSS contours are shown in **Figure 5**, alongside absolute differences in TAWSS between ILR-, LR- and HR-Laminar simulations and the LES simulation. Upon visual

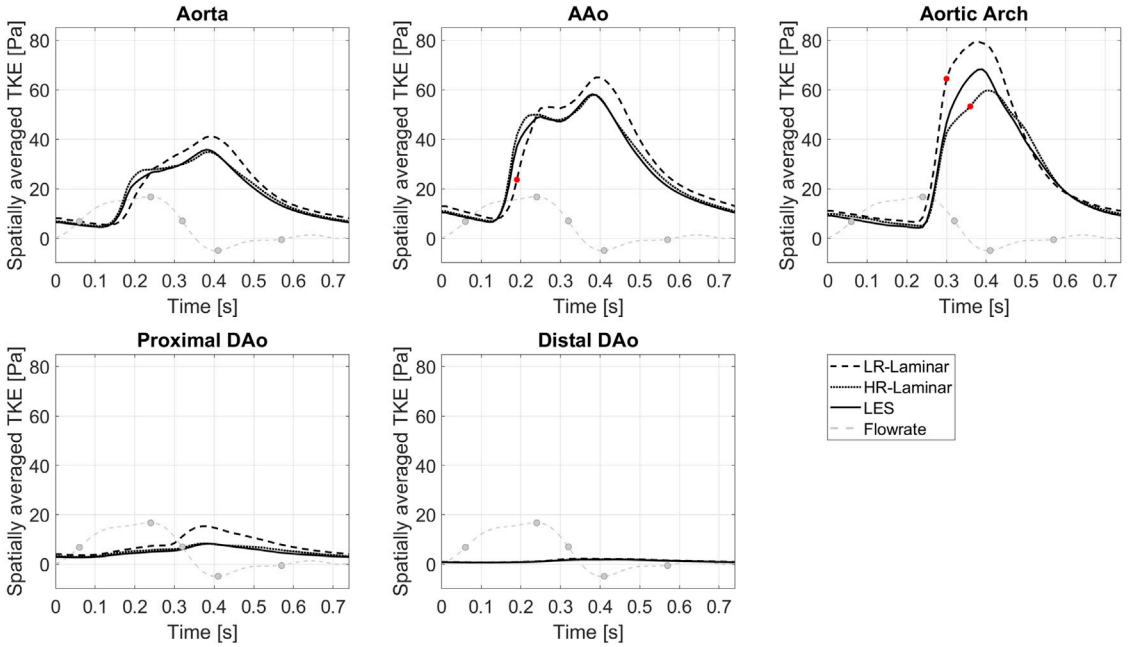

FIGURE 4 | TKE spatially averaged over the entire aorta and each ROI, plotted over the cardiac cycle. Largest differences relative to LES are indicated by red markers. Key times throughout the cardiac cycle are indicated by grey markers and refer to maximum acceleration, peak systole, maximum deceleration, end systole and mid-diastole.

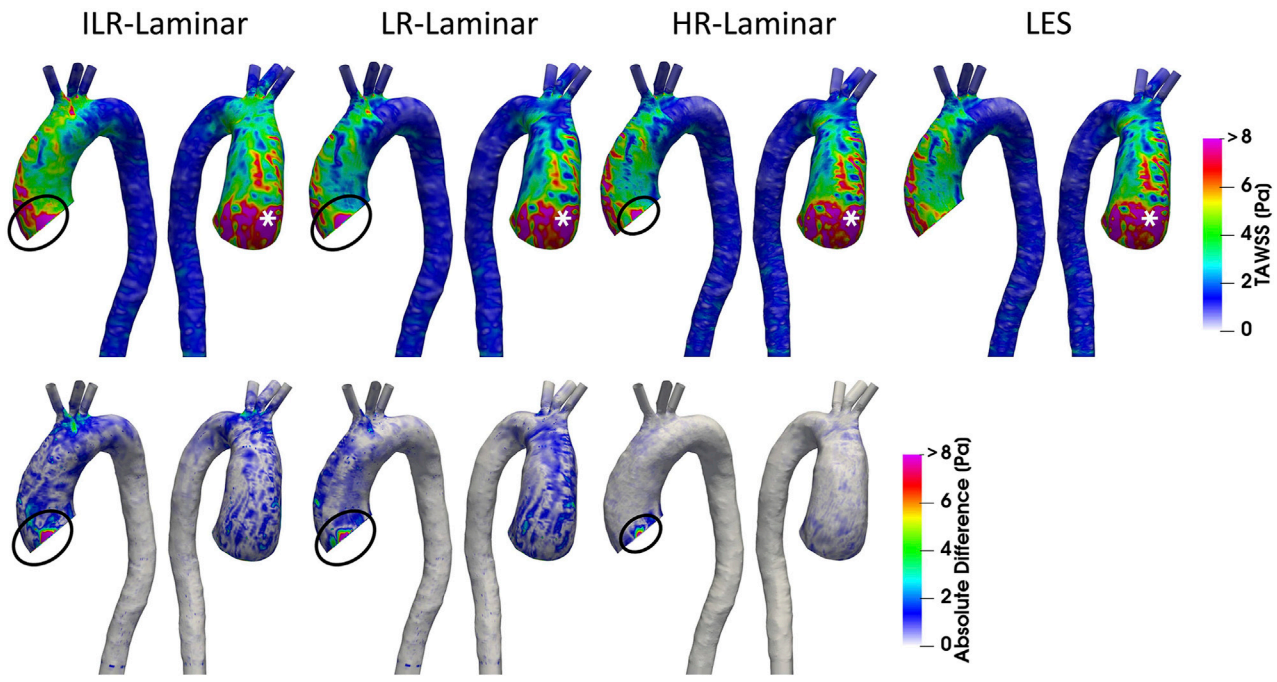

FIGURE 5 | Top row: Time-averaged wall shear stress (TAWSS) contours for ILR-Laminar, LR-Laminar, HR-Laminar and LES simulations. Bottom row: Absolute difference in TAWSS values for ILR-, LR- and HR-Laminar simulations, relative to the LES simulation. Locations of interest are circled and asterisked.

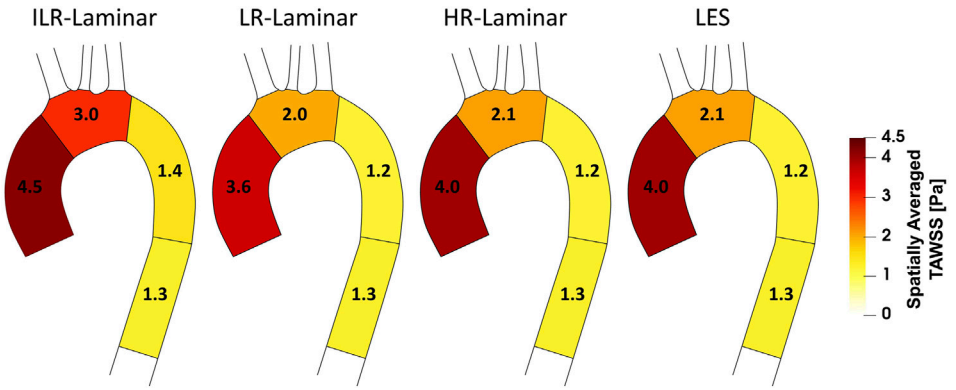

FIGURE 6 | Regional analysis visualisation. Time-averaged wall shear stress (TAWSS) spatially averaged over regions of interest for ILR-Laminar, LR-Laminar, HR-Laminar and LES simulations.

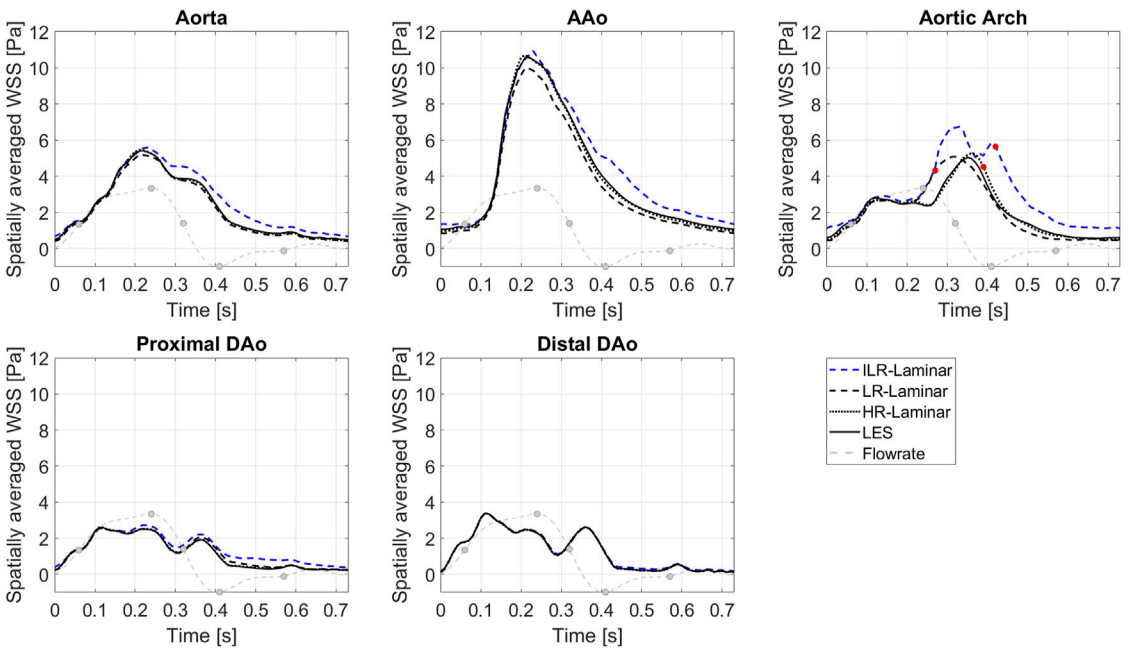

FIGURE 7 | Wall shear stress (WSS) spatially averaged over the entire aorta and each ROI, plotted over the cardiac cycle. Largest differences relative to LES are indicated by red markers. Key times throughout the cardiac cycle are highlighted and refer to maximum acceleration, peak systole, maximum deceleration, end systole and mid-diastole.

inspection, similar TAWSS patterns are seen in all simulations, regardless of post-processing approach. Largest differences occur along the left wall of the ascending aorta, near to the inlet (**Figure 5**, circled). This is likely an artefact of the inlet velocity contours which can artificially impose high near wall velocities. Excluding these regions (of potentially artificially high TAWSS), highest TAWSS's occur in the ascending aorta along the anterior wall and are in excellent agreement, reaching peak TAWSS values of 14.9, 14.7, 15.0 and 14.9 Pa in the ILR-Laminar, LR-Laminar, HR-Laminar and LES simulations, respectively. Locations of peak TAWSS are denoted by the asterisks in **Figure 5**. Relative to LES, the ILR-, LR- and HR-Laminar peak TAWSS values correspond to absolute errors 0.3%, 1.4% and 0.5%, respectively.

Figure 6 shows a schematic of TAWSS spatially averaged over each ROI, for each simulation. Each ROI is colour-coded using the average value of TAWSS in that section. HR-Laminar and LES values are in excellent agreement in all ROIs showing identical values correct to 1 decimal place. In the LR-Laminar simulation, values are underpredicted in the AAo and arch. Largest differences up to 0.4 Pa are observed in the AAo (10.6% relative error to LES). In the ILR-Laminar case, values are overpredicted in the AAo, arch, and proximal DAo. Differences are less than 1 Pa in all ROIs, with

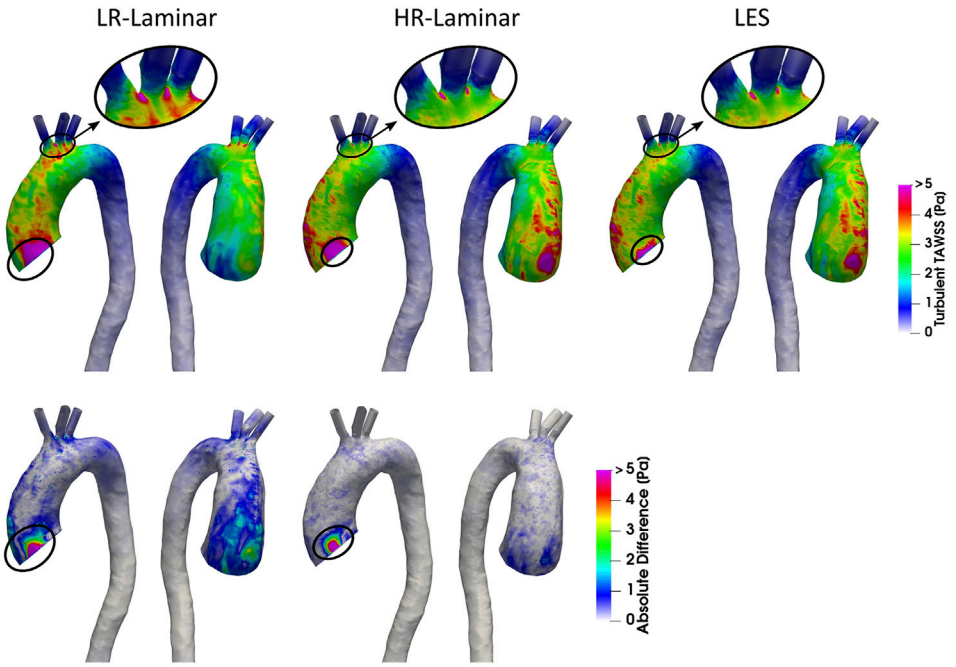

FIGURE 8 | Top row: Time-averaged turbulent wall shear stress (Turbulent-TAWSS) contours for LR-Laminar, HR-Laminar and LES simulations. Bottom row: Absolute difference in turbulent-TAWSS values for LR- and HR-Laminar simulations, relative to the LES simulation. Locations of interest are circled.

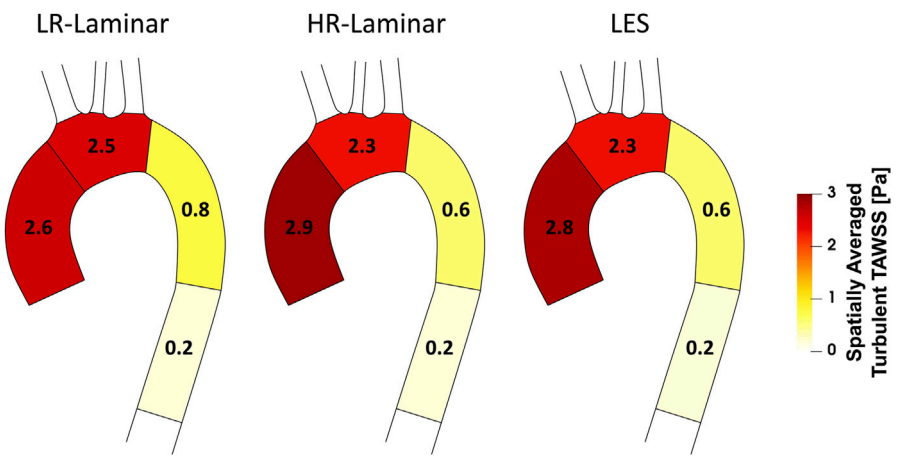

FIGURE 9 | Regional analysis visualisation. Time-averaged turbulent wall shear stress (Turbulent-TAWSS) spatially averaged over regions of interest for LR-Laminar, HR-Laminar and LES simulations.

largest differences observed in the aortic arch (44.6% relative error).

Figure 7 shows WSS spatially averaged over the entire aorta and each ROI, plotted over the entire cardiac cycle. ILR-Laminar results are based on instantaneous WSS from the final cardiac cycle and LR-, HR-Laminar and LES results are based on phase-averaged WSS. Compared to the LES simulation, HR-Laminar shows excellent agreement over the cardiac cycle in all regions. All differences are less than 0.6 Pa, with largest differences seen in the aortic arch near end systole. Both ILR- and LR-Laminar simulation results capture similar WSS trends over the cardiac cycle in all regions. Good agreement is seen in the proximal and distal DAo regions (differences less than 0.6 Pa in both simulations), with larger differences seen in the AAo and aortic arch. For ILR-Laminar, largest differences of 3.0 Pa occur in the aortic arch near end systole, and in LR-Laminar, largest differences of 1.7 Pa occur in the arch near peak systole. Largest differences are indicated by red markers in **Figure 7**.

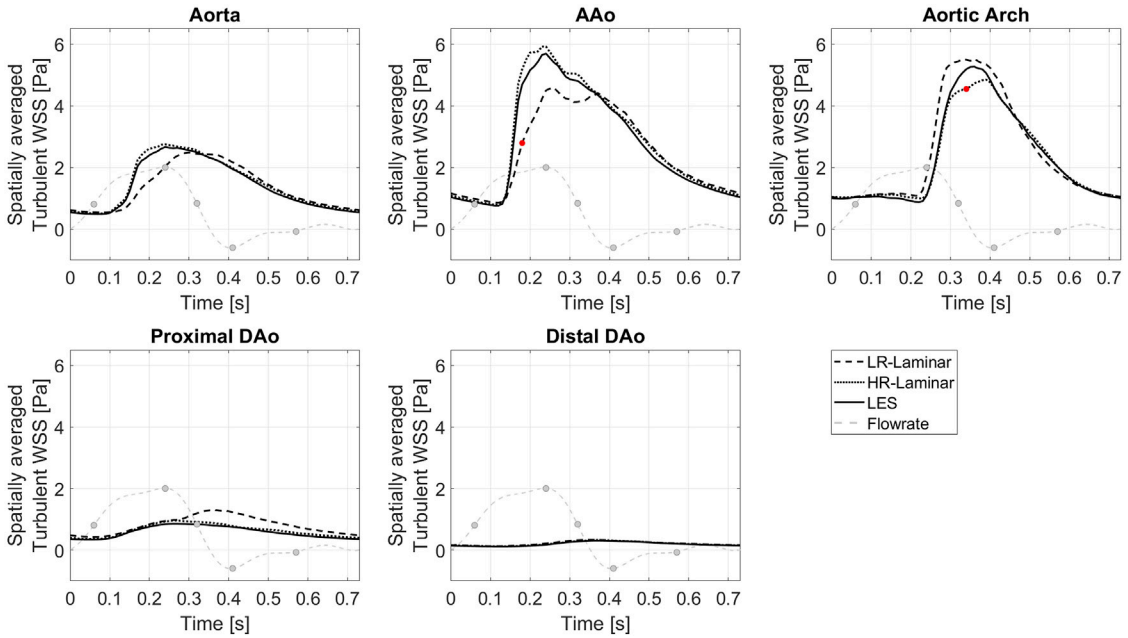

FIGURE 10 | Turbulent WSS spatially averaged over the entire aorta and each ROI, plotted over a cardiac cycle. Largest differences relative to LES are indicated by red markers. Key times throughout the cardiac cycle refer to maximum acceleration, peak systole, maximum deceleration, end systole and mid-diastole.

3.5.2 Turbulent Wall Shear Stress

Turbulent phase-averaged WSS is averaged over the cardiac cycle to give the time-averaged turbulent wall shear stress (turbulent-TAWSS) for LR-, HR-Laminar and LES simulations. Turbulent-TAWSS contours are shown in **Figure 8**, alongside absolute differences in turbulent-TAWSS between LR-, HR-Laminar simulations and the LES simulation. Visually, turbulent-TAWSS patterns agree well over the aorta, except near the inlet (**Figure 8**, circled). Excluding peak values near the inlet, highest turbulent-TAWSS's are experienced between the aortic arch branches in all simulations (**Figure 8**, circled). At these locations, the LR-Laminar, HR-Laminar and LES simulations each show peak values of 14.7, 11.5 and 11.2 Pa, respectively. Relative to LES, the LR- and HR-Laminar peak turbulent-TAWSS values correspond to maximum absolute differences of 3.5 Pa and 0.3 Pa (absolute relative errors of 31.3% and 2.7%).

A schematic of turbulent-TAWSS spatially averaged over each ROI is shown in **Figure 9** for each simulation. HR-Laminar and LES predicted values are in good agreement with differences < 0.2 Pa in all ROIs (5.1% relative error in the AAo). The LR-Laminar simulation underpredicts turbulent-TAWSS in the AAo and overpredicts turbulent-TAWSS in the aortic arch and proximal descending thoracic aorta. Relative to LES, differences are less than 0.3 Pa with largest differences observed in the proximal descending thoracic aorta (38.6% relative error).

Figure 10 shows the turbulent-WSS spatially averaged over the entire aorta and each ROI, plotted over the entire cardiac cycle. Compared to the LES simulation, HR-Laminar shows similar turbulent-WSS behaviours over the cardiac cycle in all regions except in the aortic arch, with differences up to 0.7 Pa during systolic deceleration. LR-Laminar turbulent-WSS trends differ to LES with maximum differences reaching 1.9 Pa in the AAo before peak systole. Largest differences are shown by red markers in **Figure 10**.

3.5.3 Oscillatory Shear Index

OSI is a dimensionless measure of WSS alignment and quantifies deviation of the WSS vector from the TAWSS vector over the cardiac cycle. A value of 0 indicates complete alignment throughout the cardiac cycle and a value of 0.5 indicates the converse. OSI contours are shown in **Figure 11** alongside differences in OSI between ILR-, LR- and HR-Laminar simulations and the LES simulation. OSI contours are visually similar, and best agreement is seen in HR-Laminar with differences up to 0.23. ILR- and LR-Laminar OSI both showed larger differences up to 0.48, relative to the LES simulation. This means that in certain regions ILR- and LR-Laminar simulations show opposite OSI results to the LES simulation. Locations of largest differences are indicated with an asterisk in **Figure 11**.

3.6 Energy Loss

3.6.1 Laminar Viscous Energy Loss

Viscous dissipation over the cardiac cycle is plotted in **Figure 12A**, for all three simulations. LR-, HR-Laminar and LES simulations show similar behaviours over the cardiac cycle, all peaking just ahead of peak systole. ILR-Laminar shows similar trends although values are massively overpredicted. Relative to the LES simulation, ILR-, LR- and HR-Laminar show errors of 75.6%, 1.7% and 1.5% in peak viscous dissipation values, respectively. The net viscous energy loss is calculated by integrating the viscous dissipation over the cardiac cycle and is

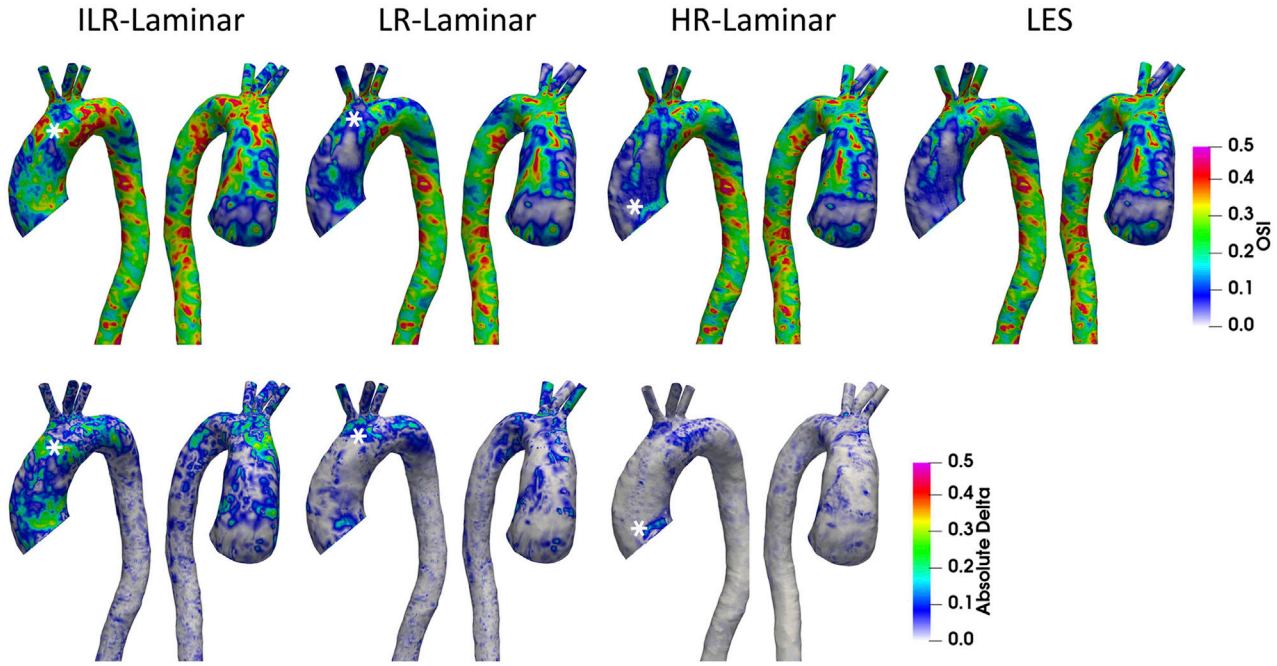

FIGURE 11 | Top row: Oscillatory shear index (OSI) contours for ILR-Laminar, LR-Laminar, HR-Laminar and LES simulations. Bottom row: Absolute difference in OSI values for ILR-, LR- and HR-Laminar simulations, relative to the LES simulation. Locations of largest differences are indicated with asterisks.

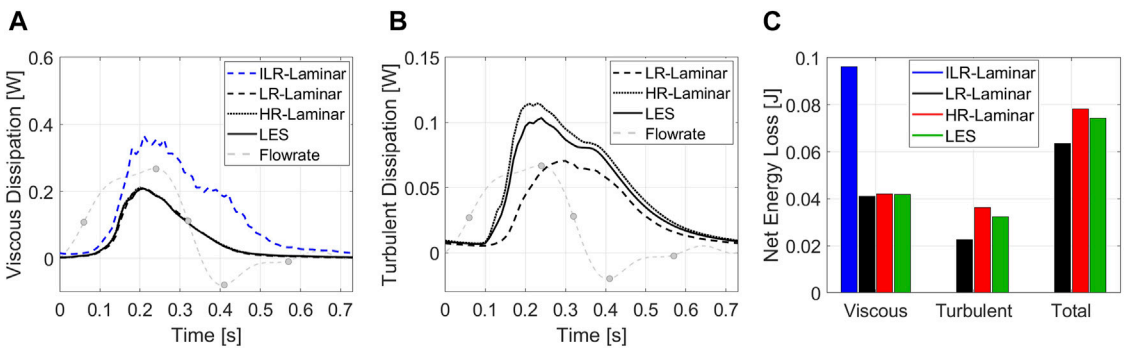

FIGURE 12 | (A) Viscous dissipation and **(B)** turbulent dissipation spatially averaged over the entire aorta, plotted over the cardiac cycle. **(C)** Net energy losses. Key times throughout the cardiac cycle are highlighted and refer to maximum acceleration, peak systole, maximum deceleration, end systole and mid-diastole.

shown in **Figure 12C**. ILR-, LR- and HR-Laminar show 130.3%, 1.7% and 0.8% errors relative to the LES simulation.

3.6.2 Turbulent Viscous Energy Loss

Turbulent dissipation over the cardiac cycle is plotted in **Figure 12B**, for all three simulations. HR-Laminar and LES simulations show similar behaviours over the cardiac cycle, although values differ. Relative to the LES simulation, LR-Laminar show largest differences near peak systole with 54.4% relative error. HR-Laminar also has largest differences near peak systole of 22.8% relative error. The net turbulent energy loss is calculated by integrating the turbulent dissipation over the cardiac cycle and is shown in **Figure 12C**. LR- and HR-Laminar show 30.4% underprediction and 11.6% overprediction, respectively, relative to the LES simulation.

4 DISCUSSION

Since the early conception of the Womersley flow model in the 1950s (Womersley, 1954; Hale et al., 1955a; Hale et al., 1955b; Womersley, 1955), blood flow in large arteries was assumed laminar and has typically been treated as such in numerical simulations. Recently, there has been a shift in attitudes towards the flow state of cardiovascular flows. In the past decade numerical studies accounting for blood flow disturbances are on the rise, finding

turbulence features in both the pathologic and healthy aorta (Lantz et al., 2012; Lantz et al., 2013; Miyazaki et al., 2017; Xu et al., 2018; Saqr et al., 2020; Xu et al., 2020; Manchester et al., 2021). One such study conducted semi-patient-specific simulations of a healthy adult aorta and a child aorta with double aortic arch (Miyazaki et al., 2017). Three modelling approaches were used: laminar, LES and the renormalisation group (RNG) $k-\epsilon$ model. Similar to this study, velocities were quantitatively compared to 4D flow MRI velocities using the Pearson's correlation method. They found that predicted velocities from the RNG $k-\epsilon$ model correlated marginally better than laminar and LES velocities, although poorer correlations (low to moderate) were observed in the child AAo owing to the flat inlet velocity profile which lacks secondary velocities. WSS values and laminar viscous energy losses from all three simulations did not correlate well with values calculated directly from 4D flow MRI because of lower spatial resolution. It was unclear which modelling approach performed the best in their study.

4.1 ILR-, LR- and HR-Laminar Comparisons with LES

In the present study, peak systolic velocities compared very well to 4D flow MRI velocities, throughout the entire aortic fluid domain. All simulations achieved a high positive correlation, except the z-component in the ILR-Laminar simulation which was just below the threshold and indicated a moderate positive correlation. Similarly, velocity streamlines were well predicted by all simulations, even during systolic deceleration when the flow-state is highly unstable. For this patient, the results suggest that any of the simulation types, including ILR-Laminar, could be used to predict velocities and flow patterns to a reasonable degree of accuracy. Visually, primary turbulence features are captured by all three simulations and spatial-temporal trends were similar. Both LR- and HR-Laminar simulations overestimated turbulence production near the inlet. Quantitatively, HR-Laminar TKE compared well to LES TKE throughout the cardiac cycle except in the aortic arch during systolic deceleration, and LR-Laminar typically overpredicted TKE over the cardiac cycle.

In terms of wall shear stresses and OSI, HR-Laminar compared best with LES predicted values. For phase-averaged (laminar) wall shear stress; maximum TAWSS was predicted within 0.5% relative accuracy, ROI analysis showed that TAWSS agreed in all regions to one decimal place, and WSS plotted over the cardiac cycle showed differences less than 0.6 Pa. In general, excellent agreement was observed between HR-Laminar and LES mean wall shear stresses. Larger differences were observed in turbulent wall shear stresses; maximum turbulent-TAWSS differed by 2.7%, ROI analysis showed that turbulent-TAWSS was overpredicted in the AAo (5.1% relative error) but was correct elsewhere, and regional-temporal analysis of turbulent-WSS showed differences less than 0.7 Pa. Overall, turbulent wall shear stresses are typically well predicted by the HR-Laminar simulation, but differences in values were observed. OSI was also fairly well predicted by HR-Laminar, although differences up to 0.23 were seen.

ILR-Laminar and LR-Laminar wall shear stresses and OSI did not compare so favourably to LES. In terms of phase-averaged (laminar) wall shear stress the lower resolution simulations were able to capture trends–both TAWSS contours and WSS plotted over the cardiac cycle are visually similar to LES—but quantitative analysis showed that values differ significantly. ILR- and LR-Laminar simulations showed relative errors of 0.3% and 1.4% in peak TAWSS values. ROI analysis showed that both simulations predicted TAWSS relatively well in the DAo, but large differences were seen in the AAo of LR-Laminar (10.6% error) and in the aortic arch of ILR-Laminar (44.6% error). Temporal and spatial analysis showed that WSS and TAWSS were better predicted in regions of laminar or lowly disturbed flow (**Figure 7**). E.g., in the proximal and distal DAo where TKE is small throughout the cardiac cycle and in the AAo and aortic arch during systolic acceleration when TKE is small. In the AAo and aortic arch during systolic deceleration and diastole, TKE levels are high and/or dissipating, and the low-resolution simulations cannot accurately predict WSS and TAWSS. These findings agree well with those of Xu et al. (2020) who compared laminar and LES simulations of three patient-specific aortas with dilation and different aortic valve morphologies. They found little difference in large-scale flow parameters, with laminar simulations underpredicting TAWSS by up to 5%. The authors observed largest differences in localised regions of highly disturbed flow—particularly in the aorta with severe aortic valve stenosis. For turbulent wall shear stresses, LR-Laminar could not accurately estimate turbulent-WSS values and typically overpredicted values, consistent with TKE overpredictions. Peak turbulent-TAWSS differed by 31.3% and ROI analysis showed differences in all regions up to 38.6%. Considering LR-Laminar could not accurately predict WSS values, it is not surprising that the spatial and temporal resolution of the simulation was not sufficient in predicting turbulent-WSS as well. OSI contours were visually similar to LES, but accuracy diminished with simulation resolution which is also not unexpected considering OSI is based on WSS.

LR- and HR-Laminar viscous dissipations and energy losses were comparable to LES with viscous energy loss values up to 1.7% relative error. ILR-Laminar viscous energy losses showed the largest relative errors of all parameters included in this study of 130.3% and viscous dissipation was overpredicted over the entire cardiac cycle. Because the instantaneous velocity field is used in the calculation which is based on the velocity gradient tensor, fluctuations are not damped and are amplified when calculating the gradient. LES turbulent dissipation values proved challenging to match with LR- and HR-Laminar simulations, although trends over the cardiac cycle were comparable in HR-Laminar. LR-Laminar underpredicted turbulent energy losses by 31.4% and HR-Laminar overpredicted it by 11.6%.

Comparing HR-Laminar and LES simulation results, it is clear that the contribution from the subgrid-scale model (or lack of) has a notable influence on predicted turbulence-based results in this case.

4.2 Post-Processing Approaches

In typical laminar-based simulations of the aorta, simulations are run until certain parameters are deemed to have reached a

periodic solution. Pressure at the branch outlets is monitored, and once this pressure has reached a periodic solution, it is assumed that all other properties have also reached a periodic solution and the simulation is stopped. Following this, results obtained in the prior cardiac cycles are neglected, and post-processing is conducted on the final cycle only using instantaneous parameters. The results from this study show that although a periodic solution in pressure is easily achieved (at 8 cardiac cycles), it does not necessarily imply that a periodic solution in all parameters is achieved and that there are still cycle-to-cycle variations. This is revealed by comparing the results from ILR- and LR-Laminar simulations, where the same simulation results were post-processed using two different approaches. Only laminar-based parameters were compared because turbulence-based parameters cannot directly be calculated from instantaneous values. There was little difference in the output velocities between the two post-processing approaches, but wall shear stresses were different. For this case, wall shear stress estimations were much better with the phase-averaged approach, although there were still deviations from the HR-Laminar and LES results. ILR-Laminar viscous energy losses were massively overpredicted, but LR-Laminar energy losses were in better agreement with LES.

4.3 Limitations, Future Work and Recommendations

In this study, the aortic wall was assumed rigid and valve leaflet motion was not directly modelled although effects were accounted for by making use of 4D flow MRI data. Whilst aortic wall motion may affect simulation results (Tan et al., 2009), the LES methods used in this paper have been thoroughly sensitivity tested and validated in idealised and patient-specific cases (Manchester and Xu, 2020; Manchester et al., 2021). Blood flow was treated as Newtonian which is widely considered an acceptable simplification in computational modelling of aortic flows. Real blood is Non-Newtonian and the length scales of red blood cells are not much smaller than the expected smallest length scales of blood flow turbulence (Antiga and Steinman, 2009). It is therefore reasonable to expect additional turbulence damping to occur at the smallest turbulence scales in Non-Newtonian flow. Andersson et al. (2015) found slight turbulence damping effects in an aortic coarctation model although this had little impact on general flow characteristics. Other studies into arterial flows found that a Newtonian flow assumption produced reasonably accurate results and that haemodynamic parameters were far more sensitive to geometric variability (Lee and Steinman, 2007; Marrero et al., 2014). Nonetheless, future studies could evaluate turbulence characteristic sensitivity to Newtonian and Non-Newtonian modelling approaches, as well as evaluate interactions with current subgrid-scale models which are designed to satisfy the properties of fully turbulent flows. In this study, an aortic case with severe aortic valve stenosis was selected to evaluate the various laminar-type simulations. Because this case showed high turbulence levels in a former study (Manchester et al., 2021), it was expected to provide a challenging test case for laminar-type simulations. Based on our findings, it is reasonable to hypothesise that laminar-type simulations of aortic flows with healthy valve types and less severe valve stenosis would perform better than the case considered in this study because turbulence levels are expected to be of smaller magnitude. Nonetheless, this study is limited to a single aortic case and in future work, a selection of aortas with a range of diseases and disturbance levels should be included to improve best practice surrounding the appropriate selection of computational approach. Only then can the results be generalised to all aortic flows.

Based on the findings from this paper, it is recommended that future numerical studies on aortic flows select the modelling approach based not only on expected flow state but the parameters of interest. For example, if only velocities are required then an ILR-Laminar type simulation may be appropriate. Considering LES simulations are computationally demanding and produce large amounts of data, an LES approach is not always feasible (e.g., in large scale studies) and alternative modelling approaches must be considered. HR-Laminar simulation results were less accurate than LES and simulation times were almost identical. Based on this, there was no benefit to running a higher resolution laminar simulation over LES. Comparing ILR-Laminar and LR-Laminar results showed that phase-averaging improved wall shear stress and viscous energy loss estimations in the lower resolution simulations. Adopting a more advanced post-processing approach is a relatively simple and low-cost way to improve simulation predictions.

5 CONCLUSION

Blood flow in a patient-specific aorta with aortic valve stenosis was simulated using different modelling approaches to assess their capabilities in capturing mean and turbulence-based parameters. Three modelling approaches were examined: LES, high-resolution (HR) laminar and low-resolution (LR) laminar. The HR-Laminar simulation used the same mesh and time-step as the LES simulation and is essentially a coarse DNS. The LR-Laminar simulation used a coarser mesh and larger time-step representative of typical laminar aortic simulations. Two post-processing approaches were compared using the LR-Laminar simulation results: one was based on the final periodic solution without phase-averaging (ILR-Laminar), and another involved phase-averaging of the same set of results over multiple cycles (LR-Laminar). A range of laminar and turbulence-based parameters were assessed.

All simulations, regardless of post-processing approach, could accurately predict velocities and flow patterns throughout the aorta. Lower resolution simulations (ILR- and LR-Laminar) were incapable of accurately predicting other laminar-based parameters calculated from velocity gradients (wall shear stress and viscous energy loss), although adopting a phase-averaged post-processing approach

improved predictions. The higher resolution simulation (HR-Laminar) produced more comparable results to LES and laminar-based parameters were better estimated than turbulence-based parameters. The findings from this study suggest that well-resolved laminar simulations (HR-Laminar) may provide accurate estimations of laminar-based parameters in disturbed flows, although LES and HR-Laminar simulation times were identical; negating the benefits of running a laminar-type simulation over LES. Post-processing simulation results with a phase-averaged approach is a simple and low-cost way to improve accuracy of lower-resolution simulation results.

DATA AVAILABILITY STATEMENT

The raw data supporting the conclusion of this article will be made available by the authors, without undue reservation.

ETHICS STATEMENT

The studies involving human participants were reviewed and approved by Health Research Authority and Regional Ethics Committee (17/NI/0160). The patients/participants provided their written informed consent to participate in this study.

AUTHOR CONTRIBUTIONS

EM: conception, methods, analysis, writing, and review; SP: methods and review; MS and TA: recruitment and review; DO'R: review; XX: conception, analysis, and review.

FUNDING

EM is supported by a PhD scholarship through the EPSRC Doctoral Training Partnership grant to Imperial College London (EP/R512540/1). This work used the Cirrus UK National Tier-2 HPC Service at EPCC (http://www.cirrus.ac.uk) funded by the University of Edinburgh and EPSRC (EP/P020267/1). This work was supported by the NIHR Imperial College BRC (P69559) and the British Heart Foundation Centre for Research Excellence (Imperial College) (RE/18/4/34215). DO'R is funded by the Medical Research Council. DO'R is supported by the UK Medical Research Council (MC-A658-5QEB0).

SUPPLEMENTARY MATERIAL

The Supplementary Material for this article can be found online at: https://www.frontiersin.org/articles/10.3389/fbioe.2022.836611/full#supplementary-material

REFERENCES

Andersson, M., and Karlsson, M. (2021). Model Verification and Error Sensitivity of Turbulence-Related Tensor Characteristics in Pulsatile Blood Flow Simulations. *Fluids* 6, 11. doi:10.3390/fluids6010011

Andersson, M., Lantz, J., Ebbers, T., and Karlsson, M. (2015). Quantitative Assessment of Turbulence and Flow Eccentricity in an Aortic Coarctation: Impact of Virtual Interventions. *Cardiovasc. Eng. Tech.* 6, 281–293. doi:10.1007/s13239-015-0218-x

Antiga, L., and Steinman, D. A. (2009). Rethinking Turbulence in Blood. *Biorheology* 46, 77–81. doi:10.3233/BIR-2009-0538

Bollache, E., Guzzardi, D. G., Sattari, S., Olsen, K. E., Di Martino, E. S., Malaisrie, S. C., et al. (2018). Aortic Valve-Mediated wall Shear Stress Is Heterogeneous and Predicts Regional Aortic Elastic Fiber Thinning in Bicuspid Aortic Valve-Associated Aortopathy. *J. Thorac. Cardiovasc. Surg.* 156, 2112–2120. doi:10.1016/j.jtcvs.2018.05.095

Borazjani, I., Ge, L., and Sotiropoulos, F. (2010). High-Resolution Fluid-Structure Interaction Simulations of Flow through a Bi-Leaflet Mechanical Heart Valve in an Anatomic Aorta. *Ann. Biomed. Eng.* 38, 326–344. doi:10.1007/s10439-009-9807-x

Cheng, Z., Kidher, E., Jarral, O. A., O'Regan, D. P., Wood, N. B., Athanasiou, T., et al. (2016). Assessment of Hemodynamic Conditions in the Aorta Following Root Replacement with Composite Valve-Conduit Graft. *Ann. Biomed. Eng.* 44, 1392–1404. doi:10.1007/s10439-015-1453-x

Chiu, J.-J., and Chien, S. (2011). Effects of Disturbed Flow on Vascular Endothelium: Pathophysiological Basis and Clinical Perspectives. *Physiol. Rev.* 91, 327–387. doi:10.1152/physrev.00047.2009

Cunningham, K. S., and Gotlieb, A. I. (2005). The Role of Shear Stress in the Pathogenesis of Atherosclerosis. *Lab. Invest.* 85, 9–23. doi:10.1038/labinvest.3700215

Davidson, L. (2009). Large Eddy Simulations: How to Evaluate Resolution. *Int. J. Heat Fluid Flow* 30, 1016–1025. doi:10.1016/j.ijheatfluidflow.2009.06.006

Davies, P. F., Remuzzi, A., Gordon, E. J., Dewey, C. F., Jr, and Gimbrone, M. A., Jr (1986). Turbulent Fluid Shear Stress Induces Vascular Endothelial Cell Turnover *In Vitro*. *Proc. Natl. Acad. Sci.* 83, 2114–2117. doi:10.1073/pnas.83.7.2114

Dolan, J. M., Kolega, J., and Meng, H. (2013). High Wall Shear Stress and Spatial Gradients in Vascular Pathology: A Review. *Ann. Biomed. Eng.* 41, 1411–1427. doi:10.1007/s10439-012-0695-0

Ge, L., Dasi, L. P., Sotiropoulos, F., and Yoganathan, A. P. (2008). Characterization of Hemodynamic Forces Induced by Mechanical Heart Valves: Reynolds vs. Viscous Stresses. *Ann. Biomed. Eng.* 36, 276–297. doi:10.1007/s10439-007-9411-x

Guzzardi, D. G., Barker, A. J., Van Ooij, P., Malaisrie, S. C., Puthumana, J. J., Belke, D. D., et al. (2015). Valve-Related Hemodynamics Mediate Human Bicuspid Aortopathy. *J. Am. Coll. Cardiol.* 66, 892–900. doi:10.1016/j.jacc.2015.06.1310

Hale, J. F., McDonald, D. A., Taylor, M. G., and Womersley, J. R. (1955a). The Counter Chronometer Method for Recording Pulse-Wave Velocity. *J. Physiol.* 129, 27–28P.

Hale, J. F., McDonald, D. A., and Womersley, J. R. (1955b). Velocity Profiles of Oscillating Arterial Flow, with Some Calculations of Viscous Drag and the reynolds Number. *J. Physiol.* 128, 629–640. doi:10.1113/jphysiol.1955.sp005330

Lancellotti, R. M., Vergara, C., Valdettaro, L., Bose, S., and Quarteroni, A. (2017). Large Eddy Simulations for Blood Dynamics in Realistic Stenotic Carotids. *Int. J. Numer. Meth Biomed. Engng* 33, e2868. doi:10.1002/cnm.2868

Lantz, J., Ebbers, T., Engvall, J., and Karlsson, M. (2013). Numerical and Experimental Assessment of Turbulent Kinetic Energy in an Aortic Coarctation. *J. Biomech.* 46, 1851–1858. doi:10.1016/j.jbiomech.2013.04.028

Lantz, J., Gårdhagen, R., and Karlsson, M. (2012). Quantifying Turbulent wall Shear Stress in a Subject Specific Human Aorta Using Large Eddy Simulation. *Med. Eng. Phys.* 34, 1139–1148. doi:10.1016/j.medengphy.2011.12.002

Lee, S.-W., and Steinman, D. A. (2007). On the Relative Importance of Rheology for Image-Based CFD Models of the Carotid Bifurcation. *J. Biomechanical Eng.* 129, 273–278. doi:10.1115/1.2540836

Manchester, E. L., Pirola, S., Salmasi, M. Y., O'Regan, D. P., Athanasiou, T., and Xu, X. Y. (2021). Analysis of Turbulence Effects in a Patient-Specific Aorta with Aortic Valve Stenosis. *Cardiovasc. Eng. Tech.* 12, 438–453. doi:10.1007/s13239-021-00536-9

Manchester, E. L., and Xu, X. Y. (2020). The Effect of Turbulence on Transitional Flow in the FDA 's Benchmark Nozzle Model Using Large-Eddy Simulation. *Int. J. Numer. Meth Biomed. Engng* 36, 1–15. doi:10.1002/cnm.3389

Mancini, V., Bergersen, A. W., Vierendeels, J., Segers, P., and Valen-Sendstad, K. (2019). High-Frequency Fluctuations in Post-stenotic Patient Specific Carotid Stenosis Fluid Dynamics: A Computational Fluid Dynamics Strategy Study. *Cardiovasc. Eng. Tech.* 10, 277–298. doi:10.1007/s13239-019-00410-9

Marrero, V. L., Tichy, J. A., Sahni, O., and Jansen, K. E. (2014). Numerical Study of Purely Viscous Non-Newtonian Flow in an Abdominal Aortic Aneurysm. *J. Biomechanical Eng.* 136, 101001. doi:10.1115/1.4027488

Miyazaki, S., Itatani, K., Furusawa, T., Nishino, T., Sugiyama, M., Takehara, Y., et al. (2017). Validation of Numerical Simulation Methods in Aortic Arch Using 4D Flow MRI. *Heart Vessels* 32, 1032–1044. doi:10.1007/s00380-017-0979-2

Mukaka, M. M. (2012). Statistics Corner: A Guide to Appropriate Use of Correlation Coefficient in Medical Research. *Malawi Med. J.* 24, 69–71.

Nicoud, F., and Ducros, F. (1999). Subgrid-Scale Stress Modelling Based on the Square of the Velocity Gradient Tensor. *Flow, Turbulence and Combustion* 62, 183–200. doi:10.1023/A:1009995426001

Petersson, S., Dyverfeldt, P., and Ebbers, T. (2012). Assessment of the Accuracy of MRI Wall Shear Stress Estimation Using Numerical Simulations. *J. Magn. Reson. Imaging* 36, 128–138. doi:10.1002/jmri.23610

Pirola, S., Cheng, Z., Jarral, O. A., O'Regan, D. P., Pepper, J. R., Athanasiou, T., et al. (2017). On the Choice of Outlet Boundary Conditions for Patient-specific Analysis of Aortic Flow Using Computational Fluid Dynamics. *J. Biomech.* 60, 15–21. doi:10.1016/j.jbiomech.2017.06.005

Puiseux, T., Sewonu, A., Meyrignac, O., Rousseau, H., Nicoud, F., Mendez, S., et al. (2019). Reconciling PC-MRI and CFD: An In-Vitro Study. *NMR Biomed.* 32, e4063. doi:10.1002/nbm.4063

Salmasi, M. Y., Pirola, S., Sasidharan, S., Fisichella, S. M., Redaelli, A., Jarral, O. A., et al. (2021). High Wall Shear Stress Can Predict Wall Degradation in Ascending Aortic Aneurysms: An Integrated Biomechanics Study. *Front. Bioeng. Biotechnol.* 9, 935. doi:10.3389/fbioe.2021.750656

Saloner, D., Acevedo-Bolton, G., Rayz, V., Wintermark, M., Martin, A., Dispensa, B., et al. (2006). "Imaging and CFD in the Analysis of Vascular Disease Progression," in Proc. SPIE 6143, Medical Imaging 2006: Physiology, Function, and Structure from Medical Images 61430G, San Diego, California, March 13, 2006. doi:10.1117/12.662791

Saqr, K. M., Tupin, S., Rashad, S., Endo, T., Niizuma, K., Tominaga, T., et al. (2020). Physiologic Blood Flow Is Turbulent. *Sci. Rep.* 10, 15492. doi:10.1038/s41598-020-72309-8

Tan, F. P. P., Torii, R., Borghi, A., Mohiaddin, R. H., Wood, N. B., and Xu, X. Y. (2009). Fluid-Structure Interaction Analysis of Wall Stress and Flow Patterns in a Thoracic Aortic Aneurysm. *Int. J. Appl. Mech.* 01, 179–199. doi:10.1142/S1758825109000095

Womersley, J. R. (1954). Flow in the Larger Arteries and its Relation to the Oscillating Pressure. *J. Physiol.* 124, 31–2P.

Womersley, J. R. (1955). Method for the Calculation of Velocity, Rate of Flow and Viscous Drag in Arteries when the Pressure Gradient Is Known. *J. Physiol.* 127, 553–563. doi:10.1113/jphysiol.1955.sp005276

Xu, H., Piccinelli, M., Leshnower, B. G., Lefieux, A., Taylor, W. R., and Veneziani, A. (2018). Coupled Morphological-Hemodynamic Computational Analysis of Type B Aortic Dissection: A Longitudinal Study. *Ann. Biomed. Eng.* 46, 927–939. doi:10.1007/s10439-018-2012-z

Xu, L., Yang, T., Yin, L., Kong, Y., Vassilevski, Y., and Liang, F. (2020). Numerical Simulation of Blood Flow in Aorta with Dilation: A Comparison between Laminar and LES Modeling Methods. *CMES-Computer Model. Eng. Sci.* 124, 509–526. doi:10.32604/cmes.2020.010719

Yen, J.-H., Chen, S.-F., Chern, M.-K., and Lu, P.-C. (2014). The Effect of Turbulent Viscous Shear Stress on Red Blood Cell Hemolysis. *J. Artif. Organs* 17, 178–185. doi:10.1007/s10047-014-0755-3

Conflict of Interest: The authors declare that the research was conducted in the absence of any commercial or financial relationships that could be construed as a potential conflict of interest.

Publisher's Note: All claims expressed in this article are solely those of the authors and do not necessarily represent those of their affiliated organizations, or those of the publisher, the editors and the reviewers. Any product that may be evaluated in this article, or claim that may be made by its manufacturer, is not guaranteed or endorsed by the publisher.

NOMENCLATURE

AAo ascending aorta
CFD computational fluid dynamics
DAo descending thoracic aorta
DNS direct numerical simulation
HR high resolution
ILR instantaneous low resolution
LES large-eddy simulation
LR low resolution
MRI magnetic resonance imaging
OSI oscillatory shear index
RNG renormalisation group
ROI region of interest
SGS subgrid-scale
TAWSS time-average wall shear stress
TKE turbulence kinetic energy
WALE wall-adapting local eddy-viscosity
WSS wall shear stress

frontiers in Bioengineering and Biotechnology

ORIGINAL RESEARCH
published: 28 March 2022
doi: 10.3389/fbioe.2022.814995

The Effects of Geometric Features of Intraluminal Thrombus on the Vessel Wall Oxygen Deprivation

Burton Carbino[†,1], Alexander Guy[†,1], Michael Durka[2,3] and Rana Zakerzadeh[,1]*

[1]Department of Engineering, Rangos School of Health Sciences, Duquesne University, Pittsburgh, PA, United States, [2]NASA Jet Propulsion Laboratory, California Institute of Technology, Pasadena, CA, United States, [3]Department of Mechanical Engineering and Materials Science, Swanson School of Engineering, University of Pittsburgh, Pittsburgh, PA, United States

The objective of this paper is to analyze the association of intraluminal thrombus (ILT) presence and morphology with oxygen transport in abdominal aortic aneurysms (AAA) and local hypoxia. The biomechanical role of the ILT layer in the evolution of the aneurysm is still not fully understood. ILT has been shown to create an inflammatory environment by reducing oxygen flux to the arterial wall and therefore decreasing its strength. It has been also hypothesized that the geometry of the ILT may further affect AAA rupture. However, no previous research has attempted to explore the effect of morphological features of ILT on oxygen distributions within the AAA, in a systematic manner. In this study, we perform a comprehensive analysis to investigate how physiologically meaningful variations in ILT geometric characteristics affect oxygen transport within an AAA. We simulate twenty-seven AAA models with variable ILT dimensions and investigate the extent to which ILT attenuates oxygen concentration in the arterial wall. Geometric variations studied include ILT thickness and ILT length, as well as the bulge diameter of the aneurysm which is related to ILT curvature. Computer simulations of coupled fluid flow-mass transport between arterial wall, ILT, and blood are solved and spatial variations of oxygen concentrations within the ILT and wall are obtained. The comparison of the results for all twenty-seven simulations supports the hypothesis that the presence of ILT in AAA correlates to significantly impaired oxygen transport to the aneurysmal wall. Mainly, we observed that ILT thickness and length are the parameters that influence decreased oxygen flow and concentration values the most, and thick thrombi exacerbate hypoxic conditions in the arterial wall, which may contribute to increased tissue degradation. Conversely, we observed that the arterial wall oxygen concentration is nearly independent of the AAA bulge diameter. This confirms that consideration of ILT size and anatomy is crucial in the analysis of AAA development.

Keywords: abdominal aortic aneurysm, intraluminal thrombus, geometric modeling, parametric study, oxygen transport, hypoxia

OPEN ACCESS

Edited by:
Chih-Yu Yang,
Taipei Veterans General Hospital, Taiwan

Reviewed by:
April J Boyd,
University of Manitoba, Canada
Lazar Davidovic,
University of Belgrade, Serbia
Paolo Di Achille,
Broad Institute, United States

***Correspondence:**
Rana Zakerzadeh
zakerzadehr@duq.edu

[†]These authors have contributed equally to this work

Specialty section:
This article was submitted to Biomechanics, a section of the journal Frontiers in Bioengineering and Biotechnology

Received: *14 November 2021*
Accepted: *21 February 2022*
Published: *28 March 2022*

Citation:
Carbino B, Guy A, Durka M and Zakerzadeh R (2022) The Effects of Geometric Features of Intraluminal Thrombus on the Vessel Wall Oxygen Deprivation. Front. Bioeng. Biotechnol. 10:814995. doi: 10.3389/fbioe.2022.814995

INTRODUCTION

Abdominal Aortic Aneurysm (AAA) is characterized by the continuous and gradual dilation of the infrarenal aorta which results from the degradation of the extracellular matrix in the arterial wall (Jana et al., 2019). The prevalence of AAA in general population ranges from 1.0 to 14.2% in men and from 0.2 to 6.4% in women (Li et al., 2013). The majority of AAAs are asymptomatic and acute AAA

ruptures are estimated to cause 4–5% of sudden death in developed countries, and is the 14th leading cause of death in the United States (Aggarwal et al., 2011). Upon rupture, this disease has a high mortality rate of 50–80%, and about 50% of patients die before ever reaching the hospital due to the asymptomatic nature of AAA. However, the processes associated with AAA development and evolution are still not fully understood. It is imperative to thoroughly understand the conditions under which AAA rupture to enhance development of more effective treatments leading to improved patient outcome. Although some clinical evidence suggests that aneurysm diameter is positively associated with the risk of rupture, it has been observed that this maximum diameter criterion may not be appropriate, since sometimes smaller AAA rupture while larger diameter aneurysms remain intact and asymptomatic (Vorp and Geest, 2005). Therefore, other parameters may also play a role in causing or predisposing the AAA to rupture. One possible reason for this variability in clinical outcomes is the formation of a layer called intraluminal thrombus (ILT). Diverse findings from the literature regarding the role of ILT in AAA progression are discussed in a review paper by Wilson et al. (Wilson et al., 2013).

Rupture of AAA is facilitated by the structural degradation of the arterial wall until the mechanical stress acting on the wall exceeds the strength of the wall tissue. It generally occurs in conjunction with the formation of the ILT in the lumen of the AAA bulge. ILT prevalence at rupture is estimated to occur in over 75% of clinically studied AAAs, though the precise role in facilitating rupture remains unclear. However, it is known that ILT presence influences the localized transluminal oxygen diffusion. It has furthermore been suggested that the geometric factors of the ILT may influence its role in AAA rupture (Riveros, 2013). Radially thicker ILT, for example, particularly inhibits oxygen diffusion through the aneurysmal wall, which leads to greater local oxygen loss, also known as hypoxia, more so than with radially thinner ILT. This resulting localized oxygen deprivation is thought to lead to degradation of the arterial wall, causing sufficient conditions for AAA rupture.

In order to maintain the health of the arterial wall, sufficient transluminal oxygen transport is essential. However, there is insufficient evidence produced to date from which definitive conclusions can be drawn towards the precise role of particularly thrombus-mediated limitations to mass transport in AAAs, though several studies have demonstrated the phenomenon of "Hypoxia-Mediated Wall Weakening" and have asserted that the morphology of ILTs can play a key role to directly influence collagen and elastin production, induce hypoxia in the arterial wall, and decrease wall strength (Vorp et al., 1998; Vorp et al., 2001). These investigations outline the potential importance of hypoxia in upsetting the local balance of protein degradation and synthesis in the AAA wall (see a comprehensive review in (Vorp and Geest, 2005)). The observed local hypoxic environment in AAA may therefore lead to a decrease in the overall structural integrity of the wall and its eventual rupture. In particular, Vorp et al. examined the hypothesis that ILT in AAA is associated with local hypoxia of the AAA wall (Vorp et al., 2001).

While hypoxia can detrimentally impact the structure and content of the wall, the mechanical stresses within the wall ultimately mediate its rupture. Most previous studies have analyzed the effect of ILT presence on transmural wall stress in AAA models (Mower et al., 1997; Wang et al., 2002; Di Martino and Vorp, 2003; Li et al., 2008; Bluestein et al., 2009; Haller et al., 2018), where qualitative information is obtained on how ILT influence aneurysm wall stress. Though the presence of ILT can inhibit physiologically healthy transluminal oxygen transport in AAA, these studies have found that from a mechanical vantage, ILT can act as structural enhancement; thus, reducing the risk of aneurysm rupture by bearing some of the arterial mechanical load. In this manner, a few studies investigated the role of geometric factors in rupture assessment of AAA. However, previous studies on the effect of AAA geometrical features have been only focused on statistical association between geometrical asymmetry, wall stress, and rupture; without considering either the ILT region or the oxygen transport within the AAA (Li and Kleinstreuer, 2007; Bhagavan et al., 2018). Yet, there has not been any research to the authors' awareness on the thrombus-mediated limitations to mass transport in AAAs; particularly towards the gross geometric ILT features which, in addition to regulating mass transport, can later provide information towards AAA structural stability. Including the ILT as a geometric feature and investigating the relation between its morphology and oxygen flow to the aneurysmal wall is the main purpose of our study.

In some previously reported experimental and computational investigations, the effect of blood flow on convective mass transfer of oxygen molecules had been neglected and only the ILT and wall regions had been considered (i.e., (Vorp et al., 1998; Polzer et al., 2012)). In particular, in (Vorp et al., 1998) a uniform oxygen concentration was assumed on the luminal surface to model the oxygen supply from the blood. However, given the advective-diffusive nature of fluid flow in luminal oxygen transport, including the hemodynamic features may provide additional insight, as previously, it has been shown that hemodynamics plays a key role in the development of ILT (Virag et al., 2015), and the blood flow field affects the oxygen transport to the arterial wall particularly in the regions of disturbed flow and reattachment. Therefore, the coupling between blood-side oxygen mass transport to the transport in the wall is necessary to accurately model local oxygen concentrations within the AAA. In (Sun et al., 2009), this coupling between hemodynamics and mass transport for a patient-specific model of AAA is considered. However, using patient-specific models without having knowledge about the variations from patient-to patient in flow rate and physical properties, prohibits a thorough sensitivity analysis of the model's parameters.

Our previous studies in (Zakerzadeh et al., 2021) and (Zakerzadeh et al., 2020) have thoroughly explored the effect of varying ILT biomechanical parameters such as permeability and oxygen diffusivity in an idealized AAA model. We extended the work by Vorp et al. (Vorp et al., 1998) in a parametric study and implemented a computational framework of coupled blood flow and oxygen transport for the purpose of assessing the effects

of different geometrical and physical features including vasa vasorum flow (in the form of varying abluminal oxygen concentration boundary condition), kinematic diffusivities within the AAA tissue, and oxygen consumption in the arterial wall. Moreover, we also analyzed the effect of AAA geometry using four similar AAA models as in (Vorp et al., 1998) and observed that geometry seems to have substantial influence on mass transport, and in particular, that ILT geometry can play a notable or negligible role on oxygen transport depending on its geometry (Zakerzadeh et al., 2021). However, only four different geometries were used which is not enough to make a conclusion.

In the current work, we augment this via parametric modeling of both luminal and ILT geometries with the purpose of systematically investigating the role of changing ILT length and thickness in idealized AAAs, which are themselves parametrically varied. Additionally, in previous studies, the correlation between oxygen diffusion and ILT geometry is not examined in detail as it is in this manuscript. This study is the first attempt to explore the association of different morphological features of ILT with the oxygen delivery to the AAA and the possible wall oxygen deprivation, in a systematic and comprehensive manner.

With the use of physiologically realistic biomechanical simulations of coupled computational fluid flow and mass transport in AAA, we simulate aortic wall oxygen transport and investigate the extent to which ILT attenuates oxygen concentration in the arterial wall. A three-dimensional computational model of AAA containing ILT is constructed which is similar to the previous research by authors presented in (Zakerzadeh et al., 2021). The parametric space is composed of twenty-seven AAA models. Geometrical parameters include AAA bulge diameter, which is related to ILT curvature, ILT thickness, and ILT length. The modeling framework accounts for fluid dynamics in the lumen and oxygen transport in the lumen, thrombus, and arterial wall. Blood flow in the lumen is modeled using Navier-Stokes equations and then coupled with advection-diffusion-reaction equations that model the transport of biomolecules in AAA and their interaction with the arterial wall living tissue. This coupled blood flow-oxygen transport model is utilized in order to analyze the influence that ILT size has on oxygen concentration attenuation in the arterial wall. Computational results on velocity fields inside the lumen and oxygen concentrations inside the ILT and wall are obtained. Twenty-seven different geometries are simulated, and concentration measures at various locations within the tissue and along the boundaries are presented and compared.

The manuscript is organized as follows. In *Materials and Methods*, we describe the tools that we use to perform AAA simulations: *Geometry Variations and Parametric Space* introduces the geometrical space, provides the geometrical representation of models that we use for each simulation, and explains how the twenty-seven cases are created. *Governing Equations and Formulation* and *Boundary Conditions and Physical Parameters* cover the governing equations for the representation of the blood flow and oxygen transport within AAA and provide the mathematical model parameters and boundary conditions. In *Solver details*, we summarize the numerical simulation techniques. In *Results*, we explore the numerical results and compare them for simulated AAA cases. Finally, the discussion of the results, conclusions and future directions are presented in *Discussion*.

MATERIALS AND METHODS

In this section, we summarize the steps to achieve a realistic simulation of the fluid flow and oxygen transport within AAA. We have constructed three-dimensional CAD models of an axisymmetric AAA containing an ILT. The maximum diameter of the AAA occurs at halfway along the vessel length and is called the bulge diameter (*BD*). A schematic of the axial and transverse cross-sections of the model is presented in **Figure 1** and **Table 1** contains the geometric parameters used to create the model and summarizes the ranges of ILT thickness and ILT length examined in our study.

Geometry Variations and Parametric Space

The parametric study space consists of twenty-seven idealized geometries. Each AAA case has three bodies: the wall, the blood, and the ILT. AAA models were designed in the commercially available Fusion 360 CAD software, and preprocessed and meshed using the ANSYS SpaceClaim, a geometry component in ANSYS Workbench (version 20.2, ANSYS Inc., Canonsburg, PA, USA). For each bulge diameter (*BD*) used, the wall was sketched and saved as a framework. Using this framework, each ILT was sketched to desired length (l) and thickness (δ). The wall and ILT sketches were then revolved around the central axis to become independent 3-D bodies. Finally, the blood body was created by filling the extra area within the vessel. This process was repeated for each of the twenty-seven AAA models. A visualization of these modeling parameters and geometric measurements can be observed in **Figure 2**. The AAA and ILT dimensions are agreeable with patient-specific morphological data (Hans et al., 2005) and are listed in **Table 1**. For each case, the AAA domain is defined as 24 cm long, with arterial wall thickness held constant at 0.1 cm. The blood vessel is defined with a radius of $R = 1$ cm at the inlet and outlet of each case, with larger bulge protrusions within the middle of the arterial domain as specified in **Figure 1**.

Bulge diameters of 4.2, 5, and 7 cm are assumed for each set of simulations, These *BD* values are in the range of baseline diameters for demographic data of patients' aneurysm size to simulate small, medium, and large aneurysm (see (Wolf et al., 1994; Cnotliwy, 2010; Zhu et al., 2020)). Bulge diameter is kept constant for each aneurysm size, and the ILT thickness and ILT length are varied to create three groups of nine AAA cases (**Figure 2**). ILT thickness and length vary with ranges of $\delta = 0.4, 0.8, 1$ cm and $l = 4, 6, 8$ cm, respectively. Thus, the analysis accounts for the combination of "short/medium/long" and "thin/medium/thick" ILTs in small, medium, and large aneurysms. The thickness of the ILT region is chosen according to relevant clinical data (Cnotliwy, 2010; Xenos et al., 2015), and the range for the ILT length is calculated

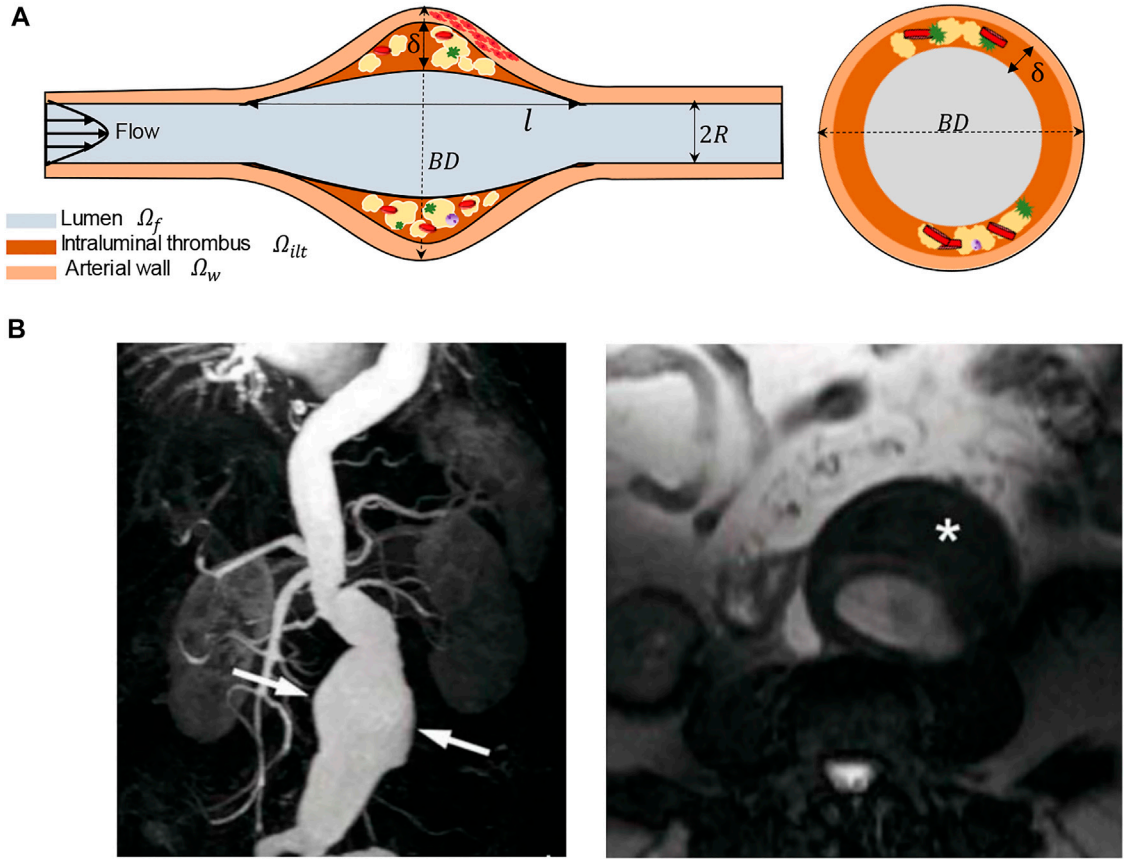

FIGURE 1 | (A) Schematic of the idealized, three-dimensional axially symmetric model of an AAA, where *BD* represents the bulge diameter, *l* denotes ILT length, and δ is the ILT thickness. **(B)** Left: coronal plane view of a magnetic resonance angiography (MRA) of a clinical infrarenal AAA. Extensive dilatation (arrows) and renal arteries on both sides can be observed. The renal arteries in MRA image are not included in the computational model. Right: the image demonstrates aneurysm formation and thrombus-covered region (asterisk). MRA images are taken from (Douek, 2005).

TABLE 1 | Geometric modelling parameters and their values in idealized lesions.

Geometric parameter	Value	Geometric parameter	Value
R (cm)	1 Hirsch, (2006)	Short ILT length (cm)	4
Length (cm)	24 Scotti et al. (2005)	Medium ILT length (cm)	6 Wolf et al. (1994)
Wall thickness (cm)	0.1	Long ILT length (cm)	8
Small-sized AAA bulge diameter (cm)	4.2 Bhagavan et al. (2018)	Thin ILT thickness (cm)	0.4 Vorp et al. (2001)
Moderate-sized AAA bulge diameter (cm)	5 Zhu et al. (2020)	Medium ILT thickness (cm)	0.8 Wang et al. (2001)
Large-sized AAA bulge diameter (cm)	7 Vorp et al. (1998); Cnotliwy, (2010)	Thick ILT thickness (cm)	1 Zhu et al. (2020)

from patient ILT volume and ILT thickness demographics measurements (Ghulam et al., 2018). An illustration of the parameter space and AAA geometries spanning the full ranges of the three explicit parameters *BD*, δ and *l* are shown in **Figure 2**. The 3-D parameter space is divided into three 2-D plots that partition cases by *BD* values (black corresponds to *BD* = 7 cm, red represents *BD* = 5.2 cm, and white signifies *BD* = 4.2 cm). In each plotted image, AAA lumen is colored white, and ILT domain is depicted in blue. Variations in ILT length (in cm) are plotted against ILT thickness (in cm) in each plot.

Governing Equations and Formulation

Our mathematical model consists of three domains: luminal blood, the ILT, and the arterial wall. Since the aorta is a large artery, blood flow in the lumen is assumed to behave as a Newtonian viscous fluid. Hence, the steady, incompressible, laminar blood flow inside the artery channel is described by the Navier–Stokes equations:

$$\rho_f\left(\boldsymbol{U}_f.\nabla\boldsymbol{U}_f\right) = \nabla.\boldsymbol{\sigma}_f \quad in\,\Omega_f \tag{1}$$

$$\nabla.\boldsymbol{U}_f = 0 \quad in\,\Omega_f \tag{2}$$

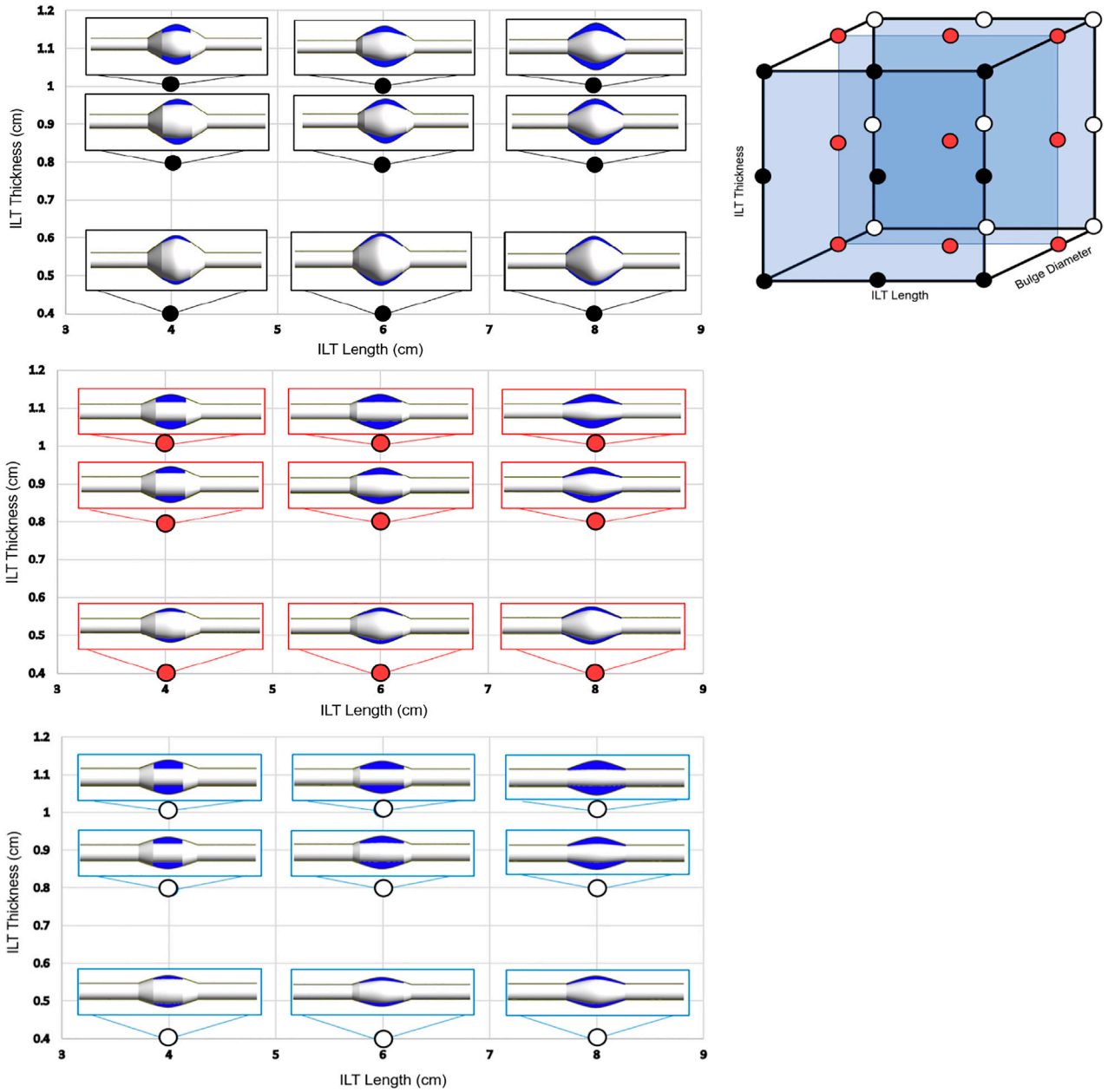

FIGURE 2 | The 3-dimensional visualization of the parametric space is shown (top-right), where each point represents one of the twenty-seven AAA geometries used in this study. Each case is characterized by a variation in ILT length, bulge diameter, and ILT thickness identified on one of the three axes, respectively. The cases are divided into three groups of nine AAA models based on bulge diameter, denoted by black (*BD* = 7 cm), red (*BD* = 5.2 cm), and white (*BD* = 4.2 cm) points on the 3D parametric space cube. The three 2D plots (left) illustrate the anatomic variations on three planes of constant *BD*, and each plane shows combined variations in thickness and length of the ILT lesion. Individual cases were designed to have ILT length of 4 cm, 6 cm, or 8 cm, and an ILT thickness of 0.4, 0.8, or 1 cm. These cases will serve as the basis of comparison for differences oxygen concentration among the simulations.

Here $\boldsymbol{U}_f$ and ρ_f stand for fluid velocity vector field in the lumen and blood density, respectively, and $\boldsymbol{\sigma_f} = -p_f\boldsymbol{I} + 2\mu_f\boldsymbol{D}(\boldsymbol{U}_f)$ is the fluid Cauchy stress tensor where p_f is fluid pressure, μ_f denotes blood dynamic viscosity, and the symmetric part of the fluid velocity gradient is defined as $\boldsymbol{D}(\boldsymbol{U}_f) = \frac{1}{2}(\nabla\boldsymbol{U}_f + \nabla\boldsymbol{U}_f^T)$. It should be noted that the subscripts f, w and ilt indicate the blood flow in the lumen, AAA wall and ILT medium respectively.

Oxygen transfer in the lumen is coupled with the blood flow and governed by the convection–diffusion equation as follows:

$$\nabla \cdot \left(-D_f \nabla C_f + \boldsymbol{U}_f C_f \right) = 0 \quad in\, \Omega_f \tag{3}$$

The symbol C_f denotes the oxygen concentration in the lumen and D_f is the diffusion coefficient for oxygen in blood.

The effect of oxygen binding to hemoglobin within the AAA lumen is neglected, as our focus is confined to the relative differences in oxygen transport across the arterial wall.

Oxygen transport in the AAA wall is modeled by the diffusion-reaction equation and therefore we have:

$$\nabla \cdot (-D_w \nabla C_w) = rC_w \ in \ \Omega_w \tag{4}$$

where C_w is the oxygen concentration in the AAA wall, D_w is the oxygen diffusivity through the AAA wall, and rC_w is the reaction term which accounts for the metabolite consumption of oxygen in cell metabolism. In particular, we introduce the consumption rate S, when the consumption of oxygen is assumed to be linearly proportional to the cell availability, namely $S = rC_w$, and r is defined as the oxygen reaction rate constant (Iannetti et al., 2016).

The ILT is assumed permeable to the transport of oxygen molecules through diffusion via the canaliculi network, without any smooth muscle cells to consume oxygen. Therefore, no reaction term is considered in the thrombus and the oxygen transfer in the ILT can be modeled by the diffusion equation, given by:

$$\nabla \cdot (-D_{ilt} \nabla C_{ilt}) = 0 \ in \ \Omega_{ilt} \tag{5}$$

where C_{ilt} is oxygen concentration in the ILT, and D_{ilt} is the oxygen diffusivity through the ILT.

It should be noted that although ILT has a porous structure arising from its highly porous canalicular network (Adolph et al., 1997), neglecting the contribution of convective oxygen transport due to interstitial fluid flow (i.e. the movement of the fluid through the extracellular matrix of the tissue) has been justified in (Polzer and Bursa, 2010; Polzer et al., 2011) where the stress fields in the aneurysmal wall changed negligibly when a poroelastic model for ILT was used. Similar conclusions were obtained in (Ayyalasomayajula et al., 2010) where simulations were performed in order to compare poroelastic and impermeable ILT models, and the ILT permeability was found to have minimal effect on interstitial velocities that have been associated with driving oxygen transport in the ILT and arterial wall. We previously explored the effect of porous ILT on oxygen transport and our findings suggest that the effect of porosity of ILT on oxygen transport within AAA is small for the reported physiological range of ILT permeability (Zakerzadeh et al., 2020).

In the next section, we summarize the parameters and boundary conditions.

Boundary Conditions and Physical Parameters

In this section, we summarize the main parameters and boundary conditions of the flow and mass transport model. At the inlet of the artery, we considered a fully developed and unidirectional velocity profile. The flowrate is chosen to match physiological Reynolds numbers and represents the flow in the abdominal aorta under the resting condition (Fraser et al., 2008). Therefore, the following parabolic velocity profile for the laminar flow taken from (Caputo et al., 2013) is specified at the inlet:

$$\boldsymbol{U}_f^{in}(r) = 2U_{med}\left(1 - \left(\frac{r}{R}\right)^2\right)\boldsymbol{n} \ on \ \Gamma_f^{in} \tag{6}$$

where $\boldsymbol{n}$ denotes the inward normal unit vector at the inlet surface, R is the radius of the vessel, and we define $r = \sqrt{y^2 + z^2}$ at the inlet. The correspondent mean velocity is obtained as U_{med} = 0.235 m/s from the measurements of the flowrate reported by (Fraser et al., 2008). The fluid is assumed to have density of ρ_f =1,050 kg/m^3 and viscosity of μ_f = 0.0035 kg/m.s, representing human blood properties. The Reynolds number of 1,100 is obtained based on the inlet lumen diameter and the inlet flow condition, which is within the realistic range for Reynolds numbers in abdominal aorta at rest (Ku, 1997). The blood oxygen partial pressure is considered a uniform 100 mmHg (Applegate et al., 2016), corresponding to the oxygen saturation of 97.7% (Severinghaus, 1979). Therefore, the oxygen concentration of C_f^{in} =5.12 × 10^{-3} kg/m^3 at the lumen inlet Γ_f^{in} is obtained by using the inlet partial pressure and molar mass of oxygen. At the lumen outlet Γ_f^{out}, the reference pressure value was prescribed, which can be arbitrarily set for incompressible flow. On the exterior of the arterial wall, the influence of the vasa vasorum is modelled by imposing the partial pressure of oxygen. Experimental studies showed that the level of adventitial oxygen tension is about one half of the oxygen tension in blood (Buerk and Goldstick, 1982; Buerk and Goldstick, 1986); therefore the abluminal wall partial pressure was fixed at 50 mmHg to model the oxygen transported by the vasa vasorum (Kemmerling and Peattie, 2018). At the cross-sectional areas of the wall representing the ends of the vascular domain a zero-flux condition on the surface normal direction is prescribed. It should be noted that an adventitial oxygen concentration of 50 mmHg, that has been used for the baseline case and previous computational models of AAA (Sun et al., 2009), corresponds to a healthy infrarenal aorta (Buerk and Goldstick, 1986). However, in the case of AAA it is expected that this value decreases significantly, since the vasa vasorum has been observed to be stenotic in both small and large AAA with the tissue being ischemic and hypoxic (Tanaka, 2015).

Conservative, interface oxygen flux conditions are employed at the ILT-wall (Γ_{ilt-w}) and ILT-lumen (Γ_{f-ilt}) interfaces, and a continuity condition was assumed between the boundaries. Moreover, the no-slip condition is defined at the interface between the lumen and wall (Γ_{f-w}), and the lumen and ILT. Therefore, the model is complemented by the following concentration interface conditions:

$$C_f = C_w \ on \ \Gamma_{f-w} \quad C_f = C_{ilt} \ on \ \Gamma_{f-ilt} \quad C_{ilt} = C_w \ on \ \Gamma_{ilt-w} \tag{7}$$

The transport equation in the fluid model describes oxygen transport with a kinematic diffusivity of D_f =1.6 × 10^{-9} m^2/s (Rappitsch and Perktold, 1996). The values for AAA wall and ILT diffusivity are taken from previous studies, where D_{ilt} =1.34 × 10^{-9} m^2/s and D_w =1.08 × 10^{-9} m^2/s are the diffusivities of oxygen through the ILT and wall respectively. The oxygen reaction rate is assumed to be r =8.4 × 10^{-3} s^{-1} under the assumption that the volume flux of oxygen is completely consumed by the smooth muscle cells. A summary of all model parameters is provided in **Table 2**.

TABLE 2 | Physical parameters and material properties for AAA model domains.

Simulation parameter	Blood	Aneurysmal wall	ILT
Thermodynamic state	Incompressible fluid	Impermeable solid	Impermeable solid
Oxygen diffusivity (m^2/s)	1.6×10^{-9} Rappitsch and Perktold, (1996)	1.08×10^{-9} Moore and Ethier, (1997)	1.34×10^{-9} Sun et al. (2009)
Density (kg/m^3)	1,060	1,000	1,000
Dynamic viscosity (kg/m.s)	0.0035		
Reaction rate (s^{-1})		8.4×10^{-3} Caputo et al. (2013)	
Reynolds number	1,100 Ku, (1997)		
Inlet oxygen concentration (kg/m^3)	5.12×10^{-3} Vorp et al. (1998)		
Vasa vasorum oxygen concentration (kg/m^3)	2.06×10^{-3} Kemmerling and Peattie, (2018)		

Solver Details

Twenty-seven fully coupled hemodynamic and oxygen transport simulations by obtaining the solutions of the Navier-Stokes equations plus diffusion-reaction equations were performed. The model was implemented in commercial code ANSYS CFX Workbench software (version 20.2, ANSYS Inc., Canonsburg, PA, USA) to carry out the fluid dynamic and mass transport simulations. Numerical simulations were performed to simulate blood flow coupled with the oxygen transport in the bloodstream and oxygen diffusion in the wall and ILT regions. The spatial discretization consists of a cell based finite volume method. A fully coupled strategy has been adopted, namely all the equations are solved simultaneously through a monolithic linear system that embraces all the degrees of freedom. The Laplace operator in the fluid momentum and oxygen transport equations is approximated by a centered scheme, while the convective terms have been discretized by means of an upwind method. The convective term in the Navier-Stokes equations is linearized by the Picard iterations ("ANSYS CFX-Solver Theory Guide", ANSYS Inc., 2010). The pressure variable in the Navier-Stokes equations is evaluated at the same nodes of the velocity field. The system is then solved using an algebraic multigrid method exploiting incomplete LU factorization as smoother. Convergence criteria were set to 10^{-5} for the normalized residuals of the global linear system of equations. Numerical simulations have been performed on parallel CPUs using a 5-Core Intel CPU, 32 GB RAM at Duquesne University. The problem was solved using the MPI parallel solver. Each simulation computes the steady-state solution using four processor cores. To obtain a reasonable resolution of the solution based on the assumed value of the Reynolds number of 1,100, we used about 1.5 million tetrahedral elements to discretize the domain representing AAA. The mesh resolutions are identical to those reported in Zakerzadeh et al. (2021). The cited study also documents a systematic mesh convergence testing which is similar to that used in the computations of the current model.

RESULTS

In this section, we investigate the dependence of oxygen distribution within a AAA domain on the variation of the ILT and AAA geometrical features including ILT thickness, ILT length and AAA bulge diameter that is directly linked to the ILT curvature. In particular, our computational solver provides a spatial prediction of oxygen concentration in the ILT and arterial tissue, as well as hemodynamic measures inside the lumen. Twenty-seven different geometries created in *Geometry variations and parametric space* are used, and the oxygen concentration profiles at different locations are presented and compared. These geometries are referred to by case (l, δ) for each *BD* values, where l is ILT length and δ is ILT thickness.

We first present the results of a baseline simulation to investigate hemodynamics and mass transport results. In the top panel of **Figure 3**, visualization of blood streamlines colored by the velocity magnitude, on the plane that cuts the AAA in half is provided. The pattern of streamlines in the blood indicates the distribution of the flow within the lumen. It is seen that blood flow in the AAA decelerates due to the enlarged diameter of the vessel and the streamlines show recirculation zones characterized by helical flow pattern in the bulge of the lumen. Additionally, the oxygen concentration distribution contour inside the whole domain that contains lumen, ILT, and wall, is shown in the middle panel of **Figure 3**. The lumen appears red, indicative of oxygen-rich blood. Moving toward the exterior of the artery, this high oxygen concentration inside the lumen that is spatially uniform, diminishes rapidly with distance inside the ILT and arterial wall. Therefore, the highest oxygen concentration is found in the lumen and the lowest is in the wall as expected. We observe more reduced oxygenation of the aortic wall in the presence of ILT which is in the middle of the lumen. This oxygen deprivation is most noticeable at the maximum diameter of the AAA, *BD*, that occurs at halfway along the length of the lumen and has the highest thickness of ILT (see **Figure 1** for a schematic illustration of the model). The oxygen concentration is higher at the straight portion of the vessel that thrombus does not exist. This observation is in line with previous conclusions in (Vorp et al., 2001). Furthermore, the bottom panel of **Figure 3** illustrates contour of oxygen concentrations on the luminal surface, defined as the interface between the lumen and ILT and between the lumen and the wall. This oxygen contour clearly shows that the concentration is not uniform at the blood-tissue interface and changes between $5.12 \times 10^{-3}\,kg/m^3$ to $4.43 \times 10^{-3}\,kg/m^3$. The observation highlights the influence of hemodynamics to compute a more realistic oxygen concentration on the luminal surface and use that to solve the oxygen diffusion within the ILT and wall tissue.

To quantify the sensitivity of oxygen flow measures to the chosen space of geometric values provided in **Table 1** and **Figure 2**, various plots are prepared and arranged that illustrate the results on different points, lines, and surfaces,

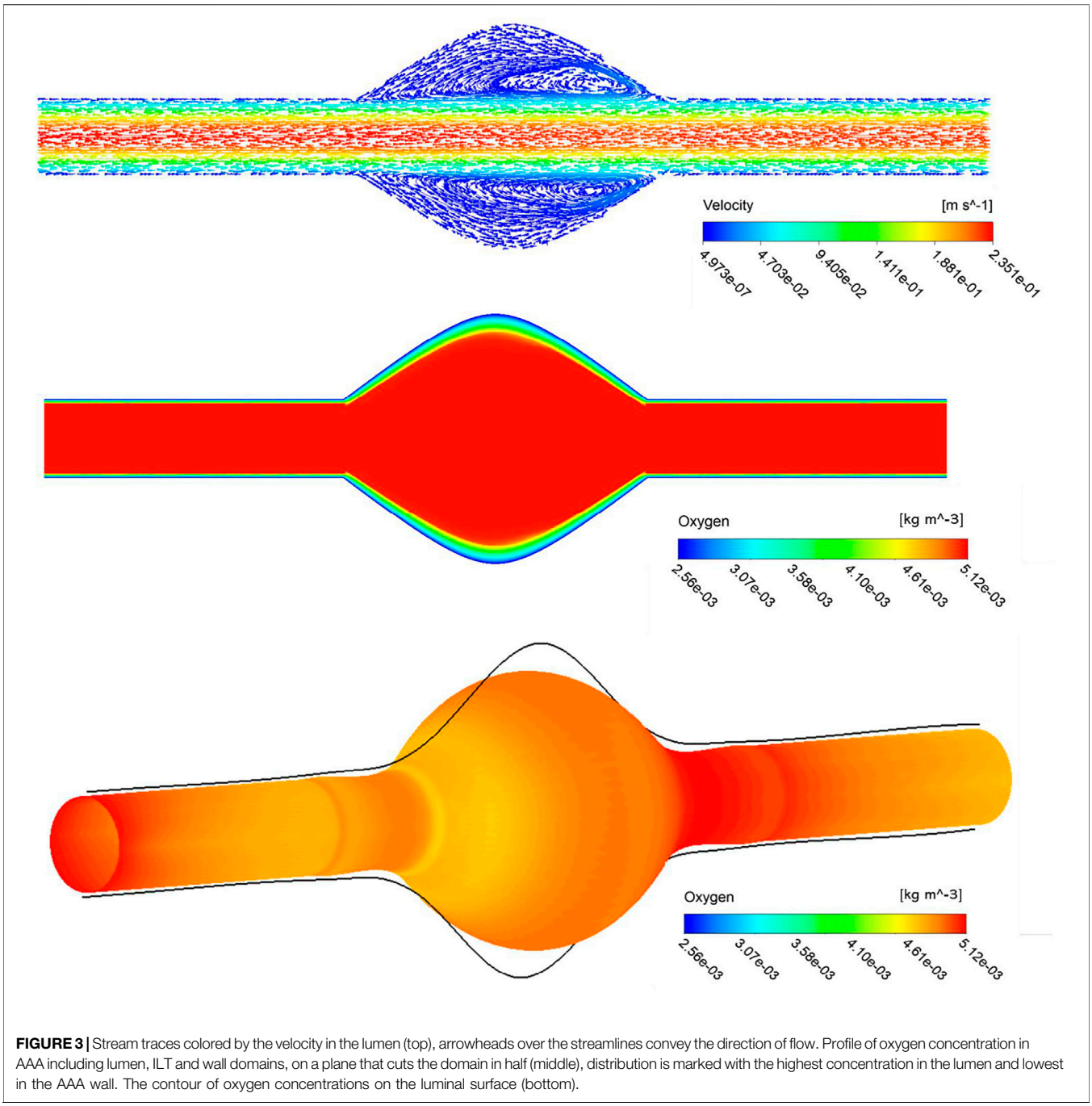

FIGURE 3 | Stream traces colored by the velocity in the lumen (top), arrowheads over the streamlines convey the direction of flow. Profile of oxygen concentration in AAA including lumen, ILT and wall domains, on a plane that cuts the domain in half (middle), distribution is marked with the highest concentration in the lumen and lowest in the AAA wall. The contour of oxygen concentrations on the luminal surface (bottom).

such as within the ILT tissue, on the abluminal ILT layer, and on the outermost layer of the arterial wall that is referred to as tunica adventitia.

The lines plots in **Figures 4–6** depict oxygen concentration fluctuation from lumen to outer wall surface as well as the change in oxygen distribution on inner wall surface on the boundary between ILT and wall. Oxygen concentration data for individual cases in each plot is differentiated by color (blue, red, or black color) for the ILT length and line type (solid, dashed, dotted) for ILT thickness, respectively. In the left panel of **Figure 4**, the concentrations for different case (l, δ) with BD= 4.2 cm and varying ILT length (l) and ILT thickness (δ) are shown along a vertical line that starts at the center of the domain. The path line is identified by blue color at the schematic representation in the top of the aforementioned figure. We observe that the concentration is constant for all nine cases in the lumen and it starts to decrease exponentially once we reach the ILT interface. For all the cases, the concentration eventually reaches the value estimated by vasa vasorum oxygen supply at the tunica adventitia. **Figure 4** (left panel), indicates

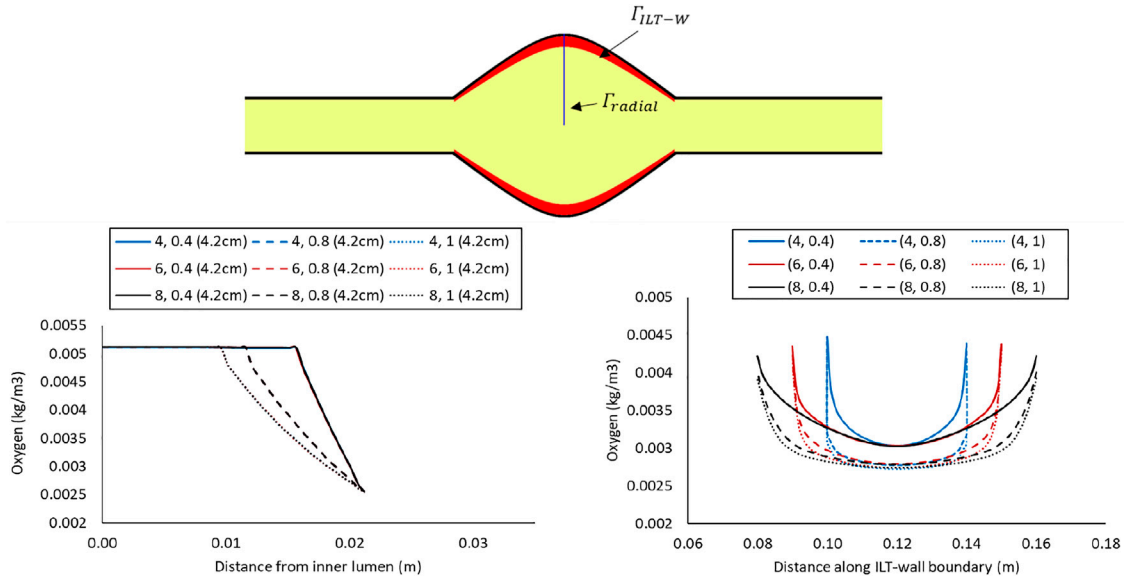

FIGURE 4 | Comparison of the oxygen concentration along a radial path line at halfway along the length of the lumen in the cases with *BD*= 4.2 cm and varying ILT length (*l*) and ILT thickness (δ) denoted by case (l, δ) (left), and comparison of the oxygen concentration along the axial length on the interior interface of the arterial wall in the same cases (right). In both plots, the blue, red, and black lines represent the short, medium, and long ILT cases information respectively; and solid, dashed, and dotted lines represent thin, moderate and thick ILT cases respectively. All nine cases are shown in **Figure 2**. At the top, these path lines are shown with blue line, Γ_{radial} for the left plot and Γ_{ILT-W} for the right plot. The Γ_{ILT-W} represents the interface between the ILT (red region) and wall domain (black region).

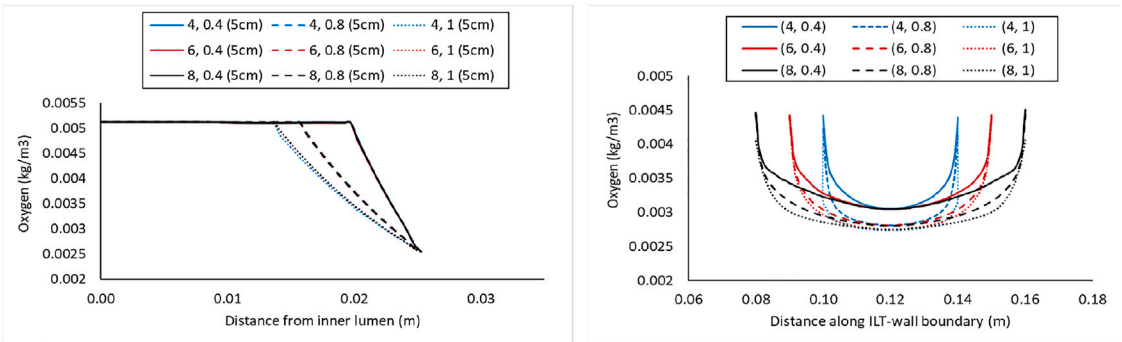

FIGURE 5 | Comparison of the oxygen concentration along a radial path line at halfway along the length of the lumen in the cases with *BD*= 5 cm and varying ILT length (*l*) and ILT thickness (δ) denoted by case (l, δ) (left), and comparison of the oxygen concentration along the axial length on the interior interface of the arterial wall in the same cases (right). In both plots, the blue, red, and black lines represent the short, medium, and long ILT cases information respectively; and solid, dashed, and dotted lines represent thin, moderate, and thick ILT cases respectively. Cases are presented in **Figure 2**. Path lines are demonstrated in **Figure 4**.

that oxygen concentration value along a radial line in the middle of AAA domain is largely affected by ILT thickness, although it is not affected by ILT length as expected. Furthermore, thinner ILTs resulted in a more sudden change in oxygen concentration from blood to the tunica adventitia that happens over a shorter length of depletion, while thicker ILTs cause a more gradual oxygen decrease that starts closer to the center of the lumen.

In the right panel of **Figure 4**, the oxygen concentration on the abluminal layer of ILT is shown for the same cases. This plot is obtained along the length of the AAA, measured on the inner wall surface that is identified by an arrow and the green line at the top of the plot. Wall oxygen concentration is captured in the middle portion of the geometry where the ILT is located. We are particularly interested in this area due to the presence of ILT. We observe that oxygen concentration on the inner interface of the aneurysmal wall has the lower values for the cases with thicker ILT tissue (**Figure 4**, right panel). The lowest concentration is captured at the ILT location where the artery has the maximum bulge. In particular, cases with the similar line pattern, which represents the same ILT thickness, result in the similar minimum value for oxygen concentration on inner wall surface. The oxygen diffusion decreases as ILT thickness increases for all cases. Therefore, the dotted and dashed lines (1 and 0.8 cm ILT thickness values, respectively) are associated with lower oxygen

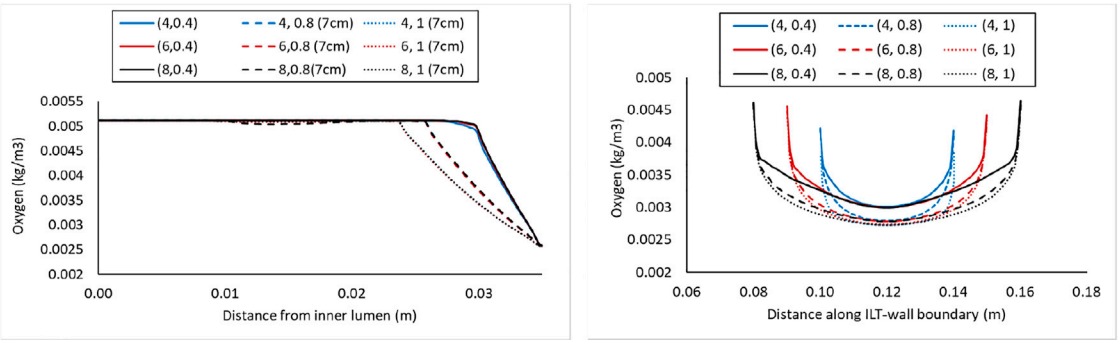

FIGURE 6 | Comparison of the oxygen concentration along a radial path line at halfway along the length of the lumen in the cases with *BD*= 7 cm and varying ILT length (*l*) and ILT thickness (δ) denoted by case (l, δ) (left), and comparison of the oxygen concentration along the axial length on the interior interface of the arterial wall in the same cases (right). In both plots, the blue, red, and black lines represent the short, medium, and long ILT cases information respectively; and solid, dashed, and dotted lines represent thin, moderate, and thick ILT cases respectively. Cases are presented in **Figure 2**. Path lines are demonstrated in **Figure 4**.

concentration compared to the solid lines (0.4 cm ILT thickness) for all the values of ILT length. Moreover, the results indicate that the longer the ILT is, the more even the oxygen distribution is along the ILT abluminal layer (i.e., ILT-wall interface). With shorter ILTs, the oxygen concentration fluctuates at a higher rate along the length of this region, while a more uniform concentration for longer ILT is observed.

Concentration values along the radial path line for all nine case (l, δ) with *BD*=5 cm is plotted in the left panel of **Figure 5**, and the oxygen concentrations on the inner wall surface along the length of the AAA are shown in the right panel of **Figure 5**. The path lines are the same as the one identified at the top of **Figure 4**. Finally, similar plots for nine cases (l, δ) with *BD*=7 cm are provided in **Figure 6**. As bulge diameter increased from **Figure 4** to **Figure 6**, we observe that oxygen reduction at the ILT domain appears at a further distance from the center of the lumen.

The simulation results for the variation of the ILT geometry and quantities of interest for each case are reported in **Figure 7** to **Figure 9**. The quantities include oxygen flux profile on the tunica adventitia layer, oxygen concentration profile within the ILT, as well as a two-level contour plot that is used as a measure to visualize the reduction in oxygen concentration inside the ILT tissue. More precisely, each grid of **Figure 7–9**, contains the simulations result for these quantities in *BD*= 4.2, 5, and 7 cm respectively. First, the contour of oxygen flux distribution on the aneurysmal wall for each case is shown, followed by the oxygen concentration contour within the cross section of the ILT tissue. Finally, the two-level concentration contour within ILT region is provided. The map has a "cutoff" value to signify low oxygen levels and is colored in red for areas that have an oxygen concentration above a particular value and blue in areas when the oxygen concentration falls below that value. Mainly, display of a two-bands color scale ranges from abluminal oxygen concentration of 2.56×10^{-3} kg/m^3 from vasa vasorum supply, defined by the blue color, to 75% of inlet oxygen concentration C_f^{in} identified by the red color. The "inflection point" is reached when the concentration values drop below 75% of the inlet concentration. This data acts as marker for the arterial wall oxygen depletion with respect to geometrical parameters.

From **Figures 7–9**, in general, the results show that increasing *l*, which corresponds to increasing the length of the ILT, causes a more uniform oxygen distribution on the outer surface of the arterial wall, while it does not affect the oxygen measurements and concentration patterns within the ILT in a sensitive manner. Decreasing *l*, which decreases the length of the ILT, slightly affects uniformity of the diffusion and reduces the concentration on the regions that are not covered by the shorter ILT significantly. We also observe that in contrast to *l*, increasing δ which correspond to increasing the thickness of the ILT has a profound effect on the oxygen distribution of the wall as well as concentration patterns within the ILT, decreases oxygen flux to the wall and depletes oxygen within the ILT at the same time. More precisely, the minimum oxygen concentration values along the inner wall interface corresponds with ILT location. Therefore, the flux on the outer surface of the arterial wall has the largest change at the ILT region. We can clearly see that thicker ILT causes a decrease in oxygen supply to the outer surface of ILT, and therefore arterial wall as well. This trend can be noticed in two-level concentration contour plots, where low oxygen regions (blue area) are larger than the red high oxygen regions. Thus, the thicker ILTs influence greater reduction of oxygen diffusion from blood flow to the inner AAA wall. These observations are in agreement with the results of **Figures 3–5**. The attenuation of oxygen flux due to increasing *l* and δ is particularly apparent for the case (8,1) in *BD*= 4.2 cm which has the longest and thickest ILT between all the cases. The oxygen supply from the lumen to the inner layer of the wall in this case is blocked by the thick ILT and the ILT-wall interface is almost depleted of oxygen (**Figure 7**). Similarly, **Figure 8** and **Figure 9** suggest that the thicker and longer ILTs inhibit the oxygen transport to the arterial wall, as oxygen concentration near the lateral bulges of the ILT is significantly lower than the medial portions of the ILT. Finally, increasing *BD*, which corresponds to the severity of the aneurysm and increases the surface curvature in the ILT region, does not seem to affect oxygen measurements significantly according to **Figures 7–9**, as all the contours for oxygen diffusion in AAA wall and ILT follow

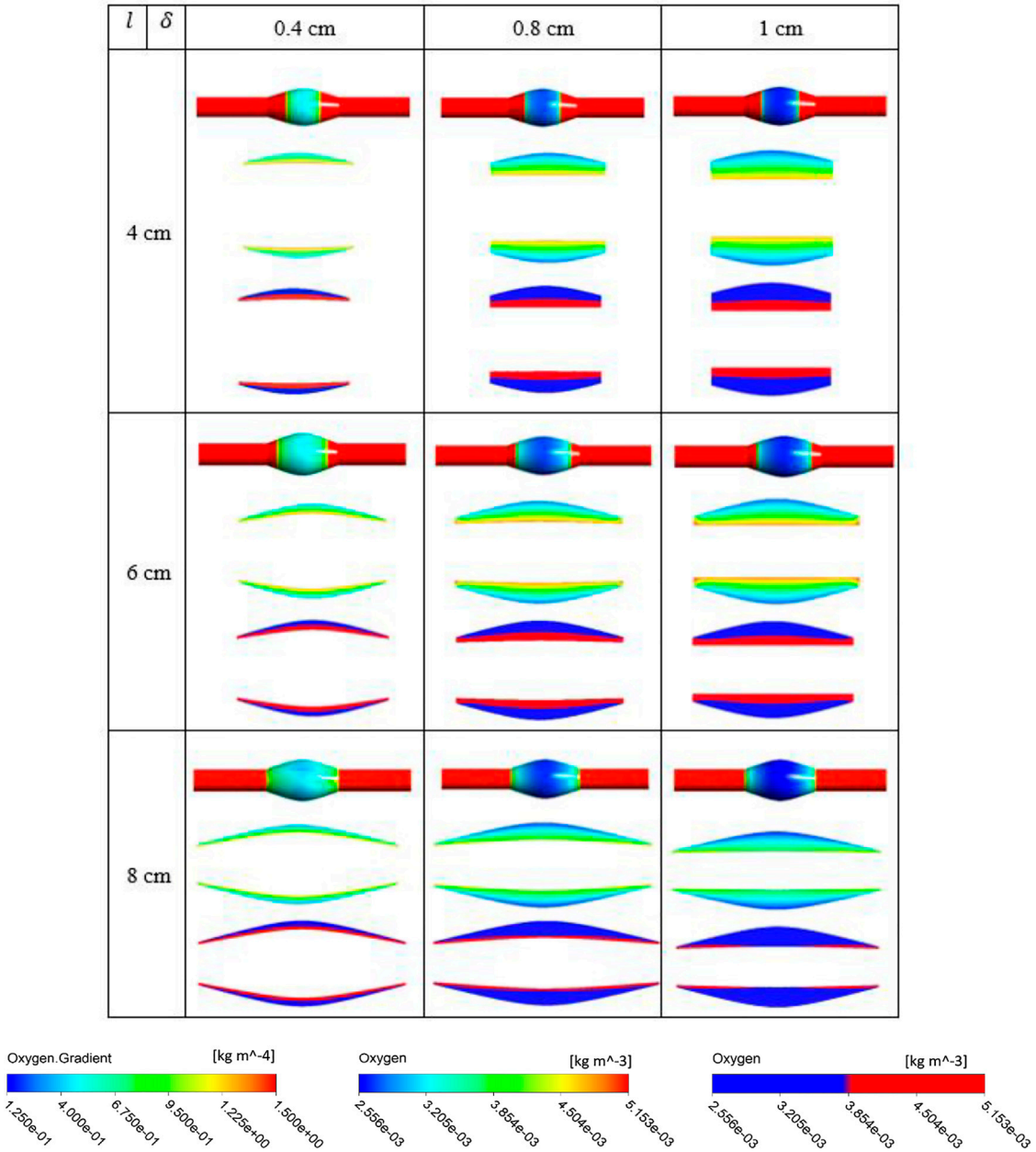

FIGURE 7 | Results of different combination of design variables ILT length (*l*) and ILT thickness (*δ*), with bulge diameter being fixed as *BD*= 4.2 cm. Each cell corresponds to the results for one case of the nine different AAA geometries provided in **Figure 2**. In each cell, three oxygen measures are plotted from top to bottom: contour of oxygen flux on the abluminal surface of the arterial wall for all analyzed cases on the same scale, contour plot of oxygen concentration in ILT on the same scale, and finally oxygen value using a two-bands color scale ranging from abluminal oxygen concentration 2.56×10^{-3} kg/m^3 (blue) to ≥75% C_f^{in} kg/m^3 (red). Scales on the bottom are used for displaying results.

relatively the same patterns for each case (l, δ) at different *BD* values.

Figure 10 analyzes the spatial distribution of the oxygen concentration on the inner AAA wall surface by collecting and comparing the concentration values at each of the three displayed points. Oxygen concentration data for varying *BD* cases are provided. Point X_1 is located on the inner wall interface before the bulge, at the straight portion of the vessel that thrombus does not exist. This point X_1 has the highest oxygen concentration value that is nearly equal to the blood flow concentration value C_f^{in}. In general, the values at X_1 are constant between all different case (l, δ), since no cases in this study have ILTs that cover this point. Points X_2 is taken at 9 cm form the AAA inlet, where will be covered by long ILT but not by the short and medium ILT. When the ILT does not cover this section of the vessel, the concentrations for X_2 remains almost

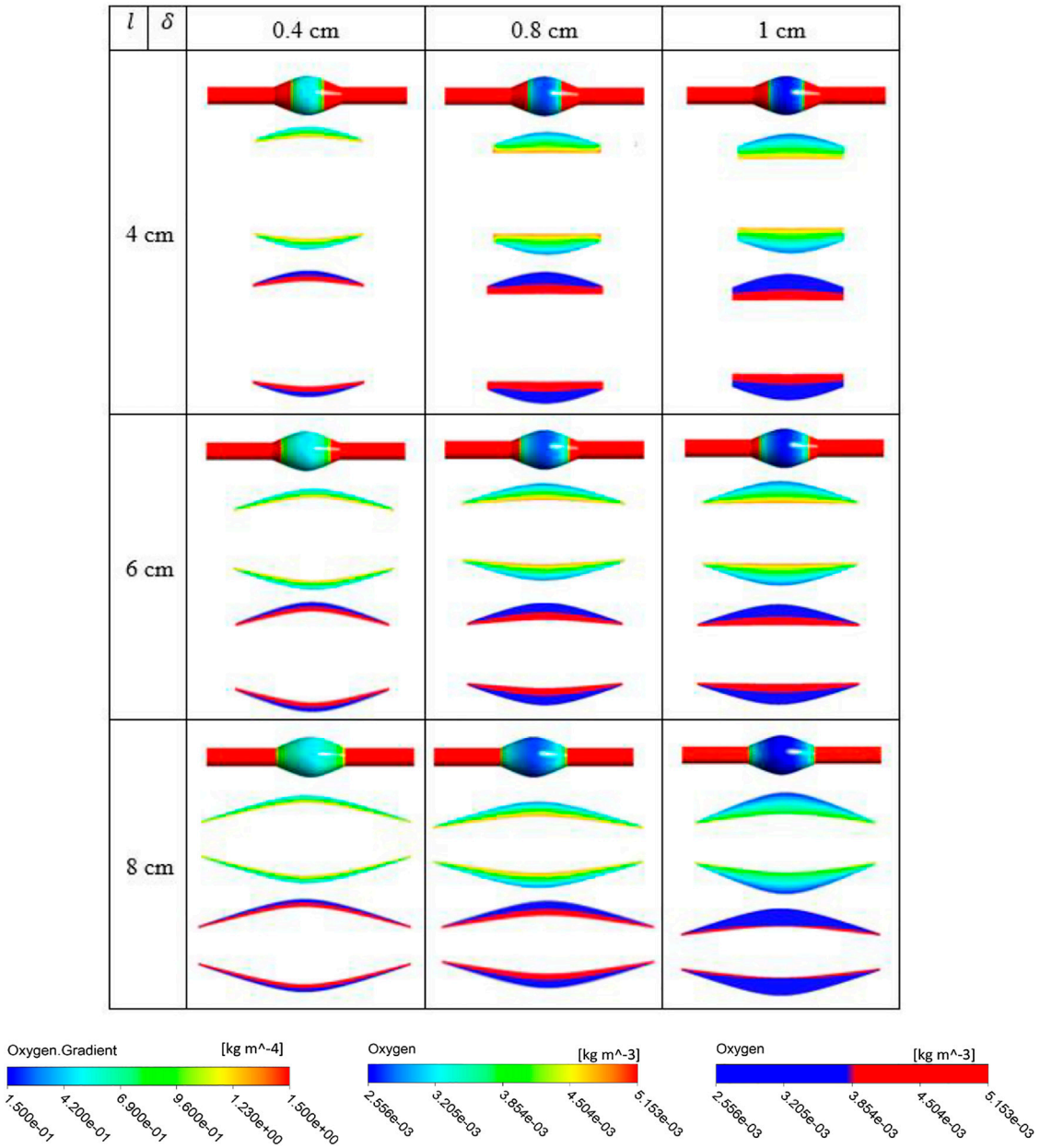

FIGURE 8 | Results of different combination of design variables ILT length (*l*) and ILT thickness (*δ*), with bulge diameter being fixed as *BD*= 5 cm. Each cell corresponds to the results for one case of the nine different AAA geometries provided in **Figure 2**. In each cell, three oxygen measures are plotted from top to bottom: contour of oxygen flux on the abluminal surface of the arterial wall for all analyzed cases on the same scale, contour plot of oxygen concentration in ILT on the same scale, and finally oxygen value using a two-bands color scale ranging from abluminal oxygen concentration 2.56×10^{-3} kg/m^3 (blue) to ≥75% C_f^{in} kg/m^3 (red). Scales on the bottom are used for displaying results.

similar to X_1, but is lower due to the bulging of the vessel. However, concentrations values significantly change when the ILT is long enough to cover that area of the vessel. Therefore, here is a significant drop in oxygen concentration at X_2 in the $l = 8$ cm ILT cases, while the cases with shorter ILTs of $l = 4$ cm and $l = 6$ cm do not cover X_2 location.

Moreover, point X_3 is located at the maximum diameter of the AAA, *BD*, which occurs at halfway along the length and has the highest thickness of ILT (see **Figure 1** for a schematic illustration of the model). As the ILT grows in thickness, the oxygen attenuation causes concentration values to decrease at this location. Similar to previous observations (**Figures 7–9**), **Figure 10** also asserts that the bulge diameter of AAA does not account for significant variation in arterial wall oxygen distribution, and therefore hypoxia. This is because the data follows the same rough pattern of oxygen concentration

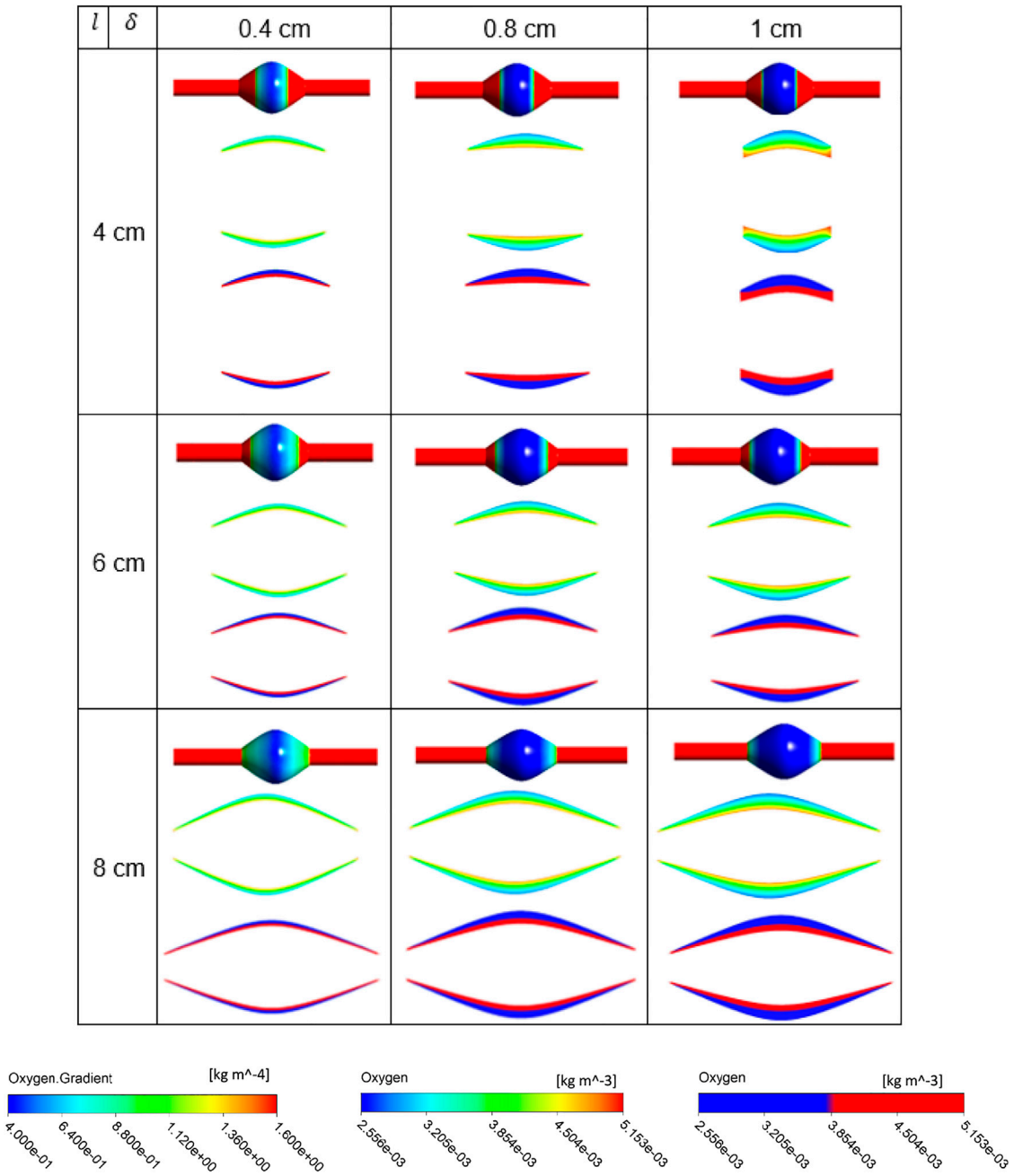

FIGURE 9 | Results of different combination of design variables ILT length (l) and ILT thickness (δ), with bulge diameter being fixed as BD= 7 cm. Each cell corresponds to the results for one case of the nine different AAA geometries provided in **Figure 2**. In each cell, three oxygen measures are plotted from top to bottom: contour of oxygen flux on the abluminal surface of the arterial wall for all analyzed cases on the same scale, contour plot of oxygen concentration in ILT on the same scale, and finally oxygen value using a two-bands color scale ranging from abluminal oxygen concentration 2.56×10^{-3} kg/m^3 (blue) to ≥75% C_f^{in} kg/m^3 (red). Scales on the bottom are used for displaying results.

among different ILT morphologies for varying bulge diameter values.

Using the numerical results presented in bar plots of **Figure 10**, we have studied the variation of oxygen concentration at the three selected points on the inner wall interface, when each geometric parameter, namely ILT length and thickness for a certain AAA bulge diameter, is varied individually. The outcome of the analysis is reported in **Figure 11**. For a better comparison of the different charts, concentration values are reported for the cases $(l, \delta = 0.4, 0.8, 1)$ in which ILT is long enough to cover point X_2. To better clarify the effects of ILT thickness, data points

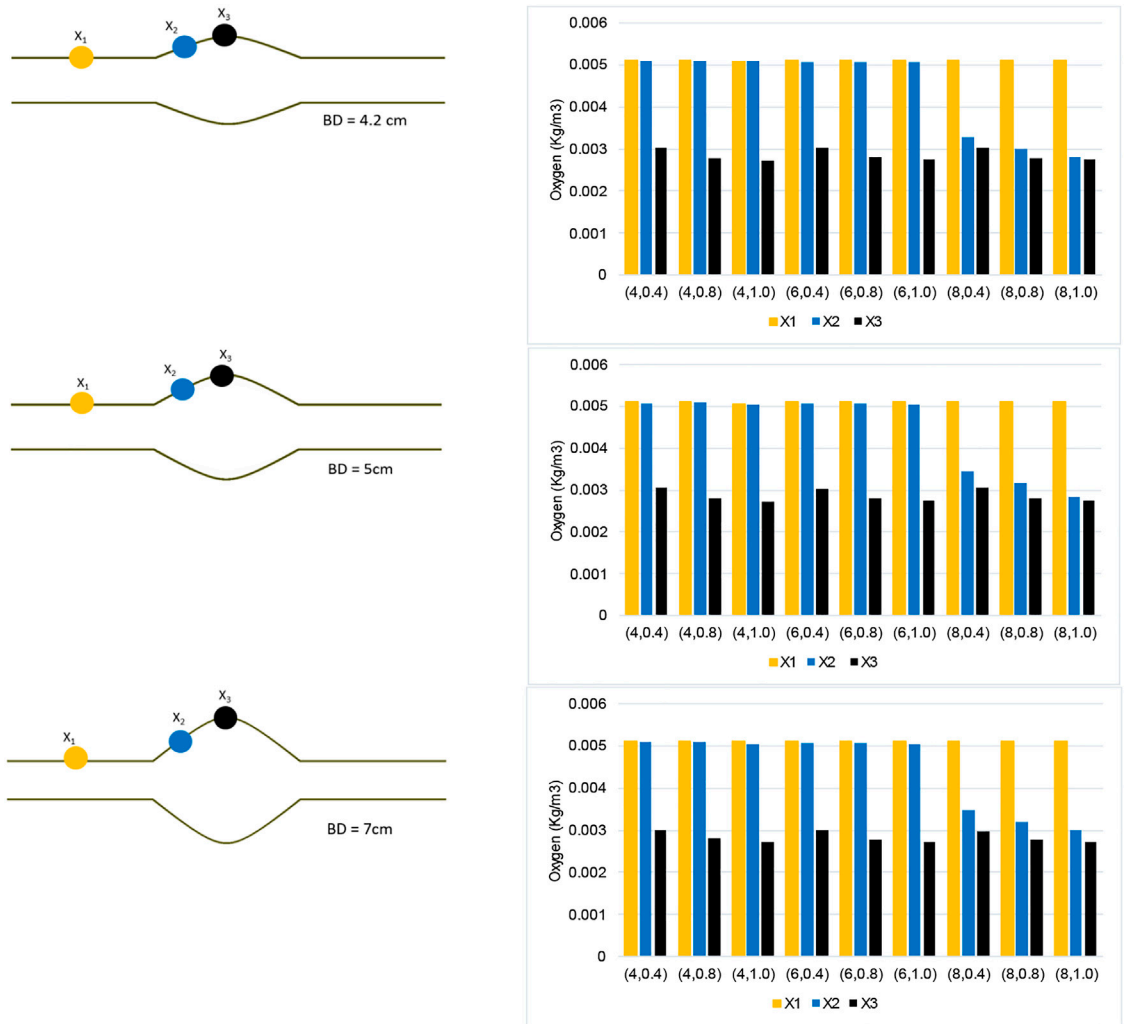

FIGURE 10 | Oxygen concentration data collected along three points of the AAA model for each case (l, δ), where l denotes ILT length and δ is ILT thickness. Plots corresponds to *BD*= 4.2 cm (top), *BD*= 5 cm (middle), and *BD*= 7 cm (bottom), respectively.

corresponding to the X_2 concentration are denoted by blue diamonds, and data points corresponding to X_3 are shown in black circles.

We observe that the dependence of the oxygen concentration at X_2 and X_3 is nonlinear and can be described using a power law model, namely $y = c.x^p$, where (p) is the exponent that quantifies the sensitivity of the quantity of interest (y) with respect to the control parameter (x) and c is a scaling constant. Since the X_2 and X_3 data for different bulge diameters demonstrates a similar trend, we have fitted them using the same power law functional relationship. We observe that all the charts show a similar behavior and that the scaling constants are comparable, but the exponents of the power law are slightly different (**Figure 11**). In particular, exponent p is a little higher for point X_3 at different bulge diameters. Oxygen concentrations in X_3 are affected by ILT thickness, while the concentration values at X_2 are affected by ILT length and only vary if ILT is long enough to cover that point. The length of the ILT had a direct relationship with increase in local ILT thickness at the lesion, and therefore the computer model demonstrated an inverse relationship of wall oxygen measures at the point X_2 that is covered by the length of ILT with ILT thickness.

DISCUSSION

The objective of this study is to quantify the key geometric parameters which cause fluctuations in oxygen transport that might lead to oxygen deprivation in the arterial wall, and to investigate if there is a relation between wall hypoxia and ILT size in AAA. The numerical experiments are designed to quantify the influence of ILT length and thickness on AAA hypoxia. In addition, we simulated varying AAA bulge diameters to confirm our findings during different stages of AAA development. Analysis is performed to model fluctuations in oxygen transport, and the oxygen

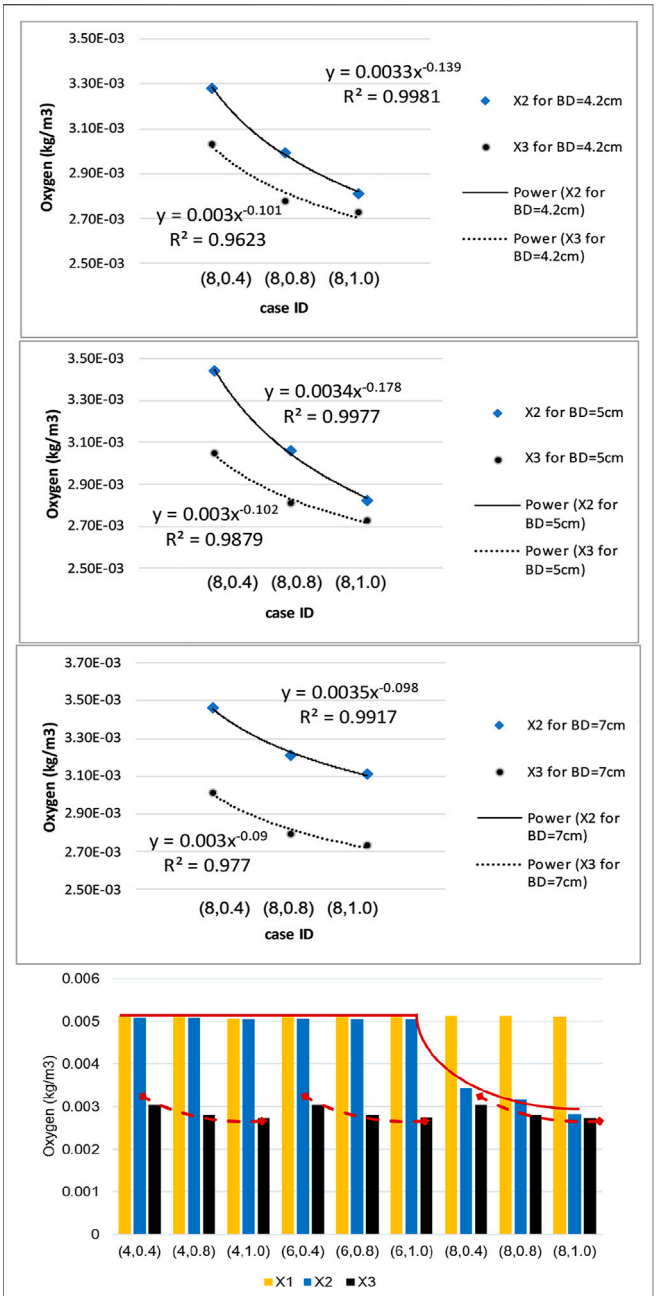

FIGURE 11 | Sensitivity results for dependence of wall oxygen concentration to the model parameters δ and l, and the schematic of the measuring indicator plots used in the analysis.

concentration profiles at different locations within an AAA model are presented and discussed.

Computer simulations predicted a gradient in oxygen concentration through the arterial wall, in particular in the region that is covered by the ILT, with maximum concentration value at the thrombus-free position, intermediate value at a medial region, and lowest value at the AAA wall (**Figure 3**). Therefore an ILT can decrease oxygen diffusion from the bloodstream to the underlying ILT and aneurysmal wall which is in agreement with observations in (Wang et al., 2002). The obtained results in **Figures 4–6** have shown that concentration values along ILT abluminal surface and within the ILT tissue are highly influenced by the ILT thickness: the thinner the ILT, the greater the oxygen concentration measurement. Moreover, the results have highlighted that AAAs with longer ILT demonstrate a more uniform oxygen distribution pattern.

Comparison of contour plots for oxygen flux to tunica adventitia layer and oxygen concentration in the ILT of all case (l, δ) geometries at different *BD* values indicates that the degree of oxygen attenuation in the wall is closely related to the ILT thickness. In the wall, there is a clear gradient of oxygen, and the flux is negatively correlated with ILT thickness. More precisely, results demonstrated that luminal oxygen diffusion through the ILT to the AAA wall decreases significantly with increasing ILT thickness, resulting in low oxygen concentration at the inner wall surface (**Figure 7**, **Figure 9** and **Figure 8**). This suggests that localized hypoxia occurs in AAA with thicker ILTs, and the thickness of the ILT layer has a profound effect on the oxygen concentration within AAA. The obtained behavior for oxygen concentration profiles were consistent with observations at Vorp et al. study (Vorp et al., 1998). Moreover, data presented in two-level oxygen contour plots (**Figures 7–9**) confirms that thicker and longer ILTs inhibit oxygen diffusion the most. This is due to the fact that thicker and longer ILTs take up more surface area and volume than other ILTs, therefore, less arterial wall surface is exposed to blood flow, and oxygen concentration to these covered areas is reduced. The thick and long cases have inflection points that are relatively more medial than their thin-and-short-ILT counterparts.

The bar plots of oxygen concentration values at different location of the wall inner surface for analyzed geometries (**Figure 10**) support this claim that ILT thickness attenuates oxygen flow most, as oxygen concentration gradually decreases as ILT thickness increases for every length of ILT. **Figure 10** also demonstrates that the diameter of the AAA bulge has minimal effect on the oxygen concentration within the arterial wall. We observe that variations in oxygen diffusion follow a similar distribution among all bulge diameter plots (**Figure 10**). Since concentration values at X_3 are directly related to ILT thickness, it is clear that the ILT thickness impacts oxygen concentration at the arterial wall most, followed by noticeable sensitivity to the ILT length (**Table 3**; **Figure 11**). More precisely, increasing ILT length leads to increase in local ILT thickness at the same time at the affected region, and therefore decreases wall oxygen concentration.

In summary, the arterial wall oxygen deprivation is nearly independent of aneurysm bulge diameter and depends only on the geometrical features of the ILT layer. The ILT thickness and wall oxygen concentration are anti-correlated, while the variation in ILT length affects the local thickness of the ILT and evens the oxygen distribution throughout the arterial wall. As such, if we increase the axial length of the ILT, the result will be an increase the area of lowered oxygen concentration within aneurysmal wall. As hypothesized, our data suggests that ILT geometry variations can have the largest effect on wall oxygen deprivation. The thicker and longer ILTs reduce oxygen diffusion to the arterial wall regardless

TABLE 3 | Exponent of the power law for different points of the sensitivity analysis.

Point	Bulge diameter (cm)	Value of the exponent (p) in $y = c.x^{-p}$
X_3	4.2	0.139
	5	0.178
	7	0.098
X_2	4.2	0.101
	5	0.102
	7	0.090

of bulge diameter and cause the most oxygen deprivation in AAA cases. Therefore, consideration of the ILT size and anatomy may be important in considering the severity of a particular AAA as recommended in (Riveros, 2013) and (Koole et al., 2013).

We would also like to point out that the high Sherwood number is a potential reason for low variation in oxygen diffusion among cases with different bulge diameters. The flow in the lumen is advection dominated and the time scale characteristic of the blood flow is too short to allow fluid movement to take place between material elements by diffusive mass transport. This indicates that bulge diameter affects oxygen flow insignificantly. Therefore, the mass transport is AAA geometry independent and more ILT geometry dependent. Instabilities in the flow can occur for certain ranges of Reynolds number and AAA severity.

The numerical methodology was validated using numerical research data of the literature, as described in Zakerzadeh et al. (Zakerzadeh et al., 2021). The blood flow with the velocity of $v \approx 0.23$ m/s matches physiological Reynolds numbers and represent the flow in the abdominal aorta under the resting condition (Fraser et al., 2008). We compared the results of wall oxygen concentration obtained from *in-situ* mass transport with experimental data for hypoxia in (Vorp et al., 2001) where normalized partial pressure of oxygen in the ILT-wall interface as well as a random point inside the AAA wall for large group of patients with thin and thick ILT has been reported. We have observed a qualitative consistency with these experimental results. However, it would be extremely difficult to find suitable clinical or *in vitro* data for quantitative validation, since precise details on variation in wall thickness, ILT thickness, and presence of vasa vasorum can significantly affect the results. As for numerical verification, mesh convergence analysis is performed (see (Zakerzadeh et al., 2021) for details of mesh independence study). The obtained oxygen concentration profiles tested against these Vorp et al.'s data (Vorp et al., 1998), and the qualitative nature of the oxygen concentration is in agreement.

Our approach, however, has some limitations. Principle among these is that a simplified geometry of idealized AAAs is used in this investigation. The idealized lesion geometries facilitate systematic variations of the three morphological features explored in this paper. In this way, we can more easily investigate the effect of these geometrical features on wall hypoxia, and thereby begin to build intuition otherwise not possible. We previously performed the analysis of combined flow and oxygen transport in a patient-specific AAA geometry (Zakerzadeh et al., 2020). However, patient-specific models prohibit creating a large number of parametric studies for the purpose of our study. In addition, to compare across AAAs, we do not have access to patient-specific blood flow rates. Nevertheless, the knowledge gained from the present work sets the ground for future research that manages patient-specific models. Moreover, the steady-state solution is obtained in the current study. The steady-state flow assumption gives a reasonable first approximation to time-averaged unsteady results, so long as Schmidt number is large (Ma et al., 1994). Given the blood oxygen diffusivity of 1.6×10^{-9} m^2/s, the calculated Schmidt number is about 2,100, and therefore considering only steady conditions is an appropriate strategy for this study while significantly reducing the computational costs of fully three-dimensional mass transfer calculations. In fact, as the transient behavior has shown to have relatively minimal impact on lumen oxygen flux (Kolandavel et al., 2006; Liu et al., 2011), it will not significantly affect the flow-driven mass transport and the conclusions of this work. It has been established that ILT is heterogeneous and oxygen diffusion coefficient fluctuates in multiple ILT layers (Yunoki et al., 2012). Moreover, the arterial wall oxygen consumption rate varies spatially as well (Buerk and Goldstick, 1982). However, to our knowledge, these parameters have never been measured for different layers of an ILT. Since such an experimental study is outside the scope of the present work, we have assumed a value of these parameters from a compilation of previously published values for thrombus. However, these observations recommend that different ILT structural composition needs to be handled more cautiously in the future AAA simulations (see (Tong and Holzapfel, 2015) for a comprehensive research summary on ILT structure and mechanical characterization). Future improvements to our AAA models could also include integrating artificial intelligence (AI) and endothelial response into our workspace. By modeling the effect of a growing ILT on oxygen diffusion and wall stress using AI, we can better predict aneurysm rupture. Additionally, modeling the layers of the arterial wall and intraluminal thrombus tissues can improve our understanding of AAA formation and rupture at the cellular level. Coupling endothelial response data with a fluid-structure interaction (FSI) framework could also allow to track immune response to AAA formation and create drug delivery pathways to cure a clinical aneurysm. In attaining a higher-fidelity model, we also plan to include the pulsatile movement of the artery in future work. This would ask for an FSI framework. While such coupling may incur high computational cost, the potential of integrating AI and immune response into our FSI framework is promising. The proposed methodology is a step forward in the personalized medicine, quantifying the aneurysm rupture risk reduction, and helping the clinicians in the preoperative planning and making informed decisions towards effective treatment.

DATA AVAILABILITY STATEMENT

The original contributions presented in the study are included in the article/Supplementary Material, further inquiries can be directed to the corresponding author.

AUTHOR CONTRIBUTIONS

RZ was responsible for project administration and designed the numerical simulations and methodology and wrote the first draft of the manuscript. BC and AG performed the simulations, collected the data, prepared figures, and contributed to the writing of the manuscript. All authors assisted with data processing and interpretation of the results and approved the final manuscript. BC and AG equally contributed and share first authorship of this work.

FUNDING

This research is supported by the Faculty Development Fund and Hunkele Dreaded Disease Award (Grant No. G2000098 and G2100064).

REFERENCES

Adolph, R., Vorp, D. A., Steed, D. L., Webster, M. W., Kameneva, M. V., and Watkins, S. C. (1997). Cellular Content and Permeability of Intraluminal Thrombus in Abdominal Aortic Aneurysm. *J. Vasc. Surg.* 25 (5), 916–926. doi:10.1016/s0741-5214(97)70223-4

Aggarwal, S., Qamar, A., Sharma, V., and Sharma, A. (2011). Abdominal Aortic Aneurysm: A Comprehensive Review. *Exp. Clin. Cardiol.* 16 (1), 11–15.

Applegate, R. L., Dorotta, I. L., Wells, B., Juma, D., and Applegate, P. M. (2016). The Relationship between Oxygen reserve index and Arterial Partial Pressure of Oxygen during Surgery. *Anesth. Analgesia.* 123 (3), 626–633. doi:10.1213/ane.0000000000001262

Ayyalasomayajula, A., Vande Geest, J. P., and Simon, B. R. (2010). Porohyperelastic Finite Element Modeling of Abdominal Aortic Aneurysms. *J. Biomech. Eng.* 132 (10), 104502. doi:10.1115/1.4002370

Bhagavan, D., Di Achille, P., and Humphrey, J. D. (2018). Strongly Coupled Morphological Features of Aortic Aneurysms Drive Intraluminal Thrombus. *Sci. Rep.* 8 (1), 13273. doi:10.1038/s41598-018-31637-6

Bluestein, D., Dumont, K., De Beule, M., Ricotta, J., Impellizzeri, P., Verhegghe, B., et al. (2009). Intraluminal Thrombus and Risk of Rupture in Patient Specific Abdominal Aortic Aneurysm - FSI Modelling. *Computer Methods Biomech. Biomed. Eng.* 12 (1), 73–81. doi:10.1080/10255840802176396

Buerk, D. G., and Goldstick, T. K. (1982). Arterial wall Oxygen Consumption Rate Varies Spatially. *Am. J. Physiology-Heart Circulatory Physiol.* 243 (6), H948–H958. doi:10.1152/ajpheart.1982.243.6.h948

Buerk, D. G., and Goldstick, T. K. (1986). Oxygen Tension Changes in the Outer Vascular wall Supplied by Vasa Vasorum Following Adenosine and Epinephrine. *Blood Vessels.* 23 (1), 9–21. doi:10.1159/000158621

Caputo, M., Chiastra, C., Cianciolo, C., Cutrì, E., Dubini, G., Gunn, J., et al. (2013). Simulation of Oxygen Transfer in Stented Arteries and Correlation with In-Stent Restenosis. *Int. J. Numer. Meth. Biomed. Engng.* 29 (12), 1373–1387. doi:10.1002/cnm.2588

Cnotliwy, M. (2010). C-Reactive Protein within the Wall of Large Abdominal Aortic Aneurysms; Pathophysiological Implications. A Preliminary Study. *Comp. Prof. Pedagogy.* 4 (82), 193–198. doi:10.2478/v10035-010-0027-8

Di Martino, E. S., and Vorp, D. A. (2003). Effect of Variation in Intraluminal Thrombus Constitutive Properties on Abdominal Aortic Aneurysm wall Stress. *Ann. Biomed. Eng.* 31 (7), 804–809. doi:10.1114/1.1581880

Douek, P. C. (2005). "Contrast-Enhanced MR Angiography of the Abdominal Aorta," in *Magnetic Resonance Angiography* (Springer), 195–208. doi:10.1007/88-470-0352-0_11

Fraser, K. H., Meagher, S., Blake, J. R., Easson, W. J., and Hoskins, P. R. (2008). Characterization of an Abdominal Aortic Velocity Waveform in Patients with Abdominal Aortic Aneurysm. *Ultrasound Med. Biol.* 34 (1), 73–80. doi:10.1016/j.ultrasmedbio.2007.06.015

Ghulam, Q. M., Bredahl, K., Sandholt, B., Taudorf, M., Lönn, L., Rouet, L., et al. (2018). Contrast Enhanced Three Dimensional Ultrasound for Intraluminal Thrombus Assessment in Abdominal Aortic Aneurysms. *Eur. J. Vasc. Endovascular Surg.* 56 (5), 673–680. doi:10.1016/j.ejvs.2018.07.029

Haller, S. J., Crawford, J. D., Courchaine, K. M., Bohannan, C. J., Landry, G. J., Moneta, G. L., et al. (2018). Intraluminal Thrombus Is Associated with Early Rupture of Abdominal Aortic Aneurysm. *J. Vasc. Surg.* 67 (4), 1051–1058. doi:10.1016/j.jvs.2017.08.069

Hans, S. S., Jareunpoon, O., Balasubramaniam, M., and Zelenock, G. B. (2005). Size and Location of Thrombus in Intact and Ruptured Abdominal Aortic Aneurysms. *J. Vasc. Surg.* 41 (4), 584–588. doi:10.1016/j.jvs.2005.01.004

Hirsch, A. T. (2006). ACC/AHA 2005 Practice Guidelines for the Management of Patients with Peripheral Arterial Disease (Lower Extremity, Renal, Mesenteric, and Abdominal Aortic): a Collaborative Report from the American Association for Vascular Surgery/Society for Vascular Surgery, Society for Cardiovascular Angiography and Interventions, Society for Vascular Medicine and Biology, Society of Interventional Radiology, and the ACC/AHA Task Force on Practice Guidelines (Writing Committee to Develop Guidelines for the Management of Patients With Peripheral Arterial Disease): Endorsed by the American Association of Cardiovascular and Pulmonary Rehabilitation; National Heart, Lung, and Blood Institute; Society for Vascular Nursing; TransAtlantic Inter-society Consensus; and Vascular Disease Foundation. *Circulation.* 113 (11), e463–e654. doi:10.1161/circulationaha.106.174526

Iannetti, L., D'Urso, G., Conoscenti, G., Cutrì, E., Tuan, R. S., Raimondi, M. T., et al. (2016). Distributed and Lumped Parameter Models for the Characterization of High Throughput Bioreactors. *PLoS One.* 11 (9), e0162774. doi:10.1371/journal.pone.0162774

Jana, S., Hu, M., Shen, M., and Kassiri, Z. (2019). Extracellular Matrix, Regional Heterogeneity of the Aorta, and Aortic Aneurysm. *Exp. Mol. Med.* 51 (12), 1–15. doi:10.1038/s12276-019-0286-3

Kemmerling, E. M. C., and Peattie, R. A. (2018). Abdominal Aortic Aneurysm Pathomechanics: Current Understanding and Future Directions. *Adv. Exp. Med. Biol.* 1097, 157–179. doi:10.1007/978-3-319-96445-4_8

Kolandavel, M. K., Fruend, E.-T., Ringgaard, S., and Walker, P. G. (2006). The Effects of Time Varying Curvature on Species Transport in Coronary Arteries. *Ann. Biomed. Eng.* 34 (12), 1820–1832. doi:10.1007/s10439-006-9188-3

Koole, D., Zandvoort, H. J. A., Schoneveld, A., Vink, A., Vos, J. A., van den Hoogen, L. L., et al. (2013). Intraluminal Abdominal Aortic Aneurysm Thrombus Is Associated with Disruption of wall Integrity. *J. Vasc. Surg.* 57 (1), 77–83. doi:10.1016/j.jvs.2012.07.003

Ku, D. N. (1997). Blood Flow in Arteries. *Annu. Rev. Fluid Mech.* 29 (1), 399–434. doi:10.1146/annurev.fluid.29.1.399

Li, X., Zhao, G., Zhang, J., Duan, Z., and Xin, S. (2013). Prevalence and Trends of the Abdominal Aortic Aneurysms Epidemic in General Population - A Meta-Analysis. *PloS one.* 8 (12), e81260. doi:10.1371/journal.pone.0081260

Li, Z.-Y., U-King-Im, J., Tang, T. Y., Soh, E., See, T. C., and Gillard, J. H. (2008). Impact of Calcification and Intraluminal Thrombus on the Computed wall Stresses of Abdominal Aortic Aneurysm. *J. Vasc. Surg.* 47 (5), 928–935. doi:10.1016/j.jvs.2008.01.006

Li, Z., and Kleinstreuer, C. (2007). A Comparison between Different Asymmetric Abdominal Aortic Aneurysm Morphologies Employing Computational Fluid-Structure Interaction Analysis. *Eur. J. Mech. - B/Fluids.* 26 (5), 615–631. doi:10.1016/j.euromechflu.2007.03.003

Liu, X., Fan, Y., Deng, X., and Zhan, F. (2011). Effect of Non-Newtonian and Pulsatile Blood Flow on Mass Transport in the Human Aorta. *J. Biomech.* 44 (6), 1123–1131. doi:10.1016/j.jbiomech.2011.01.024

Ma, P., Li, X., and Ku, D. N. (1994). Heat and Mass Transfer in a Separated Flow Region for High Prandtl and Schmidt Numbers under Pulsatile Conditions. *Int. J. Heat mass transfer.* 37 (17), 2723–2736. doi:10.1016/0017-9310(94)90389-1

Moore, J., and Ethier, C. (1997). Oxygen Mass Transfer Calculations in Large Arteries. *J. Biomech. Eng.* 119 (4), 469–475. doi:10.1115/1.2798295

Mower, W. R., Quiñones, W. J., and Gambhir, S. S. (1997). Effect of Intraluminal Thrombus on Abdominal Aortic Aneurysm wall Stress. *J. Vasc. Surg.* 26 (4), 602–608. doi:10.1016/s0741-5214(97)70058-2

Polzer, S., and Bursa, J. (2010). "Poroelastic Model of Intraluminal Thrombus in FEA of Aortic Aneurysm," in 6th World Congress of Biomechanics (WCB 2010). August 1-6, 2010 Singapore (Springer). doi:10.1007/978-3-642-14515-5_194

Polzer, S., Gasser, T. C., Swedenborg, J., and Bursa, J. (2011). The Impact of Intraluminal Thrombus Failure on the Mechanical Stress in the wall of Abdominal Aortic Aneurysms. *Eur. J. Vasc. Endovascular Surg.* 41 (4), 467–473. doi:10.1016/j.ejvs.2010.12.010

Polzer, S., Gasser, T., Markert, B., Bursa, J., and Skacel, P. (2012). Impact of Poroelasticity of Intraluminal Thrombus on wall Stress of Abdominal Aortic Aneurysms. *BioMedical Eng. OnLine.* 11, 62. doi:10.1186/1475-925x-11-62

Rappitsch, G., and Perktold, K. (1996). Computer Simulation of Convective Diffusion Processes in Large Arteries. *J. Biomech.* 29 (2), 207–215. doi:10.1016/0021-9290(95)00045-3

Riveros, F. (2013). "Influence of Intraluminal Thrombus Topology on AAA Passive Mechanics," in *Computing in Cardiology 2013* (IEEE).

Scotti, C. M., Shkolnik, A. D., Muluk, S. C., and Finol, E. A. (2005). Fluid-structure Interaction in Abdominal Aortic Aneurysms: Effects of Asymmetry and wall Thickness. *Biomed. Eng. Online.* 4, 64. doi:10.1186/1475-925x-4-64

Severinghaus, J. W. (1979). Simple, Accurate Equations for Human Blood O2 Dissociation Computations. *J. Appl. Physiol.* 46 (3), 599–602. doi:10.1152/jappl.1979.46.3.599

Sun, N., Leung, J. H., Wood, N. B., Hughes, A. D., Thom, S. A., Cheshire, N. J., et al. (2009). Computational Analysis of Oxygen Transport in a Patient-specific Model of Abdominal Aortic Aneurysm with Intraluminal Thrombus. *Br. J. Radiol.* 82 (1), S18–S23. doi:10.1259/bjr/89466318

Tanaka, H. (2015). Hypoperfusion of the Adventitial Vasa Vasorum Develops an Abdominal Aortic Aneurysm. *PloS one.* 10 (8), e0134386. doi:10.1371/journal.pone.0134386

Tong, J., and Holzapfel, G. A. (2015). Structure, Mechanics, and Histology of Intraluminal Thrombi in Abdominal Aortic Aneurysms. *Ann. Biomed. Eng.* 43 (7), 1488–1501. doi:10.1007/s10439-015-1332-5

Virag, L., Wilson, J. S., Humphrey, J. D., and Karšaj, I. (2015). A Computational Model of Biochemomechanical Effects of Intraluminal Thrombus on the Enlargement of Abdominal Aortic Aneurysms. *Ann. Biomed. Eng.* 43 (12), 2852–2867. doi:10.1007/s10439-015-1354-z

Vorp, D. A., and Geest, J. P. V. (2005). Biomechanical Determinants of Abdominal Aortic Aneurysm Rupture. *Arteriosclerosis, Thromb. Vasc. Biol.* 25 (8), 1558–1566. doi:10.1161/01.atv.0000174129.77391.55

Vorp, D. A., Lee, P. C., Wang, D. H. J., Makaroun, M. S., Nemoto, E. M., Ogawa, S., et al. (2001). Association of Intraluminal Thrombus in Abdominal Aortic Aneurysm with Local Hypoxia and wall Weakening. *J. Vasc. Surg.* 34 (2), 291–299. doi:10.1067/mva.2001.114813

Vorp, D. A., Wang, D. H. J., Webster, M. W., and Federspiel, W. J. (1998). Effect of Intraluminal Thrombus Thickness and Bulge Diameter on the Oxygen Diffusion in Abdominal Aortic Aneurysm. *J. biomechanical Eng.* 120 (5), 579–583. doi:10.1115/1.2834747

Wang, D. H. J., Makaroun, M. S., Webster, M. W., and Vorp, D. A. (2002). Effect of Intraluminal Thrombus on wall Stress in Patient-specific Models of Abdominal Aortic Aneurysm. *J. Vasc. Surg.* 36 (3), 598–604. doi:10.1067/mva.2002.126087

Wang, D. H. J., Makaroun, M., Webster, M. W., and Vorp, D. A. (2001). Mechanical Properties and Microstructure of Intraluminal Thrombus from Abdominal Aortic Aneurysm. *J. Biomech. Eng.* 123 (6), 536–539. doi:10.1115/1.1411971

Wilson, J. S., Virag, L., Di Achille, P., Karsaj, I., and Humphrey, J. D. (2013). Biochemomechanics of Intraluminal Thrombus in Abdominal Aortic Aneurysms. *J. Biomech. Eng.* 135 (2), 021011. doi:10.1115/1.4023437

Wolf, Y. G., Thomas, W. S., Brennan, F. J., Goff, W. G., Sise, M. J., and Bernstein, E. F. (1994). Computed Tomography Scanning Findings Associated with Rapid Expansion of Abdominal Aortic Aneurysms. *J. Vasc. Surg.* 20 (4), 529–538. doi:10.1016/0741-5214(94)90277-1

Xenos, M., Labropoulos, N., Rambhia, S., Alemu, Y., Einav, S., Tassiopoulos, A., et al. (2015). Progression of Abdominal Aortic Aneurysm Towards Rupture: Refining Clinical Risk Assessment Using a Fully Coupled Fluid-Structure Interaction Method. *Ann. Biomed. Eng.* 43 (1), 139–153. doi:10.1007/s10439-014-1224-0

Yunoki, K., Naruko, T., Sugioka, K., Inaba, M., Iwasa, Y., Komatsu, R., et al. (2012). Erythrocyte-rich Thrombus Aspirated from Patients with ST-Elevation Myocardial Infarction: Association with Oxidative Stress and its Impact on Myocardial Reperfusion. *Eur. Heart J.* 33 (12), 1480–1490. doi:10.1093/eurheartj/ehr486

Zakerzadeh, R., Cupac, T., and Durka, M. (2020). Oxygen Transport in a Permeable Model of Abdominal Aortic Aneurysm. *Comput. Methods Biomech. Biomed. Engin.* 24 (2), 215–229. doi:10.1080/10255842.2020.1821193

Zakerzadeh, R., Cupac, T., Dorfner, N., and Guy, A. (2021). Coupled Hemodynamics and Oxygen Diffusion in Abdominal Aortic Aneurysm: A Computational Sensitivity Study. *Cardiovasc. Eng. Tech.* 12 (2), 166–182. doi:10.1007/s13239-020-00508-5

Zhu, C., Leach, J. R., Wang, Y., Gasper, W., Saloner, D., and Hope, M. D. (2020). Intraluminal Thrombus Predicts Rapid Growth of Abdominal Aortic Aneurysms. *Radiology.* 294 (3), 707–713. doi:10.1148/radiol.2020191723

Author's Disclaimer: DM's contributions to this article were not in any official capacity from JPL.

Conflict of Interest: The authors declare that the research was conducted in the absence of any commercial or financial relationships that could be construed as a potential conflict of interest.

Publisher's Note: All claims expressed in this article are solely those of the authors and do not necessarily represent those of their affiliated organizations, or those of the publisher, the editors, and the reviewers. Any product that may be evaluated in this article, or claim that may be made by its manufacturer, is not guaranteed or endorsed by the publisher.

frontiers in Bioengineering and Biotechnology

ORIGINAL RESEARCH
published: 30 March 2022
doi: 10.3389/fbioe.2022.842754

Harmonic Distortion of Blood Pressure Waveform as a Measure of Arterial Stiffness

Nicholas Milkovich[1], *Anastasia Gkousioudi*[1], *Francesca Seta*[2], *Béla Suki*[3] *and Yanhang Zhang*[1,3,4]*

[1]Department of Mechanical Engineering, Boston University, Boston, MA, United States, [2]Vascular Biology Section, Boston University School of Medicine, Boston, MA, United States, [3]Department of Biomedical Engineering, Boston University, Boston, MA, United States, [4]Division of Materials Science and Engineering, Boston University, Boston, MA, United States

Aging and disease alter the composition and elastic properties of the aortic wall resulting in shape changes in blood pressure waveform (BPW). Here, we propose a new index, harmonic distortion (HD), to characterize BPW and its relationship with other *in vitro* and *in vivo* measures. Using a Fourier transform of the BPW, HD is calculated as the ratio of energy above the fundamental frequency to that at the fundamental frequency. Male mice fed either a normal diet (ND) or a high fat, high sucrose (HFHS) diet for 2–10 months were used to study BPWs in diet-induced metabolic syndrome. BPWs were recorded for 20 s hourly for 24 h, using radiotelemetry. Pulse wave velocity (PWV), an *in vivo* measure of arterial stiffness, was measured in the abdominal aorta *via* ultrasound sonography. Common carotid arteries were excised from a subset of mice to determine the tangent modulus using biaxial tension-inflation test. Over a 24-h period, both HD and systolic blood pressure (SBP) show a large variability, however HD linearly decreases with increasing SBP. HD is also linearly related to tangent modulus and PWV with slopes significantly different between the two diet groups. Overall, our study suggests that HD is sensitive to changes in blood pressure and arterial stiffness and has a potential to be used as a noninvasive measure of arterial stiffness in aging and disease.

Keywords: harmonic distortion, radio telemetry, tangent modulus, blood pressure waveform, pulse wave velocity

OPEN ACCESS

Edited by:
Seungik Baek, Michigan State University, United States

Reviewed by:
Matthew Bersi, Washington University in St. Louis, United States
Rudolph Gleason, Georgia Institute of Technology, United States

***Correspondence:**
Yanhang Zhang
yanhang@bu.edu

Specialty section:
This article was submitted to Biomechanics, a section of the journal Frontiers in Bioengineering and Biotechnology

Received: *24 December 2021*
Accepted: *14 March 2022*
Published: *30 March 2022*

Citation:
Milkovich N, Gkousioudi A, Seta F, Suki B and Zhang Y (2022) Harmonic Distortion of Blood Pressure Waveform as a Measure of Arterial Stiffness. Front. Bioeng. Biotechnol. 10:842754. doi: 10.3389/fbioe.2022.842754

INTRODUCTION

Arterial stiffening is a significant contributor to the progression of cardiovascular diseases, including hypertension, diabetes mellitus, stroke, heart failure, and renal failure, which are the leading cause of mortality in the developed countries (Roman et al., 2000; Yambe et al., 2004; Rucka et al., 2015; O'Rourke et al., 2016). Arteries gradually stiffen with aging, which can lead to hypertension (HT) (Sun, 2015). Diabetic patients, however, show accelerated arterial stiffening with elevated blood pressure (BP) at a relatively young age compared to nondiabetic subjects (Chaturvedi, 2007; Loehr et al., 2016). BP is routinely used as a critical clinical measure for the diagnosis of HT. Additional parameters derived from BP and artery dimensions, such as distensibility and compliance, have also been widely used both in clinics and research as indicators of the mechanical properties of arteries (Glasser et al., 1997; Kannel et al., 2003; Bundy et al., 2017). However, these parameters solely rely on the systolic, mean, and diastolic pressure values, and the inherent biomechanical information associated with the shape of the BP waveform (BPW) is not considered. For example, there is a marked difference in BPW in central aortic pressure as well as pressure measured in upper limb

arteries between young and older individuals due to wave reflection (Hirata et al., 2006). Arterial stiffening results in a pressure augmentation from the superposition of the propagating and reflected waves, which increases the peak of the waveform in the systolic phase of the cardiac cycle (van Varik et al., 2012). Therefore, the features of BPW are associated with arterial stiffness; however, the phenomenon is compounded by the nonlinear elastic behavior of the vascular wall and how pathologic changes in wall properties contribute to changes in BPW shape are not well understood.

The BPW is composed of a propagating wave, generated by cardiac contraction, and a reflected wave, from peripheral vessels to the proximal aorta. In clinical practice, indexes based on BPW are limited by their sole use of pressure differences (systolic minus diastolic) based on blood pressure measurements done on peripheral arteries (brachial arteries). One of the most widely used parameters, augmentation index (AI), quantifies the difference in pressure between the propagating wave and the reflected wave. Studies that sought to link AI to arterial stiffening and HT have shown that AI and pulse wave velocity (PWV), the gold standard clinical measure of arterial stiffness (Blacher et al., 1999; Nichols, 2005), are correlated with age, height, SBP, cholesterol and pulse pressure (Blacher et al., 1999; Brooks et al., 1999; Wilkinson et al., 2000; Brooks et al., 2001; Wilkinson et al., 2002; Nichols, 2005). Interestingly, AI and PWV were not strongly correlated with one another (Jerrard-Dunne et al., 2008). Females tend to have higher AI, an effect that seems to be independent from height and heart rate (Hayward and Kelly, 1997; Gatzka et al., 2001; Mitchell et al., 2010). This sex dependence of AI is present since prepuberty. Elevated AI is present in young girls (age 8.0 ± 0.1 years) compared to males of the same age, independent of factors that generally result in earlier wave reflection and increased AI, such as height or arterial stiffness (Ayer et al., 2010). Another BP index, reflection magnitude, is measured as the relative pressure magnitude of the reflected wave compared to the forward wave, which was suggested to better represent the overall changes due to the reflected wave (Mitchell, 2008; Mitchell et al., 2008; Mitchell et al., 2010). However, the correlation between reflection magnitude and AI is less than 0.6 (Segers et al., 2007a). Additionally, both fail to assess changes in the waveform beyond a simple increase in pressure, neglecting BPW features such as the time delay between the forward and reflected wave, which may also change the overall shape of the BPW (Ageenkova and Purygina, 2011; Theodor et al., 2014).

In this study, we aim to establish a relationship between BPW and arterial wall stiffness to understand the complex interplay between hemodynamic flow and the nonlinear mechanical properties of the arterial wall and how they manifest in BPW. To this end, we introduced a new index characterizing BPW, harmonic distortion (HD), which we hypothesize will provide a more comprehensive assessment of the BPW. A mouse model of diet-induced metabolic syndrome was used to validate the effectiveness and applicability of this new index. The BPW, collected using radiotelemetry, were analyzed for two diet groups. HD based on spectral analysis of the BPW was obtained and used to quantify the distortion of the BPW and compared to established stiffness indexes.

MATERIALS AND METHODS

Animal Model

All procedures were approved by the Boston University Institutional Animal Care and Use Committee. Male (n = 29) C57Bl/6J mice were purchased from the Jackson Laboratory (Bar Harbor, ME, United States) at 7 weeks of age. After 1 week of acclimation, the 2 month old (-mo) mice were fed a control normal diet (ND: 4.5% fat, 0% sucrose, catalog number D09071702, Research Diets, New Brunswick, NJ, United States) or high fat, high sucrose diet (HFHS: 35.5% fat, 16.4% sucrose) ad libitum (catalog numbers D09071703, Research Diets, New Brunswick, NJ, United States). In this model of diet-induced metabolic syndrome, mice develop hyperinsulinemia, glucose-intolerance, increased arterial stiffness and hypertension within 8 months on diet, closely mimicking the human metabolic syndrome, as previously described (Weisbrod et al., 2013). Mice were kept in 12 h light/dark cycles in temperature- and humidity-controlled rooms. Radiotelemetry was surgically implanted to record BPWs continuously for 20 s on the hour for 24 h in conscious, freely moving mice. Mice were divided into subsets for various experimental conditions. One subset of mice (n = 6) had baseline BPW measurements taken at 2-months, before initiation of the HFHS diet, and subsequently fed the HFHS with measurements taken longitudinally at 3- and 4-months. A second subset of mice (ND: n = 5, HFHS: n = 8) underwent radiotelemetry implantation procedures at 6-months and had BPW measurements taken at 8- and 10-months. A third subset of mice were fed ND (n = 6) or HFHS (n = 4) and euthanized at 4- and 10-months for *in vitro* mechanical analysis of their right carotid arteries.

In vivo Blood Pressure Measurements

The BPW was measured using radiotelemetry (Data Sciences International, St Paul, MI, United States) that was implanted following standard surgical procedures, as we previously described (Weisbrod et al., 2013). Briefly, mice were kept anesthetized (1–2% isofluorane) on a heating pad, while a gel-filled pressure catheter was carefully inserted in the aortic arch via catheterization of the left carotid artery (**Figure 1A**). Therefore, all BPW measurements made with radiotelemetry are local to the aortic arch and indicative of central pressure. After recovery from surgery (1–2 weeks), BPW recordings were acquired for 20 s hourly over a 24-h period in the conscious, freely moving mice. BPWs are collected wirelessly through an external receiver and a data processing matrix (**Figure 1B**). This resulted in a total of 24 distinct recordings for each mouse, with each recording consisting of many individual waveforms (**Figure 1B**). The SBP values from each waveform were then collected and separated into 16 blood pressure bins, ranging from

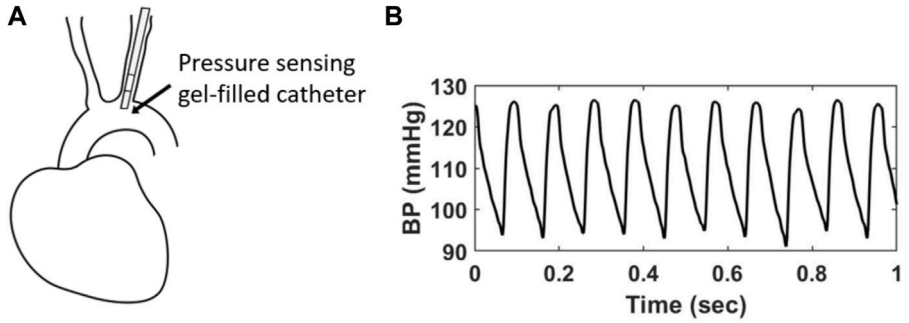

FIGURE 1 | (A) A gel-filled pressure catheter is surgically inserted in the left common carotid artery of a mouse, with the pressure-sensing region (4 mm) resting in the aortic arch. **(B)** Example of *in vivo* BPWs over 1 s time period measured using radiotelemetry.

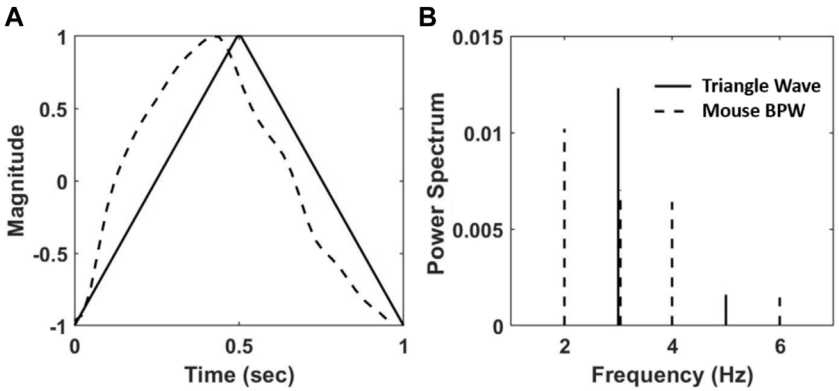

FIGURE 2 | (A) A triangular wave (solid line) and a normalized BPW from radiotelemetry (dashed line). **(B)** The normalized power spectrum, calculated as the squared fraction of Fourier coefficients at integer multiple of the fundamental frequency of the waveforms in **(A)** at 1 Hz.

80–180 mmHg, for clarity of group overlap. Normalized probability density distributions of the average SBP of each bin was then generated for every mouse. The distributions were then fitted with Gaussian functions using a MATLAB program.

Harmonic Distortion

To quantitatively compare BPWs, we introduce an index, harmonic distortion (HD), which will be used to quantify the shape change of BPW. HD is defined based on the discrete Fourier transform (DFT) of the BPW, as:

$$HD = \frac{\sum_{k=2}^{6} |A_k|^2}{|A_1|^2} \quad (1)$$

where $|A_k|^2$ are the Fourier coefficients of a single BPW multiplied by their complex conjugates. Thus, HD is essentially the ratio of energy above the fundamental frequency to that at the fundamental frequency of the waveform. Here, Fourier coefficients higher than the sixth were assumed to be negligible since they did not significantly contribute to the HD value. For an ideal sinusoidal wave, the HD value is 0. As an illustration, the normalized power spectrum, $\frac{|A_k|^2}{|A_1|^2}$, were obtained for a triangle wave and a mouse BPW (**Figure 2A**) using a custom MATLAB code according to **Eq. 1** and plotted in **Figure 2B**. The triangle wave has a HD value of 0.014 whereas the sample BPW waveform is more distorted with an HD value of 0.025.

For HD analysis of the BPW, waveforms corresponding to a single heartbeat were isolated as they appear in **Figure 2A** using custom MATLAB code by identifying the diastolic BPs. **Eq. 1** was then used to determine the HD value for each individual waveform. This analysis was performed on all mice and for all 24 BPW recordings. The corresponding SBP, the maximum value of BP in an isolated individual waveform, was also recorded and 12 evenly spaced BP bins were created between the minimum and maximum SBP values. The bin size was chosen by studying multiple bin sizes and assessing their effect on the slope of the regression line. Because the bins are weighted, the slope of these regressions is not sensitive to bin sizes (**Supplementary Figure S1**). Hence, the bin size was kept consistent for all mice. The mean and standard deviation (SD) of HD corresponding to each BP bin were calculated. HD values that were two SD outside of the mean HD value were removed. The mean and SD of HD were then recalculated for each BP bin as well as the corresponding mean BP, resulting in 12 data points for each mouse. A weighted linear regression between the mean HD and the mean BP was

performed for each age and diet group. The weight of each data point was determined by the ratio of the number of HD values in the BP bin to the total number of HD values recorded for the mouse.

Pulse Wave Velocity Measurements

Blood flow waves at two locations along the abdominal aorta, one proximal and one distal to the heart, using the renal artery as anatomical reference, were obtained in each age and diet group using high-resolution Doppler ultrasound (Vevo2100, Fujifilm-Visualsonics, Toronto, ON, Canada), as we previously described (Weisbrod et al., 2013). PWV, the rate at which BP waves travel along the aorta, was calculated as the ratio of the distance between the two locations and the difference in arrival times of two consecutive flow waves, using the foot-to-foot method and the ECG as fiducial point, over 5–10 cardiac cycles for each mouse.

In vitro Determination of Tangent Modulus

To establish the relationship between HD and arterial stiffness, tangent modulus of the common carotid arteries was obtained from a subset of mice from the 4-months ND (n = 3), 4-months HFHS (n = 2), 10-months ND (n = 3) and 10-months HFHS (n = 2) groups. Biomechanical characterization of these arteries was performed in a separate study by Gkousioudi et al. (2022), from which the circumferential Cauchy stress-stretch responses were obtained from biaxial extension-inflation tests, and then fitted using a four-fiber family constitutive model with the following strain energy function (Ferruzzi et al., 2013; Ferruzzi et al., 2018a):

$$W(\boldsymbol{C}, \boldsymbol{a}^i) = \frac{c}{2}(I_C - 3) + \sum_{i=1}^{4} \frac{c_1^i}{4c_2^i}\left\{exp\left[c_2^i\left(I_4^i - 1\right)^2\right] - 1\right\} \quad (2)$$

In this constitutive model, arterial wall is considered a composite of the isotropic extracellular matrix (elastic fibers, cells and ground substance) and anisotropic collagen fibers, which are assumed to be oriented in four directions: axial ($\alpha^1 = 0^o$), circumferential ($\alpha^2 = 90^o$), and diagonal ($\alpha^3 = -\alpha^4 = \alpha$). c and $c_{1,2}^i$ are material parameters for the isotropic matrix and the collagen fibers, respectively. $\boldsymbol{C} = \boldsymbol{F}^T\boldsymbol{F}$ is the Cauchy-Green deformation tensor with $\boldsymbol{F}$ being the deformation gradient. $I_C = trC$ is the first invariant of $\boldsymbol{C}$. $I_4^i = a^i \cdot Ca^i$ represents the invariant that is associated with the i^{th} fiber family, and $\boldsymbol{a}^i$ is the unit vector that denotes the orientation of the i^{th} fiber family.

In this study, circumferential tangent modulus, $C_{\theta\theta\theta\theta}$, was calculated as the first derivative of the Cauchy stress-stretch expressions using the best-fitted model parameter values as (Baek et al., 2007; Gkousioudi et al., 2022):

$$C_{\theta\theta\theta\theta} = 2t_{\theta\theta} + 4\lambda_\theta^4\left(\frac{\partial^2 W}{\partial\lambda_\theta^2\partial\lambda_\theta^2} + 2\sin^4\alpha\frac{\partial^2 W}{\partial\lambda_\theta^2\partial\lambda_\theta^2}\right) \quad (3)$$

where $t_{\theta\theta}$ is the Cauchy stress in the circumferential direction, λ_θ is the circumferential stretch, W is the strain energy function based on the four-fiber family constitutive model (**Eq. 2**), and α is the orientation angle of the diagonal collagen fiber families with respect to the longitudinal direction estimated during nonlinear regression model fitting (Ferruzzi et al., 2013; Ferruzzi et al., 2018a; Gkousioudi et al., 2022). Tangent modulus, $C_{\theta\theta\theta\theta}$, was then calculated as a function of the circumferential stretch λ_θ.

To establish a proper relationship between the HD obtained from *in vivo* measurements and the tangent modulus from the *in vitro* measurements, perivascular pressure, the pressure difference between the luminal and transmural pressures (Goshy et al., 1979; Kim et al., 2013; Ferruzzi et al., 2018b), needs to be considered to obtain the *in vivo* transmural pressure. Here, an estimation of average perivascular pressure 13.22 mmHg

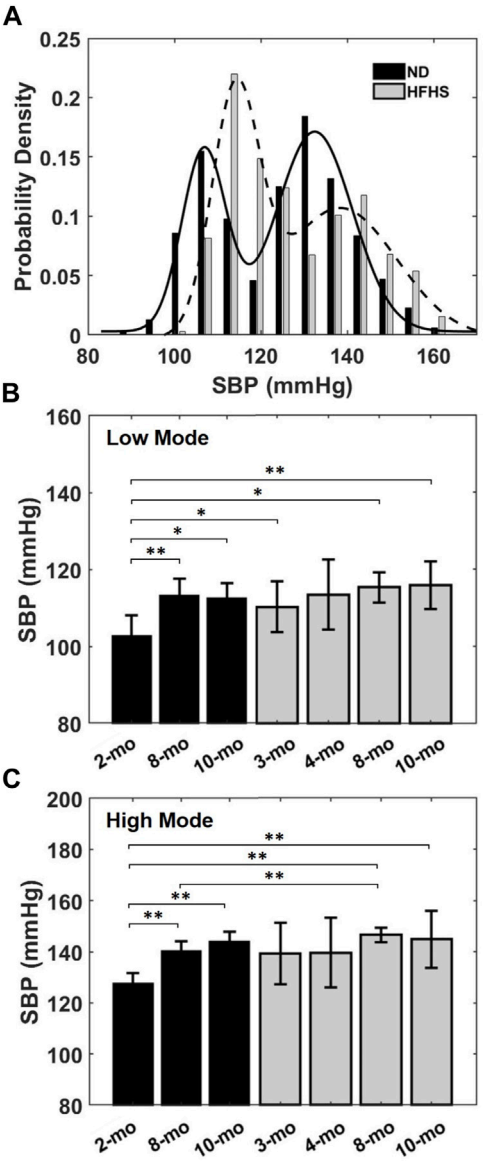

FIGURE 3 | (A) Representative bimodal probability density distribution of SBP over a 24-h period for a 2-months ND and a 3-months HFHS mouse. Solid and dashed lines are Gaussian distributions fit to the data. The low and high pressure values of the bimodal SBP distribution for each age and diet groups were averaged and showed in **(B,C)** for the low and high pressure means, respectively, for the age and diet groups (*p < 0.05; **p < 0.01).

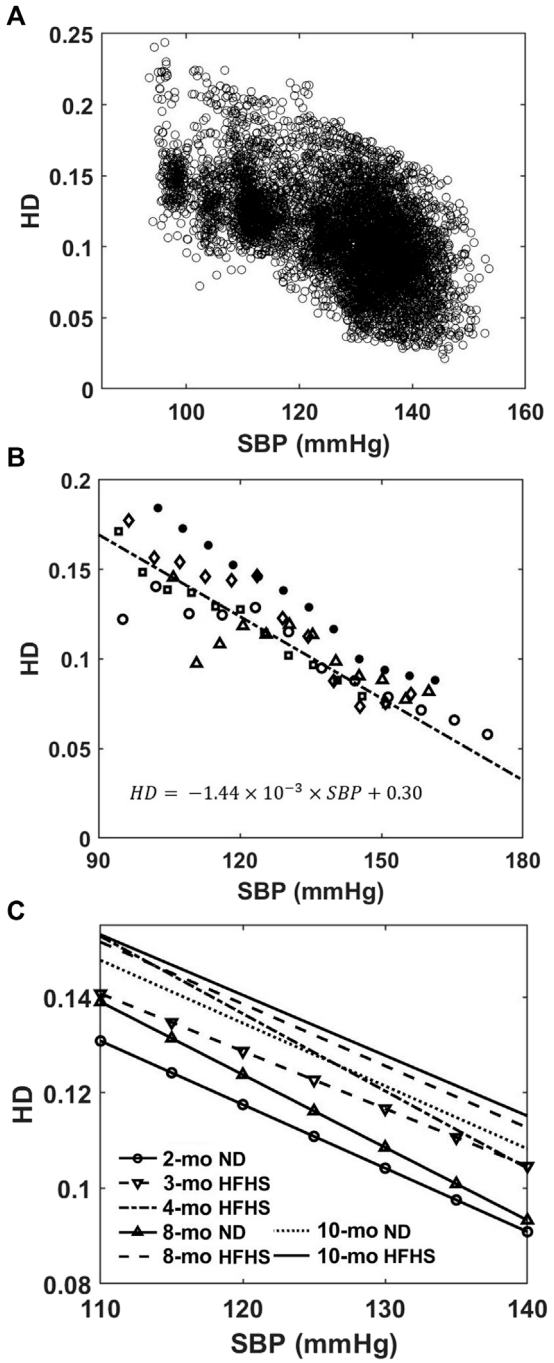

FIGURE 4 | (A) HD values of individual BPW are plotted as a function of the corresponding wave's SBP. **(B)** Mean HD values within evenly spaced BP bins for the 8-months ND group (n = 5). Different symbols represent different mice in the group. The solid line represents a weighted linear regression (r^2 = 0.78) to the data from the group. **(C)** Linear regressions between HD and luminal SBP for the 7 age and diet groups. The linear relationships consistently trend upward with increasing age and HFHS diet.

was obtained by incrementally adjusting its value for the best linear regression fit between HD and tangent modulus for each mouse. This average perivascular pressure value was then subtracted from the *in vivo* luminal SBP of each mouse to obtain transmural SBP.

Statistical Analysis

Wilcoxon rank sum tests were performed on the low and high SBP means of each mouse group after normality was not found using one-sample Kolmogorov-Smirnov tests. HD values for each mouse group were found to be not normally distributed using paired Kolmogorov-Smirnov tests. Therefore, Friedman tests were performed on HD values between mouse groups when groups had the same number of subjects and Skillings-Mack tests were performed when comparing groups with a different number of subjects. A p-value of 0.05 or lower was considered statistically significant.

RESULTS

Blood Pressure Variability

BPW data were firstly used to assess the variation of BP over a 24-h period. Probability density distributions of the SBP, i.e., the peak of the individual BPWs, were plotted for each mouse. **Figure 3A** shows a typical bimodal distribution of the SBP over a 24-h period. The data were fit with the sum of two Gaussian distributions with each peak centering at a low and high systolic blood pressure. The low- and high-pressure values at the two peaks were averaged for each age and diet group. The SBP distribution of the HFHS mouse showed a wider range of high SBP compared to the ND mouse with the two peaks correlating with age and diet. There was a significant increase in the SBP means with age in the ND groups (**Figures 3B,C**), however this trend was absent in the HFHS groups. The 2-months ND group's mean low- and high-pressure values are statistically lower than all other groups, except the 4-months HFHS and the 3-months HFHS high pressure mean.

In the current study, 5 of the 19 analyzed BPW were found to either have one or three modes (n = 2 and 3, respectively). The single mode's mean corresponded to the group high pressure average and was included as such. In the three modes case, a mean value of either high or low pressure was only included if the Gaussian distribution could be fitted to the pressure distribution, and the mode with a mean outside of one standard deviation of the low or high mean was discarded.

Harmonic Distortion

HD analysis showed that the HD values from the isolated individual BPW were inversely related to SBP over a 24-h period, as shown in **Figure 4A** for an 8-months ND mouse. The HD values range from ~0.24 to 0.03 between SBP of 93 and 153 mmHg. To study the trend between HD and SBP, evenly spaced blood pressure bins were used to find a mean HD within each bin. This mean HD is then plotted with the mean SBP of that bin for every mouse. Despite the large spread of HD seen in **Figure 4A**, following binning, a linear relation was apparent as shown for the 8-months ND group in **Figure 4B**.

Linear regression curves were then generated in a similar manner for all groups and plotted in **Figure 4C**. An upward

TABLE 1 | The *p*-values were obtained from Friedman test and Skillings-Mack test between grops. 2-months ND (n = 6), 3-months HFHS (n = 6), all other groups (n = 5). Tests were performed on average HD values with SBP bins ranging from 110–140 mmHg between each age/diet group.

	3-months HFHS	4-months HFHS	8-months ND	8-months HFHS	10-months ND	10-months HFHS
2-months ND	0.375	<0.001	<0.001	<0.001	<0.001	<0.001
3-months HFHS		<0.001	<0.001	<0.001	<0.001	<0.001
4-months HFHS			0.977	0.002	0.007	0.002
8-months ND				<0.001	0.008	0.002
8-months HFHS					<0.001	0.549
10-months ND						0.346

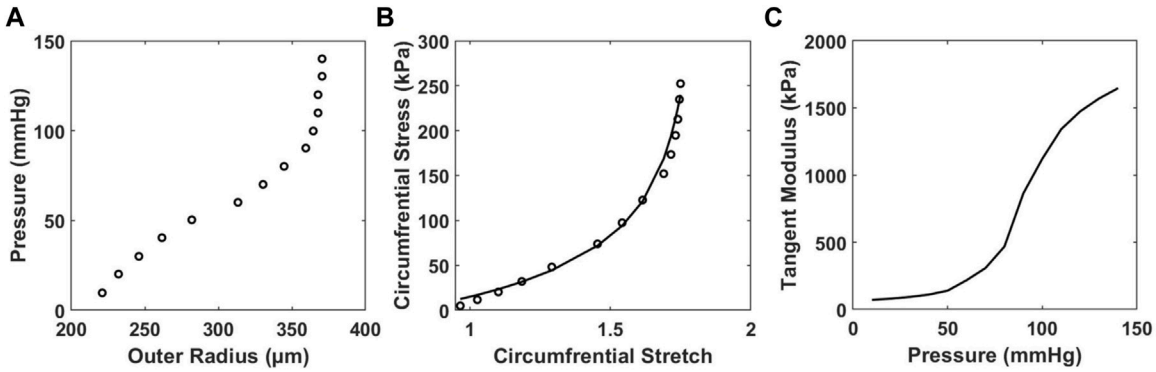

FIGURE 5 | Representative results of **(A)** *in vitro* pressure-outer radius curves from biaxial extension-inflation test; **(B)** circumferential stress-stretch curves; and **(C)** tangent modulus vs. pressure of a carotid artery sample of a 4-months ND mouse with model parameter c = 20.540 kPa, c_1^1 = 3.742 kPa; c_2^1 = 0.030; c_1^2 = 11.267 kPa; c_2^2 = 0.043; $c_1^{3,4}$ = 0.008 kPa; $c_2^{3,4}$ = 1.373 kPa, and α = 46.352° (Gkousioudi et al., 2022).

vertical shift in the curves is observed with age and diet, and the shift becomes more pronounced for older mice and mice on the HFHS diet (**Figure 4C**). In the pressure range of 110–140 mmHg SBP that all mice experience, the Friedman test, which evaluated the difference between groups' HD values, reveals the relative effect of the age on ND or HFHS diet (**Table 1**). The tests paired each of the seven age and diet groups with one another, using the rising SBP readings as repeated measures and the corresponding HD values as dependent variables. Many of these pairings were found to be highly significant with $p < 0.001$, suggesting a significant difference in HD between the age and diet groups. However, no significant difference was found the between 2-months ND and 3-months HFHS (p = 0.375), 8-months ND and 4-months HFHS (p = 0.977), 8-months HFHS and 10-months HFHS (p = 0.549), and the two 10-months groups (p = 0.346).

HD vs. Arterial Stiffness

To study the relationship between HD and arterial stiffness, we obtained tangent modulus measurements by first using the inflation test of carotid artery samples to obtain pressure-radius curves (**Figure 5A**), from which the circumferential stress-stretch relationships can be calculated (**Figure 5B**). At transmural pressures between 0–60 mmHg, the tangent modulus is nearly the same for each mouse, regardless of age and diet (**Supplementary Figure S2**). As pressure reaches about 60–70 mmHg, the tangent modulus increases prominently with pressure (**Figure 5C**, **Supplementary Figure S2**). Mice from the 10-months group were found to have a decrease in tangent modulus when compared with the 4-months group, which was accompanied by compromised energy storage capability and lower wall stress, as shown previously from others and our recent work (Gkousioudi et al., 2022). Mice on the HFHS diet appear to have lower tangent modulus values in the 4-months group, however this trend disappears in the 10-months group.

For each mouse the HD value and tangent modulus at the same transmural pressure were plotted for the 4- and 10-months groups (**Figures 6A,B**) and fitted with a linear line. The average slopes of these linear fits are displayed in **Figure 6C**. Our results demonstrate there is a linear relationship between HD and tangent modulus obtained from *in vitro* biomechanical testing. This relationship is consistent within all mice (n = 10) from both ND and HFHS groups. Furthermore, the linear trend appears to be steeper with HFHS diet. Average perivascular pressure was used in this study; however, it is not known whether perivascular pressure changes with aging and the development of metabolic syndrome. Adopting perivascular pressures at 13.22 ± 5 mmHg had an unnoticeable effect on the linear regressions between tangent modulus and HD (**Supplementary Figure S2**; **Supplementary Table S1**), although the effect of perivascular pressure on the slope of the linear regression needs to be further investigated.

The relationship between HD and PWV, a measure of arterial stiffness *in vivo*, was examined by plotting the mean HD values at 115, 135, and 155 mmHg against the average PWV

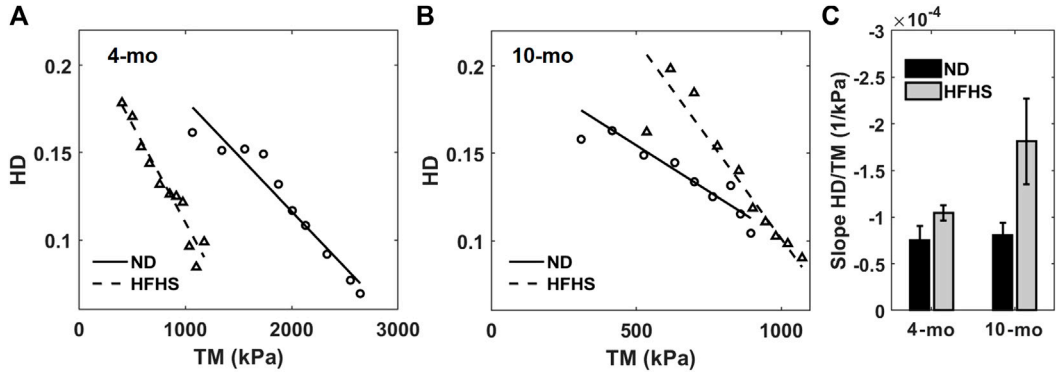

FIGURE 6 | Harmonic distortion from *in vivo* spectral analysis as function of tangent modulus measured by *in vitro* biomechanical testing for the 4-months **(A)** and 10-months mice **(B)**, normal (circles and solid line) and HFHS diet (triangles and dashed line). Linear regressions from each group are also displayed. **(C)** Average slopes of the harmonic distortion vs. tangent modulus linear fitting for the age and diet groups.

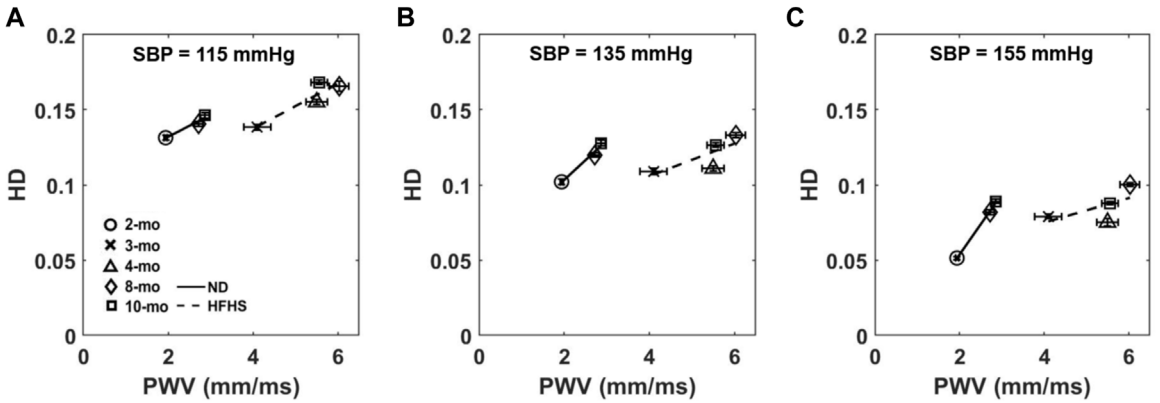

FIGURE 7 | Average HD at 115 mmHg **(A)**, 135 mmHg **(B)**, and 155 mmHg **(C)** is plotted as a function of the group's corresponding average PWV, collected *via* Doppler ultrasound, for each age and diet group.

values for each age and diet group (**Figure 7**). The slopes of the linear fits change at different pressures as well as the slope of the two diet groups. HD increases linearly with PWV for both the control ND group and the HFHS diet group with R^2 values between 0.375 and 0.998. The slopes of the linear relationship for the ND group increase with pressure with slopes being 0.015, 0.026, and 0.040 at 115, 135, and 155 mmHg, respectively. However, the plots for the HFHS groups decrease slightly with slopes being 0.015, 0.011, and 0.008 at 115, 135, and 155 mmHg, respectively.

DISCUSSION

BPW contains information on the coupled interactions among the forward propagating wave, reflected wave, as well as the arterial wall mechanics (Hirata et al., 2006; Ageenkova and Purygina, 2011; van Varik et al., 2012; Theodor et al., 2014). In this study a novel index, HD, was derived from the BPW that was measured *in vivo* using radio telemetry in mice. The nonlinear nature of the wall mechanics combined with the reflected wave alter the BPW by changing the time delay between the forward traveling and reflected waves (Amin et al., 2012) as well as the magnitude of these waves (Ageenkova and Purygina, 2011; Theodor et al., 2014). We hypothesized that HD would be sensitive to such changes. To test this, we studied the relationship between HD and other arterial stiffness measures obtained both *in vitro* and *in vivo*. Our results suggested that HD shows promise in assessing arterial stiffness as demonstrated by the linear correlation between HD and tangent modulus, an *in vitro* measure of arterial stiffness, as well as with PWV, an *in vivo* index of arterial stiffness. Furthermore, the slopes of the relationships show dependence on diet.

Blood Pressure Variability

Both SBP and HD show variability within individual subjects. The BPW has beat-to-beat variability with SBP varying considerably

based on many factors including: PWV, age, 24-h activity level, as well as brain and nerve function (Schillaci et al., 2012; Miao and Su, 2002; Stauss et al., 2008; Yoshimoto et al., 2011). From our results over the course of 24 h, SBP also varies largely with relative day-and-night activity cycles (**Figure 3A**). The distributions of SBP followed a bimodal Gaussian form, containing a low mean and high mean SBP in mice fed ND and HFHS diet (**Figure 3**), which likely corresponds with the day-and-night cycle in which subjects experience variable blood pressures related to their relative activity levels (Vliet et al., 2003; Van Vliet et al., 2006). The SBP distributions (**Figure 3**) indicate that diet-induced metabolic syndrome promotes a greater probability of high SBP. We have noted a significant increase in the low-pressure mode after just 1 month of HFHS diet (p = 0.0303). This suggests that the SBP distribution may contain an earlier manifestation of hypertension than mean BP, as used in a previous study (Weisbrod et al., 2013). High blood pressure is highly associated with increased risk of cardiovascular diseases (Kannel, 2000). Therefore, analysis of BP distribution and variability may provide insight on the physiological changes in cardiovascular function. Despite the variability in SBP and HD, our study shows that HD is linearly related to blood pressure; as SBP increases the corresponding isolated wave's HD decreases (**Figure 4A**). The trend is measurable and consistent within each age and diet group (**Figure 4C**). Elevated blood pressure is a key measure of hypertension and cardiovascular risk, though such elevation is only observed at longer time scales, in the order of months. From our study, it is important to note that beat-to-beat variability exists in SBP and BPWs. Due to the relative activity level, the mice experience high SBP in the young groups (**Figure 3A**) as well as low SBP in the old group. The relationship between HD vs. SBP was established based on the beat-to-beat variability using 20's BPW data. Such short-term fluctuations in SBP and BPW (**Figure 3A** and **Figure 4A**) and their relationships (**Figure 4C**) have demonstrated to be different between the age and diet groups. Additionally, a key finding of our study is that HD is strongly associated with arterial wall stiffness, an independent cardiovascular risk factor that cannot be derived from SBP alone.

Harmonic Distortion Index

HD analysis of the BPW indicates that the BPW undergoes changes with age and diet-induced metabolic syndrome, both of which are linked to changes in arterial wall stiffness (Blacher et al., 1999; Nichols, 2005; Wilkinson et al., 2002; Brooks et al., 2001; Brooks et al., 1999; Wilkinson et al., 2000). The inverse linear relationship between HD and SBP (**Figure 4B**) suggests that HD is sensitive to changes in arterial stiffness, since with higher mean blood pressure, arterial stiffness increases (**Figure 5C**). This is further confirmed by the inverse linear relationship between HD and the tangent modulus (**Figures 6A,B**). At higher blood pressures, there is an increase in arterial stiffness due to the gradual recruitment of collagen fibers in the adventitia (Chow et al., 2014), which would impact the BPW and thus HD. Moreover, with arterial stiffening, the waveform peak is augmented due to the overlapping of the forward and reflected waves (van Varik et al., 2012), leading to higher distortion of the BPW (**Figure 4C**). This overlap is largely originated from increased speed of both wavelets, coupled with earlier reflections during arterial remodeling (van Varik et al., 2012). Spectral decomposition of stress waveforms *via* a Fourier transform has been used in a previous study to characterize mechanical nonlinearity of isolated rat aorta (Imsirovic et al., 2018). Future study is required to understand the role of nonlinear arterial wall properties in relation to HD.

The relationship between HD and arterial stiffness is liable to shift with age and, more significantly, diet. There is also an apparent increase in slope of this relation for each age and diet group (**Figure 6C**). Consistent with previous findings that hypertension develops after 6 months of HFHS diet (Weisbrod et al., 2013), the 8-months HFHS group has significantly higher HD values than the 8-months ND group ($p < 0.001$) (**Table 1**). Further, the two 10-months groups (both ND and HFHS) are not different with regards to their HD trends, which implies that changes due to diet have slowed or subsided by 10-months. Nonetheless, the two old ND groups (8-months and 10-months) contain significantly different HD values (p = 0.008) suggesting change in HD still occurs in ND aging after the mice have reached maturity. In contrast, the 8-months HFHS group's HD values are not significantly different from 10-months HFHS ($p = 0.549$). This supports the idea that changes in the arterial wall mechanics have already occurred in the 8-months HFHS group. The efficacy of detecting this change supports HD as a noninvasive predictor of hypertension which warrants further studies.

HD vs. Pulse Wave Velocity

PWV is a broadly used *in vivo* index of arterial stiffness that measures the velocity of the forward propagating arterial pressure wave (Blacher et al., 1999; Nichols, 2005). When studying the relationship between HD and PWV (**Figure 7**), it is important to note that HD, derived from beat-to-beat BPW, is pressure dependent while PWV is not. We found that HD and PWV to be linearly related but with a diminishing R squared value in the HFHS group related to increasing pressure (**Figure 7**). Further study is needed to better understand the pressure and diet dependency of this relationship. The positive HD-PWV relation is in contrast to that of the tangent modulus and HD, which demonstrated a negative relation (**Figure 6**). While the explanation for this is not entirely clear, these results suggest that the tangent modulus is also negatively related to PWV. Possible explanations include the following. The PWV measurements were made in the abdominal aorta while HD was obtained from BPWs at the aortic arch. Abdominal aorta has been reported to be more severely affected by vascular remodeling (Hayashi et al., 2010), which could account for the more dramatic change seen in PWV with age and diet as compared to HD (**Figure 7**). Notably, the ND and HFHS diet groups follow their own linear paths (**Figure 4C**). It is also important to point out that HD is derived from local BP measurement, taken in a point within the aortic arch where the radiotelemetry is surgically implanted within the mouse,

while PWV is usually obtained over a segment length of ~1 cm. This suggests that HD can potentially be used to reveal the regional dependent condition of the arterial wall, independently of PWV.

When considering HD, it is important to mention arterial impedance as both HD and impedance rely on Fourier transforms of the BPWs (Kelly and Fitchett, 1992). Impedance is calculated by the ratio of Fourier amplitudes from the BPW and velocity waveforms, which provides an impedance modulus and phase over a range of frequencies (Kelly and Fitchett, 1992), and the modulus has been shown to increase with age-related arterial stiffening (Reddy et al., 2003). However, impedance analysis requires invasive methods and it does not consider the effect of BP on Fourier coefficients from BPWs. Previous studies on input impedance have shown inconsistencies when relating impedance directly to PWV after adjusting for factors like mean blood pressure (Mitchell et al., 2002; Segers et al., 2007b). Our results of the HD dependence on SBP (**Figure 4A**) suggest that HD, or the Fourier coefficients, of BPWs change with SBP and such changes should be considered when studying BPW.

LIMITATIONS

Our study has several limitations. Future studies including the 3 and 4 months ND groups may be necessary for direct comparison with the 3 and 4 months HFHS groups, although our previous study showed that the 2, 3, and 4 months ND groups do not show significant differences in arterial stiffness and blood pressure measures (Weisbored et al., 2013). Only male mice were used in this study. Dependence of BPW and HD index on sex also warrants further studies. Additionally, the number of mice should be increased to make quantitative comparisons between HD and tangent modulus among different age and diet groups. The radiotelemetry BPW readings were taken in the aortic arch at the left carotid artery. Due to the proximity of aortic arch and carotid arteries, it was assumed that pressure taken at the arch would be an acceptable estimation of pressure within the carotid artery in order to compare HD derived from BPWs with tangent modulus from direct *in vitro* stiffness. This study uses surgically implanted telemetry for BPW, but other more accessible approaches such as BP tonometry could produce the waveforms required for this analysis (Parry Fung et al., 2004; Feng and DiPetrillo, 2009). PWV was measured over the abdominal aorta. Differences between the material properties and the progression of arterial stiffening varies between arteries (Hayashi et al., 2010) and therefore regional variation in mechanical properties of arteries should be kept in mind while making comparisons. The interference between radiotelemetry and BPW is not known. The HD index cannot differentiate between reflection and local wall properties. Clinical studies are needed to dissect the contribution of individual factors, such as hemodynamics and wall properties, to BPW and HD.

CONCLUSION

BPW contains a wealth of information from the interactions of the forward and backward propagating waves, arterial wall mechanics, and hemodynamics. In this study, HD is proposed as a novel index to assess changes in arterial mechanical function. We showed that HD, obtained based on Fourier transform of individual BPWs, is related to SBP, and other existing *in vitro* and *in vivo* arterial stiffness measures. HD is also sensitive to age and metabolic syndrome-induced changes in BPW. Instruments used to record BPWs are more readily available clinically than instruments used to record flow. Hence, our results demonstrate that HD has the potential to be used as a noninvasive and easily accessible means to assess cardiovascular risk in future clinical settings.

DATA AVAILABILITY STATEMENT

The original contributions presented in the study are included in the article/**Supplementary Material**, further inquiries can be directed to the corresponding author.

ETHICS STATEMENT

The animal study was reviewed and approved by the Boston University Institutional Animal Care and Use Committee (IACUC).

AUTHOR CONTRIBUTIONS

NM performed the BPW analysis. AG performed the *in vitro* biomechanical testing and constitutive modeling. FS performed the *in vivo* BPW and PWV measurements. NM, BS and YZ designed the research. All authors contributed to writing and editing the manuscript.

FUNDING

This research was supported in part by Translational Research in Biomaterials Fellowship Program (TRB) at Boston University T32 EB006359, 2R01HL098028 to YZ, R01 HL136311 to FS and U01 HL-139466 to BS.

SUPPLEMENTARY MATERIAL

The Supplementary Material for this article can be found online at: https://www.frontiersin.org/articles/10.3389/fbioe.2022.842754/full#supplementary-material

REFERENCES

Ageenkova, O. A., and Purygina, M. A. (2011). Central Aortic Blood Pressure, Augmentation Index, and Reflected Wave Transit Time: Reproducibility and Repeatability of Data Obtained by Oscillometry. *Vhrm* 7, 649–656. doi:10.2147/vhrm.s24877

Amin, M., Le, V. P., and Wagenseil, J. E. (2012). Mechanical Testing of Mouse Carotid Arteries: from Newborn to Adult. *JoVE* 60, 3791–3733. doi:10.3791/3733

Ayer, J. G., Harmer, J. A., Marks, G. B., Avolio, A., and Celermajer, D. S. (2010). Central Arterial Pulse Wave Augmentation Is Greater in Girls Than Boys, Independent of Height. *J. Hypertens.* 28, 306–313. doi:10.1097/hjh.0b013e3283332286

Baek, S., Gleason, R. L., Rajagopal, K. R., and Humphrey, J. D. (2007). Theory of Small on Large: Potential Utility in Computations of Fluid-Solid Interactions in Arteries. *Computer Methods Appl. Mech. Eng.* 196, 3070–3078. doi:10.1016/j.cma.2006.06.018

Blacher, J., Asmar, R., Djane, S., London, G. M., and Safar, M. E. (1999). Aortic Pulse Wave Velocity as a Marker of Cardiovascular Risk in Hypertensive Patients. *Hypertension* 33, 1111–1117. doi:10.1161/01.HYP.33.5.1111

Brooks, B. A., Molyneaux, L. M., and Yue, D. K. (2001). Augmentation of Central Arterial Pressure in Type 2 Diabetes. *Diabetic Med.* 18, 374–380. doi:10.1046/j.1464-5491.2001.00479.x

Brooks, B., Molyneaux, L., and Yue, D. K. (1999). Augmentation of Central Arterial Pressure in Type 1 Diabetes. *Diabetes Care* 22, 1722–1727. doi:10.2337/diacare.22.10.1722

Bundy, J. D., Li, C., Stuchlik, P., Bu, X., Kelly, T. N., Mills, K. T., et al. (2017). Systolic Blood Pressure Reduction and Risk of Cardiovascular Disease and Mortality. *JAMA Cardiol.* 2, 775–781. doi:10.1001/jamacardio.2017.1421

Chaturvedi, N. (2007). The burden of Diabetes and its Complications: Trends and Implications for Intervention. *Diabetes Res. Clin. Pract.* 76, S3–S12. doi:10.1016/j.diabres.2007.01.019

Chow, M.-J., Turcotte, R., Lin, C. P., and Zhang, Y. (2014). Arterial Extracellular Matrix: a Mechanobiological Study of the Contributions and Interactions of Elastin and Collagen. *Biophysical J.* 106, 2684–2692. doi:10.1016/j.bpj.2014.05.014

Feng, M., and DiPetrillo, K. (2009). Non-Invasive Blood Pressure Measurement in Mice. *Methods Mol. Biol.* 573, 45–55. doi:10.1007/978-1-60761-247-6_3

Ferruzzi, J., Bersi, M. R., and Humphrey, J. D. (2013). Biomechanical Phenotyping of central Arteries in Health and Disease: Advantages of and Methods for Murine Models. *Ann. Biomed. Eng.* 41, 1311–1330. doi:10.1007/s10439-013-0799-1

Ferruzzi, J., Di Achille, P., Tellides, G., and Humphrey, J. D. (2018). Combining *In Vivo* and *In Vitro* Biomechanical Data Reveals Key Roles of Perivascular Tethering in Central Artery Function. *PLOS ONE* 13, e0201379–21. doi:10.1371/journal.pone.0201379

Ferruzzi, J., Madziva, D., Caulk, A. W., Tellides, G., and Humphrey, J. D. (2018). Compromised Mechanical Homeostasis in Arterial Aging and Associated Cardiovascular Consequences. *Biomech. Model Mechanobiol.* 17, 1281–1295. doi:10.1007/s10237-018-1026-7

Gatzka, C. D., Kingwell, B. A., Cameron, J. D., Berry, K. L., Liang, Y.-L., Dewar, E. M., et al. (2001). Gender Differences in the Timing of Arterial Wave Reflection beyond Differences in Body Height. *J. Hypertens.* 19, 2197–2203. doi:10.1097/00004872-200112000-00013

Gkousioudi, A., Yu, X., Ferruzzi, J., Qian, J., Wainford, R., Seta, F., et al. (2022). Biomechanical Properties of Mouse Carotid Arteries with Diet-Induced Metabolic Syndrome and Aging. *Front. Bioeng. Biotechnol.* accepted. doi:10.3389/fbioe.2022.862996

Glasser, S., Arnett, D. K., McVeigh, G. E., Finkelstein, S. M., Bank, A. J., Morgan, D. J., et al. (1997). Vascular Compliance and Cardiovascular Disease A Risk Factor or a Marker? *Am. J. Hypertens.* 10, 1175–1189. doi:10.1016/s0895-7061(97)00311-7

Goshy, M., Lai-Fook, S. J., and Hyatt, R. E. (1979). Perivascular Pressure Measurements by Wick-Catheter Technique in Isolated Dog Lobes. *J. Appl. Physiol.* 46, 950–955. doi:10.1152/jappl.1979.46.5.950

Hayashi, K., Mani, V., Nemade, A., Aguiar, S., Postley, J. E., Fuster, V., et al. (2010). Variations in Atherosclerosis and Remodeling Patterns in Aorta and Carotids. *J. Cardiovasc. Magn. Reson.* 12, 10. doi:10.1186/1532-429X-12-10

Hayward, C. S., and Kelly, R. P. (1997). Gender-Related Differences in the Central Arterial Pressure Waveform. *J. Am. Coll. Cardiol.* 30, 1863–1871. doi:10.1016/s0735-1097(97)00378-1

Hirata, K., Kawakami, M., and O'Rourke, M. F. (2006). Pulse Wave Analysis and Pulse Wave Velocity A Review of Blood Pressure Interpretation 100 Years after Korotkov. *Circ. J.* 70, 1231–1239. doi:10.1253/circj.70.1231

Imsirovic, J., Bartolák-Suki, E., Jawde, S. B., Parameswaran, H., and Suki, B. (2018). Blood Pressure-Induced Physiological Strain Variability Modulates wall Structure and Function in Aorta Rings. *Physiol. Meas.* 39, 105014. doi:10.1088/1361-6579/aae65f

Jerrard-Dunne, P., Mahmud, A., and Feely, J. (2008). Ambulatory Arterial Stiffness index, Pulse Wave Velocity and Augmentation index - Interchangeable or Mutually Exclusive Measures? *J. Hypertens.* 26, 529–534. doi:10.1097/HJH.0b013e3282f35265

Kannel, W. B. (2000). Elevated Systolic Blood Pressure as a Cardiovascular Risk Factor. *Am. J. Cardiol.* 85, 251–255. doi:10.1016/s0002-9149(99)00635-9

Kannel, W. B., Vasan, R. S., and Levy, D. (2003). Is the Relation of Systolic Blood Pressure to Risk of Cardiovascular Disease Continuous and Graded, or Are There Critical Values? *Hypertension* 42, 453–456. doi:10.1161/01.HYP.0000093382.69464.C4

Kelly, R., and Fitchett, D. (1992). Noninvasive Determination of Aortic Input Impedance and External Left Ventricular Power Output: a Validation and Repeatability Study of a New Technique. *J. Am. Coll. Cardiol.* 20, 952–963. doi:10.1016/0735-1097(92)90198-v

Kim, J., Peruski, B., Hunley, C., Kwon, S., and Baek, S. (2013). Influence of Surrounding Tissues on Biomechanics of Aortic Wall. *Ijecb* 2, 105–107. doi:10.1504/ijecb.2013.056516

Loehr, L. R., Meyer, M. L., Poon, A. K., Selvin, E., Palta, P., Tanaka, H., et al. (2016). Prediabetes and Diabetes Are Associated with Arterial Stiffness in Older Adults: The ARIC Study. *Ajhype* 29, 1038–1045. doi:10.1093/ajh/hpw036

Miao, C.-Y., and Su, D.-F. (2002). The Importance of Blood Pressure Variability in Rat Aortic and Left Ventricular Hypertrophy Produced by Sinoaortic Denervation. *J. Hypertens.* 20, 1865–1872. doi:10.1097/00004872-200209000-00033

Mitchell, G. F. (2008). Clinical Achievements of Impedance Analysis. *Med. Biol. Eng. Comput.* 47, 153–163. doi:10.1007/s11517-008-0402-3

Mitchell, G. F., Conlin, P. R., Dunlap, M. E., Lacourciere, Y., Arnold, J. M. O., Ogilvie, R. I., et al. (2008). Aortic Diameter, Wall Stiffness, and Wave Reflection in Systolic Hypertension. *Hypertension* 51, 105–111. doi:10.1161/hypertensionaha.107.099721

Mitchell, G. F., Izzo, J. L., Lacourciere, Y., Ouellet, J.-P., Neutel, J., Qian, C., et al. (2002). Omapatrilat Reduces Pulse Pressure and Proximal Aortic Stiffness in Patients with Systolic Hypertension. *Circulation* 105, 2955–2961. doi:10.1161/01.cir.0000020500.77568.3c

Mitchell, G. F., Wang, N., Palmisano, J. N., Larson, M. G., Hamburg, N. M., Vita, J. A., et al. (2010). Hemodynamic Correlates of Blood Pressure across the Adult Age Spectrum. *Circulation* 122, 1379–1386. doi:10.1161/circulationaha.109.914507

Nichols, W. (2005). Clinical Measurement of Arterial Stiffness Obtained from Noninvasive Pressure Waveforms. *Am. J. Hypertens.* 18, 3–10. doi:10.1016/j.amjhyper.2004.10.009

O'Rourke, M. F., O'Brien, C., and Edelman, E. R. (2016). Arterial Stiffening in Perspective: Advances in Physical and Physiological Science over Centuries:. *Ajhype* 29, 785–791. doi:10.1093/ajh/hpw019

Parry Fung, P., Dumont, G., Ries, C., Mott, C., and Ansermino, M. (2004). "Continuous Noninvasive Blood Pressure Measurement by Pulse Transit Time," in IEMBS'04. 26th Annual International Conference of the IEEE (IEEE), 2239–2242. doi:10.1109/iembs.2004.1403264

Reddy, A. K., Li, Y.-H., Pham, T. T., Ochoa, L. N., Treviño, M. T., Hartley, C. J., et al. (2003). Measurement of Aortic Input Impedance in Mice: Effects of Age on Aortic Stiffness. *Am. J. Physiology-Heart Circulatory Physiol.* 285, H1464–H1470. doi:10.1152/ajpheart.00004.2003

Roman, M. J., Ganau, A., Saba, P. S., Pini, R., Pickering, T. G., and Devereux, R. B. (2000). Impact of Arterial Stiffening on Left Ventricular Structure. *Hypertension* 36, 489–494. doi:10.1161/01.hyp.36.4.489

Rucka, D., Marek, J., Rucklova, Z., Lubanda, J.-C., Havranek, S., Skvaril, J., et al. (2015). Arterial Stiffening Contributes to Impairment of Cerebrovascular

Reactivity in Patients with Coronary Artery Disease without Carotid Stenosis. *Physiol. Res.* 64, 335–343. doi:10.33549/physiolres.932837

Schillaci, G., Bilo, G., Pucci, G., Laurent, S., Macquin-Mavier, I., Boutouyrie, P., et al. (2012). Relationship between Short-Term Blood Pressure Variability and Large-Artery Stiffness in Human Hypertension. *Hypertension* 60, 369–377. doi:10.1161/HYPERTENSIONAHA.112.197491

Segers, P., Rietzschel, E. R., De Buyzere, M. L., de Bacquer, D., van Bortel, L. M., de Backer, G., et al. (2007). Assessment of Pressure Wave Reflection: Getting the Timing Right!. *Physiol. Meas.* 28, 1045–1056. doi:10.1088/0967-3334/28/9/006

Segers, P., Rietzschel, E. R., de Buyzere, M. L., Vermeersch, S. J., de Bacquer, D., van Bortel, L. M., et al. (2007). Noninvasive (Input) Impedance, Pulse Wave Velocity, and Wave Reflection in Healthy Middle-Aged Men and Women. *Hypertension* 49, 1248–1255. doi:10.1161/HYPERTENSIONAHA.106.085480

Stauss, H. M., Petitto, C. E., Rotella, D. L., Wong, B. J., and Sheriff, D. D. (2008). Very Low Frequency Blood Pressure Variability Is Modulated by Myogenic Vascular Function and Is Reduced in Stroke-Prone Rats. *J. Hypertens.* 26, 1127–1137. doi:10.1097/HJH.0b013e3282fb81c8

Sun, Z. (2015). Aging, Arterial Stiffness, and Hypertension. *Hypertension* 65, 252–256. doi:10.1161/HYPERTENSIONAHA.114.03617

Theodor, M., Fiala, J., Ruh, D., Förster, K., Heilmann, C., Beyersdorf, F., et al. (2014). Implantable Accelerometer System for the Determination of Blood Pressure Using Reflected Wave Transit Time. *Sensors Actuators A: Phys.* 206, 151–158. doi:10.1016/j.sna.2013.12.006

van Varik, B. J., Rennenberg, R. J. M. W., Reutelingsperger, C. P., Kroon, A. A., de Leeuw, P. W., and Schurgers, L. J. (2012). Mechanisms of Arterial Remodeling: Lessons from Genetic Diseases. *Front. Gene* 3, 1–10. doi:10.3389/fgene.2012.00290

Van Vliet, B. N., McGuire, J., Chafe, L., Leonard, A., Joshi, A., and Montani, J.-P. (2006). Phenotyping the Level of Blood Pressure by Telemetry in Mice. *Clin. Exp. Pharmacol. Physiol.* 33, 1007–1015. doi:10.1111/j.1440-1681.2006.04479.x

Vliet, B. N., Chafe, L. L., and Montani, J. P. (2003). Characteristics of 24 H Telemetered Blood Pressure in eNOS-Knockout and C57Bl/6J Control Mice. *J. Physiol.* 549, 313–325. doi:10.1113/jphysiol.2003.041897

Weisbrod, R. M., Shiang, T., Al Sayah, L., Fry, J. L., Bajpai, S., Reinhart-King, C. A., et al. (2013). Arterial Stiffening Precedes Systolic Hypertension in Diet-Induced Obesity. *Hypertension* 62, 1105–1110. doi:10.1161/HYPERTENSIONAHA.113.01744

Wilkinson, I. B., MacCallum, H., Flint, L., Cockcroft, J. R., Newby, D. E., and Webb, D. J. (2000). The Influence of Heart Rate on Augmentation index and central Arterial Pressure in Humans. *J. Physiol.* 525, 263–270. doi:10.1111/j.1469-7793.2000.t01-1-00263.x

Wilkinson, I. B., Prasad, K., Hall, I. R., Thomas, A., MacCallum, H., Webb, D. J., et al. (2002). Increased Central Pulse Pressure and Augmentation Index in Subjects with Hypercholesterolemia. *J. Am. Coll. Cardiol.* 39, 1005–1011. doi:10.1016/s0735-1097(02)01723-0

Yambe, M., Tomiyama, H., Hirayama, Y., Gulniza, Z., Takata, Y., Koji, Y., et al. (2004). Arterial Stiffening as a Possible Risk Factor for Both Atherosclerosis and Diastolic Heart Failure. *Hypertens. Res.* 27, 625–631. doi:10.1291/hypres.27.625

Yoshimoto, T., Eguchi, K., Sakurai, H., Ohmichi, Y., Hashimoto, T., Ohmichi, M., et al. (2011). Frequency Components of Systolic Blood Pressure Variability Reflect Vasomotor and Cardiac Sympathetic Functions in Conscious Rats. *J. Physiol. Sci.* 61, 373–383. doi:10.1007/s12576-011-0158-7

Conflict of Interest: The authors declare that the research was conducted in the absence of any commercial or financial relationships that could be construed as a potential conflict of interest.

Publisher's Note: All claims expressed in this article are solely those of the authors and do not necessarily represent those of their affiliated organizations, or those of the publisher, the editors and the reviewers. Any product that may be evaluated in this article, or claim that may be made by its manufacturer, is not guaranteed or endorsed by the publisher.

frontiers | Frontiers in Bioengineering and Biotechnology

ORIGINAL RESEARCH
published: 13 April 2022
doi: 10.3389/fbioe.2022.854109

In Vitro Study of Endothelial Cell Morphology and Gene Expression in Response to Wall Shear Stress Induced by Arterial Stenosis

Lizhong Mu[1], Xiaolong Liu[1], Mengmeng Liu[2], Lili Long[1], Qingzhuo Chi[1], Ying He[1], Yue Pan[2,3], Changjin Ji[4], Ge Gao[5] and Xiaona Li[6]*

[1]Key Laboratory of Ocean Energy Utilization and Energy Conservation of Ministry of Education, School of Energy and Power Engineering, Dalian University of Technology, Dalian, China, [2]Schood of Chemical Engineering, Dalian University of Technology, Dalian, China, [3]Ningbo Institute, Dalian University of Technology, Ningbo, China, [4]School of Biomedical Engineering, Capital Medical University, Beijing, China, [5]The First Affiliated Hospital of University of Science and Technology of China, Hefei, China, [6]Key Laboratory of Industrial Ecology and Environmental Engineering (MOE), School of Environmental Science and Technology, Dalian University of Technology, Dalian, China

Objectives: We examined the correlation between changes in hemodynamic characteristics induced by arterial stenosis and vascular endothelial cell (EC) morphology and gene expression in straight silicone arteries.

Materials and methods: Transparent silicone straight artery models with four degrees of stenosis (0, 30, 50, and 70%) were fabricated. Particle image velocimetry was performed to screen silicone vessel structures with good symmetry and to match the numerical simulations. After the inner surface of a symmetric model was populated with ECs, it was perfusion-cultured at a steady flow rate. A computational fluid dynamics (CFD) study was conducted under the same perfusion conditions as in the flow experiment. The high-WSS region was then identified by CFD simulation. EC morphology in the high-WSS regions was characterized by confocal microscopy. ECs were antibody-stained to analyze the expression of inflammatory factors, including matrix metalloproteinase (MMP)-9 and nuclear factor (NF)-κB, which were then correlated with the CFD simulations.

Results: As the degree of vascular stenosis increases, more evident jet flow occurs, and the maximum WSS position moves away first and then back. ECs were irregularly shaped at vortex flow regions. The number of gaps between the cells in high-WSS regions increased. The MMP-9 and NF-κB expression did not differ between vessels with 30 and 0% stenosis. When arterial stenosis was 70%, the MMP-9 and NF-κB expression increased significantly, which correlated with the regions of substantially high WSS in the CFD simulations.

Conclusion: Stenotic arteries induce hemodynamic stress variations, which contribute to differences in EC morphology and gene expression. A high degree of vascular stenosis can directly increase inflammatory factor expression.

Keywords: vascular stenosis, silicone-endothelial cell model, wall shear stress, inflammatory factor, EC morphology

OPEN ACCESS

Edited by:
Katherine Yanhang Zhang, Boston University, United States

Reviewed by:
Shengzhang Wang, Fudan University, China
Duanduan Chen, Beijing Institute of Technology, China

****Correspondence:***
Yue Pan
panyue0811@dlut.edu.cn

Specialty section:
This article was submitted to Biomechanics, a section of the journal Frontiers in Bioengineering and Biotechnology

Received: *13 January 2022*
Accepted: *03 March 2022*
Published: *13 April 2022*

Citation:
Mu L, Liu X, Liu M, Long L, Chi Q, He Y, Pan Y, Ji C, Gao G and Li X (2022) In Vitro Study of Endothelial Cell Morphology and Gene Expression in Response to Wall Shear Stress Induced by Arterial Stenosis. Front. Bioeng. Biotechnol. 10:854109. doi: 10.3389/fbioe.2022.854109

INTRODUCTION

Atherosclerosis, one of the most common arterial diseases, seriously threatens human health. Artery stenosis caused by the presence of plaque is its typical feature (Gao et al., 2021), which often gives rise to the cardiovascular and cerebrovascular diseases, such as coronary atherosclerosis and carotid artery stenosis (Gorelick et al., 2008). An aneurysm is a local pathological congestive dilation of blood vessels caused by disease or weakening of the blood vessel wall. It is characterized by local arterial dilation and presents as a thin, distensible sac that is at risk of rupture (Sforza et al., 2009).

Post-stenotic dilation of artery is a common phenomenon in clinical diagnosis. Multiple stenoses are common in the arteries as are post-stenotic dilation of the artery (Moore, 1990). Post-stenotic dilatation of the coronary arteries can occur at high flow rates, possibly due to the wall shear stress following the constriction (Pincombe et al., 1999). In addition, clinical statistics show that in patients with intracranial artery stenosis, the proportion of the aneurysm with proximal stenosis is about 12.3%, significantly higher than the general incidence of 2–6% of intracranial aneurysm in the population (Rinkel et al., 1998). Clinical data show that *de novo* cerebral aneurysm formation is often accompanied by some degree of proximal artery stenosis (Jou et al., 2010; Kono et al., 2013; Ferns et al., 2011; Kono et al., 2014). Owing to jet flow caused by stenosis, the maximum WSS and WSSG at the aneurysm initiation site were approximately doubled and tripled, respectively (Kono et al., 2014). However, it is still unclear about the mechanobiological mechanism of how artery stenosis causes the dilation of the post-stenotic artery and how genetic expression variations respond to arterial stenosis.

It is known that the occurrence and growth of aneurysms are thought to be closely associated with abnormal hemodynamic changes, which regulate vascular biology and pathology. Interactions between biological and hemodynamic factors can cause complex arterial wall remodeling (Meng et al., 2007). Arterial endothelial cells (ECs) physiologically respond to wall shear stress (WSS) and WSS gradients (WSSGs). Computational fluid dynamics (CFD) is commonly used to evaluate hemodynamic flow and WSS/WSSG in the patient-specific vascular geometry under physiological conditions. Many studies have found that aneurysms predominantly occur at regions of high WSS (Kondo et al., 1997; Alfano et al., 2013) and that aneurysm initiation sites are correlated with high WSS (Chen et al., 2013), especially with high positive WSSGs (Metaxa et al., 2010). A major drawback of existing CFD studies is that the methods used have made it difficult to directly link the pathological effects of hemodynamic variables, such as WSS and WSSG, on biological tissues (Lu et al., 2011; Luo et al., 2011). However, the use of *in vitro* vascular models with an endothelial lining is a feasible approach to study the association between biological changes and flow dynamics (Kaneko et al., 2018; Levitt et al., 2019; Jang et al., 2020).

The EC layer is a direct barrier that isolates blood flow from the vascular wall. It is sensitive to fluid shear stress and changes in shear force caused by local flow changes. In the physiological environment, arterial WSS is around 1–2 Pa, while venous WSS is around 0.1–0.6 Pa (Kamiya et al., 1984). When the WSS exceeds the physiological threshold, ECs undergo morphological changes. Therefore, the EC layer is the earliest receptor and effector of vascular remodeling. In addition, WSS-driven EC inflammation is the first step in aneurysm formation, and nuclear factor (NF)-κB is a major inflammatory factor that mediates this step (Signorelli et al., 2018). Subsequently, proteolytic destruction of the vascular extracellular matrix by matrix metalloproteinases (MMPs) leads to aneurysm formation or rupture. MMPs and NF-κB produced in the ECs are overexpressed in aneurysm tissue (Kataoka, 2015), which is evidence of inflammation in the aneurysm occurrence.

To investigate the correlation between flow shear variations induced by vascular stenosis and the morphology and function of ECs, we carried out the *in vitro* experiments of silicone stenotic artery populated by ECs and established the relation between the artery stenosis degree and the MMPs and NF-κB expression, and the relation between the MMPs and NF-κB expression and high/low WSS.

MATERIALS AND METHODS

Fabrication of a Silicone Vascular Model

Straight transparent silicone vascular replicas with four degrees of stenosis (0, 30, 50, and 70%) were fabricated based on our brush-spin-coating method (Chi et al., 2021). An inner diameter of 5.5 mm was chosen based on the average diameter of the internal carotid artery (Liang et al., 2016). Vessel stenosis (*st*) was defined as follows: $st = (1 - d/D) \times 100\%$, where d and D are the diameters of the narrowest and normal regions, respectively.

Briefly, the vascular cores were first designed in ANSYS SpaceClaim (v17.0, ANSYS Inc., US) and saved as stereolithographical files, which were then imported into the bundled slicing software of a three-dimensional (3D) printer (Creator Pro, Zhejiang Flashforge 3D Technology, Zhejiang, China). The vascular cores of water-soluble poly(vinyl alcohol) (PVA) were generated (**Figure 1A**). The stair-like surfaces of these vascular cores were smoothened and coated with a transparent polydimethylsiloxane (PDMS; Sylgrad 184 Silicone Elastomer, US) solution to form a thin silicone layer, with a thickness of approximately 0.3 mm. A transparent silicone vascular replica was finally obtained by dissolving the PVA core in a water bath (**Figure 1B**). **Figure 1C** shows a silicone tube of 30% stenosis in glycerol and aqueous solution with a weight ratio of 1:1. When the silicone tube was submerged in the glycerol and aqueous solution, it shows a good transparency.

With consideration of that, the roughness of inner surface of the silicone tube is the main factor that influences the transparency of the silicone tube. In addition, it also makes a certain impact on the culture of ECs. Two operation specifications were adopted to smooth the inner surface of silicone tube and ensure the transparency of the silicone tube. The first step is to eliminate the stair-like texture of the water-soluble inner core. The water-soluble core is completely dipped into water 3 times, each time for 30 s, and the interval of 5 min after each dipping. The water will dissolve the texture on the

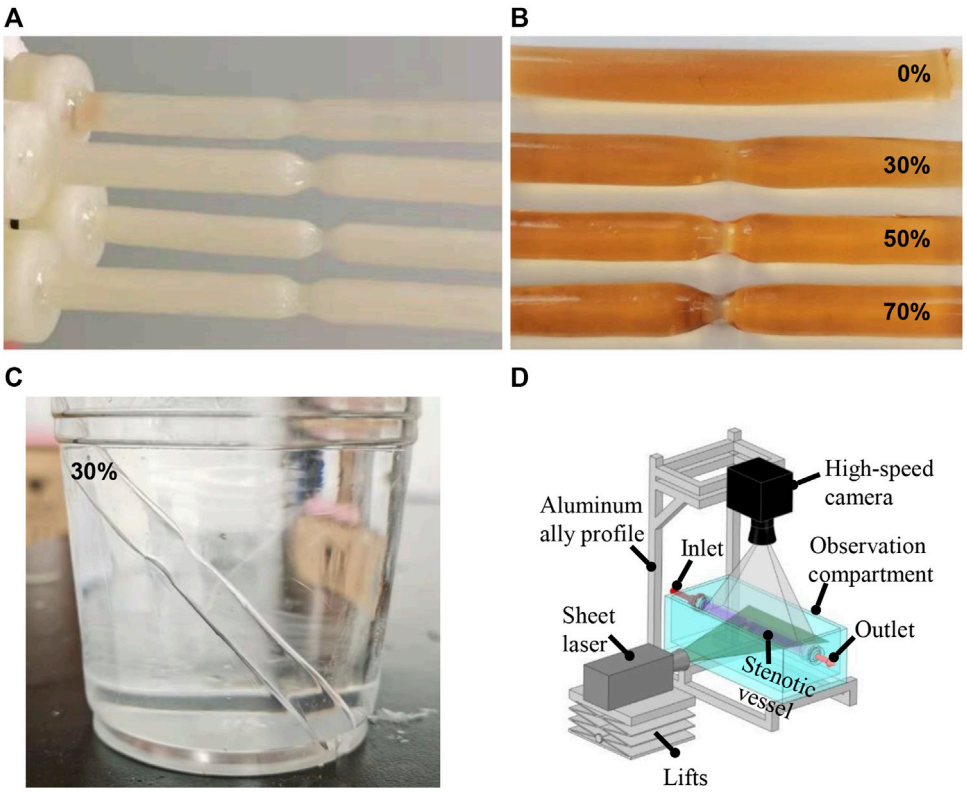

FIGURE 1 | Water-soluble inner core **(A)** and silicone vessels **(B)** with different degrees of stenosis. Silicone tube in glycerol and aqueous solution with the weight ratio of 1:1 **(C)**. PIV experimental setup **(D)**.

surface of the core. After rinsing, the core is dried in a constant temperature oven at 40°C. And the second step is to further polish the inner surface of the silicone tube. The silicone tube was dipped into the same silicone liquid for 3 s, and a 0.7 MPa high-pressure air flow was then used to blow off the excess silicone on the wall of the tube for about 1 min, and then the treated silicone tube was dried at 60°C.

Particle Image Velocimetry Analysis

As Varghese et al. (Varghese et al., 2007) reported that the flow field of the straight tube with a stenosis is extremely sensitive to the stenosis symmetry, and even a slight asymmetry can have a significant impact on the recirculation after stenosis and WSS distribution, which will differ from the CFD simulations in an extremely symmetric model. It will directly result in the variations of high-and low-WSS regions. Two smoothing treatments of silicone tube (as mentioned in *Section Fabrication of a Silicone Vascular Model*) may result in the asymmetry of the stenosis model to some extent. Hence, the main objective of the PIV study is to screen the stenosis vascular model with a symmetrical flow field and verify the CFD results.

PIV was performed using a high-speed camera (Photron, Fastcam-Mini UX 50, 2000 frames per second) with a continuous-pulse laser (MGL, 10 W, 532 nm, Changchun Institute of Laser Electronics, Changchun, China) for all the silicone vascular models before populating with human umbilical vein ECs (HUVECs) (**Figure 1D**). A solution of fluorescent beads was prepared containing 3.49% polyamide particles with a diameter of 20 μm suspended in glycerine aqueous solution with a weight ratio of 4:6. The bead solution was perfused through the silicone model using a peristaltic pump (BL600H, Baoding Zhunze Precision Pump Manufacturing Co. Ltd.) with a volumetric flow rate of 240 ml/min. PIV was focused on the predetermined positions with the stenosed region and its downstream region, and Z-plane imaging was performed through the central axis of the vessel. The PIV images were imported and processed using open source software (PIVLab in MATLAB) to screen the silicone vascular models with an axisymmetric flow and to validate the CFD simulation results.

Cell Culture Within 3D Rotation and Flow State

The clean, sterilized, and fibronectin-coated silicone models were populated with HUVECs under 3D rotation. Each model was exposed to a culture medium under flow for 24 h to set up a perfusion cell culture.

When setting up the adherent cell culture, the surface of each silicone model was first cleaned with a 75% ethanol solution for 2 h followed by a plasma cleaner. The model was then sterilized on a sterile table by ultraviolet irradiation for 30 min. To enhance EC adhesion to the PDMS, the inner surfaces of the vascular replicas were twice coated with fibronectin at 40 μg/ml for 30 s and dried in a 37°C incubator. ECs were cultured in a growth

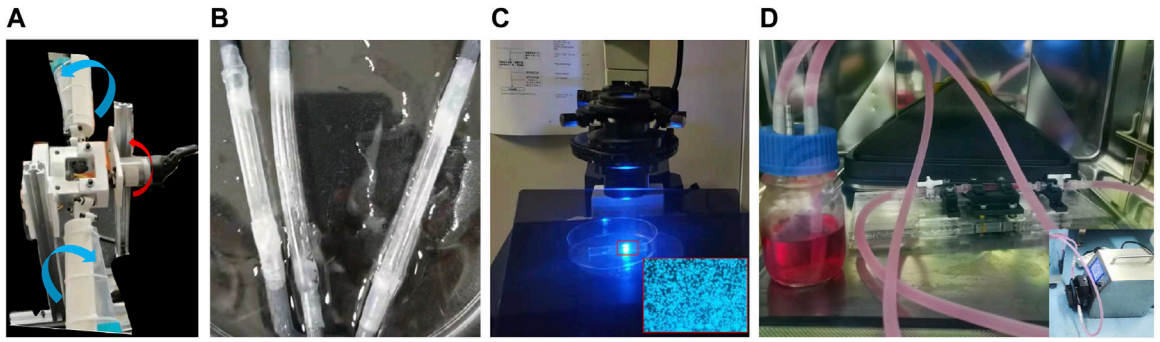

FIGURE 2 | Biaxial rotating mechanism **(A)**, the endothelialized vascular model **(B)** and its observation under the inverted microscope **(C)**, and the device used for perfusion cell culture **(D)**.

medium comprising Eagle's minimum essential medium, 10% fetal bovine serum, penicillin, and streptomycin. The silicone replicas were then immersed in a cell suspension (10^7 cells/mL), packed into a centrifuge tube covered with a cap containing a filter for gas exchange, and rotated in a carbon dioxide (CO_2) incubator at a rate of 0.25 rad/min with a biaxial rotating mechanism (**Figure 2A**). The two rotation directions are shown in blue and red arrows in **Figure 2A**. The HUVECs were adhered to the inner wall of the silicone vessels around 48 h later (**Figure 2B**), as shown in the inverted microscope (Olympus, IX73) image (**Figure 2C**).

During the perfusion cell culture, the endothelialized vascular models with different degrees of stenosis were connected to an experimental system consisting of silicone pipes, a peristaltic pump, and a liquid storage bottle with a gas exchange membrane. The EC culture medium, which contained 5% dextran (at a viscosity of 3.9 cPa), was delivered to the experimental system in a CO_2 incubator (**Figure 2D**). An approximate steady flow rate of 240 ml/min (Tanaka et al., 2006) was provided by the peristaltic pump connected with a buffer for 24 h, and the experimental conditions were maintained for each degree of stenosis tested.

Computational Fluid Dynamics Simulation

The geometric model of the stenosed artery used for the CFD simulation exactly replicated the model used for the experiment. Based on grid independence verification, a 0.2 mm mesh size was selected. The narrow part of the model required local mesh refinement, and the total number of grid points was approximately 700,000. The convergence standard of the Navier–Stokes equation was set to 10^{-6}. The inlet velocity was derived from the experimental velocity, and a uniform inlet velocity boundary condition is applied. In order to obtain a fully developed inlet flow, the length of inlet section is taken as 35 mm in the geometric model, which is about 6.4 times the inner diameter of the tube. Blood was assumed to be an incompressible Newtonian fluid with a dynamic viscosity of 0.0035 Pa·s and a density of 1,060 kg/m^3, and the wall was assumed to be rigid with no-slip boundary conditions. The outlet boundary was a zero-pressure outlet. The WSS and streamline distribution were then obtained.

When the Reynolds number (Re) was <2,300, the blood flow state of the vessels was considered to be laminar, and the laminar flow model was set. However, the jet flow and flow separation occur in the downstream regions of stenosis, and severe stenosis can induce local turbulence (Varghese et al., 2007). For the 30 and 50% stenosis models, the laminar flow model was carried out. While for the 70% stenosis model, there was an evident jet flow in the narrow part (see the white circle, **Figure 3A**), and turbulent disturbance appeared due to the jet flow with much high flow rate, as the white box indicated in **Figure 3A**. With the consideration of the low Reynolds number, the SST k–ω model can simulate the simultaneous existence of laminar, transition, and turbulent flows more accurately than other laminar or turbulent models (Chi et al., 2021), the SST k-ω model was then adopted.

Therefore, the SST k-ω model was selected for the 70% stenosis model with a local Re number of >2,300 in ANSYS 2019 Fluent. This model can more accurately simulate the concomitant existence of laminar flow, transition flow, and turbulence (Wilcox, 1994).

Endothelial Cell Morphometry and Gene Expression Analyses

ECs cultured on the inner surfaces of the vascular replicas were first washed with phosphate-buffered saline three times. Cultured ECs were then fixed in 4% paraformaldehyde. During immunofluorescent staining, the intracellular catalase was first removed using 3% hydrogen peroxide. Non-specific binding was blocked by incubating the cells with 1% rabbit serum (cat. ab7356; Abcam). The cells were stained with 4′,6-diamidino-2-phenylindole. The cells were then incubated with anti-mouse CD31 antibody (cat. 3528; CST) and either anti-rabbit NF-κB antibody (cat. ab32536; Abcam) or anti-rabbit MMP-9 antibody (cat. ab76003; Abcam) in a moist box overnight at 4°C. The following day, the cells were treated with CoraLite488-conjugated goat anti-rabbit IgG antibody (cat. SA00013-2; Proteintech) and tetramethylrhodamine-conjugated goat anti-mouse IgG antibody (cat. SA0007-1; Proteintech). Each vascular replica was then cut into pieces to examine the different regions. Finally, the images of the samples were captured at 40 × magnification using a laser scanning confocal microscope.

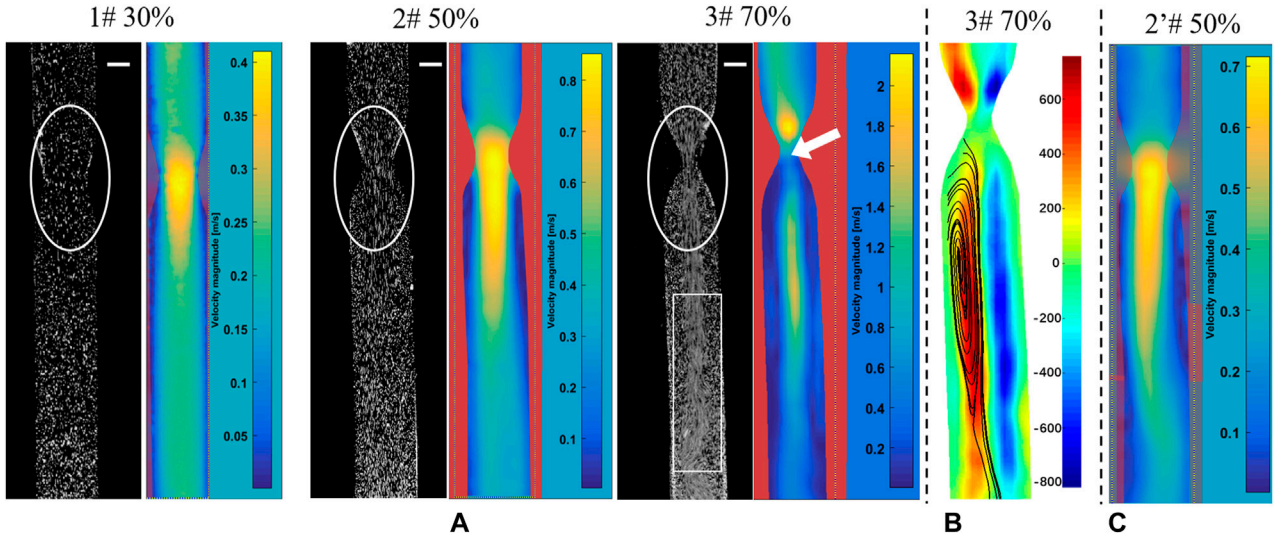

FIGURE 3 | PIV measurements to screen for silicone vessel structures with good symmetry. The snapshots in PIV experiments and flow distribution **(A)**, vorticity distribution **(B)**, and flow distribution **(C)** in a vessel with 50% stenosis. The bar scale is 2 mm.

RESULTS

Particle Image Velocimetry Measurement

Figure 3A presents the snapshots in PIV experiments and the PIV post-processed results of flow distribution, which were used to examine the silicone vessel structure with good symmetry to exclude the asymmetric model caused by model smooth treatments. The stenosed silicone tubes (1#, 2#, and 3#) had a good symmetry in terms of the velocity distribution based on the post-processed PIV results. **Figure 3B** presents the vorticity distribution in the silicone vessel with 70% stenosis. The blue and red contours represent two vortices with reverse rotation with an almost symmetric distribution. **Figure 3C** shows the flow injection through the narrow part impinged on the sidewall of the tube, which was caused by asymmetric stenosis. It was reported that asymmetric stenosis affects the extent of post-stenotic recirculation and WSS distribution, which are sensitive to blood vessel geometry (Varghese et al., 2007; Haley et al., 2021). Hence, PIV measurements play an important role in screening the vascular model of stenosis with a symmetrical flow field.

In addition, the comparisons of experimental snapshots indicated in **Figure 3A**, which are with particles in different stenotic tubes captured using a high-speed camera. It can be seen that there is more evident jet flow in the narrow part with the stenosis degree increase, in particular in the model of 70% stenosis, as the white circle indicated. However, due to the limited frame rate of 2000 fps of high-speed camera in this experiment, there is a clear trailing effect of the moving particles, especially in the model of 70% stenosis. The particles are not easy to be captured in the high jet flow state, and the positions of particles are hard to be determined. It will be difficult for the PIV analysis based on the comparison of the relative position changes of particles at two adjacent moments. That is the reason why the high velocity distribution was not detected in the PIV result in the model with 70% stenosis, as the white arrow indicated.

Validation of the Numerical Simulation Results

Figure 4 shows the numerical simulation results of flow distribution in three vascular models of stenosis. The comparisons of flow and vorticity between the PIV (**Figures 3A,B**) and CFD (**Figures 4A,B**) results are also shown. The CFD results demonstrate good agreement with the PIV measurements in terms of the flow and vorticity distribution. Thus, the selection of the related fluid models for the numerical calculation is reasonable and reliable.

Computational Fluid Dynamics Results

The WSS distribution and streamlines of the straight arteries with different degrees of stenosis were simulated by CFD using the same structural data used for 3D printing. **Figure 5A** shows the streamline and the WSS distribution in the downstream region of the vessel with 70% stenosis. The red contour shows the region in which the WSS values were >2.5 Pa. PIV revealed a clear vortex located downstream of the stenosed region (**Figure 3B**), and the high WSS was located close to the vortex. The distribution of WSS and the location of maximum WSS downstream of the 70% stenosed region are shown in **Figure 5B**. **Figure 5C** shows the location with the maximum WSS and the value distribution in different stenosed structures. The maximum WSS increased as the degree of stenosis increased. When the degree of stenosis was <50%, the maximum WSS was within 1.0 Pa. As the degree of stenosis reached 50%, the maximum WSS was >1.0 Pa. This value

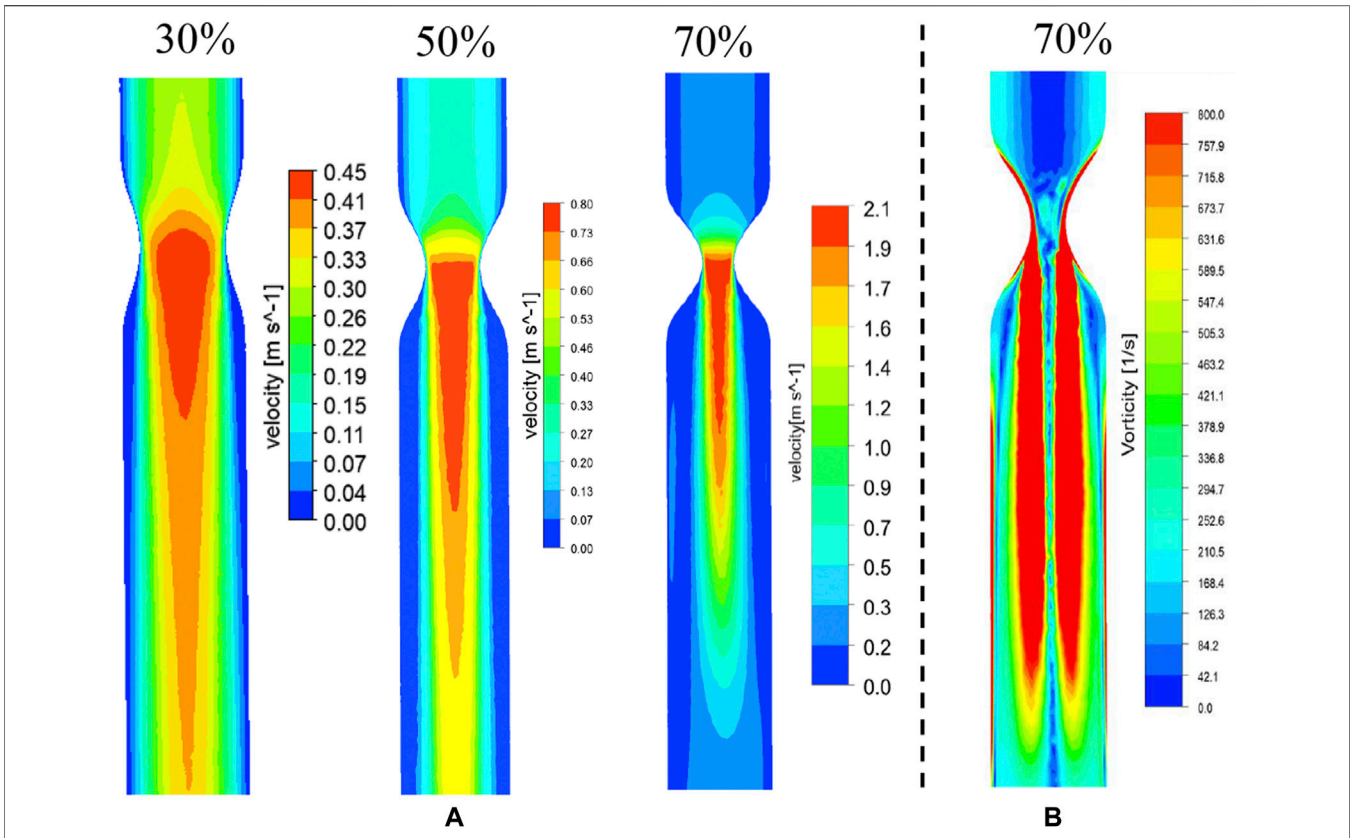

FIGURE 4 | CFD results of flow **(A)** and vorticity **(B)** distribution in vascular structures with different degrees of stenosis.

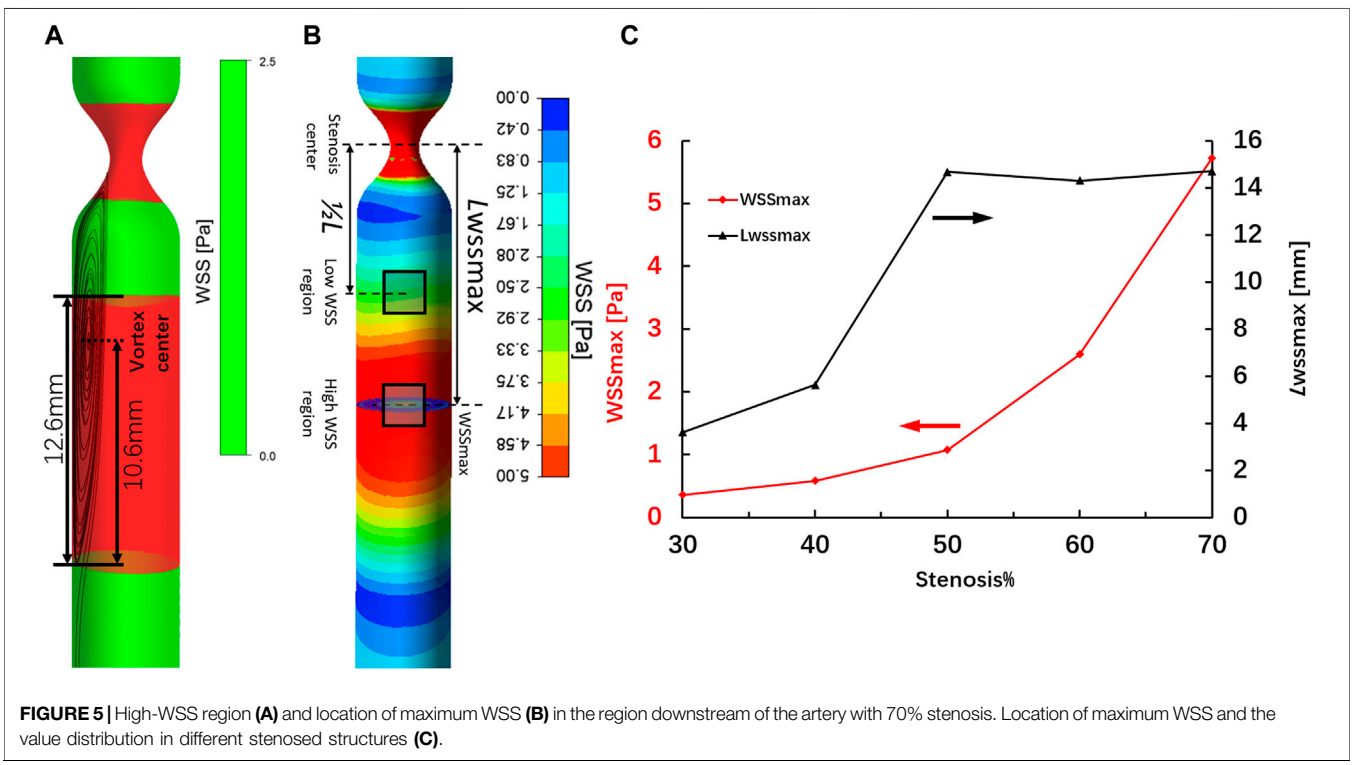

FIGURE 5 | High-WSS region **(A)** and location of maximum WSS **(B)** in the region downstream of the artery with 70% stenosis. Location of maximum WSS and the value distribution in different stenosed structures **(C)**.

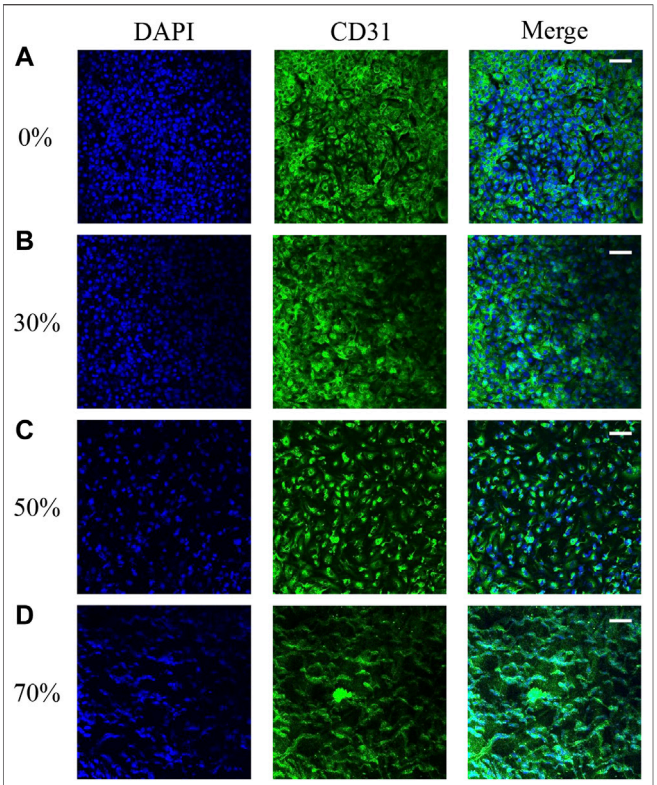

FIGURE 6 | EC morphology in 0 **(A)**, 30 **(B)**, 50 **(C)**, and 70% **(D)** stenosed structures under flow stimulation.

increased to >5.0 Pa when the degree of stenosis reached 70%. In addition, the location of maximum WSS first moved forward along the flow direction as the degree of stenosis increased, and backward against the flow after the degree of stenosis reached 50–70%. The maximum WSS was located 14–16 mm away from the center of the stenosed region.

Endothelial Cell Morphology After the Flow Stimulation

Our hemodynamic analysis showed contrasting results in vortex regions with different degrees of stenosis. The changes in EC morphology after flow culture, especially in ECs located at the regions of maximum WSS downstream of stenosis in the vascular replica, were investigated by confocal microscopy. The microscopy images show that the cytoskeletal F-actin in ECs was stained with rhodamine–phalloidin after flow stimulation induced by different degrees of stenosis. The images also show that the inner surfaces of the silicone vessels with 0 and 30% stenosis were evenly covered with ECs (**Figures 6A,B**). As the degree of stenosis increased, the ECs located downstream of 50% stenosis became elongated in the longitudinal direction. The ECs located at regions of maximum WSS downstream of stenosis showed irregular alignment due to the existence of the vortex (**Figures 6C,D**). Moreover, the gaps between the cells increased as the degree of stenosis increased (**Figures 6B–D**). In particular, when the degree of vascular stenosis reached 70%, there were clear gaps between the cells, and the EC morphology clearly changed into an undulating-ribbon structure. Kamiya reported that in physiological environments, arterial WSS is around 1–2 Pa (Kamiya et al., 1984). The flow shear induced by stenosis of <50% does not exceed the physiological range that the cell is subjected to; thus, EC morphology does not change noticeably.

Endothelial Cell Gene Expression After Flow Stimulation

We harvested ECs from the model of stenosis for gene expression analysis. The ECs were obtained downstream from the surrounding regions of maximum WSS after flow stimulation. The expression of two key vascular inflammatory factors (MMP-9 and NF-κB) is shown in **Figure 7**. The expression of MMP-9 and NF-κB in ECs from vessels with 0% stenosis did not differ from that in ECs from vessels with 30% stenosis. However, the expression of MMP-9 and NF-κB appeared to be higher in regions downstream of higher WSS due to the greater degree of stenosis. In particular, in vessels with 70% stenosis, there was a significant increase in MMP-9 and NF-κB expression. The increase in MMP-9 and NF-κB expression was correlated with substantially high vortex regions and higher WSS values downstream of stenosis (**Figure 5**). A previous study showed that the expression of inflammatory factors is consistent with variations in EC morphology, which can be explained by a stenosis degree of >50%, and WSS induced by stenosis exceeds the physiological range of the cell (Kamiya et al., 1984).

In addition, we further compared the relative fluorescence intensities of MMP-9 and NF-κB at the high-WSS (adjacent to the maximum WSS location, ~ L_{WSSmax}) and low-WSS regions (~1/2 L_{WSSmax}) as indicated in **Figure 5B**. The relative fluorescence intensities of MMP-9 and NF-κB were obtained by comparing the fluorescence intensity of current images with the one in the model of 0% stenosis located high-WSS region. As **Figures 8A,B** indicated, the expression levels of MMP-9 and NF-κB show an increased tendency with the increase in stenosis degree, and for the model of 0 and 30% stenosis, there is no clear difference between the high- and low-WSS regions. However, at 50 and 70% stenotic model, the expression levels of MMP-9 and NF-κB located at the high- and low-WSS regions show significant variations. It means that the changes in flow shear stimulation induced by stenotic arteries, in particular high WSS, will directly affect the expression of inflammatory factors which will participate in the process of vascular dilation. The fluorescence intensity of the image is calculated using the software of ImageJ (ImageJ 1.4.3.67, http://imagej.nih.gov/ij), and the data was obtained by GraphPad software (GraphPad Prism 8.0.1, https://www.graphpad-prism.cn).

DISCUSSION

In this study, we successfully created a monolayer of ECs in a silicone tube, as described in previous studies (Kaneko et al., 2018; Levitt et al., 2019). To ensure that the inner surfaces of the silicone vessel models were evenly covered with ECs and to easily obtain

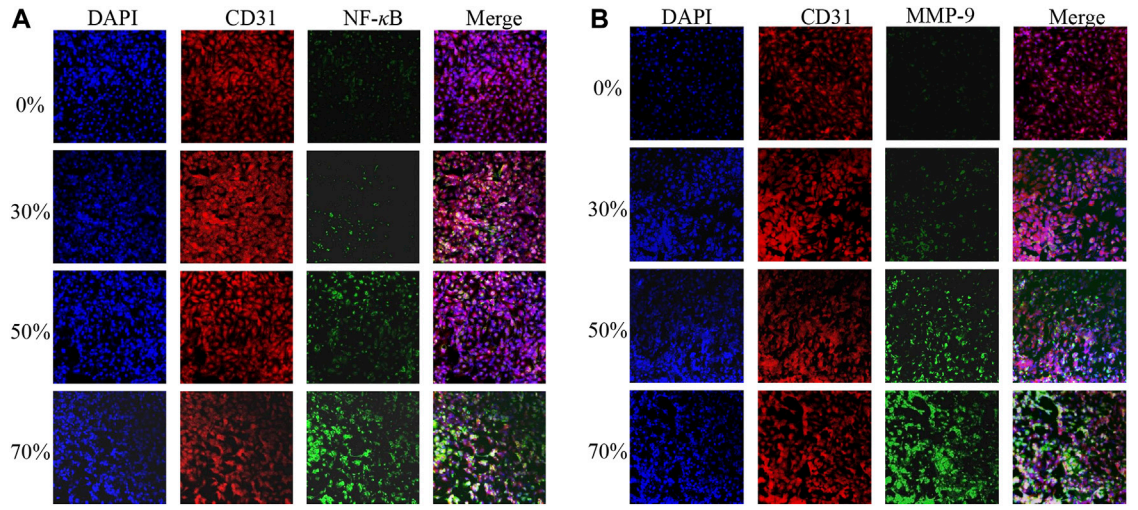

FIGURE 7 | MMP-9 **(A)** and NF-κB **(B)** expression after different degrees of flow stimulation induced by stenosis.

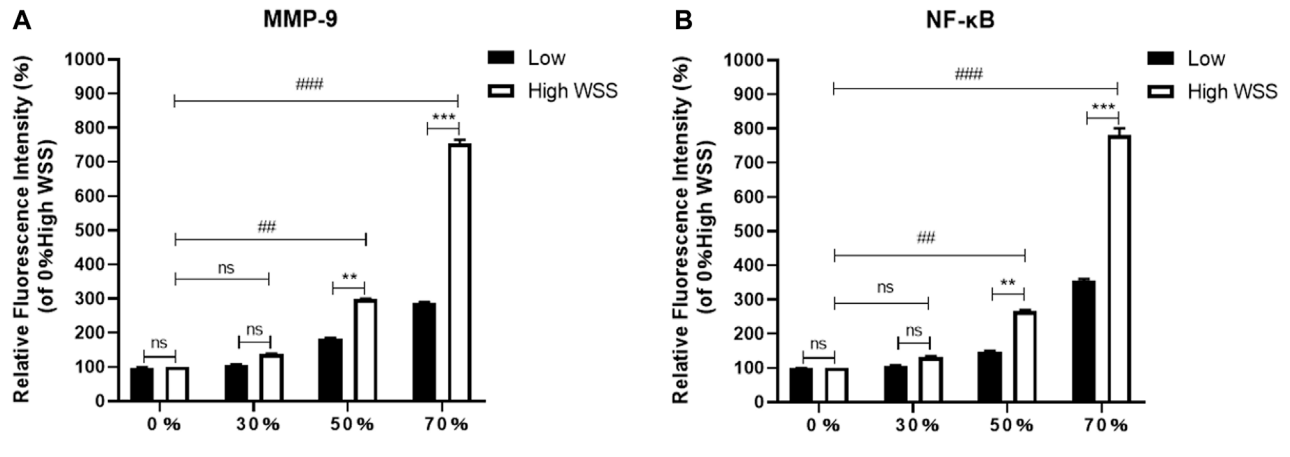

FIGURE 8 | Comparison of relative fluorescence intensity of MMP-9 **(A)** and NF-κB **(B)** at the high- and low-WSS regions in different stenosis models.

focused confocal images, the roughness and thickness of the silicone tubes, the EC concentration, and the speed of rotation were standardized.

Although fabrication of silicone vessel replicas has been described previously (Chi et al., 2021), the standardization of inner tube roughness and silicone tube thickness in this study are noteworthy. A stair-like texture of the water-soluble skeleton is difficult to avoid due to the layer-by-layer printing technique. This is not desirable as ECs are cultured and regionalized based on the surface texture. Thus, the water-soluble skeleton surface needs to be fully smoothened. However, as reported by Heley et al., the symmetric post-stenotic recirculation and WSS distribution depend on the symmetry of the stenosed vessel. The smoothing process will affect the extent of silicone vessel stenosis. Thus, it is important to screen the symmetry of vascular replicas based on PIV measurements. The thickness of the silicone replica was maintained at <0.5 mm to ensure higher transparency and better tiling of the thin silicone pieces to improve image quality by confocal microscopy. In addition, it is important to determine the appropriate cell suspension density and rotation speed to obtain evenly spread ECs. High-density suspensions and low rotation speeds can reduce the number of cells stacked together, whereas low-density suspensions and high rotation speeds can prevent ECs from adhering to the silicone wall.

Based on the CFD simulation, the WSS/WSSG and the location of maximum WSS were easily identified. The maximum WSS increased with the degree of stenosis. In addition, the location of maximum WSS fluctuated between 12 and 16 mm from the site of stenosis and was farthest at 50% stenosis. This was dependent on changes in

the location of the vortex center. Our results are in good agreement with previous statistical measurements of the distance between the narrow region and the aneurysm neck (Antonov et al., 2018).

We found that substantial changes in EC morphology and high expression of major inflammatory factors were directly related to high WSS, which may be a key factor mediating aneurysm occurrence. Our results are in line with previous observations showing that aneurysms predominantly occur at regions of high WSS (Geers et al., 2017). Excessive and abnormal WSS can also cause dysfunction or loss of the endodermis, which can lead to local vascular wall degeneration and expansion (Meng et al., 2014; Kataoka, 2015; Staarmann et al., 2019). In addition, it is known that the MMPs and NF-κB inflammation cause artery dilation. In the current study, *in vitro* experiments of silicone stenotic artery with different stenosis degrees populated by ECs were carried out, a direct relation between the artery stenosis degree and the MMPs and NF-κB expression was clearly established. The expression levels of MMP-9 and NF-κB located at the high-WSS region show significant variations in the 50 and 70% stenotic models. In addition, the expression levels of MMP-9 and NF-κB located at the high- and low-WSS regions show a significant variation in a 50% or 70% stenotic model. It means that the stenotic artery over 50% stenosis could be a potential risk factor for the post-stenotic dilation, which would pay more attention to clinical diagnosis.

This study has several limitations that should be noted. First, the physiological composition of the blood vessel wall is much more complex than that of the simplified silicone and EC layers used in our model. Second, the boundary condition setting might influence the simulation results. A steady average flow rate over a period of time in the carotid artery was set as the inlet flow condition without considering the real pulsatile wave of the blood. The differences between the steady and pulsatile inflow conditions would have influenced our WSS calculations in the CFD simulation. We set a zero-pressure outlet as the outlet boundary. If the experimentally measured pressure was adopted as the outlet boundary, the CFD result will surely make a better matching degree of experimental result in this model. Third, the frame rate of the high-speed camera is set to 2000 fps. Within the limited frame rate, there is a clear trailing effect of the moving particles. It will bring trouble in the PIV analysis based on the comparison of the relative position changes of particles at two adjacent moments. It might be difficult to capture the jet flow in PIV post-processed software of PIVLab.

CONCLUSION

In vitro experiments and CFD simulations revealed that hemodynamic stress variations induced by arterial stenosis contribute to differences in EC morphology and gene expression. A high degree of vascular stenosis can directly give rise to high WSS downstream of the stenosed region, leading to the appearance of gaps between ECs and an increase in the expression of key inflammatory factors. These inflammatory factors, which are produced by ECs, are also commonly found in aneurysm tissue. This study will be helpful for our understanding of the mechanobiological mechanism underlying the link between vascular stenosis and post-stenotic dilation.

DATA AVAILABILITY STATEMENT

The original contributions presented in the study are included in the article/Supplementary Material, further inquiries can be directed to the corresponding author.

AUTHOR CONTRIBUTIONS

LM: concept, design, development of the study, analysis of the data, and writing of the manuscript. XL: numerical simulations, manufacture of the silicone tube, and analysis of the data. ML and LL: EC culture and observation. QC: manufacture of the silicone tube YH: critical review and discussion of the article. YP: concept and design of the EC study, analysis of the data, and the discussion of the article. CJ and GG: acquisition of data and discussion. XL: preparation of confocal images of ECs.

ACKNOWLEDGMENTS

This work was partially supported by the Fundamental Research Funds for the Central Universities (DUT21JC25, DUT21LK23) and the National Natural Science Foundation of China (No. 81803024, 51976026).

REFERENCES

Alfano, J. M., Kolega, J., Natarajan, S. K., Xiang, J., Paluch, R. A., Levy, E. I., et al. (2013). Intracranial Aneurysms Occur More Frequently at Bifurcation Sites that Typically Experience Higher Hemodynamic Stresses. *Neurosurgery* 73 (3), 497–505. doi:10.1227/neu.0000000000000016

Antonov, A., Kono, K., Greim-Kuczewski, K., Hippelheuser, J. E., Lauric, A., and Malek, A. M. (2018). Proximal Stenosis Is Associated with Rupture Status in Middle Cerebral Artery Aneurysms. *World Neurosurg.* 109, E835–E844. doi:10.1016/j.wneu.2017.10.108

Chen, H., Selimovic, A., Thompson, H., Chiarini, A., Penrose, J., Ventikos, Y., et al. (2013). Investigating the Influence of Haemodynamic Stimuli on Intracranial Aneurysm Inception. *Ann. Biomed. Eng.* 41 (7), 1492–1504. doi:10.1007/s10439-013-0794-6

Chi, Q.-Z., Mu, L.-Z., He, Y., Luan, Y., and Jing, Y.-C. (2021). A brush-spin-coating Method for Fabricating *In Vitro* Patient-specific Vascular Models by Coupling 3D-Printing. *Cardiovasc. Eng. Tech.* 12 (2), 200–214. doi:10.1007/s13239-020-00504-9

Ferns, S. P., Sprengers, M. E. S., van Rooij, W. J. J., van den Berg, R., Velthuis, B. K., de Kort, G. A. P., et al. (2011). De Novo Aneurysm Formation and Growth of Untreated Aneurysms. *Stroke* 42 (2), 313–318. doi:10.1161/strokeaha.110.591594

Gao, G., Park, W., Kim, B. S., Ahn, M., Chae, S., Cho, W. W., et al. (2021). Construction of a Novel *In Vitro* Atherosclerotic Model from Geometry-

Tunable Artery Equivalents Engineered via in-Bath Coaxial Cell Printing. *Adv. Funct. Mater.* 31, 2008878. doi:10.1002/adfm.202008878

Geers, A. J., Morales, H. G., Larrabide, I., Butakoff, C., Bijlenga, P., and Frangi, A. F. (2017). Wall Shear Stress at the Initiation Site of Cerebral Aneurysms. *Biomech. Model. Mechanobiol* 16 (1), 97–115. doi:10.1007/s10237-016-0804-3

Gorelick, P. B., Wong, K. S., Bae, H.-J., and Pandey, D. K. (2008). Large Artery Intracranial Occlusive Disease. *Stroke* 39, 2396–2399. doi:10.1161/strokeaha.107.505776

Haley, A. L., Valen-Sendstad, K., and Steinman, D. A. (2021). On Delayed Transition to Turbulence in an Eccentric Stenosis Model for Clean vs. Noisy High-Fidelity CFD. *J. Biomech.* 125 (6), 110588. doi:10.1016/j.jbiomech.2021.110588

Jang, L. K., Alvarado, J. A., Pepona, M., Wasson, E. M., Nash, L. D., Ortega, J. M., et al. (2020). Three-dimensional Bioprinting of Aneurysm-Bearing Tissue Structure for Endovascular Deployment of Embolization Coils. *Biofabrication* 13 (1), 015006. doi:10.1088/1758-5090/abbb9b

Jou, L.-D., Shaltoni, H. M., Morsi, H., and Mawad, M. E. (2010). Hemodynamic Relationship between Intracranial Aneurysm and Carotid Stenosis: Review of Clinical Cases and Numerical Analyses. *Neurol. Res.* 32 (10), 1083–1089. doi:10.1179/016164110x12681290831522

Kamiya, A., Bukhari, R., and Togawa, T. (1984). Adaptive Regulation of wall Shear Stress Optimizing Vascular Tree Function. *Bull. Math. Biol.* 46 (1), 127–137. doi:10.1016/s0092-8240(84)80038-5

Kaneko, N., Mashiko, T., Namba, K., Tateshima, S., Watanabe, E., and Kawai, K. (2018). A Patient-specific Intracranial Aneurysm Model with Endothelial Lining: a Novel *In Vitro* Approach to Bridge the gap between Biology and Flow Dynamics. *J. Neurointervent Surg.* 10 (3), 306–309. doi:10.1136/neurintsurg-2017-013087

Kataoka, H. (2015). Molecular Mechanisms of the Formation and Progression of Intracranial Aneurysms. *Neurol. Med. Chir.(Tokyo)* 55, 214–229. doi:10.2176/nmc.ra.2014-0337

Kondo, S., Hashimoto, N., Kikuchi, H., Hazama, F., Nagata, I., and Kataoka, H. (1997). Cerebral Aneurysms Arising at Nonbranching Sites. *Stroke* 28 (2), 398–404. doi:10.1161/01.str.28.2.398

Kono, K., Masuo, O., Nakao, N., and Meng, H. (2013). De Novo cerebral Aneurysm Formation Associated with Proximal Stenosis. *Neurosurgery* 73 (6), E1080–E1089. doi:10.1227/NEU.0000000000000065

Kono, K., Fujimoto, T., and Terada, T. (2014). Proximal Stenosis May Induce Initiation of Cerebral Aneurysms by Increasing wall Shear Stress and wall Shear Stress Gradient. *Int. J. Numer. Meth. Biomed. Engng.* 30, 942–950. doi:10.1002/cnm.2637

Levitt, M. R., Mandrycky, C., Abel, A., Kelly, C. M., Levy, S., Chivukula, V. K., et al. (2019). Genetic Correlates of wall Shear Stress in a Patient-specific 3D-Printed Cerebral Aneurysm Model. *J. Neurointervent Surg.* 11 (10), 999–1003. doi:10.1136/neurintsurg-2018-014669

Liang, F., Liu, X., Yamaguchi, R., and Liu, H. (2016). Sensitivity of Flow Patterns in Aneurysms on the Anterior Communicating Artery to Anatomic Variations of the Cerebral Arterial Network. *J. Biomech.* 49 (15), 3731–3740. doi:10.1016/j.jbiomech.2016.09.031

Lu, G., Huang, L., Zhang, X. L., Wang, S. Z., Hong, Y., Hu, Z., et al. (2011). Influence of Hemodynamic Factors on Rupture of Intracranial Aneurysms: Patient-specific 3D Mirror Aneurysms Model Computational Fluid Dynamics Simulation. *AJNR Am. J. Neuroradiol* 32 (7), 1255–1261. doi:10.3174/ajnr.a2461

Luo, B., Yang, X., Wang, S., Li, H., Chen, J., Yu, H., et al. (2011). High Shear Stress and Flow Velocity in Partially Occluded Aneurysms Prone to Recanalization. *Stroke* 42 (3), 745–753. doi:10.1161/strokeaha.110.593517

Meng, H., Tutino, V. M., Xiang, J., and Siddiqui, A. (2014). High WSS or Low WSS? Complex Interactions of Hemodynamics with Intracranial Aneurysm Initiation, Growth, and Rupture: toward a Unifying Hypothesis. *AJNR Am. J. Neuroradiol* 35 (7), 1254–1262. doi:10.3174/ajnr.a3558

Meng, H., Wang, Z., Hoi, Y., Gao, L., Metaxa, E., Swartz, D. D., et al. (2007). Complex Hemodynamics at the apex of an Arterial Bifurcation Induces Vascular Remodeling Resembling Cerebral Aneurysm Initiation. *Stroke* 38 (6), 1924–1931. doi:10.1161/strokeaha.106.481234

Metaxa, E., Tremmel, M., Natarajan, S. K., Xiang, J., Paluch, R. A., Mandelbaum, M., et al. (2010). Characterization of Critical Hemodynamics Contributing to Aneurysmal Remodeling at the Basilar Terminus in a Rabbit Model. *Stroke* 41 (8), 1774–1782. doi:10.1161/strokeaha.110.585992

Moore, K. L. (1990). *Clinically Oriented Anatomy*. Baltimore, MD: Williams & Wilkins.

Pincombe, B., Mazumdar, J., and Hamilton-Craig, I. (1999). Effects of Multiple Stenoses and post-stenotic Dilatation on Non-newtonian Blood Flow in Small Arteries. *Med. Biol. Eng. Comput.* 37 (5), 595–599. doi:10.1007/bf02513353

Rinkel, G. J. E., Djibuti, M., Algra, A., and van Gijn, J. (1998). Prevalence and Risk of Rupture of Intracranial Aneurysms. *Stroke* 29, 251–256. doi:10.1161/01.str.29.1.251

Sforza, D. M., Putman, C. M., and Cebral, J. R. (2009). Hemodynamics of Cerebral Aneurysms. *Annu. Rev. Fluid Mech.* 41 (1), 91–107. doi:10.1146/annurev.fluid.40.111406.102126

Signorelli, F., Sela, S., Gesualdo, L., Chevrel, S., Tollet, F., Pailler-Mattei, C., et al. (2018). Hemodynamic Stress, Inflammation, and Intracranial Aneurysm Development and Rupture: A Systematic Review. *World Neurosurg.* 115, 234–244. doi:10.1016/j.wneu.2018.04.143

Staarmann, B., Smith, M., and Prestigiacomo, C. J. (2019). Shear Stress and Aneurysms: a Review. *Neurosurg. Focus* 47 (1), E2. doi:10.3171/2019.4.focus19225

Tanaka, H., Fujita, N., Enoki, T., Matsumoto, K., Watanabe, Y., Murase, K., et al. (2006). Relationship between Variations in the circle of Willis and Flow Rates in Internal Carotid and Basilar Arteries Determined by Means of Magnetic Resonance Imaging with Semiautomated Lumen Segmentation: Reference Data from 125 Healthy Volunteers. *AJNR Am. J. Neuroradiol* 27 (8), 1770–1775.

Varghese, S. S., Frankel, S. H., and Fischer, P. F. (2007). Direct Numerical Simulation of Stenotic Flows. Part 1. Steady Flow. *J. Fluid Mech.* 582, 253–280. doi:10.1017/s0022112007005848

Wilcox, D. C. (1994). Simulation of Transition with a Two-Equation Turbulence Model. *AIAA J.* 32 (2), 247–255. doi:10.2514/3.59994

Conflict of Interest: The authors declare that the research was conducted in the absence of any commercial or financial relationships that could be construed as a potential conflict of interest.

Publisher's Note: All claims expressed in this article are solely those of the authors and do not necessarily represent those of their affiliated organizations, or those of the publisher, the editors, and the reviewers. Any product that may be evaluated in this article, or claim that may be made by its manufacturer, is not guaranteed or endorsed by the publisher.

frontiers | Frontiers in Bioengineering and Biotechnology

REVIEW
published: 27 April 2022
doi: 10.3389/fbioe.2022.855791

Medical Image-Based Computational Fluid Dynamics and Fluid-Structure Interaction Analysis in Vascular Diseases

Yong He[1], *Hannah Northrup*[2,3], *Ha Le*[3], *Alfred K. Cheung*[3,4], *Scott A. Berceli*[1,5] *and Yan Tin Shiu*[3,4]*

[1]Division of Vascular Surgery and Endovascular Therapy, University of Florida, Gainesville, FL, United States, [2]Department of Biomedical Engineering, University of Utah, Salt Lake City, UT, United States, [3]Division of Nephrology and Hypertension, Department of Internal Medicine, University of Utah, Salt Lake City, UT, United States, [4]Veterans Affairs Salt Lake City Healthcare System, Salt Lake City, UT, United States, [5]Vascular Surgery Section, Malcom Randall Veterans Affairs Medical Center, Gainesville, FL, United States

OPEN ACCESS

Edited by:
Philippe Sucosky,
Kennesaw State University,
United States

Reviewed by:
Dalin Tang,
Worcester Polytechnic Institute,
United States
Farhad R. Nezami,
Brigham and Women's Hospital and
Harvard Medical School, United States

***Correspondence:**
Yan Tin Shiu
y.shiu@hsc.utah.edu

Specialty section:
This article was submitted to
Biomechanics,
a section of the journal
Frontiers in Bioengineering and
Biotechnology

Received: 16 January 2022
Accepted: 08 April 2022
Published: 27 April 2022

Citation:
He Y, Northrup H, Le H, Cheung AK,
Berceli SA and Shiu YT (2022) Medical
Image-Based Computational Fluid
Dynamics and Fluid-Structure
Interaction Analysis in
Vascular Diseases.
Front. Bioeng. Biotechnol. 10:855791.
doi: 10.3389/fbioe.2022.855791

Hemodynamic factors, induced by pulsatile blood flow, play a crucial role in vascular health and diseases, such as the initiation and progression of atherosclerosis. Computational fluid dynamics, finite element analysis, and fluid-structure interaction simulations have been widely used to quantify detailed hemodynamic forces based on vascular images commonly obtained from computed tomography angiography, magnetic resonance imaging, ultrasound, and optical coherence tomography. In this review, we focus on methods for obtaining accurate hemodynamic factors that regulate the structure and function of vascular endothelial and smooth muscle cells. We describe the multiple steps and recent advances in a typical patient-specific simulation pipeline, including medical imaging, image processing, spatial discretization to generate computational mesh, setting up boundary conditions and solver parameters, visualization and extraction of hemodynamic factors, and statistical analysis. These steps have not been standardized and thus have unavoidable uncertainties that should be thoroughly evaluated. We also discuss the recent development of combining patient-specific models with machine-learning methods to obtain hemodynamic factors faster and cheaper than conventional methods. These critical advances widen the use of biomechanical simulation tools in the research and potential personalized care of vascular diseases.

Keywords: computational fluid dynamics (CFD), finite element analysis, fluid-structure interaction (FSI), patient-specific analysis, image-based simulation

INTRODUCTION

Hemodynamic factors, the stress and strain induced by pulsatile blood flow at the surface and body of a blood vessel, play a crucial role in vascular health and diseases mainly by altering the structure and functions of endothelial and smooth muscle cells. Among the hemodynamic factors, wall shear stress (WSS), the viscous shear applied to the endothelial cells due to blood flow, has been studied the most. Endothelial cells respond to WSS *via* a variety of mechanotransduction pathways (Davies, 1995; Chiu and Chien, 2011; Ando and Yamamoto, 2022; Tanaka et al., 2021). Cell-culture and animal studies

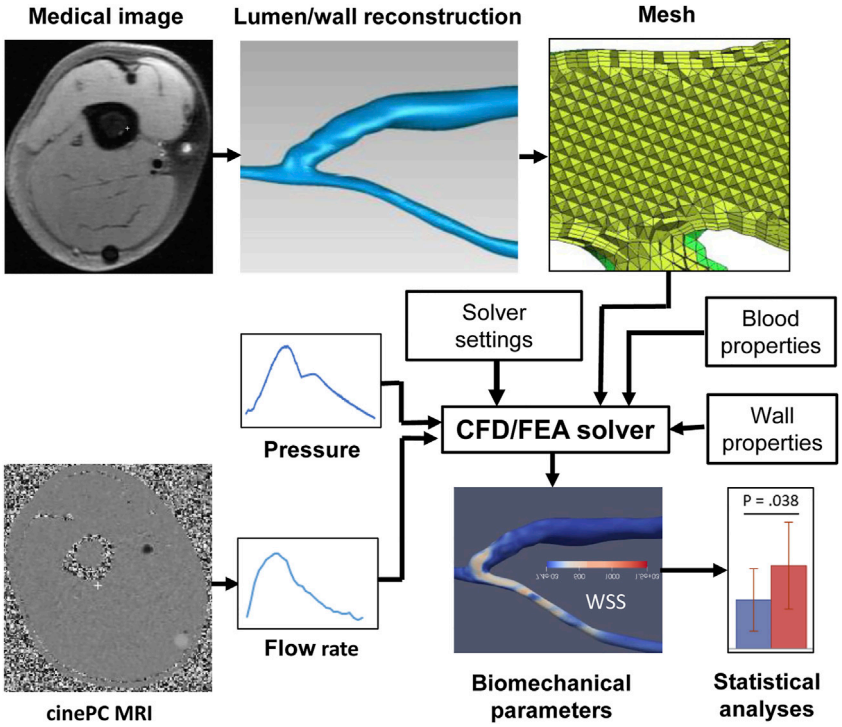

FIGURE 1 | Pipeline of a typical image-based vascular CFD/FEA simulation. CFD, computational fluid dynamics, FEA, finite element analysis, PC MRI, phase-contrast magnetic resonance imaging, WSS, wall shear stress.

have shown that different flow patterns trigger different endothelial responses. Generally, unidirectional flow is protective against atherosclerosis and neointimal formation, while complex, multidirectional flow is atherogenic and turns endothelial cells to become pro-inflammatory (Chiu and Chien, 2011). Complex, disturbed flow generates temporal and spatial gradients in luminal and wall hemodynamic parameters due to pulsatility in a cardiac cycle and the curvature, branches, and other geometric irregularities of the vasculature.

To understand the effects and mechanisms of hemodynamic factors on vascular structure and function, we first need to delineate the detailed *in vivo* three-dimensional (3D) blood flow characteristics and quantify the values of the hemodynamic forces. These data, however, cannot be obtained from analytical solutions of governing equations due to the irregular, complex geometry of the vasculature. Fortunately, with the rapid advancement of medical imaging and computational methods and power, computational fluid dynamics (CFD), finite element analysis (FEA), and fluid-structure interaction (FSI) simulations can be readily adopted and have been widely used to obtain a detailed flow field using vascular images obtained from computed tomography angiography (CTA), magnetic resonance imaging (MRI), ultrasound, intravascular ultrasound (IVUS), optical coherence tomography (OCT), and other imaging modalities. Values of the hemodynamic forces can then be derived using the detailed flow field.

Biomechanical simulations using patient-specific anatomical and physiological data have been applied to study atherosclerosis in coronary (Abbasian et al., 2020; Guvenir Torun et al., 2021), carotid (Bennati et al., 2021), cerebral (Tanoue et al., 2011), and femoral (Wood et al., 2006) arteries; thoracic (Boccadifuoco et al., 2018a) and abdominal (Taylor et al., 1998) aortas; aortic aneurysms (Mariotti et al., 2021) and dissections (Cheng et al., 2014); cerebral aneurysms (Bazilevs et al., 2010); pulmonary arterial hypertension (Zambrano et al., 2018); bypass grafts (Sankaran et al., 2012), and arteriovenous fistulas for hemodialysis (He et al., 2013). In addition to research, CFD simulations have also been used clinically to derive the coronary fractional flow reserve values in stenotic coronary arteries from CTA images, avoiding invasive coronary angiography (Min et al., 2015). We will review the multiple steps that are generally followed in these simulations (**Figure 1**). Despite the great progress in the last 2 decades, some challenges still exist, and verification and validation must be performed to assess the simulation results (Tang et al., 2014). The emerging and exciting application of machine-learning techniques to biomechanics simulations will also be reviewed. Image-based biomechanical simulations have also been used to investigate the responses of vascular tissues to and predict the outcomes of the endovascular procedures, such as stenting of stenotic arteries and stent-grafting of aortic aneurysms and dissections (Auricchio et al., 2011; Hemmler et al., 2019; Raptis et al., 2019). Simulations of the interactions of these implants with blood vessels are further complicated by the implants and not reviewed here. Our current

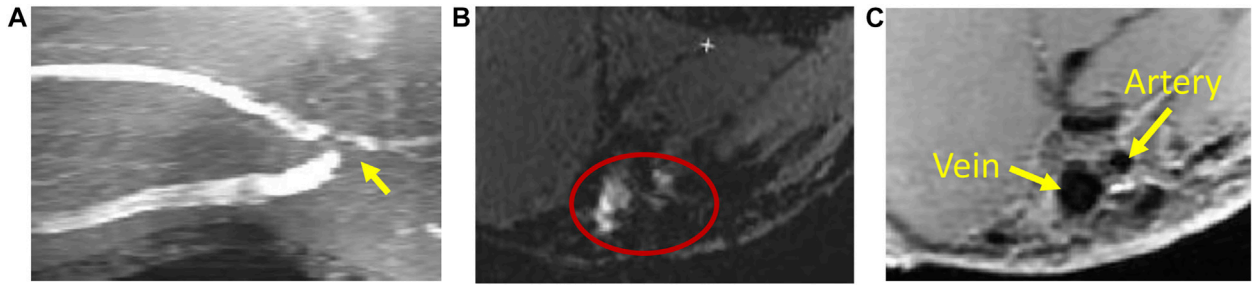

FIGURE 2 | Magnetic resonance imaging of an arteriovenous fistula. **(A)** Maximal intensity projection of white-blood time-of-flight (TOF) images. At the anastomosis (the gray region pointed by a yellow arrow), the signal is void due to complex flow. **(B)** An example of the TOF slice close to the anastomosis (enclosed by the red ellipse) where the lumen is not clearly defined. **(C)** The black-blood image shows the lumen of the fistula vein and artery clearly (the black regions pointed by yellow arrows).

review can be complemented by other reviews of image-based computational cardiovascular biomechanics (Thondapu et al., 2017; Zhong et al., 2018; Liang et al., 2019; Cameron et al., 2020; Carpenter et al., 2020; Lipp et al., 2020; Lopes et al., 2020; Ong et al., 2020; Thiyagarajah et al., 2022).

PIPELINE OF IMAGE-BASED COMPUTATIONAL BIOMECHANICAL SIMULATIONS

Imaging the Lumen

Imaging is performed to obtain the anatomical (lumen and wall) and physiological (flow) data of blood vessels that are needed for patient-specific biomechanical simulations. CTA and MRI have been the most popular modalities for vascular lumen imaging. During a spiral CTA scan, a narrow beam of x-rays is aimed at a patient and quickly rotates around the patient when the table on which a patient lies moves, producing signals that are collected by detectors opposite to the x-ray source and processed by a computer to generate cross-sectional images or slices of the body. These slices can then be digitally stacked together to form a 3D image of the patient. Multi-detector CTA uses iodinated contrast agents to enhance the vascular lumen for a quick, high-resolution scanning of the vasculature's 3D geometry. For example, the spatial and temporal resolutions of the GE CT scanner can be 0.28 mm and 0.24 s, respectively. However, exposure to ionizing X-ray radiation, the risk of acute kidney injury from using contrast agents, and artifacts from nearby bone and metal implants are the main downside of CTA (Kim et al., 2010).

MRI uses a very strong magnetic field (typically, 1.5–3.0 T for clinical scanners) and radio frequency waves to create detailed images of the organs and tissues. The main magnetic field polarizes the magnetic spins of hydrogen nuclei. The radio frequency system excites the sample and detects the resulting MR signal, whose location is determined from the gradient coil system. The contrast between different tissues is determined by the rate at which excited hydrogen nuclei return to the equilibrium state. MRI allows for non-invasive tissue characterization because of its dependence on a variety of physical and chemical characteristics of the tissue, such as physical state, molecular motion, diffusion, chemical composition and concentration, and water content (Pooley, 2005). Through the technique of time-of-flight or double inversion recovery, the 3D lumen geometry can be obtained from MRI without using a contrast agent. For vasculature with complex blood flow, such as an arteriovenous fistula, the dark-blood images obtained by the double inversion recovery technique have a better quality than the white-blood images obtained by the time-of-flight technique, which is more susceptible to complex recirculating flows (**Figure 2**). Similar to CTA, MR angiography (MRA) can be enhanced using contrast agents, but without the risk of ionizing radiation.

Imaging the Wall

The anatomical and compositional data of blood vessel walls and atherosclerotic plaques are also crucial components for studying vascular diseases and biomechanical simulations. Even though CT does not have an adequate contrast to differentiate vascular wall from adjacent perivascular tissues, it is commonly used for vascular calcification imaging because of the intrinsically higher signal intensity of calcium in CT. MRI is more versatile than CT. A variety of MRI techniques have been developed to non-invasively characterize vascular morphology and composition of atherosclerotic plaques, such as lipid core, fibrous cap, calcification, normal media, hemorrhage, and adventitia (Gold et al., 1993; Martin et al., 1995; Toussaint et al., 1996; Hatsukami et al., 2000). However, the spatial resolution of current clinical MRI scanners is limited (approximately 0.3 mm in-plane resolution with zero-filling interpolation at best) (He et al., 2013), and the thin fibrous cap (<65 μm), which is a crucial characteristic for the high-risk atherosclerotic plaque, cannot be clearly identified.

IVUS and OCT have been used to identify the components of the vascular wall at a higher spatial resolution, but they are invasive (Mantella et al., 2021). IVUS is a catheter-based procedure used to visualize the inside of a blood vessel in real time. Radiofrequency ultrasound waves, usually in the 30–60 MHz range, are emitted from the transducer at the catheter tip, and the return echo is also received by the transducer and conducted to an external computerized

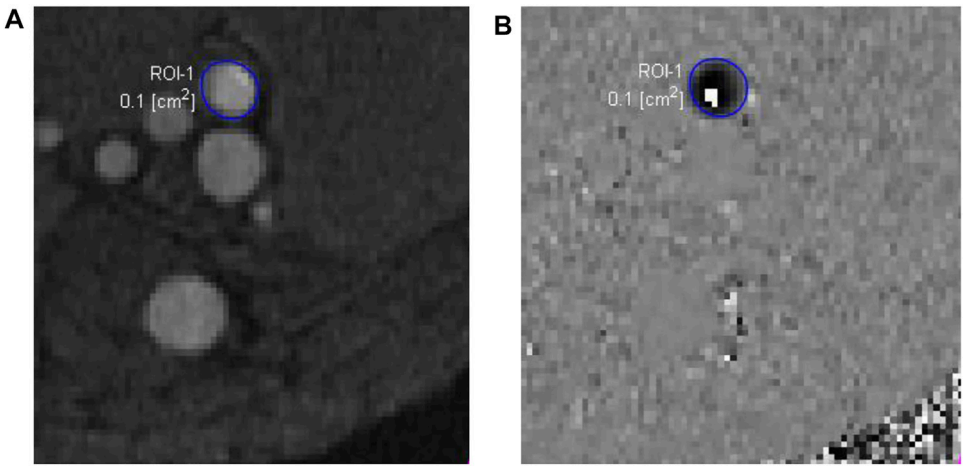

FIGURE 3 | Phase-contrast magnetic resonance images of an arteriovenous fistula. The magnitude image **(A)** is used to draw a region of interest (ROI-1) for the proximal artery (enclosed by the blue circle), which may have very high flow velocity. In this case, the velocity encoding value, 250 cm/s, was not big enough, causing a phase-wrap artifact shown by the white pixels within the ROI-1 in the phase image **(B)**.

equipment to construct and display ultrasound images of a thin cross-sectional slice of the blood vessel. Virtual histology-IVUS, through spectral analysis of IVUS backscatter signals, can reveal the fibrous, fibro-fatty, necrotic-core, and dense-calcium regions of a plaque (Nair et al., 2002; Nair et al., 2007; Campos et al., 2015). However, even with a higher resolution (65–150 μm) than MRI, IVUS still cannot adequately measure the thickness of a thin fibrous cap.

Intravascular OCT has a higher resolution than IVUS. It utilizes back-scattered infrared light to generate high-speed and high-spatial-resolution (10–20 μm) images of blood vessels after using a contrast flush to clear the intraluminal blood (Shimamura et al., 2021). It can measure the thickness of a thin fibrous cap more accurately and identify the plaque composition (Brezinski et al., 1996; Roleder et al., 2015). However, OCT has a limited penetration depth through blood vessels, so the overall plaque burden cannot be measured. Taking the advantages of both IVUS (deep penetration) and OCT (high spatial resolution) by combining the two imaging modalities seems favorable and has been increasingly used (Li et al., 2014; Guo et al., 2018; Guo et al., 2021; Lv et al., 2021). The development of other hybrid intravascular imaging modalities, such as near infrared spectroscopy-intravascular ultrasound (NIRS-IVUS), further improves vascular wall imaging. NIRS can detect lipid composition by analyzing the near-infrared absorption properties of atherosclerotic plaques. A thorough discussion of hybrid intravascular imaging modalities can be found in Bourantas et al. (2017) and Kubo et al. (2022).

Imaging the Flow

Compared to CTA, MRI also has the advantage of obtaining blood flow data using a phase-contrast sequence in either two dimensions (2D) or 3D. In 2D single-directional phase-contrast MRI, the through-plane velocity is measured by aligning the imaging plane perpendicular to the axis of the imaged blood vessel, assuming that the blood velocity is along the axial direction. The maximum intensity projection of time-of-flight images can be used to place the imaging plane. The velocity is encoded in the phase images using a velocity encoding value, which is the maximum velocity that can be measured without a phase-wrap artifact. When the phase-wrap artifact appears (**Figure 3**), the velocity encoding value needs to be increased. The flow rate can then be extracted from the phase and magnitude images using the free package Segment (Medviso AB, Lund, Sweden) (Bidhult et al., 2019) or other software. The magnitude images are used to define the lumen of imaged vessel. If the phase-wrap artifact is not severe, it can be corrected conveniently in Segment by unwrapping the affected pixels. When flow rates at several locations are needed, the scan must be repeated at each location, which is time consuming and burdensome to the patient and increases the possibility of patient-movement artifacts.

In the case of multi-directional flow measurement, four dimensional (4D, which is 3D in space plus time) phase-contrast MRI has been increasingly used to obtain time-resolved complex pulsatile blood flow velocities in three orthogonal directions within an acquired 3D volume (Markl et al., 2014; Azarine et al., 2019). Although a contrast agent is not required for phase-contrast MRI, the use of a contrast agent enhances the signal-to-noise ratio in the magnitude images and reduces noise in phase images, compared to scans without a contrast agent (Bock et al., 2010). Streamlines and velocity vectors can be used to visualize changes in blood flow pathways directly from the image data. In addition to visual flow analysis, one advantage of 4D flow MRI is that by post-processing the original data, flow rate through any plane across the volume can be obtained retrospectively. Therefore, when choosing the imaging plane orthogonal to the vessel axis is challenging, the number of measurement sites is large, and geometry of the vasculature is complex, 4D flow MRI is more accurate in flow rate quantification than 2D phase-contrast MRI by placing the

measurement plane at the locations where helical or vortical flow does not exist or is mild.

In addition to MRI, duplex Doppler ultrasonography (DUS) is also commonly used to obtain blood flow data in peripheral vasculature. In DUS, an imaging sample volume (gate) is usually placed at the middle of the vessel to obtain the maximal velocity spectrum. In commercial ultrasound scanners, to derive the flow rate from the maximal DUS velocity spectrum, a parabolic velocity profile across the lumen is assumed, resulting in the mean velocity being half of the maximal velocity across the lumen based on the Poiseuille flow theory, which is only applicable to steady laminar flow in an infinitely long straight circular tube. However, arterial blood flow is pulsatile, and the velocity profile across the lumen depends on the Womersley number α ($\alpha = R\sqrt{\rho\omega/\mu}$, where R is the lumen radius of the blood vessel, ρ is the blood density, ω is the angular frequency of blood flow pulsation, and μ is the blood dynamic viscosity) (Womersley, 1955). Consequently, a more accurate algorithm than that assuming a parabolic velocity profile has been developed by using the Womersley number to adjust the relationship between the mean and maximal velocities across the lumen (Ponzini et al., 2006). Of note, the Womersley velocity profile also depends on the assumption of a straight circular vessel. Therefore, an effort should be taken to choose a relatively straight circular segment of the blood vessel to measure flow rate. A more accurate lumen diameter measurement using a perpendicular cross-sectional view may also improve the flow rate measurement (He et al., 2018).

Lumen and Wall Geometry Reconstruction

Image segmentation, i.e., extracting lumen and wall configuration from medical images, is one of the key steps for image-based computational biomechanics. The methods of segmentation depend on the imaging modality and image quality and can be manual, semi-automatic, or automatic. For images obtained by CTA and MRA using contrast agents, the image quality of the lumen is generally high, and implicit deformable models and level set methods can be used to extract the lumen quickly by specifying a few seed points in the images to define the region of interest (Antiga et al., 2008a). This family of methods uses spatial variation in image intensity, rather than absolute intensity, and is more robust than image intensity threshold-based methods. However, for time-of-flight and black-blood MRI, the image quality of the lumen also depends on the flow characteristics and is lower at the region with disturbed flow. In this case, manual delineation of blood vessels may be needed, even though this process is time consuming and the results are user dependent. Furthermore, the slice thickness of MR images may be ≥2 mm, which causes the reconstructed surface to become non-smooth at the region with a high curvature or large diameter changes along the length of the vessel. In the Amira software (Thermo Fisher Scientific, Waltham, MA), interpolation of segmented original slices to decrease the slice thickness may improve surface quality without increasing the workload of segmentation. Other software tools also may be considered, and users should find a tool that best suits their projects.

Because of the many options of MRI sequences and complex atherosclerotic plaque compositions, segmentation and image analysis of MRI data can be complicated and require special training (Kerwin et al., 2017). The vascular wall as a whole can be semi-automatically segmented from black-blood images with an adequate quality using deformable contour based on the initial inner and outer outlines manually drawn (Ladak et al., 2001). Different plaque components based on multi-contrast MRI can also be semi-automatically (Liu et al., 2012) or automatically (Adame et al., 2004) identified.

Virtual histology-IVUS offers automatic component identification and segmentation. Automatic or computer-aided plaque component identification, segmentation, and quantification have also been developed for OCT images (Athanasiou et al., 2014; Athanasiou et al., 2018; Guo et al., 2019; Lee et al., 2020). The impact of automated characterization of mixed plaque components in complex atherosclerotic lesions has also been evaluated recently (Olender et al., 2022). Reconstruction of a 3D vascular model from 2D IVUS and OCT slices need special consideration because of the 2D nature of these images. Reconstruction by fusing IVUS or OCT and biplane angiography or CTA images has been developed and used in clinical studies (Slager et al., 2000; Bourantas et al., 2005; van der Giessen et al., 2010; Samady et al., 2011; Wang et al., 2015b; Guo et al., 2018). Anatomical landmarks visible in both IVUS or OCT and angiography or CTA images are commonly used to estimate the orientation of the IVUS or OCT slices to facilitate the generation of the 3D model. A comprehensive review of the image data fusion methodologies has been published recently (Kilic et al., 2020).

Meshing

The volumes of reconstructed lumen and wall need to be divided into small discrete elements, within which governing differential equations are solved. A high-quality mesh is a prerequisite for accurate simulation results. When creating a mesh, there are two main concerns, namely, the computational cost and the accuracy of simulation. A finer mesh gives more accurate results but requires more computational resources and time. Therefore, a common goal of meshing is to use less elements while achieving an acceptable accuracy. Due to the irregular and often complicated geometry of the vascular lumen reconstructed from medical images, an unstructured mesh is commonly used. When WSS is the target, which is often the case, a finer mesh at the blood-wall boundary, prismatic inflation layers, is required. To fill the rest of the lumen, hexahedral elements at the core can be created to reduce the number of elements if possible. Otherwise, tetrahedral elements in the core are generated. Since blood flow is more complex at the curved region and thus requires a finer mesh, a meshing algorithm using the local curvature to refine the mesh is advantageous if available. In Ansys Meshing, this is realized by adjusting the settings of the Curvature Size Function. Other software tools also may be considered, and users should find the details of the methods. In addition to more conventional tetrahedral and hexahedral mesh, polyhedral mesh has been demonstrated to be better than tetrahedral mesh in reducing the number of elements, reaching

convergence faster, and achieving WSS patterns that have less artifacts and thus are more homogeneous (Spiegel et al., 2011). To ensure an adequate mesh is created, a mesh-independence analysis should be performed based on the most important parameters in question, which are WSS parameters in most cases. The grid convergence index is recommended for the uniform reporting of grid refinement studies (Roache, 1994).

Meshing of the wall with advanced atherosclerotic plaques may be challenging due to the complex and irregular geometries of the different components. A component-fitting technique has been developed to generate mesh that can overcome this challenge (Yang et al., 2009). Using this technique, the 3D plaque components are divided into multiple small volumes to cover the irregular plaque geometry; a mesh for each volume is then generated. This approach is, however, labor intensive. More sophisticated and automatic mesh generation techniques have also been developed using an octree-based isocontouring method (Zhang et al., 2010).

Mechanical Properties

CFD/FSI simulations of blood flow require blood viscosity. The viscosity of whole blood varies with the hematocrit, leukocyte and platelet counts, plasma protein composition and concentration, as well as the shear rate. At least 15 non-Newtonian blood rheological models have been proposed to take into account the shear-thinning property (Abbasian et al., 2020). These models have different popularity; the Casson, Carreau, Carreau-Yasuda, power-law, and Quemada models are mostly used. When the shear rate is above $100\,s^{-1}$, blood behaves similarly to a Newtonian flood.

FSI simulations of blood flow require mechanical properties of blood vessel wall. Since blood vessels have complex, nearly incompressible, non-homogeneous, anisotropic, non-linear, and viscoelastic (creep, stress relaxation, and hysteresis) material behaviors, it is very difficult, if not impossible, to obtain the *in vivo* material parameters describing these behaviors. *In vivo*, *ex vivo*, *in vitro*, and *in silico* methods have been used to characterize these behaviors and derive purely phenomenological or structure-motivated constitutive models that hold only under specific conditions of interest (Holzapfel and Ogden, 2010).

Pulse wave velocity has been measured by tonometry, Doppler, or oscillometry to quantify arterial stiffness *in vivo* by many studies because its measurement is minimally invasive and inexpensive, but it only offers a single average value for the artery segment between the measuring sites, neglecting any regional variation and perivascular tethering effects (Hodis and Zamir, 2011). Medical imaging techniques have been used to obtain vascular mechanical properties. But since the *in vivo* clinical images only represent the physiologically loaded states, inverse FEA approaches, which could be used to obtain the unloaded configuration, are needed for *in vivo* material parameter identification. Therefore, medical images obtained from various imaging modalities have been combined with inverse FEA to derive *in vivo* vascular mechanical properties. For example, the *in vivo* aortic elastic properties of ascending thoracic aortic aneurysm have been identified from gated CT scans using an inverse approach (Liu et al., 2019a). An iterative procedure has also been developed to identify coronary artery mechanical properties by matching both maximum and minimum *in vivo* Cine IVUS lumen circumferences (Guo et al., 2017; Wang et al., 2021). Also using inverse FEA, the mechanical properties of infrarenal abdominal aorta and its peri-aortic structure have been assessed using displacement encoding with stimulated echoes (DENSE) MRI (Bracamonte et al., 2020). However, some assumptions were made when using inverse FEA. For example, the diastolic configuration was treated as the zero-strain reference, and the aortic wall was commonly assumed to be homogeneous (Bracamonte et al., 2020). Inverse FEA methods with more realistic conditions are needed. Recently, to overcome the previous limitation of homogenized or simplified material representations, an inverse FEA approach was developed to derive non-linear material properties of heterogeneous coronary plaque components using OCT imaging data acquired at differing pressures by incorporating interfaces between various intra-plaque components into the objective function (Narayanan et al., 2021). The importance of including multi-material plaque components has also been demonstrated by the greatly varied lesion mechanical responses (Kadry et al., 2021).

Due to their large size and a propensity for aneurysm formation and wall dissection, aortic tissues have been most extensively studied *ex vivo* (Di Martino et al., 2006; Vande Geest et al., 2006; Cebull et al., 2020; Jadidi et al., 2020). Uniaxial and biaxial tensile tests of explanted tissue strips from patients demonstrate that aortic tissues are stronger and stiffer in the circumferential than axial direction (Sokolis et al., 2012; Pichamuthu et al., 2013; Jadidi et al., 2021a). This behavior is due to preferential alignment of collagen fibers in the circumferential direction. Since a single elastic modulus value is inadequate to describe the non-linear behavior in the whole range of deformation, various forms of strain energy density functions based on deformation invariants are used to describe arterial hyperelastic behaviors under large deformation. Exponential and polynomial strain energy density functions are the most popular. Some constitutive models have also been developed to reflect the microstructural data, especially the directions of collagen fibers obtained from various optical microscopic imaging techniques (Holzapfel et al., 2000; Gasser et al., 2012; Jadidi et al., 2021b).

Boundary Conditions

Appropriate boundary conditions define the effect of the truncated vasculature and perivascular tissues within the simulated domain and are the key to obtaining accurate simulation results (Campbell et al., 2012; Gallo et al., 2012; Xu et al., 2018). Boundary conditions are needed at all the inlets and outlets. Ideally, patient-specific simulations require known velocity and blood pressure profiles at all nodes of the inlets, outlets, and wall. The velocity and flow rate can be acquired by MRI and ultrasound non-invasively. Accurate blood pressure measurement at specific locations, however, requires intravascular access by a pressure transducer and is usually unavailable. Except 4D flow MRI measurement, the 3D

velocity profiles at the inlets are unknown using other modalities. Therefore, it is common to apply the average velocity (plug flow) obtained by dividing the flow rate with the cross-sectional area at the added, extended straight inlet to achieve a fully developed flow at the location of the original inlet, but this approach may be problematic as actual flow may be skewed at the inlets that have a significant curvature and geometric irregularity. When 4D MRI velocity data are available, it is better to specify the velocity component at each direction at the inlet directly than to assume idealized velocity profiles derived from the measured flow rate (Morbiducci et al., 2013).

When patient-specific data are not available, several strategies have been devised to achieve reasonable results. Setting a zero pressure at multiple outlets has been used, but it is not a good practice because it may fail to reproduce physiologically relevant flow and pressure features (Pirola et al., 2017; Chnafa et al., 2018). Using typical or population-averaged flow rates and waveforms is common, but still not ideal because of the heterogeneity among patients. Alternatively, since lumen area or diameter data are more readily available from non-invasive clinical images, the inlet flow rate and flow split through branches can be estimated using lumen area or diameter data and various scaling laws, such as Murray's law based on minimum energy theory (Murray, 1926), or developed from measured data (Cebral et al., 2008; van der Giessen et al., 2011; Tricarico et al., 2020). In CFD simulations assuming a rigid wall, the velocity boundary condition at the wall is generally set as no-slip or zero-velocity.

In FSI simulations, blood pressure is important for accurate wall stress and strain results. When blood pressure is not available, lumped-parameter Windkessel models representing the impedance of truncated downstream vasculature can provide reasonable pressure values when the flow and parameters of the Windkessel models are appropriate (Westerhof et al., 2009; Pirola et al., 2017). However, patient-specific Windkessel parameters require patient-specific pressure and flow waveforms, which are not available in this case. Assumptions must be made to use Windkessel parameters obtained from other sources. As a way of considering the compliance, resistance, and especially wave reflection of the downstream truncated vasculature, an elastic tube terminated with a rigid contraction has been added to the outlet as a part of the computational domain (Pahlevan et al., 2011).

For structural analysis, the constraints at the nodes of the inlets and outlets differ among studies. In some studies, the translational motion was fixed while rotational motion was unconstrained for the nodes at the inlet and outlets (Nathan et al., 2011; Gomez et al., 2021), but the end nodes did not have any moving freedom (Pasta et al., 2013). In another study, nodes at the proximal end were allowed to deform only in the radial direction, while the distal ends were fixed in all directions (Martin et al., 2015).

Blood vessels are constrained radially by the surrounding perivascular tissues, and this constraint reduces the distensibility and intramural stress of an artery (Vonavkova and Horny, 2020), but it is a challenge to prescribe the *in vivo* perivascular boundary conditions. Although many studies simply ignore the perivascular constraint, some studies have attempted to model it. In one study, the radial constraint was quantified as an effective perivascular pressure applied to the outer surface of adventitia, which could be ≥50% of the intravascular pressure (Liu et al., 2007). In another study, the effect of the perivascular tissue was applied as an effective pressure waveform at the external wall of carotid arteries (Soleimani et al., 2021) or modeled as a heterogeneous elastic foundation boundary condition, which was implemented as a collection of unidimensional springs attached to the adventitial surface (Bracamonte et al., 2020).

Solution Strategies

Depending on the study objectives, a few software packages can be chosen to solve the governing differential equations of blood flow and vessel wall deformation. The common packages use finite volume (Ansys Fluent and CFX, Siemens STAR CCM+, OpenFoam) or finite element (COMSOL, SimVascular, Crimson) methods for CFD; FEA (Ansys Mechanical, Simulia Abacus, SimVascular) for structural wall stress analysis; Arbitrary Lagrangian-Eulerian (ALE) formulation (Adina, SimVascular, Simulia Abacus) or coupling the CFD and FEA solvers (Ansys Workbench) for FSI. If the focus is on hemodynamics, not detailed structural stress and strain distributions, the coupled momentum method is an efficient alternative to ALE formulation (Figueroa et al., 2006). In this method, wall deformation is assumed to be small; therefore, the fluid mesh is not updated. The vessel wall is based on a membrane model. This simplified method yields valid results in cases where the assumptions of small deformation and thin walls are indeed valid.

Several choices need to be made to balance the computational effort and accuracy. High-order numerical schemes and appropriate time-step size and residual errors should be used in addition to an appropriate mesh size (Khan et al., 2015; Dennis et al., 2017). Laminar flow is commonly assumed for most blood flow under physiological conditions, but transition to turbulence may occur in normal aorta (Ha et al., 2018), aorta with aortic valve stenosis (Manchester et al., 2021), stenotic arteries (George et al., 2008; Lantz et al., 2013; Andersson et al., 2017), intracranial aneurysms (Valen-Sendstad et al., 2011), and arteriovenous grafts (Lee et al., 2007) or fistulas (Stella et al., 2019). It has been demonstrated that flow instability can only be revealed under high spatial and time resolutions (Baek et al., 2010; Valen-Sendstad and Steinman, 2014). In the studies of turbulent blood flow, traditional Reynolds-averaged Navier–Stokes (RANS) equations-based turbulence models (k–ε and k–ω) (George et al., 2008; Perinajová et al., 2021), large eddy simulation (LES) (Lantz et al., 2013; Andersson et al., 2017; Stella et al., 2019; Manchester et al., 2021) and direct numerical simulation (DNS) (Lee et al., 2007; Valen-Sendstad et al., 2011; Arzani et al., 2012) have been used. LES directly resolves large-scale, at the size of mesh grid, velocity fluctuations. It incorporates the dissipative energy loss induced by turbulent eddies at the sub-grid level and can therefore model laminar, transitional, and turbulent features, which may all be exhibited in the different phases of the pulsatile blood flow during a cardiac cycle. Because DNS directly solves Navier–Stokes equations numerically for the scales of all turbulent eddies without using

any turbulence model, it requires much more number of mesh elements and computational resources and time than LES and is thus seldom used for complex blood flow simulations.

Image-based FEA wall stress analysis of blood vessels needs special treatment of the vascular geometry because the geometry obtained from medical images has a deformed configuration by intraluminal pressure and axial stretch. Blood vessels are stretched circumferentially, radially, and axially at the *in vivo* loaded state. In addition, there are residual stresses and strains even under the unloaded state (Chuong and Fung, 1986). However, the ideal reference configuration for FEA requires zero stresses and strains everywhere within blood vessels. Therefore, the *in vivo* vessel geometry needs to be shrunk circumferentially or radially and axially to obtain its unloaded state, which then needs to be numerically cut open radially to release the residual stresses and strains to obtain the ideal reference configuration. The *ex vivo* images of carotid arteries at a unloaded state have been stretched axially and circumferentially to match the *in vivo* MRI images in FSI simulations (Huang et al., 2009). However, the *ex vivo* unloaded state is unavailable in most patient-specific simulations. Therefore, various methods have been developed to drive the unloaded or stress-free configuration from the geometry obtained from *in vivo* clinical images. Assuming known material properties, these methods either 1) estimate the pre-stress field on the *in vivo* configuration, then depressurize the FE model to obtain the unloaded geometry (Gee et al., 2010; Weisbecker et al., 2014; Maas et al., 2016); 2) estimate the unloaded configuration by adjusting an initial geometry and running forward FE simulations (Raghavan et al., 2006; Bols et al., 2013; Riveros et al., 2013); or 3) use an inverse FE formulation (Lu et al., 2007). These methods require many FE iterations to converge and are therefore time consuming.

Biomechanical Parameter Extraction and Statistical Analysis

To quantify WSS's magnitude, multi-directionality, and pulsatility, the parameters that are most commonly extracted to characterize the local flow conditions experienced by endothelial cells at the vessel wall include time-averaged WSS magnitude over a cardiac cycle (TAWSS), maximum WSS within a cardiac cycle (WSSmax), oscillatory shear index (OSI) (He and Ku, 1996), relative residence time (RRT) (Himburg et al., 2004), WSS spatial and temporal gradients, axial WSS (WSSax), the secondary component of WSS (WSSsc), ratio of WSSsc to WSSax, transverse WSS (TAWSStrans), and cross-flow index (CFI) (Colombo et al., 2021). WSSax is the WSS component aligned with the tangent to the vessel centerline, while WSSsc is the other component of WSS in addition to WSSax (Morbiducci et al., 2015). TAWSStrans is the average over the cardiac cycle of WSS components perpendicular to the temporal mean WSS vector (Peiffer et al., 2013b). CFI is the normalized TAWSStrans by the WSS magnitude (Mohamied et al., 2017). Note that depending on the geometry, the temporal mean WSS vector at a location does not necessarily align with the direction tangent to the vessel centerline.

A recent promising advance is the development and application of an Eulerian method for obtaining WSS vector field topological skeleton that has a strong link with features of disturbed flow, such as flow separation, stagnation, impingement, and reversal (Mazzi et al., 2020; Mazzi et al., 2021). Based on the dynamical system theory, the WSS topological skeleton consists of fixed points where the WSS value is zero and manifolds that link the fixed points. In the blood flow field, the stable or unstable manifolds identify regions where the WSS vector exerts an expansion or contraction action on the endothelial cells that are potentially important for developing vascular diseases. The cycle-averaged WSS topological skeleton also relates to the fluid-phase mass transport of solutes near the wall (Arzani and Shadden, 2018). Clinically, high temporal variation of WSS contraction or expansion and high fixed-point residence times weighted by WSS contraction or expansion strength at 1 month after endarterectomy have been found to predict long-term carotid bifurcation intima-media thickness, independently from the exposure to low WSS (Morbiducci et al., 2020). The associations of WSS topological skeleton features with vascular pathophysiology need further studies.

The common biomechanical parameters of the vessel wall extracted from FEA are maximum principal stress for studying the sites of plaque rupture (Tang et al., 2009; Costopoulos et al., 2019) and aortic aneurysms (Martin et al., 2015), peak longitudinal and circumferential wall stresses for aortic aneurysms (Gomez et al., 2021) as well as Von Mises stress in normal aortas (Nathan et al., 2011) and aortic aneurysms (Rissland et al., 2009). Using FEA-derived peak stress, a multifactorial stress equation of peak stress that is based on the analysis of plaque morphological parameters has also been developed recently (Hartman et al., 2021). These plaque morphological parameters include fibrous cap thickness, necrotic core angle, necrotic core thickness, lumen area, and necrotic core calcium and plaque areas. This methodology has the potential of obtaining the peak stress within a plaque rapidly because the detailed FEA is not required.

The high spatial resolution of the data obtained from CFD or FEA simulations bring challenges in statistical analysis that investigates the relation between the focal nature of vascular diseases and biomechanical factors because these data are spatially autocorrelated (i.e., the data are more like each other when they are closer in space). Treating all the data points as independent violates the assumption of standard statistical tests and will artificially augment the sample size and obtain extremely small p values even for a very small effect size. Several methods with different mathematical complexities have been proposed to consider the spatial correlation (Peiffer et al., 2013a; Rowland et al., 2015). These methods are decorrelation length-based sampling, Dutilleul's modified t-test, iterative amplitude adjusted Fourier transform, dual-tree complex wavelet transform, and a bootstrap approach.

Linear mixed-effects regression models have also been used to accommodate the clustering of the multiple slices within a blood

vessel. A mixed-effects regression model incorporates both fixed and random effects. The random effect considers correlations among the data points due to clustering within a vessel (He et al., 2020; Hoogendoorn et al., 2020), within a plaque (Costopoulos et al., 2019) or within the slices (Wang et al., 2015a). The spatial covariance structure can also be specified in a mixed-effects model. In a study of vein bypass graft remodeling, a one-dimensional exponential spatial covariance structure was used for the strong autocorrelation among lumen diameters along the sections in each graft (He et al., 2020). Another concern is the correlation between data obtained at multiple time points from the same patient in a longitudinal study. Linear mixed-effects models can also be used in this case with the patient as a random factor (Colombo et al., 2021).

Human studies have been performed to assess the predictive power of different biomechanical parameters on the initiation, development, and rupture of atherosclerotic plaques. Low and oscillatory WSS has been widely recognized to be the key hemodynamic factor in the initiation and development of atherosclerosis. TAWSS had a higher sensitivity of predicting plaque location in both right and left coronary arteries than average WSS gradient, OSI, and RRT (Knight et al., 2010; Rikhtegar et al., 2012). However, a systematic review found that the evidence for the low/oscillatory shear theory is less robust than commonly assumed (Peiffer et al., 2013c). The definition of low WSS is important and may affect the conclusion (Hartman et al., 2021).

VERIFICATION, VALIDATION, AND UNCERTAINTY QUANTIFICATION

All image-based simulations involve uncertainties and potential errors related to every input needed in the modeling pipeline, including geometry, boundary conditions, mechanical properties, unavailable input parameters that are difficult or unethical to obtain from study subjects, solver settings, and necessary modeling assumptions (Steinman and Migliavacca, 2018; Valen-Sendstad et al., 2018; Steinman and Pereira, 2019). The sizes of these variations and their impact on predicted biomechanical factors need to be assessed through VVUQ. In the context of vascular biomechanical simulations, verification is performed to assess if the numerical simulations solve the simplified mathematical description of the vascular system correctly, and validation is implemented to determine if the model accurately represents the *in vivo* conditions. Uncertainty quantification evaluates how variations in the physical and numerical parameters affect biomechanical factors obtained from simulations. Many VVUQ studies in vascular biomechanical simulations have been performed (Steinman and Migliavacca, 2018). However, since the *in vivo* true values are usually unknown, most of these studies can only evaluate the relative differences compared to the results obtained from other methods.

Geometry (Imaging and Segmentation)

The imaging uncertainties depend on the imaging hardware, image acquisition protocols, techniques of image reconstruction from raw data, and specific characteristics of the patient. The composite effects of obliqueness, in-plane resolution, and voxel anisotropy on the accuracy of black-blood MRI-derived wall thickness measurements at the carotid bulb have been studied (Antiga et al., 2008b). Thick-slice axial acquisitions can result in artificial wall thickening due to its obliqueness to the imaging plane. Reduction of in-plane resolution can also exaggerate wall thicknesses by up to 50%.

The variation of lumen segmentation algorithms of five intracranial aneurysms from 3D digital subtraction angiography (DSA) images among the 26 participating groups has been assessed (Berg et al., 2018). Although qualitative similarity of the aneurysm representations was obtained, the inter-group differences of the aneurysm volumes, ostium surface areas, and morphology parameters (undulation and non-sphericity) were up to 20%, 30%, and 25%, respectively. These morphological variations led to 28%–51% variation in TAWSS, which may lead to an inappropriate interpretation of the simulation results (Voß et al., 2019). In another study using high-resolution OCT-derived geometry as the ground truth, the segmentation of coronary CTA images showed that the measurement uncertainty in minimum lumen diameter had the largest impact on CFD simulation-derived fractional flow reserve (FFR) (Sankaran et al., 2016). The CFD simulations based on coronary CTA images were found to overestimate the absolute TAWSS values than those based on IVUS/OCT images, although the WSS patterns were similar and the correlation and concordance were high (Eslami et al., 2021). Polynomial chaos expansion is another method for a global sensitivity analysis. It uses a stochastic approach to obtain continuous response surfaces of the hemodynamic parameters starting from a few deterministic simulations and is computationally more efficient than a Monte Carlo approach. Furthermore, using the method of polynomial chaos expansion for a global sensitivity analysis, it has been found that the sensitivity to geometry may be different during different instants of the heartbeat and in different vascular regions (Xu et al., 2021).

Blood Properties

Patient-specific blood properties are almost never available for biomechanical simulations, even though blood viscosity can vary up to 20% among individuals (Box et al., 2005). The commonly used viscosity values for the Newtonian model may vary by 10% among different patient groups (Valen-Sendstad et al., 2018). The effects of different blood rheological models on hemodynamics have been evaluated in stenotic carotid (Mendieta et al., 2020) and coronary (Abbasian et al., 2020) arteries and intracranial aneurysms (Oliveira et al., 2021). It has been found that the effects of different blood rheology models on simulation results depend on the specific hemodynamic parameters, and the difference in hemodynamic parameters can be more than 50% compared to the Newtonian model. Using a non-Newtonian blood viscosity model in a simulation requires to update viscosity after each iteration, so it takes longer to finish simulations, and it is common to use a constant blood viscosity value if the blood flow velocity and shear rate are expected to be high. Using a Newtonian model also is more appropriate when the overall flow pattern or the mean WSS

parameters are investigated; the non-Newtonian model is necessary when the low WSS region is the focus, especially for arteries with severe stenosis. When there is stenosis, the region with high velocity and WSS will not be affected significantly by the use of non-Newtonian models.

Wall Properties

In FEA, it is common to assume a constant wall thickness along the length of a blood vessel, but this assumption may be problematic. For example, this led to a significantly different wall stress distribution from that of a patient-specific model using micro-CT-measured wall thickness of an intracranial aneurysm, although the average wall stresses may be similar (Voß et al., 2016). Therefore, use of patient-specific regionally varying wall thickness is recommended for estimating peak biomechanical parameters, especially when the wall thickness is expected to be non-uniform, such as with atherosclerosis, aneurysm, and stenosis (Raut et al., 2013). Additionally, using an anisotropic material model may estimate much higher wall stresses compared to the isotropic and uniform-thickness mode (Mesri et al., 2017). Using a more general non-symmetric collagen fiber dispersion model in arterial walls (Holzapfel et al., 2015) or considering intima heterogeneity (Akyildiz et al., 2018) is needed for better describing the arterial mechanical behavior. As such, the above studies demonstrate the importance of using more realistic wall properties.

In CFD simulations, a rigid wall is most commonly assumed, but the variability in vessel lumen diameter during a cardiac cycle is approximately 5%–10% in most major normal arteries (Taylor et al., 1998). If not specifically cardiac-gated at systole, the images are more likely to be taken at diastole because systole is shorter than diastole. Therefore, the lumen size in simulations using a compliant wall is larger than that using a rigid wall, resulting in smaller velocity and WSS in simulations using a compliant wall than those using a rigid wall, although the distribution patterns of WSS parameters are similar (Kim et al., 2008). On average, the TAWSS of the compliant-wall simulation has been found to be 21.5% lower than that of a rigid-wall simulation for a hemodialysis arteriovenous fistula (McGah et al., 2014). Other studies reported a similar magnitude of difference (to be 25%) in WSS in an idealized carotid bifurcation model (Perktold and Rappitsch, 1995) or smaller (13%) in aortas reconstructed from MR images (Stokes et al., 2021). Furthermore, the effects of assuming a rigid wall on hemodynamic factors may not be uniform across different regions. At the anastomosis of an arteriovenous fistula with a more disturbed flow, the WSS difference between the compliant and rigid walls can be up to 58% (McGah et al., 2014). As expected, decreasing the Young's modulus of the aortic wall causes a more significant underestimation of the peak flow rate (Boccadifuoco et al., 2018a). Nevertheless, previous data suggest that the effect of using a rigid wall in image-based simulations may be less than that due to uncertainties in geometry and boundary conditions (Lee and Steinman, 2007). The validity of the qualitative and quantitative relations between WSS parameters and vascular diseases obtained from a rigid-wall simulations needs to be assessed.

Boundary Conditions

Using a statistical model of blood flow in internal carotid artery in CFD simulations, it has been observed that flow waveform variations at the inlet of internal carotid artery have a limited influence on the TAWSS on the saccular intracranial aneurysm surface, but the internal carotid artery flow waveform strongly affects WSS directionality in regions where the flow is highly multidirectional (Sarrami-Foroushani et al., 2016). The impact of uncertainties in the values of Windkessel model parameters at the outlets on the simulation results of an ascending thoracic aortic aneurysm has been quantified using generalized polynomial chaos expansion (Boccadifuoco et al., 2018b). Again, the results show that the uncertainties in the selected outflow parameters have only a moderate effect on TAWSS but may lead to significant variability of the instantaneous WSS in regions with complex flow. Using a similar method, it has been found that the uncertainty of the Windkessel resistance parameters at the outlets of a thoracic aorta with a coarctation induces a remarkable variability on the flow rate waveform at the peak systole but has a slighter effect on the pressure gradient across the coarctation (Antonuccio et al., 2021).

Validation of Computational Fluid Dynamics Simulations

Some *in vitro* phantom-based experiments and *in vivo* measurements by MRI have been performed to validate the results obtained from CFD simulations. Using a compliant silicone phantom aneurysm model and 3D rotational angiogram, the reliability of the CFD simulation was confirmed by comparing the actual and virtual angiograms obtained from CFD simulations of the contrast concentration (Sun et al., 2010). Another study using a rigid, patient-specific phantom of a complex abdominal aortic aneurysm showed a high degree of agreement between numerically simulated and experimentally measured velocity fields at selected slices by MRI (Kung et al., 2011). Furthermore, the pressure waveforms also had an excellent agreement with only a 3.8% difference between measured and predicted root-mean-square pressures at the light exercise condition (Kung et al., 2011). An *in vivo* 4D-flow MRI study showed the necessity of using turbulent models in simulating thoracic aortic flow (Miyazaki et al., 2017). Also based on 4D-flow MRI, it has been demonstrated that a compliant-wall computational model is needed to show the time lag at the outlets of thoracic aorta with respect to the inlet flow waveform found in MRI data (Boccadifuoco et al., 2018a). However, MRI data may not be ideal for validating CFD results. For example, the WSS and energy loss calculated from MRI data were less than those obtained from CFD simulations around the aortic arch due to the limitation of MRI spatial resolution (Boccadifuoco et al., 2018a).

MACHINE LEARNING

Promising artificial intelligence (AI) and machine learning (ML) methods have been increasingly used in various aspects of

vascular biomechanics research. These methods include imaging (Henglin et al., 2017; Rutkowski et al., 2021); segmentation of images obtained from different imaging modalities (Nasr-Esfahani et al., 2018; Guo et al., 2019; Livne et al., 2019; Zhao et al., 2019; Bajaj et al., 2021; Comelli et al., 2021; Tian et al., 2021); estimation of constitutive parameters *in vivo* (Liu et al., 2019b) or for harvested vascular tissues (González et al., 2020; Liu et al., 2020); estimation of the zero-pressure geometry of human thoracic aorta from two pressurized geometries of the same aorta at two different blood pressure levels (Liang et al., 2018); prediction of hemodynamics in human thoracic aorta trained on CFD data (Liang et al., 2020) or stresses within atherosclerotic walls trained on FEA data (Madani et al., 2019); computation of a probabilistic and anisotropic failure metric of the aortic wall (Liu et al., 2021); and prediction of plaque vulnerability (Cilla et al., 2012; Guo et al., 2021).

Deep learning in medical image analysis is a branch of ML mainly based on convolutional neural network (CNN) methodology (Litjens et al., 2017). When a neural network contains multiple layers between the input and output, it is considered a deep neural network (DNN). Vascular segmentation using well-validated deep learning methods can automatically extract the vascular structure quickly and without operator bias. To develop the deep learning model using a supervised learning approach, a large training dataset that is usually segmented manually or semi-automatically by experts is required. The most popular deep CNN used in medical image segmentation is U-Net (Ronneberger et al., 2015). U-Net has accurately segmented the images of ascending thoracic aortic aneurysm (Comelli et al., 2021) and arteries in the brain (Livne et al., 2019). Other tools, E-Net and V-Net, have also been applied successfully to ascending thoracic aortic aneurysm and coronary artery, respectively (Comelli et al., 2021; Tian et al., 2021).

Conventional image-based CFD, FEA, and FSI simulations are time consuming, limiting their potential clinical applications. Training ML algorithms using CFD and FEA simulations to combine the two methods can help generate results much faster without considerably affecting the performance. As an example, a DNN model could predict the steady velocity magnitude and pressure fields in a thoracic aorta with an average error of 2.0 and 1.4%, respectively, in one second (Liang et al., 2020) or calculate the FFR values with an excellent correlation to CFD predictions in a few seconds (Itu et al., 2016; Coenen et al., 2018). Also using DNN, the predicted peak von Mises stress magnitude in atherosclerotic artery has had an average error less than 10% (Madani et al., 2019). However, the great variations in geometry and boundary conditions among patients make data-driven models difficult to be trained in high-dimensional feature spaces. Further development of fast and real-time CFD and FEA simulations accelerated by ML algorithms may help realize clinical application potential of these biomechanical tools (Phellan et al., 2021).

CONCLUSION

Image-based simulation of the vasculature biomechanics is an active research area. From the perspective of biomechanics and mechanotransduction, it aims to partially reveal the mechanisms of the heterogeneity in the initiation, progression, and treatment response of vascular diseases in different patients. However, a completely personalized simulation, including specific, high-fidelity lumen and wall geometry, flow and pressure boundary conditions at the inlets and outlets, blood and wall properties, and interaction with perivascular tissues, is very challenging and not practical even with recent great advances in imaging and computational algorithms and power. The use of simplified models is necessary, but the validity of these simplified models needs to be thoroughly evaluated. The development and application of novel ML algorithms to all aspects of the CFD, FEA, and FSI pipelines have the potential to accelerate the application of the biomechanical analysis tools to the research and perhaps the treatment of vascular diseases. The future clinical applications may include prediction of the sites with future cardiovascular events, such as formation or rupture of atherosclerotic plaques or aneurysms, and thrombosis formation. In combination with technical advancements, large, prospective, image-based clinical studies are needed to evaluate the capability of biomechanical parameters in predicting hard-defined clinical endpoints (Gijsen et al., 2019).

AUTHOR CONTRIBUTIONS

YH and Y-TS: Conceptualization. YH: Wrote the first draft of the manuscript. YT-S: Funding. All authors critically reviewed and revised the manuscript and approved the submitted version.

REFERENCES

Abbasian, M., Shams, M., Valizadeh, Z., Moshfegh, A., Javadzadegan, A., and Cheng, S. (2020). Effects of Different Non-newtonian Models on Unsteady Blood Flow Hemodynamics in Patient-specific Arterial Models with I*n-Vivo* Validation. *Computer Methods Programs Biomed.* 186, 105185. doi:10.1016/j.cmpb.2019.105185

Adame, I. M., van der Geest, R. J., Wasserman, B. A., Mohamed, M. A., Reiber, J. H. C., and Lelieveldt, B. P. F. (2004). Automatic Segmentation and Plaque Characterization in Atherosclerotic Carotid Artery MR Images. *Magn. Reson. Mater. Phy* 16 (5), 227–234. doi:10.1007/s10334-003-0030-8

Akyildiz, A. C., Speelman, L., van Velzen, B., Stevens, R. R. F., van der Steen, A. F. W., Huberts, W., et al. (2018). Intima Heterogeneity in Stress Assessment of Atherosclerotic Plaques. *Interf. Focus.* 8 (1), 20170008. doi:10.1098/rsfs.2017.0008

Andersson, M., Lantz, J., Ebbers, T., and Karlsson, M. (2017). Multidirectional WSS Disturbances in Stenotic Turbulent Flows: A Pre- and post-intervention Study in an Aortic Coarctation. *J. Biomech.* 51, 8–16. doi:10.1016/j.jbiomech.2016.11.064

Ando, J., and Yamamoto, K. (2022). Hemodynamic Forces, Endothelial Mechanotransduction, and Vascular Diseases. *Magn. Reson. Med. Sci.* 21, 258–266. doi:10.2463/mrms.rev.2021-0018

Antiga, L., Piccinelli, M., Botti, L., Ene-Iordache, B., Remuzzi, A., and Steinman, D. A. (2008a). An Image-Based Modeling Framework for Patient-specific

Computational Hemodynamics. *Med. Biol. Eng. Comput.* 46 (11), 1097–1112. doi:10.1007/s11517-008-0420-1

Antiga, L., Wasserman, B. A., and Steinman, D. A. (2008b). On the Overestimation of Early Wall Thickening at the Carotid Bulb by Black Blood MRI, with Implications for Coronary and Vulnerable Plaque Imaging. *Magn. Reson. Med.* 60 (5), 1020–1028. doi:10.1002/mrm.21758

Antonuccio, M. N., Mariotti, A., Fanni, B. M., Capellini, K., Capelli, C., Sauvage, E., et al. (2021). Effects of Uncertainty of Outlet Boundary Conditions in a Patient-specific Case of Aortic Coarctation. *Ann. Biomed. Eng.* 49, 3494–3507. doi:10.1007/s10439-021-02841-9

Arzani, A., Dyverfeldt, P., Ebbers, T., and Shadden, S. C. (2012). *In Vivo* validation of Numerical Prediction for Turbulence Intensity in an Aortic Coarctation. *Ann. Biomed. Eng.* 40 (4), 860–870. doi:10.1007/s10439-011-0447-6

Arzani, A., and Shadden, S. C. (2018). Wall Shear Stress Fixed Points in Cardiovascular Fluid Mechanics. *J. Biomech.* 73, 145–152. doi:10.1016/j.jbiomech.2018.03.034

Athanasiou, L., Nezami, F. R., Galon, M. Z., Lopes, A. C., Lemos, P. A., de la Torre Hernandez, J. M., et al. (2018). Optimized Computer-Aided Segmentation and Three-Dimensional Reconstruction Using Intracoronary Optical Coherence Tomography. *IEEE J. Biomed. Health Inform.* 22 (4), 1168–1176. doi:10.1109/jbhi.2017.2762520

Athanasiou, L. S., Bourantas, C. V., Rigas, G., Sakellarios, A. I., Exarchos, T. P., Siogkas, P. K., et al. (2014). Methodology for Fully Automated Segmentation and Plaque Characterization in Intracoronary Optical Coherence Tomography Images. *J. Biomed. Opt.* 19 (2), 026009. doi:10.1117/1.JBO.19.2.026009

Auricchio, F., Conti, M., De Beule, M., De Santis, G., and Verhegghe, B. (2011). Carotid Artery Stenting Simulation: from Patient-specific Images to Finite Element Analysis. *Med. Eng. Phys.* 33 (3), 281–289. doi:10.1016/j.medengphy.2010.10.011

Azarine, A., Garçon, P., Stansal, A., Canepa, N., Angelopoulos, G., Silvera, S., et al. (2019). Four-dimensional Flow MRI: Principles and Cardiovascular Applications. *RadioGraphics* 39 (3), 632–648. doi:10.1148/rg.2019180091

Baek, H., Jayaraman, M. V., Richardson, P. D., and Karniadakis, G. E. (2010). Flow Instability and wall Shear Stress Variation in Intracranial Aneurysms. *J. R. Soc. Interf.* 7 (47), 967–988. doi:10.1098/rsif.2009.0476

Bajaj, R., Huang, X., Kilic, Y., Ramasamy, A., Jain, A., Ozkor, M., et al. (2021). Advanced Deep Learning Methodology for Accurate, Real-Time Segmentation of High-Resolution Intravascular Ultrasound Images. *Int. J. Cardiol.* 339, 185–191. doi:10.1016/j.ijcard.2021.06.030

Bazilevs, Y., Hsu, M.-C., Zhang, Y., Wang, W., Liang, X., Kvamsdal, T., et al. (2010). A Fully-Coupled Fluid-Structure Interaction Simulation of Cerebral Aneurysms. *Comput. Mech.* 46 (1), 3–16. doi:10.1007/s00466-009-0421-4

Bennati, L., Vergara, C., Domanin, M., Malloggi, C., Bissacco, D., Trimarchi, S., et al. (2021). A Computational Fluid-Structure Interaction Study for Carotids with Different Atherosclerotic Plaques. *J. Biomech. Eng.* 143 (9), 091002. doi:10.1115/1.4050910

Berg, P., Voß, S., Saalfeld, S., Janiga, G., Bergersen, A. W., Valen-Sendstad, K., et al. (2018). Multiple Aneurysms AnaTomy CHallenge 2018 (MATCH): Phase I: Segmentation. *Cardiovasc. Eng. Tech.* 9 (4), 565–581. doi:10.1007/s13239-018-00376-0

Bidhult, S., Hedström, E., Carlsson, M., Töger, J., Steding-Ehrenborg, K., Arheden, H., et al. (2019). A New Vessel Segmentation Algorithm for Robust Blood Flow Quantification from Two-dimensional Phase-contrast Magnetic Resonance Images. *Clin. Physiol. Funct. Imaging* 39 (5), 327–338. doi:10.1111/cpf.12582

Boccadifuoco, A., Mariotti, A., Capellini, K., Celi, S., and Salvetti, M. V. (2018a). Validation of Numerical Simulations of Thoracic Aorta Hemodynamics: Comparison with *In Vivo* Measurements and Stochastic Sensitivity Analysis. *Cardiovasc. Eng. Tech.* 9, 688–706. doi:10.1007/s13239-018-00387-x

Boccadifuoco, A., Mariotti, A., Celi, S., Martini, N., and Salvetti, M. V. (2018b). Impact of Uncertainties in Outflow Boundary Conditions on the Predictions of Hemodynamic Simulations of Ascending Thoracic Aortic Aneurysms. *Comput. Fluids* 165, 96–115. doi:10.1016/j.compfluid.2018.01.012

Bock, J., Frydrychowicz, A., Stalder, A. F., Bley, T. A., Burkhardt, H., Hennig, J., et al. (2010). 4D Phase Contrast MRI at 3 T: Effect of Standard and Blood-Pool Contrast Agents on SNR, PC-MRA, and Blood Flow Visualization. *Magn. Reson. Med.* 63 (2), 330–338. doi:10.1002/mrm.22199

Bols, J., Degroote, J., Trachet, B., Verhegghe, B., Segers, P., and Vierendeels, J. (2013). A Computational Method to Assess the *In Vivo* Stresses and Unloaded Configuration of Patient-specific Blood Vessels. *J. Comput. Appl. Mathematics* 246, 10–17. doi:10.1016/j.cam.2012.10.034

Bourantas, C. V., Jaffer, F. A., Gijsen, F. J., van Soest, G., Madden, S. P., Courtney, B. K., et al. (2017). Hybrid Intravascular Imaging: Recent Advances, Technical Considerations, and Current Applications in the Study of Plaque Pathophysiology. *Eur. Heart J.* 38 (6), 400–412. doi:10.1093/eurheartj/ehw097

Bourantas, C. V., Kourtis, I. C., Plissiti, M. E., Fotiadis, D. I., Katsouras, C. S., Papafaklis, M. I., et al. (2005). A Method for 3D Reconstruction of Coronary Arteries Using Biplane Angiography and Intravascular Ultrasound Images. *Comput. Med. Imaging Graphics* 29 (8), 597–606. doi:10.1016/j.compmedimag.2005.07.001

Box, F. M. A., van der Geest, R. J., Rutten, M. C. M., and Reiber, J. H. C. (2005). The Influence of Flow, Vessel Diameter, and Non-newtonian Blood Viscosity on the wall Shear Stress in a Carotid Bifurcation Model for Unsteady Flow. *Investig. Radiol.* 40 (5), 277–294. doi:10.1097/01.rli.0000160550.95547.22

Bracamonte, J. H., Wilson, J. S., and Soares, J. S. (2020). Assessing Patient-specific Mechanical Properties of Aortic wall and Peri-Aortic Structures from *In Vivo* Dense Magnetic Resonance Imaging Using an Inverse Finite Element Method and Elastic Foundation Boundary Conditions. *J. Biomech. Eng.* 142 (12), 121011. doi:10.1115/1.4047721

Brezinski, M. E., Tearney, G. J., Bouma, B. E., Boppart, S. A., Hee, M. R., Swanson, E. A., et al. (1996). Imaging of Coronary Artery Microstructure (*In Vitro*) with Optical Coherence Tomography. *Am. J. Cardiol.* 77 (1), 92–93. doi:10.1016/S0002-9149(97)89143-6

Cameron, J. N., Mehta, O. H., Michail, M., Chan, J., Nicholls, S. J., Bennett, M. R., et al. (2020). Exploring the Relationship between Biomechanical Stresses and Coronary Atherosclerosis. *Atherosclerosis* 302, 43–51. doi:10.1016/j.atherosclerosis.2020.04.011

Campbell, I. C., Ries, J., Dhawan, S. S., Quyyumi, A. A., Taylor, W. R., and Oshinski, J. N. (2012). Effect of Inlet Velocity Profiles on Patient-specific Computational Fluid Dynamics Simulations of the Carotid Bifurcation. *J. Biomech. Eng.* 134 (5), 051001. doi:10.1115/1.4006681

Campos, C. M., Fedewa, R. J., Garcia-Garcia, H. M., Vince, D. G., Margolis, M. P., Lemos, P. A., et al. (2015). Ex Vivovalidation of 45 MHz Intravascular Ultrasound Backscatter Tissue Characterization. *Eur. Heart J. Cardiovasc. Imaging* 16 (10), 1112–1119. doi:10.1093/ehjci/jev039

Carpenter, H. J., Gholipour, A., Ghayesh, M. H., Zander, A. C., and Psaltis, P. J. (2020). A Review on the Biomechanics of Coronary Arteries. *Int. J. Eng. Sci.* 147, 103201. doi:10.1016/j.ijengsci.2019.103201

Cebral, J. R., Castro, M. A., Putman, C. M., and Alperin, N. (2008). Flow-area Relationship in Internal Carotid and Vertebral Arteries. *Physiol. Meas.* 29 (5), 585–594. doi:10.1088/0967-3334/29/5/005

Cebull, H. L., Rayz, V. L., and Goergen, C. J. (2020). Recent Advances in Biomechanical Characterization of Thoracic Aortic Aneurysms. *Front. Cardiovasc. Med.* 7, 75. doi:10.3389/fcvm.2020.00075

Cheng, Z., Juli, C., Wood, N. B., Gibbs, R. G. J., and Xu, X. Y. (2014). Predicting Flow in Aortic Dissection: Comparison of Computational Model with PC-MRI Velocity Measurements. *Med. Eng. Phys.* 36 (9), 1176–1184. doi:10.1016/j.medengphy.2014.07.006

Chiu, J.-J., and Chien, S. (2011). Effects of Disturbed Flow on Vascular Endothelium: Pathophysiological Basis and Clinical Perspectives. *Physiol. Rev.* 91 (1), 327–387. doi:10.1152/physrev.00047.2009

Chnafa, C., Brina, O., Pereira, V. M., and Steinman, D. A. (2018). Better Than Nothing: a Rational Approach for Minimizing the Impact of Outflow Strategy on Cerebrovascular Simulations. *AJNR Am. J. Neuroradiol* 39 (2), 337–343. doi:10.3174/ajnr.A5484

Chun Yang, C., Bach, R. G., Jie Zheng, J., Ei Naqa, I., Woodard, P. K., Zhongzhao Teng, Z., et al. (2009). *In Vivo* IVUS-Based 3-D Fluid-Structure Interaction Models with Cyclic Bending and Anisotropic Vessel Properties for Human Atherosclerotic Coronary Plaque Mechanical Analysis. *IEEE Trans. Biomed. Eng.* 56 (10), 2420–2428. doi:10.1109/TBME.2009.2025658

Chuong, C. J., and Fung, Y. C. (1986). On Residual Stresses in Arteries. *J. Biomech. Eng.* 108 (2), 189–192. doi:10.1115/1.3138600

Cilla, M., Martinez, J., Pena, E., and Martinez, M. A. (2012). Machine Learning Techniques as a Helpful Tool toward Determination of Plaque Vulnerability. *IEEE Trans. Biomed. Eng.* 59 (4), 1155–1161. doi:10.1109/TBME.2012.2185495

Coenen, A., Kim, Y.-H., Kruk, M., Tesche, C., De Geer, J., Kurata, A., et al. (2018). Diagnostic Accuracy of a Machine-Learning Approach to Coronary Computed

Tomographic Angiography-Based Fractional Flow Reserve. *Circ. Cardiovasc. Imaging* 11 (6), e007217. doi:10.1161/circimaging.117.007217

Colombo, M., He, Y., Corti, A., Gallo, D., Ninno, F., Casarin, S., et al. (2021). In-stent Restenosis Progression in Human Superficial Femoral Arteries: Dynamics of Lumen Remodeling and Impact of Local Hemodynamics. *Ann. Biomed. Eng.* 49 (9), 2349–2364. doi:10.1007/s10439-021-02776-1

Comelli, A., Dahiya, N., Stefano, A., Benfante, V., Gentile, G., Agnese, V., et al. (2021). Deep Learning Approach for the Segmentation of Aneurysmal Ascending Aorta. *Biomed. Eng. Lett.* 11 (1), 15–24. doi:10.1007/s13534-020-00179-0

Costopoulos, C., Timmins, L. H., Huang, Y., Hung, O. Y., Molony, D. S., Brown, A. J., et al. (2019). Impact of Combined Plaque Structural Stress and wall Shear Stress on Coronary Plaque Progression, Regression, and Changes in Composition. *Eur. Heart J.* 40 (18), 1411–1422. doi:10.1093/eurheartj/ehz132

Davies, P. F. (1995). Flow-mediated Endothelial Mechanotransduction. *Physiol. Rev.* 75 (3), 519–560. doi:10.1152/physrev.1995.75.3.519

Dennis, K. D., Kallmes, D. F., and Dragomir-Daescu, D. (2017). Cerebral Aneurysm Blood Flow Simulations Are Sensitive to Basic Solver Settings. *J. Biomech.* 57, 46–53. doi:10.1016/j.jbiomech.2017.03.020

Di Martino, E. S., Bohra, A., Vande Geest, J. P., Gupta, N., Makaroun, M. S., and Vorp, D. A. (2006). Biomechanical Properties of Ruptured versus Electively Repaired Abdominal Aortic Aneurysm wall Tissue. *J. Vasc. Surg.* 43 (3), 570–576. doi:10.1016/j.jvs.2005.10.072

Eslami, P., Hartman, E. M. J., Albaghadai, M., Karady, J., Jin, Z., Thondapu, V., et al. (2021). Validation of wall Shear Stress Assessment in Non-invasive Coronary CTA versus Invasive Imaging: a Patient-specific Computational Study. *Ann. Biomed. Eng.* 49 (4), 1151–1168. doi:10.1007/s10439-020-02631-9

Figueroa, C. A., Vignon-Clementel, I. E., Jansen, K. E., Hughes, T. J. R., and Taylor, C. A. (2006). A Coupled Momentum Method for Modeling Blood Flow in Three-Dimensional Deformable Arteries. *Computer Methods Appl. Mech. Eng.* 195 (41), 5685–5706. doi:10.1016/j.cma.2005.11.011

Gallo, D., De Santis, G., Negri, F., Tresoldi, D., Ponzini, R., Massai, D., et al. (2012). On the Use of *In Vivo* Measured Flow Rates as Boundary Conditions for Image-Based Hemodynamic Models of the Human Aorta: Implications for Indicators of Abnormal Flow. *Ann. Biomed. Eng.* 40 (3), 729–741. doi:10.1007/s10439-011-0431-1

Gasser, T. C., Gallinetti, S., Xing, X., Forsell, C., Swedenborg, J., and Roy, J. (2012). Spatial Orientation of Collagen Fibers in the Abdominal Aortic Aneurysm's wall and its Relation to wall Mechanics. *Acta Biomater.* 8 (8), 3091–3103. doi:10.1016/j.actbio.2012.04.044

Gee, M. W., Förster, C., and Wall, W. A. (2010). A Computational Strategy for Prestressing Patient-specific Biomechanical Problems under Finite Deformation. *Int. J. Numer. Meth. Biomed. Engng.* 26 (1), 52–72. doi:10.1002/cnm.1236

Gijsen, F., Katagiri, Y., Barlis, P., Bourantas, C., Collet, C., Coskun, U., et al. (2019). Expert Recommendations on the Assessment of wall Shear Stress in Human Coronary Arteries: Existing Methodologies, Technical Considerations, and Clinical Applications. *Eur. Heart J.* 40 (41), 3421–3433. doi:10.1093/eurheartj/ehz551

Gold, G. E., Pauly, J. M., Glover, G. H., Moretto, J. C., Macovski, A., and Herfkens, R. J. (1993). Characterization of Atherosclerosis with a 1.5-T Imaging System. *J. Magn. Reson. Imaging* 3 (2), 399–407. doi:10.1002/jmri.1880030216

Gomez, A., Wang, Z., Xuan, Y., Hope, M. D., Saloner, D. A., Guccione, J. M., et al. (2021). Association of Diameter and wall Stresses of Tricuspid Aortic Valve Ascending Thoracic Aortic Aneurysms. *J. Thorac. Cardiovasc. Surg.* 1, 1. doi:10.1016/j.jtcvs.2021.05.049

González, D., García-González, A., Chinesta, F., and Cueto, E. (2020). A Data-Driven Learning Method for Constitutive Modeling: Application to Vascular Hyperelastic Soft Tissues. *Materials* 13 (10), 2319. doi:10.3390/ma13102319

Guo, X., Giddens, D. P., Molony, D., Yang, C., Samady, H., Zheng, J., et al. (2018). Combining IVUS and Optical Coherence Tomography for More Accurate Coronary Cap Thickness Quantification and Stress/strain Calculations: a Patient-specific Three-Dimensional Fluid-Structure Interaction Modeling Approach. *J. Biomech. Eng.* 140 (4), 041005. doi:10.1115/1.4038263

Guo, X., Maehara, A., Matsumura, M., Wang, L., Zheng, J., Samady, H., et al. (2021). Predicting Plaque Vulnerability Change Using Intravascular Ultrasound + Optical Coherence Tomography Image-Based Fluid-Structure Interaction Models and Machine Learning Methods with Patient Follow-Up Data: a Feasibility Study. *Biomed. Eng. Online* 20 (1), 34. doi:10.1186/s12938-021-00868-6

Guo, X., Tang, D., Molony, D., Yang, C., Samady, H., Zheng, J., et al. (2019). A Machine Learning-Based Method for Intracoronary OCT Segmentation and Vulnerable Coronary Plaque Cap Thickness Quantification. *Int. J. Comput. Methods* 16 (3), 1842008. doi:10.1142/s0219876218420082

Guo, X., Zhu, J., Maehara, A., Monoly, D., Samady, H., Wang, L., et al. (2017). Quantify Patient-specific Coronary Material Property and its Impact on Stress/strain Calculations Using *In Vivo* IVUS Data and 3D FSI Models: a Pilot Study. *Biomech. Model. Mechanobiol.* 16 (1), 333–344. doi:10.1007/s10237-016-0820-3

Guvenir Torun, S., Torun, H. M., Hansen, H. H. G., Gandini, G., Berselli, I., Codazzi, V., et al. (2021). Multicomponent Mechanical Characterization of Atherosclerotic Human Coronary Arteries: an Experimental and Computational Hybrid Approach. *Front. Physiol.* 12, 733009. doi:10.3389/fphys.2021.733009

Ha, H., Ziegler, M., Welander, M., Bjarnegård, N., Carlhäll, C.-J., Lindenberger, M., et al. (2018). Age-related Vascular Changes Affect Turbulence in Aortic Blood Flow. *Front. Physiol.* 9, 36. doi:10.3389/fphys.2018.00036

Hartman, E. M. J., De Nisco, G., Gijsen, F. J. H., Korteland, S.-A., van der Steen, A. F. W., Daemen, J., et al. (2021). The Definition of Low wall Shear Stress and its Effect on Plaque Progression Estimation in Human Coronary Arteries. *Sci. Rep.* 11 (1), 22086. doi:10.1038/s41598-021-01232-3

Hatsukami, T. S., Ross, R., Polissar, N. L., and Yuan, C. (2000). Visualization of Fibrous Cap Thickness and Rupture in Human Atherosclerotic Carotid Plaque *In Vivo* with High-Resolution Magnetic Resonance Imaging. *Circulation* 102 (9), 959–964. doi:10.1161/01.CIR.102.9.959

He, X., and Ku, D. N. (1996). Pulsatile Flow in the Human Left Coronary Artery Bifurcation: Average Conditions. *J. Biomech. Eng.* 118 (1), 74–82. doi:10.1115/1.2795948

He, Y., DeSart, K., Kubilis, P. S., Irwin, A., Tran-Son-Tay, R., Nelson, P. R., et al. (2020). Heterogeneous and Dynamic Lumen Remodeling of the Entire Infrainguinal Vein Bypass Grafts in Patients. *J. Vasc. Surg.* 71 (5), 1620–1628. e1623. doi:10.1016/j.jvs.2019.05.069

He, Y., Shiu, Y.-T., Pike, D. B., Roy-Chaudhury, P., Cheung, A. K., and Berceli, S. A. (2018). Comparison of Hemodialysis Arteriovenous Fistula Blood Flow Rates Measured by Doppler Ultrasound and Phase-Contrast Magnetic Resonance Imaging. *J. Vasc. Surg.* 68 (6), 1848–1857. e1842. doi:10.1016/j.jvs.2018.02.043

He, Y., Terry, C. M., Nguyen, C., Berceli, S. A., Shiu, Y.-T. E., and Cheung, A. K. (2013). Serial Analysis of Lumen Geometry and Hemodynamics in Human Arteriovenous Fistula for Hemodialysis Using Magnetic Resonance Imaging and Computational Fluid Dynamics. *J. Biomech.* 46 (1), 165–169. doi:10.1016/j.jbiomech.2012.09.005

Hemmler, A., Lutz, B., Kalender, G., Reeps, C., and Gee, M. W. (2019). Patient-specific In Silico Endovascular Repair of Abdominal Aortic Aneurysms: Application and Validation. *Biomech. Model. Mechanobiol.* 18, 983–1004. doi:10.1007/s10237-019-01125-5

Henglin, M., Stein, G., Hushcha, P. V., Snoek, J., Wiltschko, A. B., and Cheng, S. (2017). Machine Learning Approaches in Cardiovascular Imaging. *Circ. Cardiovasc. Imaging* 10 (10), e005614. doi:10.1161/CIRCIMAGING.117.005614

Himburg, H. A., Grzybowski, D. M., Hazel, A. L., LaMack, J. A., Li, X.-M., and Friedman, M. H. (2004). Spatial Comparison between wall Shear Stress Measures and Porcine Arterial Endothelial Permeability. *Am. J. Physiology-Heart Circulatory Physiol.* 286 (5), H1916–H1922. doi:10.1152/ajpheart.00897.2003

Hodis, S., and Zamir, M. (2011). Pulse Wave Velocity as a Diagnostic index: the Pitfalls of Tethering versus Stiffening of the Arterial wall. *J. Biomech.* 44 (7), 1367–1373. doi:10.1016/j.jbiomech.2010.12.029

Holzapfel, G. A., Gasser, T. C., and Ogden, R. W. (2000). A New Constitutive Framework for Arterial wall Mechanics and a Comparative Study of Material Models. *J. Elast.* 61 (1), 1–48. doi:10.1023/A:1010835316564

Holzapfel, G. A., Niestrawska, J. A., Ogden, R. W., Reinisch, A. J., and Schriefl, A. J. (2015). Modelling Non-symmetric Collagen Fibre Dispersion in Arterial walls. *J. R. Soc. Interf.* 12 (106), 20150188. doi:10.1098/rsif.2015.0188

Holzapfel, G. A., and Ogden, R. W. (2010). Constitutive Modelling of Arteries. *Proc. R. Soc. A.* 466 (2118), 1551–1597. doi:10.1098/rspa.2010.0058

Hoogendoorn, A., Kok, A. M., Hartman, E. M. J., de Nisco, G., Casadonte, L., Chiastra, C., et al. (2020). Multidirectional wall Shear Stress Promotes Advanced Coronary Plaque Development: Comparing Five Shear Stress Metrics. *Cardiovasc. Res.* 116 (6), 1136–1146. doi:10.1093/cvr/cvz212

Huang, X., Yang, C., Yuan, C., Liu, F., Canton, G., Zheng, J., et al. (2009). Patient-specific Artery Shrinkage and 3D Zero-Stress State in Multi-Component 3D FSI Models for Carotid Atherosclerotic Plaques Based on *In Vivo* MRI Data. *Mol. Cel. Biomech.* 6 (2), 121–134.

Itu, L., Rapaka, S., Passerini, T., Georgescu, B., Schwemmer, C., Schoebinger, M., et al. (2016). A Machine-Learning Approach for Computation of Fractional Flow reserve from Coronary Computed Tomography. *J. Appl. Physiol.* 121 (1), 42–52. doi:10.1152/japplphysiol.00752.2015

Jadidi, M., Habibnezhad, M., Anttila, E., Maleckis, K., Desyatova, A., MacTaggart, J., et al. (2020). Mechanical and Structural Changes in Human Thoracic Aortas with Age. *Acta Biomater.* 103, 172–188. doi:10.1016/j.actbio.2019.12.024

Jadidi, M., Razian, S. A., Habibnezhad, M., Anttila, E., and Kamenskiy, A. (2021a). Mechanical, Structural, and Physiologic Differences in Human Elastic and Muscular Arteries of Different Ages: Comparison of the Descending Thoracic Aorta to the Superficial Femoral Artery. *Acta Biomater.* 119, 268–283. doi:10.1016/j.actbio.2020.10.035

Jadidi, M., Sherifova, S., Sommer, G., Kamenskiy, A., and Holzapfel, G. A. (2021b). Constitutive Modeling Using Structural Information on Collagen Fiber Direction and Dispersion in Human Superficial Femoral Artery Specimens of Different Ages. *Acta Biomater.* 121, 461–474. doi:10.1016/j.actbio.2020.11.046

Kadry, K., Olender, M. L., Marlevi, D., Edelman, E. R., and Nezami, F. R. (2021). A Platform for High-Fidelity Patient-specific Structural Modelling of Atherosclerotic Arteries: from Intravascular Imaging to Three-Dimensional Stress Distributions. *J. R. Soc. Interf.* 18 (182), 20210436. doi:10.1098/rsif.2021.0436

Kagadis, G. C., Skouras, E. D., Bourantas, G. C., Paraskeva, C. A., Katsanos, K., Karnabatidis, D., et al. (2008). Computational Representation and Hemodynamic Characterization of *In Vivo* Acquired Severe Stenotic Renal Artery Geometries Using Turbulence Modeling. *Med. Eng. Phys.* 30 (5), 647–660. doi:10.1016/j.medengphy.2007.07.005

Kerwin, W. S., Miller, Z., and Yuan, C. (2017). Imaging of the High-Risk Carotid Plaque: Magnetic Resonance Imaging. *Semin. Vasc. Surg.* 30 (1), 54–61. doi:10.1053/j.semvascsurg.2017.04.009

Khan, M. O., Valen-Sendstad, K., and Steinman, D. A. (2015). Narrowing the Expertise gap for Predicting Intracranial Aneurysm Hemodynamics: Impact of Solver Numerics versus Mesh and Time-step Resolution. *Am. J. Neuroradiology* 36 (7), 1310–1316. doi:10.3174/ajnr.A4263

Kilic, Y., Safi, H., Bajaj, R., Serruys, P. W., Kitslaar, P., Ramasamy, A., et al. (2020). The Evolution of Data Fusion Methodologies Developed to Reconstruct Coronary Artery Geometry from Intravascular Imaging and Coronary Angiography Data: a Comprehensive Review. *Front. Cardiovasc. Med.* 7, 33. doi:10.3389/fcvm.2020.00033

Kim, J. J., Dillon, W. P., Glastonbury, C. M., Provenzale, J. M., and Wintermark, M. (2010). Sixty-four-section Multidetector CT Angiography of Carotid Arteries: a Systematic Analysis of Image Quality and Artifacts. *AJNR Am. J. Neuroradiol* 31 (1), 91–99. doi:10.3174/ajnr.A1768

Kim, Y.-H., Kim, J.-E., Ito, Y., Shih, A. M., Brott, B., and Anayiotos, A. (2008). Hemodynamic Analysis of a Compliant Femoral Artery Bifurcation Model Using a Fluid Structure Interaction Framework. *Ann. Biomed. Eng.* 36 (11), 1753–1763. doi:10.1007/s10439-008-9558-0

Knight, J., Olgac, U., Saur, S. C., Poulikakos, D., Marshall, W., Jr, Cattin, P. C., et al. (2010). Choosing the Optimal wall Shear Parameter for the Prediction of Plaque Location-A Patient-specific Computational Study in Human Right Coronary Arteries. *Atherosclerosis* 211 (2), 445–450. doi:10.1016/j.atherosclerosis.2010.03.001

Kubo, T., Terada, K., Ino, Y., Shiono, Y., Tu, S., Tsao, T.-P., et al. (2022). Combined Use of Multiple Intravascular Imaging Techniques in Acute Coronary Syndrome. *Front. Cardiovasc. Med.* 8, 824128. doi:10.3389/fcvm.2021.824128

Kung, E. O., Les, A. S., Medina, F., Wicker, R. B., McConnell, M. V., and Taylor, C. A. (2011). *In Vitro* validation of Finite-Element Model of AAA Hemodynamics Incorporating Realistic Outlet Boundary Conditions. *J. Biomech. Eng.* 133 (4), 041003. doi:10.1115/1.4003526

Ladak, H. M., Thomas, J. B., Mitchell, J. R., Rutt, B. K., and Steinman, D. A. (2001). A Semi-automatic Technique for Measurement of Arterial wall from Black Blood MRI. *Med. Phys.* 28 (6), 1098–1107. doi:10.1118/1.1368125

Lantz, J., Ebbers, T., Engvall, J., and Karlsson, M. (2013). Numerical and Experimental Assessment of Turbulent Kinetic Energy in an Aortic Coarctation. *J. Biomech.* 46 (11), 1851–1858. doi:10.1016/j.jbiomech.2013.04.028

Lee, J., Prabhu, D., Kolluru, C., Gharaibeh, Y., Zimin, V. N., Dallan, L. A. P., et al. (2020). Fully Automated Plaque Characterization in Intravascular OCT Images Using Hybrid Convolutional and Lumen Morphology Features. *Sci. Rep.* 10 (1), 2596. doi:10.1038/s41598-020-59315-6

Lee, S.-W., Smith, D. S., Loth, F., Fischer, P. F., and Bassiouny, H. S. (2007). Importance of Flow Division on Transition to Turbulence within an Arteriovenous Graft. *J. Biomech.* 40 (5), 981–992. doi:10.1016/j.jbiomech.2006.03.024

Lee, S.-W., and Steinman, D. A. (2007). On the Relative Importance of Rheology for Image-Based CFD Models of the Carotid Bifurcation. *J. Biomech. Eng.* 129 (2), 273–278. doi:10.1115/1.2540836

Li, J., Li, X., Mohar, D., Raney, A., Jing, J., Zhang, J., et al. (2014). Integrated IVUS-OCT for Real-Time Imaging of Coronary Atherosclerosis. *JACC: Cardiovasc. Imaging* 7 (1), 101–103. doi:10.1016/j.jcmg.2013.07.012

Liang, L., Liu, M., Martin, C., and Sun, W. (2018). A Machine Learning Approach as a Surrogate of Finite Element Analysis-Based Inverse Method to Estimate the Zero-Pressure Geometry of Human Thoracic Aorta. *Int. J. Numer. Meth Biomed. Engng* 34 (8), e3103. doi:10.1002/cnm.3103

Liang, L., Mao, W., and Sun, W. (2020). A Feasibility Study of Deep Learning for Predicting Hemodynamics of Human Thoracic Aorta. *J. Biomech.* 99, 109544. doi:10.1016/j.jbiomech.2019.109544

Liang, L., Steinman, D. A., Brina, O., Chnafa, C., Cancelliere, N. M., and Pereira, V. M. (2019). Towards the Clinical Utility of CFD for Assessment of Intracranial Aneurysm Rupture - a Systematic Review and Novel Parameter-Ranking Tool. *J. Neurointervent Surg.* 11 (2), 153–158. doi:10.1136/neurintsurg-2018-014246

Lipp, S. N., Niedert, E. E., Cebull, H. L., Diorio, T. C., Ma, J. L., Rothenberger, S. M., et al. (2020). Computational Hemodynamic Modeling of Arterial Aneurysms: a Mini-Review. *Front. Physiol.* 11, 454. doi:10.3389/fphys.2020.00454

Litjens, G., Kooi, T., Bejnordi, B. E., Setio, A. A. A., Ciompi, F., Ghafoorian, M., et al. (2017). A Survey on Deep Learning in Medical Image Analysis. *Med. Image Anal.* 42, 60–88. doi:10.1016/j.media.2017.07.005

Liu, M., Liang, L., Ismail, Y., Dong, H., Lou, X., Iannucci, G., et al. (2021). Computation of a Probabilistic and Anisotropic Failure Metric on the Aortic wall Using a Machine Learning-Based Surrogate Model. *Comput. Biol. Med.* 137, 104794. doi:10.1016/j.compbiomed.2021.104794

Liu, M., Liang, L., Sulejmani, F., Lou, X., Iannucci, G., Chen, E., et al. (2019a). Identification of *In Vivo* Nonlinear Anisotropic Mechanical Properties of Ascending Thoracic Aortic Aneurysm from Patient-specific CT Scans. *Sci. Rep.* 9 (1), 12983. doi:10.1038/s41598-019-49438-w

Liu, M., Liang, L., and Sun, W. (2020). A Generic Physics-Informed Neural Network-Based Constitutive Model for Soft Biological Tissues. *Computer Methods Appl. Mech. Eng.* 372, 113402. doi:10.1016/j.cma.2020.113402

Liu, M., Liang, L., and Sun, W. (2019b). Estimation of *In Vivo* Constitutive Parameters of the Aortic wall Using a Machine Learning Approach. *Computer Methods Appl. Mech. Eng.* 347, 201–217. doi:10.1016/j.cma.2018.12.030

Liu, W., Balu, N., Sun, J., Zhao, X., Chen, H., Yuan, C., et al. (2012). Segmentation of Carotid Plaque Using Multicontrast 3D Gradient echo MRI. *J. Magn. Reson. Imaging* 35 (4), 812–819. doi:10.1002/jmri.22886

Liu, Y., Dang, C., Garcia, M., Gregersen, H., and Kassab, G. S. (2007). Surrounding Tissues Affect the Passive Mechanics of the Vessel wall: Theory and experiment. *Am. J. Physiology-Heart Circulatory Physiol.* 293 (6), H3290–H3300. doi:10.1152/ajpheart.00666.2007

Livne, M., Rieger, J., Aydin, O. U., Taha, A. A., Akay, E. M., Kossen, T., et al. (2019). A U-Net Deep Learning Framework for High Performance Vessel Segmentation in Patients with Cerebrovascular Disease. *Front. Neurosci.* 13, 97. doi:10.3389/fnins.2019.00097

Lopes, D., Puga, H., Teixeira, J., and Lima, R. (2020). Blood Flow Simulations in Patient-specific Geometries of the Carotid Artery: a Systematic Review. *J. Biomech.* 111, 110019. doi:10.1016/j.jbiomech.2020.110019

Lu, J., Zhou, X., and Raghavan, M. L. (2007). Computational Method of Inverse Elastostatics for Anisotropic Hyperelastic Solids. *Int. J. Numer. Meth. Engng* 69 (6), 1239–1261. doi:10.1002/nme.1807

Lv, R., Maehara, A., Matsumura, M., Wang, L., Zhang, C., Huang, M., et al. (2021). Using Optical Coherence Tomography and Intravascular Ultrasound Imaging to Quantify Coronary Plaque Cap Stress/strain and Progression: a Follow-Up Study Using 3d Thin-Layer Models. *Front. Bioeng. Biotechnol.* 9, 713525. doi:10.3389/fbioe.2021.713525

Maas, S. A., Erdemir, A., Halloran, J. P., and Weiss, J. A. (2016). A General Framework for Application of Prestrain to Computational Models of Biological Materials. *J. Mech. Behav. Biomed. Mater.* 61, 499–510. doi:10.1016/j.jmbbm.2016.04.012

Madani, A., Bakhaty, A., Kim, J., Mubarak, Y., and Mofrad, M. R. K. (2019). Bridging Finite Element and Machine Learning Modeling: Stress Prediction of Arterial walls in Atherosclerosis. *J. Biomech. Eng.* 141 (8), 1. doi:10.1115/1.4043290

Manchester, E. L., Pirola, S., Salmasi, M. Y., O'Regan, D. P., Athanasiou, T., and Xu, X. Y. (2021). Analysis of Turbulence Effects in a Patient-specific Aorta with Aortic Valve Stenosis. *Cardiovasc. Eng. Tech.* 12 (4), 438–453. doi:10.1007/s13239-021-00536-9

Mantella, L. E., Liblik, K., and Johri, A. M. (2021). Vascular Imaging of Atherosclerosis: Strengths and Weaknesses. *Atherosclerosis* 319, 42–50. doi:10.1016/j.atherosclerosis.2020.12.021

Mariotti, A., Boccadifuoco, A., Celi, S., and Salvetti, M. V. (2021). Hemodynamics and Stresses in Numerical Simulations of the Thoracic Aorta: Stochastic Sensitivity Analysis to Inlet Flow-Rate Waveform. *Comput. Fluids* 230, 105123. doi:10.1016/j.compfluid.2021.105123

Markl, M., Schnell, S., and Barker, A. J. (2014). 4D Flow Imaging: Current Status to Future Clinical Applications. *Curr. Cardiol. Rep.* 16 (5), 481. doi:10.1007/s11886-014-0481-8

Martin, A. J., Gotlieb, A. I., and Henkelman, R. M. (1995). High-resolution MR Imaging of Human Arteries. *J. Magn. Reson. Imaging* 5 (1), 93–100. doi:10.1002/jmri.1880050117

Martin, C., Sun, W., and Elefteriades, J. (2015). Patient-specific Finite Element Analysis of Ascending Aorta Aneurysms. *Am. J. Physiology-Heart Circulatory Physiol.* 308 (10), H1306–H1316. doi:10.1152/ajpheart.00908.2014

Mazzi, V., Gallo, D., Calò, K., Najafi, M., Khan, M. O., De Nisco, G., et al. (2020). A Eulerian Method to Analyze wall Shear Stress Fixed Points and Manifolds in Cardiovascular Flows. *Biomech. Model. Mechanobiol.* 19 (5), 1403–1423. doi:10.1007/s10237-019-01278-3

Mazzi, V., Morbiducci, U., Calò, K., De Nisco, G., Lodi Rizzini, M., Torta, E., et al. (2021). Wall Shear Stress Topological Skeleton Analysis in Cardiovascular Flows: Methods and Applications. *Mathematics* 9 (7), 720. doi:10.3390/math9070720

McGah, P. M., Leotta, D. F., Beach, K. W., and Aliseda, A. (2014). Effects of wall Distensibility in Hemodynamic Simulations of an Arteriovenous Fistula. *Biomech. Model. Mechanobiol.* 13 (3), 679–695. doi:10.1007/s10237-013-0527-7

Mendieta, J. B., Fontanarosa, D., Wang, J., Paritala, P. K., McGahan, T., Lloyd, T., et al. (2020). The Importance of Blood Rheology in Patient-specific Computational Fluid Dynamics Simulation of Stenotic Carotid Arteries. *Biomech. Model. Mechanobiol.* 19 (5), 1477–1490. doi:10.1007/s10237-019-01282-7

Mesri, Y., Niazmand, H., and Deyranlou, A. (2017). Numerical Study on Fluid-Structure Interaction in a Patient-specific Abdominal Aortic Aneurysm for Evaluating wall Heterogeneity and Material Model Effects on its Rupture. *J. Appl. Fluid Mech.* 10 (6), 1699–1709. doi:10.18869/acadpub.jafm.73.243.2767810.29252/jafm.73.245.27678

Min, J. K., Taylor, C. A., Achenbach, S., Koo, B. K., Leipsic, J., Nørgaard, B. L., et al. (2015). Noninvasive Fractional Flow Reserve Derived from Coronary CT Angiography. *JACC: Cardiovasc. Imaging* 8 (10), 1209–1222. doi:10.1016/j.jcmg.2015.08.006

Miyazaki, S., Itatani, K., Furusawa, T., Nishino, T., Sugiyama, M., Takehara, Y., et al. (2017). Validation of Numerical Simulation Methods in Aortic Arch Using 4D Flow MRI. *Heart Vessels* 32 (8), 1032–1044. doi:10.1007/s00380-017-0979-2

Mohamied, Y., Sherwin, S. J., and Weinberg, P. D. (2017). Understanding the Fluid Mechanics behind Transverse wall Shear Stress. *J. Biomech.* 50, 102–109. doi:10.1016/j.jbiomech.2016.11.035

Morbiducci, U., Gallo, D., Cristofanelli, S., Ponzini, R., Deriu, M. A., Rizzo, G., et al. (2015). A Rational Approach to Defining Principal Axes of Multidirectional wall Shear Stress in Realistic Vascular Geometries, with Application to the Study of the Influence of Helical Flow on wall Shear Stress Directionality in Aorta. *J. Biomech.* 48 (6), 899–906. doi:10.1016/j.jbiomech.2015.02.027

Morbiducci, U., Mazzi, V., Domanin, M., De Nisco, G., Vergara, C., Steinman, D. A., et al. (2020). Wall Shear Stress Topological Skeleton Independently Predicts Long-Term Restenosis after Carotid Bifurcation Endarterectomy. *Ann. Biomed. Eng.* 48 (12), 2936–2949. doi:10.1007/s10439-020-02607-9

Morbiducci, U., Ponzini, R., Gallo, D., Bignardi, C., and Rizzo, G. (2013). Inflow Boundary Conditions for Image-Based Computational Hemodynamics: Impact of Idealized versus Measured Velocity Profiles in the Human Aorta. *J. Biomech.* 46 (1), 102–109. doi:10.1016/j.jbiomech.2012.10.012

Murray, C. D. (1926). The Physiological Principle of Minimum Work. *Proc. Natl. Acad. Sci. U.S.A.* 12 (3), 207–214. doi:10.1073/pnas.12.3.207

Nair, A., Margolis, M. P., Kuban, B. D., and Vince, D. G. (2007). Automated Coronary Plaque Characterisation with Intravascular Ultrasound Backscatter: *Ex Vivo* Validation. *EuroIntervention* 3 (1), 113–120. doi:10.4244/EIJV3I1A18

Nair, A., Kuban, B. D., Tuzcu, E. M., Schoenhagen, P., Nissen, S. E., and Vince, D. G. (2002). Coronary Plaque Classification with Intravascular Ultrasound Radiofrequency Data Analysis. *Circulation* 106 (17), 2200–2206. doi:10.1161/01.CIR.0000035654.18341.5E

Narayanan, B., Olender, M. L., Marlevi, D., Edelman, E. R., and Nezami, F. R. (2021). An Inverse Method for Mechanical Characterization of Heterogeneous Diseased Arteries Using Intravascular Imaging. *Sci. Rep.* 11 (1), 22540. doi:10.1038/s41598-021-01874-3

Nasr-Esfahani, E., Karimi, N., Jafari, M. H., Soroushmehr, S. M. R., Samavi, S., Nallamothu, B. K., et al. (2018). Segmentation of Vessels in Angiograms Using Convolutional Neural Networks. *Biomed. Signal Process. Control.* 40, 240–251. doi:10.1016/j.bspc.2017.09.012

Nathan, D. P., Xu, C., Gorman, J. H., 3rd, Fairman, R. M., Bavaria, J. E., Gorman, R. C., et al. (2011). Pathogenesis of Acute Aortic Dissection: a Finite Element Stress Analysis. *Ann. Thorac. Surg.* 91 (2), 458–463. doi:10.1016/j.athoracsur.2010.10.042

Olender, M. L., Niu, Y., Marlevi, D., Edelman, E. R., and Nezami, F. R. (2022). Impact and Implications of Mixed Plaque Class in Automated Characterization of Complex Atherosclerotic Lesions. *Comput. Med. Imaging Graphics* 97, 102051. doi:10.1016/j.compmedimag.2022.102051

Oliveira, I. L., Santos, G. B., Gasche, J. L., Militzer, J., and Baccin, C. E. (2021). Non-newtonian Blood Modeling in Intracranial Aneurysm Hemodynamics: Impact on the wall Shear Stress and Oscillatory Shear index Metrics for Ruptured and Unruptured Cases. *J. Biomech. Eng.* 143 (7), 071006. doi:10.1115/1.4050539

Ong, C. W., Wee, I., Syn, N., Ng, S., Leo, H. L., Richards, A. M., et al. (2020). Computational Fluid Dynamics Modeling of Hemodynamic Parameters in the Human Diseased Aorta: a Systematic Review. *Ann. Vasc. Surg.* 63, 336–381. doi:10.1016/j.avsg.2019.04.032

Pahlevan, N. M., Amlani, F., Hossein Gorji, M., Hussain, F., and Gharib, M. (2011). A Physiologically Relevant, Simple Outflow Boundary Model for Truncated Vasculature. *Ann. Biomed. Eng.* 39 (5), 1470–1481. doi:10.1007/s10439-011-0246-0

Pasta, S., Rinaudo, A., Luca, A., Pilato, M., Scardulla, C., Gleason, T. G., et al. (2013). Difference in Hemodynamic and wall Stress of Ascending Thoracic Aortic Aneurysms with Bicuspid and Tricuspid Aortic Valve. *J. Biomech.* 46 (10), 1729–1738. doi:10.1016/j.jbiomech.2013.03.029

Peiffer, V., Bharath, A. A., Sherwin, S. J., and Weinberg, P. D. (2013a). A Novel Method for Quantifying Spatial Correlations between Patterns of Atherosclerosis and Hemodynamic Factors. *J. Biomech. Eng.* 135 (2), 021023. doi:10.1115/1.4023381

Peiffer, V., Sherwin, S. J., and Weinberg, P. D. (2013b). Computation in the Rabbit Aorta of a New Metric - the Transverse wall Shear Stress - to Quantify the Multidirectional Character of Disturbed Blood Flow. *J. Biomech.* 46 (15), 2651–2658. doi:10.1016/j.jbiomech.2013.08.003

Peiffer, V., Sherwin, S. J., and Weinberg, P. D. (2013c). Does Low and Oscillatory wall Shear Stress Correlate Spatially with Early Atherosclerosis? A Systematic Review. *Cardiovasc. Res.* 99 (2), 242–250. doi:10.1093/cvr/cvt044

Perinajová, R., Juffermans, J. F., Mercado, J. L., Aben, J.-P., Ledoux, L., Westenberg, J. J. M., et al. (2021). Assessment of Turbulent Blood Flow and wall Shear Stress

in Aortic Coarctation Using Image-Based Simulations. *Biomed. Eng. Online* 20 (1), 84. doi:10.1186/s12938-021-00921-4

Perktold, K., and Rappitsch, G. (1995). Computer Simulation of Local Blood Flow and Vessel Mechanics in a Compliant Carotid Artery Bifurcation Model. *J. Biomech.* 28 (7), 845–856. doi:10.1016/0021-9290(95)95273-8

Phellan, R., Hachem, B., Clin, J., Mac-Thiong, J. M., and Duong, L. (2021). Real-time Biomechanics Using the Finite Element Method and Machine Learning: Review and Perspective. *Med. Phys.* 48 (1), 7–18. doi:10.1002/mp.14602

Pichamuthu, J. E., Phillippi, J. A., Cleary, D. A., Chew, D. W., Hempel, J., Vorp, D. A., et al. (2013). Differential Tensile Strength and Collagen Composition in Ascending Aortic Aneurysms by Aortic Valve Phenotype. *Ann. Thorac. Surg.* 96 (6), 2147–2154. doi:10.1016/j.athoracsur.2013.07.001

Pirola, S., Cheng, Z., Jarral, O. A., O'Regan, D. P., Pepper, J. R., Athanasiou, T., et al. (2017). On the Choice of Outlet Boundary Conditions for Patient-specific Analysis of Aortic Flow Using Computational Fluid Dynamics. *J. Biomech.* 60, 15–21. doi:10.1016/j.jbiomech.2017.06.005

Ponzini, R., Vergara, C., Redaelli, A., and Veneziani, A. (2006). Reliable CFD-Based Estimation of Flow Rate in Haemodynamics Measures. *Ultrasound Med. Biol.* 32 (10), 1545–1555. doi:10.1016/j.ultrasmedbio.2006.05.022

Pooley, R. A. (2005). Fundamental Physics of MR Imaging. *RadioGraphics* 25 (4), 1087–1099. doi:10.1148/rg.254055027

Raghavan, M. L., Ma, B., and Fillinger, M. F. (2006). Non-invasive Determination of Zero-Pressure Geometry of Arterial Aneurysms. *Ann. Biomed. Eng.* 34 (9), 1414–1419. doi:10.1007/s10439-006-9115-7

Raptis, A., Xenos, M., Spanos, K., Kouvelos, G., Giannoukas, A., and Matsagkas, M. (2019). Endograft Specific Haemodynamics after Endovascular Aneurysm Repair: Flow Characteristics of Four Stent Graft Systems. *Eur. J. Vasc. Endovascular Surg.* 58 (4), 538–547. doi:10.1016/j.ejvs.2019.04.017

Raut, S. S., Jana, A., De Oliveira, V., Muluk, S. C., and Finol, E. A. (2013). The Importance of Patient-specific Regionally Varying wall Thickness in Abdominal Aortic Aneurysm Biomechanics. *J. Biomech. Eng.* 135 (8), 081010. doi:10.1115/1.4024578

Rikhtegar, F., Knight, J. A., Olgac, U., Saur, S. C., Poulikakos, D., Marshall, W., Jr, et al. (2012). Choosing the Optimal wall Shear Parameter for the Prediction of Plaque Location-A Patient-specific Computational Study in Human Left Coronary Arteries. *Atherosclerosis* 221 (2), 432–437. doi:10.1016/j.atherosclerosis.2012.01.018

Rissland, P., Alemu, Y., Einav, S., Ricotta, J., and Bluestein, D. (2009). Abdominal Aortic Aneurysm Risk of Rupture: Patient-specific FSI Simulations Using Anisotropic Model. *J. Biomech. Eng.* 131 (3), 031001. doi:10.1115/1.3005200

Riveros, F., Chandra, S., Finol, E. A., Gasser, T. C., and Rodriguez, J. F. (2013). A Pull-Back Algorithm to Determine the Unloaded Vascular Geometry in Anisotropic Hyperelastic AAA Passive Mechanics. *Ann. Biomed. Eng.* 41 (4), 694–708. doi:10.1007/s10439-012-0712-3

Roache, P. J. (1994). Perspective: a Method for Uniform Reporting of Grid Refinement Studies. *J. Fluids Eng.* 116 (3), 405–413. doi:10.1115/1.2910291

Roleder, T., Jąkała, J., L. Kałuża, G., Partyka, Ł., Proniewska, K., Pociask, E., et al. (2015). The Basics of Intravascular Optical Coherence Tomography. *Postep Kardiol Inter* 2 (2), 74–83. doi:10.5114/pwki.2015.52278

Ronneberger, O., Fischer, P., and Brox, T. (2015). "U-net: Convolutional Networks for Biomedical Image Segmentation," in Medical Image Computing and Computer-Assisted Intervention – MICCAI 2015, 234–241. doi:10.1007/978-3-319-24574-4_28

Rowland, E. M., Mohamied, Y., Yean Chooi, K., Bailey, E. L., and Weinberg, P. D. (2015). Comparison of Statistical Methods for Assessing Spatial Correlations between Maps of Different Arterial Properties. *J. Biomech. Eng.* 137 (10), 101003. doi:10.1115/1.4031119

Rutkowski, D. R., Roldán-Alzate, A., and Johnson, K. M. (2021). Enhancement of Cerebrovascular 4D Flow MRI Velocity fields Using Machine Learning and Computational Fluid Dynamics Simulation Data. *Sci. Rep.* 11 (1), 10240. doi:10.1038/s41598-021-89636-z

Samady, H., Eshtehardi, P., McDaniel, M. C., Suo, J., Dhawan, S. S., Maynard, C., et al. (2011). Coronary Artery wall Shear Stress Is Associated with Progression and Transformation of Atherosclerotic Plaque and Arterial Remodeling in Patients with Coronary Artery Disease. *Circulation* 124 (7), 779–788. doi:10.1161/circulationaha.111.021824

Sankaran, S., Esmaily Moghadam, M., Kahn, A. M., Tseng, E. E., Guccione, J. M., and Marsden, A. L. (2012). Patient-specific Multiscale Modeling of Blood Flow for Coronary Artery Bypass Graft Surgery. *Ann. Biomed. Eng.* 40 (10), 2228–2242. doi:10.1007/s10439-012-0579-3

Sankaran, S., Kim, H. J., Choi, G., and Taylor, C. A. (2016). Uncertainty Quantification in Coronary Blood Flow Simulations: Impact of Geometry, Boundary Conditions and Blood Viscosity. *J. Biomech.* 49 (12), 2540–2547. doi:10.1016/j.jbiomech.2016.01.002

Sarrami-Foroushani, A., Lassila, T., Gooya, A., Geers, A. J., and Frangi, A. F. (2016). Uncertainty Quantification of wall Shear Stress in Intracranial Aneurysms Using a Data-Driven Statistical Model of Systemic Blood Flow Variability. *J. Biomech.* 49 (16), 3815–3823. doi:10.1016/j.jbiomech.2016.10.005

Shimamura, K., Kubo, T., and Akasaka, T. (2021). Evaluation of Coronary Plaques and Atherosclerosis Using Optical Coherence Tomography. *Expert Rev. Cardiovasc. Ther.* 19 (5), 379–386. doi:10.1080/14779072.2021.1914588

Slager, C. J., Wentzel, J. J., Schuurbiers, J. C. H., Oomen, J. A. F., Kloet, J., Krams, R., et al. (2000). True 3-dimensional Reconstruction of Coronary Arteries in Patients by Fusion of Angiography and IVUS (ANGUS) and its Quantitative Validation. *Circulation* 102 (5), 511–516. doi:10.1161/01.CIR.102.5.511

Sokolis, D. P., Kritharis, E. P., Giagini, A. T., Lampropoulos, K. M., Papadodima, S. A., and Iliopoulos, D. C. (2012). Biomechanical Response of Ascending Thoracic Aortic Aneurysms: Association with Structural Remodelling. *Computer Methods Biomech. Biomed. Eng.* 15 (3), 231–248. doi:10.1080/10255842.2010.522186

Soleimani, E., Mokhtari-Dizaji, M., Fatouraee, N., and Saberi, H. (2021). Stress Distribution Analysis in Healthy and Stenosed Carotid Artery Models Reconstructed from *In Vivo* Ultrasonography. *Ultrasonography* 40 (3), 428–441. doi:10.14366/usg.20131

Spiegel, M., Redel, T., Zhang, Y. J., Struffert, T., Hornegger, J., Grossman, R. G., et al. (2011). Tetrahedral vs. Polyhedral Mesh Size Evaluation on Flow Velocity and wall Shear Stress for Cerebral Hemodynamic Simulation. *Computer Methods Biomech. Biomed. Eng.* 14 (1), 9–22. doi:10.1080/10255842.2010.518565

Steinman, D. A., and Migliavacca, F. (2018). Editorial: Special Issue on Verification, Validation, and Uncertainty Quantification of Cardiovascular Models: towards Effective VVUQ for Translating Cardiovascular Modelling to Clinical Utility. *Cardiovasc. Eng. Tech.* 9 (4), 539–543. doi:10.1007/s13239-018-00393-z

Steinman, D. A., and Pereira, V. M. (2019). How Patient Specific Are Patient-specific Computational Models of Cerebral Aneurysms? an Overview of Sources of Error and Variability. *Neurosurg. Focus.* 47 (1), E14. doi:10.3171/2019.4.focus19123

Stella, S., Vergara, C., Giovannacci, L., Quarteroni, A., and Prouse, G. (2019). Assessing the Disturbed Flow and the Transition to Turbulence in the Arteriovenous Fistula. *J. Biomech. Eng.* 141 (10), 101010. doi:10.1115/1.4043448

Stokes, C., Bonfanti, M., Li, Z., Xiong, J., Chen, D., Balabani, S., et al. (2021). A Novel MRI-Based Data Fusion Methodology for Efficient, Personalised, Compliant Simulations of Aortic Haemodynamics. *J. Biomech.* 129, 110793. doi:10.1016/j.jbiomech.2021.110793

Sun, Q., Groth, A., Bertram, M., Waechter, I., Bruijns, T., Hermans, R., et al. (2010). Phantom-based Experimental Validation of Computational Fluid Dynamics Simulations on Cerebral Aneurysms. *Med. Phys.* 37 (9), 5054–5065. doi:10.1118/1.3483066

Tanaka, K., Joshi, D., Timalsina, S., and Schwartz, M. A. (2021). Early Events in Endothelial Flow Sensing. *Cytoskeleton* 78 (6), 217–231. doi:10.1002/cm.21652

Tang, D., Kamm, R. D., Yang, C., Zheng, J., Canton, G., Bach, R., et al. (2014). Image-based Modeling for Better Understanding and Assessment of Atherosclerotic Plaque Progression and Vulnerability: Data, Modeling, Validation, Uncertainty and Predictions. *J. Biomech.* 47 (4), 834–846. doi:10.1016/j.jbiomech.2014.01.012

Tang, D., Teng, Z., Canton, G., Yang, C., Ferguson, M., Huang, X., et al. (2009). Sites of Rupture in Human Atherosclerotic Carotid Plaques Are Associated with High Structural Stresses. *Stroke* 40 (10), 3258–3263. doi:10.1161/STROKEAHA.109.558676

Tanoue, T., Tateshima, S., Villablanca, J. P., Viñuela, F., and Tanishita, K. (2011). Wall Shear Stress Distribution inside Growing Cerebral Aneurysm. *AJNR Am. J. Neuroradiol.* 32 (9), 1732–1737. doi:10.3174/ajnr.A2607

Taylor, C. A., Hughes, T. J. R., and Zarins, C. K. (1998). Finite Element Modeling of Three-Dimensional Pulsatile Flow in the Abdominal Aorta: Relevance to Atherosclerosis. *Ann. Biomed. Eng.* 26 (6), 975–987. doi:10.1114/1.140

Thiyagarajah, N., Achey, R., Rashidi, M., and Moore, N. Z. (2022). Computational Fluid-Structure Interactions in the Human Cerebrovascular System: Part 1-A Review of the Current Understanding of Cerebrovascular Biomechanics. *J. Eng. Sci. Med. Diagn.Ther.* 5 (3), 030801. doi:10.1115/1.4053943

Thondapu, V., Bourantas, C. V., Foin, N., Jang, I.-K., Serruys, P. W., and Barlis, P. (2017). Biomechanical Stress in Coronary Atherosclerosis: Emerging Insights from Computational Modelling. *Eur. Heart J.* 38 (2), ehv689–92. doi:10.1093/eurheartj/ehv689

Tian, F., Gao, Y., Fang, Z., and Gu, J. (2021). Automatic Coronary Artery Segmentation Algorithm Based on Deep Learning and Digital Image Processing. *Appl. Intell.* 51, 8881–8895. doi:10.1007/s10489-021-02197-6

Toussaint, J.-F. o., LaMuraglia, G. M., Southern, J. F., Fuster, V., and Kantor, H. L. (1996). Magnetic Resonance Images Lipid, Fibrous, Calcified, Hemorrhagic, and Thrombotic Components of Human Atherosclerosis *In Vivo*. *Circulation* 94 (5), 932–938. doi:10.1161/01.cir.94.5.932

Tricarico, R., Laquian, L., Allen, M. B., Tran-Son-Tay, R., Scali, S. T., Lee, T. C., et al. (2020). Temporal Analysis of Arch Artery Diameter and Flow Rate in Patients Undergoing Aortic Arch Endograft Procedures. *Physiol. Meas.* 41 (3), 035004. doi:10.1088/1361-6579/ab7b40

Valen-Sendstad, K., Bergersen, A. W., Shimogonya, Y., Goubergrits, L., Bruening, J., Pallares, J., et al. (2018). Real-world Variability in the Prediction of Intracranial Aneurysm wall Shear Stress: the 2015 International Aneurysm CFD challenge. *Cardiovasc. Eng. Tech.* 9 (4), 544–564. doi:10.1007/s13239-018-00374-2

Valen-Sendstad, K., Mardal, K.-A., Mortensen, M., Reif, B. A. P., and Langtangen, H. P. (2011). Direct Numerical Simulation of Transitional Flow in a Patient-specific Intracranial Aneurysm. *J. Biomech.* 44 (16), 2826–2832. doi:10.1016/j.jbiomech.2011.08.015

Valen-Sendstad, K., and Steinman, D. A. (2014). Mind the gap: Impact of Computational Fluid Dynamics Solution Strategy on Prediction of Intracranial Aneurysm Hemodynamics and Rupture Status Indicators. *AJNR Am. J. Neuroradiol.* 35 (3), 536–543. doi:10.3174/ajnr.A3793

van der Giessen, A. G., Groen, H. C., Doriot, P.-A., de Feyter, P. J., van der Steen, A. F. W., van de Vosse, F. N., et al. (2011). The Influence of Boundary Conditions on wall Shear Stress Distribution in Patients Specific Coronary Trees. *J. Biomech.* 44 (6), 1089–1095. doi:10.1016/j.jbiomech.2011.01.036

van der Giessen, A. G., Schaap, M., Gijsen, F. J. H., Groen, H. C., van Walsum, T., Mollet, N. R., et al. (2010). 3D Fusion of Intravascular Ultrasound and Coronary Computed Tomography for Iin-Vvivo wall Shear Stress Analysis: a Feasibility Study. *Int. J. Cardiovasc. Imaging* 26 (7), 781–796. doi:10.1007/s10554-009-9546-y

Vande Geest, J. P., Sacks, M. S., and Vorp, D. A. (2006). The Effects of Aneurysm on the Biaxial Mechanical Behavior of Human Abdominal Aorta. *J. Biomech.* 39 (7), 1324–1334. doi:10.1016/j.jbiomech.2005.03.003

Voňavková, T., and Horný, L. (2020). Effect of Axial Prestretch and Adipose Tissue on the Inflation-Extension Behavior of the Human Abdominal Aorta. *Computer Methods Biomech. Biomed. Eng.* 23 (3), 81–91. doi:10.1080/10255842.2019.1699544

Voß, S., Beuing, O., Janiga, G., and Berg, P. (2019). Multiple Aneurysms AnaTomy CHallenge 2018 (MATCH)-Phase Ib: Effect of Morphology on Hemodynamics. *PLoS One* 14 (5), e0216813. doi:10.1371/journal.pone.0216813

Voß, S., Glasser, S., Hoffmann, T., Beuing, O., Weigand, S., Jachau, K., et al. (2016). Fluid-structure Simulations of a Ruptured Intracranial Aneurysm: Constant versus Patient-specific wall Thickness. *Comput. Math. Methods Med.* 2016, 1–8. doi:10.1155/2016/9854539

Wang, L., Wu, Z., Yang, C., Zheng, J., Bach, R., Muccigrosso, D., et al. (2015a). IVUS-based FSI Models for Human Coronary Plaque Progression Study: Components, Correlation and Predictive Analysis. *Ann. Biomed. Eng.* 43 (1), 107–121. doi:10.1007/s10439-014-1118-1

Wang, L., Zheng, J., Maehara, A., Yang, C., Billiar, K. L., Wu, Z., et al. (2015b). Morphological and Stress Vulnerability Indices for Human Coronary Plaques and Their Correlations with Cap Thickness and Lipid Percent: an IVUS-Based Fluid-Structure Interaction Multi-Patient Study. *Plos Comput. Biol.* 11 (12), e1004652. doi:10.1371/journal.pcbi.1004652

Wang, L., Zhu, J., Maehara, A., Lv, R., Qu, Y., Zhang, X., et al. (2021). Quantifying Patient-specific *In Vivo* Coronary Plaque Material Properties for Accurate Stress/strain Calculations: an IVUS-Based Multi-Patient Study. *Front. Physiol.* 12, 721195. doi:10.3389/fphys.2021.721195

Weisbecker, H., Pierce, D. M., and Holzapfel, G. A. (2014). A Generalized Prestressing Algorithm for Finite Element Simulations of Preloaded Geometries with Application to the Aorta. *Int. J. Numer. Meth. Biomed. Engng.* 30 (9), 857–872. doi:10.1002/cnm.2632

Westerhof, N., Lankhaar, J.-W., and Westerhof, B. E. (2009). The Arterial Windkessel. *Med. Biol. Eng. Comput.* 47 (2), 131–141. doi:10.1007/s11517-008-0359-2

Womersley, J. R. (1955). Method for the Calculation of Velocity, Rate of Flow and Viscous Drag in Arteries when the Pressure Gradient Is Known. *J. Physiol.* 127 (3), 553–563. doi:10.1113/jphysiol.1955.sp005276

Wood, N. B., Zhao, S. Z., Zambanini, A., Jackson, M., Gedroyc, W., Thom, S. A., et al. (2006). Curvature and Tortuosity of the Superficial Femoral Artery: a Possible Risk Factor for Peripheral Arterial Disease. *J. Appl. Physiol.* 101 (5), 1412–1418. doi:10.1152/japplphysiol.00051.2006

Xu, H., Baroli, D., and Veneziani, A. (2021). Global Sensitivity Analysis for Patient-specific Aortic Simulations: the Role of Geometry, Boundary Condition and Large Eddy Simulation Modeling Parameters. *J. Biomech. Eng.* 143 (2), 021012. doi:10.1115/1.4048336

Xu, P., Liu, X., Zhang, H., Ghista, D., Zhang, D., Shi, C., et al. (2018). Assessment of Boundary Conditions for CFD Simulation in Human Carotid Artery. *Biomech. Model. Mechanobiol.* 17 (6), 1581–1597. doi:10.1007/s10237-018-1045-4

Zambrano, B. A., McLean, N. A., Zhao, X., Tan, J.-L., Zhong, L., Figueroa, C. A., et al. (2018). Image-based Computational Assessment of Vascular wall Mechanics and Hemodynamics in Pulmonary Arterial Hypertension Patients. *J. Biomech.* 68, 84–92. doi:10.1016/j.jbiomech.2017.12.022

Zhang, Y., Hughes, T. J. R., and Bajaj, C. L. (2010). An Automatic 3D Mesh Generation Method for Domains with Multiple Materials. *Computer Methods Appl. Mech. Eng.* 199 (5), 405–415. doi:10.1016/j.cma.2009.06.007

Zhao, F., Chen, Y., Hou, Y., and He, X. (2019). Segmentation of Blood Vessels Using Rule-Based and Machine-Learning-Based Methods: a Review. *Multimedia Syst.* 25 (2), 109–118. doi:10.1007/s00530-017-0580-7

Zhong, L., Zhang, J.-M., Su, B., Tan, R. S., Allen, J. C., and Kassab, G. S. (2018). Application of Patient-specific Computational Fluid Dynamics in Coronary and Intra-cardiac Flow Simulations: Challenges and Opportunities. *Front. Physiol.* 9, 742. doi:10.3389/fphys.2018.00742

Conflict of Interest: The authors declare that the research was conducted in the absence of any commercial or financial relationships that could be construed as a potential conflict of interest.

frontiers | Frontiers in Bioengineering and Biotechnology

ORIGINAL RESEARCH
published: 18 May 2022
doi: 10.3389/fbioe.2022.836990

Microvascular Dynamics and Hemodialysis Response of Patients With End-Stage Renal Disease

Jen-Shih Lee[1,2]* *and Lian-Pin Lee*[2]

[1]Department of Biomedical Engineering, University of Virginia, Charlottesville, VA, United States, [2]Global Monitors, Inc., San Diego, CA, United States

In our previous analysis of three sets of hemodialysis studies, we found that patients possessing higher hematocrit have a higher filtration coefficient KSo and more fluid being restituted from the tissue. A new dynamic analysis is developed to reveal how the plasma protein concentration, restitution volume, and plasma volume are changing over the time course of 240 min hemodialysis. For patients with the filtration coefficient KSo as 0.43 or 5.88 ml/min/mmHg, we find that the restitution rate would reach 50% of the extraction rate in 5.3 or 57.4 min, respectively. By the end of hemodialysis, the restitution rate of both patients asymptotically approaches a value of 0.93 ml/min which is slightly higher than the extraction rate of 9.03 ml/min. The plasma volume drops by 10% of the total plasma volume in 11 min for patients with low KSo and drops by 2.1% and turns around to an increasing trend in 5.6 min for patients with high KSo. These results suggest that the filtration coefficient acts like a facilitator in restituting more fluid from the tissue to compensate for the loss of plasma volume due to extraction. The hematocrit data of three sets of hemodialysis also indicate that significant microvascular blood volume is shifted from small veins toward the venous side of macrocirculation. A better understanding of how the factors examined here cause hypovolemia can be the basis for one to modify the hemodialysis process such that the development of hypovolemia can be avoided over the course of hemodialysis.

Keywords: blood volume, microcirculation, plasma protein concentration, hematocrit, hemodialysis

OPEN ACCESS

Edited by:
Der-Cherng Tarng, Taipei Veterans General Hospital, Taiwan

Reviewed by:
John S. Clemmer, University of Mississippi Medical Center, United States
Ying He, Dalian University of Technology, China

***Correspondence:**
Jen-Shih Lee
JL@globalmonitors.com

Specialty section:
This article was submitted to Biomechanics, a section of the journal Frontiers in Bioengineering and Biotechnology

Received: *16 December 2021*
Accepted: *23 March 2022*
Published: *18 May 2022*

Citation:
Lee J-S and Lee L-P (2022) Microvascular Dynamics and Hemodialysis Response of Patients With End-Stage Renal Disease . Front. Bioeng. Biotechnol. 10:836990. doi: 10.3389/fbioe.2022.836990

1 INTRODUCTION

Over the course of hemodialysis (HD), the continuous extraction of ultrafiltrate from the blood by the dialyzer will increase the plasma protein concentration (PPC) from Cp to Cp'. For three groups of patients with normal, anemic, and more anemic hematocrit, the PPC increment (Cp'-Cp)/Cp' is found as 11.7, 10.2, and 7.9%, respectively (Schneditz et al., 1992; Minutolo et al., 2003). The full circulation analysis (FCA) of these end-point protein data reveals that the large drop in the PPC increment is mainly due to the patients having these arterial hematocrits Ha (42.4 ± 3.5%, 33.5 ± 2.4%, and 27.9 ± 3.1%, respectively) have these filtration coefficients KSo (0.43, 0.85, and 5.88 ml/min/mmHg, respectively, personal communication). A larger filtration coefficient is also shown by the FCA to associate with more fluid being restituted from the tissue and lesser reduction in the total plasma volume for patients with lower hematocrit. This impact of the filtration coefficient on plasma volume reduction suggests that the filtration coefficient acts like a factor facilitating the prevention of hypovolemia. In this article, we will expand the end-point analysis to one that can predict how these

variables, namely, PPC, restitution volume, plasma volume, microvascular blood pressure, and rate of the restitution are changing over the course of HD. A total of three sets of computations are made for patients having the three filtration coefficients mentioned previously. By comparing the temporal changes of the variables so calculated will help us better understand how and why that the filtration coefficient can be a facilitating factor for the patient to generate a fluid restitution to adequately compensate for the fluid extracted by the dialyzer and hence the prevention of the development of hypovolemia.

In the FCA, the full circulation is divided into three compartments: the macrocirculation, microcirculation, and the splenic microcirculation. The blood flowing in six groups of microvessels (the small arteries, arterioles, capillaries, post-capillaries, venules, and small veins) has a microvessel hematocrit in the range of 90–20% of Ha (Lipowsky et al., 1980). The blood pressure in the small arteries can be 100 mmHg, while that in the small veins is 2–4 mmHg. The organs in our body may have different filtration coefficients. In the FCA, the six groups are grouped into one microcirculation compartment with Pmic being its blood pressure, Hmic as its microvascular hematocrit of the microcirculation, and KSo as its filtration coefficient. Because the red blood cells (RBCs) in the splenic microcirculation are tethered by the microvessel wall, the hematocrit there can be 2.07 times of Ha (Gibson et al., 1946). Equations are formulated in our previous study to describe the transvascular fluid and protein movement between the microcirculation and the tissue. The equations are used to deduce from the measured PPC increment (Cp'-Cp')/Cp' and hematocrit increment (Ha'-Ha)/Ha', the filtration coefficient KSo, the change in plasma volume ΔVp, and the reduction in microvascular blood volume ΔVmic. We will use the morphometric and hemodynamic characteristics of the microcirculation to deduce a value for Pmic and Hmic and to partition the calculated microvascular blood volume reduction to the six microvessel groups. The FCA simulates the transvascular protein movement as the transport of a fluid across the endothelia having γCp as its protein concentration. The constant γ is termed as the permeability fraction. A way to find the value of γ is described.

A hematocrit equation has been established in FCA to show how these three factors, namely, a change in plasma volume (ΔVp), a change in microvascular blood volume (ΔVmic), and a splenic RBC release change of the arterial hematocrit. Graphical results are generated to show how these three factors alter the arterial hematocrit over the course of HD. With known ΔVmic, we can calculate the change in macrovascular blood volume. The meaning of a change in microvascular blood volume and the impact of a change in macrovascular blood volume on cardiac filling are elaborated from the perspective of a 13-generation circulation model (Rothe 2011).

For many hypovolemia studies, the increase in hematocrit over the course of HD is used to determine the reduction in plasma volume over the course of HD (Schneditz et al., 1992; Calvacanti et al., 2006; Dasselaar et al., 2007; Booth et al., 2011). The Van Beaumont (1972) hematocrit equation (VBHE) used in those studies can be derived from the hematocrit equation of the FCA under the assumption of no microvascular volume change and no splenic RBC release. In the study carried out by Schneditz et al. (1992), the blood volume change calculated from VBHE is used in their numerical procedure to determine the filtration coefficient of the more anemic patients. In FCA, we use the PPC data and the protein equation to determine the reduction in plasma volume and the filtration coefficient. The differences that are generated by these two computation procedures are examined.

2 ANALYSES, RESULTS, AND DISCUSSIONS

The process on changing plasma protein concentration. In this part of FCA, the plasma space in the entire circulation is treated as one compartment. Before HD, there is a constant filtration flux Jf (0) flowing out of the plasma compartment to the tissue. The 0 in the parenthesis identifies the quantity as one at the initiation of HD ($t = 0$). This flux carries a protein concentration Cf. Meanwhile, there is a constant lymphatic return Qlym which carries a protein concentration Clym. As the plasma volume and the PPC are not likely to change before the initiation of HD, we have the following requirements:

$$\mathrm{Qlym} = \mathrm{Jf}\,(0) \text{ and } \mathrm{Qlym}\,\mathrm{Clym} = \mathrm{Jf}\,(0)\mathrm{Cf} \tag{1}$$

As the interstitial space is being flushed by the filtration, these two equalities also indicate that the protein concentration in the interstitial fluid space Ct equals Cf. We regard that the transvascular fluid movement Jf(t) is governed by the Starling hypothesis, that is,

$$\mathrm{Jf}\,(\mathrm{t}) = \mathrm{KSo}\{\mathrm{Pmic}\,(\mathrm{t}) - \mathrm{Pt} - \sigma[\pi\mathrm{p}\,(\mathrm{t}) - \pi\mathrm{t}]\} \tag{2}$$

where KSo is the filtration coefficient, Pmic (0) is a representative hydrostatic pressure of the microcirculation, Pt is the hydrostatic pressure on the tissue side, σ is the reflection coefficient, πp(t) is the plasma colloidal osmotic pressure (COP) at time t, and πt is the tissue COP. Over the course of HD, the total volume of the fluid restituted from the tissue is given by:

$$\Delta\mathrm{Vr} = \int_0^{\Delta\mathrm{T}} \mathrm{KSo}\left[\sigma\left(\pi\mathrm{p}\,(\mathrm{t}) - \pi\mathrm{t}\right) - \left(\mathrm{Pmic}\,(\mathrm{t}) - \mathrm{Pt}\right)\right]\mathrm{dt} + \Delta\mathrm{T}\cdot\mathrm{Qlym} \tag{3}$$

We consider that the volume of fluid being restituted from the tissue to the circulation is much smaller than the fluid volume of the interstitial fluid space. Thus, we can assume that the interstitial fluid pressure and the tissue COP are not altered by HD. Thus, the replacement of Qlym in **Eq. 3** by Jf (0) converts **Eq. 3** to the following form:

$$\Delta\mathrm{Vr} = \int_0^{\Delta\mathrm{T}} \mathrm{KSo}\{\sigma[\pi\mathrm{p}\,(\mathrm{t}) - \pi\mathrm{p}\,(0)] - [\mathrm{Pmic}\,(\mathrm{t}) - \mathrm{Pmic}\,(0)]\}\mathrm{dt} \tag{4}$$

As derived later, **Eq. 4** can be converted to the following algebraic equation:

$$\Delta Vr = k\,KSo\left[\sigma\Delta\pi p - \Delta Pmic\right] \quad (5)$$

where $\Delta\pi p$ is $\pi p'$-πp, $\Delta Pmic$ is Pmic'-Pmic, and k is an integration constant (**Eq. 8**). From now on, quantity without ' is identified as one at $t = 0$, quantity with ' as one at $t = \Delta T$, and that with (t) as one at time t. Later on, Pmic is identified as a surface average of the blood pressure over the entire surface area of the microcirculation, and the pressure change $\Delta Pmic$ can be calculated as:

$$\Delta Pmic = \zeta\Delta Vb/Vb \quad (6)$$

where ζ is termed as the autonomous constant, and ΔVb is Vb'-Vb.

The volume of restitution subtracted by the extraction volume ΔVe is the change in plasma volume:

$$\Delta Vp \equiv Vp' - Vp = \Delta Vr - \Delta Ve \quad (7)$$

As we regard that the splenic RBC release does not change the blood volume of the splenic microvasculature, the change in total blood volume ΔVb is given by:

$$\Delta Vb = \Delta Vp \quad (8)$$

Let Cr be the protein concentration of the restituted fluid. Then, the protein mass added to the plasma compartment is $Cr\Delta Vr$. Thus, the increase in the protein mass over the course of HD is given by:

$$Cp'\,Vp' = Cp\,Vp + Cr\Delta Vr \quad (9a)$$

Eqs 7 and **9a** can be combined to form the following equation:

$$\Delta Cp/Cp' = \Delta Ve/Vp - \left(\Delta Vr/Vp\right)\left(1 - Cr/Cp'\right) \quad (9b)$$

where ΔCp is Cp'-Cp. As described later, we use the permeability fraction γ to characterize Cr as a fraction of Cp:

$$Cr = \gamma Cp \quad (10)$$

Termed the protein equation, **Eq. 9b** uses the change in PPC to calculate $\Delta Vr/Vp$. The first term $\Delta Cp/Cp'$ in **Eq. 9b** is termed as the PPC increment (the increase in PPC induced by HD and then normalized by Cp'), the second term $\Delta Ve/Vp$ is termed as the extraction increment (the increment in PPC induced by the extraction), and the third term is the restitution dilution (the dilution of PPC by fluid restitution). As Cr is smaller than Cp, the value of restitution dilution is negative. The negativity makes us to name this third term as dilution.

Overall, we have six algebraic equations (**Eqs. 5–10**) to characterize the transvascular fluid and protein movements. The equations contain four modeling constants: KSo, σ, γ, and ζ. Here, KSo is treated as an input parameter, while σ is taken as 1, γ as 0.09, and ζ as 36.67 mmHg. The hemodialysis process is defined by two parameters: ΔT and ΔVe. Once the initial values of plasma volume Vp, blood volume Vb, and PPC Cp are given, then we can use the equations to solve for these six end-values: Cp' or ΔCp, Cr, Vp' or ΔVp, Vb' or ΔVb, ΔVr, and $\Delta Pmic$. The value of $\Delta\pi p$ is derived from Cp and Cp' through the Landis and Pappenheimer (1963) equation (**Eq. A6**).

The two HD studies carried out by Minutolo et al. (2003) on patients with normal and anemic (N and A) hematocrit and the high ultrafiltration experiment carried out by Schneditz et al. (1992) on patients with more anemic (MA) hematocrit are to be identified as N78%, A72%, and MA18%20 HD, respectively. The percentage defines the $\Delta Ve/Vp$ imposed to the HD. The first two HDs have 240 min as ΔT. The two digits 20 in the last HD is used to highlight that its HD time ΔT is 20 min. These HD parameters, ΔVe, ΔT, and the initial value of Cp, Vp, and Vb and the final PPC Cp', can be found or derived from the publications. In our previous analysis, we used **Eqs 5–10** and **Eq. A6** to calculate these seven variables: Cr, ΔVr, ΔVp, ΔVb, $\Delta\pi p$, $\Delta Pmic$, and kKSo. Here, we use the equations in the Appendix to calculate the temporal changes of Vr(t), Vp(t), Vb(t), Pmic (t), $\pi p(t)$, and the integration constant k and filtration coefficient KSo.

The second series of HDs will be identified as low KSo, medium KSo, and high KSo HD. They are to have these filtration coefficients: 0.43, 0.85, and 5.88 ml/min/mmHg, which are the filtration coefficients found for N78%, A72%, and MA18%20 HD, respectively. The initial conditions and the settings of ΔVe and ΔT for this second series are those of N78% HD.

Microvascular morphometry, hemodynamics, and hemodialysis. In formulating FCA, two new modeling constants, the permeability fraction γ and the autonomous constant ζ, and the microvascular blood pressure are introduced. In this section, a procedure based on the morphometry and hemodynamics of the microcirculation is presented to assess what likely values are to be set for the two constants and one pressure variable.

The morphometry data (generation number, vessel type, number of vessels, diameter, and length) of a central vascular tree model are reproduced in the first five columns of **Table 1** (Rothe 2011). The surface areas and volumes of these vessels are listed in the 5th and 7th column of the table. With So and Vo being the total surface area and the total blood volume of the vascular tree, the surface and volume fractions (Sn/So and Vn/Vo) of the 13-generations circulation are depicted in **Figures 1A,B**.

Through the relation between the *in vivo* microvascular hematocrit and vessel diameter (Lipowsky et al., 1980), we use the diameter reported in the table to set a value as the microvessel hematocrit Hmic,n of the *n*th generation and present it through this ratio α_n (= Hmic,n/Ha) in the 9th column of **Table 1**. For the current investigations, the vessels of the 5th to 10th generation are categorized as microvessels, as their hematocrit ratios are all smaller than unity. Among these six generations, only the capillaries may be considered as rigid (Fung 1966), while other larger microvessels are distensible.

It is noted from **Figure 1A** that almost 99% of the surface area of the circulation resides in the microcirculation. All blood vessels are lined by endothelial cells, and the filtration and permeation characteristics of various microvessels may be similar to each other. Thus, the total surface area of the microcirculation should be taken as the So in **Eq. 2**. For this surface distribution, we form an S-axis (the 7th column) to mark the location of a point within the vascular network. As an example, the entrance of the microcirculation (i.e., the entrance of small arteries) is located at an S of 0.35%

TABLE 1 | Morphometry and hemodynamics of a central vascular tree[a] (Rothe 2011).

n	Vessel type	Number N_n	Diameter D_n, mm	Length L_n, mm	Surface area S_n, m^2	S-axis (%)	Volume V_n, mL	Ht_n/Ha	R_n
1	Aorta	1	10	400	0.01	0.00	31.4	1	2.8
2	Large arteries	40	3	200	0.08	0.01	56.5	1	4.3
3	Main arterial branches	600	1	100	0.19	0.10	47.1	1	11.5
4	Terminal branches	1800	0.6	10	0.03	0.32	5.1	1	3.0
5	Small arteries	4.0E+07	0.019	3.5	8.36	0.35	39.7	0.52	25.1
6	Arterioles	4.0E+08	0.007	0.9	7.92	9.90	13.9	0.46	32.5
7	Capillaries	1.8E+09	0.0037	0.2	4.18	18.95	3.9	0.46	20.6
8	Post-capillary Venules	5.8E+09	0.0073	0.2	26.60	23.73	48.6	0.46	0.4
9	Venules	1.2E+09	0.021	0.1	7.92	54.12	41.6	0.48	0.0
10	Small veins	8.0E+07	0.037	3.4	31.62	63.17	292.5	0.59	0.9
11	Main venule branches	600	2.4	100	0.45	99.29	271.4	1	0.3
12	Large veins	40	6	200	0.15	99.81	226.2	1	0.3
13	Vena cava	1	12.5	400	0.02	99.98	49.1	1	1.1
	Total				87.5	100	1127		101.7

[a]*By including the blood volume in the lungs and heart chambers, the total blood volume is 1376 ml. The cardiac output generating the pre-HD pressure is 1.376 L/min. The unit of resistance R_n is mmHg/(L/min).*

which is the sum of the surface areas of all vessel upstream of the entrance divided by the total surface area (87.5 m^2). Correspondently, the exit of the microcirculation is located at an S of 99.3%. The blood volumes tabulated in the 8th column indicate that 70% of the total blood volume resides in the 10th to 12th generation. We calculate the relative viscosity of blood $\mu^\star$ as 13.2 α_n^2 + 1.30 α_n +1.45 and then take the resistance of the *n*th generation as $A\cdot\mu^\star\ L_n/(N_n\cdot D_n^4)$. The resistance for each generation so calculated is shown in the last column of **Table 1**.

In the next five paragraphs, we will use the data in **Table 1** to determine what value should be set for ΔPmic in **Eq. 5**. Suppose the cardiac output for the central circulation of **Table 1** is set at 1.38 L/min, the arterial blood pressure at 140 mmHg, and the venous blood pressure at 0, then we can find a value for A to generate the distribution of blood pressure (the solid line) shown in **Figure 2A**. This distribution of blood pressure along the S-axis will be taken as that of the patient whose HD has been just initiated.

Based on the studies of Minutolo et al. (2003) and LaForte et al. (1994), the drop in the arterial blood pressure at the end of HD ΔPa is 20 mmHg while the drop in venous blood pressure ΔPv is −3 mmHg. By guessing the cardiac output as 1.21 L/min, setting Pv' as −3 mmHg, and using the resistance distribution shown in **Table 1** to do the pressure calculation, the distribution of blood pressure at the end of HD is shown as the solid line in **Figure 2B**. The pressure distribution shown in **Figure 2A** indicates that the pressure in the microcirculation to drop from 110 to 4 mmHg at the beginning of HD, while **Figure 2B** indicate that the drop is from 94 to 0.2 mmHg at the end of HD.

Let Pb be σ πp (0) + Pt - σ πt. These four pressures Pb, πp, Pt, and πt may be considered as constants as one moves along from the arterial end to the venous end of the microcirculation. The fluid flux Jf in Eq. 2 generated over the microvascular surface at time 0 is now calculated as:

$$Jf = \int_0^1 KSo\,(P - Pb)\ dS = KSo\,(Pmic - Pb) \qquad (11)$$

If KSo is a constant, then the last equality of **Eq. 11** shows that Pmic is a surface average of the blood pressure in the microcirculation. The integration of the beginning pressure P shown in **Figure 2A** yields 19.2 mmHg as the value of Pmic. It is noted that Pb is used in **Eq. 11** to show that P-Pb is the net pressure driving the fluid flux Jf. The presence of Pb in **Eq. 11** has no effect on the determination of Pmic. With Pmic so determined, we plot the line P = Pmic as the dotted line in **Figure 2A**. The intercept between the dotted line and solid line as pointed by an arrow in **Figure 2A** corresponds to an S of 0.22, a location that is slightly downstream of the entrances of capillaries. We choose Pb as 17.2 mmHg so that there is a net driving pressure of 2 mmHg to produce the filtration flux before the initiation of HD (Patients with anemic hematocrit and a body weight of 54 Kg has the KS product as 0.85 ml/min/mmHg. This 2-mmHg pressure is chosen such that the fluid flows through the interstitial corresponding to a lymphatic flow of 1.7 L/day (= 2 mmHg · 0.85 ml/min/mmHg)). The line P = Pb is plotted as the broken line in **Figure 2A**. Then, the up arrows in **Figure 2A** originated from the broken line represent filtration for that portion of microcirculation, while the down arrows represent absorption.

We can add the resistances up to form a R-axis like the formation of the S-axis. Then, the plot of the blood pressure P against the R-axis will be a straight line with a negative slope. Let the total resistance be Rt. The intercept pointed at by the big

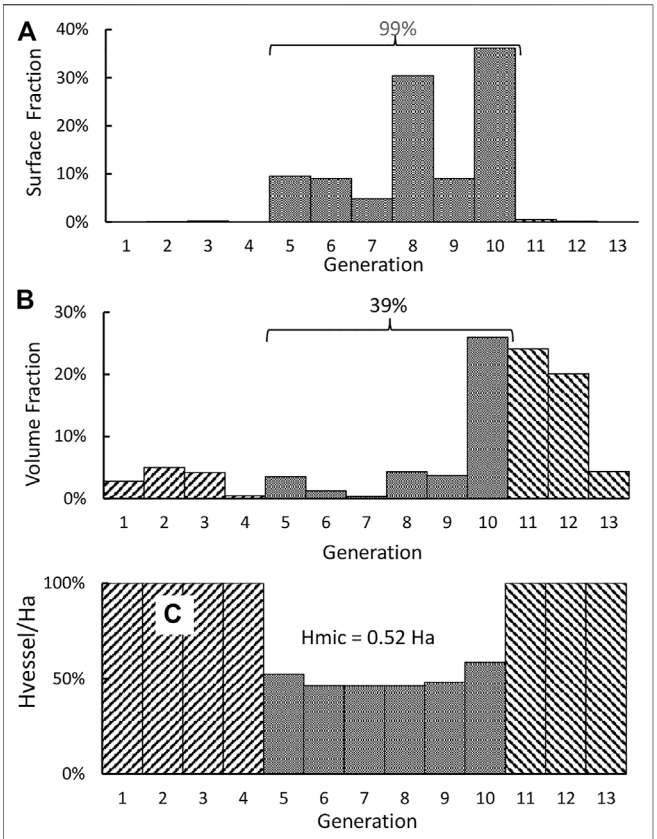

FIGURE 1 | (A) Distribution of the surface fraction of a 13-generation central vascular tree. **(B)** Distribution of the volume fraction. **(C)** Distribution of the hematocrit ratio Hvessel/Ha.

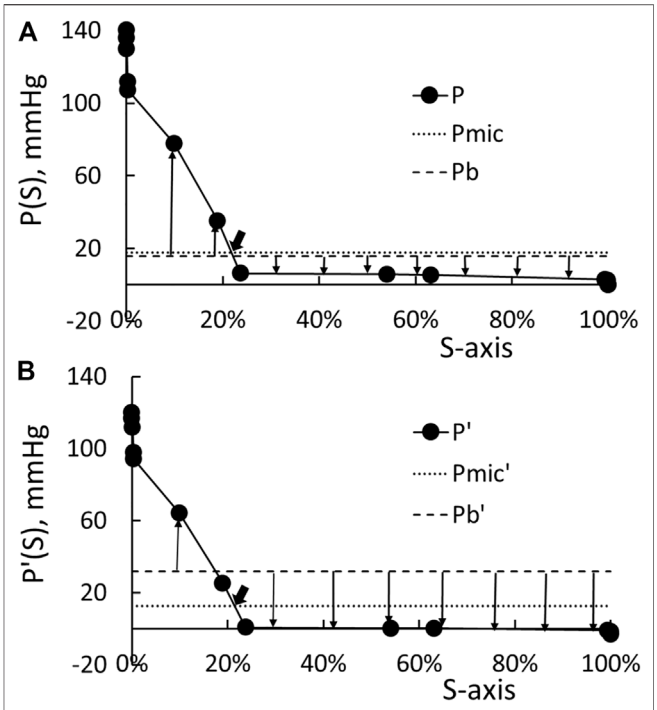

FIGURE 2 | (A) Distribution of the pre-HD blood pressure P. Pmic is the surface weighted average of the pressure in the microcirculation, and Pb is the base pressure (**Eq. 7**). The up arrows indicate fluid filtration to the tissue, and the down arrow indicates fluid absorption by the circulation. **(B)** Distribution of post-HD blood pressure and the correspondent Pmic' and Pb.

arrow in **Figure 2A** has f Rt as its resistance with the resistance fraction f taking 0.9 as its value. This is to say that the Pmic can be calculated as:

$$\text{Pmic} = (1 - \text{f})\text{Pa} + \text{fPv} \tag{12}$$

The computation of the area over the part of blood pressure covered by the up arrows yields the filtration flux Qf as one driven by a pressure differential of 11.3 mmHg (i.e., the flux is 11.3 mmHg KSo), while the absorption flux Qa as one driven by −9.3 mmHg. The sum of the filtration and absorption flux is the net flux which is driven by 2 mmHg.

By the end of HD, the arterial blood pressure drops by about 20 mmHg while the venous blood pressure by 3 mmHg (LaForte et al., 1994; Minutolo et al., 2003). We then guess a cardiac output, set the venous pressure at −3 mmHg, and use the resistances listed in **Table 1** to calculate the pressure distribution such that the calculated arterial blood pressure will now be 120 mmHg. The distribution of P′ so calculated is shown as the solid line in **Figure 2B**. The microvascular blood pressure Pmic' now takes 14 mmHg as its value. It is located at an S′ of 0.215 and its correspondent resistance fraction f′ takes 0.88 as its value. Because these S′ and f′ closely approximate the S and f derived from the blood pressure before the HD, we use the following formula to determine the change in microvascular blood pressure ΔPmic:

$$\Delta\text{Pmic} = (1 - \text{f})\Delta\text{Pa} + \text{f}\Delta\text{Pv} \tag{13}$$

In the CHRE of LaForte et al. (1994), they found that the drops in arterial and venous blood pressure are linearly related to the reduction in blood volume. The substitution of the linear relations to **Eq. 13** yields **Eq. 6** given earlier. The value of ζ is calculated as 36.7 mmHg for conscious rabbits and 23.7 mmHg for anesthetized rabbits. Because of the dependence on the consciousness of the rabbits, we term ζ as an autonomous constant.

In the following three paragraphs, we describe how ΔVr, Cr, and γ are related to the transvascular fluid and protein movement and what value should be used as γ. For patients with normal hematocrit, the HD induces the COP to increase by 16 mmHg (= Δπp). The new base pressure Pb' (= Pt + πp' - πt = Pb + Δπp) is now set as 33.2 mmHg (= 17.2 mmHg +16 mmHg). The line P' = Pmic' and P' = Pb' are plotted as the dotted and broken line in **Figure 2B**, respectively. As one sees the filtration arrows in **Figure 2B** are shorter than those depicted in **Figure 2A**, while the absorption arrows in **Figure 2B** are longer than those in **Figure 2A**. The pressure producing the filtration flux Qf', absorption flux Qa', and net flux (= Qf'−Qa') are driven by these pressure differences 6.0, −25.2, and −19.2 mmHg, respectively.

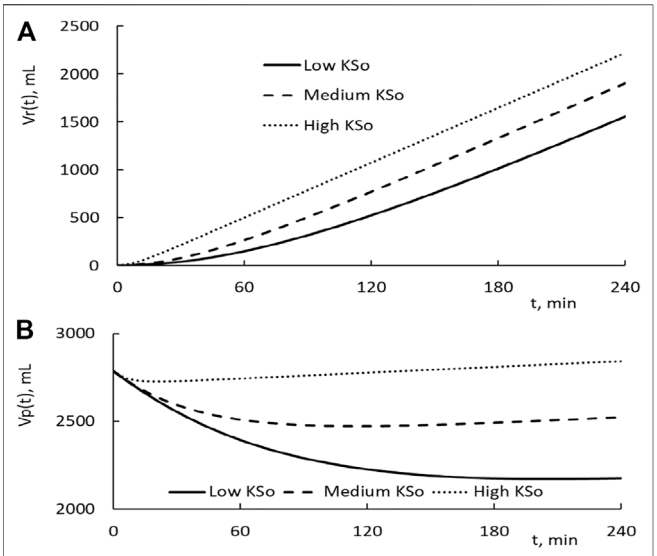

FIGURE 3 | (A) Temporal changes in fluid restitution volume Vr(t) over the course of HD. The patients taking the HD have low, medium, and high filtration coefficient KSo. The plasma volume of the patient is set at 2,785 ml, and the HD is performed with the relative extraction ΔVe/Vp as 77.8%. **(B)** Temporal changes in plasma volume induced by HD.

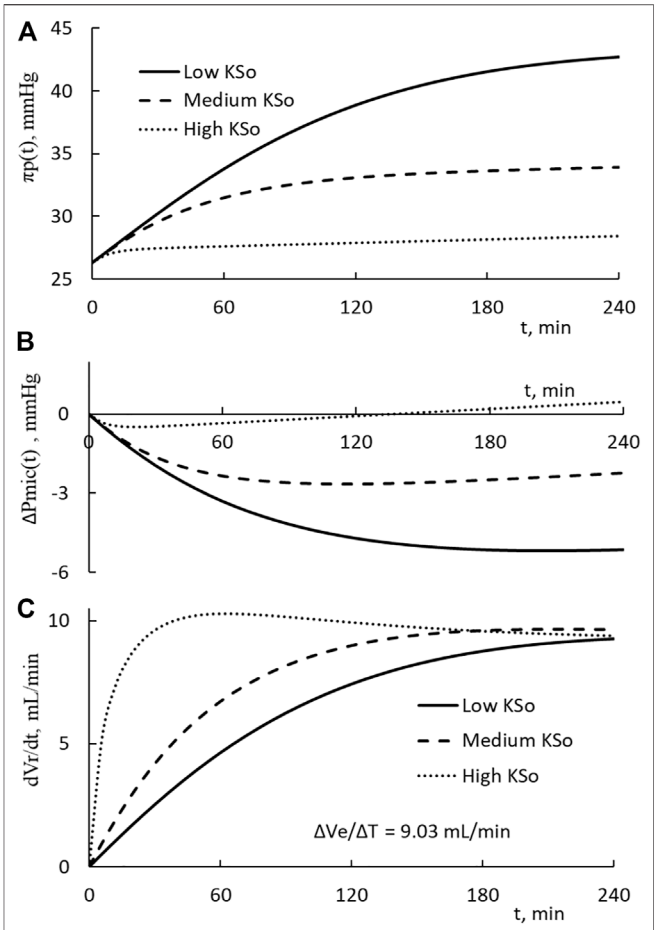

FIGURE 4 | (A) Temporal increases on the plasma COP for patients with low, medium, and high filtration coefficient KSo. The HD is performed with the relative extraction ΔVe/Vp as 77.8%. **(B)** Temporal decreases in microvascular blood pressure. **(C)** Temporal changes of the rate of restitution.

On the arterial side of the microcirculation, the fluid in the vascular side is being filtrated at the rate Qf(t) from the circulation to the tissue. Let the protein concentration of the filtrated fluid be Cr,f. The semi-permeability of the endothelial lining may only allow a fraction of the protein in the plasma to filtrate to the tissue, i.e. Cr,f will be smaller than Cp. On the venous side, the fluid in the tissue is being absorbed to the circulation at a rate of Qa. Let the protein concentration of the interstitial fluid be Ct and that of the absorbed or restituted fluid be Cr,a which is a fraction of Ct. The integration of these fluid and protein fluxes over the HD time yields the following two integrals:

$$\Delta Vr = \int_0^{\Delta T} [Qa(t) - Qf(t)]dt \tag{14}$$

$$\Delta Vr\ Cr = \int_0^{\Delta T} (Qa(t)Cr,a(t) - Qf(t)Cr,f(t))dt = \Delta Vr\,\gamma\,Cp \tag{15}$$

The permeability fraction: γ is the integral in **Eq. 15** divided by ΔVr Cp. Beyond the formula given by Yuan and Rigor (2011) on transvascular protein movement, more information on the quantities within the two integrals in **Eqs 14**, **15** are required for calculating the value of γ.

As an alternative, we used in our previous analysis the following reasoning to deduce 0.09 as the value for γ. First, we set over the pre-HD time, the protein concentration of the filtration to the tissue Cr,f in this form $\gamma^{1/2}$ Cp. As the interstitial fluid space is being flushed by this fluid for a long time, the protein concentration of the interstitial fluid Ct can take Cr,f as its value. Over the course of HD, the endothelia may allow a similar fraction of protein to be restituted back to the circulation. Thus, we take the protein concentration of the restituted fluid as $\gamma^{1/2}$ Ct which is also γCp. On their study of the composition of interstitial fluid, Fogh-Andersen et al. (1995) reported that the PPC of their subjects in supine position is 6.86 g/dl and the protein concentration of interstitial fluid is 2.06 g/dl. These two protein concentrations lead us to set the value of $\gamma^{1/2}$ as 0.3 (≈2.06/6.86). This selection is equivalent to set γ as 0.09. As a sensitivity check, some computations on ΔVp/Vp are made later on with 0.4 as the value of γ.

Dynamics of transvascular fluid and protein movement. The time courses of the restitution volume Vr(t) for the HD with low, medium, and high KSo are depicted as the solid, broken, and dotted line, respectively, in **Figure 3A**. As one can see that the initial rise in restitution volume is much higher for patients with higher KSo. Over the later time, the rate of increase in Vr becomes comparable for the three HDs. Because of their difference over the early stage of HD, more fluid is restituted from the tissue for patients with higher KSo.

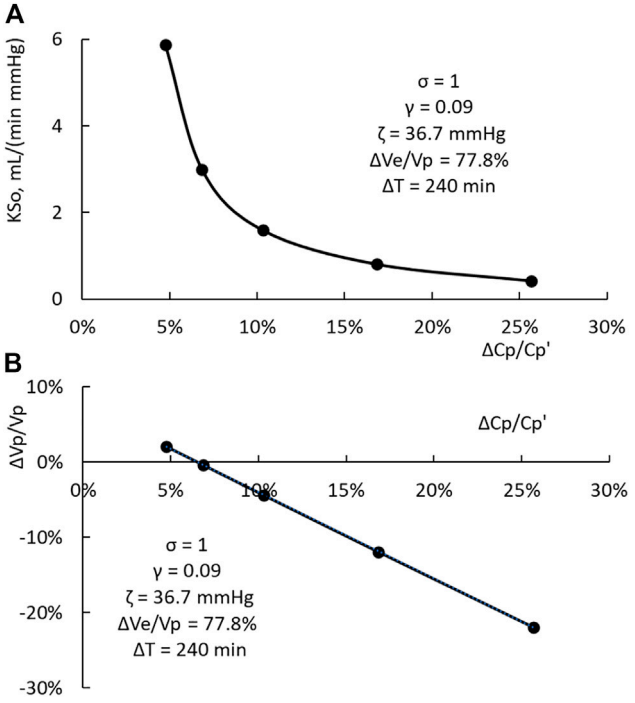

FIGURE 5 | (A) One-to-one relation between KSo and the PPC increment ΔCp/Cp'. **(B)** One-to-one relation between the relative change in plasma volume ΔVp/Vp and the PPC increment.

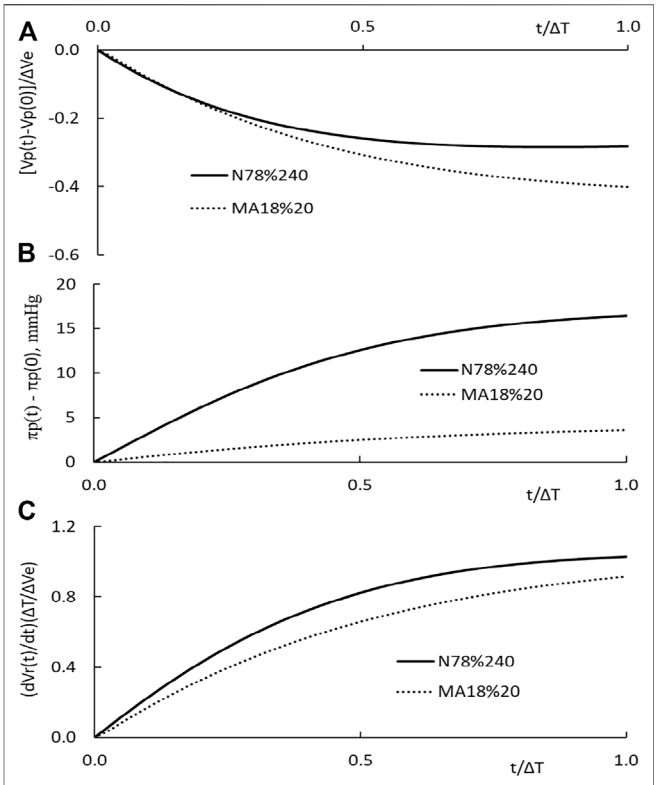

FIGURE 6 | (A) Temporal changes in plasma volume of N78% HD carried out in patients with normal hematocrit (solid line) and that MA18%20 HD carried out in patients with more anemic hematocrit (dotted line). **(B)** Temporal changes in plasma COP πp(t) of the two HDs. **(C)** Temporal changes in the normalized rate of restitution dVr(t)/dt.

The subtraction of the extraction from the restitution is the reduction in plasma volume. Its time courses for the three HDs are depicted in **Figure 3B**. As the HD is initiated, the plasma volume is in a decreasing trend. Around the time of 24, 114, and 210 min, the plasma volume of the high, medium, and low KSo HD turns to an increasing trend, respectively. An increasing trend means that the rate of fluid restitution at that time is higher than the extraction rate. The decrease in Vp at the end of HD is larger for patients with lower KSo.

The changes in plasma COP, microvascular blood pressure, and the rate of fluid restitution are shown in **Figures 4A–C**. The results on COP indicate that the PPC is in a monotonic increasing trend over the course of HD. The end COP is the largest for patients with the lowest KSo. The rate of restitution is shown to rise as the time progresses and then approaches asymptotically to about 9.3 ml/min which is slightly higher than the extraction rate of 9.03 ml/min.

The calculations presented in **Figures 3**, **4** are made with the same initial conditions of Vp, Vb, and Cp, the same modeling constant γ, ζ and the same HD parameters ΔVe and ΔT. The differences among the three HDs shown in **Figures 3**, **4** are the result that the filtration coefficient set for HD is different. However, there is one exception on the rate of restitution near the end of dialysis. At that time, the rates of the three HDs are about the same. **Eq. 9b** is made up of ΔVe/Vp, which describes how the extraction is to increase the PPC, and a term proportional to ΔVr(t)/Vp, which describes how the restitution is to dilute the PPC. Initially the increase in restitution volume is small and the restitution dilution is low. The high initial increment in PPC (ΔCp(t)/Cp'(t)) leads to a rapid increase in πp(t), Vr(t), and restitution dilution. Then, the increase in restitution dilution as indicated by **Eq. 9b** will slow down the rise in PPC. As the rate of restitution rises to the rate extraction, the PPC will increase no more. The plateauing of the restitution rate to the extraction rate, as shown in **Figure 4C**, is a condition projected by **Eqs 5, 9b**.

We can calculate the total driving pressure and the pressure fraction, ΔPmic(t)/[(Δπp(t)-ΔPmic(t)]. At 1 h, the fractions of low, medium, and high KSo HD take these percentages 31, 32, and 23.6%, respectively. The correspondent values at the end of HD are 23.9%, 22.6%, and -28.9%. These percentages indicate that the reduction in microvascular blood pressure contributes about 30% of the driving pressure to restitute the fluid from the tissue.

For these three HDs, the filtration coefficient is the only variable being changed. The computation results indicate that KSo and ΔVp/Vp, as shown in **Figure 5**, have a one-to-one relation with the PPC increment ΔCp/Cp'. The data points in **Figure 5A**, computed from **Eqs 8**, **9b**, can be matched by a straight line with a slope of 1.09 and a correlation coefficient (R^2) of 0.9996. If 0.4 is set as γ, the relation between ΔCp/Cp' and ΔVp/Vp is slightly curvilinear. The slope of the straight line fit is

TABLE 2 | Organ weights, volumes of minute vessels, microvascular hematocrit, and the organ KSn product of a normal dog[a].

	OWn, g	Vmic,n, mL	Vmic,n/OWn mL/g	Vb,n, mL	Hmic,n/Ha	KSn/OWn	KSn
Spleen	72	36.7	0.510	47.5	2.07		
Liver	99	37.1	0.375	76.2	0.31	0.80	1.15
Lungs	252	29.9	0.119	65.2	0.78	4.55	0.15
Kidneys	58	4.7	0.081	25.7	0.21		
Heart	83	5.6	0.067	11.2	0.52		
Bowel	350	14.4	0.041	38.3	0.36		
Muscle	3540	57.1	0.016	130.4	0.45	0.14	0.50
Brain	62	2.0	0.032	6.6	0.21		

[a]*The data in the 2nd to 6th column are derived from* ***Table 1*** *of Gibson et al. (1946). OWn stands for organ weight. The total blood volume Vb of the dog is 1,150 ml, and the dog weighs 11.9 kg. The units of KSn/OWn and KSn are mL/(min mmHg kg) and mL/min/mmHg, respectively.*

1.47 and the R^2 is 0.994. For a HD, ΔCp/Cp' can be measured readily. If the HD is done with a ΔVe and ΔT similar to those used to derive the results shown in **Figure 5**, then the relations depicted in **Figure 5A** can be used to provide the first estimate of KSo and ΔVp/Vp.

The time course of the plasma volume, PPC, and the restitution rate of N78% and MA18%20 HD is depicted in **Figure 6**. The HD with patients of normal hematocrit has ΔVe/Vp as 77.8%, and ΔT as 240 min. The ΔVe/Vp of the MA18%20 HD is 18.4%, and its ΔT as 20 min. The filtration coefficients used in the computations are 0.43 and 5.88 ml/min/mmHg, respectively. Their rate of extraction ΔVe/ΔT is 9.0 and 36.5 ml/min. To put these results for comparison, we normalize the time scale t of the figure by ΔT, the plasma volume change by ΔVe, and the rate of restitution by ΔVe/ΔT. A comparison of these results with those shown in **Figure 3** indicates that a change in ΔVe and ΔT can significantly change the time courses of Vp(t) and dVr(t)/dt.

Multiple circulation system. Gibson et al. (1946) obtain tissue samples cleared of visible blood vessels and used the tagged RBC and plasma protein methodology to measure the blood volume of minute vessels in eight organs and the hematocrit of blood in minute vessels. The organ weight, total microvascular blood volume, and total blood volume of the eight organs are given in **Table 2** The distribution of microcirculation volume Vmic,n and the ratio of the microvascular hematocrit Hmic,n to Ha of the eight organs are listed in the 6th column of **Table 2**. In reference to the weight of the *n*th organ (OWn), Vmic,n/OWn for these eight organs is in the range of 0.016–0.77 ml/g. We also calculate the normalized total blood volume of the *n*th organ (Vb,n)/OWn to highlight that the organ blood volume count is distributed over a wide range of 0.11–0.77 ml/g. The microvascular hematocrit of the spleen is 2.07 times of the arterial hematocrit. The other seven organs have a microvascular hematocrit in the range of 0.22–0.78 times of Ha. The volume weighted microvascular hematocrit for the seven organs (no spleen) is 0.47 Ha.

Measured by the isogravimetric technique, the KSn/OWn of the liver (Bennett and Rothe 1981), lung lobe (Lee et al., 1996), and hindlimb (identified as the muscle, Michel 1984) are listed in the 8th column of **Table 2**. In view of the alveolar structure of the lung and the dense vasculature of the liver, the endothelial surface area of the lungs per unit lung weight (Sn/OWn) may be the largest of the three organs and that of the muscle is the smallest. The value of KSn/Own and KSn are listed in the last two columns of **Table 2**.

The circulatory system is consisted of the vascular trees of various organs. From the perspective of the circulatory system, these trees can be viewed as multiple circulations arranged in parallel. Let the filtration coefficient of the *n*th circulation be KSn and its plasma volume be Vp,n. Then, we set the filtration coefficient KSo and the total plasma volume Vp of the circulatory system at:

$$\mathrm{KSo} = \sum_{n=1}^{m} \mathrm{Ksn} \tag{16a}$$

$$\mathrm{Vp} = \sum_{n=1}^{m} \mathrm{Vp,n} \tag{16b}$$

For the given ΔVe and Cp, we can use the values of KSo and Vp so determined to calculate Cp', ΔCp/Cp', ΔVr, ΔVp, ΔPmic, and Δπp .

Let us define the KS fraction λn of the *n*th circulation as:

$$\lambda n = \mathrm{KSn}/\mathrm{Kso} \tag{17}$$

and assign λn ΔVe as the extraction imposed to the *n*th circulation, λnVp as its plasma volume, and λnVb as its blood volume. λn ΔVr will be set at the fluid volume restituted from the *n*th circulation. The substitution of these parameters into **Eqs 5–10** will reveal that all λn values are canceled out, and the five equations remain in the same forms. Remaining in the same form means that the values of Cp', ΔCp/Cp', ΔPmic, and Δπp calculated for the *n*th circulation will be identical to those derived for the multiple circulation system. This identity justifies the use of **Eq. 16a** to derive the KSo of the entire circulatory system. The limited data on KSn shown in **Table 2** suggest that a significant fraction of the fluid restituted from the tissue through HD would be derived from the liver.

The plasma volume Vp,n set for the *n*th organ with the λ_n in **Eq. 17** may not be the true plasma volume of that organ. Thus, the PPC of the plasma coming out from the *n*th organ will be different from the one calculated for the multiple system. As the plasma is being mixed in the heart chambers, the mixed final PPC becomes the one predicted by the FCA for the multiple system.

The FCA of PPC increment induced by the HD of more anemic patients indicates that the value of KSo/BW is 0.11 ml/(min mmHg kg). If we apply this value to a dog of 11.9 Kg, then its KSo will be 1.33 ml/(min mmHg), which is smaller

than the sum of the three values given in the last column of **Table. 2**.

Microvessel hematocrit, whole body hematocrit, and Fcell ratio. In FCA, the circulation (not including the splenic microcirculation) is divided into a microcirculation and a macrocirculation compartment. Their blood volumes are designated as Vmic and Vmac. The hematocrit of the blood in these two compartments are Hmic and Ha. We use the fractional numbers α and β to describe the following relations:

$$\mathrm{Hmic} = \alpha\,\mathrm{Ha} \quad \mathrm{Vmic} = \beta\,\mathrm{Vb} \quad \mathrm{Vmac} = (1-\beta)\mathrm{Vb} \tag{18}$$

The whole blood hematocrit Hw, the total RBC volume of the two compartments divided by the blood volume, and the Fcell ratio (=Hw/Ha) of the two compartment circulation can be calculated as:

$$\mathrm{Hw} = (\mathrm{Ha}\,\mathrm{Vmac} + \mathrm{Hmic}\,\mathrm{Vmic})/\mathrm{Vb} = (1-\beta)\mathrm{Ha} + \alpha\beta\,\mathrm{Ha} \tag{19a}$$

$$\mathrm{Fcell} \equiv \mathrm{Hw}/\mathrm{Ha} = 1 - \beta + \alpha\beta \tag{19b}$$

Eq. 19a indicates that Hw is a volume weighted average hematocrit of the two compartments. We can form a full circulation by adding the pulmonary circulation and the four heart chambers to the central circulation shown in **Table 1**. The sum of the microvessel blood volumes in this full circulation yields a value of β close to 0.326. The volume weighted hematocrit of the full circulation yields a value of α close to 0.54. The selection of 0.326 and 0.54 will make the Fcell defined in **Eq. 19b** to take 0.85 as its value. If we set the volume of splenic microcirculation that contains high hematocrit blood as 4.2% of Vb and its hematocrit as 2.07 Ha, the Fcell for the micro- and macrocirculation and the splenic microcirculation will be increased to 0.90.

For comparison, Dasselaar et al. (2007) reported that the Fcell ratio measured for their HD patients is 0.896 ± 0.036. In their article, Chien and Gregersen (1962) point out that Fcell of subjects is 0.9 and that of subjects with no spleen is 0.85.

The initial value of β is 0.326. As the time progresses, the microvascular blood volume and the blood volume will be decreased by the HD. As calculated for N78% HD, the value of β derived from the FCA is reduced to 0.273 and the Fcell ratio is increased to 0.874. For calculations, we assume that the fractional constant α is not altered by the change in microvascular blood volume.

Factors changing the arterial hematocrit. A change in plasma volume ΔVp, a change in microvascular blood volume ΔVmic, and a shift of the concentrated RBC from the spleen ΔVrbc to the circulation lead to the following change in the arterial hematocrit of blood circulating through the macrocirculation:

$$\Delta\mathrm{Ha}/\mathrm{Ha}' = [-\Delta\mathrm{Vp}/\mathrm{Vb} + (1-\alpha)\Delta\mathrm{Vmic}/\mathrm{Vb} + (\Delta\mathrm{Vrbc}/\mathrm{Vb})/\mathrm{Ha}']/\mathrm{Fcell} \tag{20}$$

This equation is derived from the conservation of RBC in the macrocirculation compartment and is termed as the hematocrit equation.

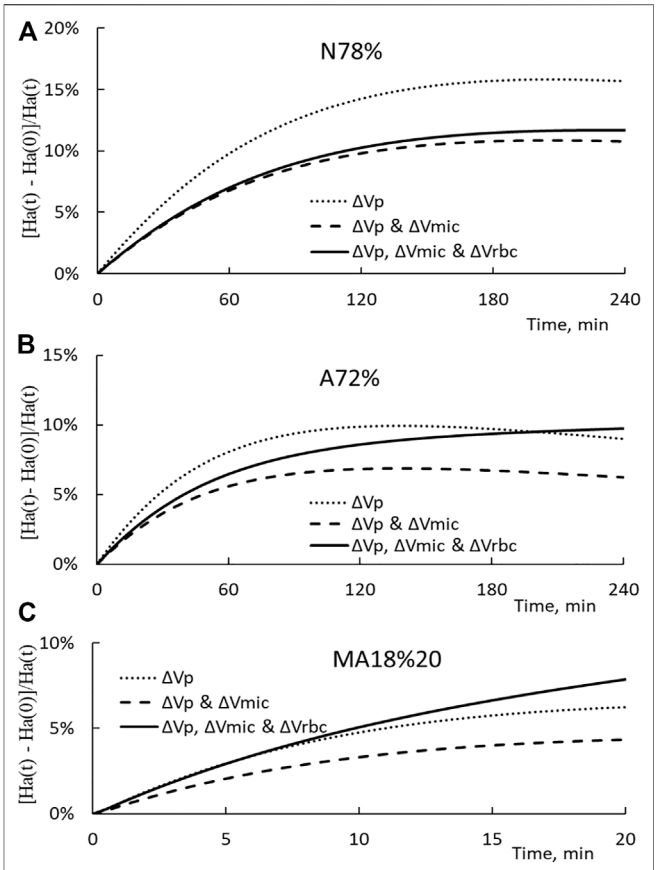

FIGURE 7 | (A) Temporal changes in the arterial hematocrit increment Ha(t)-Ha (0)/Ha(t) for the N78% HD. The dotted, broken, and solid lines show the increment induced only by ΔVp, ΔVp, and ΔVmic, and all three ΔVp, ΔVmic, and ΔVrbc, respectively. **(B)** Temporal changes in the arterial hematocrit increment for A72% HD. **(C)** Temporal changes in the arterial hematocrit increment for MA18%20 HD.

The results of CHRE indicate that the reduction in microcirculation blood volume due to hemorrhage is linearly related to the reduction in blood volume by the following equation:

$$\Delta\mathrm{Vmic} = \eta\Delta\mathrm{Vb} \tag{21}$$

The constant η takes 0.65 as its value (LaForte et al., 1994). In view of the large volume distributions in the small veins (**Table 1**), most of the ΔVmic could be originated from the volume reduction of small veins (the 10th generation).

In our previous analysis on the data of A72% and Ma18%20, if ΔVrbc is set as zero, the FCA projects that the microcirculation would be dilated by 3.3%Vb and 2.5%Vb, respectively. The arterioles are the only microvessel generation that could be induced by HD to dilate. As shown in **Table 1**, the arterioles contain only 1.2% of the blood volume. The large dilatation percentages estimated for ΔVmic/Vb indicate that the spleen is activated by the HD to release the concentrated RBC at these volumes (ΔVrbc*): 0.03%Vb (N78%), 1.09%Vb (A78%), and 0.91%Vb (MA18%). These percentages are derived with η set

as 0.65. If we decrease η to 0.4 (i.e., the microcirculation is more rigid), the FCA projects that the spleen of patients of normal hematocrit is induced by N78% HD to retain 0.74% Vb of the concentrated RBC from the general circulation. The reduction in total radioactivity of the tagged RBC in the spleen found by Yu et al. suggests that the spleen is not likely to be activated by the HD to retain RBC from the central circulation.

To illustrate how splenic RBC release and microvascular volume reduction change arterial hematocrit over the course of HD, we set ΔVp/Vp as the one derived from **Eq. 7**, ΔVmic as the one derived from **Eq. 21** with η set at 0.65, and ΔVrbc(t) computed from the following linear function of t:

$$\Delta Vrbc(t) = \Delta Vrbc^{*} \cdot \frac{t}{\Delta T} \tag{22}$$

The arterial hematocrit Ha(t) is calculated first with ΔVp only (the dotted line), then ΔVp and ΔVmic (the broken line), and finally with ΔVp, ΔVmic, and ΔVrbc (the solid line). The hematocrit changes for N78%, A72%, and MA18%20 HD are presented in **Figures 7A–C** respectively. It is noted that the end point of the solid line corresponds to the hematocrit Ha' measured in the experiments. The results shown in the figure indicate that the reduction in the microvascular blood volume will reduce the hematocrit from that induced by the plasma volume change. In the opposite direction and as expected, splenic RBC releases will lead to an increase in the arterial hematocrit.

If HD does not induce the spleen to release its highly concentrated blood to the circulation (i.e. ΔVrbc = 0) and the microcirculation is rigid so that ΔVmic = 0, then **Eq. 20** is simplified to the following form:

$$\Delta Ha/Ha' = -\Delta Vb/Vb/Fcell \tag{23}$$

If we set Fcell at unity and replace ΔVp by ΔVb (**Eq. 8**), then **Eq. 23** is further simplified to VBHE, which is widely used to determine the relative change in the blood volume (RCBV and ΔVb/Vb) induced by HD. For the N78%, A72%, and MA18%20 HD, the VBHE projects that the patients would have RCBV as -11.7%, -10.2%, and -7.9%, respectively. The correspondent changes derived from the previous FCA are -14.5%, -8.3%, and -5.6%.

The RCBV measured by a tagging technology is assessed as −17.3% and that calculated by VBHE is −8.2% (Dasselaar et al., 2007). They conclude that the VBHE underestimates RCBV for patients with normal hematocrit and overestimates for patients with anemic hematocrit. The hematocrit of their patients is about 40% which is slightly below the normal hematocrit (42.4%) referred in thisarticle. Their conclusion is compatible to our finding that the RCBV derived from the VBHE for patients with normal hematocrit is smaller than the RCBV derived from the FCA.

Reduction in macrovascular blood volume. Since the sum of macro- and microvascular blood volume is the total blood volume, we have the change in macrovascular blood volume as:

$$\Delta Vmac = \Delta Vb - \Delta Vmic \tag{24}$$

In view of the large volume fractions of the venous macrocirculation (**Table 1**), most of the ΔVmac could be originated from the venous macrocirculation. For N78%, A72%, and MA18% HD, the FCA projects the macrovascular volume reduction values (ΔVmac/Vb) are −4.9%, −2.9%, and −2.0, respectively.

The venous macrocirculation has been regarded as a volume reservoir that can be used to improve venous return and cardiac filling. Because the right atrium resides downstream of the venous macrocirculation, it is likely that the macrovascular blood volume reduction derived from the FCA can be used as an index in characterizing whether the cardiac filling is being reduced by the HD.

Comparisons with other experimentations and analyses. LaForte et al. (1994) carried out their hemorrhage (5, 10, and 15% of the blood volume) in 2 min and then reinfusion in the next 2 minutes. Over this short period, the volume of the fluid restituted from the tissue will be much smaller than that of HD performed over 4 h. Similar changes in the hematocrit are also found for rabbits with their spleen removed (LaForte et al., 1992). Thus, the hematocrit decreases over the 2-min hemorrhage is generated mostly by a reduction in the microvascular volume. For 10% hemorrhage experiments, they found that the PPC is reduced by 0.027 ± 0.008 g/dl and the hematocrit by 1.20 ± 0.04%. The correspondent PPC increment ΔCp/Cp' is 0.5%, and the hematocrit increment ΔHa/Ha' is 3.6%. The analysis of the protein and hematocrit data yields these estimations:

(i) The splenic RBC release is minimally induced by CHRE, and the rabbit's microcirculation functions like a passive elastic system.
(ii) The hemorrhage volume of 7% is derived from the fluid being restituted from the tissue over 2 min, 60% from the reduction in microvascular blood volume (= ΔVmic), and 33% from the reduction in macrocirculation blood volume (= ΔVmac),
(iii) The filtration coefficient of rabbit as projected by FCA is 0.21 ml/(min mmHg kg). The correspondent estimate derived from FCA of three HDs has the filtration coefficient in the range of 0.008–0.085 ml/(min mmHg kg).
(iv) If the VBHE is used to compute ΔVb and **Eq. 7** to calculate ΔVr, then the calculation by **Eq. 5** will yield 1.08 ml/(min mmHg kg) as the filtration coefficient of the rabbit, which is almost 5 times larger than the one estimated by the FCA.

For the HDs analyzed here, the dialysis is done over a long period of time, the fluid volume restituted from the tissue can be significantly larger than that generated from the CHRE of rabbits. As a result, the PPC and hematocrit increments found for the three HDs analyzed here have comparable values. The difference between these two increments indicates that the HD does induce significant change in microvascular blood volume and cause the spleen to release RBC to the circulation.

On the MA18%20 HD, Schneditz et al. (1992) used a protein analysis to derive the RCBV. Then the matching of the RCBV with that derived from the hematocrit data leads to a projection that the filtration coefficient of the more anemic patients is 5.6 ml/(min mmHg 50 Kg). This is equivalent to set the value

of KSo as 7.74 ml/min/mmHg (= 69.1 Kg (BW) X 5.6 ml/(min mmHg 50 Kg)). In our FCA, we match the projected Cp' with the measured one and deduced KSo as 5.9 ml/min/mmHg. The difference in data matching (hematocrit vs PPC) may be the reason that the estimate of Schneditz et al. (1992) on KSo is different from our estimate.

3 CONCLUDING REMARKS

In this article, we use the FCA to determine from the protein data of the three HD studies, namely, the restitution volume, the change in plasma volume, and the filtration coefficient of patients with normal, anemic, and more anemic hematocrit. To further verify FCA and the modeling of the circulation, we recommend that the following experiments be performed:

(i) The making of hourly PPC measurements over the course of HD. The measurements will verify whether the FCA projected the temporal changes in PPC correctly.
(ii) A total of two HDs with two different relative extractions (i.e., at two $\Delta Ve/Vp$) deriving the filtration coefficients from the protein data of these two HDs should have the same value. In cases that they do not, a different guess on the filtration coefficient and permeability fraction may lead FCA to generate results that can match the two measured PPC increments.
(iii) The performance of the tagged protein and RBC experiments of Dasselaar et al. (2007) and the use of their procedure projected the reduction in plasma volume. With the PPC also measured in these experiments, then we can examine whether the reduction in plasma volume projected by FCA matches that by the tagging technology.
(iv) The performance of the CHRE for the determination of η so that **Eq. 20** can be used to determine the splenic RBC release.
(v) Yu et al. (1997) found that the splanchnic radioactivity decreases to 90% of the baseline value after 2 h of the accelerated fluid removal during dialysis. The volume reduction of the splanchnic macrocirculation can cause a decrease in radioactivity. If this radioactive technology can be shown to measure the splenic RBC release, then we have an independent way to verify the splenic RBC release projected by FCA.

The analysis of HD data with patients grouped according to their hematocrits leads to the recognition that patients having higher hematocrits are to have a smaller filtration coefficient and the suggestion that the filtration coefficient is a facilitator to generate more fluid restitution. As a result, we have a better compensation to the fluid extraction by the dialyzer and a lesser reduction in plasma volume for patients with lower hematocrit. It will be of interest to group patients according to their frequency of having intradialytic hypotension and/or their blood pressure variability (Flythe and Brunelli 2014) so that we can better understand what other factors can also be a limiting factor on having more fluid restitution. Through these experiments and data comparison, a better understanding of the factors inducing hypovolemia for patients taking HD can be the basis for one to modify the HD process such that the development of hypovolemia can be avoided over the course of HD.

DATA AVAILABILITY STATEMENT

The raw data supporting the conclusion of this article will be made available by the authors, without undue reservation.

AUTHOR CONTRIBUTIONS

These authors J-SL and L-PL have contributed equally to this work and share first authorship.

FUNDING

The funding for this research was provided by Global Monitors, Inc.

REFERENCES

Bennett, T. D., and Rothe, C. F. (1981). Hepatic Capacitance Responses to Changes in Flow and Hepatic Venous Pressure in Dogs. *Am. J. Physiol.* 240, HI8–H28. doi:10.1152/ajpheart.1981.240.1.H18

Booth, J., Pinney, J., and Davenport, A. (2011). Do Changes in Relative Blood Volume Monitoring Correlate to Hemodialysis-Associated Hypotension. *Nephron Clin. Pract.* 117, c179–c183. doi:10.1159/000320196

Cavalcanti, S., Cavani, S., Ciandrini, A., and Avanzolini, G. (2006). Mathematical Modeling of Arterial Pressure Response to Hemodialysis-Induced Hypovolemia. *Comput. Biol. Med.* 36, 128–144. doi:10.1016/j.compbiomed.2004.08.004

Chien, S., and Gregersen, M. I. (1962). "Determination of Body Fluid Volumes," in *Physical Techniques in Biological Research*. Editor W. L. Nastuk (Cambridge, Massachusetts, United States: Academic Press), 1–105. Chapter 1. doi:10.1016/b978-1-4831-6742-8.50008-2

Dasselaar, J. J., Lub-de Hooge, M. N., Pruim, J., Nijnuis, H., Wiersum, A., de Jong, P. E., et al. (2007). Relative Blood Volume Changes Underestimate Total Blood Volume Changes during Hemodialysis. *Cjasn* 2, 669–674. doi:10.2215/CJN.00880207

Flythe, J. E., and Brunelli, S. M. (2014). Blood Pressure Variability and Dialysis: Variability May Not Always Be the Spice of Life. *J. Am. Soc. Nephrol.* 25, 650–653. doi:10.1681/ASN.2013111237

Fogh-Andersen, N., Altura, B. M., Altura, B. T., and Siggaard-Andersen, O. (1995). Composition of Interstitial Fluid. *Clin. Chem.* 41, 1522–1525. doi:10.1093/clinchem/41.10.1522

Fung, Y. C. (1966). Theoretical Considerations of the Elasticity of Red Cells and Small Blood Vessels. *Fed. Proc.* 25, 1761–1772.

Gibson, J. G., II, Seligman, A. M., Peacock, W. C., Aub, J. C., Fine, J., and Evans, R. D. (1946). The Distribution of Red Cells and Plasma in Large and Minute Vessels of the Normal Dog, Determined by Radioactive Isotopes of Iron and Iodine 1. *J. Clin. Invest.* 25, 848–857. doi:10.1172/jci101772

LaForte, A. J., Lee, L. P., Rich, G. F., Skalak, T. C., and Lee, J. S. (1994). Blood Volume Redistribution from a Passive Elastic Permeable Microcirculation Due to Hypovolemia. *Am. J. Physiology-Heart Circulatory Physiol.* 266, H2268–H2278. doi:10.1152/ajpheart.1994.266.6.h2268

LaForte, A. J., Lee, L. P., Rich, G. F., Skalak, T. C., and Lee, J. S. (1992). Fluid Restitution and Shift of Blood Volume in Anesthetized Rabbits Subject to Cyclic Hemorrhage. *Am. J. Physiology-Heart Circulatory Physiol.* 262, H190–H199. doi:10.1152/ajpheart.1992.262.1.h190

Landis, E. M., and Pappenheimer, J. R. (1963). "Exchange of Substances through the Capillary walls," in *Handbook of Physiology, Section 2, Circulation (Vol II)*. Editors W. F. Hamilton, P. Dow, and D. C. Washington (Rockville, Md: APS), 961–034.

Lee, J. S., Lee, L. P., and Rothe, C. F. (1996). Assessing Microvascular Volume Change and Filtration from Venous Hematocrit Variation of Canine Liver and Lung. *Ann. Biomed. Eng.* 24, 25–36. doi:10.1007/BF02770992

Lipowsky, H. H., Usami, S., and Chien, S. (1980). *In Vivo* measurements of "apparent Viscosity" and Microvessel Hematocrit in the Mesentery of the Cat. *Microvasc. Res.* 19, 297–319. doi:10.1016/0026-2862(80)90050-3

Michel, C. C. (1984). "Fluid Movement through Capillary walls," in *Handbook of Physiology, Cardiovascular System, Microcirculation*. Editors A. R. Pries and P. W. Secomb (Rockville, Md: APS), 375–409. Chap. 9.

Minutolo, R., Nicola, L. D., Bellizzi, V., Iodice, C., Rubino, R., Aucella, F., et al. (2003). Intra- and post-dialytic Changes of Haemoglobin Concentrations in Non-anaemic Haemodialysis Patients. *Nephrol. Dial. Transplant.* 18, 2606–2612. doi:10.1093/ndt/gfg387

Rothe, C. F. (2011). "Venous System: Physiology of the Capacitance Vessels," in *Handbook of Physiology - Cardiovascular System*. Editors D. F. Bohr, A. P. Somlyo, and H. V. SparksJr. (Oxford, United Kingdom: Oxford University Press), 397–452. Chapter 13. doi:10.1002/cphy.cp020313

Schneditz, D., Roob, J., Oswald, M., Pogglitsch, H., Moser, M., Kenner, T., et al. (1992). Nature and Rate of Vascular Refilling during Hemodialysis and Ultrafiltration. *Kidney Int.* 42, 1425–1433. doi:10.1038/ki.1992.437

Van Beaumont, W. (1972). Evaluation of Hemoconcentration from Hematocrit Measurements. *J. Appl. Physiol.* 32, 712–713. doi:10.1152/jappl.1972.32.5.712

Yu, A. W., Nawab, Z. M., Barnes, W. E., Lai, K. N., Ing, T. S., and Daugirdas, J. T. (1997). Splanchnic Erythrocyte Content Decreases during Hemodialysis: A New Compensatory Mechanism for Hypovolemia. *Kidney Int.* 51, 1986–1990. doi:10.1038/ki.1997.270

Yuan, S. Y., and Rigor, R. R. (2011). "Regulation of Endothelial Barrier Function," in *Colloquium Series on Integrated Systems Physiology: From Molecule to Function*. Editors D. N. Granger and J. P. Granger (San Rafael CA: Morgan & Claypool Life Sciences), 1–146. Chapter 1. doi:10.4199/c00025ed1v01y201101isp013

Conflict of Interest: The authors JS. Lee and LP. Lee are the owners of Global Monitors Inc. and are employed by Global Monitor Inc. Funding for this research was provided by Global Monitors, Inc.

Publisher's Note: All claims expressed in this article are solely those of the authors and do not necessarily represent those of their affiliated organizations, or those of the publisher, the editors and the reviewers. Any product that may be evaluated in this article, or claim that may be made by its manufacturer, is not guaranteed or endorsed by the publisher.

4 APPENDIX: EQUATIONS AND COMPUTATION PROCEDURE

The entire HD period is divided into M segments. For each segment [i·dt to (i + 1)dt], the volume of fluid extracted by the dialyzer is dVe (= ΔVe/M). The initial value Cp(0), Vp(0), and Vb(0) are correspondent to the one set for Cp, Vp, and Vb in **Eqs 3–5**. In addition, we also have Vr (0) as zero. To start the calculations, we will set a value as KSo. Then, we guess the PPC increment for the *i*th segment as dCp. The values of various variables are computed by the following equations:

$$\mathrm{Cp}(\mathrm{i}+1) = \mathrm{Cp}(\mathrm{i}) + \mathrm{dCp} \tag{A1}$$

$$\mathrm{Vr}(\mathrm{i}+1) = \mathrm{Vr}(\mathrm{i}) + \left[\mathrm{dVe} - \mathrm{dCp}\,\mathrm{Vp}(0)/\mathrm{Cp}(\mathrm{i}+1)\right]/\left(1 - \gamma\mathrm{Cp}(0)/\mathrm{Cp}(\mathrm{i}+1)\right) \tag{A2}$$

$$\mathrm{Vp}(\mathrm{i}+1) = \mathrm{Vp}(\mathrm{i}) + \mathrm{Vr}(\mathrm{i}+1) - \mathrm{Vr}(\mathrm{i}) - \mathrm{dVe} \tag{A3}$$

$$\mathrm{Vb}(\mathrm{i}+1) = \mathrm{Vb}(\mathrm{i}) + \mathrm{Vp}(\mathrm{i}+1) - \mathrm{Vp}(\mathrm{i}) \tag{A4}$$

$$\mathrm{Pmic}(\mathrm{i}+1) = \mathrm{Pmic}(0) + \zeta[\mathrm{Vb}(\mathrm{i}+1) - \mathrm{Vb}(0)]/\mathrm{Vb}(0) \tag{A5}$$

$$\pi\mathrm{p}(\mathrm{i}+1) = 2.1\mathrm{Cp}(\mathrm{i}+1) + 0.16\mathrm{Cp}(\mathrm{i}+1)^2 + 0.009\mathrm{Cp}(\mathrm{i}+1)^3 \tag{A6}$$

$$\mathrm{KS1} = 2[\mathrm{Vr}(\mathrm{i}+1) - \mathrm{Vr}(\mathrm{i})]/\mathrm{dt}/\{\sigma[\pi\mathrm{p}(\mathrm{i}+1) + \pi\mathrm{p}(\mathrm{i}) - 2\pi\mathrm{p}(0)] - \mathrm{Pmic}(\mathrm{i}+1) - \mathrm{Pmic}(\mathrm{i}) + 2\mathrm{Pmic}(0)\} \tag{A7}$$

The value of dCp is changed until the value of KS1 takes the value of KSo. Then, similar computations are performed for the next segment. The value of Cp(M), Vr(M), and Vp(M)-Vp(0) is taken as Cp', ΔVr, and ΔVp, respectively. The value of k in **Eq. 4** is computed as

$$(\sigma\Delta\pi\mathrm{p} - \Delta\mathrm{Pmic})k = \left[\int_0^{\Delta T}\{\sigma\pi\mathrm{p}(\mathrm{t}) - \sigma\pi\mathrm{p}(0) - \mathrm{Pmic}(\mathrm{t}) + \mathrm{Pmic}(0)\}\mathrm{dt}\right] \tag{A8}$$

Experimentally, the value of Cp' is reported. Then, we can use **Figure 5** to set a likely value for KSo. Iterations will be performed until the resulting Cp' takes the experimentally measured value. The final value found for KSi is taken as KSo of that patient.

GLOSSARY

(t) Quantity without ' is that at beginning time 0 and with ' that at the end time ΔT. For temporal calculations, (t) is added to the quantity.

BW Body weight in kg.

CHRE Cyclic hemorrhage and reinfusion experiment.

COP Colloidal osmotic pressure.

Cr The protein concentration in fluid restituted from the tissue to the circulation, **Eqs 9, 10**.

FCA Full circulation analysis. The full circulation is represented by a macrocirculation, a microcirculation, and a splenic microcirculation.

Fcell The ratio of the whole body hematocrit to the arterial hematocrit, **Eq. 19b**.

HD Hemodialysis.

Hw Whole body hematocrit, **Eq.19a**.

k Constant in **Eq. 5** and **Eq. A8**.

KSo Filtration coefficient with So representing the surface available for filtration

Pa Arterial blood pressure.

Pb Base pressure which is πp−πt−Pt. See **Eq. 11**.

Pmic Microvascular blood pressure. See **Eqs. 2, 11, 12**.

PPC Plasma protein concentration.

Pv Venous blood pressure.

RBC Red blood cell.

RCBV Relative change in blood volume.

Rn Flow resistance of the *n*th generation

S-axis Summation of the surface areas upstream of the point in the vasculature divided by So.

Vb Blood volume which is the sum of Vmac and Vmic.

VBHE van Beaumont hematocrit equation, **Eq. 23** with Fcell set at 1.

Vmac Macrocirculation volume = (1-β) Vb.

Vmic Microcirculation volume = β Vb.

Vp Plasma volume = (1-Hw) Vb.

Vr Restitution volume.

α = Hmic/Ha.

β = Vmic/Vb. The value of β can change over the course of HD.

γ Permeability fraction, **Eq. 10**. γCp is taken as the protein concentration Cr in the fluid being restituted from the tissue to the circulation.

ΔPmic Change in microvascular blood pressure = Pmic'-Pmic. **Eqs 5**, **6**.

ΔT HD time.

ΔVe Extraction volume or volume of ultrafiltrate being extracted by the dialyzer.

ΔVp Change in plasma volume = Vp'-Vp.

ΔVr Restitution volume or the total volume of the fluid restituted from the tissue.

Δπp Change in plasma COP = πp'-πp. **Eq. 5**.

ζ Autonomous constant which defines how the autonomous control changes the relation between ΔPmic and ΔVb. **Eq. 6**

η Fraction constant relating the change in microvascular blood volume to the change in total blood volume, See **Eq. 21**.

λ_n = KSn/KSo, where KSn is the filtration coefficient of the *n*th organ and KSo is that of the microcirculation. **Eq. 17**.

πp Plasma COP.

πt Tissue COP.

σ Reflection coefficient, **Eq. 2**.

Advantages of publishing in Frontiers

OPEN ACCESS
Articles are free to read for greatest visibility and readership

FAST PUBLICATION
Around 90 days from submission to decision

HIGH QUALITY PEER-REVIEW
Rigorous, collaborative, and constructive peer-review

TRANSPARENT PEER-REVIEW
Editors and reviewers acknowledged by name on published articles

Frontiers
Avenue du Tribunal-Fédéral 34
1005 Lausanne | Switzerland

Visit us: www.frontiersin.org
Contact us: frontiersin.org/about/contact

REPRODUCIBILITY OF RESEARCH
Support open data and methods to enhance research reproducibility

DIGITAL PUBLISHING
Articles designed for optimal readership across devices

FOLLOW US
@frontiersin

IMPACT METRICS
Advanced article metrics track visibility across digital media

EXTENSIVE PROMOTION
Marketing and promotion of impactful research

LOOP RESEARCH NETWORK
Our network increases your article's readership